Universidad de Valladolid

FACULTAD DE CIENCIAS

**DEPARTAMENTO QUÍMICA FÍSICA
Y QUÍMICA INORGÁNICA**

TESIS DOCTORAL:

GAS PHASE STUDIES OF MOLECULES OF BIOLOGICAL AND ASTROPHYSICAL INTEREST

Presentada por María Celina Bermúdez Arias
para optar al grado de
Doctor por la Universidad de Valladolid

Dirigida por:
José Luis Alonso Hernández

INDEX - ÍNDICE

CHAPTER I. SUMMARY / RESUMEN

La presente Tesis Doctoral se ubica dentro del proyecto de investigación CTQ2010-19008 (Estructuras e Interacciones en Biomoléculas) otorgado por el Ministerio de Ciencia e Innovación al Grupo de Espectroscopia Molecular (GEM) de la Universidad de Valladolid. Durante el periodo 2011-2015 se han realizado estudios sobre el comportamiento conformacional y tautomérico de biomoléculas así como la relación entre su estructura y su funcionalidad.

En esta investigación se han considerado los constituyentes elementales de las biomoléculas (denominados *building blocks*: aminoácidos, monosacáridos, o bases nitrogenadas) caracterizándolos en detalle para así poder predecir su comportamiento como un todo. El reconocimiento celular,[1-2] el plegamiento y desdoblamiento de proteínas,[3] el dulzor de los azúcares,[4-5] así como las combinaciones de las bases nitrogenadas para formar ácidos nucleicos,[6] son ejemplos de procesos que dependen de la estructura de estas biomoléculas. Por todo ello, un estudio detallado de su estructura en términos de conformaciones, tautomería y de las fuerzas intramoleculares que las estabilizan es necesario para lograr entender la funcionalidad de éstos sistemas biológicos.

Las biomoléculas, en general, no presentan una única estructura tridimensional, sino que se caracterizan por su elevada flexibilidad. La rotación en torno a sus enlaces sencillos genera diferentes estructuras tridimensionales denominadas

conformaciones o confórmeros. Además de distintos confórmeros, algunos *building blocks* presentan tautomería: dos especies, denominadas tautómeros, están en equilibrio tautomérico cuando la trasposición de un hidrógeno de una parte a otra de la molécula da lugar a la otra especie. Las bases nitrogenadas son un claro ejemplo de tautomería (véase apartado I.2).[7-10] La estabilidad relativa tanto de las formas tautoméricas como de las conformaciones, viene determinada por las fuerzas intramoleculares que las estabilizan, de entre las que destacan por su importancia los enlaces de hidrógeno.[11-19]

El mayor inconveniente de los estudios conformacionales y tautoméricos radica en el medio en el que se encuentran naturalmente las biomoléculas, los medios condensados. En este entorno, la estabilidad de sus conformaciones así como de sus tautómeros viene determinada no sólo por las interacciones intramoleculares ya mencionadas, sino también por las intermoleculares; ya que al poderse formar diferentes enlaces no covalentes entre las biomoléculas y el medio, la distribución conformacional de las sustancias se puede ver afectada. Estas interacciones intermoleculares pueden llegar incluso a alterar la forma de las biomoléculas; un ejemplo de ello son los aminoácidos que pasan de presentarse en su forma neutra cuando están aislados, a la forma zwiteriónica en los medios condensados[20-21] (grupo amino cargado positivamente y carboxilo negativamente, debido a la transposición de un

protón). Por tanto, para poder estudiar la distribución conformacional y el equilibrio tautomérico intrínseco a las biomoléculas, es preciso hacerlo en condiciones de aislamiento, donde las interacciones con el medio sean nulas y, por consiguiente, únicamente se pongan de manifiesto las interacciones intramoleculares propias del sistema. Esta condición se cumple, por ejemplo, en fase gaseosa.

Tal y como se explicará en el Capítulo III, la sinergia entre las técnicas que combinan ablación láser (LA) con espectroscopia de microondas con transformada de Fourier (FTMW) y los cálculos *ab initio* de alto nivel, han resultado ser idóneas para la identificación de las especies más abundantes de estas biomoléculas en fase gaseosa.[22] Gracias a la capacidad para volatilizar sustancias de alto punto de fusión mediante ablación láser y el gran poder de resolución (sub-doppler) y sensibilidad asociados a FTMW, se ha podido abordar por primera vez los estudios de biomoléculas aisladas: azúcares,[23-28] aminoácidos proteicos,[29-42] bases nitrogenadas,[7-10] o neurotransmisores[43-44]. La información conformacional y aportada en estos estudios es de gran utilidad, no sólo para lograr entender la funcionalidad de estas moléculas, sino que, además, los datos espectroscópicos de cada una de las especies identificadas posibilitan una futura detección de estas biomoléculas en el espacio interestelar.

Haciendo uso de estas técnicas, durante el periodo de tesis, se ha abordado el estudio de diversos aspectos relacionados con las biomoléculas como: el dulzor de los azúcares (Capítulo IV-V), la estructura del azúcar constituyente del ADN (desoxirribosa, Capítulo VI), las características conformacionales del primer aminoazúcar (Capítulo VII), el tautomerismo en aminoácidos (Capítulo VIII), la microsolvatación de bases nitrogenadas (Capítulo IX) y el panorama conformacional de los neurotransmisores (Capítulo X). Se ha de hacer una especial mención a los azúcares recogidos en esta memoria (Capítulos IV-VIII), debido a que esta línea de investigación se ha iniciado recientemente en el laboratorio y la cual está dando excelentes resultados.

Además de los trabajos realizados sobre el comportamiento conformacional y tautomérico de las biomoléculas, se ha abordado la problemática de la identificación de moléculas en el medio interestelar (ISM). Dicha identificación precisa de parámetros espectroscópicos obtenidos en el laboratorio. De este modo, más de 180 moléculas han sido detectadas.[45] Sin embargo aún faltan por ser identificadas numerosas especies.[46] Con ese fin, en el laboratorio se ha actualizado los espectrómetros en el dominio de frecuencias que trabajan en las regiones del espectro de microondas, milimétricas y submilimétricas (véase apartado III.1.4) que son las mismas que son registradas en muchos observatorios astronómicos. Como resultado de estas mejoras y del extenso trabajo espectroscópico realizado se han logrado identificar numerosas transiciones pertenecientes a los estados vibracionalmente excitados de los cianuro de etilo y

de vinilo en el ISM (Anexos I y II). Además, con el fin de poder corroborar su detección tentativa en el ISM,[47] se ha realizado un análisis detallado del propenal, una molécula considerada como un azúcar del espacio y que está estrechamente ligada a la síntesis de aminoácidos[48]. El isocianuro de metilo (CH₃OCN) es otra molécula que podría estar presente en el ISM dado que moléculas similares ya han sido detectadas en diferentes zonas de la galaxia.[49-52] Con el fin de facilitar su identificación en el ISM, se ha realizado un análisis rotacional del estado fundamental de torsión del isocianuro hasta 350GHz (Capítulo XII).

En el transcurso de la presente tesis doctoral, no sólo se han tratado aspectos puramente

espectroscópicos sobre biomoléculas y moléculas de interés atrsofísico, sino que también se ha realizado una incursión en temáticas relacionadas con el análisis de drogas mediante la combinación de técnicas de ablación laser con espectrometría de masas en tiempos de vuelo (LA-TOF-MS). Se han analizador muestras sólidas evitando el siempre tedioso pretratamiento, intrínseco a las técnicas más convencionales. De esta forma, la sustancia estupefaciente MDMA se ha logrado detectar satisfactoriamente a partir de una muestra decomisada. (véase Capítulo XIII)

A continuación se procede a desglosar más detenidamente cada una de las temáticas que se recogen en la presente memoria de tesis.

I.1. AZÚCARES

Los carbohidratos son las biomoléculas más abundantes en la tierra. Son, además, la principal fuente de energía del organismo, por lo que su ingesta es esencial para la vida humana. Como tales nutrientes, están involucrados en numerosos procesos biológicos.[53] Dada su relevancia, numerosas son las investigaciones que se pueden encontrar en la literatura, hasta el punto que existen diversas revistas científicas indexadas especializadas en su estudio.[54]

Los carbohidratos más complejos están constituidos por los monosacáridos, o azúcares simples, a los cuales se les asocia generalmente con el sabor dulce. Estas sustancian se caracterizan por

la gran variedad de configuraciones en las que se pueden presentar. Hay dos principales grupos de monosacáridos, las adosas y las cetosas. La diferencia entre ellos radica en la posición del grupo carbonilo (ver Figura I.1); las primeras poseen un grupo carbonilo terminal, un aldehído, mientras que las últimas, un grupo cetona en la posición segunda. En general, no se encuentran en su forma lineal
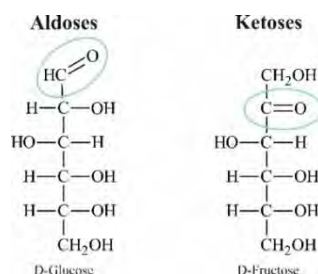
FIGURA I.1: *Proyección de Fisher de los dos principales representantes de aldosas y cetosas: D-glucosa y D-fructosa.*
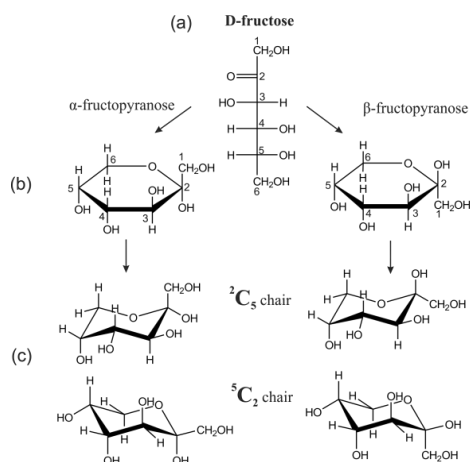
FIGURA I.2: *Esquema de las configuraciones de la D-fructosa. (a) Proyección de Fisher. (b) Proyección de Harworth de las formas piranosas. (c) Distintas configuraciones de la silla.*

como la representada en la Figura I.1, sino que se estabilizan en sus formas cíclicas de cinco miembros, denominadas furanosas, o de seis miembros, llamadas piranosas (véase ejemplo fructosa en Figura I.2). Durante el proceso de ciclación el grupo carbonilo se reduce a alcohol formándose dos nuevos isómeros: los anómeros α y β (Figura I.2.b). La distribución más estable de las formas piranosas es la tipo silla[55] bien en su configuración $^2C_5$ o $^5C_2$, (el superíndice indica el carbono que está por encima del plano de referencia de la silla y subíndice, el que está por debajo,[56] véase Figure I.2.c, en el caso de las adosas conrresponderían con $^1C_4$ y $^4C_1$).

La problemática asociada a la estabilidad relativa de las diferentes estructuras de los azúcares se ha tratado con diversos métodos espectroscópicos (RMN,[57-58] VROA,[59] Rayos X,[60-61]). A raíz de estos resultados, se han enunciado teorías para la justificación de la estabilidad preferencial de unas conformaciones frente a otras, como por ejemplo el

efecto anómerico,[62-63] el efecto $\Delta 2$,[64] o el efecto gauche[65]. Sin embargo estos estudios no tienen en general resolución conformacional y están realizados en fases condensadas donde existen interacciones intermoleculares que pueden alterar la estabilidad de las especies. Tal y como se explica en el apartado III.1, las técnicas que combinan ablación laser con espectroscopia de rotación han resultado ser idóneas[22] para desvelar el panorama conformacional de pequeñas biomoléculas como son los azúcares y así poder aportar información sobre los efectos anteriormente enunciados y de los enlaces de hidrógeno intramoleculares. En los últimos años se ha realizado el análisis conformacional mediante esta técnica de diversos monosacáridos, como la eritrosa,[23] xilosa[24] o glucosa[25].

Partiendo de la base de los nuevos resultados sobre el comportamiento conformacional de los azúcares, uno de los aspectos que no se ha tratado hasta el momento es la relación entre su estructura y su sabor dulce. En la literatura, numerosas han sido las teorías que han surgido durante este último siglo tratando de identificar las características estructurales que ha de presentar una sustancia para
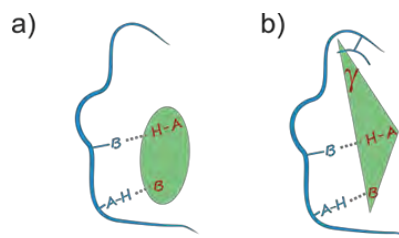
FIGURA I.3: *Representación de las teorías sobre el dulzor. En azul un esquema del receptor y el rojo del edulcorante. Los enlaces de hidrógeno que los unen se representan con líneas punteadas entre ambos. a) Teoría de Shallenberger donde la zona verde se marca la zona de interacción (glucoporo). b) Marcado en verde el diagrama del "triángulo del dulzor".*
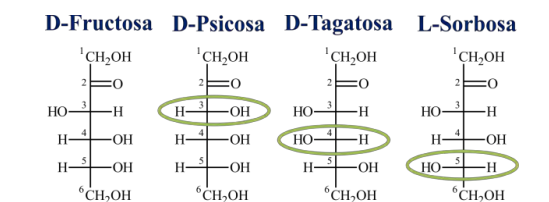
FIGURA I.4: *Esquema de las configuraciones de la D-fructosa. (a) Proyección de Fisher. (b) Proyección de Harworth de las formas piranosas. (c) Distintas configuraciones de la silla.*

poseer un sabor dulce.[5] La teoría más extendida es la postulada por Shallenberger y Acree,[4] en la cual establecen que el dulzor de una sustancia depende de la fortaleza de los dos enlaces de hidrógeno que se establecen entre el edulcorante y el receptor biológico (Figura I.3.a). A esta teoría inicial se le han ido añadiendo modificaciones; entre las que destacan la inclusión de un tercer punto hidrofóbico de unión,[66] el sitio γ, (Figura I.3.b) y la posterior postulación que afirma que el receptor puede contener hasta 8 zonas de anclaje con el edulcorante.[67] Es necesario mencionar que cuando estas teorías fueron planteadas, no había datos experimentales precisos sobre el comportamiento conformacional de los edulcorantes que pudiesen corroborar lo postulado.

Las cetohexosas (Figura I.4) son un caso especialmente interesante para el estudio de la relación entre la estructura y el sabor dulce. Estos epímeros (azúcares que sólo se diferencian en la configuración de un carbono asimétrico) son todos igual de dulces que el azúcar común, a excepción de la D-fructosa, que es el doble de dulce que todas. De esta forma, se puede tratar de identificar los posibles glucóforos basándose en las características conformacionales que tienen en común. Asimismo, la comparativa en el comportamiento

conformacional aportará datos para tratar de justificar las discrepancias en el grado de dulzor.

Los Capítulos IV y V de la presente Memoria recogen el estudio conformacional de las cetohexosas **D-fructosa, D-tagatosa, D-psicosa y L-sorbosa**, donde se analizan la relación entre su estructura y el sabor dulce que les caracteriza. El primero de ellos se dedica al estudio de la D-fructosa donde dos conformaciones han sido encontradas en fase gas (Figura I.5.a), siendo la β $^2C_5$ g- cc mucho más abundante que la β $^2C_5$ g- cc (98% frente al 2%). El estudio conformacional de sus epímeros junto con el análisis de la relación estructura-dulzor se trata en el Capítulo V. Se han encontrado tres, dos y una conformaciones de la D-
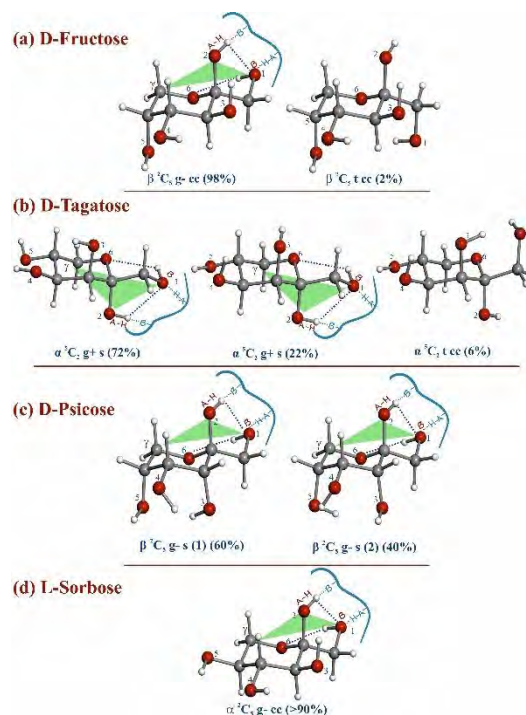
FIGURA I.5: *Confórmeros observados para las cetohexosas. Las líneas punteadas señalan los enlaces de hidrógeno que comparten los confórmeros más abundantes (en paréntesis se encuentra la abundancia de cada confórmero). El triángulo del dulzor A-H, B and γ está marcado de acuerdo con las teorías que se encuentran en la literatura.[68-70] (a) D-Fructosa. (b) D-Tagatosa. (c) D-Psicosa (d) L-Sorbosa*
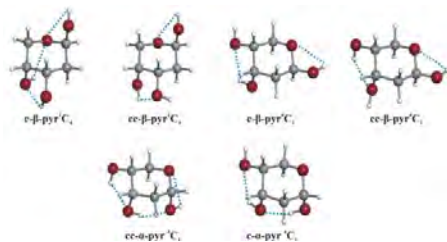
FIGURA I.6: *Confórmeros observados de la 2-desoxy-D-ribosa.*

tagatosa, D-psicosa y L-sorbosa respectivamente (Figura I.5.b, I.5.c y I.5.d). Todos ellos no están estabilizados en la misma configuración de la silla, pero, sí que se ha encontrado que en el entorno de los grupos OH(1), OH(2) y O_ring, es análoga para todos ellos. Esta característica que tienen común podría estar relacionada con el dulzor de estas sustancias al ser el punto de anclaje con el receptor.

En el Capítulo VI se presenta el primer estudio conformacional de la **2-desoxirribosa,** constituyente del ADN**.** El comportamiento estructural de este monosacárido puede jugar un papel muy importante en la funcionalidad de los ácidos nucleicos (ADN y ARN), ya que la estructura primaria de ambos se diferencia principalmente en el azúcar que contienen: 2-desoxirribosa el ADN y ribosa el ARN. Estos azúcares también son muy similares entre sí; la 2-desoxirribosa es igual que la ribosa pero eliminando el grupo hidroxilo en la posición dos. A pesar de parecer que la estructura primaria es muy similar, tanto las estructuras secundaria y terciaria como la funcionalidad del ADN y ARN es muy diferente. En el presente trabajo se ha analizado el comportamiento conformacional de la 2-desoxi-D-ribosa, encontrándose dos conformaciones de su forma α-piranosa y cuatro de la β-piranosa (Figura

I.6), todos estabilizadas mediante enlaces de hidrógeno intramoleculares. En este caso, la conformación análoga a la más estable de la α-ribosa[71] no ha podido ser detectada en la 2-desoxirribosa, debido, posiblemente, a un debilitamiento en la red de enlaces intramoleculares resultado de la eliminación del hidroxilo.

Los aminoazúcares son monosacáridos donde que se ha sustituido un grupo hidroxilo por un amino. Esta sustitución es una de las principales formas de anclaje de los azúcares a las proteínas para formar las glucoproteínas. A raíz del estudio sobre el comportamiento conformacional del monosacárido por excelencia, la D-glucosa,[25] donde se han logrado estudiar tanto los efectos estereoelectrónicos como los enlaces de hidrógeno cooperativos de cuatro confórmeros de α-D-glucopiranosa y tres de la β-glucopiranosa, se inició el estudio del primer amino azúcar, la **D-glucosamina**. En el Capítulo VII, se recoge su estudio conformacional donde se discuten las similitudes encontradas entre los tres confórmeros observados de la α-D-glucosamina y los correspondientes de la α-glucosa (ver Figura I.7).
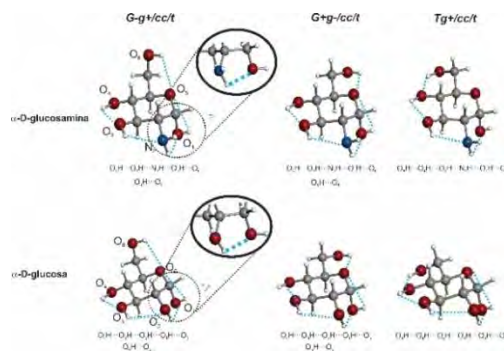
FIGURA I.7: *Confórmeros observados de la α-D-glucosamina (arriba) y de la α-D-glucosa (abajo).*
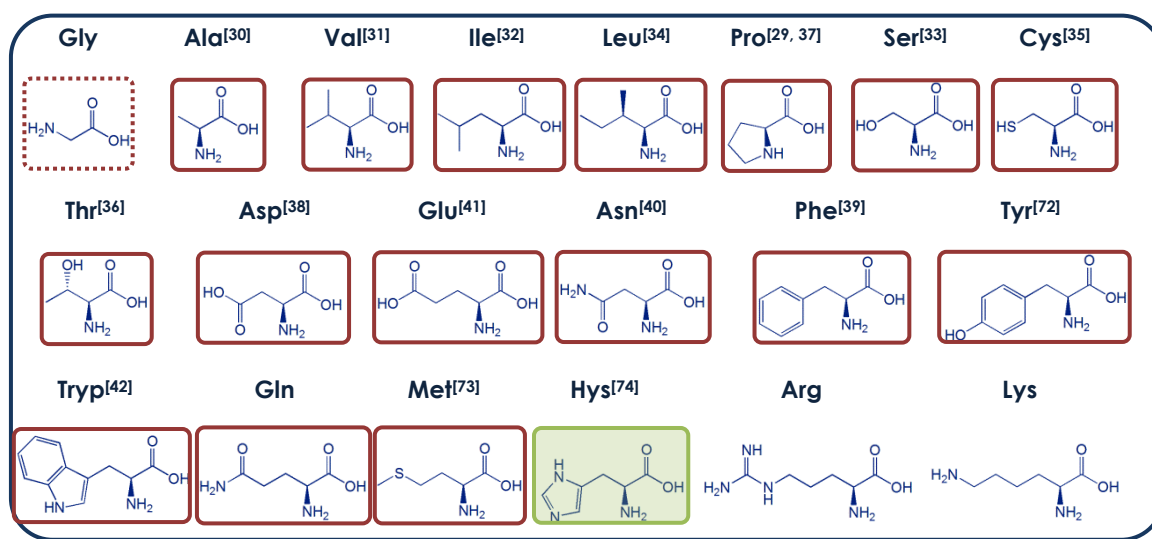
FIGURA I.8: *Esquema de los 20 aminoácidos proteicos. Los aminoácidos marcados en línea continua roja son los estudiados en el GEM mientras que el marcado en línea punteada, lo ha sido en otros laboratorios. El aminoácido histidina, recuadrado en verde, es objeto de estudio en la presente Memoria*

I.2. AMINOÁCIDOS

El comportamiento conformacional de los aminoácidos, que son los constituyentes elementales de las proteínas, tiene una gran influencia en su estructura, su plegamiento y desdoblamiento.[3] Esta temática ha venido siendo objeto de estudio en el GEM desde el 2002 cuando se publicaron los primeros resultados sobre la prolina.[29] Tal y como se muestra en la Figura I.8, gracias a la técnica LA-MB-FTMW[36, 74-75] se ha podido observar el comportamiento conformacional de la mayoría de estos relevantes sistemas biológicos. Se ha de destacar, por ejemplo, el estudio sobre la metionina con ocho confórmeros observados,[73] o las seis especies identificadas para la serina.[33]

Dado que el gran mapa conformacional de los aminoácidos proteicos está casi concluido, se han podido observar ciertas características comunes en estas biomoléculas. Para poder evaluarlas, se hará una distinción entre aquellos aminoácidos con cadena lateral apolar y aquellos con cadena lateral polar. Los de cadena apolar, por definición, no
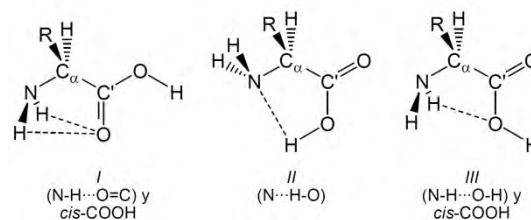
FIGURA I.9: *Esquema de los tres posibles enlaces de hidrógeno intramoleculares entre los grupos amino e carboxilo de los α-aminoácidos*

poseen ningún grupo funcional que pueda formar enlaces de hidrógeno intramoleculares a excepción de los grupos amino y carboxilo. Por lo que serán los enlaces entre ambos grupos los que dominarán sus preferencias conformacionales. En la Figura I.9 se muestran los tres tipos de enlaces de hidrogeno posibles. Se ha encontrado que en una expansión supersónica los enlaces de hidrógeno que se establecen preferentemente son los de tipo I y tipo II, siendo más estables los primeros. Se postula que los confórmeros con enlaces de hidrógeno tipo III se relajan conformacionalmente a los tipo I; esto es debido a que la barrera energética correspondiente al giro del grupo carboxilo es lo suficientemente baja para que durante la expansión supersónica se dé esta interconversión.[76-79] De tal forma que si este giro no está impedido, como en el caso de Ac₃C,[80] los confórmeros tipo III no podrán ser observados.

A diferencia de los anteriores, los aminoácidos de cadena lateral polar pueden establecer enlaces de hidrógeno entre el resto polar y los grupos amino y ácido; estos enlaces pueden alterar sustancialmente el comportamiento de los confórmeros, ya que su formación puede aumentar la energía de la barrera correspondiente al giro del grupo carboxilo, impidiendo así la interconversión entre los tipo I y tipo III[35, 38]. Además, se ha encontrado que estos enlaces pueden llegar a estabilizar preferencialmente los confórmeros tipo III sobre los de tipo I.[36]
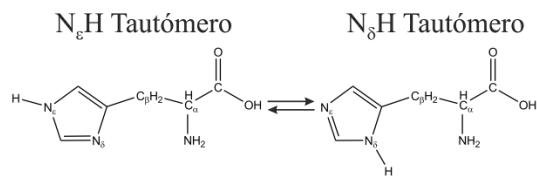
FIGURA I.10: *Equilibrio tautomérico de la histidina*

Hasta el momento, de entre todos los aminoácidos estudiados, ninguno de ellos presentaba en su cadena lateral la posibilidad de estar en equilibrio tautomérico. Motivados por la falta de información sobre la influencia de la tautomería en la estabilidad conformacional, se plantea el estudio de la **histidina**, uno de los dos únicos aminoácidos proteicos que presentan esta singularidad. La histidina (His) en su cadena lateral posee un grupo imidazol que está en equilibrio tautomérico entre sus formas $N_\varepsilon H$ y $N_\delta H$ (mostradas en la Figura I.10). Esta particularidad de la histidina hace que este aminoácido juegue un papel importante en muchos procesos biológicos.[81-84]

Sin embargo, el estudio rotacional de la histidina presenta la dificultad añadida de la presencia de tres ^{14}N no equivalentes. La distribución de carga no esférica de los núcleos de ^{14}N (I=1), hace que las transiciones rotacionales se rompan en numerosas
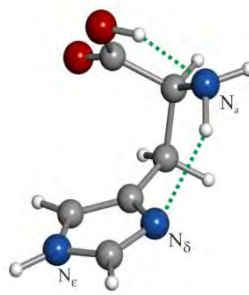
FIGURA I.11: *Confórmero observado de la histidina*

componentes, formando una compleja estructura hiperfina de cuadrupolo nuclear.[85] El análisis de una estructura hiperfina de cuadrupolo de tres núcleos de ^{14}N no equivalentes es de suma complejidad y muy pocos casos se pueden encontrar en la literatura[86] y menos para nitrógenos no equivalentes.[10] Con el fin de facilitar el análisis, se construyó un nuevo LA-MB-FTMW (ver apartado II.1) que permite recoger el espectro de microondas a bajas frecuencias donde las componentes hiperfinas de cuadrupolo están normalmente mejor resueltas.

En el Capítulo VIII se presentan los resultados del análisis del espectro de rotación de la histidina, donde se identificó una única especie conformacional perteneciente al tautómero $N_\varepsilon H$. Éste confórmero se encuentra estabilizado por dos enlaces de hidrógeno intramoleculares: uno tipo II entre el carboxilo y el grupo amino y el otro entre el grupo amino y el N_δ del grupo imidazol (Figura I.11).

I.3. MICROSOLVATACIÓN DE BASES NITROGENADAS

Al igual que el aminoácido histidina, las cinco bases nitrogenadas constituyentes de los ácidos nucleicos ADN y ARN también pueden presentar tautomería. Hasta el momento, se ha estudiado mediante espectroscopia de rotación el comportamiento conformacional y tautomérico tanto de la base púrica guanina (G),[9] como las tres bases pirimidínicas citosina (C),[10] timina (T)[7] y uracilo (U)[8]. De entre todos estos estudios cabe destacar los resultados encontrados para citosina en fase gas donde se ha logrado identificar las cinco formas tautoméricas[10] (Figura I.12) siendo la más abundante la enol-amino-trans (EAt). Sin embargo, la citosina en fases condensadas y en el ADN, el tautómero identificado es la forma canónica keto-amino.[6, 87-88] Tal y como se ha mencionado al inicio del Capítulo, los enlaces de hidrogeno intermoleculares con el disolvente (agua) pueden

alterar el equilibrio tautomérico al estabilizar preferentemente una especie, en este caso la KA, frente al resto. Es en este momento, cuando cabe la pregunta sobre cuántas moléculas de agua son necesarias para la inversión del equilibrio tautomérico, ¿sería suficiente una molécula de agua?

Para estudiar cómo afecta el disolvente a la estabilidad de los confórmeros / tautómeros, se han llevado a cabo con anterioridad diversos estudios sobre microsolvatación, que es aquella situación en la que un sistema molecular se encuentra rodeado
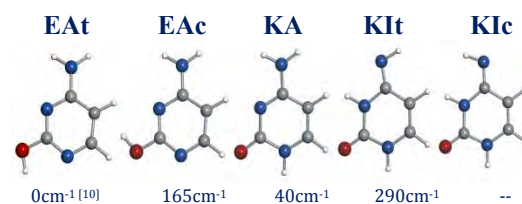
FIGURA I.12: *Las cinco especies tautoméricas observadas de la citosina. Debajo de las figuras se muestra la energía de Gibbs experimental (KIc no pudo ser calculada dada la baja intensidad del espectro)*
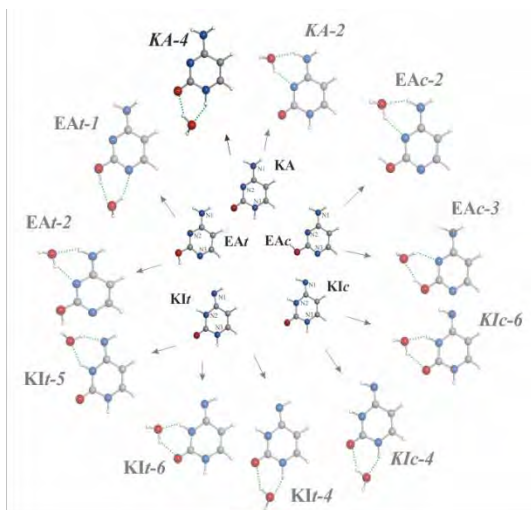
FIGURA I.13: *Posibles microsolvatos de la citosina. Destacado el KA-4 al ser el único observado.*

por un pequeño número de moléculas de agua. En concreto en este laboratorio se ha podido explorar la influencia una y dos moléculas de agua sobre los aminoácidos glicina[89-90] y alanina[91] mediante la técnica LA-MB-FTMW. Asimismo, los monohidratos de las bases pirimidínicas timina y uracilo han sido también caracterizados en detalle por primera vez.[92]

Basándonos en la experiencia en microsolvatación de biomoléculas del grupo, en el Capítulo IX se ha tratado de dar respuesta a los interrogantes sobre la **microsolvatación de la citosina**. Sin embargo, la intensidad de las transiciones pertenecientes a los microsolvatos de la citosina está por debajo del límite de detección del instrumento LA-MB-FTMW. Por este motivo, este espectrómetro ha sido modificado para incluir un sistema de acumulación de múltiples espectros (hasta un máximo de diez) por cada ciclo instrumental (explicado en apartado III.1.3). De esta forma se ha reducido el consumo de muestra y se ha facilitado la acumulación de un mayor número de espectros sin tener que parar interrumpir la experimentación para realizar labores de limpieza del nozzle de ablación. Haciendo uso de este sistema, se logró identificar, una única especie de entre todas las posibles (destacada en la Figura I.13). Todo parece indicar que se trata de la forma KA a la que se le ha unido el agua entre el grupo amino pirimidínico y el grupo cetona. Por tanto, una molécula de agua sí parece ser capaz de invertir el equilibrio tautomérico de la citosina.

I.4. NEUROTRANSMISORES

Los neurotransmisores son las moléculas encargadas de la comunicación entre neuronas a través del espacio sináptico. La naturaleza de estas sustancias es muy diversa (ver ejemplos en Figura I.14). En general, todas ellas poseen un alto grado de flexibilidad que suele derivar en un elevado número de conformaciones posibles. Un estudio del panorama conformacional de estos sistemas puede ayudar a lograr entender la actividad de los neurotransmisores así como el proceso de reconocimiento que se da en la célula postsipnáptica. En la literatura se pueden encontrar diversos estudios que tratan de desvelar el panorama conformacional de los neurotransmisores mediante espectroscopia electrónica.[100-107]
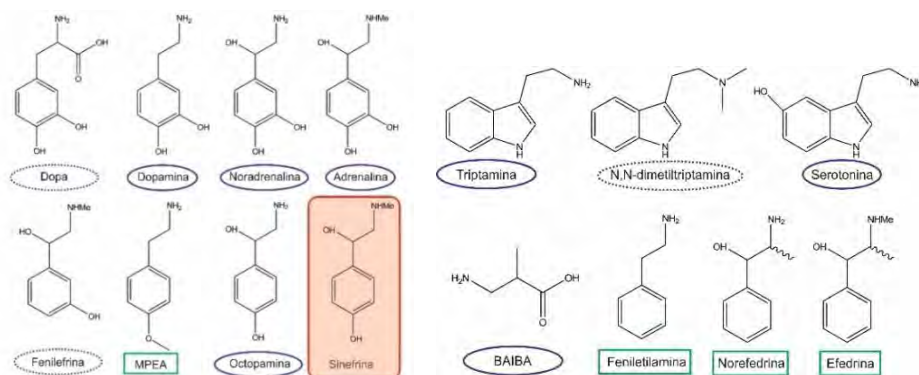
FIGURA I.14: *Ejemplos de neurotransmisores estudiados en el laboratorio.[43-44, 93-99] Marcados en elipse azul los analizados mediante la técnica MB-FTMW combinada con ablación láser y los recuadrados en verde combinada con calentamiento. Los que están en línea punteada se encuentra actualmente bajo estudio. El estudio de la sinefrina, sombreada en rojo, se encuentra recogido en la presente memoria.*

El estudio de neurotransmisores mediante espectroscopia de rotación se inició en el laboratorio con los estudios conformacionales de la feniletilamina[96] y p-metoxifeniletilamina,[99] y a las que se han sumado moléculas como la triptamina,[95] efedrina,[94] serotonina,[43] dopamina,[44] adrenalina,[97] BAIBA,[93] etc. (ver ejemplos en Figura I.14) Continuando con esta línea de investigación, en el Capítulo XI se explica el comportamiento conformacional de la **sinefrina** (sombreada en rojo en la Figura I.14). Este neurotransmisor es comercialmente usado en seres humanos como agente reductor de grasa, dado su poder estimulante.[108] Su estructura es similar a la adrenalina pero con un único grupo hidroxilo en posición para. Seis han sido las conformaciones de la sinefrina (Figura I.15), todos ellos estabilizados por un enlace de hidrógeno intramolecular entre el grupo hidroxilo de la cadena lateral y el nitrógeno (OH···N). Los confórmero tipo GG tienen además una estructura favorable para la formación de una interacción entre el grupo amino y la nube π del anillo aromático (NH···π). Los resultados obtenidos para la sinefrina han sido, además, comparados con el MPEA (2-metilamino-1-feniletanol), homólogo a la sinefrina pero con el hidroxilo del anillo.
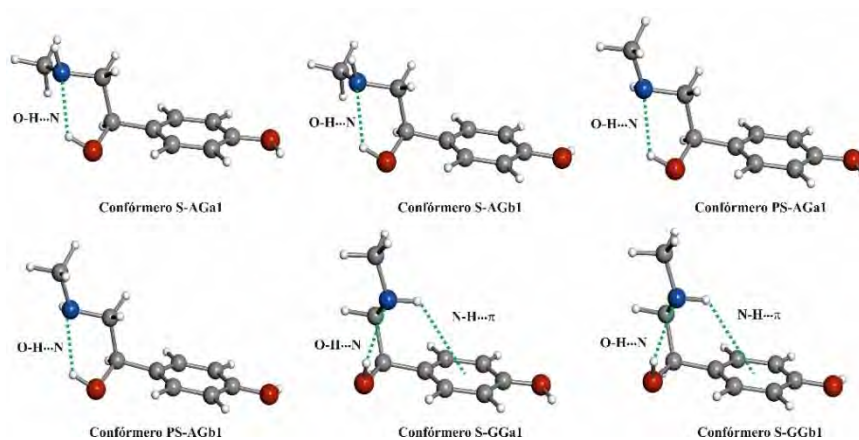
FIGURA I.15: *Confórmeros observados para la sinefrina, donde se indican los enlaces intramoleculares que los estabilizan.*

I.5. OTROS ESTUDIOS

I.5.1 Especies de interés astrofísico.

El fin último de la astroquímica es entender la formación de moléculas en el universo, para lo cual es necesario conocer las sustancias químicas que lo forman. Hasta el momento más de 180 moléculas han sido detectadas en el ISM[45] basándose en la comparación de los espectros recogidos en los observatorios astronómicos con los parámetros espectroscópicos obtenidos en los laboratorios. Pero aún existe un gran número de transiciones que están sin identificar (U-lines). En los registros del radio telescopio de 30m IRAM (Pico Veleta, España), a pesar de haber identificado unas 4000 transiciones,[109-114] hay más de 8000 U-lines.[46] Gracias al Proyecto ALMA (Atacama Large Millimeter/submillimeter Array), donde ya se han detectado moléculas en nuevas regiones del espacio,[115] la sensibilidad de las observaciones del ISM se esta incrementando enormemente, lo que lleva consigo un aumento considerable del número de U-lines que puede llegar al límite de la confusión. Estas transiciones podrían pertenecer tanto a nuevas moléculas no identificadas aún en el ISM, como a moléculas que ya han sido observadas pero de cuyos estados vibracionalmente excitados, isotopólogos o conformaciones de mayor energía no hay datos precisos sobre sus parámetros rotacionales. A partir de la identificación de estas últimas especies se puede obtener información sobre características de la región del espacio ISM donde se encuentran, como, por ejemplo, la temperatura de la nebulosa, opacidad o presencia de fuentes de radiación próximas.[116-117]

Con el fin de proporcionar parámetros rotacionales lo suficientemente precisos para permitir la identificación de las U-lines, en nuestro laboratorio se han actualizado los espectrómetros en el dominio de frecuencias (véase Capítulo III.1.3). Estos sistemas instrumentales permiten recoger el espectro de rotación hasta frecuencias cercanas al terahercio.[118] De esta forma se pueden registrar las mismas regiones del espectro que las que se registran en los observatorios astrofísicos y que, normalmente, están fuera del ámbito de uso de los espectrómetros en el dominio de frecuencia utilizados en los apartados anteriores relativos a biomoléculas.

Haciendo uso de estas técnicas, se ha analizado el espectro de rotación pura de los estados vibracionalmente excitados de los **cianuros de etilo y vinilo** (Anexos I y II, respectivamente). Estas sustancias son muy abundantes en el ISM, tanto que, gracias a este trabajo, se han detectado transiciones puramente rotacionales pertenecientes a estados vibracionalmente excitados con energías hasta de 600 cm^{-1} sobre el fundamental en Orión KL.

Además del estudio de moléculas ya detectadas, se ha realizado el análisis de sustancias candidatas a estar en el ISM como el **propenal** (Capítulo XI) y **isocianuro de metilo** (Capítulo XII), con el fin de proporcionar datos espectroscópicos que posibiliten su detección.

El propenal ($CH_2=CH-CHO$) es el aldehído insaturado más simple. Su relevancia viene dada por su relación con la síntesis de aminoácidos[48] y porque, como tal aldehído, es considerado uno de los azúcares del espacio.[119] Mientras que en el caso de otros aldehídos, como el glicoladehido, más de 40 transiciones diferentes han sido observadas en distintas zonas del espacio,[120-123] para el propenal únicamente se han encontrado dos transiciones en las región de Sagitario B2.[47] Dado que la sensibilidad de los observatorios del ISM está en aumento constante, es probable que se puedan detectar otras transiciones del propenal, incluyendo a sus estados excitados y a su isómero de mayor energía (cis). Es por ello que en el Capítulo XI se recoge el análisis de los estados fundamentales los dos isómeros (cis y trans), los isotopólogos del trans y sus primeros estados vibracionalmente excitados.

El isocianuro de metilo (CH_3OCN) es otra molécula candidata a ser detectada en el ISM debido a que moléculas de similares características como el ácido isocianídricomo (HOCN) o el ácido fulmínico (HCNO), han sido observadas en diferentes zonas del ISM.[49-52] Por este motivo, se

ha analizado el espectro de rotación del estado fundamental de torsión del CH_3OCN hasta 350GHz donde se han identificado más de 700 transiciones (Capítulo XII).

I.5.2. Análisis de drogas mediante LA-TOF-MS.

El análisis de drogas representa un interesante campo de trabajo debido al alto impacto social que suponen las drogas en la sociedad actual. La ablación láser de compuestos sólidos posibilita el análisis evitando tediosos procedimientos de preparación o muestreo. En el Capítulo XIII se describe la construcción de un sistema experimental que combina ablación láser de muestras sólidas y espectrometría de masas de tiempos de vuelo que tiene como fin el análisis drogas y otras sustancias orgánicas sin necesidad de disolver la muestra. Hasta el momento se ha logrado caracterizar los espectros de masas de diversos fármacos (aspirina y paracetamol) y de drogas tales como el MDMA, comúnmente conocida como éxtasis. Mediante el análisis de los espectros se han observado diferentes patrones de fragmentación de las muestras cuando éstas son ionizadas mediante ablación láser o con métodos más convencionales como impacto electrónico. Por lo tanto, éste sistema no sólo permite la detección de drogas ilícitas sino que también aporta información sobre la fotofragmentación que se produce al hacer interaccionar un láser con la muestra.

I.6. REFERENCIAS

[1]   J. M. Lehn, *Nobel Lecture* **1987**, *8*, 444.

[2]   M. J. Zigmond, *Fundamental Neuroscience*, Academic Press: London, **1998**.

[3]   K. A. Dill, H. S. Chan, *Nat Struct Mol Biol* **1997**, *4*, 10-19.

[4]   R. S. Shallenberger, T. E. Acree, *Nature* **1967**, *216*, 480-482.

[5]   G. G. Birch, R. S. Shallenberger, *C R C Critical Reviews in Food Science and Nutrition* **1976**, *8*, 57-95.

[6]   J. D. Watson, F. H. C. Crick, *Nature* **1953**, *171*, 737-738.

[7]   J. C. Lopez, M. I. Peña, M. E. Sanz, J. L. Alonso, *Journal of Chemical Physics* **2007**, *126*.

[8]   V. Vaquero, M. E. Sanz, J. C. Lopez, J. L. Alonso, *Journal of Physical Chemistry A* **2007**, *111*, 3443-3445.

[9]   J. L. Alonso, I. Peña, J. C. Lopez, V. Vaquero, *Angewandte Chemie-International Edition* **2009**, *48*, 6141-6143.

[10]   J. L. Alonso, V. Vaquero, I. Peña, J. C. López, S. Mata, W. Caminati, *Angewandte Chemie* **2013**, *48*, 5934-5936.

[11]   S. Antolínez, J. C. López, J. L. Alonso, *Angewandte Chemie International Edition* **1999**, *38*, 1772-1774.

[12]   M. E. Sanz, J. C. López, J. L. Alonso, *Chemistry – A European Journal* **1999**, *5*, 3293-3298.

[13]   M. E. Sanz, A. Lesarri, J. C. López, J. L. Alonso, *Angewandte Chemie International Edition* **2001**, *40*, 935-938.

[14]   J. L. Alonso, S. Antolínez, S. Blanco, A. Lesarri, J. C. López, W. Caminati, *Journal of the American Chemical Society* **2004**, *126*, 3244-3249.

[15]   S. Blanco, J. C. López, A. Lesarri, W. Caminati, J. L. Alonso, *ChemPhysChem* **2004**, *5*, 1779-1782.

[16]   W. Caminati, J. C. López, J. L. Alonso, J.-U. Grabow, *Angewandte Chemie International Edition* **2005**, *44*, 3840-3844.

[17]   E. J. Cocinero, R. Sánchez, S. Blanco, A. Lesarri, J. C. López, J. L. Alonso, *Chem. Phys. Lett.* **2005**, *402*, 4-10.

[18]   P. Ottaviani, W. Caminati, L. B. Favero, S. Blanco, J. C. López, J. L. Alonso, *Chemistry – A European Journal* **2006**, *12*, 915-920.

[19]   J. C. López, W. Caminati, J. L. Alonso, *Angewandte Chemie International Edition* **2006**, *45*, 290-293.

[20]   T. J. Kistenmacher, G. A. Rand, R. E. Marsh, *Acta Crystallographica Section B* **1974**, *30*, 2573-2578.

[21]   C. H. Gorbitz, B. Dalhus, *Acta Crystallographica Section C* **1996**, *52*, 1754-1756.

[22]   J. L. Alonso, J. C. López, Springer Berlin Heidelberg, **2015**, pp. 1-67.

[23]   C. Cabezas, I. Peña, A. M. Daly, J. L. Alonso, *Chemical Communications* **2013**, *49*, 10826-10828.

[24]   I. Peña, S. Mata, A. Martín, C. Cabezas, A. M. Daly, J. L. Alonso, *Physical Chemistry Chemical Physics* **2013**, *15*, 18243-18248.

[25]   J. L. Alonso, M. A. Lozoya, I. Peña, J. C. Lopez, C. Cabezas, S. Mata, S. Blanco, *Chemical Science* **2014**, *5*, 515-522.

[26]   C. Bermúdez, I. Peña, C. Cabezas, A. M. Daly, J. L. Alonso, *Chemphyschem* **2013**, *14*, 893-895.

[27] I. Peña, E. J. Cocinero, C. Cabezas, A. Lesarri, S. Mata, P. Écija, A. M. Daly, Á. Cimas, C. Bermúdez, F. J. Basterretxea, S. Blanco, J. A. Fernández, J. C. López, F. Castaño, J. L. Alonso, *Angewandte Chemie International Edition* **2013**, *52*, 11840-11845.

[28] I. Peña, L. Kolesnikova, C. Cabezas, C. Bermúdez, M. Berdakin, A. Simao, J. L. Alonso, *Physical Chemistry Chemical Physics* **2014**, *16*, 23244-23250.

[29] A. Lesarri, S. Mata, E. J. Cocinero, S. Blanco, J. C. Lopez, J. L. Alonso, *Angewandte Chemie-International Edition* **2002**, *41*, 4673-4676.

[30] S. Blanco, A. Lesarri, J. C. Lopez, J. L. Alonso, *Journal of the American Chemical Society* **2004**, *126*, 11675-11683.

[31] A. Lesarri, E. J. Cocinero, J. C. Lopez, J. L. Alonso, *Angewandte Chemie-International Edition* **2004**, *43*, 605-610.

[32] A. Lesarri, R. Sanchez, E. J. Cocinero, J. C. Lopez, J. L. Alonso, *Journal of the American Chemical Society* **2005**, *127*, 12952-12956.

[33] S. Blanco, M. E. Sanz, J. C. Lopez, J. L. Alonso, *Proceedings of the National Academy of Sciences of the United States of America* **2007**, *104*, 20183-20188.

[34] E. J. Cocinero, A. Lesarri, J. U. Grabow, J. C. Lopez, J. L. Alonso, *Chemphyschem* **2007**, *8*, 599-604.

[35] M. E. Sanz, S. Blanco, J. C. Lopez, J. L. Alonso, *Angewandte Chemie-International Edition* **2008**, *47*, 6216-6220.

[36] J. L. Alonso, C. Perez, M. E. Sanz, J. C. Lopez, S. Blanco, *Physical Chemistry Chemical Physics* **2009**, *11*, 617-627.

[37] S. Mata, V. Vaquero, C. Cabezas, I. Peña, C. Perez, J. C. Lopez, J. L. Alonso, *Physical Chemistry Chemical Physics* **2009**, *11*, 4141-4144.

[38] M. E. Sanz, J. C. Lopez, J. L. Alonso, *Physical Chemistry Chemical Physics* **2010**, *12*, 3573-3578.

[39] C. Perez, S. Mata, S. Blanco, J. C. Lopez, J. L. Alonso, *Journal of Physical Chemistry A* **2011**, *115*, 9653-9657.

[40] C. Cabezas, M. Varela, I. Peña, S. Mata, J. C. Lopez, J. L. Alonso, *Chemical Communications* **2012**, *48*, 5934-5936.

[41] I. Peña, M. Eugenia Sanz, J. C. Lopez, J. L. Alonso, *Journal of the American Chemical Society* **2012**, *134*, 2305-2312.

[42] M. E. Sanz, C. Cabezas, S. Mata, J. L. Alonso, *The Journal of Chemical Physics* **2014**, *140*, -.

[43] C. Cabezas, M. Varela, I. Peña, J. C. Lopez, J. L. Alonso, *Physical Chemistry Chemical Physics* **2012**, *14*, 13618-13623.

[44] C. Cabezas, I. Peña, J. C. López, J. L. Alonso, *The Journal of Physical Chemistry Letters* **2013**, *4*, 486-490.

[45] E. Herbst, J. T. Yates, *Chemical Reviews* **2013**, *113*, 8707-8709.

[46] B. Tercero, J. Cernicharo, J. Pardo, J. Goicoechea, *Astronomy & Astrophysics* **2010**, *517*, A96.

[47] J. M. Hollis, P. R. Jewell, F. J. Lovas, A. Remijan, H. Mollendal, *Astrophysical Journal* **2004**, *610*, L21-L24.

[48] J. E. Van Trump, S. L. Miller, *Science* **1972**, *178*, 859-860.

[49] S. Brünken, C. A. Gottlieb, M. C. McCarthy, P. Thaddeus, *The Astrophysical Journal* **2009**, *697*, 880.

[50] N. Marcelino, J. Cernicharo, B. Tercero, E. Roueff, *The Astrophysical Journal Letters* **2009**, *690*, L27.

[51] N. Marcelino, S. Brünken, J. Cernicharo, D. Quan, E. Roueff, E. Herbst, P. Thaddeus, *A&A* **2010**, *516*, A105.

[52] S. Brünken, A. Belloche, S. Martín, L. Verheyen, K. M. Menten, *A&A* **2010**, *516*, A109.

[53] B. Wang, G.-J. Boons, Wiley, **2011**.

[54]   *Advances in Carbohydrate Chemistry and Biochemistry, Carbohydrate Research, Journal of Carbohydrate Chemistry, etc.*

[55]   R. E. Reeves, *Journal of the American Chemical Society* **1950**, *72*, 1499-1506.

[56]   A. D. McNaught, *Carbohydr Res* **1997**, *297*, 1-92.

[57]   R. U. Lemieux, J. D. Stevens, *Canadian Journal of Chemistry* **1966**, *44*, 249-262.

[58]   S. Angyal, V. Pickles, *Australian Journal of Chemistry* **1972**, *25*, 1695-1710.

[59]   Z. Q. Wen, L. D. Barron, L. Hecht, *Journal of the American Chemical Society* **1993**, *115*, 285-292.

[60]   S. H. Kim, Rosenste.Rd, *Acta Crystallographica* **1967**, *22*, 648-&.

[61]   S. Takagi, R. D. Rosenstein, *Carbohydrate Research* **1969**, *11*, 156-158.

[62]   E. Juaristi, G. Cuevas, *Tetrahedron* **1992**, *48*, 5019-5087.

[63]   C. L. Perrin, K. B. Armstrong, M. A. Fabian, *Journal of the American Chemical Society* **1994**, *116*, 715-722.

[64]   T. D. Buley, A. M. Striegel, *Carbohydrate Polymers* **2010**, *79*, 241-249.

[65]   S. Wolfe, *Accounts of Chemical Research* **1972**, *5*, 102-111.

[66]   L. B. Kier, *Journal of Pharmaceutical Sciences* **1972**, *61*, 1394-1397.

[67]   C. Nofre, J.-M. Tinti, *Food Chemistry* **1996**, *56*, 263-274.

[68]   R. S. Shallenberger, *Pure and Applied Chemistry* **1978**, *50*, 1409-1420.

[69]   M. G. Lindley, G. G. Birch, *Journal of the Science of Food and Agriculture* **1975**, *26*, 117-124.

[70]   G. G. Birch, S. Shamil, Z. Shepherd, *Experientia* **1986**, *42*, 1232-1234.

[71]   E. J. Cocinero, A. Lesarri, P. Écija, F. J. Basterretxea, J.-U. Grabow, J. A. Fernández, F. Castaño, *Angewandte Chemie International Edition* **2012**, *51*, 3119-3124.

[72]   C. Pérez, Valladolid **2010**.

[73]   I. Peña, Valladolid **2011**.

[74]   C. Bermúdez, S. Mata, C. Cabezas, J. L. Alonso, *Angewandte Chemie International Edition* **2014**, *53*, 11015-11018.

[75]   A. Lesarri, S. Mata, J. C. Lopez, J. L. Alonso, *Rev. Sci. Instrum.* **2003**, *74*, 4799-4804.

[76]   R. S. Ruoff, T. D. Klots, T. Emilsson, H. S. Gutowsky, *The Journal of Chemical Physics* **1990**, *93*, 3142-3150.

[77]   P. D. Godfrey, R. D. Brown, F. M. Rodgers, *Journal of Molecular Structure* **1996**, *376*, 65-81.

[78]   P. D. Godfrey, R. D. Brown, *Journal of the American Chemical Society* **1998**, *120*, 10724-10732.

[79]   G. M. Florio, R. A. Christie, K. D. Jordan, T. S. Zwier, *Journal of the American Chemical Society* **2002**, *124*, 10236-10247.

[80]   A. I. Jiménez, V. Vaquero, C. Cabezas, J. C. López, C. Cativiela, J. L. Alonso, *Journal of the American Chemical Society* **2011**, *133*, 10621-10628.

[81]   J. C. Kendrew, R. E. Dickerson, B. E. Strandberg, R. G. Hart, D. R. Davies, D. C. Phillips, V. C. Shore, *Nature* **1960**, *185*, 422-427.

[82]   M. F. Perutz, M. G. Rossmann, A. F. Cullis, H. Muirhead, G. Will, A. C. T. North, *Nature* **1960**, *185*, 416-422.

[83]   A. Volbeda, M.-H. Charon, C. Piras, E. C. Hatchikian, M. Frey, J. C. Fontecilla-Camps, *Nature* **1995**, *373*, 580-587.

[84]   S. Dementin, V. Belle, P. Bertrand, B. Guigliarelli, G. Adryanczyk-Perrier, A. L. De Lacey, V. M. Fernandez, M. Rousset, C. Leger, *Journal of the American Chemical Society* **2006**, *128*, 5209-5218.

[85]   W. Gordy, R. L. Cook, *Microwave Molecular Spectra, Vol. IX and XIV*, Wiley-Interscience, New York, **1984**.

[86]   H. Hopf, C. Mlynek, R. J. McMahon, J. L. Menke, A. Lesarri, M. Rosemeyer, J. U. Grabow, *Chemistry-A European Journal* **2010**, *16*, 14115-14123.

[87]   C. E. Crespo-Hernández, B. Cohen, P. M. Hare, B. Kohler, *Chemical Reviews* **2004**, *104*, 1977-2020.

[88]   M. K. Shukla, J. Leszczynski, *Journal of Biomolecular Structure and Dynamics* **2007**, *25*, 93-118.

[89]   J. L. Alonso, E. J. Cocinero, A. Lesarri, M. E. Sanz, J. C. Lopez, *Angewandte Chemie-International Edition* **2006**, *45*, 3471-3474.

[90]   J. L. Alonso, I. Pena, M. Eugenia Sanz, V. Vaquero, S. Mata, C. Cabezas, J. C. Lopez, *Chemical Communications* **2013**, *49*, 3443-3445.

[91]   V. Vaquero, M. E. Sanz, I. Peña, S. Mata, C. Cabezas, J. C. López, J. L. Alonso, *The Journal of Physical Chemistry A* **2014**, *118*, 2584-2590.

[92]   J. C. Lopez, J. L. Alonso, I. Peña, V. Vaquero, *Physical Chemistry Chemical Physics* **2010**, *12*, 14128-14134.

[93]   N. Kuş, A. Sharma, I. Peña, M. C. Bermúdez, C. Cabezas, J. L. Alonso, R. Fausto, *The Journal of Chemical Physics* **2013**, *138*, 144305.

[94]   J. L. Alonso, M. E. Sanz, J. C. Lopez, V. Cortijo, *Journal of the American Chemical Society* **2009**, *131*, 4320-4326.

[95]   J. L. Alonso, V. Cortijo, S. Mata, C. Perez, C. Cabezas, J. C. Lopez, W. Caminati, *Journal of Molecular Spectroscopy* **2011**, *269*, 41-48

[96]   J. C. Lopez, V. Cortijo, S. Blanco, J. L. Alonso, *Physical Chemistry Chemical Physics* **2007**, *9*, 4521-4527

[97]   C. Cabezas, Valladolid **2011**

[98]   C. Cabezas, A. Simao, C. Bermudez, M. Varela, I. Pena, S. Mata, R. Fausto, J. L. Alonso, *J Phys Chem A* **2013**, *117*, 4907-4915.

[99]   V. Cortijo, J. L. Alonso, J. C. López, *Chem. Phys. Lett.* **2008**, *466*, 214-218.

[100] H. Mitsuda, M. Miyazaki, I. B. Nielsen, P. Carcabal, C. Dedonder, C. Jouvet, S.-i. Ishiuchi, M. Fujii, *J. Phys. Chem. Lett.* **2010**, *1*, 1130-1133.

[101] S.-i. Ishiuchi, T. Asakawa, H. Mitsuda, M. Miyazaki, S. Chakraborty, M. Fujii, *The journal of physical chemistry. A* **2011**, *115*, 10363-10369.

[102] S.-i. Ishiuchi, H. Mitsuda, T. Asakawa, M. Miyazaki, M. Fujii, *Physical Chemistry Chemical Physics* **2011**, *13*, 7812-7820.

[103] P. Carcabal, L. C. Snoek, T. Van Mourik, *Molecular Physics* **2005**, *103*, 1633-1639.

[104] T. A. Legreve, J. R. Clarkson, T. S. Zwier, *The journal of physical chemistry. A* **2008**, *112*, 3911-3920.

[105] S. J. Martinez, J. C. Alfano, D. H. Levy, *Journal of Molecular Spectroscopy* **1992**, *156*, 421-430.

[106] L. Snoek, E. Robertson, R. Kroemer, J. Simons, *Chem. Phys. Lett.* **2000**, *321*, 49-56.

[107] G. Von Helden, I. Compagnon, M. Blom, M. Frankowski, U. Erlekam, J. Oomens, B. Brauer, R. Gerber, G. Meijer, *Physical Chemistry Chemical Physics* **2008**, *10*, 1248-1256.

[108] L. G. Rossato, V. M. Costa, R. P. Limberger, M. d. L. Bastos, F. Remião, *Food and chemical toxicology : an international journal published for the British Industrial Biological Research Association* **2011**, *49*, 8-16.

[109] K. Demyk, H. Mäder, B. Tercero, J. Cernicharo, J. Demaison, L. Margulès, M. Wegner, S. Keipert, M. Sheng, *Astronomy & Astrophysics* **2007**, *466*, 255-259.

[110] L. Coudert, B. Drouin, B. Tercero, J. Cernicharo, J.-C. Guillemin, R. A. Motiyenko, L. Margulès, *The Astrophysical Journal* **2013**, *779*, 119.

[111] M. Carvajal, L. Margulès, B. Tercero, K. Demyk, I. Kleiner, J. Guillemin, V. Lattanzi, A. Walters, J. Demaison, G. Wlodarczak, *Astronomy & Astrophysics* **2009**, *500*, 1109-1118.

[112] L. Margules, R. Motiyenko, K. Demyk, B. Tercero, J. Cernicharo, M. Sheng, M. Weidmann, J. Gripp, H. Mäder, J. Demaison, *Astronomy & Astrophysics* **2009**, *493*, 565-569.

[113]   R. Motiyenko, B. Tercero, J. Cernicharo, L. Margulès, *Astronomy & Astrophysics* **2012**, *548*, A71.

[114]   B. Tercero, L. Margulès, M. Carvajal, R. A. Motiyenko, T. Huet, E. Alekseev, I. Kleiner, J.-C. Guillemin, H. Møllendal, J. Cernicharo, *Astronomy & Astrophysics* **2012**, *538*, A119.

[115]   M. Cordiner, M. Palmer, C. Nixon, P. Irwin, N. Teanby, S. Charnley, M. Mumma, Z. Kisiel, J. Serigano, Y.-J. Kuan, *The Astrophysical Journal Letters* **2015**, *800*, L14.

[116]   A. M. Daly, C. Bermúdez, A. López, B. Tercero, J. C. Pearson, N. Marcelino, J. L. Alonso, J. Cernicharo, *The Astrophysical Journal* **2013**, *768*, 81.

[117]   A. Lopez, B. Tercero, Z. Kisiel, A. M. Daly, C. Bermudez, H. Calcutt, N. Marcelino, S. Viti, B. J. Drouin, I. R. Medvedev, C. F. Neese, L. Pszczolkowski, J. L. Alonso, J. Cernicharo, *Astronomy & Astrophysics* **2014**, *572*, A44.

[118]   A. Daly, L. Kolesniková, S. Mata, J. Alonso, *Journal of Molecular Spectroscopy* **2014**, *306*, 11-18.

[119]   L. E. Snyder, D. Buhl, B. Zuckerman, P. Palmer, *Physical Review Letters* **1969**, *22*, 679-681.

[120]   J. M. Hollis, F. J. Lovas, P. R. Jewell, *Astrophysical Journal* **2000**, *540*, L107-L110.

[121]   D. T. Halfen, A. J. Apponi, N. Woolf, R. Polt, L. M. Ziurys, *The Astrophysical Journal* **2006**, *639*, 237.

[122]   M. T. Beltrán, C. Codella, S. Viti, R. Neri, R. Cesaroni, *The Astrophysical Journal Letters* **2009**, *690*, L93.

[123]   J. K. Jørgensen, C. Favre, S. E. Bisschop, T. L. Bourke, E. F. v. Dishoeck, M. Schmalzl, *The Astrophysical Journal Letters* **2012**, *757*, L4.

CHAPTER II. INTRODUCTION

The present Doctoral Thesis incorporates the goals of the research project CTQ2010-19008 (Structure and interactions in Biomolecules) supported by Spanish "Ministerio de Ciencia e Innovación" upon "Grupo de Espectroscopia Molecular – GEM" from University of Valladolid. A wide range of research concerning the conformational and tautomeric behavior of biomolecules as well as its relation between structure and functionality has been executed between 2011 and 2015.

The present investigation has been focused primary on the elemental constituents of biomolecules, named as building blocks: amino acids, monosaccharides, or nitrogen bases. Our aim was characterizing their structure in detail in order to being able to understand their global behavior. Cellular recognition,[1-2] protein folding and unfolding,[3] sweetness of sugars[4-5] as well as the combination of nitrogen bases that form nucleic acids[6] are examples of processes that depend on the structure of these building blocks. As such, a detailed investigation in terms of conformations, and tautomerization is required in order to gain insight into the functionality of these relevant biological systems.

Generally, biomolecules are characterized by their structural high flexibility. The rotation of their single bonds rotations lead to different three dimensional structures that they can be stabilized. These forms are called conformer or conformation. Besides different conformations, the building blocks can exhibit tautomeric equilibrium: each tautomer is transformed into other tautomers by means of a hydrogen transposition. Nitrogen bases bare a clear example of this tautomerism (see section II.3).[7-10] Generally, the intrinsic stability of these tautomers and conformers is determined by their intramolecular interactions, predominantly, by the hydrogen bond interactions.[11-19]

These biomolecules naturally occurs in condensed phases, where their conformational behavior is not only affected by the aforementioned intramolecular interactions, but also by the intermolecular interactions. The latter interactions could even alter the form of the biomolecules, as occur in amino acids, which are stabilized as zwitterions instead of being neutrals.[20-21] In zwitterions, the amine is positively charged (it becomes a quaternary amine) and the carboxylic group is negatively owing to its deprotonation. As such, isolation conditions, where only intramolecular interactions dominate the stabilization, are required in order to explore the conformational distribution and the tautomeric equilibrium intrinsic to biomolecules. This condition is fulfilled using gas phase experiments.

As it will be explained in Chapter III, the synergy between *ab initio* calculation and the techniques that combines laser ablation (LA) with Fourier transform microwave spectroscopy (FTMW) have been proved to be ideal for unveiling the conformational behavior of biomolecules in gas phase.[22] Equipped with the capacity of volatilizing substances with high melting point by laser ablation as well as with the high resolution (sub-Doppler)

and sensitivity associated with the FTMW instrument, the first studies of several isolated biomolecules were possible by rotational spectroscopy. To date, the conformational behavior of sugars,[23-28] amino acids,[29-43] nitrogen bases,[7-10] neurotransmitters,[44-45] have been explored.

The present dissertation reports on several conformational and tautomeric studies that investigate different aspects of biomolecules: sweetness of sugars (Chapter IV-V), the structure of the DNA sugar (deoxyribose, Chapter VI), conformational characteristics of amino sugars (Chapter VII), tautomerism of amino acids (Chapter VIII), microsolvation of nucleobases (Chapter IX) and conformational panorama of neurotransmitters (Chapter X). In the following sections, further details of each topic are described.

Besides exploring the conformational and tautomeric behavior of biomolecules, some research has been done regarding the identification of molecules in the interstellar medium (ISM). This identification requires from precise spectroscopic parameters obtained in the laboratory. So far, more than 180 molecules have been detected[46] but a great deal of species remains unidentified, including their vibrational excited states and their isotopologues.[47] For this purpose, our laboratory upgraded the frequency domain instruments in the microwave, millimeterwave and sub-millimeterwave

spectral regions that the astronomical observatories register (see sections III.1.4), in order to provide new rotational data of molecules of astronomical interest. As a result of this improvements and a vast spectroscopic work, more than 3000 transitions belonging to vibrational excited states of ethyl and vinyl cyanides (Annexes I and II) has been detected in the ISM. Furthermore, propenal (acrolein), considered a "sugar of the space"[48] and closely related to amino acid synthesis[49] was analyzed in detail (Chapter XI) in order to facilitate the rotational parameters required to confirm the tentative identification of this molecule in the ISM[50]. Methyl isocyanate (CH_3OCN) is another molecule that may be present in the ISM since similar molecules have been already detected.[51-54] A detail analyisis of its rotational spectrum up to 350GHz is presented in Chapter XII.

In this dissertation not only pure rotational studies of biomolecules were treated but also we have been introduced to the analysis of illicit drugs. An instrument that combines laser ablation and time-of-flight mass spectrometry (LA-TOF-MS) was built with the aim of being able to analyze drugs from the solid avoiding tedious pretreatments. In Chapter XIII the successful analysis of the illicit drug MDMA based on its laser ablated mass spectrum is presented.

II.1. SUGARS

Carbohydrates are the main source of energy for human beings, thus, their intake is essential. As nutrients, they are involved in a numerous biological processes.[55] Due to their relevance, a large number of investigations can be found in the literature that are captured in diverse journals which are specialized in different aspects of their study.[56]
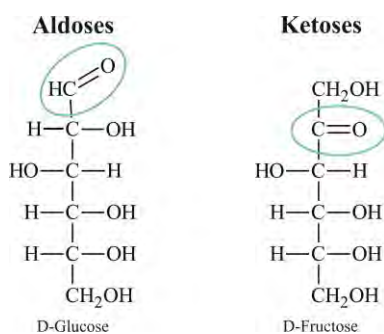
FIGURE II.I: *Fisher projection of the two main representatives of aldoses and ketoses: D-glucose and D-fructose.*

Complex carbohydrates are built by sequences of monosaccharides, named also as simple sugars, which are normally associated to the sweet flavor. These elemental sugars can be stabilized in multitude of configurations. In function of the position of their carbonyl group sugars are divided in aldoses (aldehyde group) and ketoses (ketone group), whose main representatives are depicted in Figure II.1. Although they are often represented in linear configuration (Fisher projections), in their chemical environment are stabilized as rings. These rings are formed by four carbon atoms and one oxygen (furanores) or five carbons one oxygen (pyranoses, see examples of Figure II.2). During the cyclization process, the carbonyl group is reduced

to alcohol forming two new isomers: the anomers α and β (see Figure II.2.b). The most stable distribution of pyranose rings is the chair type configuration[57] either as $^2C_5$ or $^5C_2$, (superscript indicates the carbon that is above the reference plain and the subscript, the one that is below,[58] see Figure II.2.c).

Several spectroscopic methods have been employed to explore the relative stability of sugar configurations (NMR,[59-60] VROA,[61] X Ray[62-63]). On the basis of their initial results, anomeric effect,[64-65] $\Delta 2$ effect,[66] or gauche effect[67] theories have been proposed to justify sugars configuration preferences. Nevertheless, these methods do not usually have resolution enough to observe their conformational behavior, or the experiments were not conducted under isolation conditions, where intermolecular interactions, that may alter their
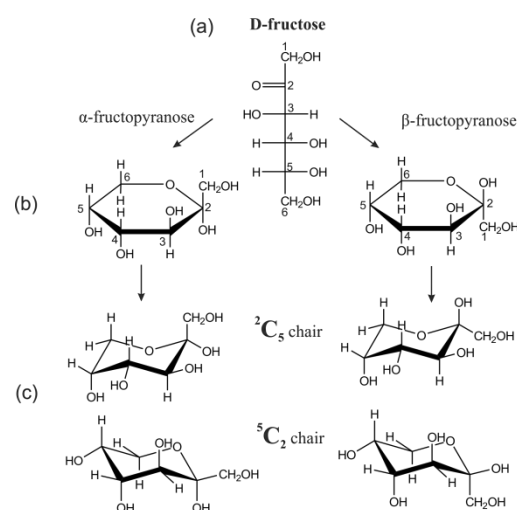
FIGURE II.2. *Esquema de las cofiguraciones de la D-fructosa. (a) Proyección de Fisher. (b) Proyección de Harworth de las formas piranosas. (c) Distintas configuraciones de la silla.*
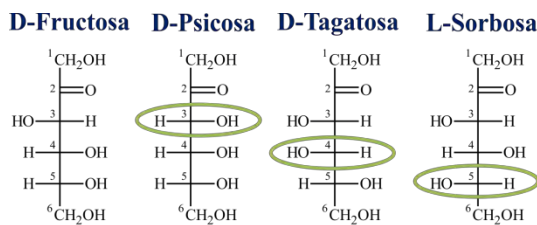
FIGURE II.3: *Fisher projection of ketohexoses. Green ellimpses indicate the asymmetric carbon that changes the configuration with regard to D-fructose.*

stability, are avoided. As it is explained in section III.1, the combination of laser ablation with Fourier transform microwave spectroscopy is suitable to unveil the intrinsic conformational behavior of sugars, hence to explore the hydrogen bond interactions as well as the stereoelectronic effects mentioned above. So far, it have been accomplished the study of aldoses like: erythrose,[23] xylose[24] and glucose.[25]

The aspect of the sweet flavor of sugars, which is related to their structure,[5] has yet to be explored on the basis of the new capabilities of unveiling the conformational behavior of sugars. Long time, numerous investigations have been performed in order to identify the requirements that must contain a substance to be sweet.[5] To date, everything seems to indicate a close relation between the structure and the sweetness. The most expanded theory was postulated by Shallenberger and Acree,[4] where they established that sweetness depends on the strength of the two H-bond interactions that are formed between the sweetener and the biological receptor. (Figure II.4.a). This initial theory was soon modified adding a third binding site, γ site (Figure II.4.b).[68] Most recently, based on a hyperpotent sweetener study, Tinti and

Nofre[69] stated that sweet receptors are capable of being linked through up to eight intermolecular interactions. However, substances to be sweet do not have to contain the homologous eight binding sites, although the more linkages the more sweet. It is worth mentioning that at the time these theories were proposed, the experimental information available was unable to offer much detail concerning the sweeteners conformational behavior that could confirm their postulations.

In the present dissertation, we have focused on the exploration of the conformational behavior of ketohexoses **D-fructose**, **D-tagatose**, **D-psicose** and **L-sorbose** (Figure II.3), and their relation between structure and sweetness. This group of sugars represents an interesting group of analysis in terms of sweetness behavior. All of them are epimers of D-fructose: they only differ in the configuration of an asymmetric carbon. However, D-fructose is almost twice as sweet as the rest, which have the same sweetness degree as table sugar. Taking the advantage that all of them are sweet, one can try to identify the possible grucophores based on the common conformational
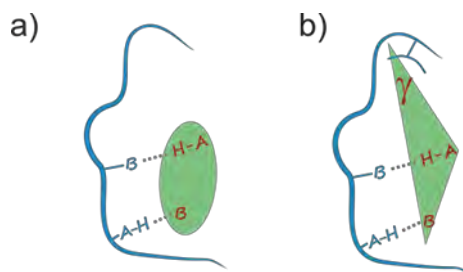
FIGURE II.4: *Representation of sweetness theories. Receptor scheme is in blue, sweetener in red and hydrogen bond interactions are point out with grey dashed lines. a) Shallenberger and Acree theory. b) Sweetness triangle formed with the new γ site.*

charascteristics they posses. In Chapter IV the rotational spectrum ofD-fructose is analyzed in order to unveil its conformational behavior. The rotational studies of D-Tagatose, D-Psicose and L-sorbose are presented in Chapter V. In both sections, the conformational behavior is explored in terms of their sweetness. There, the common conformational signatures of their conformations are analyzed in order to identify their glucophores. Moreover, the conformational differences of these sugars are discussed with the aim of rationalize their different degree of sweetnes (D-Fructose is twice as sweet as the rest)

In the following sugar sections, the conformational changes that suffer a sugar produced by the elimination of an hydroxyl group (Chapter VI, of **2-deoxyribose**) of by the substitution of one of its hydroxyl group by an amine group (see Chapter VII of **D-glucosamine**) will be investigated.

The change between ribose and 2-deoxyribose consist on the elimination of the hydroxyl group in position two. It seems a simple change, but it is one of the main differences between the nucleic acids RNA and DNA, whose functions are very different.

Structurally, the elimination of an hydroxyl group might change the conformational behavior of the sugar since not all intramolecular H-bonds can be formed, leading to weakening of the H-bond intermolecular network, thus, altering the energy of the different conformations. The study of 2-deoxyribose will provide information regarding the influence of a hydroxyl group in the conformational stability of these sugars.

As it was mentioned previously, our group has unveiled recently the conformational behavior of D-glucose,[25] which is the monosaccharide par excellence. In this work, four conformers of α-D-glucopyranose and three of β-D-glucopyranose were identified. In these conformers, both stereoelectonic effects (anomeric and Gauche effects) and H-bond interactions were studied. On the basis of these results, the conformational study of amino-sugars were initiated with D-glucosamine. This group of sugars is relevant since the substitution of an hydroxyl group by an amino groups is one of ways of binding sugars to proteins. Moreover, D-glucosamine is essential for the generation of nitrogen compounds as glycoproteins or glycolipids.[70]

II.2. AMINO ACIDS

The structure and folding of proteins depends on the conformational behavior of its elemental constituents, the amino acids.[3] The conformational behavior of the 20 natural amino acids has been object of investigation in our laboratory since 2002 when it was published the first results of proline.[29] LA-MB-FTMW technique[37, 71-72] allowed us to unveil the conformational characteristics of these relevant biological systems. Some results worth mentioning
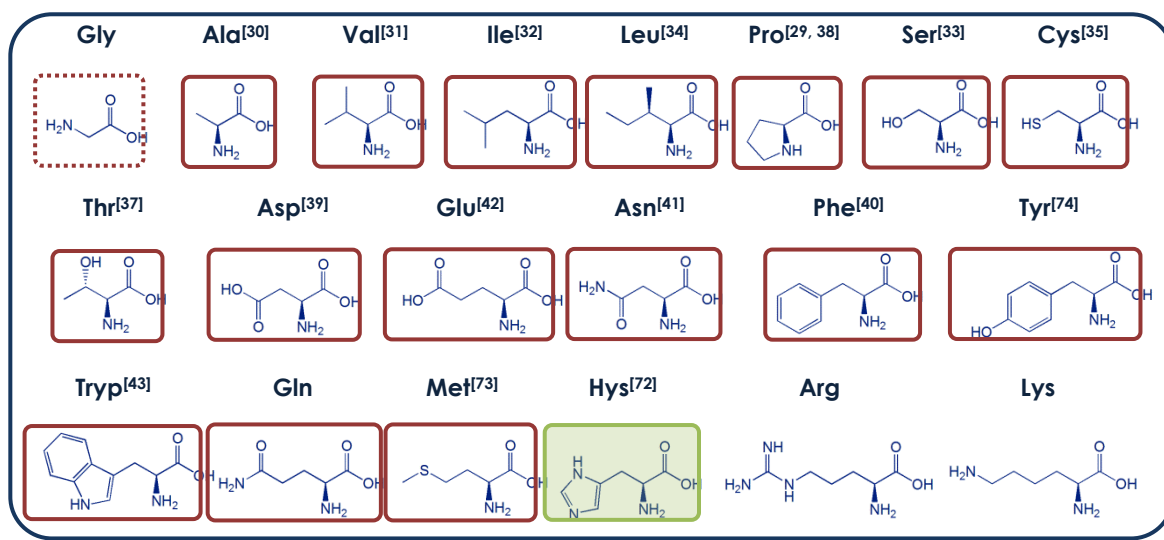
FIGURE II.5: *20 natural amino acids. Those that are pointed out with a continuous red square were studied in our group; if the line is dashed, it was analyzed in other laboratories. The conformational analyisis of histidine (Hys), highlighted in green, is explored in the present dissertation.*

include, for instance, the study of methionine with eight conformers observed, [73] or the six different structures of serine.[33] The conformational information provided by these investigations is useful not only to gain insight in the functionality of these molecules, but the spectroscopic data of each of these species permits moreover their further detection in the ISM.

Provided that the conformational panorama of the natural amino acids is almost concluded (see Figure II.5), some common characteristics of these biomolecules were observed. In order to explain them, we will distinguish between those amino acids with polar or non-polar side chains. Non-polar side chain amino acids, by definition, cannot have any functional group that can form any H-bond intramolecular interaction except for the α-amino and carboxyl groups. Thus, its conformational preferences will be dominated by the H-bond interaction between these two groups (see Figure II.6 where the three types of possible hydrogen bonds are shown). Based on our rotational research, non-polar amino acids are preferentially stabilized by H-bonds type I and II, being the first ones more stable. So far, type III conformers were not observed. It has been proposed that type III species relax to type I ones through the rotation of the -COOH torsion angle, owing to the low energy of the barrier that interconverts them during the supersonic expansion.[75-78] As such, unless the rotation is blocked, as for Ac₃C,[79] type III conformers will not be observed for non-polar amino acids.
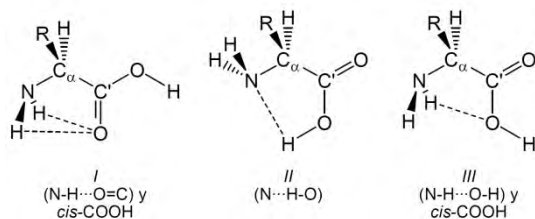
FIGURE II.6: *Three posible H-bond interactions between amino and carboxylic groups.*

Polar side chain amino acids, in contrast, can establish intramolecular hydrogen bonds between their polar chain and the amino and carboxylic groups. These interactions might alter substantially their conformational behavior since the hyper-potential surface may change stabilizing type III species more than type I ones[37] or elevating the interconversion barrier between type I and type III conformers which allows the observation of type III species.[35, 39]

To date, none of the amino acids studied contained a side chain in tautomeric equilibrium. In the present dissertation, we explore in Chapter VIII the influence of tautomerism in the conformational behavior of a natural amino acid for the first time. This amino acid is **histidine** (His), one of the two that present this singularity. Its side chain is formed by a methyl imidazol group that is in tautomeric equilibrium between its forms $N_\varepsilon H$ y $N_\delta H$ (see Figure II.7). The versatility resulting from this tautomeric equilibrium of histidine makes it extremely important in **biological processes**.[80-83]
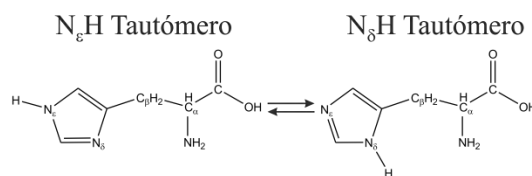
FIGURE II.7: *Tautomeric equilibrium of histidine*

The rotational study of histidine presents an important drawback: the presence of three non-equivalent ^{14}N nuclei. The non-spherical charge distribution of the ^{14}N (I=1) creates an electric nuclear quadrupole moment that interacts with the electric field gradient generated at the site of the quadrupole nuclei by the rest of the electric and nuclear charges of the molecule. This interaction gives rise to a coupling between the ^{14}N nuclear spins with the overall angular momentum, which results in a characteristic hyperfine structure observable in the rotational spectrum. The analysis of a quadrupole hyperfine structure arising from three non-equivalent ^{14}N nuclei is of utmost complexity and only a few examples can be found in the literature.[10]

II.3. MICROSOLVATION OF NITROGEN BASES

Likewise histidine, the five nitrogen bases constituents of the nucleic acids DNA and RNA can present tautomeric equilibria. The secondary structure of these acids is hold due to the formation of hydrogen bonds between pairs of nitrogen bases.[6] In so doing, altering the tautomerism of these nitrogen bases, intermolecular interactions can be affected, which could led to mutation processes in beings.[84-85] For this reason the study of the tautomeric equilibrium of nitrogen bases is of utmost importance to understand their biological functionality.

To date, both the purine base guanine (G) [9] and the three pyrimidinic bases citosine (C), [10] thymine (T) [7] and uracil (U) [8] have been probed

EAt	EAc	KA	KIt	KIc
0cm⁻¹ [10]	165cm⁻¹	40cm⁻¹	290cm⁻¹	--
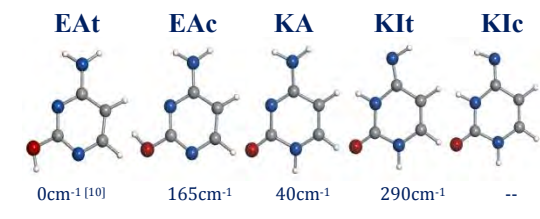
FIGURA I.8: *Five tautomeric species observed for cytosine. The experimental Gibbs energies are shown below each figure. (KIc could not be calculate provided its low intensity in the spectrum.)*

by rotational spectroscopy under isolation conditions were the interactions with the environment do not have influence in the equilibrium. It is worth mentioning the results obtained for the pyrimidinic cytosine:[10] all five tautomeric forms were identified being the most abundant the enol-amine trans (EAt). This is in contrast to what happen in condensed phases and in DNA where the tautomer found is the canonic form keto amino (KA)[6, 86-87]. As mentioned early in this Chapter, intermolecular hydrogen bond interactions with the solvent (water) may alter the tautomeric equilibrium, leading to stabilizing one tautomer against the rest. In Chapter IX we were wondering if a single water molecule is enough to overstabilize KA versus EAt.

To explore how water affects to the conformational / tautomeric stability, some microsolvation studies were previously carried out in our laboratory. Microsolvation is that situation where a molecular system is surrounded by a small number of water molecules. To date, it was explored the influence of one and two water molecules over the amino acids glycine[88-89] and alanine[90] by means of LA-MB-FTMW technique. Applying the same procedure, the monohydrates of purine bases thymine and uracil were characterized.

On the basis of the group experience on solvation of biomolecules, Chapter IX describes the investigation concerning the influence of a water molecule in the tuatumerism of **cytosine**. The goal was unveiling if only one water molecule is able to invert the equilibrium towards the keto specie instead of the enolic form. Moreover, it will be explored which of the multiple binding sites of cytosine is water firstly linked.

II.4. NEUROTRANSMITTERS

Neurotransmitters are molecules in charge of the communication between neurons through the synaptic space. They have diverse origins as shown in the Figure II.10. In general all of them are characterized by its high flexibility that might lead to a great deal of possible conformations. A comprehensive research regarding the

conformational panorama of neurotrasnmitters may help to understand their activity as well as the recognizing process in the post symnactic cell. .In the literature multiple electronic spectroscopic investigations can be found.[91-98]

The first studies performed in our laboratory concerning the conformational behavior of
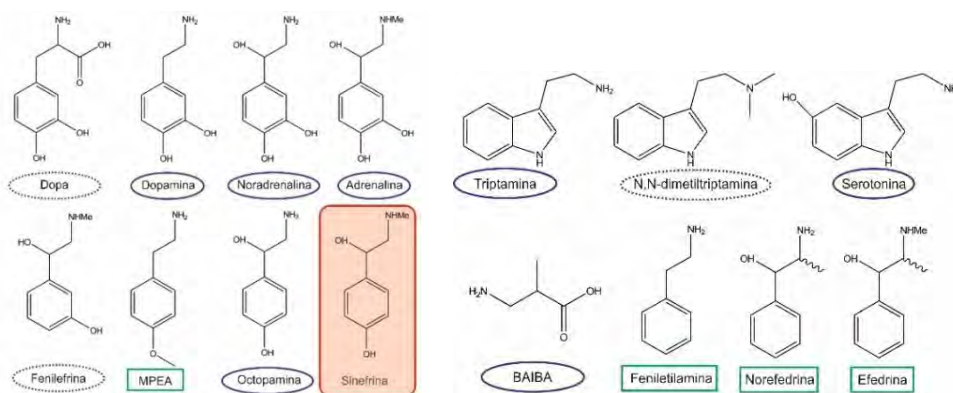
FIGURA I.14: *Ejemplos de neurotransmisores estudiados en el laboratorio.[44-45, 99-105] Marcados en elipse azul los analizados mediante la técnica MB-FTMW combinada con ablación láser y los recuadrados en verde combinada con calentamiento. Los que están en línea punteada se encuentra actualmente bajo estudio. El estudio de la sinefrina, sombreada en rojo, se encuentra recogido en la presente memoria.*

neurotrasmitters were those of phenylethylamine[99] and p-metoxyphenylethylamine.[100] Following them several molecules have been investigated: tryptamine,[101] ephedrine,[102] serotonin,[44] dopamine,[45] adrenaline,[103] BAIBA,[104] etc. (see further examples in Figure II.10) In the same research line, in Chapter XI is presented the conformational behavior of **synephrine** Its structure is analogous to adrenalin but with only one hydroxyl group linked to the aromatic ring. Synephrine is commercially used as grass reductant, provided its big stimulant power in human beings.

II.5. OTHER STUDIES

I.5.1 Species of astrochemical interest

The ultimate goal of astrochemistry is to understand the formation of molecules in the universe; as such, it is necessary to know the substances that compose it. So far, more than 180 molecules were detected in the ISM from comparing the spectra taken in astronomical observatories with the spectroscopic parameters obtained in laboratories. There is still a great deal of transitions that has yet to be identified (U-lines). In the registers of 30m radio telescope IRAM (Pico Veleta, Spain), although 4000 transitions were identified,[106-111] there are more than 8000 U-lines remaining.[47] Owing to ALMA developing project (Atacama Large Millimeter/submillimeter Array), where there have already been detected some molecules in new regions of the ISM, the sensitivity of the observations will be highly enhanced, which may lead to significantly increase the number of U-lines, lying the line confusion limit. These lines could belong both to molecules not yet studied in laboratories as well as to molecules already observed but whose vibrationally excited states, isotopologues or higher energy conformations but there are not still precise spectroscopic parameters.

The detection of the latter is moreover essential to obtain information about the conditions of the ISM region, such as nebulous temperatures, opacity or presence of high energy radiation sources.[112-113]

In order to provide the rotational parameters precise enough to identify U-lines, in our laboratory, it have been upgraded the frequency domain spectrometers (see Chapter III.1.3), which are able to measure up to frequencies close to 1 THz.[114] In so doing, the spectra from observatories can be directly compared to those taken in our laboratory.

Appling these techniques, the pure rotational spectra of the vibrational excited states of **ethyl and vinyl cyanide** have been analyzed (see Appendixes I and II, respectively). These substances are very abundant in the ISM. Owing to these works, it was detected pure rotational transitions belonging to vibrational excited states of energies of $600cm^{-1}$ in the in the star forming region of Orion KL.

Besides molecules already detected in the ISM, the analysis of substances susceptible to be in the space was performed in order to provide the spectroscopic parameters required for its identification. Chapter XI and Chapter XII describe the analysis of **propenal** and **methyl isocyanate**, respectively.

Propenal ($CH_2-CH-CHO$) is the simplest unsaturated aldehyde. It is related to amino acids[49] synthesis and to sugar decomposition.[26, 115] As aldehyde it is consider as a sugar of the space.[48] Some aldehydes have been already detected in the

ISM.[50, 116-119]. While more than 40 transitions have been reported in different regions of the space for glycoladehyde, for propenal, solely two transitions were observed in Sagitarius B2[50]. Providing that the sensitivity of the observations is continuously increasing, further detection of propenal transtions are possible, including those belonging to vibrational excited states, its isotopologues or its higher energy isomer (cis). Chapter XI is dedicated to a comprehensive rotational analysis of all these species.

Methyl isocyanate (CH_3OCN) is another molecule that can be detected in the ISM, since other species of similar characteristics have already been observed; isocyanic acid or fulminic acid were reported in different regions of the ISM.[51-54] As such, we have analyzed the rotational spectrum of the torsional ground state of CH_3OCN up to 350GHz (Chapter XII).

I.5.2. Illicit drug analysis by LA-TOF-MS

Analysis of illicit drugs rises as an interesting field of work given the high social impact presented by drugs in the modern society. Direct laser ablation of solid compounds enables their analysis without sampling or preparation procedures. For that purpose, we have constructed an experimental setup that combines laser ablation with time-of-flight mass spectrometry and ulteriorly perform studies on the mass spectra of such drugs as MDMA, commonly known as ecstasy. Analysis of the observed fragmentation pattern in mass spectra

may   elucidate   upon   the   ablation-induced photofragmentation   phenomena   produced   by ablation, which differs from those previously observed with conventional ionization methods.

II.6. REFERENCES

[1]   J. M. Lehn, *Nobel Lecture* **1987**, *8*, 444.

[2]   M. J. Zigmond, *Fundamental Neuroscience*, Academic Press: London, **1998**.

[3]   K. A. Dill, H. S. Chan, *Nat Struct Mol Biol* **1997**, *4*, 10-19.

[4]   R. S. Shallenberger, T. E. Acree, *Nature* **1967**, *216*, 480-482.

[5]   G. G. Birch, R. S. Shallenberger, *C R C Critical Reviews in Food Science and Nutrition* **1976**, *8*, 57-95.

[6]   J. D. Watson, F. H. C. Crick, *Nature* **1953**, *171*, 737-738.

[7]   J. C. Lopez, M. I. Peña, M. E. Sanz, J. L. Alonso, *Journal of Chemical Physics* **2007**, *126*.

[8]   V. Vaquero, M. E. Sanz, J. C. Lopez, J. L. Alonso, *Journal of Physical Chemistry A* **2007**, *111*, 3443-3445.

[9]   J. L. Alonso, I. Peña, J. C. Lopez, V. Vaquero, *Angewandte Chemie-International Edition* **2009**, *48*, 6141-6143.

[10]   J. L. Alonso, V. Vaquero, I. Peña, J. C. López, S. Mata, W. Caminati, *Angewandte Chemie* **2013**, *48*, 5934-5936.

[11]   S. Antolínez, J. C. López, J. L. Alonso, *Angewandte Chemie International Edition* **1999**, *38*, 1772-1774.

[12]   M. E. Sanz, J. C. López, J. L. Alonso, *Chemistry – A European Journal* **1999**, *5*, 3293-3298.

[13]   M. E. Sanz, A. Lesarri, J. C. López, J. L. Alonso, *Angewandte Chemie International Edition* **2001**, *40*, 935-938.

[14]   J. L. Alonso, S. Antolínez, S. Blanco, A. Lesarri, J. C. López, W. Caminati, *Journal of the American Chemical Society* **2004**, *126*, 3244-3249.

[15]   S. Blanco, J. C. López, A. Lesarri, W. Caminati, J. L. Alonso, *ChemPhysChem* **2004**, *5*, 1779-1782.

[16]   W. Caminati, J. C. López, J. L. Alonso, J.-U. Grabow, *Angewandte Chemie International Edition* **2005**, *44*, 3840-3844.

[17]   E. J. Cocinero, R. Sánchez, S. Blanco, A. Lesarri, J. C. López, J. L. Alonso, *Chem. Phys. Lett.* **2005**, *402*, 4-10.

[18]   P. Ottaviani, W. Caminati, L. B. Favero, S. Blanco, J. C. López, J. L. Alonso, *Chemistry – A European Journal* **2006**, *12*, 915-920.

[19]   J. C. López, W. Caminati, J. L. Alonso, *Angewandte Chemie International Edition* **2006**, *45*, 290-293.

[20]   T. J. Kistenmacher, G. A. Rand, R. E. Marsh, *Acta Crystallographica Section B* **1974**, *30*, 2573-2578.

[21]   C. H. Gorbitz, B. Dalhus, *Acta Crystallographica Section C* **1996**, *52*, 1754-1756.

[22]   J. L. Alonso, J. C. López, Springer Berlin Heidelberg, **2015**, pp. 1-67.

[23]   C. Cabezas, I. Peña, A. M. Daly, J. L. Alonso, *Chemical Communications* **2013**, *49*, 10826-10828.

[24]   I. Peña, S. Mata, A. Martín, C. Cabezas, A. M. Daly, J. L. Alonso, *Physical Chemistry Chemical Physics* **2013**, *15*, 18243-18248.

[25]   J. L. Alonso, M. A. Lozoya, I. Peña, J. C. Lopez, C. Cabezas, S. Mata, S. Blanco, *Chemical Science* **2014**, *5*, 515-522.

[26]   C. Bermúdez, I. Peña, C. Cabezas, A. M. Daly, J. L. Alonso, *Chemphyschem* **2013**, *14*, 893-895.

[27]   I. Peña, E. J. Cocinero, C. Cabezas, A. Lesarri, S. Mata, P. Écija, A. M. Daly, Á. Cimas, C. Bermúdez, F. J. Basterretxea, S. Blanco, J. A. Fernández, J. C. López, F. Castaño, J. L. Alonso, *Angewandte Chemie International Edition* **2013**, *52*, 11840-11845.

[28]   I. Peña, L. Kolesnikova, C. Cabezas, C. Bermúdez, M. Berdakin, A. Simao, J. L. Alonso, *Physical Chemistry Chemical Physics* **2014**, *16*, 23244-23250.

[29]   A. Lesarri, S. Mata, E. J. Cocinero, S. Blanco, J. C. Lopez, J. L. Alonso, *Angewandte Chemie-International Edition* **2002**, *41*, 4673-4676.

[30]   S. Blanco, A. Lesarri, J. C. Lopez, J. L. Alonso, *Journal of the American Chemical Society* **2004**, *126*, 11675-11683.

[31]   A. Lesarri, E. J. Cocinero, J. C. Lopez, J. L. Alonso, *Angewandte Chemie-International Edition* **2004**, *43*, 605-610.

[32]   A. Lesarri, R. Sanchez, E. J. Cocinero, J. C. Lopez, J. L. Alonso, *Journal of the American Chemical Society* **2005**, *127*, 12952-12956.

[33]   S. Blanco, M. E. Sanz, J. C. Lopez, J. L. Alonso, *Proceedings of the National Academy of Sciences of the United States of America* **2007**, *104*, 20183-20188.

[34]   E. J. Cocinero, A. Lesarri, J. U. Grabow, J. C. Lopez, J. L. Alonso, *Chemphyschem* **2007**, *8*, 599-604.

[35]   M. E. Sanz, S. Blanco, J. C. Lopez, J. L. Alonso, *Angewandte Chemie-International Edition* **2008**, *47*, 6216-6220.

[36]   C. Perez, S. Blanco, J. C. Lopez, J. L. Alonso, in *IBBI*, Valladolid, **2008**.

[37]   J. L. Alonso, C. Perez, M. E. Sanz, J. C. Lopez, S. Blanco, *Physical Chemistry Chemical Physics* **2009**, *11*, 617-627.

[38]   S. Mata, V. Vaquero, C. Cabezas, I. Peña, C. Perez, J. C. Lopez, J. L. Alonso, *Physical Chemistry Chemical Physics* **2009**, *11*, 4141-4144.

[39]   M. E. Sanz, J. C. Lopez, J. L. Alonso, *Physical Chemistry Chemical Physics* **2010**, *12*, 3573-3578.

[40]   C. Perez, S. Mata, S. Blanco, J. C. Lopez, J. L. Alonso, *Journal of Physical Chemistry A* **2011**, *115*, 9653-9657.

[41]   C. Cabezas, M. Varela, I. Peña, S. Mata, J. C. Lopez, J. L. Alonso, *Chemical Communications* **2012**, *48*, 5934-5936.

[42]   I. Peña, M. Eugenia Sanz, J. C. Lopez, J. L. Alonso, *Journal of the American Chemical Society* **2012**, *134*, 2305-2312.

[43]   M. E. Sanz, C. Cabezas, S. Mata, J. L. Alonso, *The Journal of Chemical Physics* **2014**, *140*, -.

[44]   C. Cabezas, M. Varela, I. Peña, J. C. Lopez, J. L. Alonso, *Physical Chemistry Chemical Physics* **2012**, *14*, 13618-13623.

[45]   C. Cabezas, I. Peña, J. C. López, J. L. Alonso, *The Journal of Physical Chemistry Letters* **2013**, *4*, 486-490.

[46]   E. Herbst, J. T. Yates, *Chemical Reviews* **2013**, *113*, 8707-8709.

[47]   B. Tercero, J. Cernicharo, J. Pardo, J. Goicoechea, *Astronomy & Astrophysics* **2010**, *517*, A96.

[48]   L. E. Snyder, D. Buhl, B. Zuckerman, P. Palmer, *Physical Review Letters* **1969**, *22*, 679-681.

[49]   J. E. Van Trump, S. L. Miller, *Science* **1972**, *178*, 859-860.

[50]   J. M. Hollis, P. R. Jewell, F. J. Lovas, A. Remijan, H. Mollendal, *Astrophysical Journal* **2004**, *610*, L21-L24.

[51]   S. Brünken, C. A. Gottlieb, M. C. McCarthy, P. Thaddeus, *The Astrophysical Journal* **2009**, *697*, 880.

[52]   N. Marcelino, J. Cernicharo, B. Tercero, E. Roueff, *The Astrophysical Journal Letters* **2009**, *690*, L27.

[53]   N. Marcelino, S. Brünken, J. Cernicharo, D. Quan, E. Roueff, E. Herbst, P. Thaddeus, *A&A* **2010**, *516*, A105.

[54]   S. Brünken, A. Belloche, S. Martín, L. Verheyen, K. M. Menten, *A&A* **2010**, *516*, A109.

[55]   B. Wang, G.-J. Boons, Wiley, **2011**.

[56]   *Advances in Carbohydrate Chemistry and Biochemistry, Carbohydrate Research, Journal of Carbohydrate Chemistry, etc.*

[57]   R. E. Reeves, *Journal of the American Chemical Society* **1950**, *72*, 1499-1506.

[58]   A. D. McNaught, *Carbohydr Res* **1997**, *297*, 1-92.

[59]   R. U. Lemieux, J. D. Stevens, *Canadian Journal of Chemistry* **1966**, *44*, 249-262.

[60]   S. Angyal, V. Pickles, *Australian Journal of Chemistry* **1972**, *25*, 1695-1710.

[61]   Z. Q. Wen, L. D. Barron, L. Hecht, *Journal of the American Chemical Society* **1993**, *115*, 285-292.

[62]   S. H. Kim, Rosenste.Rd, *Acta Crystallographica* **1967**, *22*, 648-&.

[63]   S. Takagi, R. D. Rosenstein, *Carbohydrate Research* **1969**, *11*, 156-158.

[64]   E. Juaristi, G. Cuevas, *Tetrahedron* **1992**, *48*, 5019-5087.

[65]   C. L. Perrin, K. B. Armstrong, M. A. Fabian, *Journal of the American Chemical Society* **1994**, *116*, 715-722.

[66]   T. D. Buley, A. M. Striegel, *Carbohydrate Polymers* **2010**, *79*, 241-249.

[67]   S. Wolfe, *Accounts of Chemical Research* **1972**, *5*, 102-111.

[68]   L. B. Kier, *Journal of Pharmaceutical Sciences* **1972**, *61*, 1394-1397.

[69]   C. Nofre, J.-M. Tinti, *Food Chemistry* **1996**, *56*, 263-274.

[70]   S. Roseman, *Journal of Biological Chemistry* **2001**, *276*, 41527-41542.

[71]   A. Lesarri, S. Mata, J. C. Lopez, J. L. Alonso, *Rev. Sci. Instrum.* **2003**, *74*, 4799-4804.

[72]   C. Bermúdez, S. Mata, C. Cabezas, J. L. Alonso, *Angewandte Chemie International Edition* **2014**, *53*, 11015-11018.

[73]   I. Peña, Valladolid **2011**.

[74]   C. Pérez, Valladolid **2010**.

[75]   R. S. Ruoff, T. D. Klots, T. Emilsson, H. S. Gutowsky, *The Journal of Chemical Physics* **1990**, *93*, 3142-3150.

[76]   P. D. Godfrey, R. D. Brown, F. M. Rodgers, *Journal of Molecular Structure* **1996**, *376*, 65-81.

[77]   P. D. Godfrey, R. D. Brown, *Journal of the American Chemical Society* **1998**, *120*, 10724-10732.

[78]   G. M. Florio, R. A. Christie, K. D. Jordan, T. S. Zwier, *Journal of the American Chemical Society* **2002**, *124*, 10236-10247.

[79]   A. I. Jiménez, V. Vaquero, C. Cabezas, J. C. López, C. Cativiela, J. L. Alonso, *Journal of the American Chemical Society* **2011**, *133*, 10621-10628.

[80]   J. C. Kendrew, R. E. Dickerson, B. E. Strandberg, R. G. Hart, D. R. Davies, D. C. Phillips, V. C. Shore, *Nature* **1960**, *185*, 422-427.

[81]   M. F. Perutz, M. G. Rossmann, A. F. Cullis, H. Muirhead, G. Will, A. C. T. North, *Nature* **1960**, *185*, 416-422.

[82]   A. Volbeda, M.-H. Charon, C. Piras, E. C. Hatchikian, M. Frey, J. C. Fontecilla-Camps, *Nature* **1995**, *373*, 580-587.

[83]   S. Dementin, V. Belle, P. Bertrand, B. Guigliarelli, G. Adryanczyk-Perrier, A. L. De Lacey, V. M. Fernandez, M. Rousset, C. Leger, *Journal of the American Chemical Society* **2006**, *128*, 5209-5218.

[84]   M. D. Topal, J. R. Fresco, *Nature* **1976**, *263*, 285-289.

[85]   L. C. Sowers, G. V. Fazakerley, R. Eritja, B. E. Kaplan, M. F. Goodman, *Proceedings of the National Academy of Sciences* **1986**, *83*, 5434-5438.

[86]   C. E. Crespo-Hernández, B. Cohen, P. M. Hare, B. Kohler, *Chemical Reviews* **2004**, *104*, 1977-2020.

[87]   M. K. Shukla, J. Leszczynski, *Journal of Biomolecular Structure and Dynamics* **2007**, *25*, 93-118.

[88]   J. L. Alonso, E. J. Cocinero, A. Lesarri, M. E. Sanz, J. C. Lopez, *Angewandte Chemie-International Edition* **2006**, *45*, 3471-3474.

[89]   J. L. Alonso, I. Pena, M. Eugenia Sanz, V. Vaquero, S. Mata, C. Cabezas, J. C. Lopez, *Chemical Communications* **2013**, *49*, 3443-3445.

[90]   V. Vaquero, M. E. Sanz, I. Peña, S. Mata, C. Cabezas, J. C. López, J. L. Alonso, *The Journal of Physical Chemistry A* **2014**, *118*, 2584-2590.

[91]   H. Mitsuda, M. Miyazaki, I. B. Nielsen, P. Carcabal, C. Dedonder, C. Jouvet, S.-i. Ishiuchi, M. Fujii, *J. Phys. Chem. Lett.* **2010**, *1*, 1130-1133.

[92]   S.-i. Ishiuchi, T. Asakawa, H. Mitsuda, M. Miyazaki, S. Chakraborty, M. Fujii, *The journal of physical chemistry. A* **2011**, *115*, 10363-10369.

[93]   S.-i. Ishiuchi, H. Mitsuda, T. Asakawa, M. Miyazaki, M. Fujii, *Physical Chemistry Chemical Physics* **2011**, *13*, 7812-7820.

[94]   P. Carcabal, L. C. Snoek, T. Van Mourik, *Molecular Physics* **2005**, *103*, 1633-1639.

[95]   T. A. Legreve, J. R. Clarkson, T. S. Zwier, *The journal of physical chemistry. A* **2008**, *112*, 3911-3920.

[96]   S. J. Martinez, J. C. Alfano, D. H. Levy, *Journal of Molecular Spectroscopy* **1992**, *156*, 421-430.

[97]   L. Snoek, E. Robertson, R. Kroemer, J. Simons, *Chem. Phys. Lett.* **2000**, *321*, 49-56.

[98]   G. Von Helden, I. Compagnon, M. Blom, M. Frankowski, U. Erlekam, J. Oomens, B. Brauer, R. Gerber, G. Meijer, *Physical Chemistry Chemical Physics* **2008**, *10*, 1248-1256.

[99]   J. C. Lopez, V. Cortijo, S. Blanco, J. L. Alonso, *Physical Chemistry Chemical Physics* **2007**, *9*, 4521-4527.

[100]   V. Cortijo, J. L. Alonso, J. C. López, *Chem. Phys. Lett.* **2008**, *466*, 214-218.

[101]   J. L. Alonso, V. Cortijo, S. Mata, C. Perez, C. Cabezas, J. C. Lopez, W. Caminati, *Journal of Molecular Spectroscopy* **2011**, *269*, 41-48.

[102]   J. L. Alonso, M. E. Sanz, J. C. Lopez, V. Cortijo, *Journal of the American Chemical Society* **2009**, *131*, 4320-4326.

[103]   C. Cabezas, Valladolid **2011**.

[104]   N. Kuş, A. Sharma, I. Peña, M. C. Bermúdez, C. Cabezas, J. L. Alonso, R. Fausto, *The Journal of Chemical Physics* **2013**, *138*, 144305.

[105]   C. Cabezas, A. Simao, C. Bermudez, M. Varela, I. Pena, S. Mata, R. Fausto, J. L. Alonso, *J Phys Chem A* **2013**, *117*, 4907-4915.

[106]   K. Demyk, H. Mäder, B. Tercero, J. Cernicharo, J. Demaison, L. Margulès, M. Wegner, S. Keipert, M. Sheng, *Astronomy & Astrophysics* **2007**, *466*, 255-259.

[107]   L. Coudert, B. Drouin, B. Tercero, J. Cernicharo, J.-C. Guillemin, R. A. Motiyenko, L. Margulès, *The Astrophysical Journal* **2013**, *779*, 119.

[108]   M. Carvajal, L. Margulès, B. Tercero, K. Demyk, I. Kleiner, J. Guillemin, V. Lattanzi, A. Walters, J. Demaison, G. Wlodarczak, *Astronomy & Astrophysics* **2009**, *500*, 1109-1118.

[109]   L. Margules, R. Motiyenko, K. Demyk, B. Tercero, J. Cernicharo, M. Sheng, M. Weidmann, J. Gripp, H. Mäder, J. Demaison, *Astronomy & Astrophysics* **2009**, *493*, 565-569.

[110]   R. Motiyenko, B. Tercero, J. Cernicharo, L. Margulès, *Astronomy & Astrophysics* **2012**, *548*, A71.

[111]   B. Tercero, L. Margulès, M. Carvajal, R. A. Motiyenko, T. Huet, E. Alekseev, I. Kleiner, J.-C. Guillemin, H. Møllendal, J. Cernicharo, *Astronomy & Astrophysics* **2012**, *538*, A119.

[112]   A. M. Daly, C. Bermúdez, A. López, B. Tercero, J. C. Pearson, N. Marcelino, J. L. Alonso, J. Cernicharo, *The Astrophysical Journal* **2013**, *768*, 81.

[113]   A. Lopez, B. Tercero, Z. Kisiel, A. M. Daly, C. Bermudez, H. Calcutt, N. Marcelino, S. Viti, B. J. Drouin, I. R. Medvedev, C. F. Neese, L. Pszczolkowski, J. L. Alonso, J. Cernicharo, *Astronomy & Astrophysics* **2014**, *572*, A44.

[114]   A. Daly, L. Kolesniková, S. Mata, J. Alonso, *Journal of Molecular Spectroscopy* **2014**, *306*, 11-18.

[115]   S. Moldoveanu, *Pyrolysis of Organic Molecules: Applications to Health and Environmental Issues, Vol. 28th*, Elsevier, **2010**.

[116]   J. M. Hollis, F. J. Lovas, P. R. Jewell, *Astrophysical Journal* **2000**, *540*, L107-L110.

[117]   D. T. Halfen, A. J. Apponi, N. Woolf, R. Polt, L. M. Ziurys, *The Astrophysical Journal* **2006**, *639*, 237.

[118]   M. T. Beltrán, C. Codella, S. Viti, R. Neri, R. Cesaroni, *The Astrophysical Journal Letters* **2009**, *690*, L93.

[119]   J. K. Jørgensen, C. Favre, S. E. Bisschop, T. L. Bourke, E. F. v. Dishoeck, M. Schmalzl, *The Astrophysical Journal Letters* **2012**, *757*, L4.

CHAPTER III. METHODOLOGY

This Chapter is divided in three main sections. After explaining the necessity of employing rotational spectroscopy for the research proposals described in the Introduction, a description of each instrument employed during the investigation is summarized in the first part. The general strategy is presented in the section III.2, where the synergy between experiment and theory is evidenced. Finally, the tools for a correct analysis of the rotational spectra are introduced briefly in the last part of this chapter.

III.1. EXPERIMENTAL TECHNIQUES

As described in the previous Chapter, the conformational study of biomolecules is best performed under isolated conditions in order to eliminate the influence of the intermolecular interactions with the environment so that we evaluate the intrinsic properties of these systems. The development of spectroscopic techniques combined with supersonic jets has been essential for the investigation of molecules in an environment free of collisions.[1-3] A supersonic jet is generated during an adiabatic expansion of a gas at high pressure (1-20bar) against a high vacuum (10^{-5}-10^{-7}mbar) both connected through a small hole called nozzle (≤1mm of diameter). In so doing, at the exit of the nozzle the gas is accelerated to supersonic speeds. The pulse of gas is normally entrained in a carrier gas, generally a noble gas, and a small portion of the sample to be analyzed. In the first step of the expansion, binary collisions between the sample and the carrier gas lead to cooling in the rotational and vibrational levels in order to acquire the speed of the carrier gas. As such, the sample is embedded in a flux free of collisions, where the molecules can be considered as isolated. This molecular cooling simplifies and increases the intensity of the spectra since only the lowest rotational levels of the lowest vibrational states of each conformer are populated.

Supersonic jets have been combined with diverse spectroscopic techniques to obtain information of the species present in the jet.[1-4] Between them, the most common methods for exploring biomolecules are based on laser techniques.[5-6] The combination of double resonance UV-UV (hole burning) or IR-UV (IR ion-dip spectroscopy with LIF detection (light induced fluorescence or mass spectrometry detection of the ions produced by REMPI processes (Resonance enhanced Multiphoton Ionization)[7-12] were found appropriate to provide information about the conformers presents in the supersonic jet. However, they require that the sample possesses an electronic band well resolved in the vibronic components (a chromophore group allows it), and that the electronic excited states do not undergo into quick deactivation processes that provoke an inefficient ionization. Only a few biomolecules fulfill these two conditions: barely, three out of the 20 amino acids[13-17], none of the carbohydrates and, nitrogen bases have had difficulties to be analyzed owing to deactivation processes that occur in their exited states[18-28]. Signals produced by the different conformations are not often well-resolved, which may lead to missing conformations and speculative and ambiguous assignments.[24, 28-31]

Fourier transform microwave spectroscopy combined with supersonic jets (MB-FTMW) allows to exploring the rotational spectra of each conformation present in the supersonic jet as if they were different chemical species, as long as they have a non-zero dipole moment (almost all biomolecules does it). The main drawback of applying this

technique to biomolecules lies in vaporizing the sample since they usually have high melting point and low vapor pressure. Furthermore, conventional thermal heating methods are often useless owing to the sample decomposition previous to its vaporization. During last decade, laser ablation has emerged as an exceptional technique to overcome this inconvenience associated with the solid samples vaporization. In our laboratory, we have successfully combined laser ablation with Fourier transform microwave spectroscopy in supersonic jet.[32-34] In so doing, we were able to unveil the conformational and tautomeric behavior of different types of biomolecules:[35] amino acids, sugars, nitrogen basis, vitamins, etc…

Contained in this thesis, distinct FTMW techniques have been adapted to each type of biomolecule under study (described in sections III.1.1 to III.1.3). Sugars are analyzed using a broad-band technique based on Chirped pulses,[36] combined with laser ablation[33, 37] which allows a rapid acquisition of the entire rotational spectrum (6-18GHz) per instrumental cycle (see Section III.1.1). Biomolecules containing a ^{14}N need higher resolution systems, as the LA-MB-FTMW,[32, 38] to observe its hyperfine structure (see Section III.3.3 for quadrupole hyperfine structure explanation). For the particular case of the amino acid histidine with a very complex hyperfine structure due to its three inequivalents ^{14}N (Figure III.1.a), it required the construction of a new design of the LA-MB-FTMW spectrometer that covered lower frequency ranges (section III.1.2), where the hyperfine
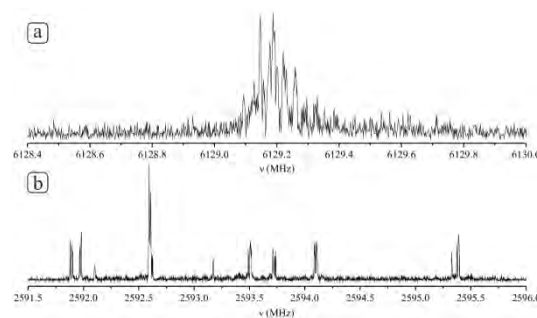
FIGURE III.1: *Comparative of the quadrupole hyperfine structure of histidine at different frequencies (same scales) (a) 4_{14}-3_{13}. transition (b) 1_{11}-0_{00} transition.*

components of low J transitions are much more resolved (see Figure III.1.b). The cytosine-water complex eluded detection under the normal conditions of this LA-MB-FTMW configuration. The proportion of water complexes during the ablation process is scared, which would involve much higher accumulation and time consuming experiment. The number of accumulations in these experiments is limited by the laser ablation system, which demands certain cleaning of the ablation nozzle to avoid its blockage. At this point, a multi-FID (Free Induction Decay) step was implemented. It consists on, instead of only acquiring a single spectrum per ablation pulse, accumulating up to ten (section III.1.3). As such, the sensitivity of the instrument per cycle was increased. With this experimental condition, cytosine water complex was analyzed.

These FTMW instruments have been proven to be ideal for the analyzing the conformational and tautomeric behavior of biomolecules.[35] They typically work up to frequencies not higher than 26 GHz. However, the observations of the ISM are registered normally at higher frequencies. In order

to be able to make a direct comparison of the laboratory spectra and the observations, the rotational analysis of molecules of astrophysical interest will be done in frequency domain spectrometers that cover higher frequency ranges. Reported in this dissertation, two types of frequency domain spectrometers have been upgraded with new synthesizers and new multipliers: Stark modulation and frequency modulation (FM) instruments (sections III.1.4 and III.1.5). The Stark (12-110GHz) is normally employed to make the initial assignments of the excited vibrational states of the molecules due to the characteristic shape of the transitions that matches the transitions of the ground and vibrational excited states. This pattern comes from the breaking of the M-degeneracy of the rotational transitions when an electric field is applied. These Stark initial assignments are used as starting point for the higher frequency measurements performed in the FM modulation spectrometers that can register the spectrum up to 1080GHz.

III.1.1. LA-CP-FTMW

A schematic block diagram of the design of the spectrometer used is shown in Figure III.2 and some pictures on Figures III.3 and III.4. Details of the components, which are numbered in parenthesis in the text, are given in the footnote of Figure II.2. In the general procedure, cylindrical rods of the sugars' samples (see sample preparation in section III.2) are placed in the ablation nozzle
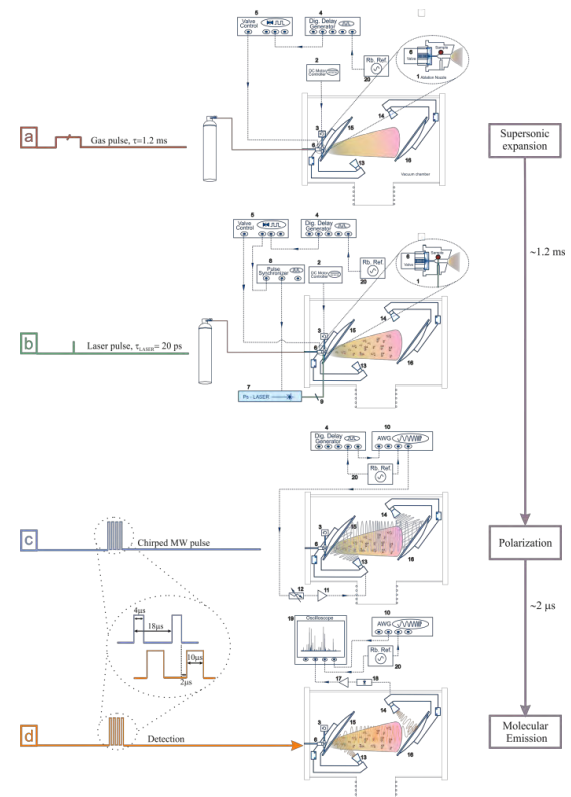
FIGURE III.2: *Scheme of the working sequence of LA-CP-FTMW. (1) Ablation nozzle. (2) DC motor controller. (3) DC Motor: Oriel Motor Mike 18074. (4) Digital Delay generator: Stanford Research Systems, DG645. (5) Valve driver: IOTA ONE. (6) Injection Valve. (7) Nd:YAG laser: Ekspla, 20ps,15mJ. (8)Pulse syncrhronizer. (9) Mechanical shutter. (10) Arbitrary Waveform Generator: Tektronix AWG7122B, 24Gsamples/s[-1]. (11)Traveling Wave Tube Amplifier, TWT: IFI, GT186-300, 300W. (12) Variable attenuator. (13-16) Parabolic reflector system: Satimo reflector with interface for SH2000, 2-32GHz. (13) Ridge polarization horn. (14-15) Parabolic reflectors. (16) Ridge detection horn. (17) VLN amplifier. (18) Pin diode limiter. (19) Digital Oscilloscope: Tektronix DPO72004B, 50Gsamples/s[-1], 20GHz hardware bandwidth. (20) 10MHz Rubidium Frequency Standard Oscillator: Stanford Research Systems FS725.*

(1) where a motor (2-3) allows the solid rod to rotating and translating up and down along the injection system during the whole process, in order to achieve the maximum exploitation of the sample. A digital delay generator (4) sends a pulse to a valve driver (5), opening the nozzle valve for 1200μs (6). This makes the carrier gas (Ne at backing pressure of 15bar) to expand adiabatically into the vacuum chamber creating the supersonic expansion (Figure
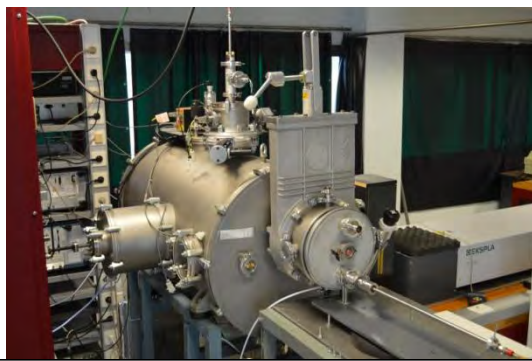
FIGURE III.3: *General aspect of vacuum chamber and laser of the LA-CP-FTMW spectrometer*

III.2.a). After an adequate delay (~850 μs), a picosecond pulse of a Nd:YAG laser (7) hits the solid rod and vaporizes the sample seeding the molecules into the carrier gas (Figure III.2.b). In order to adjust the laser repetition rate from 10Hz (standard of this laser) to 2Hz (repetition rate for this experiment), a pulse synchronizer (8) and a shutter (9) are used. The fast chirp microwave pulse that macroscopically polarize the species present in the supersonic jet is created by an arbitrary waveform generator (10), which is time controlled by the digital delay generator (4). A traveling wave tube amplifier (TWT) (11) is used to amplify this chirped pulse. The power level necessary for the polarization of the molecular systems is adjusted
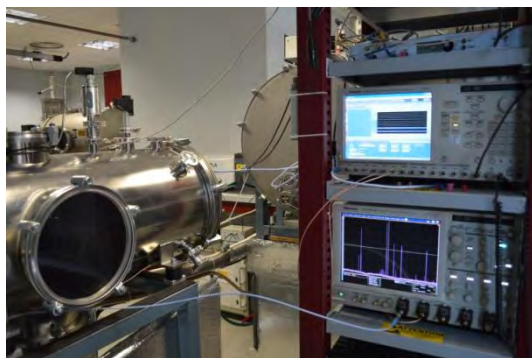
FIGURE III.4: *Arbitrary wave function generator and Oscilloscope.*

using a variable attenuator (12). The amplified chirped pulse is broadcasted across the vacuum chamber (Figure III.2.c) during 4μs using a parabolic reflector system (13-16). To reduce sample consumption, four separate broadband rotational spectra spaced by 18μs emerge from the first horn antenna (13) to polarize the molecular beam in each injection cycle. 2 μs after each excitation pulse ceases, the second horn (14) is used to acquire for 10μs the free induction decay signal (FID) emitted by the sample as response to the microwave excitation (Figure III.2.d). The FID is further amplified by a sensitive amplifier (17) which is protected from the high-power of the TWT amplifier by a pin diode limiter (18). The amplified rotational free induction decay (FID) is recorded in the time domain by a digital oscilloscope (19) and Fourier transformed to the frequency domain. The phase reproducibility of the experiment is achieved by locking all frequency sources and the digital oscilloscope to a 10 MHz rubidium frequency standard oscillator (20). Around 100 000 individual FIDs (four per each molecular expansion) were normally averaged in the time domain and Fourier transformed to obtain the rotational spectra of a molecule.

III.1.2. LA-MB-FTMW

Based on previous designs of LA-MB-FTMW spectrometers constructed at the University of Valladolid,[1] we have developed a new instrument
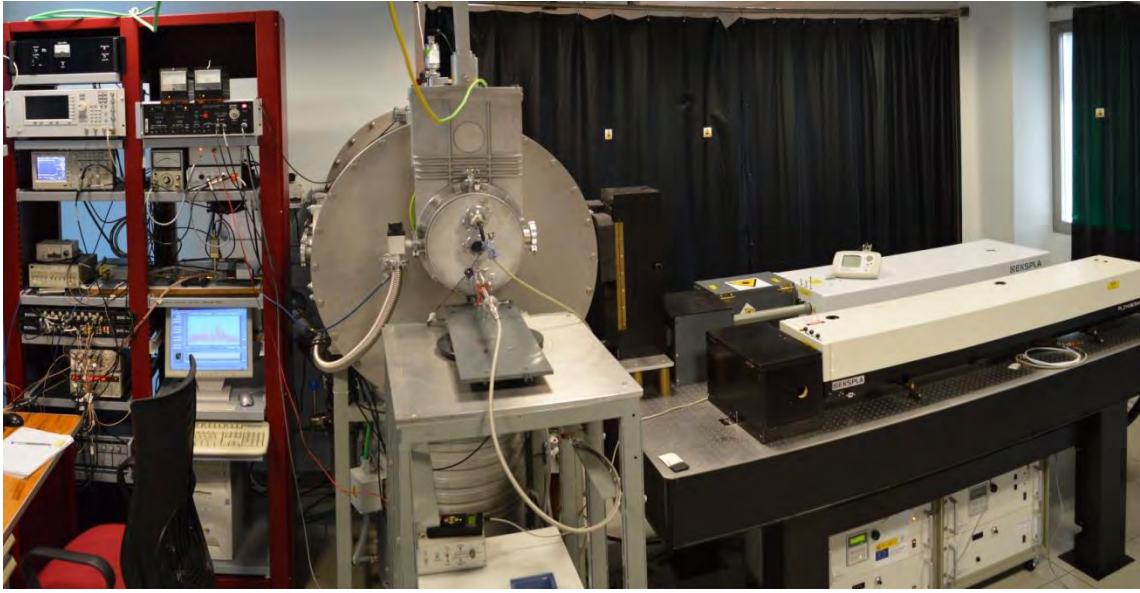
FIGURE III.5 *Picture of the LA-MB-FTMW instrument*

specially dedicated to maximize performances at low frequency ranges (2 to 8 GHz) (see Figure III.5). It is composed by three main parts: a Fabry-Pérot resonator, a laser ablation system and a Fourier transform microwave spectrometer.

The resonator is formed by two spherical aluminum mirrors of 70 cm of diameter and 70 cm of radius of curvature. The resonator is housed in a cylindrical stainless-steel high vacuum tank (~113 cm long, 80 cm diameter), evacuated by a diffusion pump (~12000 l/s, Leybold Dip 12000) backed by a roots blower (~500 m^3/h, Leybold Ruvac 500). One of the mirrors is kept fixed and the other is mounted on a 20 cm long motorized support (Rexroth and Berger-Lahr RDM545/100LTA) which provides incremental translation steps of 1.25 µm, so the distance between the mirrors can be adjusted for each polarization frequency. The stepper motor is controlled by the computer through a motor control unit, to allow automatic tuning when scanning. The resonator is tuned measuring the transmitted power with a coaxial detector (HP 8473C) connected to the antenna on the moving mirror. A single antenna covering the full 2-8 GHz band is connected to the FTMW spectrometer and serves for both polarizing and detection stages.

The pulsed nozzle of the laser ablation system is accommodated in the backside of the fixed mirror, with a coaxial arrangement of the jet and the resonator axis. It is made from a commercial solenoid valve (General Valve Series 9, nozzle diameter 1.0 mm) with an extension channel to hold the cylindrical sample rod in a vertical position. The sample rod is obtained from the pulverized solid by appropriate pressing. The laser is focused in the sample through a lateral orifice of the nozzle and a vacuum-tight window of the expansion chamber.

A motorized micrometer is used to simultaneously rotate and translate the sample rod each laser pulse, so the laser hits a different point of the sample surface in successive pulses, minimizing the problem of shot-to-shot fluctuation in the amount of the desorbed material. A commercial driver opens the pulsed nozzle when triggered by the pulse control unit of the instrument, expanding a high pressure carrier gas (15 bar) through the desorption nozzle. A picosecond Nd:YAG pulsed laser (Ekspla PL2251, 20 ps pulse width) working in the third harmonic (355 nm) is used as ablation source. In order to focus and direct the laser beam to the ablation nozzle an appropriate converging lens is inserted between two steering mirrors on a vertical support outside the vacuum tank. Adjustment of the position of the focusing lens permits some control of the laser spot size, which is about 0.6 mm in diameter on the target rod.

In the FTMW spectrometer, a microwave synthesizer (Agilent E8257D) at a frequency v-30 MHz is used as the radiation source of the spectrometer, which is alternatively switched to the polarization or detection branches of the spectrometer. The exciting radiation (v-30 MHz) is then shifted in frequency to v to allow a later superheterodyne detection using a single-sideband (SSB) upconverter. A variable attenuator located before the microwave amplifier (Miteq AMF-5F-200800-15) serves to regulate the desired microwave power, which is monitored with a power meter (Agilent E4418B). The excitation pulse is fed into the resonator through a wire antenna ($\lambda/4$).

Once the excitation is extinguished the molecular emission at microwave frequencies is amplified with a low-noise-amplifier (noise figure NF = 1.5 dB) and down-converted to the radio-frequency region in two mixing steps. A first image-rejection mixer mixes the FID at frequency v MHZ with the microwave signal at frequency v-30 MHz, shifting the molecular spectra to the 30 MHz region. In a second step the spectrum is mixed with a radiofrequency source at 27.5 MHz signal, shifting down the spectrum to the 2.5 MHz region where it can be easily digitized. The time-domain spectrum is digitized at 40 ns sampling intervals, taking up to 16k data points per cycle (frequency resolution of 1.5 kHz). Real-time Fourier transformation and accumulation of successive experiments is implemented in the control software.

III.1.3. LA-MB-FTMW with Multi-FID

A multi FID step has been introduced in the previously described LA-MB-FTMW spectrometer in order to enhance the sensitivity of the instrument. The experimental procedure is now as follows.

Solid rods are ablated using the third harmonic of a Nd:YAG picoseconds laser. The vaporized species are seeded in a carrier gas that is later expanded adiabatically into a Fabry-Pérot cavity to produce a supersonic expansion. Since this system is employed for a microsolvation experiment, a water reservoir was placed just before the gas valve. The clusters of cytosine-water were formed in the jet and

later probed with a sequence of short polarizing microwave pulses. The number of pulses and the delay between pulses is selected to get a compromise between sensitivity and resolution. The more number of pulses the better sensitivity whereas the longer the delay the higher resolution. Each FID produced by each microwave pulse is recorded, added together and Fourier transformed to obtain the spectrum in the frequency domain.

III.1.4 Frequency domain spectrometers

III.1.4.1. Stark modulation spectroscopy

The Stark-modulated spectrometer[39] has been recently upgraded to reach frequencies up to 170GHz (Figure III.6). The sources from 12.5 to 40 GHz are backward wave oscillators (BWO)´s HP8695A (12.5 to 18 GHz), HP8696 (18-26.5 GHz) and HP8697A (26.5-40GHz) stabilized by a phase lock loop (PLL) using harmonics generated from a Fluke 6060A frequency synthesizer. The mixed signal of the BWO and harmonic generator is sent to a HP-8709A synchronizer. For frequencies 50-170 GHz, a Virginia Diode quadrupler (WR15 50-75 GHz), hextupler (WR10 75-110 GHz) and nonupler (WR6.5 110-170 GHz) were used with either a BWO s HP8695A (12.5 to 18 GHz) or an Agilent 8247D as the input and stabilized as described above. Solid state Schottky detectors were used, WR15, WR10, WR6.5 with appropriate

FIGURE III.6: *Stark modulation spectrometer.*

waveguide transitions for both source and detector to emit and receive through the X-Band cell. The signal is amplified and sent to a phase sensitive detector. The output is recorded by a PICO 1012 data recorder which is controlled by an in-house LabVIEW program. The data is taken in both directions and averaged. The resulting spectrum is imported into the AABS program and the top of the signal was fit to a Gaussian lineshape. The accuracy of this measurement is given as 50 kHz. Stark voltages ranging from 80V to 500V at 33.3333 kHz frequency were applied to sufficiently modulate the transitions for detection.

III.1.4.2. FM modulation spectroscopy

Schemes of the two configurations of the millimeter and submillimeter wave spectrometer used in this work covering the spectral range from 50 to 1080 GHz are shown in Figure III.8 and their corresponding images on Figure III.7. The microwave source (1) is a frequency modulated
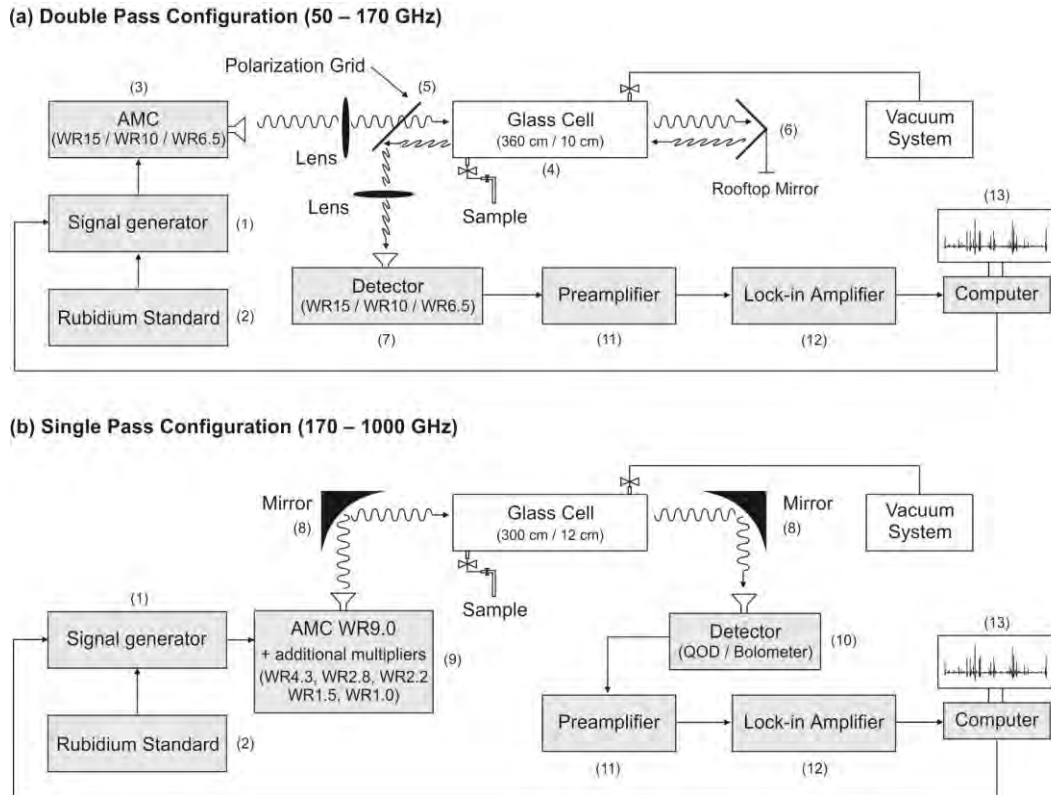
FIGURE III.8. *Schemes of the single (a) and double path (b) configurations of the millimeter- and submillimeter wave spectrometer.*

signal generator (Agilent E8257D) operating from 250 kHz to 20 GHz, phase locked to a Rubidium standard (2). In the double pass configuration (Figure III.8.a), the microwave frequency is multiplied by 4, 6 or 9 using amplifier multiplier chains AMC WR15, AMC WR10, or AMC WR6.5 (3) from VDI, Inc., with average powers of 34 mW, 17 mW, and 4 mW, to reach the frequency ranges of 50 – 75 GHz, 75 – 110 GHz or 110 – 170 GHz, respectively. The optical path length of the free space cell (4) of 3.6 m is doubled using a polarization grid (5) (Millitech, Inc.) and a home-made rooftop mirror (6). The output signal, after the second pass through the cell, is detected by the corresponding solid state Schottky diodes detectors

WR15, WR10 and WR6.5 (7) from VDI, Inc. Rotational spectra above 170 GHz are measured in a single pass mode configuration shown in Figure 2b using parabolic metal mirrors (Edmund Optics, Inc.) as focusing optic elements (8). An active VDI sextupler AMC WR9.0 (average power of 25 mW) is initially used to produce a suitable frequency input for additional active and passive multipliers (VDI, Inc.) connected by wave guide to its output (9). The active doublers WR4.3 and WR 2.2 are connected to a 12V bias implemented directly in the WR9.0 while the passive triplers, WR 2.8, WR 1.5, and WR1.0 require no bias. Using combinations of these multipliers, the frequencies of 170 – 240 GHz (WR4.3), 240 – 360 GHz

FIGURE III.7: *FM modulation spectrometers*

(WR2.8), 340 – 480 GHz (WR4.3 and WR2.2), 510 – 720 GHz (WR4.3 and WR1.5), and 720 – 1080 GHz (WR2.8 and WR1.0) are reached with average powers of 3 mW, 0.9 mW, 0.2 mW, 50 μW, and 9 μW, respectively. A broadband Quasi-Optical Detector (QOD) from VDI, Inc. and liquid helium cooled silicon bolometer (Infrared Laboratories, Inc.) are used as the detection elements (10). For both configurations, detected source frequency-modulated signal is amplified (11) and sent to the lock-in amplifier (SR510, Stanford Research Systems, Inc.) where 2*f* detection is applied, where *f* is the modulation frequency, to increase the sensitivity of the measurements (12). Modulation frequency of 10.2 kHz is used for the non-cooled (room temperature) detectors while 90 Hz for the cryogenic detector and the modulation depth is determined to give the Doppler line width. The generator and the lock-in amplifier are connected by standard GPIB to the computer (13) and controlled by a laboratory developed LabVIEW program.

III.1.5. Laser ablation time of flight spectrometer

The LA-TOF-MS experimental setup employed for the analysis of illicit drugs has been developed in-house by using a combination of commercial components. Figure III.9 shows a diagram of the overall system. The ionization chamber is a multiport stainless steel vacuum cavity where samples are introduced through port 1. The samples present the shape of a pill, with 8 mm diameter and 5 mm long, and are linked to the holder via heat shrink tube. A gate valve is used to avoid vacuum loses each time a new sample is inserted. The horizontal position of the sample can be adjusted to obtain the best signal. Samples are vertically fixed at halfway point between the TOF extractor and repeller plates. Port 1 is coupled to the time-of-flight (TOF) tube in such a way that its extractor and repeller plates are located in the middle of the chamber. The TOF tube employed is a Jordan type tube of 1 meter long which can operate in reflectron mode (RM Jordan, model D-850). Along the tube, there are several voltage adjustable plates that are adjusted to optimize the signal of the samples. All of them are working in continuous mode with the exception of the repeller and extractor plates, which have been modified by two high voltage rapid switches in order to pulse them. The laser beam is introduced inside the ionization chamber though a glass window placed in port 3. This beam is aligned by two external mirrors in such a way that it is equally spaced from both extractor and repeller

plates; as such, the laser ablation/ionization is produced perpendicularly to the sample. The laser employed is a Nd:YAG (Quantel Brilliant, model C07.BR) in the third harmonic (λ= 355 nm) with pulse width ~ 5 ns. Its power is adjusted modifying the time delay between the flash lamp and the Q-S pulse. A single lens (Melles Griot), with a focal distance of 750 mm, which is placed between the above mentioned two mirrors, is employed to focus the laser beam onto the sample. The distance from the lens to the target is tuned by employing a translation stage, which allows to modifying the beam spot area in order to obtain a stable signal. The laser spot size is around 0.6 cm^2. Two turbo molecular pumps (Leybold, model TDL RS 458 and TURBOVAC, model 361) connected though port 4 and in the TOF tube are used to maintain the ultra-high vacuum required for the experiment. The ionization chamber is generally at 10^{-7} Torr while the reflectron TOF is at 10^{-8} Torr.

The experimental sequence is controlled by a commercial delay generator (Stanford Research Systems, model DG-645) working at a repetition rate of 10 Hz. Both flash lamp and Q-switch of the laser are externally triggered by the delay generator, being the Q-switch delayed from the flash lamp around 300μs; this time changes in function of the energy that requires the sample to be ionized. A few micro seconds after the Q-switch, the extractor and repeller plates are pulsed during a period that may range from less than a microsecond to 20μs. Delays and pulsed widths are tuned to accomplish the maximum signal of the interested ions. The output signal of the extraction plates is used to trigger the oscilloscope (Agilent model 5464D, 2Gs/s), which digitalizes the signal coming from the multichannel plate of the TOF tube. Afterwards, the data is sent to a computer where the analysis and graphing is performed.
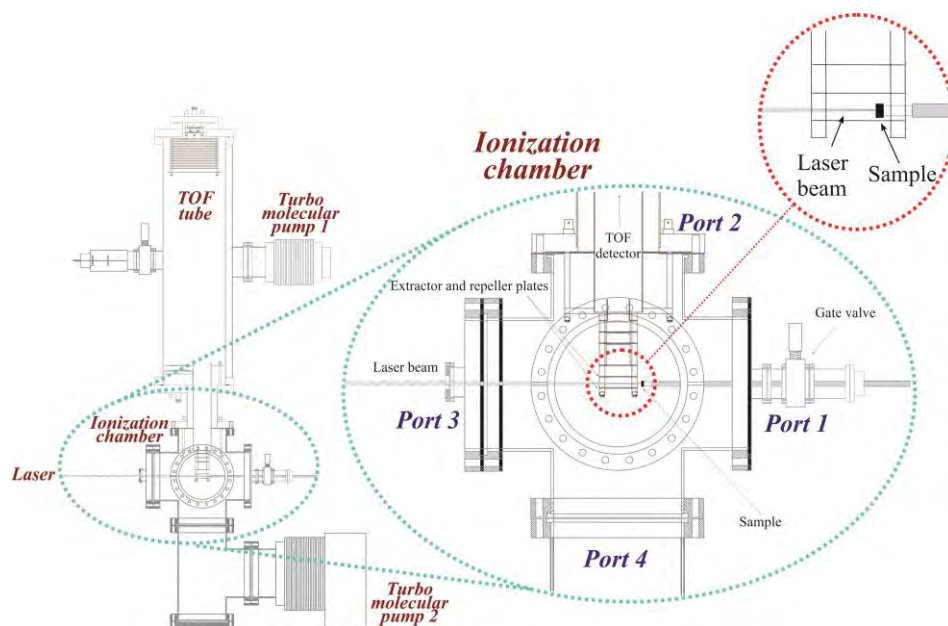
FIGURE III.9: *Scheme of LA-TOF-MS instrument*
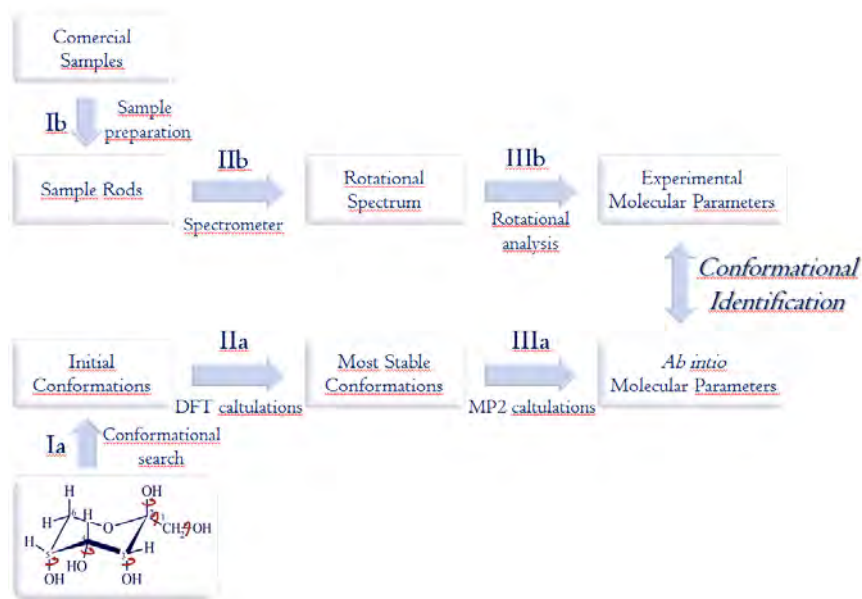
FIGURE III.10: *General strategy scheme*

III.2. GENERAL STRATEGY

As mentioned, rotational spectroscopy is used to unveil the conformational and tautomeric behavior of the building blocks. The general strategy to identify species present in the gas phase is schematically presented in Figure III.10. It is divided into two sequence lines: **block a,** which describes the process calculating the *ab initio* molecular properties of the most stable species, and **block b,** which explains the experimental procedure to obtain the experimental molecular properties from the analysis of the spectrum. Both blocks are executed in parallel to finally converge in the conformational / tautomeric identification by comparing the *ab initio* and experimental molecular properties. These molecular properties are the rotational constants, which depend on the mass distribution of the molecule, quadrupole coupling constants, which provide information about the electric field of the ^{14}N and the electric dipole moments, which are related with the intensity of the rotational transitions (see section III.3 for further details).

In block a, the first step (**Ia**) is finding all possible conformations. Sometimes, if we are dealing with simple molecules, chemical intuition would be enough to make an initial proposal, but normally, this is not the case for biomolecules and a systematic search helped by theoretical calculations is required. For each configuration, the minima of the potential energy surface are searched employing low computational cost methods, such as molecular mechanics[40] or semiempiric calculations.[41-42] The programing package Hyperchem (Hyper Cube Inc.), was employed for the conformational search.

Conformations resulted from this search were submitted[43] to higher level calculation using density functional theory (DFT) methods like B3LYP (Becke, three-parameter, Lee-Yang.Parr)[44] with the People basis set (6-31G(d,p)) (**step IIa**). Considering that the higher energy conformers are not sufficiently populated to be detected, the molecular properties of the possible conformers (those within an energy window of 1500cm^{-1}) are calculated *ab initio* employing a second order Moller-Plesset perturbative method (MP2)[45] with the standard Pople basis set 6-311++G(d,p)[46] (**step IIIa**). The final selection of the possible conformers is done based on the energy: normally, those whose energy is less than 1000 cm^{-1} above the global minimum.

In case of molecules of astrophysical interest, the goal of the investigation is not the identification of the conformations. On the contrary, it is to analyze vibrational excited states and to extend the measurements up to higher frequencies in order to obtain rotational parameters precise enough for astrophysical detection. As such, the molecular properties that need to be calculated *ab initio* in these works are the corrections of rotational constants for the vibrationally excited states, centrifugal distortion constants and coupling terms parameters. For these propose, frequency calculations are performed[43] at MP/6-311++G(d,p) using anharmonic potential. This calculation will give the first-order correction to the ground state rotational constants that can be employed to estimate the molecular parameters of the vibrational excited states.

Block b is initiated in parallel to block a. Sample preparation corresponds to **step Ib**. Biomolecules under study are normally solids with high melting point that requires laser ablation to be effectively vaporized. Samples are prepared grounding about 1g of these solids to form a pine power (Figure II.11.a), which is later mixed with few drops of a commercial binder. The mixture is then pressed at 300 MPa in a hydraulic press (Figure III.11.b) in order to obtain solid rods like the one shown in Figure III.11.c. After being dried, rods are placed in the ablation nozzle.
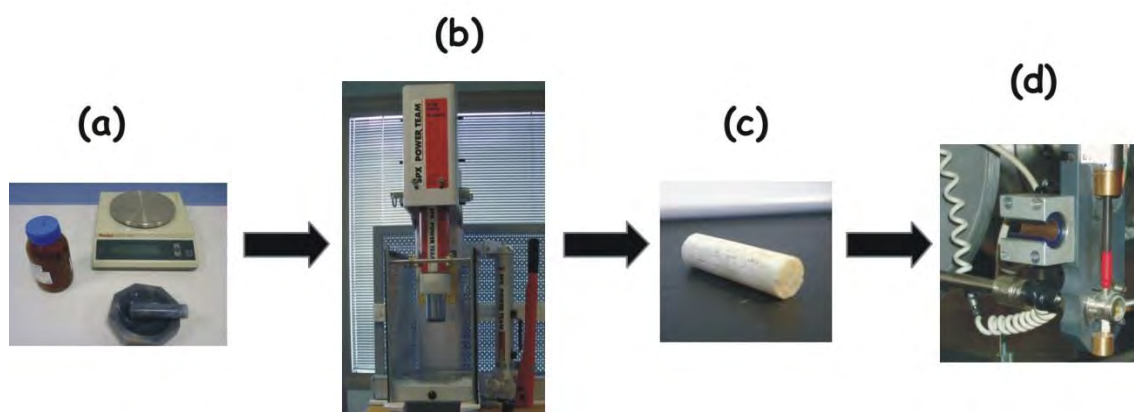
FIGURE III.11: *Sample preparation procedure*

In case of molecules of astrophysical interest, sample preparation is different since these molecules are liquids easily vaporized. These liquids are placed into a glass cell and degassed using the common freeze-pump-thaw method to remove the sample. Afterwards, the cell of the spectrometer is filled up at a pressure of about 2 10^{-2} mbar.

Once the samples are in the corresponding spectrometers, the instrumental conditions are optimized (power, timing, pressure, ablation process, etc.). The experimental procedure followed to record the spectra (**step IIb**) will depend on the spectrometer employed and the type of molecule. Generally, in LA-CP-FTMW spectrometer, the complete spectrum from 6 to 12 GHz is recorded. The conformational search in LA-MB-FTMW techniques is initiated by long scans in the surroundings of the predicted transition frequencies

of the lowest energy conformers. When several transitions are found, they are analyzed (see section III.3) in order to predict further lines to measure. This process is repeated iteratively until obtaining rotational parameters precise enough. In case of molecules of astrophysical interest the strategy changes. As mentioned in section III.1, the Stark spectrometer is used to make scans around the transitions to observe its satellites, which normally correspond to the vibrational excited states. Once several transitions are recorded, an initial analysis is made to obtain preliminary rotational constants that allow identifying further transitions at higher frequencies. At this point, a complete spectrum of the molecule is recorded using the different configurations of the FM modulation spectrometer. The analysis of this spectrum is carried out assisted by the software package AABS[47].

III.3. TOOLS FOR ROTATIONAL ANALYSIS

Analyzing a rotational spectrum means to extract all possible information about the molecule from it. This is achieved by fitting the constants present in the eigenvalues of the Hamiltonian that describes the rotation of the molecule. Rotational constants *A*, *B* and *C*, dipole moments, quadrupole coupling constants, centrifugal distortion constants and Coriolis and Fermi perturbation terms are the constants obtained in the analysis. Once known them the spectrum of any molecule can be reproduced with exceptional accuracy. The first three are molecular parameters related to the

structure of the molecule. As such, they are used as a tool for the conformational identification. A brief description of them is given in the following sections. Further details can be found in the literature.[48-51] Unless it is explicitly mentioned, SPCAT/SPFIT[52] program package is used for predicting the spectra and fitting parameters derived from the analysis of the spectra.

III.3.1. Rotational Constants

The frequency of the transitions that appear in a rotational spectrum correspond to the energy

difference between two rotational energy levels of the molecule. The energy levels are the eigenvalues of the Hamiltonian operators, which are usually expressed in terms of angular momentum operators. The resulting eigenvalues can be constituted from linear combination of the three rotational constants (A, B and C), being these ones directly related to the mass distribution of the molecular system. They are inversely proportionate to the moments of inertia (I_a, I_b, I_c), which results from the product of each mass multiply by their distances to the axis $\left(I_\alpha = \sum m_i \cdot r_{i,\alpha}^2\right)$, being α the a, b or c axis. Thus, they are specific for a given molecule. As such, obtaining their values from the analysis of a section of the spectrum allows to predicting each rotational transition of the entire spectrum as well as identifying the structure of the species (conformer, tautomer, etc) that is being analyzed.

The relation between the rotational constants, molecules are classified as: linear tops $(I_a = 0, I_b = I_c)$, spherical tops $(I_a = I_b = I_c)$, symmetric oblate tops $(I_a = I_b < I_c)$, symmetric prolate tops $(I_a < I_b = I_c)$ or asymmetric tops $(I_a < I_b < I_c)$. The asymmetric degree of a molecule is estimated by Ray constant, defined as $\kappa = (2B - A - C)/(A - C)$, whose values range from 1 for oblate type molecules and -1 for prolate. The type of the top dictates the relation between the rotational angular momenta $\mathbf{P}$ and $\mathbf{P_x}$ $\mathbf{P_y}$ $\mathbf{P_z}$, thus, the eigenvalues of the rotational Hamiltonian. The rotational Hamiltonian under the rigid rotor approximation can be written as:

$$H_R = A J_a^2 + B J_b^2 + C J_c^2 \tag{III.1}$$

where A, B, C are the rotational constants and J_a^2, J_b^2, J_c^2 are the diagonal elements of the Jacobian matrix of the molecule. The elements of the Jacobian are $J_{ij} = \left(\delta I_i / \delta P_j\right)$, where the I_i are the moments of inertia and P_j the angular momenta.

In case of a symmetric top, $\mathbf{P_z}$, where z is selected as the symmetry axis (a for prolate-tops and c for oblate-tops), and $\mathbf{P^2}$, commute with the Hamiltonian since they are constants during the motion. The resulting eigenvalues expressed as:

Prolate: $E_{J,K} = h\left[BJ(J + 1) + (A - B)K^2\right]$ (III.2)

Oblate: $E_{J,K} = h\left[BJ(J + 1) + (C - B)K^2\right]$

where $J = 0,1,2 \ldots$ and $K = 0, \pm 1, \pm 2 \ldots \pm J$. Thus the energy levels are degenerated in K.

In asymmetric rotors none of the three principal moments of inertia is zero and no two are equal, as such, the rotational frequencies can no longer be expressed in convenient equation as was done for symmetric tops. $\mathbf{P_z}$ does no longer commute with the Hamiltonian thus, K is not a good quantum number. The general procedure to solve this is to assume that the wave functions can be expanded in terms of the symmetric-top functions (see representation in Figure III.12). In so doing, the quantum number K is replaced by the combination of the quantum numbers K_a and K_c, which correspond to the limit cases of symmetric prolate (κ=-1) and symmetric oblate (κ=1). SPFIT/SPCAT software package[52] incorporates these Hamiltonians and it is used to fit the spectra to the rotational constants.
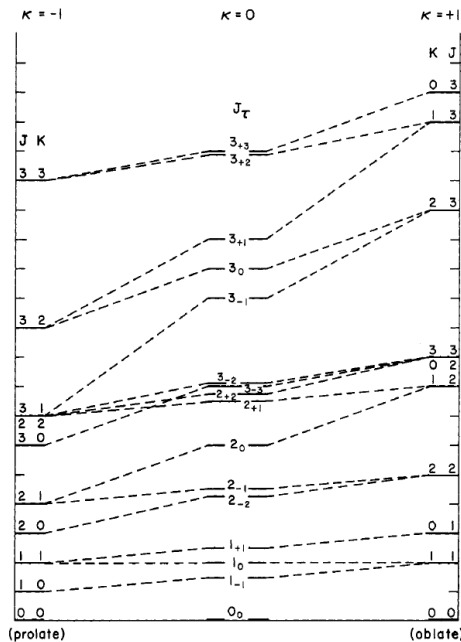
FIGURE III.12: *Relation of the asymmetric rotor energy levels (center) to those of the limiting prolate (left) and oblate (right).*

III.3.2. Dipole moments

Rotational transition intensities are related to the dipole moment of the molecule, particularly to its projection along the molecular axes a, b, c (μ_a, μ_b, μ_c). The transition intensity is directly proportional to the transition moment integral defined as:

$$\langle \psi_1 \, | \mu_{a,b,c} | \psi_2 \, \rangle \qquad (\text{III.3})$$

where ψ_1 and ψ_2 are the initial and final states and $\mu_{a,b,c}$ is the projection of the dipole moment. Thus, a transition is allowed when the direct product of the irreducible symmetric representation of the elements of the transition moment integral $(\Gamma(\psi_1) \otimes \Gamma(\mu_{a,b,c}) \otimes \Gamma(\psi_2))$ contains the totally symmetric representation. Selection rules for rotational spectroscopy are derived from this expresion:

$$\Delta J = -1, 0, 1 \qquad \text{P, Q, R branches} \qquad (\text{III.4})$$
$$\Delta K_a = 0; \ \Delta K_c = \pm 1 \qquad a - type$$
$$\Delta K_a = \pm 1; \ \Delta K_c = \pm 1 \qquad b - type$$
$$\Delta K_a = \pm 1; \ \Delta K_c = 0 \qquad c - type$$

As such, a-type transitions depend on the projection of the dipole moment along a axis (μ_a). The optimum polarization power of this transitions is inversely proportional to μ_a: low dipole moment implies higher polarization power to observe the lines. Taking this advantage, playing around with the polarization power get information of the three components of the dipole moment of the molecular system, which is useful for the conformational identification.

III.3.3. Quadrupole Coupling Constants

Most biomolecules contains at least a nitrogen in its structure. Its most abundant isotope, ^{14}N, possess a nuclear spin angular momentum *I*=1. As such it has non-spherical nuclear charge distribution that generates a non-vanished nuclear quadrupole momentum (eQ)[53]:

$$eQ = \int \rho \, r^2 (3 \cos \alpha - 1) \, dr \qquad (\text{III.5})$$

where ρ is the nuclear charge density and *r* and α the distance to the volume element and the angle between *r* and the spin axis. This momentum interacts with the electric field gradient generated by the rest of the molecular charges. As a consequence, *I* and the angular momentum of the molecule *J* are coupled leading to a splitting of the rotational levels. The quantum number generated that labeled account for this coupling is F which is equal to (I+J). Thus the rotational transitions show

a quadrupole hyperfine structure that requires from high resolution spectroscopy techniques to be appreciated (see Figure III.1). The presence of more than one ^{14}N atoms increases the complexity of the analysis. Histidine (Chapter VIII) has three non-equivalent nitrogens, leading to a very complicated hyperfine structure (see Figure III.X). Only few examples of the analysis of a quadrupole hyperfine structure resulting from the present of three inequivalent ^{14}N can be found in the literature.[54]

The rotational Hamiltonian of the molecule used to analyze the spectrum is compound by the rigid rotor Hamiltonian (H_R) described in the previous section plus a term that accounts for the nuclear quadrupole coupling (H_Q):

$$H = H_R + H_Q \tag{III.6}$$

H_Q is expressed as follows:

$$H_Q = \frac{eQq_{ij}}{2J(2J-1)I(2I-1)}\left[3(IJ)^2 + \frac{3}{2}IJ - I^2J^2\right] \tag{III.7}$$

where q_{ij} (i,j=a,b,c) are the coefficients that represent the average electronic field gradient expressed in terms of the coordinates in the principal axis orientation. These coefficients are related to the components of the nuclear quadrupole coupling tensor χ:

$$\chi = \begin{pmatrix} \chi_{aa} & \chi_{ab} & \chi_{ac} \\ \chi_{ba} & \chi_{bb} & \chi_{bc} \\ \chi_{ca} & \chi_{cb} & \chi_{cc} \end{pmatrix}; \chi_{ij} = eQq_{ij}; \tag{III.8}$$

The diagonal elements of the tensor represent the electric field along the principal axes which can be also fitted in SPFIT/SPCAT[52]. Their values are very sensitive to the electronic environment of the

^{14}N atom. Thus, they can be used for the conformational identification.

III.3.4. Centrifugal distortion constants

The treatment of the Hamiltonian presented in section III.3.1. is performed under the rigid rotor approximation. This approach assumes that all atoms in the molecule are fixed during the rotation motion hence the potential energy does not change, which means that the energy is entirely kinetic. However, molecules are not completely rigid. It would be more accurate to consider that atoms are held together by finite restoring forces. As the speed of the rotation increases (higher J), the centrifugal forces tend to increase their bond length, resulting in a decrease of the moment of inertia. Thus, analyzing molecules at higher frequencies (higher J) requires incorporating the effect of the distortion in the Hamiltonian (H_D):

$$H = H_R + H_D \tag{III.9}$$

The perturbation treatment developed by Watson[55] is the most extended to account for the centrifugal distortion of asymmetric molecules. Two Hamiltonian reductions, asymmetric (A) and symmetric (S) where derived. The A reduction including up to the sextic terms were used to analyze the rotational spectra of propenal and methyl cyanate (Chapter XI and XII). It is expressed as:

$$H = H_R + H_D^{(A)} = AJ_a^2 + BJ_b^2 + CJ_c^2 \tag{III.10}$$

$$-\Delta_J J^4 - \Delta_{JK}J^2J_a^2 - \Delta_K J_a^4 +$$

$$\frac{1}{2}\left[\delta_J J^2 + \delta_K J_a^2, J_+^2 + J_-^2\right]_+$$

$$+\phi_J J^6 + \phi_{JK}J^4J_a^2 + \phi_{KJ}J^2J_a^4 + \phi_{JK}J_a^6$$

$$+\frac{1}{2}\left[\varphi_J J^4 + \varphi_{JK}J^2J_a^2 + \varphi_K J_a^4, J_+^2 + J_-^2\right]_+$$

where A, B, C are the rotational constants, Δ_J, Δ_{JK}, Δ_K, δ_J, δ_K are quartic Φ_J, Φ_{JK}, Φ_{KJ}, Φ_K, φ_J, φ_{JK}, φ_J are sextic centrifugal distortion constants.

III.3.5. Vibrational-rotation interactions: Coriolis and Fermi

When analyzing the pure rotational spectrum of a vibrational excited state, in some occasions, including higher order terms to the semirrigid rotor Hamiltonian is not enough to account for several transition sequences. The reason might be the coupling between vibrational excited states. If symmetry allows it, when two levels are close enough in energy, they interact with each other perturbing their energy with opposite signs. The consequence in the spectrum is that for one state, transitions are found at certain frequency below the prediction and, in the other one, they are perturbed the same amount but with opposite singne, above the prediction. This can be appreciated in Figure III.13 where the difference between the frequencies of unperturbed state ν_0 and the frequency observed of two coupling states is shown. Perturbations can be beforehand predicted using the reduced plots (Figure III.14). They are built employing an initial set of rotational constants and vibrational energy values (experimental or *ab initio*) The crossing place, as that pointed out in a green ellipse, may
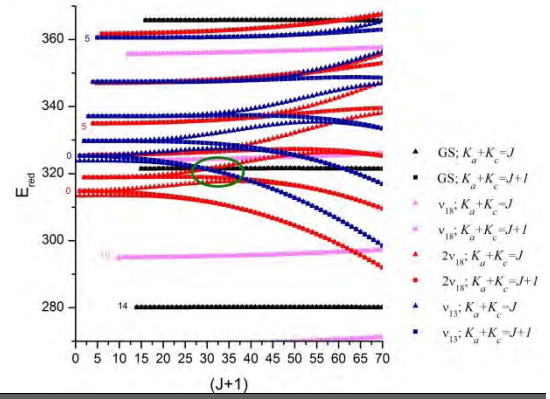
FIGURE III.14: *Reduced energies diagram, $E_{red} = E - E(\nu_{24} = 1) - J(J + 1)(B + C)/2$, for excited states involving the rotational energy of propenal. Each visible sequence represents one value of the K_a quantum number. Green circle highlights the perturbation between the rotational levels of ν_{13} and $2\nu_{18}$ of Figure III.13.*

correspond to transition sequences that are perturbed by Coriolis or Fermi interactions.

In terms of symmetry, Fermi interactions can occur between two interacting vibrational excited states that belong to the same irreducible representations. The off-diagonal Hamiltonian operator that describes the Fermi coupling is given as: [56]

$$H_F = W_F + W_F^J J^2 - W_F^K J^2 + W_\pm(J_x^2 - J_y^2) \tag{III.11}$$

where W_F, W_F^J, W_F^K, and $W_\pm$ are the Fermi-type
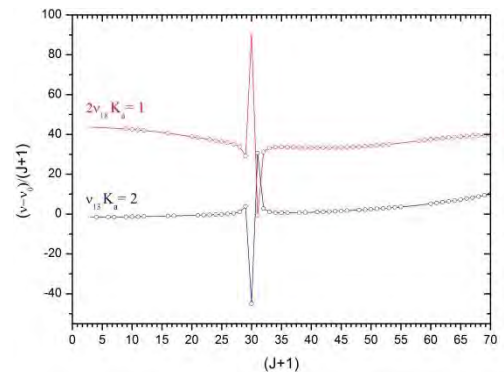
FIGURE III.13: *Example of some observed perturbations between the rotational levels of ν_{13} and $2\nu_{18}$ of propenal. The $(\nu-\nu_0)$ quantity represents the difference of the frequency of a given excited state transition and the corresponding transition in the ground state. Each circle represents the experimentally measured frequency and the continuous line is a result of the predictions based on the final set of the spectroscopic constants.*

coupling constants.

Coriolis type interactions are allowed by symmetry when the direct product of the symmetric representation of the interacting states and that for the J_α operator (α=a, b, c) contains the totally symmetric representation of the group[57].

$$\Gamma(\nu_i) \otimes \Gamma(\nu_j) \otimes \Gamma(J_\alpha) \subseteq A, A', A_1, A_g, \Sigma_g^+ \ldots \qquad \text{(III.12)}$$

The type of operator (α) dictates the type of Coriolis coupling that might be given. Taking c-type Coriolis as an example, the Hamiltonian would be[56]:

$$H_C^{i,j} = iG_c J_c + F_{ab}(J_a J_b - J_b J_a) \qquad \text{(III.13)}$$

where G_c and F_{ab} are named as the first-order and second-order Coriolis coupling constants, respectively. The last F_{ab} is a centrifugal distortion term that provides corrections to the matrix.[57-59] An initial value of G_c can be estimated by means of the harmonic frequencies of the modes involved in the coupling ($\omega_{i,j}$) and the dimensionless Coriolis (ζ^c) obtained and from force field calculations:[58]

$$G_C^{i,j} = C_e \zeta_{i,j} \left[(\omega_i / \omega_j)^{1/2} + (\omega_j / \omega_i)^{1/2} \right] \qquad \text{(III.14)}$$

Both Coriolis and Fermi terms are defined elsewere[60] in terms of parameters of the SPFIT/SPCAT program package employed in the analysis.

III.4. REFERENCES

[1]   D. H. Levy, *Annual Review of Physical Chemistry* **1980**, *31*, 197-225.
[2]   D. H. Levy, *Science* **1981**, *214*, 263-269.
[3]   D. H. Levy, (Eds.: J. M. Hollas, D. Phillips), Spinger Science, London, **1995**.
[4]   W. H. Flygare, T. J. Balle, Google Patents, **1983**.
[5]   W. Demtröder, (Ed.: r. Ed.), Springer-Verlag, Berlin, **2002**.
[6]   D. L. Andrews, *Lasers in Chemistry*, Springer-Verlag, Berlin, **1990**.
[7]   R. Weinkauf, J.-P. Schermann, M. S. de Vries, K. Kleinermanns, *Eur. Phys. J. D* **2002**, *20*, 309-316.
[8]   R. J. Lipert, S. D. Colson, *Chem. Phys. Lett.* **1989**, *161*, 303-307.
[9]   T. R. Rizzo, Y. D. Park, L. A. Peteanu, D. H. Levy, *The Journal of chemical physics* **1986**, *84*, 2534-2541.
[10]   T. S. Zwier, *The Journal of Physical Chemistry A* **2001**, *105*, 8827-8839.
[11]   E. G. Robertson, J. P. Simons, *Physical Chemistry Chemical Physics* **2001**, *3*, 1-18.
[12]   P. M. Johnson, M. R. Berman, D. Zakheim, *The Journal of Chemical Physics* **1975**, *62*, 2500-2502.
[13]   S. J. Martinez, J. C. Alfano, D. H. Levy, *Journal of Molecular Spectroscopy* **1992**, *156*, 421-430.
[14]   L. Snoek, E. Robertson, R. Kroemer, J. Simons, *Chem. Phys. Lett.* **2000**, *321*, 49-56.
[15]   T. R. Rizzo, Y. D. Park, L. Peteanu, D. H. Levy, *The Journal of chemical physics* **1985**, *83*, 4819-4820.
[16]   F. Piuzzi, I. Dimicoli, M. Mons, B. Tardivel, Q. Zhao, *Chem. Phys. Lett.* **2000**, *320*, 282-288.
[17]   L. C. Snoek, R. T. Kroemer, M. R. Hockridge, J. P. Simons, *Physical Chemistry Chemical Physics* **2001**, *3*, 1819-1826.
[18]   J. Peon, A. H. Zewail, *Chem. Phys. Lett.* **2001**, *348*, 255-262.
[19]   T. Gustavsson, A. Sharonov, D. Onidas, D. Markovitsi, *Chem. Phys. Lett.* **2002**, *356*, 49-54.
[20]   T. Gustavsson, A. Sharonov, D. Markovitsi, *Chem. Phys. Lett.* **2002**, *351*, 195-200.
[21]   A. Sharonov, T. Gustavsson, V. Carré, E. Renault, D. Markovitsi, *Chem. Phys. Lett.* **2003**, *380*, 173-180.
[22]   D. Onidas, D. Markovitsi, S. Marguet, A. Sharonov, T. Gustavsson, *The Journal of Physical Chemistry B* **2002**, *106*, 11367-11374.
[23]   T. Gustavsson, Á. Bányász, E. Lazzarotto, D. Markovitsi, G. Scalmani, M. J. Frisch, V. Barone, R. Improta, *Journal of the American Chemical Society* **2006**, *128*, 607-619.
[24]   M. Mons, F. Piuzzi, I. Dimicoli, L. Gorb, J. Leszczynski, *The Journal of Physical Chemistry A* **2006**, *110*, 10921-10924.
[25]   M. Shukla, J. Leszczynski, *Chem. Phys. Lett.* **2006**, *429*, 261-265.
[26]   H. Chen, S. Li, *The Journal of Physical Chemistry A* **2006**, *110*, 12360-12362.
[27]   C. M. Marian, *The Journal of Physical Chemistry A* **2007**, *111*, 1545-1553.
[28]   K. Seefeld, R. Brause, T. Häber, K. Kleinermanns, *The Journal of Physical Chemistry A* **2007**, *111*, 6217-6221.
[29]   H. Mitsuda, M. Miyazaki, I. B. Nielsen, P. Carcabal, C. Dedonder, C. Jouvet, S.-i. Ishiuchi, M. Fujii, *J. Phys. Chem. Lett.* **2010**, *1*, 1130-1133.
[30]   C. Cabezas, I. Peña, J. C. López, J. L. Alonso, *The Journal of Physical Chemistry Letters* **2013**, *4*, 486-490.

[31]   J. L. Alonso, I. Peña, J. C. Lopez, V. Vaquero, *Angewandte Chemie-International Edition* **2009**, *48*, 6141-6143.

[32]   A. Lesarri, S. Mata, J. C. Lopez, J. L. Alonso, *Rev. Sci. Instrum.* **2003**, *74*, 4799-4804.

[33]   S. Mata, I. Peña, C. Cabezas, J. C. López, J. L. Alonso, *Journal of Molecular Spectroscopy* **2012**, *280*, 91-96.

[34]   I. Peña, A. M. Daly, C. Cabezas, S. Mata, C. Bermúdez, A. Niño, J. C. López, J.-U. Grabow, J. L. Alonso, *The Journal of Physical Chemistry Letters* **2012**, *4*, 65-69.

[35]   J. L. Alonso, J. C. López, Springer Berlin Heidelberg, **2015**, pp. 1-67.

[36]   G. G. Brown, B. C. Dian, K. O. Douglass, S. M. Geyer, S. T. Shipman, B. H. Pate, *Review of Scientific Instruments* **2008**, *79*.

[37]   I. Peña, S. Mata, A. Martín, C. Cabezas, A. M. Daly, J. L. Alonso, *Physical Chemistry Chemical Physics* **2013**, *15*, 18243-18248.

[38]   J. L. Alonso, C. Perez, M. E. Sanz, J. C. Lopez, S. Blanco, *Physical Chemistry Chemical Physics* **2009**, *11*, 617-627.

[39]   A. G. Lesarri, M. E. Charro, R. M. Villamañán, D. G. Lister, J. C. López, J. Alonso, *Journal of Molecular Spectroscopy* **1991**, *149*, 317-328.

[40]   W. D. Cornell, P. Cieplak, C. I. Bayly, I. R. Gould, K. M. Merz, D. M. Ferguson, D. C. Spellmeyer, T. Fox, J. W. Caldwell, P. A. Kollman, *Journal of the American Chemical Society* **1995**, *117*, 5179-5197.

[41]   J. J. P. Stewart, *Journal of Computational Chemistry* **1989**, *10*, 209-220.

[42]   M. J. S. Dewar, E. G. Zoebisch, E. F. Healy, J. J. P. Stewart, *Journal of the American Chemical Society* **1985**, *107*, 3902-3909.

[43]   M. J. Frisch, G. W. Trucks, H. B. Schlegel, G. E. Scuseria, M. A. Robb, J. R. Cheeseman, G. Scalmani, V. Barone, B. Mennucci, G. A. Petersson, H. Nakatsuji, M. Caricato, X. Li, H. P. Hratchian, A. F. Izmaylov, J. Bloino, G. Zheng, J. L. Sonnenberg, M. Hada, M. Ehara, K. Toyota, R. Fukuda, J. Hasegawa, M. Ishida, T. Nakajima, Y. Honda, O. Kitao, H. Nakai, T. Vreven, J. A. Montgomery, J. E. Peralta, F. Ogliaro, M. Bearpark, J. J. Heyd, E. Brothers, K. N. Kudin, V. N. Staroverov, T. Keith, R. Kobayashi, J. Normand, K. Raghavachari, A. Rendell, J. C. Burant, S. S. Iyengar, J. Tomasi, M. Cossi, N. Rega, J. M. Millam, M. Klene, J. E. Knox, J. B. Cross, V. Bakken, C. Adamo, J. Jaramillo, R. Gomperts, R. E. Stratmann, O. Yazyev, A. J. Austin, R. Cammi, C. Pomelli, J. W. Ochterski, R. L. Martin, K. Morokuma, V. G. Zakrzewski, G. A. Voth, P. Salvador, J. J. Dannenberg, S. Dapprich, A. D. Daniels, O. Farkas, J. B. Foresman, J. V. Ortiz, J. Cioslowski, D. J. Fox, Wallingford CT, **2010**.

[44]   P. J. Stephens, F. J. Devlin, C. F. Chabalowski, M. J. Frisch, *The Journal of Physical Chemistry* **1994**, *98*, 11623-11627.

[45]   C. Moller, M. S. Plesset, *Physical Review* **1934**, *46*, 0618-0622.

[46]   R. Krishnan, J. S. Binkley, R. Seeger, J. A. Pople, *The Journal of Chemical Physics* **1980**, *72*, 650-654.

[47]   Z. Kisiel, L. Pszczółkowski, I. R. Medvedev, M. Winnewisser, F. C. De Lucia, E. Herbst, *Journal of Molecular Spectroscopy* **2005**, *233*, 231-243.

[48]   W. Gordy, R. L. Cook, *Microwave Molecular Spectra, Vol. IX and XIV*, Wiley-Interscience, New York, **1984**.

[49]   J. A. Wollrab, *Rotational Spectra and Molecular Structure*, Academic Press, New York & London, **1967**.

[50]   H. W. Kroto, *Molecular Rotation Spectra*, Dover Publications Inc., New York, **1992**.

[51]   J. M. Hollas, *High Resolution Spectroscopy*, Jonh Wiley & Sons, United Kingdom, **1998**.

[52]   H. M. Pickett, *Journal of Molecular Spectroscopy* **1991**, *148*, 371-377.

[53]   W. Gordy, R. L. Cook, *Microwave Molecular Spectroscopy*, John Wiley & Sons, New York, **1984**.

[54]   J. L. Alonso, V. Vaquero, I. Peña, J. C. López, S. Mata, W. Caminati, *Angewandte Chemie* **2013**, *48*, 5934-5936.

[55]   J. K. G. Watson, *Vibrational Spectra and Structure, Vol. 6*, Elsevier: Amsterdam, **1977**.

[56]   V. I. Perevalov, V. G. Tyuterev, *Journal of Molecular Spectroscopy* **1982**, *96*, 56-76.

[57]   P. R. Bunker, P. Jensen, *Molecular Symmetry and Spectroscopy*, NRC Research Press, Ottawa, **2006**.

[58]   D. Papousek, M. R. Aliev, *Molecular Vibrational-Rotational Spectra*, Academia, Prague, **1982**.

[59]   J. Plíva, *Journal of Molecular Spectroscopy* **1986**, *120*, 5-10.

[60]   R. A. H. Butler, D. T. Petkie, P. Helminger, F. C. De Lucia, *Journal of Molecular Spectroscopy* **2003**, *220*, 150-152.

CHAPTER IV. UNVEILING THE SWEET CONFORMATIONS OF D-FRUCTOPYRANOSE
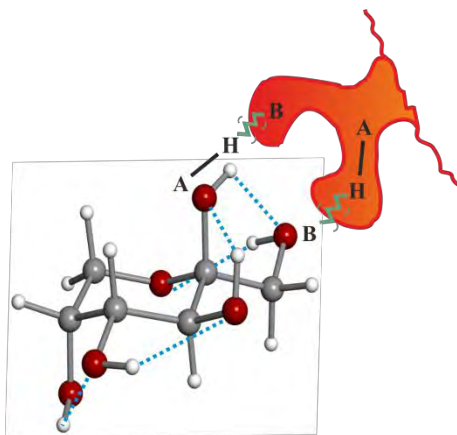
Two conformers of D-fructopyranose have been characterized using laser ablation and broadband Fourier transform microwave spectroscopy. Both species are stabilized by complicated intramolecular hydrogen bonding networks. Structural motifs related to the sweetness of D-fructopyranose have been revealed for the most stable conformer.

The physical and chemical properties that make carbohydrates so relevant are directly related to their structure. A clear example is the sweetness.[1] D-fructose $(C_6H_{12}O_6)$, a six-carbon polyhydroxyketone (see Scheme IV.1 (a)), is the sweetest naturally occurring carbohydrate. It is present in most of the vegetables and fruits, and it is a structural component of sucrose. Previous studies have established that its sweetness in solution decreases while the proportion of fructopyranose drops off assuming that the sweetness is directly related to the D-fructopyranose structure.

Although ketohexoses as fructose can exhibit linear form, D-fructose rapidly cyclize in aqueous solution to form mixtures of pyranose and furanose forms.[2] The cyclation reaction converts the C_2 in a chiral carbon yielding two enantiomers designated α and β (Scheme IV.1 (b)). For D-fructose, the equilibrium concentrations in water are around 57% of β-D-pyranose; 31% of β-D-furanose; 9% of α-D-furanose and 3% of α-D-pyranose).[3] However, in its crystalline form, the unique species found is the β-D-fructropyranose, according to the crystal structure experiments.[4] Besides other higher energy forms, pyranoses adopt preferably a rigid chair backbone with the conformations $^5C_2$ and $^2C_5$ shown in Scheme IV.1(c).

Despite the important role of D-fructopyranose in sugar chemistry, there exists no detailed experimental information about its conformational behavior. In addition to steric and anomeric effects, the conformational analysis of D-fructopyranoses requires the consideration of intramolecular hydrogen bonding between vicinal OH groups. The relative arrangement of the hydroxyl groups is relevant to distinguish between the different conformers. Unveiling the most stable structures of fructopyranose in isolated conditions of gas phase may contribute to a better understanding of this sweet property attributed to D-fructopyranose.
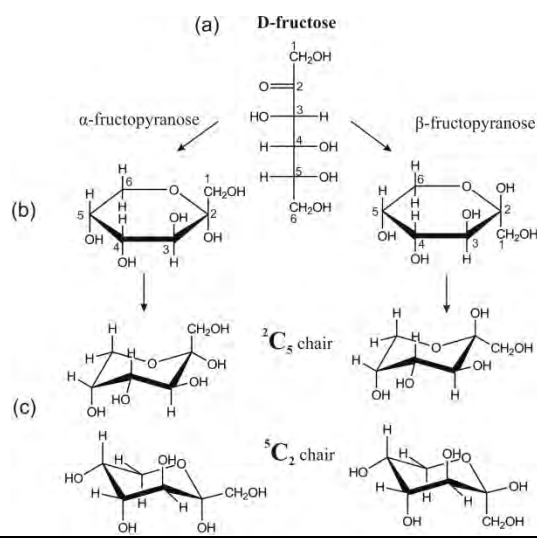
SCHEME IV.1: (a) Fisher projection of D-fructose; (b) Haworth projections of α and β anomers; (c) $^2C_5$ and $^5C_2$ chair configurations.

The determination of the three-dimensional molecular geometry by microwave spectroscopy is feasible for D-fructopyranose. A high-resolution rotational spectrum unambiguously distinguishes among different conformations.[5] In addition, molecules entrained in an expanding supersonic jet provides a powerful means of isolated them and probing their most stable conformers by their rotational spectrum. The transfer of molecules into the gas phase most commonly involves classical heating methods of vaporization. However, D-fructose suffers thermal decomposition and the ring
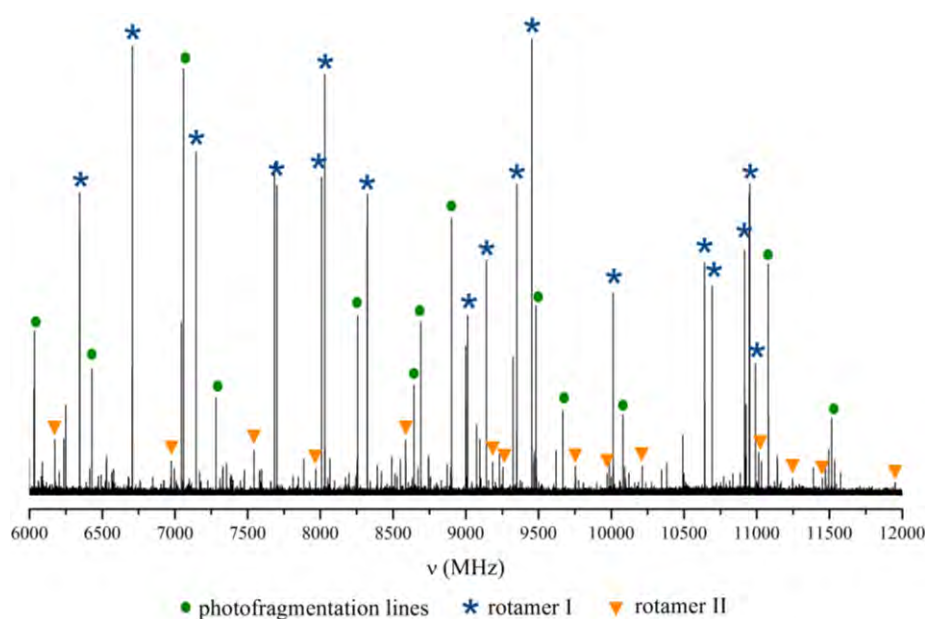
FIGURE IV.1: Broadband microwave spectrum of D-fructose

structure becomes uncertain due to mutarotation.[6] Although D-fructopyranose cannot undergo transition from a pyranose to a furanose form in the gas phase, this transition may be possible (prior) during vaporization. The way to minimize this process is by using a technique that vaporizes neutral molecules rapidly. Such a technique is laser ablation which involves desorbing the sample from the solid by a short laser pulse.[7] This process is fast enough to prevent any transition of D-fructopyranose into other form.

Taking into account all above, we have used our laser ablation technique combined with Fourier transform microwave spectroscopy in a supersonic expansion[8] to bring crystalline D-fructopyranose into the gas phase and probe all plausible conformers by their rotational spectra. A new broadband microwave spectrometer (CP-FTMW), described in detail elsewhere,[8-9] has been used to

rapidly acquire the rotational spectra in wide frequency ranges, making more efficient the search of different coexisting species in the supersonic jet. LA-MB-FTMW spectroscopy,[10] which has been used in our group in the study of amino acids,[11] nitrogen bases,[12] neurotransmitters[13] and glucopyranose[14], is relatively slow since the use of a resonator Fabry-Pérot cavity limits the measurable frequency bandwidth.

The recorded broadband spectrum from 6-12 GHz of D-fructopyranose shown in Figure IV.1, allowed us to identify two intense μ_c-type R-branch progressions of the type $J+1_{1,J} \leftarrow J_{0,J}$ and $J+1_{2,J} \leftarrow J_{1,J}$ (J quantum number ranging from 3 to 5), as corresponding to a first rotamer I. Once the lines from rotamer I and those belonging to known spectra of photofragmentation species (glyceraldehyde, ethylene glycol, acetic acid, oxoacetic acid, formaldehyde and acrolein) were

	Rotamer I cc β $^2C_5$ g-[a]		Rotamer II cc β $^2C_5$ t	
	Exp.	Theor.	Exp.	Theor.
A^b/MHz	1465.27642(57)[f]	1469.07	1241.55585(61)	1244.58
B/MHz	770.56891(32)	777.03	837.27557(54)	843.84
C/MHz	609.96826(32)	614.09	712.1201(17)	717.72
μ_a/D	...	-0.2	...	-0.3
μ_b/D	...	0.0	...	-0.1
μ_c/D	observed	1.4	observed	3.6
σ^c/kHz	4.0	...	9.9	...
N^d	18	...	22	...
$\Delta E_{MP2}{}^e$	...	0	...	735

removed from the spectra, an exhaustive search on the remaining weaker lines conducted to the assignment of a new set of μ_c-type R-branch progressions ascribed to a second rotamer II. μ_a- and μ_b-type transitions were predicted for both rotamers but they could not be detected in the spectrum. The measured rotational transitions given in Tables IV.S1 and IV.S2 of the Supplementary Information were analyzed[15] using a rigid rotor Hamiltonian to give the sets of rotational constants collected in Table IV.1 for both rotamers.

Conformational assignments of the detected rotamers I and II can be based upon the combination of several factors which collectively provide unique identifications. These include the quantitative match between the experimental and calculated *ab initio* values of the rotational constants and the correlation between the predicted dipole moment components and the intensity of the corresponding rotational transition. We took into consideration conformers below 1100 cm⁻¹ resulting from a conformational search[16] carried out on all plausible ring configurations of α- and β-D-fructopyranoses. The final set of spectroscopic constants were generated by performing a series of *ab initio* geometry optimization[17] using MP2 perturbation theory at the (MP2/6-311G++(d,p)) level. The results are collected in Table IV.S3 and IV.S4 of the Supplementary Information.

The experimental and predicted *ab initio* values of the rotational constants in Table IV.1 allows the irrefutable identification of rotamer I to conformer cc β $^2C_5$ g- and rotamer II to conformer cc β $^2C_5$ t. Additionally, the predicted small values of μ_a and μ_b dipole moment components for both conformers are consistent with the non-observation of the corresponding spectra. From relative intensity measurements we have estimated the population ratio of fructopyranose forms β $^2C_5$ g-: cc β $^2C_5$ t as 1: 0.02 which is in excellent accordance with the computed energies; conformer cc β $^2C_5$ t is predicted 700 cm⁻¹ above the global minimum cc β $^2C_5$ g-. The exceptional matching between experimental rotational constants and those predicted from the equilibrium structure (relative errors less than 0.8%) allows to assuming the actual structures of both conformers as those predicted by *ab initio* calculations depicted in Figure IV.2. Both conformers are present in the most favorable chair configuration $^2C_5$, with the largest substituent in

equatorial position and the anomeric hydroxyl group ($OH_{(2)}$) in axial position (anomeric effect).[18]

The most abundant conformer cc β $^2C_5$ g- is stabilized by a five cooperative intramolecular hydrogen bond network, (see Figure IV.2) $OH_{(5)}\cdots OH_{(4)}\cdots OH_{(3)}\cdots OH_{(2)}\cdots OH_{(1)}\cdots O_{(ring)}$, with a counter clockwise arrangement of the OH groups. This hydrogen bond cooperative interaction associated to this conformer is a form of intramolecuar solvation which reinforces the stability. In the same way, conformer cc β $^2C_5$ t shows a chain of three cooperative $OH_{(5)}\cdots OH_{(4)}\cdots OH_{(3)}\cdots OH_{(2)}$ and one non-coperative $OH_{(1)}\cdots O_{(ring)}$ hydrogen bonds.

A simple rationalization of structure-sweetness relationship is based on the existence of a basic structural unit common to sweet molecules, and formed by a proton donating A-H and proton accepting B electronegative groups[1a-e]. The concept of a tripartite glucophore AH-B ("sweetness triangle") has its merit as a unifying
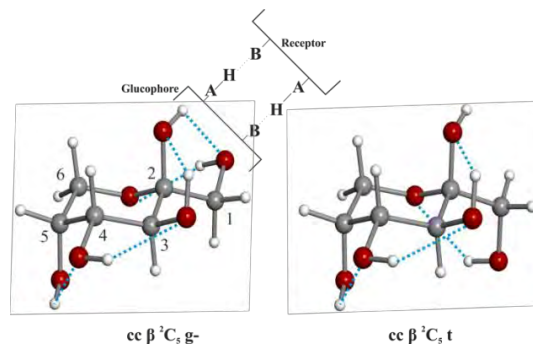
FIGURE IV.2: *The three dimensional structures of the two observed conformers of β-D-fructopyranose showing the intramolecular hydrogen bonding networks and the glucophore unit.*

criterion proved useful in rationalizing the sweetness in diverse classes of compounds.[1a-c] The assignment of the AH-B tripartite in detected conformers of Figure IV.2 is very complicated by the fact each OH group can function as AH and/or B. After the examination of structure of cc β $^2C_5$ g-conformer, one can state that $OH_{(1)}$ and $O_{(2)}$ can be considered as the most likely AH-B glucophore causing the sweet response via interaction with a complementary hydrogen bond donor and acceptor in the taste receptor. Hence, the most abundant conformer cc β $^2C_5$ g- might be responsible of the sweetness of D-fructose.

IV.1. EXPERIMENTAL SECTION

The rotational spectrum of D-fructose was investigated by using a chirped pulse Fourier transform microwave spectrometer (CP-FTMW),[8] which works in the 6-18 GHz frequency region. Solid samples of D-fructose (m.p. ~ 120ºC) were ground and mixed with a minimum amount of a commercial binder and pressed into cylindrical

rods which were placed into our ablation nozzle and vaporized using a Nd:YAG picosecond laser. The vaporized molecules were seeded in the carrier gas Ne to expand adiabatically into a vacuum chamber where they were probed by Fourier transform microwave spectroscopy. An arbitrary waveform generator created a microwave pulse containing a

fast linear sweep (chirp) over the entire frequency region from 6 to 12 GHz, which was directly amplified by a 300W TWT (travelling wave tube) amplifier. The amplified pulse was broadcast into the vacuum chamber through two microwave horns interacting with the vaporized molecules in the pulsed jet. The free induction decay signal (FID) was amplified and digitized on a fast oscilloscope. 150000 averages were acquired to obtain the rotational spectrum (See Figure IV.1). The estimated accuracy of the frequency measurements is better than 10 kHz.

VI.2. REFERENCES

[1]   a) R. S. Shallenberger, T. E. Acree, *Nature* **1967**, *216*, 480-482; b) L. B. Kier, *J. Pharm. Sci.* **1972**, *61*, 1394-1397; c) van der Heijden, *Pure Appl. Chem.* **1997**, *69*, 667-674; d) R. J. Woods, W. A. Szarek, V. H. Smith, *J. Am. Chem. Soc.* **1990**, *112*, 4732-4741; e) R. S. Shallenberger, *Pure Appl. Chem.* **1978**, *50*, 1409-1420; f) E. W. Deutsch, C. Hansch, *Nature* **1966**, *211*, 75.

[2]   A. L. Lehninger, *Principles of Biochemistry*, 4th ed., W.H. Freeman, **2004**.

[3]   D. Doddrell, Allerhan.A, *J. Am. Chem. Soc.* **1971**, *93*, 2779-2781.

[4]   a) J. A. Kanters, G. Roelofsen, B. P. Alblas, I. Meinders, *Acta Cryst. B* **1977**, *33*, 665-672; b) S. Takagi, G. A. Jeffrey, *Acta Cryst. B* **1977**, *33*, 3510-3515. 10.

[5]   J. P. Schermann, *Spectroscopy and Modeling of Biomolecular Building Blocks*, Elsevier, 2008.

[6]   M. Hurtta, I. Pitkänen, J. Knuutinen, *Carbohydrate Research* **2004**, *339*, 2267-2273.

[7]   R. J. Levis, *Annu. Rev. Phys. Chem.* **1994**, *45*, 483-518.

[8]   S. Mata, I. Peña, C. Cabezas, J. C. López, J. L. Alonso, , *J. Mol. Spectrosc.* **2012**, *280*, 91-96.

[9]   G. G. Brown, B. C. Dian, K. O. Douglass, S. M. Geyer, S. T. Shipman, B. H. Pate, *Rev. Sci. Instrum.* **2008**, *79*.

[10]   J. L. Alonso, C. Pérez, M. E. Sanz, J. C. López, S. Blanco, *Phys. Chem. Chem. Phys.* **2009**, *11*, 617-627.

[11]   See, for example, a) E. J. Cocinero, A. Lesarri, J. U. Grabow, J. C. López, J. L. Alonso, *Chemphyschem* **2007**, *8*, 599-604; b) I. Peña, M. Eugenia Sanz, J. C. López, J. L. Alonso, *J. Am. Chem. Soc.* **2012**, *134*, 2305-2312.

[12]   J. L. Alonso, I. Peña, J. C. López, V. Vaquero, *Angew. Chem. Int. Ed.* **2009**, *48*, 6141-6143 and references therein.

[13]   C. Cabezas, M. Varela, I. Peña, J. C. López, J. L. Alonso, *Phys. Chem. Chem. Phys.* **2012**, *14*, 13618-13623

[14]   M. Lozoya, C. Cabezas, S. Mata, J. C. López, J. L. Alonso in *LA-MB-FTMW Studies of Sugars*, Communication MH13, International Symposium on Molecular Spectroscopy, *66th Meeting* – Ohio State University, USA, **2011**.

[15]   H. M. Pickett, *J. Mol. Spectrosc.* **1991**, *148*, 371-377.

[16]   M. J. S. Dewar, E. G. Zoebisch, E. F. Healy, J. J. P. Stewart, *J. Am. Chem. Soc.* **1985**, *107*, 3902-3909.

[17]   M. J. Frisch, *et al. Gaussian 09, Revision B.01*, Wallingford CT, **2010**.

[18]   E. Juaristi, G. Cuevas, *Tetrahedron* **1992**, *48*, 5019-5087.

CHAPTER V . SWEETNESS AND KETOHEXOSES CONFORMATIONAL BEHAVIOUR

A comparative analysis of the conformational behavior of D-fructose epimers has been executed in order to rationalize the diverse and, sometimes, contradictory theories concerning sweetness on the basis of this new structural information. Rotational spectroscopy combined with laser ablation was employed to identify three, two and one conformational species for ketohexoses D-tagatose, D-psicose and L-sorbose, respectively. These species were found to be stabilized by different cooperative H-bond networks stablished between all hydroxyl groups of each molecule. Several parallels in the distribution of these H-bonds were found indicating that there are common conformational signatures that might be related with the place where they interact with the sweet receptor.

V.1. INTRODUCTION

Human beings feel attracted to food owing to its flavors and the pleasure experienced when tasting them. The sense of taste, located in the oral cavity, is able to recognize up to five different tastes from food: salty, sour, bitter, sweet and umami (from the Japanese *umai*; meaning delicious). Perceiving salty and sour tastes is due to the presence of protons and ions. There is no relation with the structure of the substance. In contrast, sensing the latter three flavors (bitter, sweet and umami) is due to a response induced by chemoreceptors in the taste bud recognizing specific molecular structures. Inquiry into these taste receptors has identified the structures responsible for perceiving each flavor:[1] taste receptors (TRB), which are members of G-protein-coupled receptors (GPCRs) present in tongue and palate epithelia.[2] Particularly, within this TRB group, type T2R taste receptors recognize bitterness whereas sweetness and umami are detected by type T1R, assigning T1R1 and T1R3 to umami and T1R2 and T1R3 to sweetness.[3-5] Therefore, only two receptors are responsible for recognizing all of the many and diverse sweeteners that exist. In order to account for all of them, these receptors have been conjectured to contain different binding sites, each responsible for detecting sweeteners of similar sizes. Thus, all small-size sweeteners, like monosaccharides or amino acids, are due to interactions with the same receptor site.[6] Nonetheless, not all similar size molecules

are equally sweet. This therefore raises the question concerning which structural characteristics provide sweeteners with their flavor, while other substances with similar structures are not sweet, in other words, what the relation is between sweetness and structure.

Since early last century, abundant research has addressed the link between sweetness and the structure of sweeteners.[11] Several studies have assigned the sweet properties of a molecule to the presence of particular pairs of functional groups,[12-13] while, others have assigned it to a specific disposition of an atom.[11, 14] Yet, none of these theories had been able to offer a unified explanation regarding the sweetness-structure relation until Shallenberger and Acree's proposal.[15-16] They observed that the hydrogen bonds of sweet molecules strongly affected their sweetness. Under these circumstances, they stated that the degree of sweetness depends on the strength of two H-bonds
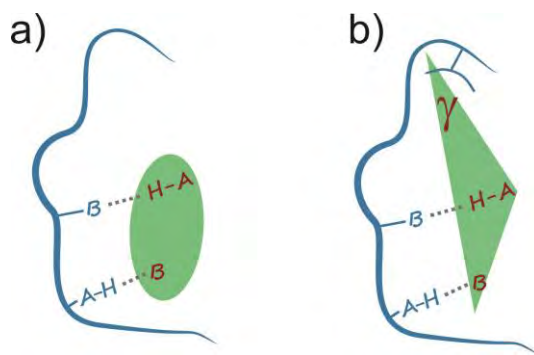
FIGURE V.I. *Representation of the sweetness theories. a) Shallenberger's theory: green area represents the glucophore of the sweetener. b) Diagram of the "sweetness triangle" in the sweetener (marked in green).[7-10]*

by which the sweetener is bound to the sweet receptor (see Figure V.1a). They established that one of the two electronegative atoms might act as proton donor (AH) in the hydrogen bond interaction and the other as acceptor (B). These two groups form what is called the glucophore, which generally refers to the part of the sweetener that interacts with the sweet receptor.

A third binding site was later proposed by Kier, the γ-site, forming the "sweetness triangle" Figure V.1.b).[17] This new γ-site might interact with the receptor via hydrophobic or van der Waals' interaction. Nonetheless, the γ-site was postulated as unnecessary. Indeed, it was stated that it merely enhances the sweet flavor depending on the γ-AH-B distance.[18]

Evolution of sweetness theories continued with the introduction of the multipoint attachment theory. Tinti et al. proposed that, besides the complementary sites for the AH-B-γ triangle, the sweet receptor must contains at least five other linking sites where the sweetener can interact, making eight sites in all.[19] However, the glucophore in the sweetener need not contain the analogous eight binding sites, although, the greater the number of interactions, the sweeter the substance. This and other related theories always concur with Shallenberger's initial idea that in order to be sweet a molecule needs to establish two H-bonds with the receptor.

At the time all these theories were proposed, experimental data regarding the structure of
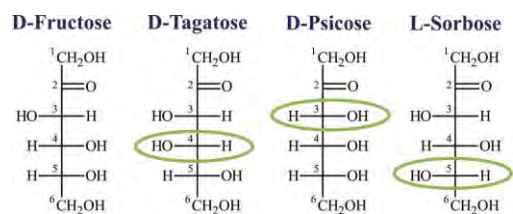
FIGURE V.2. *Fisher projection of ketohexoses indicating the carbon that changes the configuration with regard to D-Fructose.*

sweeteners was restricted to information from condensed phases, and was unable to offer much detail concerning either the spatial distribution of hydrogen atoms or the intrinsic intramolecular H-bond interactions that stabilize the molecules. A 3D conformational study of these sweet substances might provide such information, shedding some light on the discussion regarding the relation between sweetness and structure.

The particular case of ketohexoses (ketoses with six carbon atoms, see Figure V.2) is extremely appealing since these epimers (sugars that only differ in the configuration of one asymmetric carbon) are as sweet as table sugar (sucrose) with the exception of D-Fructose which is twice as sweet. If we drew a comparison between the conformational behaviour of their most stable structures, we could extract common structural features that may endow them with their sweet flavor. Likewise, seeking the different characteristics of sweeteners with varying degrees of sweetness, we would be able to identify those conformational aspects that enhance the flavor of the sweetest ones.

In light thereof, in the present work, we have vaporized the solid samples of D-fructose,[20] D-tagatose, D-psicose and L-sorbose (m.p. from 103

to 165ºC) and their most stable structures characterized in the isolation conditions of a supersonic expansion by Fourier transform microwave spectroscopy. The results of this conformational analysis are used to evaluate the theories proposed to date concerning sweetness.

Nowadays, the food industry is looking to design tasty new substances, not only maintaining sweet taste but also avoiding undesirable health effects. Consequently, there is keen interest in identifying the structural requirements that a sweet substance must contain in order to planify the synthesis of new artificial sweetners.

V.2. BACKGROUND

The rotational spectroscopic studies of monosaccharides undertaken under the isolation conditions of the gas phase has proven ideal for exploring conformational behaviour.[21] *Detailed structural information concerning the intramolecular hydrogen bond networks that contribute to stabilizing the observed conformers can be extracted from high resolution rotational studies.*[22] However, these studies have been hampered by vaporization problems; sugars thermally decompose before being vaporized by classical heating methods. Laser techniques have emerged as an alternative solution. The first conformational characterization of the archetypal monosaccharide D-glucose has recently become possible by combining laser ablation (LA) with molecular beam Fourier transform microwave (MB-FTMW) spectroscopy.[21] Four conformers of α-D-glucopyranose and three conformers of β-D-glucopyranose have been unequivocally identified. More recently, a new generation of broadband microwave spectrometers has allowed to record the spectrum in wide frequency ranges, making

conformational research more efficient.[23] In our laboratory, we recently combined the lattest broad-band chirped-pulse Fourier transform microwave technology (CP-FTMW) introduced by Pate with our laser ablation sources (LA)[24] and applied to make the first rotational studies of D-erythose,[25] D-xylose[26], D-glucosamine[27] and 2-deoxyribose.[28]

A scheme of our LA-CP-FTMW spectrometer constructed at the University of Valladolid as well as the operating sequence is shown in Figure V.3. A 4 μs chirped-pulse is directly generated by an arbitrary waveform generator (1) and amplified by the adjustable (3) traveling wave tube (2) amplifier with a 300 W maximum output power. Following amplification, a parabolic reflector system comprising dual ridge horns (5-6) and two parabolic reflectors (6-7) in a paraxial beam configuration is used to broadcast the excitation pulse into the vacuum chamber and receive the broadband molecular emission. This molecular free induction decay (FID) signal is directly digitized using a digital oscilloscope (8) after it has been

(a) Scheme of LA-CP-FTMW instrument

(b) Operation sequence of LA-CP-FTMW instrument
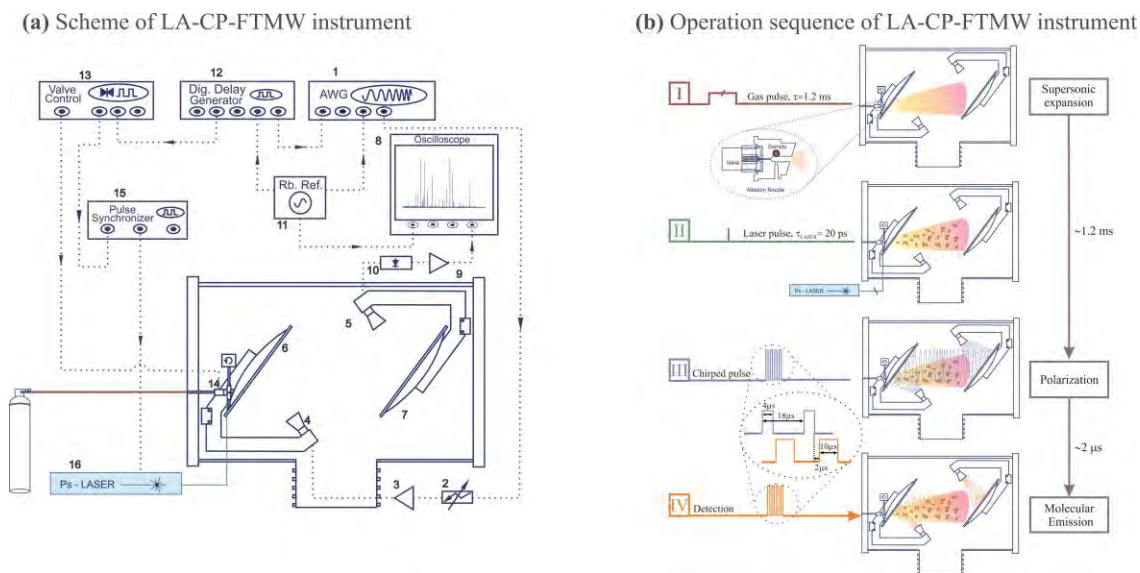
FIGURE V.3. *Pulse sequence for a single experimental cycle including generation of a supersonic expansion and laser ablation, polarization and detection. (1) Arbitrary Waveform Generator: Tektronix AWG7122B, 24Gsamples/s[1]. (2) Variable attenuator. (3) Traveling Wave Tube Amplifier, TWT: IFI, GT186-300, 300W. (4-7) Parabolic reflector system: Satimo reflector with interface for SH2000, 2-32GHz. (4) Ridge polarization horn. (5) Ridge detection horn. (6-7) Parabolic reflectors. (8) Digital Oscilloscope: Tektronix DPO72004B, 50 Gsamples/s[1], 20GHz hardware bandwidth. (9) Low nose amplifier. (10) Pin diode limiter. (11) 10MHz Rubidium Frequency Standard Oscillator: Stanford Research Systems (12) Digital Delay generator: Stanford Research Systems, DG645. (13) Valve driver: IOTA ONE. (14) Injection Valve. (15) Pulse synchronizer. (16) Nd:YAG laser: Ekspla,*

amplified with a low-noise microwave amplifier (9). The rotational spectrum in the frequency domain is obtained by taking a fast Fourier transformation of the FID, following the application of a Kaiser-Bessel window to improve baseline resolution. All frequency and trigger sources as well as the digital oscilloscope are phase-locked to a 10 MHz Rb-disciplined quartz oscillator (11).

The spectrometer operating sequence (see Figure V.3.b) , commences with a molecular pulse of 700 µs duration which drives the carrier gas flow through the pulsed valve source (a). After a slight delay, a laser pulse hits the solid and vaporizes the sample (b). Four separate broadband rotational spectra are acquired in each injection cycle (c). The four individual broadband chirped excitation pulses,

of 4 µs duration, are spaced by 18 µs. 2 µs after each excitation pulse ceases, the rotational free induction decay is then acquired for 10 µs (d). Around 100 000 individual FIDs (four per each molecular expansion) were normally averaged in the time domain and Fourier transformed to obtain the rotational spectra Using the aforementioned technique, the conformational behaviour of the first ketohexose, the archetypal D-fructose, was recently revealed.[20] Crystalline β-D-fructopyranose was transferred into gas phase by laser ablation and probed in supersonic expansion. From the analysis of the rotational spectrum, two pyranoside conformers were detected β $^2C_5$ g- cc and β $^2C_5$ t cc (Figure V.4), where α or β denote the anomer type, $^2C_5$ or $^5C_2$ refer to pyranose ring configuration, g- (-
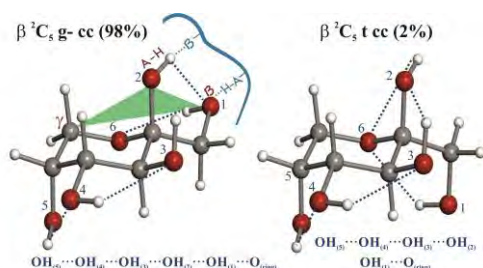
FIGURE V.4. *Observed conformers of D-fructopyranose[20] and their intramolecular H-bond networks.*

60°), $g+$ ($+60^o$) and t (180°) describe the values of the torsion angle $O_{(1)}$-$C_{(1)}$-$C_{(2)}$-$O_{(2)}$, which determines the orientation of the hydroxymethyl group and "c", "cc" and "s" describe the clockwise, counter-clockwise and split arrangements of the intramolecular hydrogen bond networks. If had been required, an additional number would be added to provide energy ordering for conformers inside the same families. These two conformers differ in the orientation of the torsion angle formed between the CH_2OH ring substituent and the anomeric OH ($O_{(1)}$-$C_{(1)}$-$C_{(2)}$-$O_{(2)}$). As such, the hydrogen bond interactions that stabilize them form different arrangements (see dashed lines of Figure V.3). The most abundant β $^2C_5$ g- cc conformer (98%) is stabilized by a network of five cooperative[29] intramolecular H-bonds in a counterclockwise (*cc*) arrangement over the entire molecule:

$OH_{(5)}\cdots OH_{(4)}\cdots OH_{(3)}\cdots OH_{(2)}\cdots OH_{(1)}\cdots O_{(ring)}$. In the least abundant (β $^2C_5$ t cc), the H-bond network is split into two: $OH_{(5)}\cdots OH_{(4)}\cdots OH_{(3)}\cdots OH_{(2)}$ and $OH_{(1)}\cdots O_{(ring)}$. The spatial disposition of the most abundant conformer of D-fructopyranose seems to indicate that $OH_{(1)}$ and $OH_{(2)}$ hydroxyl pairs are appropiate candidates to be assigned as AH and B sites of the glucophore, respectively, as it was already announced by Shallenberger et al.[30-31] Equipped with both the potential of the LA-CP-FTMW experimental tool to unveil the conformational behaviour of monosaccharides and the first results concerning D-fructose, we faced the challenge of exploring the conformational behaviour of D-fructose epimers: D-tagatose, D-psicose and L-sorbose. In the following section, we analyze their rotational spectrum in order to reveal common structural signatures that might be correlated to their sweetness, shedding some light on the identification of the glucophore. As such, theories which seek to explain the relation between sweetness and structure can be evaluated on the basis of this fresh experimental information.

V.3. RESULTS

V.3.1 D-Tagatose.

D-Tagatose is the C-4 epimer of D-fructose (Figure V.2). It is a sweetener which is 90% as sweet as sucrose (table sugar) but has only 38% of its calories. Due to its antidiabetic properties and its low glycemic index (GI=3) compared to sucrose (GI=100),[32] D-tagatose is considered to be a healthy sweetener.[33] In condensed phases, D-tagatose cyclizes into a six-member ring (pyranose) by reducing its reactive carbonyl group. Hence, the
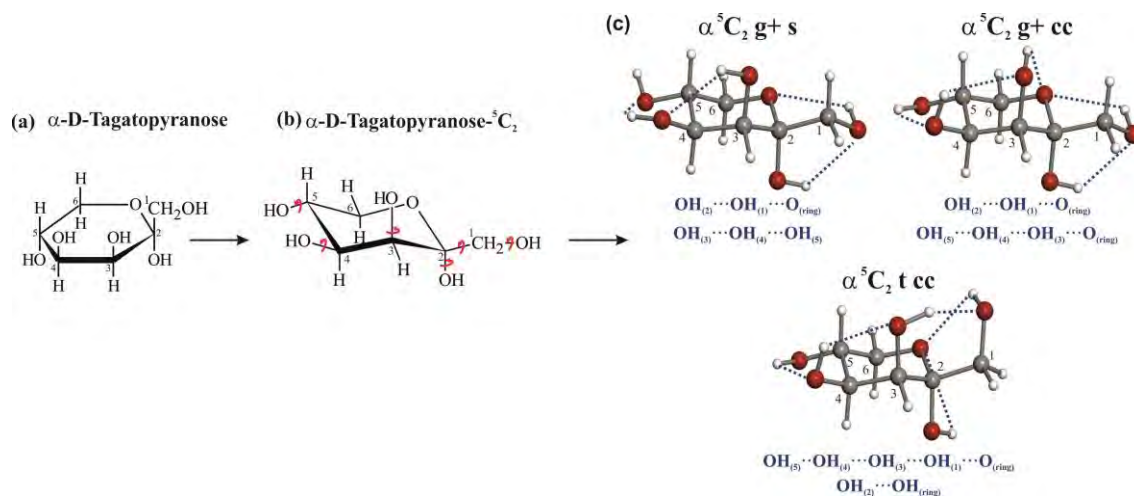
FIGURE V.5. *α-D-tagatopyranose species. (a) Haworth projection of the pyranose α anomer, which is the one found in crystalline phase.[35] α or β nomenclature is selected according to IUPAC,[36] thus, for ketohexoses, cis disposition of OH(5) and OH(2) is labeled as α and trans as β. (b) [5]C[2] and [2]C[5] chair configurations.[36] Red arrows indicate the torsion angles to be optimized ab initio. (c) Conformers observed for D-tagatose. Dashed lines mark the H-bond interactions described below. The actual structure of these three conformers are taken from those predicted ab intio (see Tables V.S5-S7 of SI) given the exceptional matching between theoretical and experimental rotational constants (Table V.1).*

$C_{(2)}$ becomes an asymmetric center, which results in two possible α and β species, called anomers (see the Haworth projection in Figure V.5.a). In aqueous solution, D-tagatose mainly exists as a mixture of α and β pyranoses, adopting the $^5C_2$ or the $^2C_5$ chair configurations (Figure V.5.b),[34] which can be interconverted by ring inversion. In crystalline form, D-tagatose exists only in α pyranoside form in the $^5C_2$ configuration,[35] where the CH_2OH ring substituent is in equatorial position.

In our experiment, which aimed to reveal its most stable conformations, solid rods of crystalline α-D-tagatopyranose (m.p.=134ºC) were vaporized by laser ablation and tested proved by CP-FTMW spectroscopy following the procedure described in the previous section. The 6 to 12GHz broadband spectrum, shown in Figure V.6.a, appeared to be dominated by decomposition lines shared by most sugars (see footnote to Figure V.6).[27] A rotameric species, labelled as I, was first identified on the basis of identifying a-type R-branch $(J+1)_{0\ J+1} \leftarrow J_{0\ J}$ and $(J+1)_{1\ J+1} \leftarrow J_{1\ J}$ pairs of rotational progressions ranging from $J=4$ to $J=8$ (Figure V.6.a). After iterative fitting and prediction, a total of 63 a-, b- and c-type R-branch transitions were collected for this rotamer (Table V.S1 of Supplementary Information (SI)). Deeper insights into the low intense background of the broadband spectrum made it possible to assign rotamers II and III (Figure V.6.b and V.6.a). For rotamer II, 22 a- and c-type R-branch transitions were measured whereas for rotamer III 16 a-type were identified (Tables V.S2-S3 of SI). Rigid rotor analysis[37] of all the frequencies measured led to the rotational constants listed in Table V.1. These values are related to the mass distribution of a molecule and
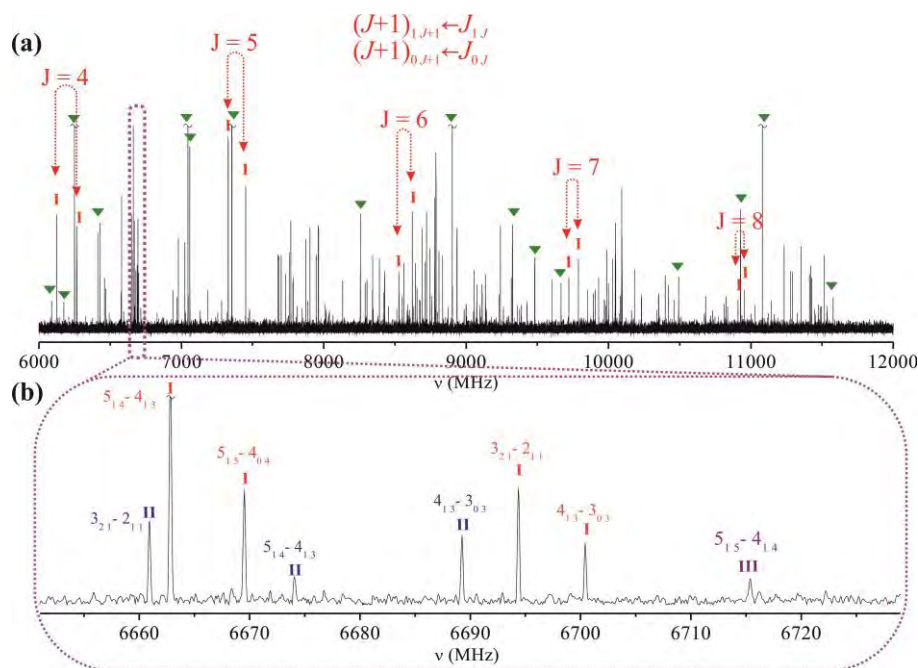
FIGURE V.6. *Broadband rotational spectrum of D-tagatose. (a) D-tagatose rotational spectrum (6-12GHz 80 000 acquisitions) obtained by LA-CP-FTMW technique. Green triangles indicate the common decomposition lines of sugars (formaldehyde, acrolein, etc). Marked in red are the a-type R-branch $(J+1)_1 J+1\leftarrow J1 J$ and $(J+1)0 J+1\leftarrow J0 J$ pairs of rotational progressions ranging from J=4 to J=8 of rotamer I. (b) Small section of the spectrum that shows a-type R-branch rotational transitions of rotamers I and II (c) Small section of the spectrum that shows rotational transitions of the three rotamers observed for D-tagatose.*

can be used in the conformational identification of these rotamers.

The resemblance between the rotational constants of rotamers I and II strongly indicates that they correspond to conformers with the same skeletal framework but different orientation of hydroxyl groups. We then took into consideration the lowest energy conformers for the $^5C_2$ ring configuration

arising from *ab initio* calculation. The five species found in an energy window of 1500cm^{-1} (see Table V.S4 of SI) were submitted[35] to full geometry optimization at MP2/6-311++g(d,p) level of theory to derive their corresponding rotational constants. A scale factor ranging from 0.991 to 0.997 makes the theoretical values for conformers α $^5C_2$ g+ s, α $^5C_2$ g+ cc and α $^5C_2$ t cc concur with the

Table V.1: Experimental rotational parameters for the observed conformers of D-tagatose

	Rotamer I	α $^5C_2$ g+ s	Rotamer II	α $^5C_2$ g+ cc	Rotamer III	α $^5C_2$ cc t
A/MHz[a]	1627.89919(33)[f]	1636.6	1614.28940(51)	1618.6	1462.359(24)	1474.9
B/MHz	698.29606(15)	701.9	699.11441(25)	703.6	747.26266(56)	750.3
C /MHz	588.40040(10)	592.3	591.15555(28)	595.7	650.90140(53)	653.6
$\|\mu_a\|$/D[b]	Observed	1.9	Observed	1.0	Observed	2.7
$\|\mu_b\|$/D	Observed	1.7	...	0.1	...	1.4
$\|\mu_c\|$/D	Observed	1.4	Observed	1.7	...	0.0
σ^c / kHz	6.5		6.3		9.6	
N[d]	63		22		16	
ΔE_{MP2}[e]/cm^{-1}		0		91		288

[a] Experimental rotational constants.[b] Experimental observation of the a, b and c-type spectrum. [c] rms deviation of the fit. [d] Number of fitted rotational transitions. [e] Relative energies (MP2/6-311++G(d,p) basis set) with respect to the global minimum. [f] Standard error in parenthesis in the units of the last digit.

experimental values for rotamers I, II and III, respectively. As anticipated, conformers, α $^5C_2$ g+ s and α $^5C_2$ g+ cc, only differ in the orientation of their hydroxyl groups. This change does not significantly affect their rotational constant values although it does drastically alter the μ_b dipole moment, which changes from 1.7D to zero when passing from the α $^5C_2$ g+ s conformer to α $^5C_2$ g+ cc. This is thus reflected in the experimental selection rules. b-type transitions are not observed for rotamer II

The configuration of all detected conformers of α-D-tagatose is the chair $^5C_2$, where the most bulky substituent is in equatorial position. The population distribution of these species was estimated from the transition intensities, taking into account the square of the dipole moments values from Table V.1. Assuming that cooling in the supersonic expansion brings all molecular systems to the lowest vibrational states, the resulting population is distributed as follows: α $^5C_2$ g+ s, 72%; α $^5C_2$ g+ cc, 22%; and α $^5C_2$ t cc, 6%. All these conformers are stabilized by H-bonds involving all hydroxyl groups of the molecule (Figure V.5.c) forming small networks which might over-stabilize them due to H-bond cooperativity.[29] Under this $^5C_2$ α configuration, every conformation of sugar exhibits two vicinal hydroxyl groups in axial disposition ($OH_{(2)}$ and $OH_{(3)}$), not allowing any hydrogen bond interaction between them to be established (see Figure V.5.c).Thus, any plausible H-bond network over the entire molecule is broken. The two most stable conformers (α $^5C_2$ g+ s and α $^5C_2$ g+

cc), which have a very similar structure, are arranged forming two split H-bond networks depicted in Figure V.5.c. The two only differ in the orientation of the network established around the hydroxyl groups $OH_{(3)}$, $OH_{(4)}$ and $OH_{(5)}$; in the most stable form, it has a clockwise orientation whereas in the latter it displays a counter-clockwise arrangement, which allows it to form an extra H-bond with the $O_{(ring)}$. As such, the α $^5C_2$ g+ cc has one H-bond more than α $^5C_2$ g+ s although it is less stable. The discrepancy in the stability of these species might be explained in terms of an anti-cooperative H-bond which might involve the $O_{(ring)}$ ($OH_{(3)}\cdots O_{(ring)}$ and $OH_{(1)}\cdots O_{(ring)}$). In the least abundant species found (α $^5C_2$ t cc), $OH_{(1)}$ does not present the same orientation as the previous two; this hydroxyl group is in anti-orientation compared to the anomeric glycol. In this way, the hydroxyl groups $OH_{(5)}$, $OH_{(4)}$, $OH_{(3)}$, $OH_{(1)}$ and $O_{(ring)}$ form an H-bond network and the remaining $OH_{(2)}$ interacts with the $O_{(ring)}$ to form an additional single H-bond, which can also lead to anti-cooperative effects.

V.3.2 D-Psicose

D-Psicose, also known as D-allulose or D-ribo-2-hexulose, is the C-3 epimer of D-fructose (Figure V.2). Its sweetness is calculated to be 70% of D-sucrose.[40] Although it is a rare sugar, D-psicose has attracted much attention recently for its promising health properties[41-44] as a no-energy sweetener.[45] In crystalline phase, D-psicose (m.p.=105ºC) appears as a β anomer (Figure V.7.a) in a $^2C_5$
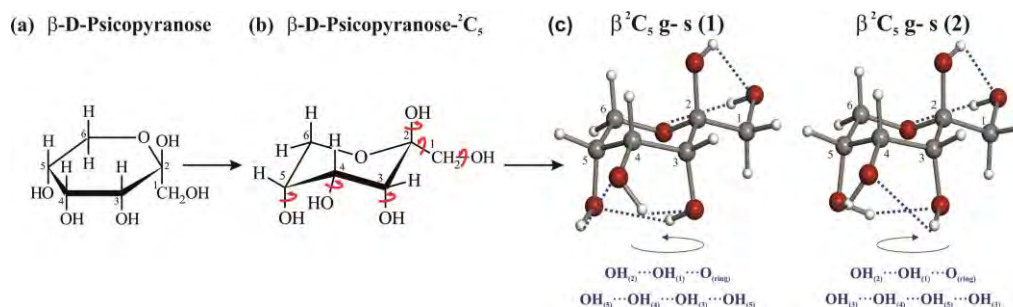
FIGURE V.7. *Species of β-D-psicopyranose. (a) Haworth projection of the pyranose β anomer[36] which is the one found in crystalline phase.[38-39] (b) [2]C[5] chair configurations, where the hydroxymethyl group is equatorial. Red arrows indicate the torsion angles to be optimized ab initio. (c) Conformers observed for D-psicose. Dashed lines mark the H-bond interactions described below. The actual structure of these three conformers are taken from those predicted ab intio (see Tables V.S11-S12 of SI) given the exceptional matching between theoretical and experimental rotational constants (Table V.2).*

pyranoside ring configuration (Figure V.7.b)[38-39]. Ab initio computation carried out on this form indicates the existence of six plausible conformations below 1500cm[-1](Table V.S8 of SI). Guided by this prediction, its broadband rotational spectrum (Figure V.8) was analysed. After removing the spectroscopy features that are common for sugars (green triangles of Figure V.8), it was easy to identify intense pairs of b-type R-branch $(J+1)_{0\,J+1} \leftarrow J_{1\,J}$ and $(J+1)_{1\,J+1} \leftarrow J_{0\,J}$ progressions (J ranging from J=4 to J=7), as belonging to a first rotamer I (Figure V.8.a). Neither a- nor c-type

transitions were observed for this rotamer. This is consistent with the near zero values of the μ_a and μ_c dipole moment components predicted for the two lowest energy conformers β [2]C[5] g- s (1) and β [2]C[5] g-s (2) (Table V.2). Rigid rotor analysis of all measured lines, (listed in Table V.S9 of SI), leads to the set of rotational constants listed in the first column of Table V.2.

A more detailed inspection of the spectrum revealed the existence of the same b-type R-branch progressions very close to each transition of rotamer I, but with much lower intensity (see Figure V.8.b),
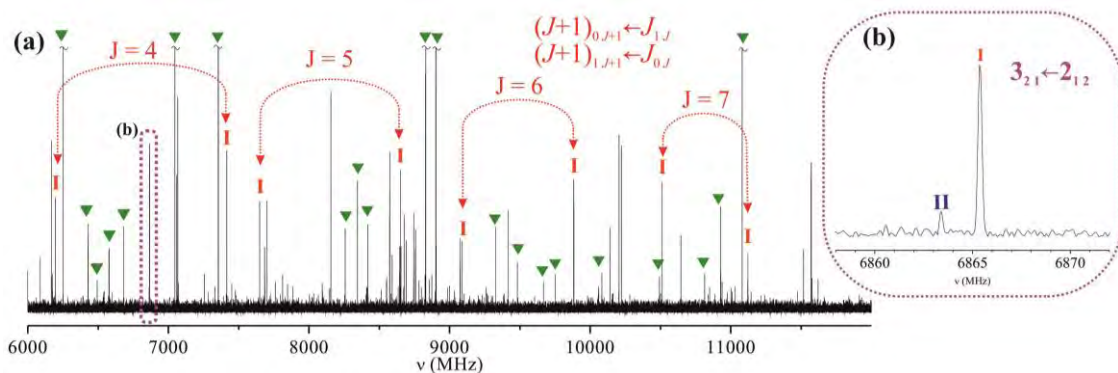
FIGURE V.8. *Broadband rotational spectrum of D-psicose. (a) D-psicose rotational spectrum (6-12GHz 103000 acquisitions) obtained by LA-CP-FTMW technique. Yellow triangles indicate all decomposition lines. Marked in red are the b-type R-branch $(J+1)_{0J+1} \leftarrow J_{1J}$ and $(J+1)_{1J+1} \leftarrow J_{0J}$ pairs of rotational progressions ranging from J=4 to J=7 of rotamer I. (b) Small section of the spectrum that shows rotational transitions of the two rotamers observed for D-psicose.*

Table V.2: Experimental rotational parameters for the observed conformers of D-Psicose.

	Rotamer I	β ^{2}C$_5$ g- s (1)	Rotamer 2	β ^{2}C$_5$ g- s (2)
A/MHz[a]	1626.7540(38)[f]	1631.8	1626.75480(84)	1635.8
B/MHz	723.03579(12)	728.3	724.68772(41)	728.3
C /MHz	660.98104(16)	665.3	661.03584(48)	664.9
$\|\mu_a\|$/D[b]	Observed	1.9	Observed	1.0
$\|\mu_b\|$/D	Observed	1.7	...	0.1
$\|\mu_c\|$/D	Observed	1.4	Observed	1.7
σ[c] / kHz	5.3		9.4	
N[d]	24		15	
ΔE[e]/cm^{-1}		0		73

[a] Experimental rotational constants.[b] Experimental observation of the a, b and c-type spectrum. [c] rms deviation of the fit. [d] Number of fitted rotational transitions. [e] Relative energies (MP2/6-311++G(d,p) basis set) with respect to the global minimum. [f] Standard error in parenthesis in the units of the last digit.

which were ascribed to rotamer II. As with rotamer I, a- and c- type transitions were predicted but not found (see list of transitions in Table V.S10 of SI). Rotational constants emerging from rigid rotor analysis are listed in Table V.2. The close resemblance between the rotational constants of rotamers I and II, (Table V.2) indicates that both conformers will show minimal discrepancies in their structure. On account of their rotational parameters and dipole moments, rotamers I and II are only consistent with the two lowest energy conformers β ^{2}C$_5$ g- s (1) and β ^{2}C$_5$ g- s (2), shown in Figure

V.7.c. Each is stabilized by two intramolecular hydrogen bonding networks, a common feature they share being the short network that involves OH$_{(2)}$···OH$_{(1)}$···O$_{(ring)}$. The only difference between them is the clockwise or counter clockwise orientation of the cyclic H-bond network established between another three hydroxyl groups (OH$_{(3)}$, OH$_{(4)}$ and OH$_{(5)}$). Due to the extraordinary similarities in their rotational parameters, no conclusive identification can be attained on this basis. However, if we attribute rotamer I to β^{2}C$_5$ g- s (1) and rotamer II to β ^{2}C$_5$ g- s (2), the relative intensity of the experimental transitions, corrected by the corresponding values of μ_b^2, will give rise to a population distribution of β ^{2}C$_5$ g- s (1) 60% and β ^{2}C$_5$ g- s (2) 40%, which is consistent with the relative stability predicted *ab initio*. In light thereof, it could be a reasonable assignment to ascribe rotamer I to conformer β ^{2}C$_5$ g- s (1) and rotamer II to β ^{2}C$_5$ g- s (2)

V.3.3 L-Sorbose
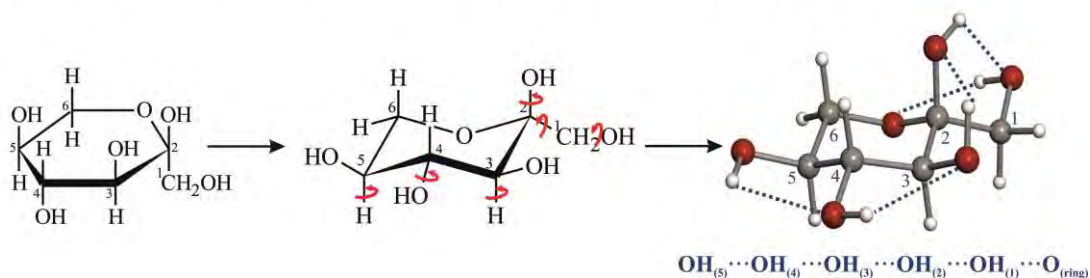
FIGURE V.9. *Observed species of α-L-sorbopyranose. (a) Haworth projection of the pyranose α anomer[36] which is the one found in crystalline phase.[46] (b) ^{2}C$_5$ chair configurations, where the hydroxymethyl group is equatorial. Red arrows indicate the torsion angles to be optimized ab initio. (c) Conformer observed for L-sorbose. Dashed lines mark the H-bond interactions described below. The actual structure of these three conformers are taken from those predicted ab intio (see Table V.SI5 of SI) given the exceptional matching between theoretical and experimental rotational constants (Table V.3).*
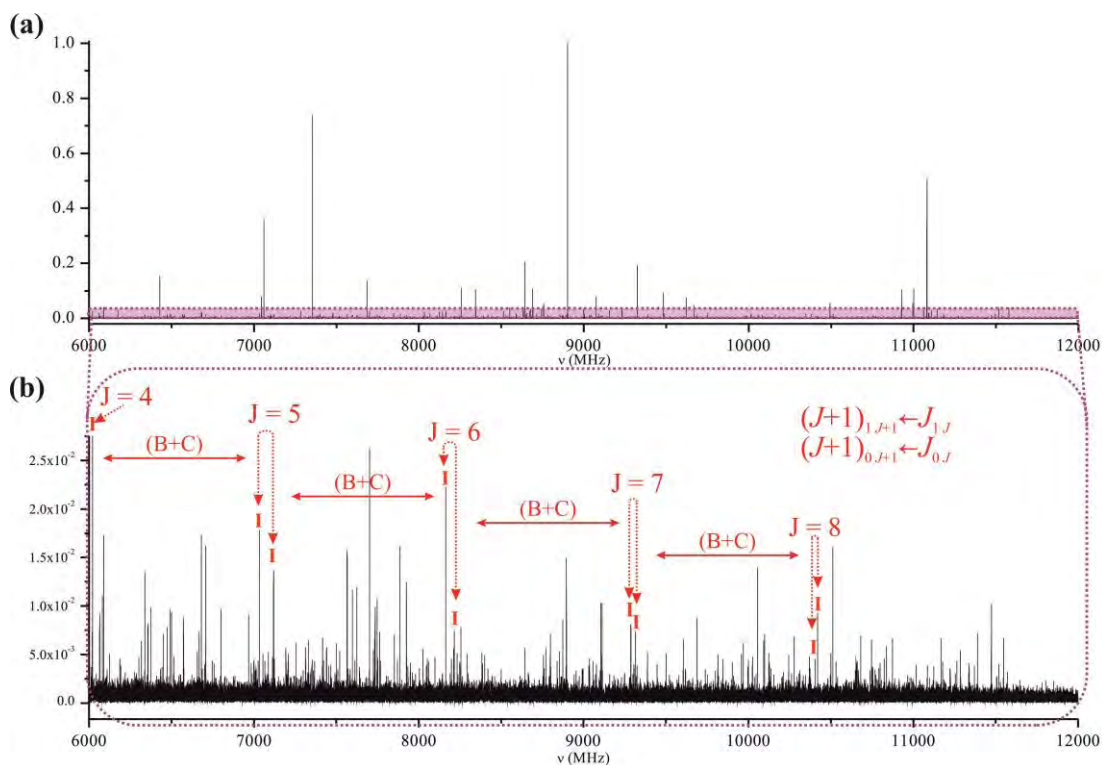
FIGURE V.10. *Broadband rotational spectrum of L-sorbose. (a) Normalized rotational spectrum of L-sorbose obtained by LA-CP-FTMW technique (6-12GHz, 133000 acquisitions). (b) Amplification of the shadow area after removing all decomposition lines. Marked in red are the a-type R-branch $(J+1)_{1,J+1} \leftarrow J_{1,J}$ and $(J+1)_{0,J+1} \leftarrow J_{0,J}$ pairs of rotational progressions ranging from J=4 to J=8 of rotamer I.*

L-sorbose is the C-5 epimer of D-fructose (Figure V.2). It is a sweetener about as sweet as sucrose although its main use is as an intermediate in the industrial synthesis of Vitamin C.[47-49] In crystalline phase, L-sorbose is found in the α anomer in the most stable $^2C_5$ pyranoside ring configuration (Figure V.9)[46] (see Footnote of Figure V.4 for nomenclature of L species).

Crystalline samples of α-L- sorbopyranose (m.p.=165°C) were placed into the gas phase using laser ablation and probed by LA-CP-FTMW spectroscopy to obtain the broadband rotational spectrum in the 6 to 12 GHz frequency region (Figure V.10.a). After removing the common photofragmentation products of sugars, only low intense transitions remain in the spectrum (Figure V.10.b), indicating that α-L-sorbopyranose conformations present low dipole moments. Analysis of this spectrum was carried out guided by

Table V.3. Experimental and predicted rotational parameters for the observed conformer of L-sorbose.

	Rotamer I	α $^2C_5$ g- cc
A/MHz[a]	1525.5027(80)[f]	1527.9
B/MHz	722.08428(33)	727.5
C /MHz	556.05153(30)	559.0
$\|\mu_a\|$/D[b]	Observed	0.8
$\|\mu_b\|$/D	...	0.1
$\|\mu_c\|$/D	...	0.1
σ^c / kHz	8.4	
N[d]	34	
ΔE_{MP2}[e]/cm^{-1}		0

[a] Experimental and predicted rotational constants. (A, B, C) [b] Absolute value of the electric dipole moment components predicted from MP2 calculations indicating whether the a, b and c-type spectrum is observed. [c] Experimental values obtained from spectrum analysis. The rms deviation of the fit is 8.4 kHz and the number of fitted rotational transitions is 34.[e] Standard error in parenthesis in the units of the last digit.

the results of *ab initio* computations showing three plausible conformers lying in an energy window of 1500cm^{-1} (Table V.S13 of SI). In the spectrum, a-type R-branch $(J+1)_{0\ J+1} \leftarrow J_{0\ J}$ and $(J+1)_{1\ J+1} \leftarrow J_{1\ J}$ pairs of rotational progressions ranging from $J=4$ to $J=8$ were observed (Figure V.10.b). Once these lines were analyzed[50] using a rigid rotor Hamiltonian, further higher K_a a-type R-branch transitions were included in the fitting of this rotamer I (see list of transitions in Table V.S14 of SI). The derived rotational constants are shown in Table V.3. No signals of any other type of transition belonging to this rotamer I or to other species could be identified. The experimental rotational constants of rotamer I can only be compatible with those for the conformer α $^2C_5$ g- cc. This is reinforced by the fact that only a-type transitions are observed, in accordance with the dipole moment components values predicted for this conformer (see SI).

The α $^2C_5$ g- cc conformation of L-sorbose shows a strong analogy to that found as the most stable for D-fructose, with the sole exception of the disposition of the OH$_{(5)}$, which is axial in D-fructose whereas in L-sorbose it is equatorial. As such, the hydrogen bond network that stabilizes the α $^2C_5$ g-cc conformer is the same as is found in fructose: OH$_{(5)}$···OH$_{(4)}$···OH$_{(3)}$···OH$_{(2)}$···OH$_{(1)}$···O$_{(ring)}$.

However, in contrast to D-fructose, where two forms were observed, we could not find the second abundant species (α $^2C_5$ t cc) for L-sorbose, probably due to its predicted low dipole moment component values and thus, its lower abundance in the supersonic expansion.

V.4. SWEETNESS AND STRUCTURE

As already mentioned in the introduction, the first unified postulation concerning the relation between sweetness and structure, announced by Shallenberger et al.,[15-16] established that the sweetener-receptor linkage was caused by two hydrogen bond interactions (type AH-B) that form the glucophore (Figure V.1a). In light of this new experimental information regarding the conformational behaviour of ketohexoses (depicted in the panel of Figure V.11), theories explaining sweetness in terms of structure can be revisited in order to discuss their agreement with the present conformational results D-fructose, which is the sweetest natural-occurring sugar and is about twice as sweet as its epimers, has been used as a model to identify the structural motifs forming the glucophore.[11, 15-16, 30] Initially, the hydroxyl groups OH$_{(1)}$ and OH$_{(2)}$ of ketohexoses were ascribed to AH and B sites of the glucophore, respectively.[30-31] Looking at the panel of the conformational panorama of ketohexoses (Figure V.11), it is easy to realize that all the most abundant species of ketohexoses: β $^2C_5$ g- cc (98%) for D-fructose, α $^5C_2$ g+ s (72%) and α $^5C_2$ g+ cc (22%) for D tagatose, β $^2C_5$ g- s (1) (60%) and β $^2C_5$ g- s (2) (40%) for D-psicose and α $^2C_5$ g- cc for L-sorbose, have a

(a) D-Fructose

β $^2C_5$ g- cc (98%)   β $^2C_5$ t cc (2%)

(b) D-Tagatose

α $^5C_2$ g+ s (72%)   α $^5C_2$ g+ s (22%)   α $^5C_2$ t cc (6%)

(c) D-Psicose

β $^2C_5$ g- s (1) (60%)   β $^2C_5$ g- s (2) (40%)

(d) L-Sorbose

α $^2C_5$ g- cc (>90%)
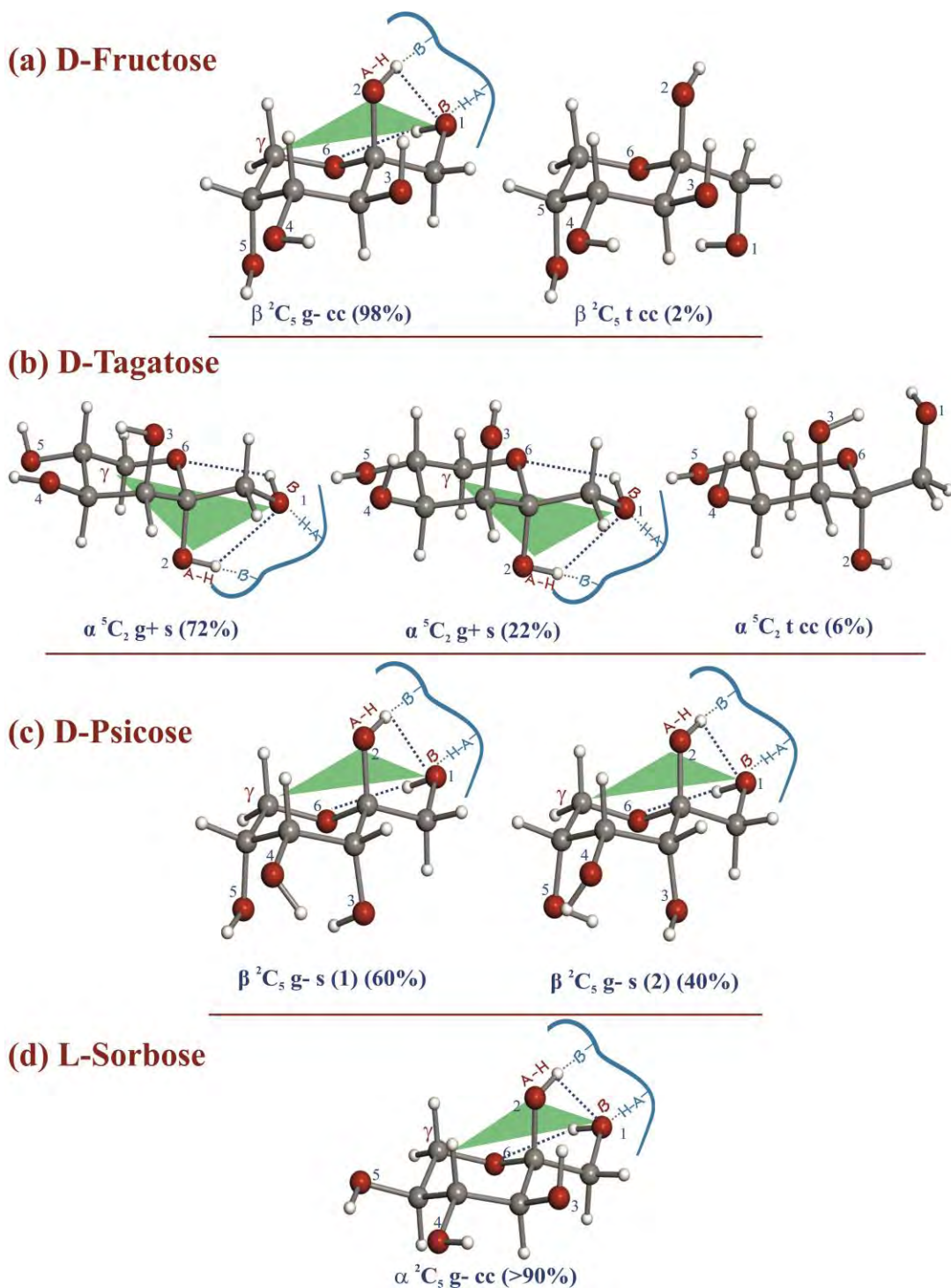
FIGURE 11. *Observed conformers for all ketohexoses. Blue dashed lines indicate the H-bon interaction that share the most stable conformers of ketohexoses. A-H, B and γ sweetness triangle is pointed our according to the sweetness theories of the literature.[30-31, 52] In parenthesis, the abundance of each conformer are shown. (a) D-Fructose. (b) D- Tagatose. (c) D-Psicose (d) L-Sorbose*

common orientation of the hydroxymethyl group. Despite their distinct $^2C_5$ or $^5C_2$ ring configuration, the anomeric $OH_{(2)}$ is always in axial orientation while the $OH_{(1)}$ points towards the $O_{(ring)}$ forming the H-bond network $OH_{(2)}\cdots OH_{(1)}\cdots O_{ring}$ (see dahed lines in the Figure).

As such, these conformers share the common conformational signature $OH_{(2)}\cdots O_{(1)}$, which could be ascribed to the AH and B sites of glucophore. Owing to the spatial disposition of the hydroxyl groups, $OH_{(1)}$ seems to have a major tendency to act as proton donor (AH) and $OH_{(2)}$ as acceptor (B), which would concur with Shallenberger's proposal.[30-31] The reverse identification of AH as $OH_{(1)}$ and B as $OH_{(2)}$, proposed in the literature,[51] does not appear to be consistent with the detailed structural information provided in this study.

Nevertheless, the presence of an elevated number of hydroxyl groups in ketohexoses allows additional assignments to the glucophore. *A priori,* all pairs of vicinal OH could act as AH-B in the glucophore. The $OH_{(2)}$-$OH_{(3)}$ pair could be discarded since in D-tagatose and D-psicose conformations are axial-axial in a spatial disposition that seem not proper for the linkage with the receptor (see Figure V.11.b and V.11.c). The most abundant conformers of ketohexoses always shows an hydrogen bond interaction between the other two hydroxyl pairs $OH_{(3)}$-$OH_{(4)}$ and $OH_{(4)}$-$OH_{(5)}$ that could be easily adapted to the linkage to the receptor forming the glucophore. However, neither the orientation of these hydroxyl groups (clockwise -

counterclokwise) or their relative distribution (equatorial-equatorial - axial-equatorial) is common for ketohexoses conformations (Figure V.11). Thus, if the glucophore were ascribed to $OH_{(3)}$-$OH_{(4)}$[52] or $OH_{(4)}$-$OH_{(5)}$, large discrepancies would be expected in terms of their sweetness degree; though, D-tagatose, D-psicose and L-sorbose are almost equally sweet.

Concerning the idea of a glucophose unit forming an AH-B-γ triangle[17] (mentioned in the introduction), identifying the hydrophobic γ site proved relatively straightforward. As can be observed in Figure V.11, all conformations have in common that the surroundings of $C_{(6)}$ are free of any hydrophilic group. Thus, this site constitutes the main hydrophobic environment, and, consequently, is the most suitable for being assigned as γ, in accordance with the initial postulations.[17] Thus, based on the common conformational signatures of ketohexoses, everything seem to indicate that the glucophore (sweetness triangle) might be formed by $OH_{(2)}$, $OH_{(1)}$ and $C_{(6)}$ (see green triangles in Figure V.11).

However, the rationalization of sweetness degree of ketohexoses assuming the aforementioned triangle (see Figure V.11) presents an inconvenient when it comes to explain why D-fructose is twice as sweet as L-sorbose. Exploring the conformational behaviour of these sugars has unveiled extraordinary similarities between their structures. β $^2C_5$ g- cc species of D-fructose and α $^2C_5$ g- cc of L-sorbose are stabilized by the same H-bond network exteded

over the entire molecule. The only difference between them arises from the orientation of the $OH_{(5)}$ (Figure V.11.a and V.11d). In the literature, this difference in sweetness was rationalized in terms of a possible H-bond interaction between the $OH_{(5)}$ and $O_{(ring)}$ in β-D-fructopyranose,[31, 53] which might leave the $OH_{(1)}$ free to be linked with the receptor. and which cannot be formed in α-L-sorbopyranose. According to our experimental results, this hydrogen bond interaction does not exist in any of the observed species of β-D-fructopyranose. Therefore, there is no explanation for the differences in their sweetness if the glucophore does not involve somehow to the $OH_{(5)}$ group as it can occur if it existed an extra binding site that links to $OH_{(5)}$, or if steric hindrance was generated at that place when $OH_{(5)}$ is axial.

V.5. CONCLUSIONS

Combining microwave spectroscopy with laser ablation allows the intrinsic conformational behaviour of sugars to be revealed for the first time. The present investigation into ketohexoses has opened a new window to explore the old subject regarding the linkage between sweetness and structure. In so doing, established theories can be evaluated on the basis of this initial experimental information concerning the conformations of these sweeteners. Identifying a common conformational signature involving $OH_{(2)}$, $OH_{(1)}$ and O_{ring} of the most abundant species of ketohexoses seem to indicate that anchoring to the sweet receptor could occur here.

V.6. REFERENCES

[1]   M. Behrens, W. Meyerhof, C. Hellfritsch, T. Hofmann, *Angewandte Chemie International Edition* **2011**, *50*, 2220-2242.

[2]   E. Adler, M. A. Hoon, K. L. Mueller, J. Chandrashekar, N. J. P. Ryba, C. S. Zuker, *Cell* **2000**, *100*, 693-702.

[3]   X. Li, L. Staszewski, H. Xu, K. Durick, M. Zoller, E. Adler, *Proceedings of the National Academy of Sciences* **2002**, *99*, 4692-4696.

[4]   G. Q. Zhao, Y. Zhang, M. A. Hoon, J. Chandrashekar, I. Erlenbach, N. J. P. Ryba, C. S. Zuker, *Cell* **2003**, *115*, 255-266.

[5]   G. Nelson, M. A. Hoon, J. Chandrashekar, Y. Zhang, N. J. P. Ryba, C. S. Zuker, *Cell* **2001**, *106*, 381-390.

[6]   G. Morini, A. Bassoli, P. A. Temussi, *Journal of Medicinal Chemistry* **2005**, *48*, 5520-5529.

[7]   A. van der Heijden, L. B. P. Brussel, H. G. Peer, *Food Chemistry* **1978**, *3*, 207-211.

[8]   P. A. Temussi, F. Lelj, T. Tancredi, M. A. C. Morelli, A. Pastore, *International Journal of Quantum Chemistry* **1984**, *26*, 889-906.

[9]   C. H. Gorbitz, *Acta Chemica Scandinavica Series B-Organic Chemistry and Biochemistry* **1987**, *41*, 83-86.

[10]   T. Yamazaki, E. Benedetti, D. Kent, M. Goodman, *Angewandte Chemie International Edition in English* **1994**, *33*, 1437-1451.

[11]   G. G. Birch, R. S. Shallenberger, *C R C Critical Reviews in Food Science and Nutrition* **1976**, *8*, 57-95.

[12]   G. Cohn, *Die organischen Geschmacksstoffe*, F. Siemenroth, **1914**.

[13]   E. Oertly, R. G. Myers, *Journal of the American Chemical Society* **1919**, *41*, 855-867.

[14]   T. Kaneko, *Journal of Chemical Society (Japan)* **1938**, *29*, 433-439.

[15]   R. S. Shallenberger, T. E. Acree, *Nature* **1967**, *216*, 480-482.

[16]   R. S. Shallenberger, T. E. Acree, C. Y. Lee, *Nature* **1969**, *221*, 555-556.

[17]   L. B. Kier, *Journal of Pharmaceutical Sciences* **1972**, *61*, 1394-1397.

[18]   S. C. Ebeling, *Food Chemistry* **1998**, *61*, 107-112.

[19]   C. Nofre, J.-M. Tinti, *Food Chemistry* **1996**, *56*, 263-274.

[20]   C. Bermúdez, I. Peña, C. Cabezas, A. M. Daly, J. L. Alonso, *Chemphyschem* **2013**, *14*, 893-895.

[21]   J. L. Alonso, M. A. Lozoya, I. Peña, J. C. Lopez, C. Cabezas, S. Mata, S. Blanco, *Chemical Science* **2014**, *5*, 515-522.

[22]   J. L. Alonso, J. C. López, Springer Berlin Heidelberg, **2015**, pp. 1-67.

[23]   G. G. Brown, B. C. Dian, K. O. Douglass, S. M. Geyer, S. T. Shipman, B. H. Pate, *Review of Scientific Instruments* **2008**, *79*.

[24]   S. Mata, I. Peña, C. Cabezas, J. C. López, J. L. Alonso, *Journal of Molecular Spectroscopy* **2012**, *280*, 91-96.

[25]   I. Peña, E. J. Cocinero, C. Cabezas, I. Peña, Alberto, S. Mata, P. Écija, A. M. Daly, Á. Cimas, C. Bermúdez, F. J. Basterretxea, S. Blanco, J. A. Fernández, J. C. López, F. Castaño, J. L. Alonso, *Chemical CommunicationsAngewandte Chemie International Edition* **2013**, *4952*, 10826-1082811840-1082811845.

[26]   I. Peña, S. Mata, A. Martín, C. Cabezas, A. M. Daly, J. L. Alonso, *Physical Chemistry Chemical Physics* **2013**, *15*, 18243-18248.

[27]   I. Peña, L. Kolesnikova, C. Cabezas, C. Bermúdez, M. Berdakin, A. Simao, J. L. Alonso, *Physical Chemistry Chemical Physics* **2014**, *16*, 23244-23250.

[28]   I. Peña, E. J. Cocinero, C. Cabezas, A. Lesarri, S. Mata, P. Écija, A. M. Daly, Á. Cimas, C. Bermúdez, F. J. Basterretxea, S. Blanco, J. A. Fernández, J. C. López, F. Castaño, J. L. Alonso, *Angewandte Chemie International Edition* **2013**, *52*, 11840-11845.

[29]   G. A. Jeffrey, W. Saenger, *Hydrogen Bonding in Biological Structures*, Springer-Verlag, New York, **1991**.

[30]   R. S. Shallenberger, *Pure and Applied Chemistry* **1978**, *50*, 1409-1420.

[31]   M. G. Lindley, G. G. Birch, *Journal of the Science of Food and Agriculture* **1975**, *26*, 117-124.

[32]   Y. Lu, G. V. Levin, T. W. Donner, *Diabetes, Obesity and Metabolism* **2008**, *10*, 109-134.

[33]   G. V. Levin, *Journal of Medicinal Food* **2002**, *5*, 23-36.

[34]   S. Köpper, S. Freimund, *Helvetica Chimica Acta* **2003**, *86*, 827-843.

[35]   S. Takagi, R. D. Rosenstein, *Carbohydrate Research* **1969**, *11*, 156-158.

[36]   A. D. McNaught, *Carbohydr Res* **1997**, *297*, 1-92.

[37]   W. Gordy, R. L. Cook, *Microwave Molecular Spectroscopy*, John Wiley & Sons, New York, **1984**.

[38]   A. Kwiecień, K. Slepokura, T. Lis, *Carbohydrate Research* **2008**, *343*, 2336-2339.

[39]   K. Fukada, T. Ishii, K. Tanaka, M. Yamaji, Y. Yamaoka, K.-i. Kobashi, K. Izumori, *Bulletin of the Chemical Society of Japan* **2010**, *83*, 1193-1197.

[40]   H. Oshima, I. Kimura, K. Izumori, *Food Science and Technology Research* **2006**, *12*, 137-143.

[41]   W. Mu, W. Zhang, Y. Feng, B. Jiang, L. Zhou, *Appl Microbiol Biotechnol* **2012**, *94*, 1461-1467.

[42]   T. Matsuo, K. Izumori, *Bioscience, Biotechnology, and Biochemistry* **2006**, *70*, 2081-2085.

[43]   T. Matsuo, Y. Baba, M. Hashiguchi, K. Takeshita, K. Izumori, H. Suzuki, *Asia Pacific Journal of Clinical Nutrition* **2001**, *10*, 233-237.

[44]   S. H. Baek, S. J. Park, H. G. Lee, *Journal of Food Science* **2010**, *75*, H49-H53.

[45]   T. Matsuo, H. Suzuki, M. Hashiguchi, K. Izumori, *Journal of Nutritional Science and Vitaminology* **2002**, *48*, 77-80.

[46]   S. H. Kim, Rosenste.Rd, *Acta Crystallographica* **1967**, *22*, 648-&.

[47]   A. H., *Nature* **1934**, *134*, 724-725.

[48]   T. Reichstein, A. Grüssner, *Helvetica Chimica Acta* **1934**, *17*, 311-328.

[49]   P. De Wulf, W. Soetaert, E. J. Vandamme, *Biotechnology and Bioengineering* **2000**, *69*, 339-343.

[50]   J. K. G. Watson, *Vibrational Spectra and Structure, Vol. 6*, Elsevier: Amsterdam, **1977**.

[51]   M. Mathlouthi, M. O. Portmann, *Journal of Molecular Structure* **1990**, *237*, 327-338.

[52]   G. G. Birch, S. Shamil, Z. Shepherd, *Experientia* **1986**, *42*, 1232-1234.

[53]   R. J. Woods, W. A. Szarek, V. H. Smith, *Journal of the American Chemical Society* **1990**, *112*, 4732-4741.

CHAPTER VI.   Six Pyranoside Forms of free 2-Deoxy-D-Ribose
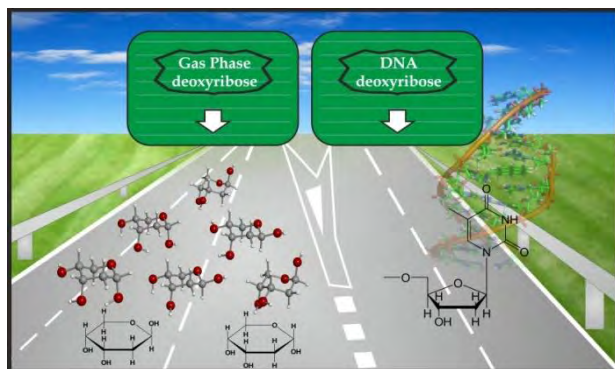
A clear picture of the conformational panorama of isolated 2-deoxy-D-ribose has been obtained using chirped pulse and Balle-Flygare Fourier transform microwave spectrometers both coupled with laser ablation sources. Two conformers of α-D-deoxyribopyranose and four of β-D-deoxyribopyranose have been unveiled on the basis of the spectroscopic rotational parameters in conjunction with *ab initio* predictions. The anomeric effect and intramolecular hydrogen bonding are the main factors which control the conformational behavior. The substitution and effective structures of the most abundant conformer have been determined.

Carbohydrates are one of the most versatile biochemical building blocks, widely acting in energetic, structural or recognition processes.[1] The interpretation of biological activity of saccharides is based on the structure and relative stability of their conformers. One of the obstacles in resolving the basic structure issues arises from their ability of forming strong intermolecular hydrogen bonds with polar solvent, which in turn can result in conformational changes. A clear picture of the conformational panorama of isolated 2-deoxy-D-ribose has been unveiled using Fourier transform microwave spectroscopy in conjunction with a UV ultrafast laser ablation source. Additionally, the

availability of rotational data has been recognized as the main bottle-neck to examine the presence of these building blocks in interstellar space,[2] so these studies can be also useful for the astrochemistry community.

2-Deoxy-D-ribose (2DR, $C_5H_{10}O_4$) (Figure VI.1.a) is an important naturally occurring monosaccharide, present on nucleotides' structure, known as the building blocks of DNA.[3] In DNA, 2DR is present in the furanose (five-membered) ring form, whereas in aqueous solution it cyclizes, producing five and six-membered rings, with the latter - the pyranoid form - being dominant.[4] By
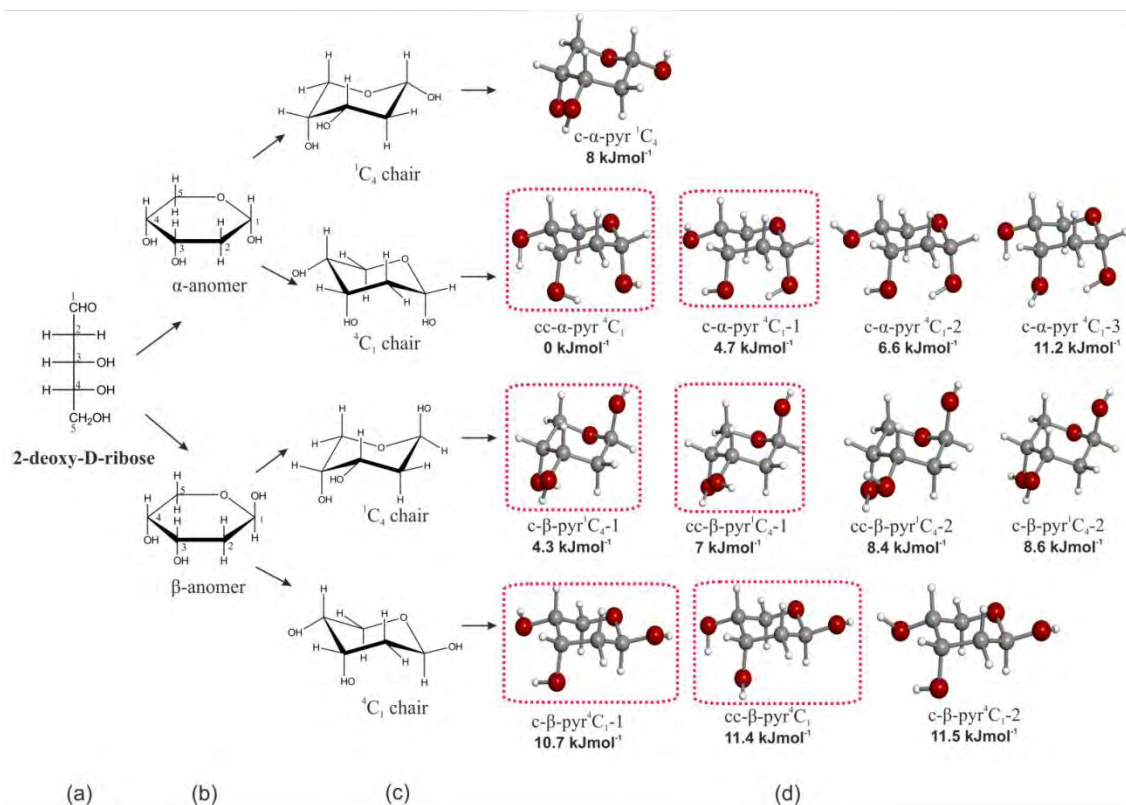
FIGURE VI.1: . (a) Fisher projection of 2-deoxy-D-ribose. (b) Haworth projections of α and β anomers. (c) $^1C_4$ and $^4C_1$ chair conformations. (d) Predicted conformers within 12 kJmol^{-1} from MP2(full)/6-311++G(d,p) ab initio computations; the observed conformers are encircled.

closing the chain into a six-membered ring, the C_1 carbon atom is thus converted into an asymmetric centre, yielding two possible stereochemical α and β anomeric species (Figure VI.1.b). In aqueous solution, 2DR primarily exists as a mixture of nearly equal amounts of α and β pyranose forms, present in their low energy chair conformations, $^4C_1$ and $^1C_4$ (Figure VI.1.c).[4] Such configurations are connected through ring inversion, thus establishing the axial or equatorial position of the OH for each conformer. In addition, the monossacharides exhibit an unusual preferential stabilization of pyranose rings containing an axial OH at the C_1 carbon over the equatorial orientation known as anomeric effect, which is widely described in the literature,[5] although its physical origin still generates a considerable controversy nowadays.[6] Nevertheless, structural analysis of 2DR must take into consideration the intramolecular hydrogen bonding between adjacent OH groups. Plausible formation of hydrogen bond networks reinforces their stability due to hydrogen bond cooperativity effects.[7] Such networks are a fundamental piece in carbohydrate molecular recognition.[8] The key to dissect all these factors arises from unveiling the most stable conformers of 2DR and the relative arrangement of the different hydroxy groups in isolation conditions, such as those found in gas phase.

In vacuo theoretical calculations, carried out on α-/β-pyranoses, α-/β-furanoses and open–chain conformations, predict 15 furanose and pyranose forms (Figure VI.1.d, Table VI.1) in an energy window of 12 kJmol^{-1} above the predicted cc-α-pyr-$^4C_1$ global minimum. The notation used to label the different conformers include the symbols α and β to denote the anomer type, $^4C_1$ and $^1C_4$ to denote the pyranose chair form, C2-endo or C3-endo to
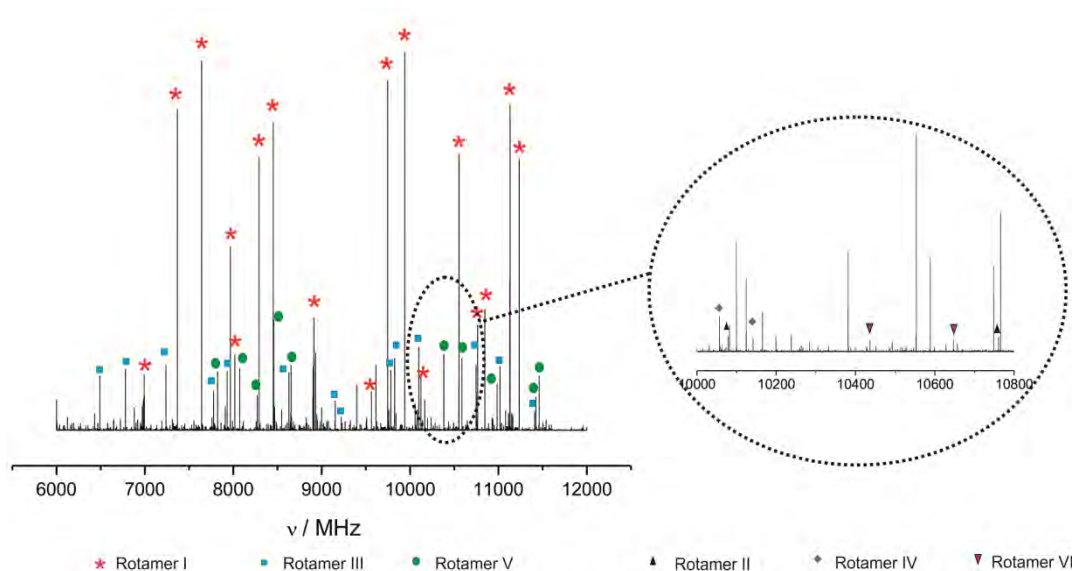
FIGURE VI.2. Broadband microwave spectrum of 2-deoxy-D-ribose.

TABLE VI.1: Calculated spectroscopic parameters and relative energies for the α and β lowest-energy conformers of 2-deoxy-D-ribose (below 1300 cm^{-1}) from *ab initio* computations.

	A[a]	B	C	$|\mu_a|$	$|\mu_b|$	$|\mu_c|$	ΔE[b]	ΔG[c]
cc-α-pyr $^4C_1$	2492	1533	1250	2.9	0.3	0.3	0	0
c-α-pyr $^4C_1$-1	2518	1535	1259	3.0	0.6	1.4	4.7	4.7
c-α-pyr $^4C_1$-2	2512	1531	1258	3.6	0.7	2.8	6.6	6.0
c-α-pyr $^1C_4$	2503	1395	1077	1.8	1.6	1.9	8.0	6.7
c-α-pyr $^4C_1$-3	2511	1520	1249	1.0	3.3	1.6	11.2	10.6
c-β-pyr $^1C_4$-1	2447	1527	1158	2.6	1.2	0.5	4.3	3.3
cc-β-pyr $^1C_4$-1	2463	1524	1150	1.0	2.1	0.6	7.0	5.6
cc-β-pyr $^1C_4$-2	2446	1528	1150	0.2	1.1	2.2	8.4	6.8
c-β-pyr $^1C_4$-2	2455	1522	1154	1.2	2.6	0.3	8.6	6.7
c-β-pyr $^4C_1$-1	2956	1279	1030	1.7	2.0	0.2	10.7	8.9
cc-β-pyr $^4C_1$	2948	1273	1028	0.2	2.2	1.0	11.4	9.4
c-β-pyr $^4C_1$-2	2947	1279	1029	2.2	0.6	1.1	11.5	9.4
cc-α-fur-C_2-endo-1	2527	1379	1155	0.6	2.6	0.6	6.7	3.5
cc-α-fur-C_2-endo-2	2627	1261	1035	1.3	2.0	1.5	10.2	6.5
cc-α-fur-C_2-endo-3	2576	1371	1172	1.9	2.0	0.5	12.0	8.5

[a] A, B, and C represent the rotational constants (in MHz), μ_a, μ_b and μ_c are the absolute values of electric dipole moment components (in D) [b] MP2/6-311++G(d,p) electronic energies (in cm-1). [c] Gibbs energies calculated at 298 K at the MP2/6-311++G(d,p) level of theory (in cm-1).

denote the furanose envelope forms and the symbols "c" or "cc" to indicate the clockwise or counter-clockwise configuration of the adjacent OH bonds, respective-

ly. A number is added to provide the MP2 energy ordering within the same family. To validate the predicted conformational behavior, comparison with precise experimental data of 2DR is needed. Former experiments to determine the conformation of monosaccharides were based on X-ray and NMR measurements.[9,4] However, their data are influenced by environmental effects associated with the solvent or crystal lattice. Recently, IR spectrum of 2DR in an inert matrix in the region of the stretching OH vibration has been interpreted by summing the modeled spectra for several α and β conformers.[10] Gas phase studies of some phenyl substituted monosaccharides,[11a] polisaccharides[11b] or sugar complexes[11c] have

been investigated by UV and IR double resonance hole burning spectroscopy experiments, but no data have been reported for the corresponding 2DR derivative. The intrinsic difficulty of working with gas phase 2DR (actually, with carbohydrates, in general) takes root in the labile nature of the solid sample (m.p. = 89-90ºC) and the difficulties inherent to vaporization. A suite of powerful strategies has evolved employing a combination of laser ablation for transferring intact molecules into the gas phase, rapid cooling in a free jet expansion to stabilize their conformers and highly selective Fourier transform microwave spectroscopy to probe the most stable conformers.[12] Structural studies of amino acids,[13] nucleic acid bases,[14] neurotransmitters,[15] drugs like aspirin[16] and sugars such as glucose[17] benefit from this LA-MB-FTMW technique.[12] Recently, the microwave spectra of ribose[18] and fructose[19a] have been characterized using a UV ultrafast laser ablation

source with a Balle-Flygare FTMW spectrometer. In the last years, new broadband Fourier transform microwave techniques[20] have allowed the fast acquisition of the rotational spectrum in wide frequency ranges. Recently, a picoseconds laser ablation source has been assembled to these techniques[21,22] at the University of Valladolid and successfully applied to the conformational studies of vitamin C[22] and D-fructose.[19b] The spectrum of 2DR was observed and assigned independently in Valladolid and Bilbao using the CP-FTMW technique and a Balle-Flygare FTMW spectrometer, respectively, in both cases combined with a UV picoseconds laser source (For more details see Section III.1.2). Six different rotameric species labeled I to VI were identified, once the known lines belonging to photo-fragmentation species[19b] were removed from the broadband spectra recorded in Valladolid (see Figure VI.2). Assignments were mainly based on the identification of characteristic patterns of μ_a-R-branch progressions in the 6-12 GHz frequency range. The rotational constants collected in Table VI.2 (see the complete results in Table V.S1 of SI) were determined by a Watson semirigid rotor Hamiltonian[23] of the measured transitions (Tables VI.S2-S7 of the Supplementary Information).

TABLE VI.2. Experimental spectroscopic parameters for the six observed conformers of 2-deoxy-D-ribose

Parameter	Rotamer I c-β-pyr $^1C_4$	Rotamer II cc-β-pyr $^1C_4$	Rotamer III c-β-pyr $^4C_1$	Rotamer IV cc-β-pyr $^4C_1$	Rotamer V cc-α-pyr $^4C_1$	Rotamer VI c-α-pyr $^4C_1$
$A^{[a]}$ /MHz	2437.81949 (50)[e]	2449.4937 (10)	2934.15179 (76)	2921.37810 (82)	2484.416 (14)	2505.0150 (12)
B /MHz	1510.72594 (34)	1508.31836 (62)	1271.16669 (33)	1266.98987 (44)	1517.76450 (62)	1521.47507 (52)
C /MHz	1144.97968 (34)	1137.47992 (43)	1022.34736 (33)	1020.28118 (42)	1238.99514 (62)	1246.45004 (53)
$\mu_a^{[b]}$/D	Obs[f]	Obs	Obs	...	Obs	Obs
μ_b/D	Obs	Obs	Obs	Obs	...	...
μ_c/D	Obs	Obs	...	Obs	...	Obs
$\sigma^{[c]}$ / KHz	11.1	7.3	12.5	10.0	4.3	5.9
$N^{[d]}$	51	21	45	20	12	16

[a] A, B and C are the rotational constants. [b] Electric dipole moment. 1 D ≈ 3.3356×10-30 C m. [c] rms deviation of the fit. [d] Number of fitted transitions. [e] Standard error in parenthesis in the units of the last digit. [f] Observation of a-, b-, and c-type transitions for each structure.

A comparison of the experimentally determined values (Table VI.2) with those predicted *ab initio* (Table VI.1) enables the identification of the six detected rotamers as particular conformers of 2DR. All structures observed were α/β-pyranoses forms. We found no evidence of either α/β-furanoses or any linear forms in gaseous 2DR. The conformational assignment used the rotational constants, type and magnitude of the observed spectrum and the relative intensity of the microwave transitions. The experimental rotational constants of rotamers I and II are only consistent with those predicted for the couple of conformers c-β-pyr-$^1C_4$-1 and cc-β-pyr-$^1C_4$-1. However, their

absolute values do not allow discrimination between them. Considering that one departs from the clockwise orientation of the OH groups of the c-β-pyr-$^1C_4$-1 conformer towards the cc-β-pyr-$^1C_4$-1 conformer counterclockwise orientation, the predicted changes in rotational constants (ΔA = -16 MHz, ΔB = 3 MHz, and ΔC = 8 MHz) are in good agreement with those calculated from experimental values (ΔA = -11.7 MHz, ΔB = 2.4 MHz, and ΔC = 7.5 MHz), thus allowing to ascribe rotamer I as conformer c-β-pyr-$^1C_4$-1 and rotamer II as conformer cc-β-pyr-$^1C_4$-1. Also, the intensities of the measured transitions are in agreement with the predicted values of the dipole moment components and the selection rules, further supporting this assignment. Analogously, the rotational constants of rotamers III and IV should be related to either c-β-pyr-$^4C_1$-1 or cc-β-pyr-$^4C_1$ conformers. Only μ_a- and μ_b-type spectra, for rotamer III and μ_b- and μ_c-type spectra, for rotamer IV were observed. Based on the predicted values of the dipole moment components, rotamer III can only be ascribed as c-β-pyr-$^4C_1$-1, whereas rotamer IV as cc-β-pyr-$^4C_1$. For rotamers V and VI, rotational constants are consistent with those predicted for α $^4C_1$ pyranoses. Again, the selection rules and intensities observed indicate that rotamers V and VI should be assigned to conformers cc-α-pyr-$^4C_1$ and c-α-pyr-$^4C_1$, respectively. The non-observation of conformers c-α-pyr $^4C_1$-2, cc-β-pyr $^1C_4$-2, c-β-pyr $^1C_4$-2 and c-β-pyr $^4C_1$-2 in Table VI.1 can be safely attributed to a collisional relaxation in the jet,[24] since it differs from the observed conformers only in the
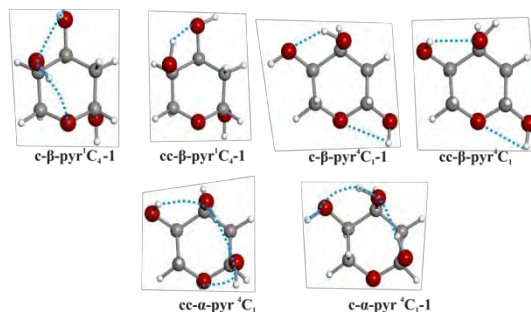
FIGURE VI.3: *The six observed conformers of 2-deoxy-D-ribose showing the intramolecular hydrogen bond arrangements.*

orientation of one of the hydroxy groups at C_3 or C_4 (see some examples of the calculated interconversion barriers in Figures VI.S1 and VI.S2 of Supplementary Information)

The population ratios for α and β conformers - c-β-pyr-$^1C_4$-1(I): cc-β-pyr-$^1C_4$-1(II) : c-β-pyr-$^4C_1$-1(III) : cc-β-pyr-$^4C_1$ (IV): cc-α-pyr-$^4C_1$(V) : c-α-pyr-$^4C_1$-1(VI) = 1 : 0.06(1) : 0.38(4) : 0.11(1) : 0.15(1) : 0.02(2) - have been estimated from transition intensities,[25] taking into account the values of dipole moment components from Table VI.1 and by assuming that the cooling in the supersonic expansion brings all the molecular systems to the lowest vibrational state of each observed conformer. Prior to the interpretation of these data, it is necessary to retain that, although the cc-α-pyr-$^4C_1$ conformer has been predicted to be 4.3 kJmol^{-1} more stable than the c-β-pyr-$^1C_4$ one, it is only reasonable to assume that the 2DR rotational spectra will reflect the composition of the α and β forms in the commercial solid sample. The interconversion between α and β anomers is a solvent-mediated reaction and would not occur that

easily during evaporation,[26] specially if the sample is completely dry.[27] Hence, results indicate that 2DR exists in the gas phase as a mixture of approximately 10% of α and 90 % of β pyranose forms, thus displaying the dominant β-$^1C_4$ pyranose form, as found in the previous X-ray crystalline study.[9] The hypothetical equilibrium relative populations for the β forms - c-β-pyr-$^1C_4$-1(I): cc-β-pyr-$^1C_4$-1(II) : c-β-pyr-$^4C_1$-1(III) : cc-β-pyr-$^4C_1$(IV) = 1 : 0.39 : 0.11 : 0.08 - predicted from the Gibbs energies, are not in total agreement with the above experimental abundances, particularly in the case of the pair cc-β-pyr-$^1C_4$(II) : c-β-pyr-$^4C_1$(III). This fact must be associated either to a wrong evaluation of the *ab initio* energies, collisional relaxation of high energy conformers to low-energy conformers[24] or to the result of a series of processes that include the laser-vaporization of the solid.[28] In this way, the observed relative population ratio can be only tentatively related to a population distribution close to those of equilibrium at the temperature of the carrier gas assuming that a high collisional rate exists in the seeding region.[29] Nevertheless, our experimental results reflect the observed most abundant α and β anomers are predicted as the global minimum.

In Bilbao, with Balle-Flygare FT-MW technique thanks to the high sensitivity reached allowed to extend the spectral measurements to all five monosubstituted ^{13}C species and the endocyclic ^{18}O species in their natural abundance ($\sim$1.1% and $\sim$0.2%) for the most abundant c-β-pyr-$^1C_4$-1

conformer (see Tables VI.S8-S10 of Supplementary Information). The isotopic information was used to derive substitution and effective structures for this species, shown in Table VI.S11 and interactive 3D-model of Supplementary Information.

The detected conformers of 2DR, depicted in Figure VI.3, can be rationalized in terms of factors that may contribute to their stabilization. The two observed α conformers, cc-α-pyr-$^4C_1$ and c-α-pyr-$^4C_1$-1, are stabilized by anomeric effect; they have a $^4C_1$ ring configuration, thus leading the anomeric OH group towards the axial position. The hydroxy groups of both conformers are located at the same side of the ring, and are able to form chains of hydrogen bonds, which in turn, are strongly reinforced by sigma hydrogen bond cooperativity.[7] The most abundant α form cc-α-pyr-$^4C_1$ presents a counter-clockwise arrangement of the OH groups with a chain of three hydrogen bonds $O_{(4)}H\cdots O_{(3)}H\cdots O_{(1)}H\cdots O_{ring}$, while the less abundant c-α-pyr-$^4C_1$-1 shows a chain of two $O_{(1)}H\cdots O_{(3)}H\cdots O_{(4)}H$. The anomeric effect in the most abundant β form c-β-pyr-$^1C_4$-1 is reinforced by the intramolecular hydrogen bond network $O_{(3)}H\cdots O_{(4)}H\cdots O_{ring}$. Conformers c-$\beta$-pyr-$^4C_1$-1 and cc-$\beta$-pyr-$^4C_1$, with the anomeric hydroxy group in equatorial position, are stabilized by two non-cooperative intramolecular hydrogen bonds. All the conformers exhibit a mutual gauche configuration for the hydroxy groups at C_3 and C_4 positions, thus establishing that the gauche effect is not a discriminating stability factor. Another kind of

stabilizations as Hassel-Ottar and delta-two effects has a secondary role in monosaccharides.[30]

Compared to ribose the absence of the hydroxy group at C_2 in 2-deoxyribose limits the possibility of forming hydrogen bonds and in practice leads to weakening of the cooperative hydrogen bond network, altering the relative abundances. For example, the most stable α-pyranose form c-α-pyr-$^1C_4$ of ribose has not been detected in 2DR. The absence of an $O_{(2)}H$ group reverses the arrangement of the OH groups in the most stable β-pyranose forms (from clockwise c-β-pyr $^1C_4$ of 2DR to counter-clockwise in ribose cc-β-pyr $^1C_4$) to maximizes the number of hydrogen bonds (2 in cc-orientation vs. 1 in the clockwise arrangement).

In summary, the anomeric effect and hydrogen bonding are the main factors controlling the conformational behavior of isolated 2DR, represented by two α- and four β-pyranose conformers. Hydroxy groups orientate preferentially in such way for yielding a cooperative hydrogen bonding as efficiently as possible. When 2DR is vaporized, it exists predominantly in the pyranose form with a relative abundance of 10% of α and 90 % of β forms in accordance with its crystalline composition. In this context, the experimental ionization energy of 9.1 eV of gas-phase 2DR, obtained using tunable vacuum UV synchrotron radiation,[31] which has been previously ascribed to α pyranose forms, should actually correspond to the β forms.

It remains an open question how solvation affects the equilibrium between pyranose and furanose forms. Anyhow, the evidence collected so far supports that pyranoses are more stable both in gas-phase and solution, so the biological pathway to the insertion of ribose and deoxyribose in RNA or DNA cannot be merely attributed to a preference for furanoses in the physiological medium. Some structural arguments could be based on the existence of an exocyclic hydroxymethyl group (at C-5) in the furanose form. Both DNA and RNA involve a phosphate-linked chain, connected through bonds between the (exocylic) CH_2OH OH-5' and (cyclic) OH-3' groups. This could not occur if the ribose/deoxyribose units were in the pyranose form. On this argument the evolutionary preference might be structural and connected with the availability of the "CH2O-" linker. The question on why the nature chose to grow via OH3' and OH5' could then be an option of suitability, since there are several combinations of hydroxy groups which may build biologically useful shapes.

Alternatively, Eschenmoser[32,33] has suggested that biological selection of RNA is not due to base-paring strength, but to overtolerance to base-pair mismatches. However, the issue remains opened since no experiment has yet proved that any nucleotide has a reasonable ability to replicate nonenzymatically under "natural conditions".[34]

VI.1. EXPERIMENTAL SECTION

2-deoxy-D-ribose (m.p.: 89-90ºC) was purchased from Sigma-Aldrich, without further purification, and prepared by mixing the powder of the solid with a commercial binder. The mixture was pressed to form cylindrical rods, which were placed in a laser ablation nozzle[10] to be vaporized using a 20ps Nd:YAG laser. The vaporized molecules were seeded in the Ne carrier gas at backing pressure of 15 bar, to expand adiabatically into the vacuum chamber, and probed by broadband CP-FTMW spectroscopy. Four separate broadband rotational spectra were acquired in each injection cycle with a total of 150000 averages.

Conformational searches were first carried out using semiempirical methods, followed by optimizations at the B3LYP/6-31G(d,p) level of theory, using the Gaussian suite of programs[23]. Rotational constants and the electric dipole moment components, together with the relative energies and Gibbs free energies (see Table 1) were derived from optimized structures computed at the MP2/6-311++G(d,p) level of theory on the predicted most stable conformers.

VI.2. REFERENCES

[1]   a) R. S. Shallenberger, T. E. Acree, *Nature* **1967**, *216*, 480-482; b) L. B. Kier, *J. Pharm. Sci.* **1972**, *61*, 1394-1397; c) van der Heijden, *Pure Appl. Chem.* **1997**, *69*, 667-674; d) R. J. Woods, W. A. Szarek, V. H. Smith, *J. Am. Chem. Soc.* **1990**, *112*, 4732-4741; e) R. S. Shallenberger, *Pure Appl. Chem.***1978**, *50*, 1409-1420; f) E. W. Deutsch, C. Hansch, *Nature* **1966**, *211*, 75.

[2]   A. L. Lehninger, *Principles of Biochemistry*, 4th ed., W.H. Freeman, **2004**.

[3]   D. Doddrell, Allerhan.A, *J. Am. Chem. Soc.* **1971**, *93*, 2779-2781.

[4]   a) J. A. Kanters, G. Roelofsen, B. P. Alblas, I. Meinders, *Acta Cryst. B* **1977**, *33*, 665-672; b) S. Takagi, G. A. Jeffrey, *Acta Cryst. B* **1977**, *33*, 3510-3515. 10.

[5]   J. P. Schermann, *Spectroscopy and Modeling of Biomolecular Building Blocks*, Elsevier, 2008.

[6]   M. Hurtta, I. Pitkänen, J. Knuutinen, *Carbohydrate Research* **2004**, *339*, 2267-2273.

[7]   R. J. Levis, *Annu. Rev. Phys. Chem.* **1994**, *45*, 483-518.

[8]   S. Mata, I. Peña, C. Cabezas, J. C. López, J. L. Alonso, , *J. Mol. Spectrosc.* **2012**, *280*, 91-96.

[9]   G. G. Brown, B. C. Dian, K. O. Douglass, S. M. Geyer, S. T. Shipman, B. H. Pate, *Rev. Sci. Instrum.* **2008**, *79*.

[10]   J. L. Alonso, C. Pérez, M. E. Sanz, J. C. López, S. Blanco, *Phys. Chem. Chem. Phys.* **2009**, *11*, 617-627.

[11]   See, for example, a) E. J. Cocinero, A. Lesarri, J. U. Grabow, J. C. López, J. L. Alonso, *Chemphyschem* **2007**, *8*, 599-604; b) I. Peña, M. Eugenia Sanz, J. C. López, J. L. Alonso, *J. Am. Chem. Soc.* **2012**, *134*, 2305-2312.

[12]   J. L. Alonso, I. Peña, J. C. López, V. Vaquero, *Angew. Chem. Int. Ed.* **2009**, *48*, 6141-6143 and references therein.

[13]   C. Cabezas, M. Varela, I. Peña, J. C. López, J. L. Alonso, *Phys. Chem. Chem. Phys.* **2012**, *14*, 13618-13623

[14]   M. Lozoya, C. Cabezas, S. Mata, J. C. López, J. L. Alonso in *LA-MB-FTMW Studies of Sugars,* Communication MH13, International Symposium on Molecular Spectroscopy, *66th Meeting* – Ohio State University, USA, **2011**.

[15]   H. M. Pickett, *J. Mol. Spectrosc.***1991**, *148*, 371-377.

[16]   M. J. S. Dewar, E. G. Zoebisch, E. F. Healy, J. J. P. Stewart, *J. Am. Chem. Soc.* **1985**, *107*, 3902-3909.

[17]   M. J. Frisch, *et al. Gaussian 09, Revision B.01*, Wallingford CT, **2010**.

[18]   E. Juaristi, G. Cuevas, *Tetrahedron* **1992**, *48*, 5019-5087.

[1]   a) P. Colins, R. Ferrier, *Monosacccharides: Their Chemistry and Their Roles in Natural Products*, Wiley, New York, **1995**; b) W. Pigman, D. Horton, *The Carbohydrates: Chemistry and Biochemistry*; Academic Press, New York, **1972**.

[2]   E. Herbst, E. F. van Dishoeck, *Annu. Rev. Astron. Astr.* **2009**, *47*, 427.

[3]   a) J. D. Watson, F. H. C. Crick, *Nature* **1953**, *171*, 737–738; b) W. Saenger, Principles of Nucleic Acid Structure, Springer, New York, 1984, pp. 1-556.

[4]   a) S. J. Angyal, *Angew. Chem. Int. Ed.* **1969**, *8*, 157-226; b) M. Rudrum, D. F. Shaw, *J. Chem. Soc.* **1965**, 52; c) R. U. Lemieux, J. D. Stevens, *Can. J. Chem.* **1966**, *44*, 249; d) S. J. Cortes, T. L. Mega, R. L Van Etten, *J. Org. Chem.* **1991**, *56*, 943-947.

[5]   a) E. Juaristi, G. Cuevas, *Tetrahedron* **1992**, *48*, 5019-5087; b) C. L. Perrin, K. B. Armstrong, M. A. Fabian, *J. Am. Chem. Soc.* **1994**, 116, 715-722.

[6]   a) E. J. Cocinero, P. Çarçabal, T. D. Vaden, J. P. Simons, B. G. Davis, *Nature* **2011**, *469*, 76; b) M. P. Freitas, *Org. Biomol. Chem.* **2013**, *11*, 2885; c) C. Wang, Z. Chen, W. Wu, Y. Mo, *Chem. Eur. J.* **2013**, *19*, 1436; d) G. F. Bauefeldt, T. M. Cardozo, M. S. Pereira, C. O. da Silva, *Org. Biomol. Chem.* **2013**, *11*, 299.

[7]   a) M. López de la Paz, G. Ellis, M. Pérez, J. Perkins, J. Jiménez-Barbero, C. Vicent, *Eur. J. Org. Chem.* **2002**, 840-855; b) G. A. Jeffrey and W. Saenger, Hydrogen Bonding in Biological Structures; Springer-Verlag: New York, 1991.

[8]   a) G. A. Jeffrey, *Food Chem.* **1996**, *56*, 241-246; b) Hunter, C. A. *Angew. Chem., Int. Ed.* **2004**, *43*, 5310-5324; c) Greenspan, N. S. *Curr. Top. Microbiol. Immunol.* **2001**, *260*, 65-85.

[9]   S. Furberg, *Acta Chem. Scand.* **1960**, *14*, 1357-1363.

[10]   T. Yu. Nikolaenko, L. A. Bulavin, D. N. Govorun, *Journal of Applied Spectroscopy,* **2011**, *78,* 751-754.

[11]   a) P. Çarçabal, R. A. Jockusch, I. Hünig, L. C. Snoek, R. T. Kroemer, B. G. Davis, D. P. Gamblin, I. Compagnon, J. Oomens, J. P. Simons, *J. Am. Chem. Soc.* **2005**, *127*, 11414-11425 and references therein; b) E. J. Cocinero, D. P. Gamblin, B. G. Davis and J. P. Simons, *J. Am. Chem. Soc.,* **2009**, *131*, 11117; c) E. J. Cocinero, P. Çarçabal, T. D. Vaden, B. G. Davis and John P. Simons J. *Am. Chem. Soc.,* **2011**, *133*, 4548.

[12]   a) J. L. Alonso, C. Pérez, M. E. Sanz, J. C. López, S. Blanco, *Phys. Chem. Chem. Phys.* **2009**, 11, 617-627 and references therein; b) E. J. Cocinero, A. Lesarri, P. Écija, J.-U. Grabow, J. A. Fernández, F. Castaño, *Phys. Chem. Chem. Phys.* **2010**, *12*, 12486.

[13]   I. Peña, M. E. Sanz, J. C. López, J. L. Alonso, *J. Am. Chem. Soc.* **2012**, *134*, 2305-2312 and references therein.

[14]   J. L. Alonso, V. Vaquero, I. Peña, J. C. López, S. Mata, W. Caminati, *Angew. Chem.* **2013**, *125*, 2387-2390 and references therein.

[15]   C. Cabezas, I. Peña, J. C. López, J. L. Alonso, *J. Phys. Chem. Lett.* **2013**, *4*, 486-490 and references therein.

[16]   C. Cabezas, J.L. Alonso, J.C. López, S. Mata, *Angew.Chem. Int. Ed.* **2012**, *51*, 1375-1378.

[17]   M. Lozoya, C. Cabezas, S. Mata, J. C. López, J. L. Alonso, in *LA-MB-FTMW Studies of Sugars,* Communication MH13, International Symposium on Molecular Spectroscopy, 66th Meeting – Ohio State University, USA, June, **2011**.

[18]   E. J. Cocinero, A. Lesarri, P. Écija, F. J. Basterretxea, J.-U. Grabow, J.A. Fernández, F. Castaño, *Angew. Chem. Int. Ed.* **2012**, *51*, 3119-3124.

[19]   a) E. J.Cocinero, A. Lesarri, P. Écija, A. Cimas, B. J. Davis, F. J. Basterretxea, J. A. Fernández, F. Castaño, *J. Am. Chem. Soc.* **2013**, *135*, 2845; b) C. Bermúdez, I. Peña, C. Cabezas, A. M. Daly and J. L. Alonso, *ChemPhysChem.* **2013**, *14*, 893-895.

[20]   a) G. G. Brown, B. C. Dian, K. O. Douglass, S. M. Geyer, S. T. Shipman, B. H. Pate, *Rev. Sci. Instrum.* **2008**, *79,* 053103; b) B. C. Dian, G. G. Brown, K. O. Douglass, B. H. Pate, *Science* **2008**, *320,*924; c) J.-U. Grabow, S. Mata, J. L. Alonso, I. Peña, S. Blanco, J. C. López and C. Cabezas, *Phys. Chem. Chem. Phys.* **2011**, *13*, 21063.

[21]   S. Mata, I. Peña, C. Cabezas, J. C. López, J. L. Alonso, *J. Mol. Spectrosc.* **2012**, *280*, 91-96.

[22]   I. Peña, A. M. Daly, C. Cabezas, S. Mata, C. Bermúdez, A. Niño, J. C. López, J-U. Grabow, J. L. Alonso, *J. Phys. Chem. Lett.* **2013***, 4,* 65–69.

[23]   Watson, J. K. G. in *Vibrational Spectra and Structure,* Vol. 6 (Ed.: J. R.Durig), Elsevier, New York, 1977, pp. 1– 78.

[24]   R. S. Ruoff, T. D. Klots, T. Emilsson, H. S. Gutowsky, *J. Chem. Phys.* 1990, *93*, 3142.

[25]   G. T. Fraser, R. D. Suenram, C. L. Lugez, *J. Phys. Chem. A* **2000**, *104,*1141.

[26]   Finch, P. *Carbohydrates: Structures, Syntheses and Dynamics* Kluwer Academic Publishers: Netherlands **1999**.

[27]   L. P. Guler, Y.-Q. Yu, and H. I. Kenttämaa, *J. Phys. Chem. A* **2002**, *106*, 6754-6764.

[28]   a) R. L. Levis, *Annu. ReV. Phys. Chem.* **1994**, *45*, 483 and references therein; b) L. V. Zhigilei, P. B. S. Kodali, B. J. Garrison, *J. Phys. Chem. B* **1998**, *102*, 2845; c) L. V. Zhigilei, E. Leveugle, B. J. Garrison, Y. G. Yingling, M. I. Zeifman, *Chem. ReV.* **2003**, *103*, 321.

[29]   S. Blanco, A. Lesarri, J. C. López, J. L. Alonso, *J. Am. Chem. Soc.* **2004**, *126*, 11675.

[30]   a) B. Ma, H. F. Schaefer III, N. L. Allinger, *J. Am. Chem. Soc.* **1998**, *120*, 3411; b) S. Wolfe, *Acc. Chem. Res.* **1972**, *5*, 102-111.

[31]   D. Ghosh, A. Golan, L. K. Takahashi, A. Krylov, M. A Ahmed, *J. Phys. Chem. Lett.* **2012**, *3*, 97-101.

[32]   Eschenmoser, A., *Science* **1999**, *284*, 2188.

[33]   Beier, M.; Reck, F., Wagner, T.; Krishnamurthy, R.; Eschenmoser, A., *Science* **1999**, *283,* 69.

[34]   D. H. Lee, J. R. Granja, J. A. Martínez, K. Severin, R. Ghadiri, *Nature* **1996**, *382,* 525.

CHAPTER VII. THE SHAPE OF D-GLUCOSAMINE

The bioactive amino monosaccharide D-glucosamine has been generated in gas phase via laser ablation of D-glucosamine hydrochloride. Three cyclic α-$^4C_1$ pyranose forms have been identified using Fourier transform microwave techniques. Stereoelectronic hyperconjugative forces – essentially linked with the anomeric or gauche effect – and cooperative OH···O, OH···N and NH···O chains, extended along the entire molecule, are found to be the main factors driving the conformational behavior. The orientation of the NH_2 group within each conformer has been determined by the values of the nuclear quadrupole constants. The results have been compared with those recently obtained for the archetypical D-glucose

VII.1. INTRODUCTION

The first conformational characterization of isolated D-glucose molecule in gas phase became recently possible due to the latest developments of Fourier tranform microwave techniques coupled with laser ablation vaporizations methods.[1] For this archetypical monosaccharide, four conformers of α-D-glucopyranose and three of β-D-glucopyranose have been unequivocally identified. D-glucosamine ($C_6H_{13}NO_5$, see Figure VII.1.a) is a bioactive amino monosaccharide that differs structurally from the parent D-glucose by replacement of the hydroxyl group on C_2 by an amino group. In the human body, glucosamine is biochemically formed as glucosamine-6-phosphate,[2] which is an essential precursor for subsequent synthesis of important nitrogen-containing macromolecules, such as glycoproteins, glycolipids and glycosaminoglycans, known as building blocks of the joint cartilage and connective tissues, contributing to their strength and flexibility.3 Glucosamine salts, derivatives and glucosamine-containing polymers have potential to be used in numerous biomedical applications.[3-7]
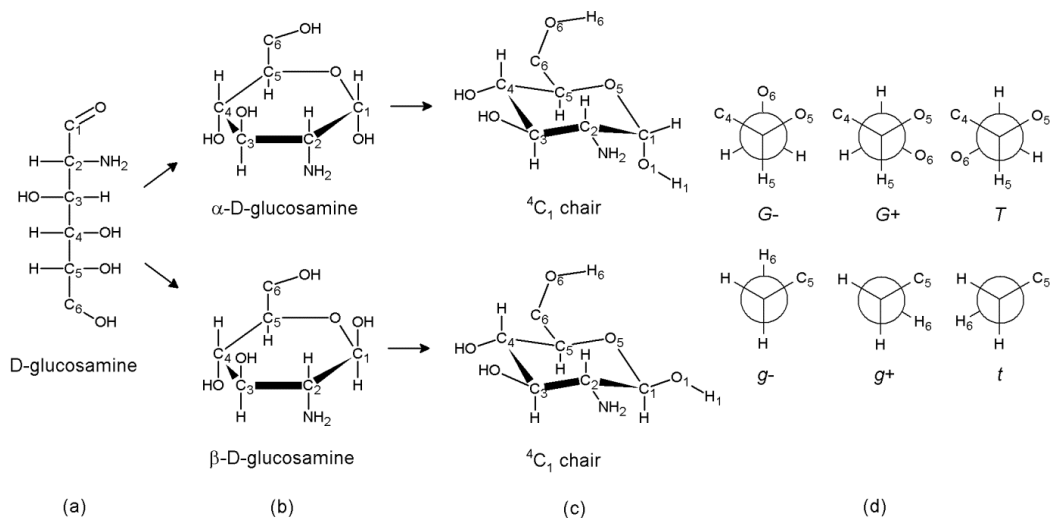
FIGURE *VII.I* (a) Fisher projection of D-glucosamine; (b) α- and β-anomers of D-glucosamine in Haworth projection; (c) $^4C_1$ conformations of α- and and β-D-glucosamine; (d) Newman projections of plausible conformations of the hydroxymethyl group around the C_5–C_6 (G–, G+, T) and C_6–O_6 (g–, g+, t) bonds

In the pure form, D-glucosamine is chemically unstable; promptly reacting when exposed to the atmosphere, and is thus only commercially available as a salt, where it appears in the protonated form. Hence, most of the experimental studies on D-glucosamine salts have been performed in either the solid[8-10] or liquid phases.[10-15] X-ray crystallography experiments on D-glucosamine hydrochloride indicate that the protonated glucosamine exists in the α-anomeric pyranose

form, in the preferred $^4C_1$ chair conformation.[8,9] When dissolved in water, the α-pyranose form is slowly transformed into the β-form, until it reaches the equilibrium anomeric composition of α: β ~ 63:37 as observed from optical rotation and nuclear magnetic resonance (NMR) experiments.[11,12] Interestingly, these results contrast with those obtained for D-glucose, where the reversed ratio of the two anomeric forms has been reported.[12,14-16] Despite the biological and medical importance of D-glucosamine, no experimental data on the conformational behavior of its neutral form has been reported hitherto.

At the University of Valladolid, efficient procedures have been developed for generation of neutral forms of proteogenic amino acids in supersonic expansion by laser ablation of its zwitterionic forms, allowing their conformational investigation using Fourier transform microwave techniques.[17,18] These experimental approaches have also been applied successfully to many other biologically relevant molecules, and, recently, several conformers of the monosaccharides D-glucose,[1] D-xylose,[19] D-fructose,[20] 2-deoxy-D-ribose[21] and D-erythrose[22] have been identified and characterized structurally. In the present study, the conformational behavior of D-glucosamine, successfully generated in the gas phase by laser ablation of its hydrochloride salt, is reported for the first time.
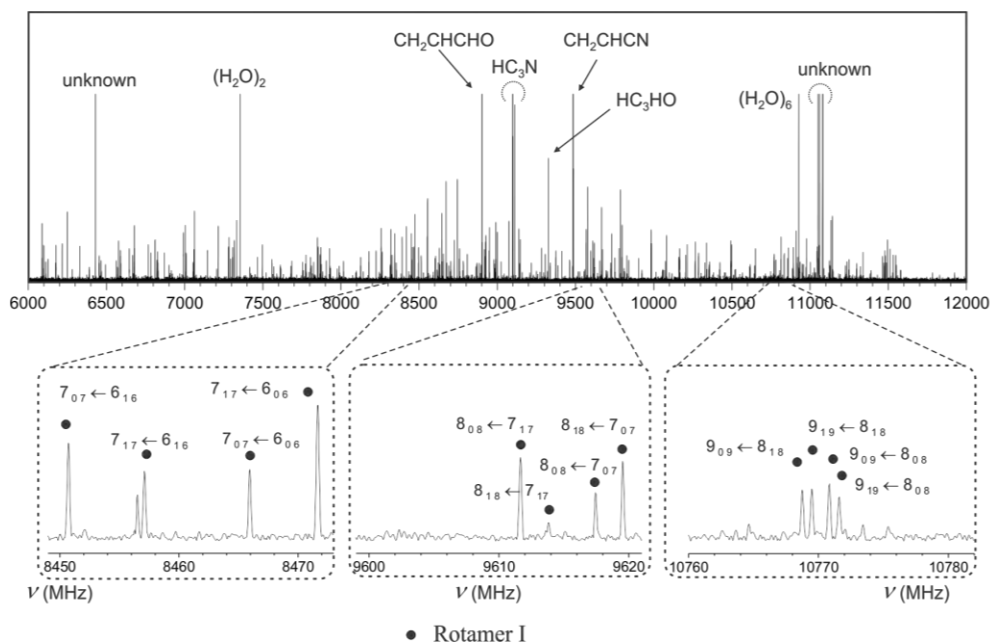
FIGURE *VII.2* Upper panel: overview CP-FTMW spectrum of the laser ablated α-D-glucosamine with assigned decomposition lines; lower panels: a-type $(J + 1)_{0J+1} \leftarrow J_{0J}$ and $(J + 1)_{1J+1} \leftarrow J_{1J}$ and b-type $(J + 1)_{1J+1} \leftarrow J_{0J}$ and $(J + 1)_{0J+1} \leftarrow J_{1J}$ progressions in detail corresponding to the observed rotamer I; rotational transitions become degenerated with the increasing J

VII.2. EXPERIMENTAL DETAILS

A commercial sample of D-glucosamine hydrochloride (m.p. = 190 – 194 °C) was used without any further purification. A solid rod was prepared by pressing the compound's fine powder mixed with a small amount of commercial binder and was placed into the ablation nozzle. A picosecond Nd:YAG laser (10 mJ per pulse, 35 ps pulse width) was used as vaporization tool. Products of the laser ablation were supersonically expanded using the flow of carrier gas (Ne, 15 bar) into the vacuum chamber of the spectrometers. D-glucosamine was first investigated using a chirped pulse Fourier transform microwave (CP-FTMW) spectrometer coupled with laser ablation to sample swiftly the rotational spectra of the different conformers present in the gas-phase mixture. Details of the experimental setup have been given elsewhere.[17] Up to 70 000 individual free induction decays were averaged in the time domain and Fourier transformed to obtain the rotational spectrum from 6 to 12 GHz shown in the upper panel of Figure VII.2. A Kaiser-Bessel window was applied to increase the baseline resolution. The sub-Doppler resolution of the laser ablation molecular beam Fourier transform microwave (LA-MB-FTMW) technique,[18] operating from 4 to 18 GHz, was used to resolve the hyperfine structure due to the ^{14}N nucleus. A short microwave radiation pulse of 0.3 μs duration was applied to polarize all the vaporized molecules. The registered free induction decay was then converted to the frequency domain by Fourier transformation. All the transitions appeared as Doppler doublets due to the parallel configuration of the molecular beam and the microwave radiation. The resonance frequency was determined as the arithmetic mean of the two Doppler components. Frequency accuracy better than 5 kHz and an estimated resolution of 7 kHz are achieved in the experiment.

VII.3. RESULTS

VII.3.1 Modelling

Symilarly to D-glucose and other hexoses, D-glucosamine may exist in linear or cyclic forms, with the six-membered aldopyranose ring being the most stable species[23] (see Figure VII.1.b). The formation of this ring structure is the result of a cyclization process through the nucleophilic attack of the hydroxyl group located at C_5 to the carbonyl carbon atom (C_1), which may lead to formation of α and β anomeric forms. The pyranose ring might assume either of two chair $^1C_4$ or $^4C_1$ configurations (see Figure VII.1c), but being dominant the latter, where the hydroxymethyl -CH_2OH group is in

Table VII.1. Molecular properties for the α- and β- lowest energy conformers of D-glucosamine (below 600 cm^{-1})

	A^a	B	C	χ_{aa}	χ_{bb}	χ_{cc}	$|\mu_a|$	$|\mu_b|$	$|\mu_c|$	ΔE^b	ΔG^c
α-G-g+/*cc*/t	1276	784	581	2.21	−3.92	1.70	3.0	3.8	0.1	0	0
α-G+g-/*cc*/t	1313	763	534	0.66	−2.44	1.78	3.0	3.2	1.2	31	19
α-Tg+/*cc*/t	1398	740	538	2.54	−4.33	1.79	4.1	1.7	0.9	113	205
α-G-g+/*cl*/g-	1296	788	573	2.76	0.51	−3.26	1.0	0.7	1.2	329	327
α-Tt/*cl*/g-	1404	752	544	2.76	0.46	−3.22	2.4	0.6	0.3	541	613
α-Tg-/*cl*/g-	1400	748	542	2.75	0.40	−3.15	0.1	0.5	0.0	587	672
β-G-g+/*cc*/t	1177	818	535	2.34	-3.37	1.03	2.8	2.2	2.5	0^d	0
β-G+g-/*cc*/t	1180	790	495	0.70	-2.38	1.68	2.6	2.0	1.0	37	16
β-Tg+/*cc*/t	1317	735	495	2.40	-4.10	1.71	3.2	0.4	1.0	140	230

^{a} A, B, and C represent the rotational constants (in MHz); χ_{aa}, χ_{bb} and χ_{cc} are the diagonal elements of the ^{14}N nuclear quadrupole coupling tensor (in MHz); μ_a, μ_b and μ_c are the electric dipole moment components (in D). ^{b} Relative energies (in cm^{-1}) with respect to the global minimum calculated at the MP2/6-311++G(d,p) level. ^{c} Gibbs energies calculated at 298 K. ^{d} The α-anomer species is predicted to be 579 cm^{-1} more stable than the β-anomer.

equatorial position and is energetically favored[1] (see Figure VII.1.c).

On this basis, *ab initio* calculations were performed on α- and β- $^4C_1$ configurations to obtain the lower-energy conformations and their relative Gibbs energies. Six α and three β forms have been predicted below 600 cm^{-1} (see Table VII.1). The α and β glucosamine´s conformers have been labeled according to the hydroxymethyl group configurations.[1,24] Three staggered forms, designated *G−*, *G+* (*gauche*) and *T* (*trans*) (see Figure VII.1.d), and represented by the O_6–C_6–C_5–O_5 dihedral angle with the values of approximately −60°, 60° and 180°, respectively, have been considered. In the same way, the symbols *g−*, *g+* and *t* describe the conformations defined by the H_6–O_6–C_6–C_5 dihedral angle. The symbols *cc* or *cl* after the first slash denote, respectively, the counterclockwise or clockwise arrangement of the cooperative network of intramolecular hydrogen bonds. Finally, after the second slash, the symbols *g−*, *g+* and *t* represent the orientation of the

anomeric hydroxyl group hydrogen atom defined by the H_1–O_1–C_1–C_2 dihedral angle.

The Moller-Plesset second order method (MP2) and the 6–311++G(d,p) basis set[25] were used to geometrically optimize the structures and to calculate the relevant spectroscopic properties. The values of the rotational constants (A, B, C), electric dipole moment components (μ_a, μ_b, μ_c) and the electric quadrupole coupling constants (χ_{aa}, χ_{bb}, χ_{cc}) for these conformers are reported in Table VII.1.

VII.3.2 Broadband CP-FTMW rotational spectrum analysis

The recorded broadband rotational spectrum of laser ablated of D-glucosamine hydrochloride from 6 to 12 GHz is shown in Figure VII.2. Soon, decomposition products lines common to other studies of sugars[20] and amino acids[26] (see Figure VII.2, upper panel) attributable to cyanoderivatives, formadelhyde, etc. were easily identified. After excluding the aforementioned signals from the spectral analysis, the identification of rotational transitions belonging to a first species, labeled as

rotamer I, was accomplished. Assignments were based on the identification in the broadband spectrum of a-type $(J+1)_{0\,J+1} \leftarrow J_{0\,J}$, $(J+1)_{1\,J+1} \leftarrow J_{1\,J}$ and b-type $(J+1)_{1\,J+1} \leftarrow J_{0\,J}$, $(J+1)_{0\,J+1} \leftarrow J_{1\,J}$ pairs of rotational progressions, which became degenerated with increasing J (Figure VII.2, lower panels). Following an iterative procedure of fitting and subsequent predictions, more a-type and b-type transitions were assigned in the range from $J = 3$ to $J = 8$. On the same basis, further searches in the broadband spectrum made possible the assignment of rotational transitions of another two rotamers: II and III. For rotamer III, only a-type rotational transitions were observed. No other rotamers were found in the broadband rotational spectrum.

Table VII.2. Experimental spectroscopic parameters for the three observed rotamers of D-glucosamine obtained from CP-FTMW spectra.

Parameter	Rotamer I	Rotamer II	Rotamer III
A[a] / MHz	1269.4108 (23)[c]	1305.3545 (29)	1389.896 (18)
B / MHz	781.1783 (13)	760.1481 (12)	738.65091 (94)
C / MHz	577.43929 (36)	531.25706 (33)	535.50479 (54)
a-type [b]	observed	observed	observed
b-type	observed	observed	–
c-type	–	–	–
N[c]	31	42	21
σ_{fit}[d] / kHz	23.3	26.1	19.2

[a] A, B, and C represent the rotational constants. [b] Observation of a-, b-, and c-type transitions for each structure. [c] Number of fitted transitions. [d] RMS deviation of the fit. [e] Standard error in parenthesis in the units of the last digit.

Some observed transitions show partial resolved hyperfine structure as corresponding to a compound with one ^{14}N nucleus. This experimental fact confirmed the generation of neutral glucosamine in the gas phase by laser ablation of crystalline D-glucosamine hydrochloride. Thus, the three observed rotamers can be ascribed to different glucosamine conformers. Since the spectral resolution attainable in the CP-FTMW experiments is not sufficient to completely resolve these hyperfine effects, only transitions with unresolved hyperfine structure (see Tables VII.S1-S3 of the SI) were fit[27] to a rigid rotor Hamiltonian to derive a first set of the rotational constants listed in Table VII.2.
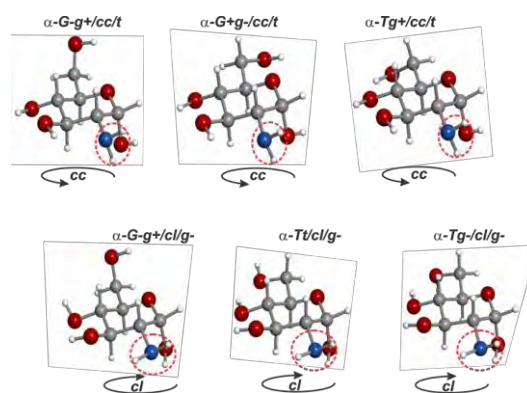
FIGURE VII.3 *The most stable conformers of α-D-glucosamine (below 600 cm^{-1}), showing the cc configuration in conformers G-g+/cc/t, G+g-/cc/t and Tg+/cc/t and the cl one in conformers G-g+/cl/g-, Tt/cl/g- and Tg-/cl/g-.*

The comparison of these experimental values with those predicted in Table VII.1 for the α and β forms of glucosamine clearly indicates that the three observed rotamers belong to α forms of glucosamine shown in Figure VII.3. The values of the rotational constants reflect directly the mass distribution of the conformers, which is substantially different in α and β forms. Dealing with α forms, it could be hypothesized that rotamer I could be the *G-g+/cc/t* or *G-g+/cl/g-* conformers and rotamer III the *Tg+/cc/t*, *Tt/cl/g-*, or *Tg-/cl/g-* conformers, while rotamer II can be definitively assigned to *G+g-/cc/t* conformer. If two conformers present similar mass distribution, the
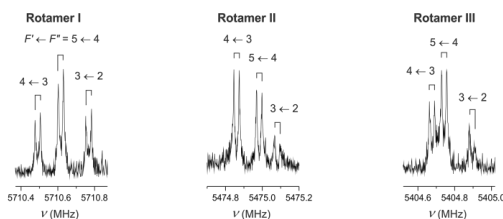
FIGURE VII.4 *Nuclear quadrupole hyperfine structure of the 4_{13} ← 3_{12} rotational transition for rotamers I, II and III. Each component labeled as $F'\leftarrow F''$ is observed as a doublet due to the Doppler effect. The molecular frequency is the arithmetic mean of the Doppler doublets*

rotational constants cannot be used to unambiguously distinguish between them. Hence, other conformational tools are needed for a conclusive identification.

The intramolecular hydrogen bond network arrangements, counterclockwise (*cc*) or clockwise (*cl*) (see Figure VII.3), significantly changes the predicted values of the dipole moment components for the six plausible low-energy conformes of the α forms (see Table VII.1). It, consequently, affects the observable type of transitions. Table VII.2 documents that none of *c*-type transition was observed for the various rotamers. If rotamer I was indeed the *G-g+/cl/g-* conformer, *c*-type transitions

should be observable, since $\mu_a \approx \mu_c$. Thus, rotamer I could be tentatively assigned to *G-g+/cc/t* conformer. For rotamer III, only *a*-type transitions were observed, so conformer Tg-/*cl*/*g-* should be excluded due to very low predicted value for this dipole moment component. It is still not possible to distinguish between conformers *Tg+/cc/t* and *Tt/cl/g-*.

A more straightforward way to distinguish unambiguously between conformers is to take into account the values of nuclear quadrupole hyperfine constants that can be extracted from the hyperfine structure of rotational transitions. The nuclear quadrupole coupling constants derived from the analysis are very sensitive to the orientation of the $-NH_2$ group with respect to the principal axes system. As shown in Table VII.1, the predicted values for the diagonal elements of the quadrupole coupling tensor χ_{aa}, χ_{bb}, χ_{cc} change dramatically going from the *cc* configuration in conformers *G-g+/cc/t* and *Tg+/cc/t* to the *cl* ones in conformers *G-g+/cl/g-* and *Tg-/cl/g-* (see Figure VII.3), since the $-NH_2$ group shows opposite orientation in both *cc* and *cl* arrangements to participate in the intramolecular hydrogen bond networks. A high resolution rotational study by LA-MB-FTMW spectroscopy is needed to completely resolve the ^{14}N nuclear quadrupole hyperfine structure, and to achieve a conclusive identification of the observed rotamers

Table VII.3. Experimental spectroscopic parameters for the three observed rotamers of D-glucosamine obtained from LA-MB-FTMW spectra.

Parameter	Rotamer I (α-G-g+/cc/t)	Rotamer II (α-G+g-/cc/t)	Rotamer III (α-Tg+/cc/t)
A^a / MHz	1269.4100(15)[c]	1305.34810(82)	1390.0011(14)
B / MHz	781.18234(26)	760.14999 (14)	738.65282 (13)
C / MHz	577.437380(86)	531.255624(50)	535.499914(56)
$\chi_{aa}{}^b$ / MHz	2.159 (16)	0.637 (5)	2.487 (6)
χ_{bb} / MHz	−3.727 (14)	−2.278 (4)	−4.129 (5)
χ_{cc} / MHz	1.567 (14)	1.641 (4)	1.642 (5)
N^c	32	30	18
$\sigma_{fit}{}^d$ / kHz	1.3	1.3	1.1

[a] A, B, and C represent the rotational constants. [b] χ_{aa}, χ_{bb} and χ_{cc} are the diagonal elements of the ^{14}N nuclear quadrupole coupling tensor. [c] Number of fitted transitions. [d] RMS deviation of the fit. [e] Standard error in parenthesis in the units of the last digit

VII.4. HIGH RESOLUTION LA-MB-FTMW SPECTRA

A new series of experiments on laser ablated D-glucosamine hydrochloride were carried out using our LA-MB-FTMW technique. The nuclear quadrupole coupling hyperfine structure for the rotational transitions of the observed rotamers was fully resolved as shown in Figure VII.4 for the 4_{13}-3_{12} transition. A total of 32, 30 and 18 quadrupole hyperfine components were measured for rotamers I, II and III, respectively (Tables VII.S4-S6 of the SI). They were analyzed using the effective Hamiltonian $H = H_{ROT} + H_Q$, where H_{ROT} represents the rigid rotor Hamiltonian and H_Q the quadrupole coupling Hamiltonian.[28] Using the $F = J + I$ angular momentum coupling scheme, the energy levels involved in each transition were thus labeled with the quantum numbers J, K_{-1}, K_{+1}, and F. Experimentally derived rotational constants A, B, C together with the diagonal elements of the quadrupole coupling tensor χ_{aa}, χ_{bb}, χ_{cc} for each rotamer are given in Table VII.3. Contributions of the off-diagonal elements of the nuclear quadrupole coupling tensor to the observed frequencies were
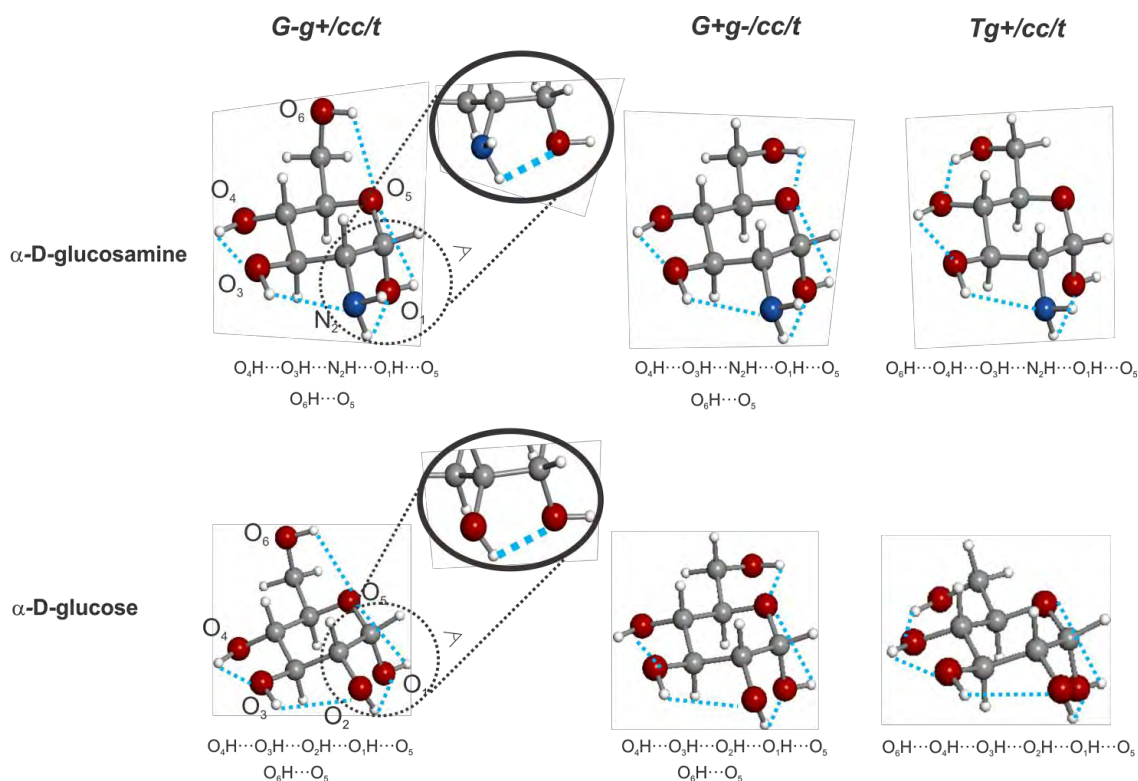
FIGURE VII.5 *The three observed conformers of α-D-glucosamine in comparison with those observed for α-D-glucose.[1] Inlet: detail of the N₂H···O₁ and O₂H···O₁ hydrogen bonds for G-g+/cc/t conformers of α-D-glucosamine and α-D-glucose, respectively. The amino group NH₂ in α-D-glucosamine assumes the same role in the intramolecular hydrogen bonding than the hydroxyl group OH in α-D-glucose*

found to be negligible, and therefore these parameters were not determined.

At first, a comparison of the experimentally obtained values of the electric quadrupole coupling constants for rotamer II (see Table VII.3) with the predicted ones (see Table VII.1) was made to confirm its assignment to the $G+g$-/cc/t conformer. The excellent agreement among both sets of data confirms the assignment based on the rotational constants. Similarly, the experimental electric quadrupole coupling constants for rotamers I and III werecompared with those predicted for the related conformers' candidates (see Tables VII.3 and VII.1), unambiguously showing that rotamer I corresponds to the G-$g+$/cc/t conformer and rotamer III corresponds to the $Tg+$/cc/t conformer

VII.4. DISCUSSION

The observation of only α-forms deserves some explanation. It should be noted that, as observed in previous studies,[29,30] the laser ablation of solid samples of the crystalline D-glucosamine hydrochloride generates into the gas phase neutral D-glucosamine in its α-pyranose form, thus preserving the α-pyranose species present in the X-ray studies.[1,19] The interconversion between the α and β anomers is a solvent-mediated reaction and thus should not occur that easily during evaporation,[31] especially if the sample is completely dry.[32] In any case, the most stable β form, β-G-$g+$/cc/t, is predicted 579 cm^{-1} above the most stable α-G-$g+$/cc/t one.

The three observed α-pyranose forms of D-glucosamine, G-$g+$/cc/t, G+g-/cc/t and T$g+$/cc/t, are stabilized by the anomeric effect; they present a $^4C_1$ ring configuration, thus leading the anomeric OH group towards the axial position.[33] The hydroxyl groups are located at the same side of the ring to form a hydrogen bond network, which in turn, is reinforced by sigma hydrogen-bond cooperativity.[34] In this way, the two most stable conformers G+g-/cc/t and G-$g+$/cc/t are stabilized by a chain of four cooperative hydrogen bonds ($O_4H \cdots O_3H \cdots N_2H \cdots O_1H \cdots O_5$) and one non-cooperative $O_6H \cdots O_5$ bond, as depicted in Figure VII.5. The least stable conformer $Tg+$/cc/t exhibits five cooperative hydrogen bonds ($O_6H \cdots O_4H \cdots O_3H \cdots N_2H \cdots O_1H \cdots O_5$), including the stronger H-bond between O_6H and O_4H which is, for sugars with O_4H equatorial group, favorable only in the *trans* configuration. Relative abundances of the three conformers have been estimated from the relative intensities of the rotational transitions, and found to be G-$g+$/cc/t : G+g-/cc/t : Tg+/cc/t ≈ 0.7(1) : 1 : 0.2(1), in qualitatively agreement with those predicted for Gibbs energies in Table VII.1.

The observation of a *trans* configuration for α-D-glucosamine, *Tg+/cc/t*, represents a remarkable fact, since numerous experimental studies on glucopyranosides in condensed phases,[35-37] have shown that the dihedral angle (O6–C6–C5–O5) displays a preference towards G- and G+ gauche configuration, with an almost complete absence of the *trans* (T). Our results are in agreement with *ab initio* computations, which predict the *trans* conformer enough populated to be detected in the supersonic expansion. In any case, the hydroxymethyl group's gauche (G) configurations of D-glucosamine also dominate in the gas phase, which can in principle be seen as a consequence of contributions of factors like the so-called gauche effect,[38] associated with the stabilization of the synclinal (gauche) conformation of two vicinal electronegative groups bonded to a two carbon unit. The same conformational behavior has been observed in the archetypical α-D-glucopyranose.

As shown in Figure VII.5, the three observed conformers of α-D-glucosamine and the three lower-energy conformers of α-D-glucose[1] exhibit the same configuration of the exocyclic hydroxymethyl group, as well as the same orientation of the intramolecular hydrogen bond network (*cc*). Their relative abundances are also comparable with those previously reported for the corresponding conformers of α-D-glucose.[1] The fourth conformer in order of increasing energy (*G-g+/cl/g-*) of α-D-glucosamine has not been detected, in contrast to that observed for α-D-glucose. This fact can be easily explained by its higher relative energy and, consequently, to its small abundance in the supersonic expansion.

The high resolution reached by LA-MB-FTMW experiments allows the determination of the nuclear quadrupole coupling constants, χ_{aa}, χ_{bb}, χ_{cc}. They inform on the orientation of the NH$_2$ group with respect to the molecular frame, and allow establishing the intramolecular interactions in which this functional group is involved. The inlet of Figure VII.5 shows how the amino group inserts into the hydrogen bond network; it adopts such as orientation to assume the same role of the OH-group at the C$_2$ carbon in α-D-glucopyranose. Therefore, the amino group does not introduce any changes into the gas phase conformational shape of α-D-glucosamine respect to that observed for α-D-glucose.

VII.5. CONCLUSSION

The present study provides the first experimental investigation of the gas phase structures of D-glucosamine, which has led to the determination of the conformational behavior of this important amino monosaccharide. Three different conformers have been conclusively identified through their rotational spectra. As with α-D-glucopyranose, the observed conformers are stabilized by a mesh of

stereoelectronic hyperconjugative forces – essentially linked with the anomeric or *gauche* effect – and cooperative OH···O chains extended along the entire molecule. The three observed conformers of α-D-glucosamine and the three most abundant conformers of α-D-glucose have the same configurations of the hydroxymethyl group as well as the same counterclockwise arrangement of the OH groups. The orientation of the NH₂ group within each conformer has been delineated by the values of the nuclear quadrupole constants. The NH₂ group adopts the same role than the OH group in the intramolecular hydrogen bonding network, which leads to the conclusion that the substitution of the hydroxyl group on C-2 by the amino group does not affect the gas phase conformational behavior found in the archetypal D-glucose

VII.7. REFERENCES

[1]. J. L. Alonso, M. A. Lozoya, I. Peña, J. C.López, C. Cabezas, S. Mata, S. Blanco, *Chem. Sci.*, 2014, **5**, 515.

[2]. S. Ghosh, H. J. Blumenthal, E. Davidson, S. Roseman, *J. Biol. Chem.*, 1960, **235**, 1265.

[3]. G. S. Kelly, *Altern. Med. Rev.*, 1998, **3**, 27.

[4]. Y. Henrotin, A. Mobasheri, M. Marty, *Arthritis Research & Therapy*, 2012, **14**, 201.

[5]. T. H. Fischer, A. P. Bode, M. Demcheva, J. N. Vournakis, *J. Biomed. Mat. Res. A*, 2007, **80A**, 167.

[6]. H. Nakamura, K. Masuko, K. Yudoh, T. Kato, T Kamada, T. Kawahara, *International Journal of Rheumatology*, 2007, **27**, 213.

[7]. S. X. Wang, S. Laverty, M. Dumitriu, A. Plaas, M. D. Grynpas, *Arthritis & Rheumatism*, 2007, **56**, 1537.

[8]. S. S. C. Chu, G. A. Jeffrey, *P. Roy. Soc. Lond. A. Mat.*, 1965, **285**, 470.

[9]. W. T. A. Harrison, H. S. Yathirajan, B. Narayana, T. V. Sreevidya, B. K. Sarojini, *Acta Crystallogr. E*, 2007, **63**, o3248.

[10]. S. C. Sahoo, A. Tharalekshmy, S. W. Ng, P. Naumov, *Crystal Growth & Design*, 2012, **12**, 5148.

[11]. S. Bunel, C. Ibarra, E. Moraga, A. Blaskó, C. A. Bunton, *Carbohyd. Res.*, 1993, **244**, 1.

[12]. D. Horton, J. S. Jewell, K. D. Philips, *J. Org. Chem.*, 1966, **31**, 4022.

[13]. J. C. Irvine, J. C. Earl, *J. Chem. Soc. Trans.*, 1922, **121**, 2370.

A. Neuberger, A. P. Fletcher, *Carbohyd. Res.*, 1971, **17**, 79.

[14]. Neuberger, A. P. Fletcher, *J. Chem. Soc. B: Phys. Org.*, 1969, 178.

[15]. T. Taga, K. Osaki, *Bull. Chem. Soc. Jpn.*, 1975, **48**, 3250.

[16]. S. Mata, I. Peña, C. Cabezas, J. C. López, J. L. Alonso, *J. Mol. Spectrosc.*, 2012, **280**, 91.

[17]. Peña, M. E. Sanz, J. C. López, J. L. Alonso, *J. Am. Chem. Soc.*, 2012, **134**, 2305-2312.

[18]. Peña, S. Mata, A. Martin, C. Cabezas, A. M. Daly, J. L. Alonso, *Phys. Chem. Chem. Phys.*, 2013, **15**, 18243.

[19]. Bermúdez, I. Peña, C. Cabezas, A. M. Daly, J. L. Alonso, *ChemPhysChem*, 2013, **14**, 893.

[20]. Peña, E. J. Cocinero, C. Cabezas, A. Lesarri, S. Mata, P. Écija, A. M. Daly, Á. Cimas, C. Bermúdez, F. J. Basterretxea, S. Blanco, J. A. Fernández, J. C. López, F. Castaño, J. L. Alonso, *Angew. Chem. Int. Ed.*, 2013, **52**, 11840.

[21]. Cabezas, I. Peña, A. M. Daly, J. L. Alonso, *Chem. Commun.*, 2013, **49**, 10826.

[22]. L. Lehninger, *Principles of Biochemistry*; 4th ed.; W.H. Freeman, 2004.

[23]. M. Hoffmann, J. Rychlewski, *J. Am. Chem. Soc.*, 2001, **123**, 2308.

[24]. M. J. Frisch, G. W. Trucks, H. B. Schlegel, G. E. Scuseria, M. A. Robb, J. R. Cheeseman, G. Scalmani, V. Barone, B. Mennucci, G. A. Petersson, H. Nakatsuji, M. Caricato, X. Li, H. P. Hratchian, A. F. Izmaylov, J. Bloino, G. Zheng, J. L. Sonnenberg, M. Hada, M. Ehara, K. Toyota, R. Fukuda, J. Hasegawa, M. Ishida, T. Nakajima, Y. Honda, O. Kitao, H. Nakai, T. Vreven, J. A. Montgomery Jr., J. E. Peralta, F. Ogliaro, M. Bearpark, J. J. Heyd, E. Brothers, K.

N. Kudin, V. N. Staroverov, R. Kobayashi, J. Normand, K. Raghavachari, A. Rendell, J. C. Burant, S. S. Iyengar, J. Tomasi, M. Cossi, N. Rega, J. M. Millam, M. Klene, J. E. Knox, J. B. Cross, V. Bakken, C. Adamo, J. Jaramillo, R. Gomperts, R. E. Stratmann, O. Yazyev, A. J. Austin, R. Cammi, C. Pomelli, J. W. Ochterski, R. L. Martin, K. Morokuma, V. G. Zakrzewski, G. A. Voth, P. Salvador, J. J. Dannenberg, S. Dapprich, A. D. Daniels, O¨. Farkas, J. B. Foresman, J. V. Ortiz, J. Cioslowski and D. J. Fox, Gaussian 09, Revision B.01, Gaussian, Inc., Wallingford, CT, 2009.

[25].   M. E. Sanz, C. Cabezas, S. Mata, J. L. Alonso, *J. Chem. Phys.*, 2014, **140**, 204308.

[26].   H. M. Pickett, J. Mol. Spectrosc., 1991, **148**, 371–377.

[27].   W. Gordy and R. L. Cook, Microwave Molecular Spectra, John Wiley & Sons, New York, 3rd edn, 1984.

[28].   Cabezas, I. Peña, J. C. López, J. L. Alonso, *J. Phys. Chem. Lett.*, 2013, **4**, 486.

[29].   C. Cabezas, M. Varela, I. Peña, J. C. López, J. L. Alonso, *Phys. Chem. Chem. Phys.*, 2012, **14**, 13618.

[30].   P. Finch, *Carbohydrates: Structures, Syntheses and Dynamics*, Kluwer Academic Publishers, Netherlands, 1999.

[31].   L. P. Guler, Y.-Q. Yu, H. I. Kenttämaa, *J. Phys. Chem. A*, 2002, **106**, 6754 – 6764.

[32].   Juaristi and G. Cuevas, Tetrahedron, 1992, **48**, 5019–5087.

[33].   A. Jeffrey, W. Saenger, *Hydrogen Bonding in Biological Structures*, Springer, New York, 1991.

[34].   R. H. Marchessault, S. Pérez, *Biopolymers*, 1979, **18**, 2369.

[35].   Bock, J. Ø. Duus, *J. Carbohydr. Chem.*, 1994, **13**, 513.

[36].   Y. Nishida, H. Hori, H. Ohrui, H. Meguro, *J. Carbohydr. Chem.*, 1988, **7**, 239.

[37].   S. Wolfe, Acc. Chem. Res., 1972, **5**, 102

CHAPTER VIII: TAUTOMERISM IN NEUTRAL HISTIDINE
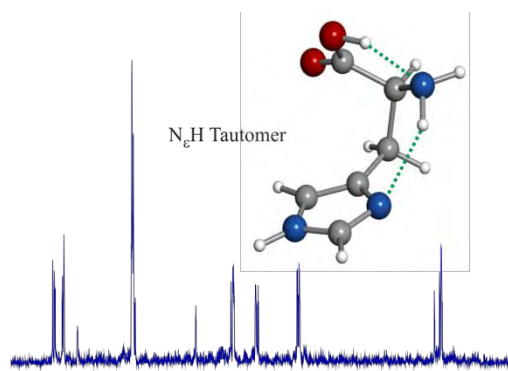
Histidine is an important natural amino acid, involved in many relevant biological processes, which, due to its physical properties, proved difficult to characterize experimentally in its neutral form. In this work, neutral histidine has been generated in the gas phase by laser ablation of solid samples and its $N_\varepsilon H$ tautomeric form unraveled through its rotational spectrum. The quadrupole hyperfine structure, arising from the existing three ^{14}N nuclei, constituted a site-specifically probe for revealing the tautomeric form as well as the side chain configuration of this proteogenic amino acid.

Histidine (His, $H_2N\text{-}CH\text{-}(CH_2\text{-}C_3N_2H_3)\text{-}COOH$) is one of the twenty proteogenic amino acids present in many relevant proteins.[1] The imidazol group (Scheme VIII.1) of its side chain, makes His to be one of the two natural amino acids that can exhibit tautomeric equilibrium. Either N_δ or N_ε of the imidazol ring might be protonated, and, thus, both can participate in *inter-* and *intra-*molecular hydrogen bonds, acting as donor or as acceptor. As such, His residue is an excellent binding site either for other molecules, or to induce stabilization by intramolecular interactions within the protein structure.[2-5] Several spectroscopic techniques have been devoted to analyze His tautomeric balance in condensed phases, where His is stabilized as a zwitterion ($^+H_3N\text{-}CH(CH_2\text{-}C_3N_2H_3)\text{-}COO^-$),[6-11] and, thus, it does not represent the neutral canonical form present in peptide side chains. The tautomeric fraction of the imidazole ring of His for proteins in solution varies significantly among different positions of His in the same protein, reflecting the importance of the environment in determining the tautomeric behavior.[12] For these reasons, the determination of tautomeric behavior of His in gas phase, where it is stabilized in its neutral canonical form, is of utmost importance to gain knowledge on their intrinsic tautomeric/conformational properties.

His, a solid with high melting point (m.p.~290ºC) and low vapor pressure, is well known for their thermal instability, preventing easy measurements of their gas-phase spectra in static thermally heated gas cells. Hence, studies on the
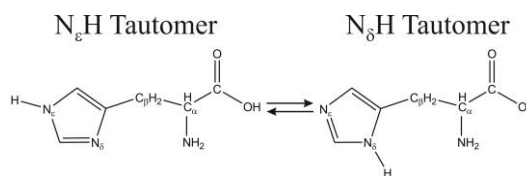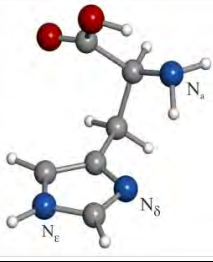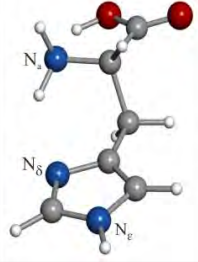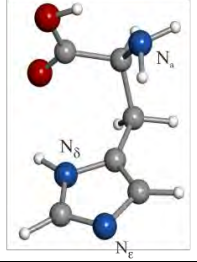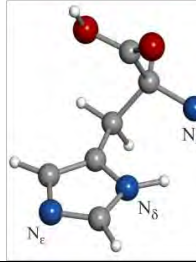
SCHEME VIII.1: *Tautomeric equilibrium in histidine.*

tautomeric/conformational preferences of neutral form have been, until now, restricted solely to the theoretical field.[13-16] Nowadays, advances in laser ablation of solid biomolecules have allowed to overcome vaporization problems. Thus, high resolution spectroscopy techniques have enabled scientific community to observe individual conformers of biomolecules with unprecedented clarity.[17] Particularly, the combination of Fourier transform microwave spectroscopy with laser ablation techniques conducted in a supersonic expansion (LA-MB-FTMW) has provided a new approach to the structural studies of amino acids,[18-19] nitrogen bases[20] and other relevant building blocks.[21-22]

Nevertheless, His still remains as a challenging problem for a rotational spectroscopic study. His possesses three ^{14}N nuclei with nuclear spin $I=1$, one located in the amino group ($^{14}N_a$) and the other two in the imidazole ring (N_ε and N_δ). These three interact with the electric field gradient created by the rest of the molecule at the nucleus, splitting into a very complex hyperfine pattern each rotational transition and, thus, increasing the difficulty of spectral interpretation. In this project, we have faced these challenges successfully and here we report the first rotational study of neutral His using

TABLE VIII.1: *Ab initio* predicted rotational and quadrupole coupling constants for the four lowest-energy conformers[a] *of histidine*

	εII$_a$	εII$_b$	δII$_a$	δI$_a$
A/B/C[b]	1818/862/772	2993/568/501	1917/826/729	1805/847/785
$\chi_{aa}/\chi_{bb}/\chi_{cc}$ (N$_\delta$)	1.66/-3.51/1.85	0.67/-2.18/1.51	0.14/1.22/-1.36	0.20/-0.17/-0.03
$\chi_{aa}/\chi_{bb}/\chi_{cc}$ (N$_\varepsilon$)	-0.19/1.09/-0.90	1.15/1.02/-2.16	-2.27/1.63/0.64	-1.77/0.05/1.72
$\chi_{aa}/\chi_{bb}/\chi_{cc}$ (N$_a$)	0.58/1.93/-2.52	-1.53/2.08/-0.55	-0.67/1.41/-0.74	-4.04/2.69/1.35
$|\mu_a|/|\mu_b|/|\mu_c|$	3.5/1.5/0.2	7.8/0.4/1.9	1.8/3.1/1.3	4.4/2.3/1.6
ΔE	0	742	422	838
ΔG	0	678	480	731

[a] Conformers are labelled following the nomenclature used in previous studies of amino acids. The first label distinguishes between tautomers; ε (for tautomer N$_\varepsilon$H) and δ (for tautomer N$_\delta$H). The second index indicates the type of hydrogen bond between the amino and the carboxylic group [Ref. 7b]. Finally, lower labels a and b designate the increasing energy order within each type of hydrogen bonding. [b] A, B, C are the rotational constants (in MHz); χ$_{aa}$, χ$_{bb}$, χ$_{cc}$ are the ^{14}N nuclear quadrupole coupling constants (N$_\varepsilon$, N$_\delta$ and N$_a$ correspond to three different ^{14}N nuclei); $|\mu_a|$, $|\mu_b|$, $|\mu_c|$ are the absolute values of the electric dipole moment components (in D); ΔE and ΔG are the MP2/6-311++G(d,p) electronic energies and Gibbs free energies (298K), respectively (in cm^{-1}), with respect to the global minimum.

a newly constructed Fourier transform microwave spectrometer (see Section III.1.2).

With this aim, solid His has been transferred into the gas phase by laser ablation. Vaporized molecules are then seeded in a stream of Ne carrier gas, and supersonically expanded, becoming ideally frozen in their most stable forms. These can be interrogated by a microwave radiation pulse in the prepared solvent-free environment of the supersonic expansion. Spectroscopic searches in wide frequency regions revealed the rotational spectrum of only one rotamer with the characteristic pattern of a near-prolate asymmetric top with sets of a-type R-branch transitions. As anticipated, all observed transitions were split into many close hyperfine components, arising from the coupling of three non-equivalent ^{14}N$_\varepsilon$, ^{14}N$_\delta$ and ^{14}N$_a$ nuclei. At first glance, the assignment of hyperfine structure

seemed impossible. Hence, the rotational frequencies of nine a-type transitions were roughly measured as the intensity-weighted mean of the line clusters and fitted[23] to a rigid rotor Hamiltonian leading to a preliminary set of rotational constants $A \approx 1848$, $B \approx 832$ and $C \approx 746$ (all in MHz). To ascertain which His structure is responsible for the observed spectrum, theoretical values of the rotational constants of the most stable forms of His are required. Thus, the lowest energy conformations reported in previous theoretical studies[5] were re-optimized using *ab initio* calculations[11] at MP2/6-311++G(d,p) level of theory. The spectroscopic parameters for the conformers lying in an energy window of 1000 cm^{-1} are collected in Table VIII.1. The values of the experimental rotational constants were found to be consistent with those predicted for the conformers

TABLE VIII.2: Experimental and predicted rotational and quadrupole coupling constants for the observed rotamer of histidine.

	Experimental	Theoretical MP2/cc-pVTZ
A[a]	1847.53472 (52)[b]	1839[c]
B	831.71551 (16)	859
C	745.94445 (18)	770
Δ_J	0.2651 (53)	-
χ_{aa} / N_δ	1.6113 (17)	1.62
χ_{bb} / N_δ	-3.4973 (16)	-3.49
χ_{cc} / N_δ	1.8860 (16)	1.87
χ_{aa} / N_ε	-0.17933 (26)	-0.18
χ_{bb} / N_ε	1.12207 (87)	0.97
χ_{cc} / N_ε	-0.94273 (87)	-0.79
χ_{aa} /NH$_2$	0.0052 (22)	0.04
χ_{bb} /NH$_2$	2.0982 (43)	2.10
χ_{cc} /NH$_2$	-2.1034 (43)	-2.14
N	75	-
σ	1.9	-

[a]A, B, C are the rotational constants (in MHz); D$_J$ is a quartic centrifugal distortion constant (in kHz); χ_{aa}, χ_{bb}, χ_{cc} are the ^{14}N nuclear quadrupole coupling constants (in MHz); N is the number of fitted transitions; s is the rms deviation of the fit (in kHz). [b]Standard error in parentheses in units of the last digit. [c]Values calculated at MP2/ccpVTZ level of theory.

labeled as εII_a, δI_a and δII_a. Unfortunately, the difference in the rotational constants values for these three species is not large enough to allow discrimination and a conclusive identification cannot be reached on this basis.

A different and independent way of identifying structures is based on the presence of ^{14}N nuclei in the molecule. While rotational constants are strongly related to mass distribution, nuclear quadrupole coupling interactions depend critically on the electronic environment, position and orientation of the ^{14}N nuclei. The quadrupole coupling constants[24] have been used as fingerprints in conformational analysis of amino acids,[18-19] as well as for tautomeric identification of nucleobases.[20] For His, the predicted values of the quadrupole coupling constants (χ_{aa}, χ_{bb} and χ_{cc}) for the ^{14}N nuclei (see Table 1) are distinct due to the

dissimilar nature of bonding in the vicinity of the nucleus. Thus, they could provide an independent approach to discriminate tautomeric species. In order to unveil, in a conclusive fashion, the observed tautomeric species, it becomes necessary to resolve and interpret the quadrupole hyperfine structure of His, an asymmetric top with three ^{14}N nuclei of different electronic environment. The next stage of the investigation covered the analysis of the nuclear quadrupole hyperfine structure. b-type R-branch transition whose hyperfine components are predicted as being most spread in frequency have to be first analyzed. The construction of the new LA-MB-FTMW spectrometer, covering lower frequency regions, made possible to record the b-type R-branch transition $1_{1,1} \leftarrow 0_{0,0}$ at about 2.5 GHz (Figure VIII.1). Interpretation of the quadrupole coupling pattern led to the assignment of ten hyperfine components of this transition, essential as starting point of the analysis. New predictions allowed the assignment of a total of 75 hyperfine components (Table VIII.S1 of Supplementary
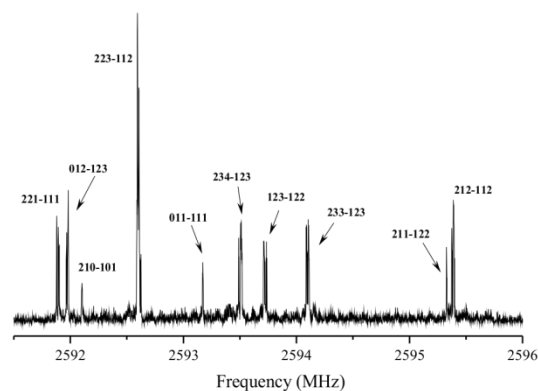
FIGURE VIII.1: *1_{11} - 0_{00} rotational transition in 2 GHz frequency region for the observed rotamer of His. The ^{14}N quadrupole components are labeled with the quantum numbers F_1', F_2', F- F_1'', F_2'', F' (nuclear quadrupole scheme: I_1+J=F_1, I_2+F_1=F_2, I_3+F_2=F where I stands for the nuclear spin for each ^{14}N)*

Information) belonging to nine a- and three b-type R-branch transitions. They were analyzed[23] using a Watson's A-reduced semirigid rotor Hamiltonian in the I^r-representation[25] supplemented with a term to account for the nuclear quadrupole coupling contribution.[24] Table VIII.2 illustrates how such analysis rendered accurate rotational and nuclear quadrupole constants.

Comparison of experimental quadrupole coupling constants with those predicted for conformers εII_a, δI_a and δII_a allowed the unequivocal identification of the observed rotamer as conformer εII_a. This assignment is further confirmed attending to the predicted values of the dipole moments and the type of spectra observed. A close look into the values of nuclear quadrupole coupling constants for $^{14}N_a$ nucleus indicates small discrepancies between experimental and theoretical values. Although the difference is not large enough to raise doubts about the identity of the conformer detected, it suggests the existence of some discrepancy between the calculated geometries and the actual ones. Such discrepancies have lead to the correction of the orientation of the amino group in the εII_a conformer, by performing ab initio calculations for different values of the dihedral angle (> $HN_aC_aC_\beta$). An improved matching was found when this angle was rotated from the initial ab initio value of -16° to -23° (See Figure VIII.S1 of Supplementary Information). This fact prompted us to make other MP2 optimizations using a larger basis as cc-pVTZ in an attempt to find a more suitable calculation basis set to reproduce our
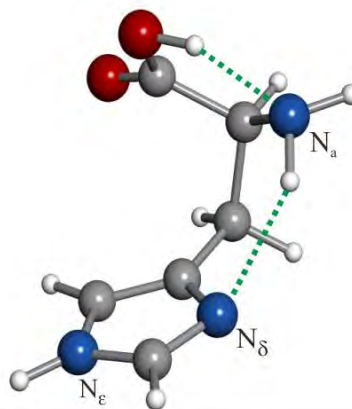
FIGURE VIII.2: *Observed conformer for the histidine molecule, showing the intramolecular hydrogen bonds that stabilize the structure,*

experimental nuclear quadrupole coupling constants. This fact prompted us to make other MP2 optimizations using a larger basis set as cc-pVTZ in an attempt to find a more suitable calculation basis set to reproduce our experimental nuclear quadrupole coupling constants. In this manner, we have re-optimized the ab initio structure at the MP2/cc-pVTZ level of theory obtaining a value for this dihedral angle of -21° and, consequently, a closer concordance between the experimental and predicted quadrupole coupling constants (See Table VIII.2). This results in a more favorable arrangement to the establishment of N_a-H···N_δ interactions between the amino group and imidazol ring analogous to the H bond that stabilized one of the species found for its homologue histamine.[26] The 3D structure of εII_a conformer, shown in the Figure VIII.2, has been taken from that predicted by ab initio calculations (Cartesian coordinates are given in Table VIII.S2 of the Supplementary Information), based in the good agreement between experimental and theoretical

values of rotational constants (relative errors less than 3%).

Summarizing, the present study provides the first experimental information on the conformational and tautomeric properties of neutral His. The capability of LA-MB-FTMW spectroscopy to undertake very accurate spectroscopic constants and their direct comparison with *ab initio* computations provides an unmatched means for the unequivocal identification of the observed species. The three $^{14}N_\varepsilon$, $^{14}N_\delta$ and $^{14}N_a$ nuclei of His present at defined sites introduce hyperfine rotational probes that further expand the utility of this spectroscopic technique. Our results indicate that neutral His exits in the gas phase in the $N_\varepsilon H$ tautomeric form in a single εII_a conformation which is the one predicted as the global minimum. This is stabilized by an O-H$\cdots N_a$ hydrogen bond in an α-COOH trans configuration also found in the rest of essential aromatic amino acids.[27-28] One of the hydrogen atoms of the amino group is pointing towards the imidazol ring indicating the existence of an N_a-H$\cdots N_\delta$ interaction, since none H is attached to the N_δ atom, this can act as a proton acceptor in the intramolecular H-bond. Both intramolecular hydrogen bonds form an intramolecular hydrogen bond network O-H$\cdots N_a$-H$\cdots N_\delta$, which could be the stabilization motif of the observed species. The present state-of-the-art of microwave spectroscopy, as illustrated in the present study, is paving the way towards the study of larger, more complex, biological systems which have been previously considered as being out of reach of high resolution spectroscopic studies.

VIII.1. REFERENCES

[1]   A. L. Lehninger, *Principles of Biochemistry*, 4th ed., W.H. Freeman, **2004**.

[2]   J. C. Kendrew, R. E. Dickerson, B. E. Strandberg, R. G. Hart, D. R. Davies, D. C. Phillips, V. C. Shore, *Nature* **1960**, *185*, 422-427.

[3]   M. F. Perutz, M. G. Rossmann, A. F. Cullis, H. Muirhead, G. Will, A. C. T. North, *Nature* **1960**, *185*, 416-422.

[4]   S. Dementin, V. Belle, P. Bertrand, B. Guigliarelli, G. Adryanczyk-Perrier, A. L. De Lacey, V. M. Fernandez, M. Rousset, C. Leger, *Journal of the American Chemical Society* **2006**, *128*, 5209-5218.

[5]   A. Volbeda, M. H. Charon, C. Piras, E. C. Hatchikian, M. Frey, J. C. Fontecillacamps, *Nature* **1995**, *373*, 580-587.

[6]   M. S. Lehmann, T. F. Koetzle, W. C. Hamilton, *International Journal of Peptide and Protein Research* **1972**, *4*, 229-239.

[7]   J. J. Madden, E. L. McGandy, N. C. Seeman, *Acta Crystallographica Section B* **1972**, *28*, 2377-2382.

[8]   P. Edington, M. M. Harding, *Acta Crystallographica Section B* **1974**, *30*, 204-206.

[9]   F. Blomberg, W. Maurer, H. Ruterjans, *Journal of the American Chemical Society* **1977**, *99*, 8149-8159.

[10]   F. Pfluger, B. Hernandez, M. Ghomi, *J. Phys. Chem. B* **2010**, *114*, 9072-9083.

[11]   S. H. Li, M. Hong, *Journal of the American Chemical Society* **2011**, *133*, 1534-1544.

[12]   J. A. Vila, Y. A. Arnautova, Y. Vorobjev, H. A. Scheraga, *Proceedings of the National Academy of Sciences* **2011**, *108*, 5602-5607.

[13]   Z. J. Huang, W. B. Yu, Z. J. Lin, *Journal of Molecular Structure-Theochem* **2006**, *801*, 7-20.

[14]   Z. J. Huang, Z. J. Lin, C. Song, *Journal of Physical Chemistry A* **2007**, *111*, 4340-4352.

[15]   Z. A. Tehrani, E. Tavasoli, A. Fattahi, *Journal of Molecular Structure: THEOCHEM* **2010**, *960*, 73-85.

[16]   B. Kovacevic, M. Rozman, L. Klasinc, D. Srzic, Z. B. Maksic, M. Yanez, *Journal of Physical Chemistry A* **2005**, *109*, 8329-8335.

[17]   J. P. Shermann, *Spectroscopy and Modelling of Biomolecular Builiding Blocks*, Elsevier, Amsterdam, **2008**.

[18]   C. Cabezas, M. Varela, I. Peña, S. Mata, J. C. Lopez, J. L. Alonso, *Chemical Communications* **2012**, *48*, 5934-5936.

[19]   I. Peña, M. E. Sanz, J. C. López, J. L. Alonso, *Journal of the American Chemical Society* **2012**, *134*, 2305-2312.

[20]   J. L. Alonso, V. Vaquero, I. Peña, J. C. López, S. Mata, W. Caminati, *Angewandte Chemie* **2013**, *48*, 5934-5936.

[21]   C. Cabezas, M. Varela, J. L. Alonso, *Chemphyschem* **2013**, *14*, 2539-2543.

[22]   J. L. Alonso, M. A. Lozoya, I. Peña, J. C. Lopez, C. Cabezas, S. Mata, S. Blanco, *Chemical Science* **2014**, *5*, 515-522.

[23]   H. M. Pickett, *Journal of Molecular Spectroscopy* **1991**, *148*, 371-377.

[24]   W. Gordy, R. L. Cook, *Microwave Molecular Spectra, Vol. IX and XIV*, Wiley-Interscience, New York, **1984**.

[25]   J. K. G. Watson, *Vibrational Spectra and Structure, Vol. 6*, Elsevier: Amsterdam, **1977**.

[26]   P. D. Godfrey, R. D. Brown, *Journal of the American Chemical Society* **1998**, *120*, 10724-10732.

[27]   C. b. Perez, S. Mata, S. Blanco, J. C. López, J. L. Alonso, *J. Phys. Chem. A* **2011**, *115*, 9653.
[28]   M. E. Sanz, C. Cabezas, S. Mata, J. L. Alonso, *J. Phys. Chem. A* **2014**, *accepted.*

CHAPTER IX. THE MONOHYDRATED CYTOSINE

The preference of cytosine for it keto-amino tautomer when water is present has been revealed by the analysis of the rotational spectrum of the monohydrated cluster of cytosine. In these clusters, water is bound to the ketone and the adjacent amino group by two hydrogen bond interactions that close a six member ring.

Huge scientific efforts have been devoted to the study of physical chemistry properties of the nucleic acids DNA and RNA. Among all the features of these macromolecules, the study of the conformational and tautomeric behavior of its building blocks is of fundamental interest to understand DNA recognition and replication mechanisms. A recent study of cytosine,[1] one of their nucleobases, has shown that, in isolation conditions, it can be present in five different forms arising from keto-enolic and amino-imino tautomeric equilibria (see Figure IX.1.a). Contrary as occur in crystal structure and in nucleic acid chains[2-4], where the most stable tautomer is the keto-amino (KA), the trans-enol-amino (EAt) form has been found to be slightly more populated than the keto-amino (ratio 1:0.82 in favour of the EAt species). Moving to an environment closer to the biological medium, it remains to be investigated how the tautomeric behavior is altered by docking water molecules to bare cytosine. Therefore, in the present work, we were wondering about the effect of solvation in tautomeric behavior of cytosine: is it one water molecule enough to provide a tautomeric selection? which binding site (s) is water attached to?

On the basis on prior ab initio calculations,[5-6] which are the only data available since the experimental research, so far, are restricted to cytosine protonated[7] and to the crystal structure,[8] it has been found that eleven monohydrate complexes of cytosine with water, in which water can be attached via seven different pairs of

hydrogen bonds, are plausible (see Supplementary Information for the ab initio calculation and Figure IX.1 for the results). To the complexity of finding which of these complexes are stabilized, it is added the experimental difficulties of generating them. Fortunately, the latest improvements in microwave spectroscopy have made possible to observe clusters of glycine[9-10] and alanine[11] with one and two water molecules attached, as well as, the monohydrate of the nucleobases uracil and thymine.[12] This approach consists on ablating with laser solid rods of cytosine whose vaporized molecules interact with a carrier gas containing water. All together are swept along towards a cavity where the complexes generated are submitted to a detailed structural interrogation through pulsed jet Fourier transform microwave spectroscopy.[13] Thus, provided the success on previous investigations, we have faced the challenge of researching about the conformational behavior of the monohydrated cytosine, whose analysis by microwave spectroscopy is even more complicated due to the presence of three ^{14}N that results in a very complicated hyperfine structure.

The experimental procedure was started by conducting long frequency scans in the 3 to 8 GHz microwave region with the aim of finding rotational transitions belonging to cytosine-water complex. During the search, the rotational spectrum of bare cytosine[1] was easily found. After removing these lines, none new lines were identified, apart from those produced during the photofragmentation process. At this point, it was taken the advantage of

FIGURE IX.1. a) All five forms of bare cytosine (in the central part of the figure) surrounded by the eleven minima of the complex cytosine-water predicted by *ab initio* calculations; wich are named using the nomenclature employed for the monomer[3] followed by a number indicating the binding site

H-bonds[a]	EAt-1	EAt-2	EAc-2	EAc-3	KA-4	KA-2	KIt-4	KIt-5	KIt-6	KIc-4	KIc-6
	$O_cH\cdots O_w$	$N_1H\cdots O_w$	$N_1H\cdots O_w$	$O_cH\cdots O_w$	$N_3H\cdots O_w$	$N_1H\cdots O_w$	$N_3H\cdots O_w$	$N_2H\cdots O_w$	$N_2H\cdots O_w$	$N_3H\cdots O_w$	$N_2\cdots O_w$
	$O_wH\cdots N_3$	$O_wH\cdots N_2$	$O_wH\cdots N_2$	$O_wH\cdots N_2$	$O_wH\cdots O_c$	$O_wH\cdots N_2$	$O_wH\cdots O_c$	$O_wH\cdots N_1$	$O_wH\cdots O_c$	$O_wH\cdots O_c$	$O_wH\cdots O_c$
A[b]/MHz	3735	2154	2163	2168	3697	2171	3610	2192	2185	3623	2174
B/MHz	980	1363	1345	1386	980	1356	980	1342	1349	974	1354
C/MHz	778	842	836	847	776	841	775	836	836	771	837
μ_a[c] / D	3.2	0.6	2.5	2.3	2.9	2.8	1.2	3.5	3.4	2.2	0.9
μ_b / D	3.2	2.0	2.8	5.4	4.0	4.8	4.0	4.7	2.9	1.1	3.3
μ_c / D	0.9	0.2	1.2	2.3	0.2	0.0	-0.9	0.5	0.6	1.0	0.8
Δ_c[d] /uÅ²	-1.29	-5.21	-4.45	-1.41	-1.19	-4.65	-3.37	-2.69	-1.71	-3.28	-1.80
ΔE_{MP2}[e]/cm⁻¹	0	7	1080	779	247	370	1084	1216	1869	1764	1929
D_e[f]/KJmol⁻¹	33.27	34.64	34.28	37.84	40.40	39.56	36.54	34.49	37.02	35.61	33.50

[a] O_c is the oxygen of the cytosine, O_w is oxygen of the water molecule and the subscript in the nitrogen stands for the number of the nitrogen. [b] A, B, and C represent the rotational constants; μ_a, μ_b, and μ_c are the electric dipole moment components. 1 D ≈ 3.3356 x 10⁻³⁰ C m. [d] $\Delta_c = I_c - I_a - I_b$ is the inertial defect. Conversion factor: 505379.1 MHz/uÅ². [e] Relative energies (in cm⁻¹) with respect to the global minimum calculated at MP2/6-311++G(d,p) level. [f] *Ab initio* values for the dissociation energy have been corrected for basis set superposition error (BSSE) using the counterpoise procedure and including fragment relaxation.

the recently implementation of a multi-FID device (see Supplementary information), which allows to accumulate up to 10 spectra per laser pulse. Under this new experimental condition, a new set of a-type R-branch transitions could be observed in the spectrum. All of these lines disappeared when either the laser pulses or the water reservoir were removed. Furthermore, although they were too weak to be properly measured and assigned, all transitions were split into many hyperfine quadrupole components (see Figure IX.2) arising from the presence of the three ¹⁴N atoms (I=1) of the cytosine. The centers of the transitions were fitted[14] to a rigid rotor Hamiltonian[15] obtaining the rotational constants of a specie that correspond

to the monohydrated cytosine. Moreover, R-branch b-type transitions belonging to this rotamer where also measured and added to the fitting. No other lines attributable to cytosine water complexes remained unassigned in the spectrum.

At first glance (comparison), the comparison between the experimental rotational constants (Table IX.2) with those predicted for all the above dimers (Figure IX.1) allows ensuring that water is not linked to cytosine through the binding sites 2, 3, 5 and 6, in other words, water is attached by the cytosine oxygen and the nitrogen 3. The distinction between these species seems more complicated. Nevertheless, there are several statements to discard the species KIt-4 and KIc-4. Firstly, it has recently been shown that both keto-imino conformers of the bare cytosine are the least abundant species under the same experimental conditions.[3] In addition, not only differs their A rotational constants more than 100 MHz from the predicted values, but also, the predicted dipole moments of KIc-4 (μ_b) and Kit-4 (μ_a) are too low to account for the experimental

Table IX.2. Experimental rotational constants for the observed rotamer of the cytosine water complex

Parameter	Experimental Value
A^a/MHz	3725.40(15)^b
B/MHz	980.744(44)
C/MHz	777.329(31)
$\Delta_c{}^c$ /uÅ^2	-0.8(2)
N^d	10
σ^e /kHz	22.7
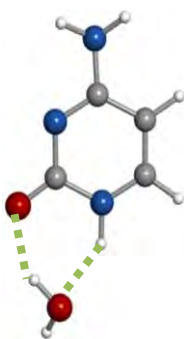
^{a}A, B and C are the rotational constants; ^{b} Standard error in parentheses in the units of the last digit. $^d \Delta_c = I_c - I_a - I_b$ is the inertial defect. ^{c}Conversion factor: 505379.1 MHz/uÅ^2. Number of transitions. ^{d}rms deviation of the fit.
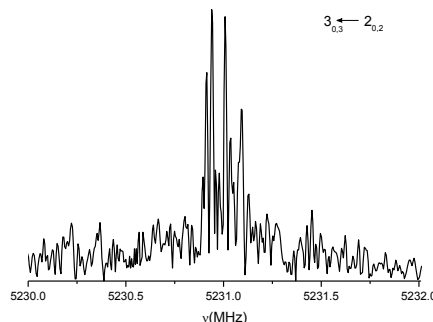
FIGURE IX.2. *Hyperfine structure of the a-type R-branch transition $3_{0,3} - 2_{0,2}$ of the observed rotamer of cytosine water complex.*

observations, attending to the power required for the polarization of the a- and b-type R-branch transitions. And, finally, the clustering stabilization energy predicted for both keto-imino complexes are around 4 kJ/mol smaller than the correspondent energy for the KA-1 cluster.

At this moment, the two complexes under consideration are the EAt-1and KA-4 whose bare tautomers (EAt and KA, respectively) are almost equally populated in isolation conditions. However, due to the resemblance between them in terms of geometry and mass distribution, the determination of the rotational constants are not enough to ensure which of both complexes is the one that exist in gas phase. Yet, we can bring some light over this issue considering several facts. If the rotational values obtained corresponded to the EAt-1, the EAt-2 would have to be also observed since it has lower dissociation energy and the energy of both minima are similar. However, although a dedicated search was performed applying the ultimate optimal conditions, any transition belonging to this EAt-2

monohydrate could be detected. Furthermore, the dissociation energy of the KA-1 complex, it is predicted to be around 7 kJ/mol higher than the EAt-1 complex, which means that it formation is more stabilizing. Thus, these arguments indicate that KA-4 monohydrate of cytosine is the species present in the supersonic expansion, which is not the most abundant for the bare conformers.[1] The change in the relative abundance between the keto-amino and the enol-amino species triggered by the presence of a molecule of water has been also found in the system 2-hydroxypyridine/2-pyridone, which is a mimetic of cytosine that also contains a keto-enol tautomerism.[16] In this case, the 2-hydroxypyridine (enolic form) is more abundant without water attached (the population ratio found was 1:0.27), whereas the ratio is inverted to 1:1.67 in favor of the 2-pyridone for the monohydrated species.

As it is shown in the figure of Table IX.2, the KA-4 cytosine complex is stabilized by two hydrogen bond interaction between the water molecule and the carbonylic oxygen of cytosine and the amino group number 3 (N_3 H···O_w and O_w H···O_c). As a consequence of the formation of the complex with water, the inertial defect (Δ_c), which can be used to investigate the planarity of a system), has been slightly augmented. From the close zero value of the inertial defect for bare KA (-0.2212(3)u$Å^2$), which indicates that it is a planar molecule, to the -0.8(2) u$Å^2$ found for the complex KA-4. This fact points out that there are only small contributions of out-of-plain atoms as occur in case of uracil-water complex.[12]

IX.1. EXPERIMENTAL DETAILS

The rotational spectra of cytosine–water complexes have been investigated using an upgrade spectrometer of the LA-MB-FTMW spectrometer already reported.[17] Details of the modifications are described in the Supplementary Information. Briefly, a multi FID step has been introduced in order to enhance the sensitivity of the instrument. Thus, the experimental procedure is now as follows.

Commercial samples of cytosine powder, without further purification, are ground and mixed with a commercial binder in order to obtain compact rods by pressing the mixture in a hydraulic press. The solid rods are ablated using the third harmonic of a Nd:YAG picoseconds laser. The vaporized species are seeded in a carrier gas that is later expanded adiabatically into a Fabry-Pérot cavity to produce a supersonic expansion. A water reservoir was placed just before the gas valve to add water to the inert carrier gas. The clusters of cytosine-water were formed in the jet and later probed with a sequence of short polarizing microwave pulses. The number of pulses and the delay between pulses is selected to get a compromise between sensitivity and resolution. The more number of pulses the better sensitivity whereas the longer the delay the higher

resolution. Each FID produced by each microwave pulse is recorded, added together and Fourier transformed to obtain the spectrum in the frequency domain

IX.2. REFERENCES

[1]   J. L. Alonso, V. Vaquero, I. Peña, J. C. López, S. Mata, W. Caminati, *Angewandte Chemie* **2013**, *48*, 5934-5936.

[2]   J. D. Watson, F. H. C. Crick, *Nature* **1953**, *171*, 737-738.

[3]   C. E. Crespo-Hernández, B. Cohen, P. M. Hare, B. Kohler, *Chemical Reviews* **2004**, *104*, 1977-2020.

[4]   M. K. Shukla, J. Leszczynski, *Journal of Biomolecular Structure and Dynamics* **2007**, *25*, 93-118.

[5]   G. Fogarasi, P. G. Szalay, *Chem. Phys. Lett.* **2002**, *356*, 383-390.

[6]   A. K. Chandra, D. Michalska, R. Wysokiñsky, T. Zeegers-Huyskens, *The Journal of Physical Chemistry A* **2004**, *108*, 9593-9600.

[7]   J. M. Bakker, J.-Y. Salpin, P. Maître, *International Journal of Mass Spectrometry* **2009**, *283*, 214-221.

[8]   G. A. Jeffrey, Y. Kinoshita, *Acta Crystallographica* **1963**, *16*, 20-28.

[9]   J. L. Alonso, E. J. Cocinero, A. Lesarri, M. E. Sanz, J. C. Lopez, *Angewandte Chemie-International Edition* **2006**, *45*, 3471-3474.

[10]   J. L. Alonso, I. Pena, M. Eugenia Sanz, V. Vaquero, S. Mata, C. Cabezas, J. C. Lopez, *Chemical Communications* **2013**, *49*, 3443-3445.

[11]   V. Vaquero, M. E. Sanz, I. Peña, S. Mata, C. Cabezas, J. C. López, J. L. Alonso, *The Journal of Physical Chemistry A* **2014**, *118*, 2584-2590.

[12]   J. C. Lopez, J. L. Alonso, I. Peña, V. Vaquero, *Physical Chemistry Chemical Physics* **2010**, *12*, 14128-14134.

[13]   I. Peña, M. Eugenia Sanz, J. C. Lopez, J. L. Alonso, *Journal of the American Chemical Society* **2012**, *134*, 2305-2312.

[14]   H. M. Pickett, *Journal of Molecular Spectroscopy* **1991**, *148*, 371-377.

[15]   J. K. G. Watson, *Vibrational Spectra and Structure, Vol. 6*, Elsevier: Amsterdam, **1977**.

[16]   S. Mata, V. Cortijo, W. Caminati, J. L. Alonso, M. Eugenia Sanz, J. C. Lopez, S. Blanco, *Journal of Physical Chemistry A* **2010**, *114*, 11393-11398.

[17]   C. Bermúdez, S. Mata, C. Cabezas, J. L. Alonso, *Angewandte Chemie International Edition* **2014**, *53*, 11015-11018.

CHAPTER X.   CONFORMATIONAL ANALYSIS OF SYNEPHRINE IN THE GAS PHASE
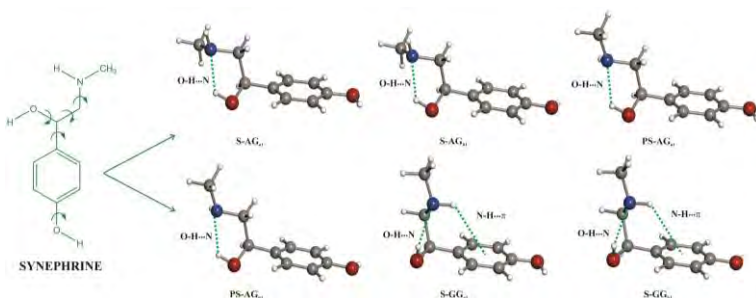
Six conformers of the neurotransmitter synephrine have been identified in gas phase using a laser ablation device in combination with a molecular beam Fourier-transform microwave spectrometer operating in the 4–10 GHz frequency range. The identification of all the conformers was based on the comparison of the experimental rotational and ^{14}N quadrupole coupling constants with those predicted by *ab initio* calculations, and relative values of their electrical dipole moment components. The conformational preferences have been rationalized in terms of the various intramolecular forces operating in the different conformers of the studied molecules. All observed species are characterized by an intramolecular hydrogen-bond of type O–H$\cdots$N established in the side chain of the neurotransmitters, which adopt an extended disposition in their most stable forms. For conformers with a folded side chain an extra N-H$\cdots\pi$ hydrogen-bond type interaction is established between the amino group and the π-system of the aromatic ring.

X.1. INTRODUCTION

Neurotransmitters are substances produced and secreted by a neuron to cross the synapse space between neurons. They are comprised by several different families of compounds, including amino acids, peptides and biogenic amines. A key structural feature of neurotransmitters is their high conformational flexibility. This dictates molecular shape, which, in turn, has great influence on the transport properties, as well as on the molecular recognition processes at the receptor site.[1-3]

The study of the intricate processes of neurotransmission at molecular level and on interactions of neurotransmitters in complex biological conditions must be preceded by detailed characterization of the neurotransmitters conformational properties in the absence of intermolecular interactions, thus avoiding alterations of their intrinsic structural preferences, matching the conditions found in gas phase. Howbeit, pure neurotransmitters at room temperature normally present themselves as solids with low to very low vapor pressure and high melting point. Hence, the question of how to efficiently populate the gas phase with these compounds is a critical one for the success of these investigations. Conventional heating methods can be used to achieve the necessary amount of compound in the gas phase, but they are only useful for a handful of these compounds, easily vaporizable neurotransmitters. Combining Fourier transform microwave spectroscopy in supersonic jets (MB-FTMW) with heating methods we have characterized the conformational panorama of several neurotransmitters in the gas phase such as, 2-phenylethylamine,[4] p-methoxyphenylethylamine,[5] norephedrine, ephedrine, and pseudoephedrine[6]. However, investigation of complete series of neurotransmitters escaped MB–FTMW spectroscopy studies due to their high melting points and associated very low vapor pressures. In these cases, laser ablation has been shown to be an efficient method for vaporizing solid samples without the decomposition problems encountered using heating methods. Indeed, laser ablation in combination with supersonic molecular beams and microwave spectroscopy (LA-MB-FTMW)[7-10] has proven to be a powerful tool in the investigation of the gas phase conformational behavior of solid neurotransmitters such as taurine,[11] tryptamine,[12] GABA,[13] serotonin[14] and dopamine.[15]

In the continuation of our [16]ongoing investigation about the conformational study of neurotransmitters in the gas phase using rotational spectroscopy, in the present investigation we have considered synephrine (4-[1-hydroxy-2-(methylamino) ethyl]phenol) as target compound. This molecule (see Figure X.1) is endogenous biogenic amines that has been shown to act as important neurotransmitters. Synephrine is a naturally occurring alkaloid in many cactus and citrus juice fruits,[16-17] which is commonly marketed as a weight-loss drug, acting as a stimulant in humans.[18] As far as we could ascertain in the literature, synephrine has been studied using a combination of electronic and IR Dip spectroscopy techniques.[19] A related systems 2-amino-1-phenylethanol (APE) and 2-methylamino-1-phenylethanol (MAPE), without the phenolic OH group in para position, have been studied[20] by free jet absorption microwave spectroscopy.

On this basis, we have tackled the problem of characterizing the conformational preferences of synephrine, and the nature of the intramolecular interactions which determine its preferences, taking advantage of the high resolution of LA-MB-FTMW spectroscopy. The obtained results allow us to conclusively identifying six conformers of synephrine. The role of the intramolecular hydrogen bonding interactions is discussed in terms of the stabilization of all observed conformers.

X.2. EXPERIMENTAL AND COMPUTATIONAL METHODS

X.2.1. Experimental setup

A laser ablation molecular beam Fourier transform microwave (LA-MB-FTMW) spectrometer, described elsewhere,[7-10] which operates in the 4–10 GHz frequency region, was used in order to record the rotational spectra of both studied molecules. Solid rods of fine-powdered synephrine (Sigma-Aldrich, 98%, m. p. = 187 ºC) were mixed with minimum quantities of a commercial binder to form a cylindrical rod. The samples were then vaporized using the third harmonic (355 nm) of a Nd:YAG picosecond laser (20 ps length pulse) using energies of ~13 mJ/pulse. The neutral vaporized molecules were seeded in the carrier gas (Ne, 15 bar) and
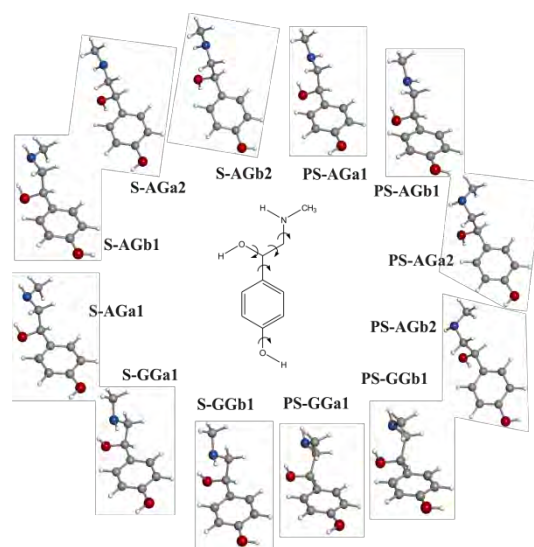
FIGURE X.1: *The twelve lowest-energy conformers of synephrine predicted by ab initio calculations. The sketch is in the center for which the hindered single-bond rotations which govern conformational equilibrium are shown.*

expanded into a Fabry-Pérot resonator. After sending the microwaves pulses through the cavity, the emission FID (free induction decay) of the molecules was recorded in the time-domain and Fourier transformed to yield the frequency-domain spectrum. Since the supersonic jet and the microwave resonator axis are collinearly placed, signals appeared split into Doppler doublets (see Figure X.2). The arithmetic mean of the doublets was taken as the final frequency. The estimated accuracy of the frequency measurements is better than 3 kHz.

X.1.1. *Ab initio* calculations

Ab initio calculations were performed to guide the identification of the species detected in the supersonic expansion. The calculations were performed at the MP2/6-311++G(d,p) level of theory, using the Gaussian 09[21] suite of programs. Twelve conformers for synephrine (depicted in Figures X.1) were found in an energy window of

800 cm^{-1} above the global minimum. According to the herein adopted nomenclature, each conformer of synephryne is specified by a combination of four symbols: the pair of capital letters indicates the orientation of the $CC_\alpha C_\beta N$ and $OC_\alpha C_\beta N$ chains, *e.g.* AG or GG (where A and G stays for *anti* and *gauche* arrangements, respectively), subscripts "a" and "b" specify the different orientations of the OH group of the ring, and the subscripts "1" and "2" designate the increasing order in energy. Furthermore, the presence of the methyl group attached to the amino group induces chirality at the nitrogen atom, thus giving rise to two distinct forms: synephrine (S) and pseudo-synephrine (PS). Hence, in the designation of the conformers of synephrine a prefix ("S" or "PS") is used to distinguish between the two possible configurations of the amino group. The predicted rotational constants, ^{14}N nuclear quadrupole coupling constants and the electric dipole components are collected in Tables X.1.

Table X.1 Calculated spectroscopic parameters and relative energies at MP2/6–311++G(d,p) level of theory of the lowest energy conformers of synephrine.

		B	C	χ_{aa}	χ_{bb}	χ_{cc}	μ_a	μ_b	μ_c	ΔE^b	ΔG^c
S-AG$_{a1}$	2596.0	418.5	387.9	2.61	-2.93	0.32	-1.6	0.8	2.0	50	21
S-AG$_{b1}$	2599.9	417.2	389.0	2.62	-2.60	-0.03	-1.7	3.3	-1.3	103	117
S-AG$_{a2}$	2361.9	395.6	389.1	2.87	0.54	-3.42	1.0	0.9	-1.1	472	393
S-AG$_{b2}$	2367.7	394.9	389.5	2.87	0.60	-3.47	-1.3	0.7	1.1	483	331
PS-AG$_{a1}$	2403.1	400.7	387.5	2.58	-4.82	2.24	-1.7	1.4	-1.3	94	0
PS-AG$_{b1}$	2408.6	398.4	389.4	2.59	-4.71	2.12	1.7	3.6	0.3	145	133
PS-AG$_{a2}$	2575.8	414.7	393.3	2.14	2.27	-4.41	-1.3	-0.5	1.1	772	755
PS-AG$_{b2}$	2587.6	414.1	393.4	2.14	2.28	-4.42	1.4	-2.1	-1.9	793	707
S-GG$_{a1}$	1729.0	498.0	471.2	1.77	-0.76	-1.00	-0.3	-2.2	0.5	0	173
S-GG$_{b1}$	1726.0	497.8	472.1	1.75	-0.40	-1.35	-0.2	-3.0	-2.3	76	202
PS-GG$_{a1}$	1719.2	563.8	529.3	2.06	-0.70	-1.36	0.7	2.3	0.4	206	420
PS-GG$_{b1}$	1715.6	564.3	530.3	2.05	-0.54	-1.51	0.1	2.9	2.3	289	383

[a] *A*, *B* and *C* are the rotational constants, in MHz; χ_{aa}, χ_{bb} and χ_{cc} are elements of the ^{14}N nuclear quadrupole coupling tensor, in MHz; μ_a, μ_b and μ_c are the electric dipole moment components, in Debye. [b] Relative energies respect to the global minimum calculated at MP2-6-311++G(d,p) level of theory, in cm^{-1}. [c] Gibbs energies calculated at 298 K at the MP2-6-311++G(d,p) level of theory in cm^{-1}.

X.3. RESULTS AND DISCUSSION

Taking into account the predicted values of the μ_a electric dipole moment components shown in Table X.1, scans were directed to look for μ_a-type R-branch transitions. Several sets of transitions corresponding to four different rotamers labeled as I, II, III and IV were identified in the spectrum. Preliminary fittings[22] and predictions allowed the measurement of μ_b and μ_c-type R-branch transitions for all the species with the exception of μ_c-type lines for rotamer IV. Additional scans allowed identification of two sequences of μ_b-type R-branch $J+1_{1,J+1}\leftarrow J_{0,J}$ transitions for two new rotamers, named as V and VI; μ_c-type lines were added for the rotamer VI while not for species V. As it was expected, all transitions found exhibit hyperfine structure, as shown in Figure X.2. All measured rotational transitions are collected in Tables X.S1-S6 of the Supplementary Information. A small number of weak signals remain unassigned in the wide frequency regions scanned. They probably belong to other species of synephrine predicted to lie at higher energies. Due to the weakness of these lines and their insufficient number it has not been possible to attribute them to new rotamers.

In the conformational assignment, it is possible to pair the conformers as I/II; III/IV and V/VI based on the rotational and quadrupole coupling constants provided in Table X.2. The rotational constants of the first pair, I/II, resemble those theoretically predicted for both the PS-AG$_{a1}$, PS-AG$_{b1}$, S-AG$_{a1}$ and S-AG$_{b1}$ conformers. However, one can quickly sort between the two families (PS and S) by comparing the observed quadrupole coupling constants of this pair of rotamers. While the experimentally determined values for the χ_{aa} constant match reasonably well both families, the χ_{bb} and χ_{cc} elements allows undoubtedly to conclude that rotamers I and II belong to the S-AG$_{a1/b1}$ pair and, moreover, ascribing them to S-AG$_{a1}$ and S-AG$_{b1}$ respectively. This fact is further confirmed by the optimum microwave power to polarize the μ_b-type lines, much lower in rotamer II than in I as it was predicted by the μ_b dipole moments (AG$_{a1}$: 0.8 D and AG$_{b1}$: 3.3 D). Secondly, based on their rotational constants, III and IV are in concordance to the other extended pairs PS-AG$_{a1}$/PS-AG$_{b1}$ and S-AG$_{a2}$/S-AG$_{b2}$. Once again, the determined values of the χ_{bb} and χ_{cc} constants allowed identification of this pair as belonging to the PS-AG$_{a1/b1}$ conformer family. Given the low MW power needed to polarize μ_b-type lines of rotamer IV, along with the absence of μ_c-type R-branch for this rotamer (but present in rotamer III), it is possible to assign rotamers III and IV to conformers PS-AG$_{a1}$ (μ_b=1.4 D and μ_c=1.3 D) and PS-AG$_{b1}$ (μ_b=3.6 D and μ_c=0.3 D), respectively. Using a similar approach in the analysis of the experimental data for rotamers V and VI, the rotational constants indicate that both belong to the S-GG family and distinction between them could be done based on the electric dipole

TABLE X.2 Experimental spectroscopic parameters of the six observed rotamers of synephrine.

	Rotamer I	Rotamer II	Rotamer III	Rotamer IV	Rotamer V	Rotamer VI
A^a	$2619.31951(91)^d$	$2621.43704(81)$	$2431.79192(93)$	$2429.8036(26)$	$1751.6139(17)$	$1749.29934(76)$
B	$417.815936(90)$	$416.712685(80)$	$401.522388(86)$	$399.97472(24)$	$491.43186(17)$	$491.01374(10)$
C	$386.003079(87)$	$387.043532(75)$	$383.211109(81)$	$385.16449(25)$	$464.06642(12)$	$465.271378(96)$
χ_{aa}	$2.524(18)$	$2.587(16)$	$2.537(19)$	$2.580(72)$	$1.573(47)$	$1.596(12)$
χ_{bb}	$-3.054(13)$	$-2.778(12)$	$-4.767(15)$	$-4.764(62)$	$-1.187(31)$	$-0.9142(93)$
χ_{cc}	$0.530(13)$	$0.250(12)$	$2.231(14)$	$2.184(62)$	$-0.387(31)$	$-0.6818(93)$
μ_a	Y^e	Y	Y	Y	N	N
μ_b	Y	Y	Y	Y	Y	Y
μ_c	Y	Y	Y	N	N	Y
N^b	31	32	18	20	14	20
σ^c	2.1	1.8	2.3	3.1	1.7	2.1

[a] A, B and C are the rotational constants, in MHz; χ_{aa}, χ_{bb} and χ_{cc} are elements of the ^{14}N nuclear quadrupole coupling tensor, in MHz. [b] Number of fitted transitions. [c] Root mean square of the fit, in kHz. [d] Standard errors are indicated in parentheses in units of the last digit. [e] "Yes" or "No" to observation of a-, b-, and c-type transitions for each structure.

moments. Thus, V and VI species were identified as S-GG$_{a1}$ and S-GG$_{b1}$, respectively.

Given the high resolution of the LA-MB-FTMW spectroscopic technique, independent analysis of the rotational spectra of individual conformers becomes possible, thus leading to the conclusive ascription of six different conformers of the synephrine, in contrast previously reported study on the same molecule using electronic spectroscopy.[23] In that work, the authors interpreted the hole burning spectra in terms of the

coexistence of six conformers in the molecular beam, classified into three groups based on spectral similarity. Each group is originated from the two different orientations of the phenolic OH group. They assigned conformational geometries by comparing the experimental and theoretical IR spectra, except the orientation of the phenolic OH group.

As it can be seen from Figure X.3, all detected forms of synephrine are stabilized by an O–H···N bond between the lone electron pair of the N atom and the hydroxyl group of the side chain. Conformers bearing an N–H···O hydrogen-bond follow in order of increasing energy those possessing the dominant O–H···N stabilizing interaction, and conformers of S-GG type, with a folded side chain, present an extra N-H···π hydrogen-bond type interaction between the amino group and the π-system of the aromatic ring. On the other hand, steric hindrance induced by the methylamino moiety precludes it from interacting favorably with the π-system of the aromatic ring, thus preventing further stabilization and leading to an increase in the conformer relative
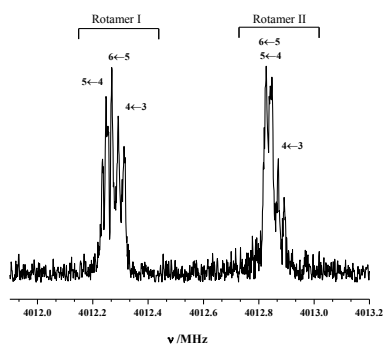
FIGURE X.2 *A 3 MHz section of the rotational spectrum of synephrine showing the 5_{05}-4_{04} rotational transition for rotamers I and II. The nuclear quadrupole hyperfine components are labelled with the quantum numbers $F' \leftarrow F''$. The coaxial arrangement of the adiabatic expansion and the resonator axis produces an instrumental Doppler doubling.*

Rotamer I/S-AG$_{a1}$ Rotamer II/S-AG$_{b1}$ Rotamer III/PS-AG$_{a1}$

Rotamer IV/PS-AG$_{b1}$ Rotamer V/S-GG$_{a1}$ Rotamer VI/S-GG$_{b1}$
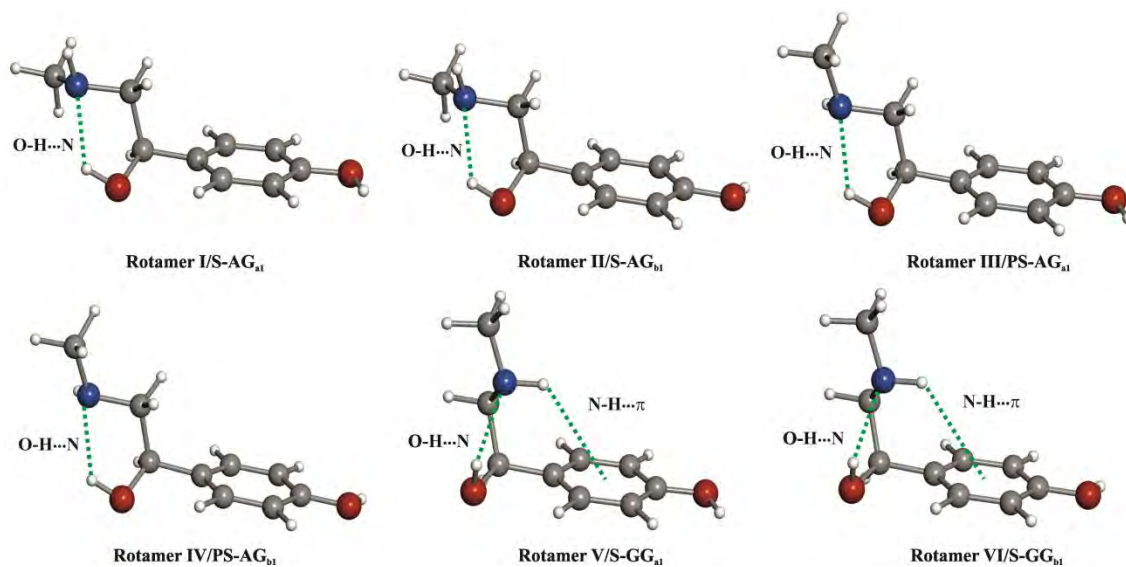
FIGURE X.3 *The six observed conformers of synephrine showing the intramolecular interactions that stabilize the structures.*

energies for instance in the case of the PS-GG family of conformers.

These results on synephrine can be contrasted with those reported for the analog molecule MAPE, for which AG$_{1a}$, AG$_{1b}$ and GG$_{1a}$ conformers where

found in the gas phase.[20] In this case, there is also a doubling of the number of conformers in synephrine respect to MAPE, resulting of the different orientations of the phenyl *para*-OH group.

X.4. CONCLUSIONS

In summary, the present study has probed the conformational landscape of the neurotransmitter synephrine by rotational spectroscopy. Interpretation of the experimental results was supported by an extensive series of theoretical calculations on the two molecules performed at the MP2/6-311++G(d,p) level of approximation. Six conformers of conformers of synephrine have been experimentally identified. The observed species of

both molecules correspond to the predicted most abundant conformers, all of them being characterized by having a strongly stabilizing O–H···N intramolecular hydrogen-bond.

This investigation can contribute to improvement in our understanding of the role of intramolecular forces in the conformational preferences of neurotransmitters.

X.5. REFERENCES

[1]   N. R. Goldberg, T. Beuming, O. S. Soyer, R. A. Goldstein, H. Weinstein, J. A. Javitch, *European journal of pharmacology* **2003**, *479*, 3-12.

[2]   Y. Zhao, D. Terry, L. Shi, H. Weinstein, S. C. Blanchard, J. A. Javitch, *Nature* **2010**, *465*, 188-193.

[3]   D. Majumdar, S. Guha, *Journal of Molecular Structure: THEOCHEM* **1988**, *180*, 125-140.

[4]   J. C. López, V. Cortijo, S. Blanco, J. L. Alonso, *Physical Chemistry Chemical Physics* **2007**, *9*, 4521-4527.

[5]   V. Cortijo, J. L. Alonso, J. C. López, *Chem. Phys. Lett.* **2008**, *466*, 214-218.

[6]   J. L. Alonso, M. E. Sanz, J. C. Lopez, V. Cortijo, *Journal of the American Chemical Society* **2009**, *131*, 4320-4326.

[7]   S. Antolínez, A. Lesarri, S. Mata, S. Blanco, J. C. López, J. L. Alonso, *Journal of Molecular Structure* **2002**, *612*, 125-131.

[8]   A. Lesarri, S. Mata, J. C. Lopez, J. L. Alonso, *Rev. Sci. Instrum.* **2003**, *74*, 4799-4804.

[9]   A. Lesarri, S. Mata, S. Blanco, J. C. Lopez, J. L. Alonso, *Journal of Chemical Physics* **2004**, *120*, 6191-6196.

[10]   J. L. Alonso, C. Perez, M. E. Sanz, J. C. Lopez, S. Blanco, *Physical Chemistry Chemical Physics* **2009**, *11*, 617-627.

[11]   V. Cortijo, M. E. Sanz, J. C. López, J. L. Alonso, *The Journal of Physical Chemistry A* **2009**, *113*, 14681-14683.

[12]   J. L. Alonso, V. Cortijo, S. Mata, C. Perez, C. Cabezas, J. C. Lopez, W. Caminati, *Journal of Molecular Spectroscopy* **2011**, *269*, 41-48.

[13]   S. Blanco, J. C. Lopez, S. Mata, J. L. Alonso, *Angewandte Chemie-International Edition* **2010**, *49*, 9187-9192.

[14]   C. Cabezas, M. Varela, I. Peña, J. C. Lopez, J. L. Alonso, *Physical Chemistry Chemical Physics* **2012**, *14*, 13618-13623.

[15]   C. Cabezas, I. Peña, J. C. López, J. L. Alonso, *The Journal of Physical Chemistry Letters* **2013**, *4*, 486-490.

[16]   T. Wheaton, I. Stewart, *Lloydia* **1970**, *33*, 244-254.

[17]   S. M. Vieira, K. H. Theodoro, M. B. A. Glória, *Food Chemistry* **2007**, *100*, 895-903.

[18]   L. G. Rossato, V. M. Costa, R. P. Limberger, M. de Lourdes Bastos, F. Remião, *Food and chemical toxicology* **2011**, *49*, 8-16.

[19]   S.-i. Ishiuchi, T. Asakawa, H. Mitsuda, M. Miyazaki, S. Chakraborty, M. Fujii, *The Journal of Physical Chemistry A* **2011**, *115*, 10363-10369.

[20]   S. Melandri, S. Ragno, A. Maris, *The Journal of Physical Chemistry A* **2009**, *113*, 7769-7773.

[21]   M. J. Frisch, G. W. Trucks, H. B. Schlegel, G. E. Scuseria, M. A. Robb, J. R. Cheeseman, G. Scalmani, V. Barone, B. Mennucci, G. A. Petersson, H. Nakatsuji, M. Caricato, X. Li, H. P. Hratchian, A. F. Izmaylov, J. Bloino, G. Zheng, J. L. Sonnenberg, M. Hada, M. Ehara, K. Toyota, R. Fukuda, J. Hasegawa, M. Ishida, T. Nakajima, Y. Honda, O. Kitao, H. Nakai, T. Vreven, J. A. Montgomery, J. E. Peralta, F. Ogliaro, M. Bearpark, J. J. Heyd, E. Brothers, K. N. Kudin, V. N. Staroverov, T. Keith, R. Kobayashi, J. Normand, K. Raghavachari, A. Rendell, J. C. Burant, S. S. Iyengar, J. Tomasi, M. Cossi, N. Rega, J. M. Millam, M. Klene, J. E. Knox, J. B. Cross, V. Bakken, C. Adamo, J. Jaramillo, R. Gomperts, R. E. Stratmann, O. Yazyev, A. J. Austin, R. Cammi, C. Pomelli, J. W. Ochterski, R. L. Martin, K.

Morokuma, V. G. Zakrzewski, G. A. Voth, P. Salvador, J. J. Dannenberg, S. Dapprich, A. D. Daniels, O. Farkas, J. B. Foresman, J. V. Ortiz, J. Cioslowski, D. J. Fox, Wallingford CT, **2010**.

[22]   H. M. Pickett, *Journal of Molecular Spectroscopy* **1991**, *148*, 371-377.

[23]   S.-i. Ishiuchi, T. Asakawa, H. Mitsuda, M. Miyazaki, S. Chakraborty, M. Fujii, *The journal of physical chemistry. A* **2011**, *115*, 10363-10369.

CHAPTER XI. COMPREHENSIVE ANALYSIS OF PREBIOTIC PROPENAL UP TO 660GHZ

Since interstellar detection of propenal is only based on two rotational transitions in the centimeter wave region, its high resolution rotational spectrum has been measured up to 660 GHz and fully characterized by assignment of more than 12 000 transitions to provide direct laboratory data to the astronomical community. Spectral assignments and analysis include transitions from the ground state of the *trans* and *cis* isomers, three *trans*-^{13}C isotopologues and ten excited vibrational states of the *trans* form. Combining new millimeter and submillimeter data with those from the far-infrared region has yielded the most precise set of spectroscopic constants of *trans*-propenal obtained to date. Newly determined rotational constants, centrifugal distortion constants, vibrational energies, Coriolis and Fermi interaction constants are given with high accuracy and were used to predict transition frequencies and intensities over a wide frequency range. Results of this work should facilitate astronomers further observation of propenal in the interstellar medium.
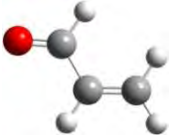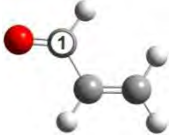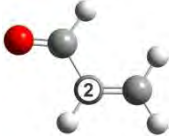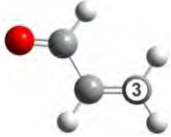
XI.1. INTRODUCTION

Ever since the discovery of the simplest aldehyde (formaldehyde) in the interstellar medium (ISM), aldehydes have also been called the "sugars of space" [1]. Detection of these "sugars of space" is associated mainly to molecular clouds, which may indicate that the reactions occurring in grains facilitate their formation.[2] So far, the observation of lines belonging to these aldehydes is restricted to molecules with chains containing no more than three carbon atoms, with propenal (acrolein), CH_2CHCHO, the simplest conjugated aldehyde, being one of the largest. Additionally, propenal is considered to be a prebiotic molecule owing both to its formation in the decomposition of sugars[3-4] and its implication in the synthesis of amino acids, such as methionine and glutamic acid, via Strecker-type reactions [5]. Its generation in the ISM has been postulated to be a product of a simple hydrogen addition reaction from a known interstellar aldehyde, propynal.[6-7] Nevertheless, while more than 40 transitions have been found belonging to other relevant aldehydes, such as glycolaldehyde, in different regions of the ISM,[8-10] positive detection of propenal has thus far been based on only two transitions of its lower energy trans isomer in the ground vibrational state, namely $2_{11} \leftarrow 1_{10}$ and the $3_{13} \leftarrow 2_{12}$ at 18221.164(2) and 26079.449(1)MHz, respectively, observed by the 100m Green Bank Telescope pointing toward the star-forming region of Sagittarius B2(N).[11-12] With the increasing

sensitivity of astrophysical detection facilities, it might now be possible to identify not only further lines of trans-propenal but also transitions from ^{13}C isotopologues, excited vibrational states or the higher energy cis isomeric form. The key to success in this astrophysical identification lies in analyzing propenal pure rotational transitions, especially those that fall into the millimeter- and submillimeter-wave regions, which are the working domains for the IRAM, NRAO, SEST, CSO telescopes or ALMA interferometers

Propenal can be observed in two trans and cis planar C_s conformers that interchange by rotation around the single C−C bond (see figures in Table XI.1), the cis being 600 cm^{-1} higher in energy than the trans one.[13] Ground state rotational spectra of both conformers, their isotopologues and the lowest-energy excited vibrational state have already been studied in the microwave region.[13-17] However, apart from the ground vibrational state of trans-propenal, which has been analyzed up to 170GHz,[18] no further information exists on the rotational spectrum of propenal. Since there is always an uncertainty involved in predicting transitions at higher frequencies, interstellar detection of new propenal lines should be based on transitions measured directly in the laboratory or transitions predicted from a data set that includes higher frequency lines. In the present work, the pure rotational spectrum of propenal up to 660GHz has

TABLE XI.1: Ground state spectroscopic constants of the trans-propenal parent and ^{13}C-species and *cis*-propenal

Constant	Unit	*Trans*-propenal	*Trans*-[13]C[1]	*Trans*-[13]C[2]	*Trans*-[13]C[3]	*Cis*-propenal
A	MHz	47353.7074 (17)	46781.0275 (67)	46518.9165 (64)	47255.1934 (73)	22831.6487 (43)
B	MHz	4659.499468 (61)	4644.74135 (19)	4642.43842 (17)	4520.79374 (15)	6241.04728 (35)
C	MHz	4242.689488 (56)	4225.83534 (20)	4221.74338 (19)	4126.64084 (18)	4902.20757 (21)
Δ_J	kHz	1.042067 (19)	1.03970 (10)	1.03172 (10)	0.988410 (65)	5.11335 (24)
Δ_{JK}	kHz	-8.78538 (44)	-8.6890 (24)	-8.7575 (13)	-8.9704 (14)	-29.1854 (13)
Δ_K	kHz	360.363 (64)	348.56 (23)	367.21 (22)	363.31 (26)	108.07 (12)
δ_J	kHz	0.1202675 (76)	0.120817 (20)	0.121459 (18)	0.111595 (18)	1.48116 (12)
Δ_K	kHz	5.7481 (24)	5.643 (10)	5.745 (10)	5.441 (10)	11.3386 (76)
Φ_J[b]	mHz	0.2994 (25)	0.209 (20)	0.274 (21)	0.287 (11)	1.601 (89)
Φ_{JK}	mHz	-6.576 (46)	[-6.576][c]	[-6.576][c]	[-6.576][c]	92.04 (49)
Φ_{KJ}	mHz	-510.0 (12)	-382 (19)	-536.1 (64)	-459.1 (70)	-1153.0 (21)
φ_J	mHz	0.0740 (11)	[0.0740][c]	[0.0740][c]	[0.0740][c]	1.082 (43)
φ_{JK}	mHz	5.00 (62)	[5.00][c]	[5.00][c]	[5.00][c]	-19.3 (20)
J range		5-73	1-55	1-55	1-67	1-61
K_a range		0-19	0-12	0-16	0-16	0-23
N_{lines}/N_{ex}[d]		1606/28	492/103	531/85	485/93	574/78
σ_{fit}[e]	kHz	37	40	40	41	39

aThe numbers in parentheses are 1σ uncertainties in the units of the last decimal digit. bPurely K-dependent sextic centrifugal distortion constants ΦK and φK could not be determined from the present data sets. cFixed to the parent species value. dNumber of distinct frequency fitted lines/number of excluded lines based on the 2u fitting criterion of the SPFIT program[21] where u is the uncertainty of the measured frequency. The uncertainties between 50 and 500kHz were given to the millimeter and submillimeter data from this work and 100kHz to the microwave data from[13, 17]. eStandard deviation of the fit.

been analyzed for the ground vibrational state of *cis*- and *trans*-propenal, the three ^{13}C isotopologues of the latter and ten lowest energy excited vibrational states below 700cm^{-1}. Given the strong Coriolis and Fermi perturbations observed, a global fit analysis combining our pure rotational and previously published vibrational rotational data[19-20] was required. A highly accurate set of spectroscopic parameters that reproduce the spectrum and can facilitate detections of propenal in the ISM was thus obtained.

XI.2. EXPERIMENTAL DETAILS

A commercially available sample of liquid propenal (b.p.= 125ºC) was used without further purification. Propenal spectrum was acquired using two different spectrometers. A recently upgraded Stark-modulation spectrometer employing 33kHz modulation frequency and phase-sensitive detection[22] was used to cover the 26−110GHz range. Millimeter and submillimeter-wave measurements, over the 50 to 660~GHz range, were performed using a direct absorption spectrometer recently constructed at the University of Valladolid.[23] It is based on the frequency multiplier chains (VDI, Inc.) driven by an Agilent E8257D microwave synthesizer. The signal was

detected using solid-state zero-bias detectors (VDI, Inc.) at twice the modulation frequency ($2f = 20.4$kHz) and with a modulation depth between 20 and 50kHz resulting in the second derivative line shape. All spectra were taken at room temperature with sample pressure less than 30mTorr and recorded in 1GHz sections in both directions.

Rotational spectra of all three ^{13}C isotopologues were measured in their natural abundances. Transition lines were measured using a Gaussian profile function (AABS package[24] with accuracy better than 50kHz for isolated well-developed lines (the accuracy up to 500kHz was given to lines with poor signal-to-noise ratio).

XI.3. ROTATIONAL SPECTRA AND ANALYSIS

XI.3.1 Ground vibrational state.

The ground state rotational spectrum of *trans*-propenal is dominated by strong a-type R-branch transitions and weaker b-type R-branch and Q-branch transitions, in agreement with the values of the dipole moment components $\mu_a = 3.052(4)$D and $\mu_b = 0.630(1)$D.[13] Starting with the predictions based on the previous results and following an iterative process of assignment and fitting, over 1900 lines were assigned up to J = 76 and K_a = 24. The following Watson's A-reduced semi-rigid Hamiltonian up to the sixth order[25] was used in the analysis

$$H_{Rot}^{(v)} = AJ_a^2 + BJ_b^2 + CJ_c^2 - \Delta_J J^4 - \Delta_{JK}J^2J_a^2$$

$$-\Delta_K J_a^4 + \frac{1}{2}\left[\delta_J J^2 + \delta_K J_a^2, J_+^2 + J_-^2\right]_+$$

$$+\phi_J J^6 + \phi_{JK}J^4J_a^2 + \phi_{KJ}J^2J_a^4 + \phi_{JK}J_a^6$$

$$+\frac{1}{2}\left[\varphi_J J^4 + \varphi_{JK}J^2J_a^2 + \varphi_K J_a^4, J_+^2 + J_-^2\right]_+ \qquad (1)$$

where A, B, C are the rotational constants, Δ_J, Δ_{JK}, Δ_K, δ_J, δ_K are quartic Φ_J, Φ_{JK}, Φ_{KJ}, Φ_K, φ_J, φ_{JK}, φ_J are sextic centrifugal distortion constants. Some series

of high K_a-rotational transitions were found to be perturbed and could not be fitted within the distortable rotor model, hence, they were not included in the current stage of the fit. These perturbations were later treated in the global analysis presented in the following section. The spectroscopic parameters derived are listed in the first column of Table XI.1.

Around 500 distinct frequency ground state lines for each ^{13}C-species were analyzed in terms of the same Hamiltonian given by Equation 1 with Φ_{JK}, φ_J, and φ_{JK} constants fixed to the values of the parent species. Since our measurements were performed in natural abundance (intensities about 1% of the parent species), only the intense a-type transitions were observed. These transitions were combined with the a- and b-type ones measured by[17] using isotopically highly enriched samples. The final sets of the spectroscopic constants are also given in Table XI.1.

For cis-propenal ($\mu_a = 2.010(5)$D and $\mu_a = 1.573(3)$D)[13], more than 500 lines were assigned

TABLE XI.2: Laboratory assigned and fitted transitions frequencies for the *trans*-propenal parent, its ^{13}C isotopologues and *cis*-propenal ground states and ten excited vibrational states of *trans*-propenal.

Species	J'	K_a'	K_c'	v'	J''	K_a''	K_c''	v''	ν_{obs} [b] (MHz/cm^{-1})	$\nu_{obs} - \nu_{calc}$ [c] (MHz/cm^{-1})	Comment[d]	Ref
Trans-$^{13}C_1$	16	1	16	0	15	1	15	0	138100.896	0.040		(2)
Trans-$^{13}C_1$	16	0	16	0	15	0	15	0	139964.297	0.020		(2)
Trans-$^{13}C_2$	20	7	13	0	19	7	12	0	177365.923	-0.031		(2)
Trans-$^{13}C_1$	20	6	14	0	19	6	13	0	177394.047	0.053	B	(2)
Trans-$^{13}C_2$	20	6	15	0	19	6	14	0	177394.047	0.056	B	(2)
Trans-$^{13}C_3$	16	0	16	0	15	0	15	0	136624.069	0.005		(2)
Trans-$^{13}C_3$	20	1	19	0	19	1	18	0	175805.698	0.121	U	(2)
Cis	17	1	16	0	16	1	15	0	182121.954	-0.030		(2)
Cis	16	2	14	0	15	2	13	0	184240.673	-0.006		(2)
Trans	23	2	22	0	22	2	21	0	203709.166	-0.031		(2)
Trans	23	2	22	3	22	2	21	3	203716.290	0.012		(2)
Trans	23	2	22	10	22	2	21	10	203840.124	-0.005		(2)

This table is published in its entirety in the electronic edition of the *Astrophysical Journal Supplement Series*. A portion is shown here for guidance regarding its form and content. [a]Upper and lower state quantum numbers are indicated by ' and '', respectively. The assignment of the individual vibrational states to v is as following: $0 \rightarrow$ ground state, $1 \rightarrow v_{18} = 1$, $2 \rightarrow v_{18} = 2$, $3 \rightarrow v_{13} = 1$, $4 \rightarrow v_{18} = 3$, $5 \rightarrow (v_{18} = 1, v_{13} = 1)$, $6 \rightarrow v_{12} = 1$, $7 \rightarrow v_{17} = 1$, $8 \rightarrow v_{18} = 4$, $9 \rightarrow (v_{18} = 2, v_{13} = 1)$, and $10 \rightarrow v_{13} = 2$. [b]Observed frequency. Microwave, millimeter and submillimeter data are in MHz while the far-infrared data are in cm^{-1}. [c]Observed minus calculated frequency. [d]Blended transitions were fitted to their intensity weighted averages and are labeled by B. Unfitted transitions are labeled by U.
References: (1)Blom *et al.*[17]; (2) This work; (3)Blom *et al.*[13]; (4)Winnewisser *et al.*[18]; (5) McKellar *et al.*[20].

to a- and b-type R-branch transitions up to J = 60 and K_a = 23 and were analyzed using the above-mentioned Hamiltonian. The derived spectroscopic constants are listed in the last column of Table XI.1. Line assignments, observed frequencies ν_{obs}, ν_{obs} - ν_{cal} values, where ν_{cal}, is the calculated frequency based on the Hamiltonian model used, and references of the data sources included in the final fits for the *trans*-^{13}C-species and *cis*-propenal ground states are presented in Table XI.2.

XI.3.2 Excited vibrational states.

Trans-propenal has four low-lying vibrational modes involving skeletal C–C torsion (v_{18}), C=C–C bending (v_{13}), O=C–C bending (v_{12}), and =CH$_2$ twisting mode (v_{17}). Up to 10 vibrational states below 700 cm^{-1} (see Figure XI.1) can be sufficiently populated at the room temperature of the experiment to generate a highly rich vibrational satellite spectrum. Stark-modulation microwave spectroscopy is a very useful tool for analyzing these

rotational satellite lines as has recently been shown in works on ethyl[23] and vinyl cyanide[26]. A section of the Stark spectrum around the ground state $4_{14} \leftarrow 3_{13}$ rotational transition of *trans*-propenal is presented in Figure XI.2. At the higher frequency side of the ground state line, a harmonic progression formed by four satellite lines with the same Stark pattern as the ground state line can easily be identified and assigned to pure rotational transition in successive excited vibrational states of the v_{18} torsional mode. Moreover, pure rotational spectra in other excited states corresponding to $v_{13} = 1$, $v_{12} = 1$, $v_{17} = 1$ as well as combination states ($v_{18} = 1, v_{13} = 1$) and ($v_{18} = 2, v_{13} = 1$,) were also observed. Preliminary spectroscopic constants obtained for these 10 excited states were used to predict the corresponding rotational spectra in the millimeter- and submillimeter-wave region. Loomis-Wood type plots, originally described by Loomis and Wood,[27] from the AABS package[24, 28]

were used to facilitate identification of rotational transitions for each vibrational state

During the analysis of propenal in the millimeter and submillimeter region, the major complication is due to the mutual interactions between excited vibrational states belonging to low-lying vibrational modes leading to strong perturbations in the spectrum. The possible interactions between two states depends on the symmetry classification of the states involved which is marked in Figure XI.1 according to the C_s symmetry point group. Vibrational states belonging to different symmetry species may be connected by a- and b-type Coriolis interaction terms, and excited states with the same symmetry species may be coupled through c-type Coriolis and Fermi interactions. Figure XI.1 shows how the lowest-energy $v_{18} = 1$ excited state should be free of interactions due to its energy spacing with respect to other excited states. Over 1000 pure rotational transitions could be included in the fit using Equation 1. Nonetheless, several K_a series
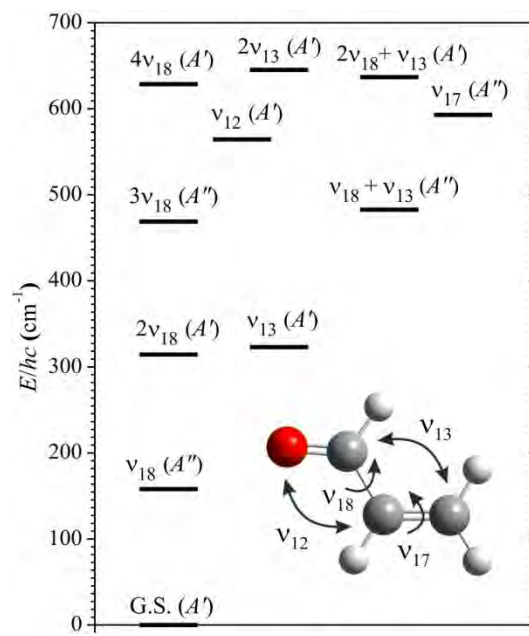
FIGURE XI.1: *Vibrational energy levels of trans-propenal below 700cm^{-1} obtained by McKellar[20] and schematic illustration of the four lowest-energy normal vibrational modes, v_{18}: C−C torsion, v_{13}: C=C−C bending mode, v_{12}: O=C−C bending mode, v_{17}: =CH$_2$ twisting mode. The symmetry specifications are given in accordance with C$_s$ point group.*

revealed deviations that could not be taken into account by adding higher-order centrifugal distortion effects. Some of these anomalies were observed exactly within the same range of the J quantum numbers as those already observed for
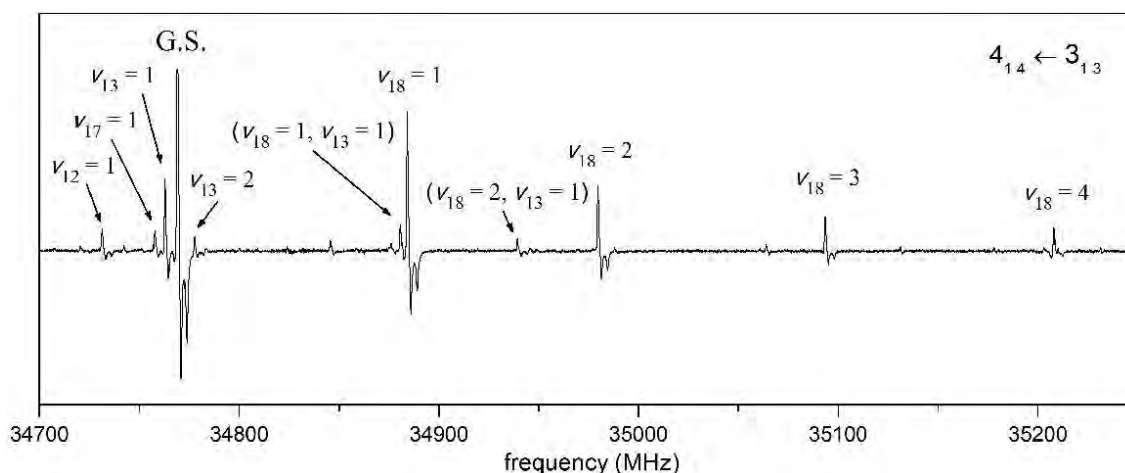
FIGURE XI.2. *Stark modulated spectrum of the $J'_{K'_a,K'_c} \leftarrow J''_{K''_a,K''_c} = 4_{14} \leftarrow 3_{13}$ transition (200 V) showing the assignments of the vibrational states below 700 cm^{-1}.*

ground state transitions. This clearly indicates that the ground state is in mutual interaction with the v_{18} = 1 excited state and, as a result, they were analyzed together. Even though both a- and b-type Coriolis couplings are allowed in this case, only b-type Coriolis terms were found to be significant in the fitting. Including the Coriolis terms in the analysis improved the fit considerably, although, several K_a series of transitions in v_{18} = 1 could still not be reproduced. A deeper insight into the v_{18} = 1 rotational energy levels showed further interactions with higher-energy v_{18} = 2 state. This significantly complicates the analysis since the v_{18} = 2 state cannot be analyzed without the neighboring almost iso-energetic v_{13} = 1 state due to strong c-type Coriolis and Fermi interactions between them. A close look at the microwave spectrum in Figure XI.2 shows a small shift of the v_{18} = 2 transition from the equidistant pattern which reflects the strong coupling between this state and v_{13} = 1. A 4-state Hamiltonian analysis was thus performed to correctly reproduce all the perturbed transitions in the ground state, v_{18} = 1, v_{18} = 2 and v_{13} = 1 excited vibrational states. Two excited vibrational states, v_{18} = 3 and $(v_{18}$ = 1, v_{13} = 1), were then also analyzed as an interacting pair connected through c-type Coriolis and Fermi interactions. Possible interactions of this pair with other states were ignored. Analysis of the five remaining excited vibrational states above 500cm^{-1} led to the identification of many local perturbations. Although the v_{12} = 1 and v_{17} = 1 pair was initially treated separately, a 5-state Hamiltonian including v_{12} = 1,

v_{17} = 1, v_{18} = 4, $(v_{18}$ = 2, v_{13} = 1), and v_{13} = 2 excited vibrational states was inevitable.

XI.3.3 Global analysis.

Over 10 000 distinct frequency lines treated in the above-mentioned 4-state, 2-state and 5-state analyses were finally combined with more than 8000 lines available from high resolution vibration-rotation study of McKellar et al.[20] The uncertainties between 50 and 500 kHz were given to the millimeter and submillimeter data and between 0.0003 and 0.001 cm^{-1} to the far-infrared data for weighing purposes of the non-linear least-square fit. The Hamiltonian matrix constructed for this problem can be written in standard block form with 11×11 array size. Each diagonal block consists of $H_{Rot}^{(v)} + \Delta E_v$ term where $H_{Rot}^{(v)}$ is the Watson's A-reduced rotational Hamiltonian for given vibrational state v defined by Equation 1 and $\Delta E_v = E_v - E_0$ is the vibrational energy difference from the ground state. The vibrational identifiers v are assigned to individual vibrational states as follows: 0 → ground state, 1 → v_{18} = 1, 2 → v_{18} = 2, 3 → v_{13} = 1, 4 → v_{18} = 3, 5 →$(v_{18}$ = 1, v_{13} =1), 6 → v_{12} = 1, 7 → v_{17} = 1, 8 → v_{18} = 4, 9 →$(v_{18}$ = 2, v_{13} =1), and 10 → v_{13} = 2. The off-diagonal blocks are composed by the Coriolis and Fermi interaction Hamiltonians $^{\alpha}H_{Cor}^{(v,v')}$ and $H_F^{(v,v')}$, respectively, and were used when clear evidence of the mutual interactions between two states v and v' was found. The leading terms of the α-type Coriolis Hamiltonian up to the second power in angular momentum are described in equation 2.[29]

TABLE XI.3: Spectroscopic constants of *trans*-propenal for each vibrational state v included in the global 11-state fit (A reduction, I^r representation).

OC[b]	Constant[c]	Unit	v[a] 0	1	2	3	4	5
100vv'	A	MHz	47353.6999 (17)[d]	45782.9630 (50)	44374.617 (61)	48755.457 (49)	43101.272 (93)	46956.217 (86)
200vv'	B	MHz	4659.499451 (93)	4666.24463 (33)	4672.9124 (10)	4659.3132 (10)	4679.4475 (17)	4665.4082 (17)
300vv'	C	MHz	4242.689513 (86)	4259.62456 (32)	4276.62153 (90)	4238.35294 (96)	4293.6518 (14)	4255.7034 (11)
2vv'	$-\Delta_J$	kHz	-1.042093 (30)	-1.087069 (83)	-1.13228 (17)	-1.02736 (16)	-1.18057 (18)	-1.06618 (13)
11vv'	$-\Delta_{JK}$	kHz	8.79047 (56)	8.5734 (12)	8.2463 (68)	10.2970 (59)	8.3705 (97)	9.667 (10)
20vv'	$-\Delta_K$	kHz	-360.260 (44)	64.74 (10)	327.99 (35)	-803.12 (23)	507.10 (41)	-149.07 (36)
401vv'	$-\delta_J$	kHz	-0.120239 (11)	-0.119011 (66)	-0.11652 (15)	-0.11803 (15)	-0.11483 (15)	-0.116933 (68)
410vv'	$-\delta_K$	kHz	-5.7747 (39)	0.769 (28)	6.258 (67)	-11.756 (68)	10.237 (63)	-2.335 (38)
3vv'	Φ_J	mHz	0.3090 (39)	0.513 (13)	0.688 (35)	0.185 (33)	1.068 (33)	[0.3090][e]
12vv'	Φ_{JK}	mHz	12.2 (17)	-101.1 (22)	-232 (11)	95 (11)	-74.7 (91)	-58.7 (84)
21vv'	Φ_{KJ}	Hz	-0.5951 (64)	0.9430 (99)	2.460 (50)	-1.905 (41)	1.805 (41)	1.065 (42)
30vv'	Φ_K	Hz	1.42 (25)	-217.87 (48)	-277.53 (71)	161.49 (49)	-299.60 (66)	-232.43 (82)
402vv'	φ_J	mHz	0.0760 (17)	0.0858 (83)	-0.069 (21)	0.151 (23)	0.182 (19)	[0.0760][e]
411vv'	φ_{JK}	mHz	7.99 (96)	60.7 (49)	93 (12)	-78 (11)	142 (11)	[7.99][e]
420vv'	φ_K	Hz	2.63 (25)	-13.72 (33)	-31.5 (15)	16.7 (17)	-10.0 (12)	-6.8 (11)
vv'	ΔE	cm^{-1}	0	157.883986 (22)	314.19009 (26)	323.05132 (25)	468.94645 (68)	482.82732 (68)
	J range[f]		0–77	2–74	2–70	3–73	2–71	3–70
	K$_a$ range[f]		0–24	0–22	0–20	0–21	0–17	0–15
	N$_{lines}$/N$_{ex}$[g]		1983/1	1728/23	936/0	947/1	977/10	811/12

OC[b]	Constant[c]	Unit	6	7	8	9	10
100vv'	A	MHz	47416.470 (69)	47190.191 (58)	41959.25 (94)	45351.42 (89)	50229.95 (13)
200vv'	B	MHz	4656.00325 (58)	4653.5032 (10)	4686.1597 (97)	4671.2440 (83)	4659.2597 (25)
300vv'	C	MHz	4237.96030 (46)	4242.15421 (76)	4310.8450 (53)	4273.1641 (46)	4234.0391 (24)
2vv'	$-\Delta_J$	kHz	-1.04737 (16)	-1.04841 (19)	-1.22103 (33)	-1.09837 (54)	-1.02430 (53)
11vv'	$-\Delta_{JK}$	kHz	9.074 (12)	9.410 (13)	7.935 (28)	9.036 (23)	12.082 (18)
20vv'	$-\Delta_K$	kHz	-357.36 (47)	-368.38 (15)	584.0 (46)	279.9 (41)	-1365.53 (91)
401vv'	$-\delta_J$	kHz	-0.119715 (39)	-0.11940 (16)	-0.10875 (21)	-0.11748 (59)	-0.11000 (53)
410vv'	$-\delta_K$	kHz	-6.242 (53)	-5.413 (59)	-13.143 (90)	-10.39 (20)	20.47 (19)
3vv'	Φ_J	mHz	0.332 (26)	0.412 (32)	1.488 (36)	-0.75 (13)	-1.10 (13)
12vv'	Φ_{JK}	mHz	82.1 (53)	8.3 (18)	-192 (28)	-955 (20)	1022 (35)
21vv'	Φ_{KJ}	Hz	[-0.5951][e]	-0.339 (16)	3.90 (15)	5.49 (14)	-6.34 (10)
30vv'	Φ_K	Hz	5.5 (15)	-25.65 (36)	-223.4 (95)	-409.5 (77)	426.5 (18)
402vv'	φ_J	mHz	[0.0760][e]	0.087 (20)	-0.531 (37)	-1.09 (11)	0.79 (10)
411vv'	φ_{JK}	mHz	18.5 (93)	50 (11)	[7.99][e]	-206 (56)	-617 (52)
420vv'	φ_K	Hz	13.14 (75)	[2.63][e]	-23.2 (37)	-130.8 (32)	145.9 (49)
vv'	ΔE	cm^{-1}	564.340326 (23)	593.079293 (15)	621.8530 (40)	641.0928 (41)	647.83644 (57)
	J range[f]		3–70	3–69	2–70	3–67	3–66
	K$_a$ range[f]		0–15	0–17	0–15	0–15	0–17
	N$_{lines}$/N$_{ex}$[g]		798/7	649/20	602/42	505/34	463/7

[a]The assignment of the vibrational states to v is as following: 0 → ground state, 1 → $v_{18} = 1$, 2 → $v_{18} = 2$, 3 → $v_{13} = 1$, 4 → $v_{18} = 3$, 5 →($v_{18} = 1$, $v_{13} = 1$), 6 → $v_{12} = 1$, 7 → $v_{17} = 1$, 8 → $v_{18} = 4$, 9 →($v_{18} = 2$, $v_{13} = 1$), and 10 → $v_{13} = 2$. [b]SPFIT/SPCAT operator code. These operators are each within a defined state v where $v = v' = 0,1,...10$. [c]Common constant symbol. [d]The numbers in parentheses are 1σ uncertainties in the units of the last decimal digit. [e]Fixed to the ground state value. [f]Quantum number range corresponding to the millimeter and submillimeter data. [g]Number of distinct frequency fitted lines/number of excluded lines corresponding to the pure rotational data based on the 9u fitting criterion of the SPFIT program where u is the uncertainty of the measured frequency.

$$^{\alpha}H_{Cor}^{(v,v')} = iG_{\alpha}J_{\alpha} + F_{\beta\gamma}(J_{\beta}J_{\gamma} + J_{\gamma}J_{\beta}) \qquad (2)$$

where G_{α} and $F_{\beta\gamma}$ are the Coriolis coupling constants and α, β, γ are the permutations of a, b, c. The Fermi interaction Hamiltonian up to the second power in angular momentum is given as[29]

$$H_F^{(v,v')} = W + W_J J^2 + W_K J_{\alpha}^2 + W_{\pm} (J_b^2 - J_c^2) \quad (3)$$

where W, W_J, W_K and $W_{\pm}$ are the Fermi coupling constants. Despite the huge convergence problems, a stable fit was eventually achieved by finally selecting 211 adjusted and 7 fixed parameters leading to root-mean-square deviation of 168kHz. Analysis of many interstate perturbations allowed to derive precise values of vibrational energies for all the excited vibrational states and together with the rotational and centrifugal distortion constants are assembled in Table 3. Determinable Coriolis and Fermi coupling constants are listed in Table 4. Choice of the Coriolis and Fermi coupling constants related to higher powers of angular momentum operators, than those presented in Equations 2 and 3, has been established empirically during the fitting procedure. Those producing a significant improvement of the fit were retained. Some of these constants, however, do not have generally known symbol. SPFIT/SPCAT operator codes (OC) are thus provided in Tables 3 and 4 to be able to derive the corresponding operator form. In the basis of J^2, J_{α}^2 and $J_{\pm}$, where $J_{\pm} = J_b \pm iJ_c$, definition of such operators can be found in Butler

TABLE XI.4: Coriolis and Fermi coupling constants for interacting states $(v \leftrightarrow v')$ of *trans*-propenal obtained from the global 11-state fit (I^r representation)

OC[b]	Constant[c]	Unit	$(v \leftrightarrow v')$[a]					
			$(0\leftrightarrow1)$	$(1\leftrightarrow2)$	$(6\leftrightarrow7)$	$(7\leftrightarrow8)$	$(7\leftrightarrow9)$	$(7\leftrightarrow10)$
2000vv'	G_a	MHz	...	...	11272.5 (21)[d]	131.3 (20)	-413 (15)	...
2001vv'	G_a^J	MHz	...	...	-0.02270 (44)	...	...	...
2100vv'	F_{bc}	MHz	...	...	...	...	...	1.0621 (30)
4000vv'	G_b	MHz	...	...	1132.26 (13)	43.37 (70)	-69.9 (69)	...
4001vv'	G_b^J	kHz	...	...	0.0239 (88)	...	...	...
4010vv'	G_b^K	MHz	...	...	-0.1287 (14)	...	...	...
4100vv'	F_{bc}	MHz	...	...	...	...	5.48 (26)	...
4200vv'		kHz	5.606 (49)	...	...	...	...	...
4210vv'		kHz	...	0.02467 (19)	...	...	...	...
OC[b]	Constant[c]	Unit	$(2\leftrightarrow3)$	$(4\leftrightarrow5)$	$(6\leftrightarrow8)$	$(8\leftrightarrow9)$	$(8\leftrightarrow10)$	$(9\leftrightarrow10)$
6000vv'	G_c	MHz	-345.488 (34)	550.203 (35)	77.54 (10)	650.24 (30)	-98.8 (13)	534.61 (40)
6001vv'	G_c^J	kHz	0.388 (13)	...	..	..	..	..
6100vv'	F_{ab}	MHz	-1.6356 (22)	2.2549 (25)	..	..	..	3.432 (22)
6200vv'		kHz	-0.571 (10)	0.9216 (34)	..	..	3.997 (73)	0.210 (23)
vv'	W	MHz	81372 (13)	-134480 (32)	..	168296 (202)	..	116018 (15)
1vv'	W_J	MHz	-0.2174 (16)	0.5528 (30)	..	..	..	-0.2685 (27)
10vv'	W_K	MHz	-52.12 (15)	56.78 (18)	..	-111.5 (28)	..	-73.86 (29)
11vv'	W_{JK}	kHz	-1.015 (29)	0.993 (28)	..	..	..	..
400vv'	$W_{\pm}$	MHz	..	...	..	-0.0790 (57)	..	..
410vv'	$W_{\pm}^K$	kHz	..	0.308 (28)	..	..	..	..
1200vv'		kHz	..	..	..	..	0.797 (47)	..

[a]The assignment of the vibrational states to v is as following: 0 → ground state, 1 → $v_{18} = 1$, 2 → $v_{18} = 2$, 3 → $v_{13} = 1$, 4 → $v_{18} = 3$, 5 →($v_{18} = 1$, $v_{13} = 1$), 6 → $v_{12} = 1$, 7 → $v_{17} = 1$, 8 → $v_{18} = 4$, 9 →($v_{18} = 2$, $v_{13} =1$), and 10 → $v_{13} = 2$. [b]SPFIT/SPCAT operator code. These operators each connect defined vibrational states v and $\square^{v'}$ where $v, \square^{v'} = 0, 1,...10$. [c]Common constant symbol. [d]The numbers in parentheses are 1σ uncertainties in the units of the last decimal digit.

TABLE XI.5: Predicted transition frequencies of the *trans-* and *cis*-propenal ground states and ten excited vibrational states of *trans*-preopenal

Species	Transition[a]								ν_{cal}[b]	$u(\nu_{calc})$[c]	$S(\mu^2)$[d]	(E')[d]	(E'')[d]
	J'	K_a'	K_c'	v'	J''	K_a''	K_c''	v''	(MHz/cm^{-1})	(MHz/cm^{-1})	(D^2)	(cm^{-1})	(cm^{-1})
Trans	10	2	8	3	9	2	7	3	89423.789	0.005	733.300	346.055	343.072
Trans	10	5	6	2	9	5	5	2	89431.879	0.010	574.612	363.332	360.349
Trans	10	2	8	0	9	2	7	0	89436.162	0.001	733.476	22.098	19.115
Cis	8	6	2	0	7	6	1	0	89445.730	0.002	101.415	34.124	31.140
Cis	21	4	17	0	21	3	18	0	89523.928	0.025	182.948	97.469	94.483
Cis	8	5	4	0	7	5	3	0	89527.729	0.003	141.241	27.803	24.817

This table is published in its entirety in the electronic edition of the *Astrophysical Journal Supplement Series*. A portion is shown here for guidance regarding its form and content. Only transitions with predicted uncertainties $u(\nu_{calc}) \leq 1MHz$ are included. [a]Upper and lower state quantum numbers are indicated by ' and ", respectively. The assignment of the individual vibrational states to v is as following: $0 \to$ ground state, $1 \to v_{18} = 1$, $2 \to v_{18} = 2$, $3 \to v_{13} = 1$, $4 \to v_{18} = 3$, $5 \to (v_{18} = 1, v_{13} = 1)$, $6 \to v_{12} = 1$, $7 \to v_{17} = 1$, $8 \to v_{18} = 4$, $9 \to (v_{18} = 2, v_{13} = 1)$, and $10 \to v_{13} = 2$. [b]Predicted frequency. [c]1σ uncertainty of the predicted frequency. [d]Line strength S multiplied by the square of the dipole moment component. Experimentally available values of the dipole moment of $\mu_a = 3.052D$ and $\mu_b = 0.630D$ for *trans*-propenal and $\mu_a = 2.010D$ and $\mu_b = 1.573D$ [13] *cis*-propenal were used in the calculation. Dipole moment components for *trans*-propenal excited vibrational states were approximated by corresponding ground state values. [e]Upper level energy. [f]Lower level energy.

et al.[30] or Pearson *et al.*[31]. Spectroscopic constants reported in Tables XI.3 and XI.4 can be considered as effective parameters that reproduce precisely the rotational spectrum *trans*-propenal in the ground and ten excited vibrational states.

Since the intensities are prerequisite for a correct molecular identification in the interstellar medium, the spectroscopic constants from Tables XI.1, XI.3 and XI.4 were used to predict the transition frequencies and line strengths of both isomers studied in this work in the frequency region through 760 GHz. The predicted transition frequencies are gathered in Table XI.5 along with the rotational quantum numbers, estimated uncertainties, intensities in terms of line strengths multiplied by the square of the corresponding dipole moment component and energies of the lower and upper energy levels.

To sum up, present laboratory measurements and complete analysis of the propenal millimeter and submillimeter spectra have allowed to determine new sets of the spectroscopic constants and, using the available values of the dipole moment components, it was possible to predict the transition frequencies and intensities of many additional lines through 760 GHz. Rotational transitions of propenal can now be searched for over a wide frequency range toward appropriate interstellar sources.

XI.4. REFERENCES

[1]   L. E. Snyder, D. Buhl, B. Zuckerman, P. Palmer, *Physical Review Letters* **1969**, *22*, 679-681.

[2]   M. Ikeda, M. Ohishi, A. Nummelin, J. E. Dickens, P. Bergman, Å. Hjalmarson, W. M. Irvine, *The Astrophysical Journal* **2001**, *560*, 792.

[3]   S. Moldoveanu, *Pyrolysis of Organic Molecules: Applications to Health and Environmental Issues, Vol. 28th*, Elsevier, **2010**.

[4]   C. Bermúdez, I. Peña, C. Cabezas, A. M. Daly, J. L. Alonso, *Chemphyschem* **2013**, *14*, 893-895.

[5]   J. E. Van Trump, S. L. Miller, *Science* **1972**, *178*, 859-860.

[6]   B. E. Turner, *Astrophysical Journal Supplement Series* **1991**, *76*, 617.

[7]   W. M. Irvine, R. D. Brown, D. M. Cragg, P. Friberg, P. D. Godfrey, N. Kaifu, H. E. Matthews, M. Oshishi, H. Suzuki, H. Takeo, *Astrophysical Journal* **1988**, *335*, L89.

[8]   J. M. Hollis, F. J. Lovas, P. R. Jewell, *Astrophysical Journal* **2000**, *540*, L107-L110.

[9]   D. T. Halfen, A. J. Apponi, N. Woolf, R. Polt, L. M. Ziurys, *The Astrophysical Journal* **2006**, *639*, 237.

[10]   M. T. Beltrán, C. Codella, S. Viti, R. Neri, R. Cesaroni, *The Astrophysical Journal Letters* **2009**, *690*, L93.

[11]   J. M. Hollis, P. R. Jewell, F. J. Lovas, A. Remijan, H. Mollendal, *Astrophysical Journal* **2004**, *610*, L21-L24.

[12]   M. A. Requena-Torres, J. Martín-Pintado, S. Martín, M. R. Morris, *The Astrophysical Journal* **2008**, *672*, 352.

[13]   C. E. Blom, A. Bauder, *Chem. Phys. Lett.* **1982**, *88*, 55-58.

[14]   J. Fine, J. H. Goldstein, J. W. Simmons, *Journal of Chemical Physics* **1955**, *23*, 601-601.

[15]   R. Wagner, J. Fine, J. W. Simmons, J. H. Goldstein, *Journal of Chemical Physics* **1957**, *26*, 634-637.

[16]   E. A. Cherniak, C. C. Costain, *Journal of Chemical Physics* **1966**, *45*, 104-&.

[17]   C. E. Blom, G. Grassi, A. Bauder, *Journal of the American Chemical Society* **1984**, *106*, 7427-7431.

[18]   M. Winnewisser, G. Winnewisser, T. Honda, E. Hirota, *Z. Naturforsch., A* **1975**, *30A*, 1001-1014.

[19]   A. R. W. McKellar, D. W. Tokaryk, L.-H. Xu, D. R. T. Appadoo, T. May, *Journal of Molecular Spectroscopy* **2007**, *242*, 31-38.

[20]   A. R. W. McKellar, D. R. T. Appadoo, *Journal of Molecular Spectroscopy* **2008**, *250*, 106-113.

[21]   H. M. Pickett, *Journal of Molecular Spectroscopy* **1991**, *148*, 371-377.

[22]   J. L. Alonso, e. al., **(to be published)**.

[23]   A. M. Daly, C. Bermúdez, A. López, B. Tercero, J. C. Pearson, N. Marcelino, J. L. Alonso, J. Cernicharo, *The Astrophysical Journal* **2013**, *768*, 81.

[24]   Z. Kisiel, L. Pszczółkowski, I. R. Medvedev, M. Winnewisser, F. C. De Lucia, E. Herbst, *Journal of Molecular Spectroscopy* **2005**, *233*, 231-243.

[25]   J. K. G. Watson, *Vibrational Spectra and Structure, Vol. 6*, Elsevier: Amsterdam, **1977**.

[26]   A. López, B. Tercero, Z. Kisiel, A. M. Daly, C. Bermúdez, H. Calcutt, N. Marcelino, S. Viti, B. J. Drouin, I. R. Medvedev, C. F. Neese, L. Pszczółkowski, J. L. Alonso, J. Cernicharo, *A&A* **2014**, *572*, A44.

[27]   F. W. Loomis, R. W. Wood, *Physical Review* **1928**, *32*, 223-236.

[28]   Z. Kisiel, L. Pszczółkowski, B. J. Drouin, C. S. Brauer, S. Yu, J. C. Pearson, I. R. Medvedev, S. Fortman, C. Neese, *Journal of Molecular Spectroscopy* **2012**, *280*, 134-144.
[29]   V. I. Perevalov, V. G. Tyuterev, *Journal of Molecular Spectroscopy* **1982**, *96*, 56-76.
[30]   R. A. H. Butler, D. T. Petkie, P. Helminger, F. C. De Lucia, *Journal of Molecular Spectroscopy* **2003**, *220*, 150-152.
[31]   J. C. Pearson, C. S. Brauer, B. J. Drouin, *Journal of Molecular Spectroscopy* **2008**, *251*, 394-409.

CHAPTER XII. DETAIL ANALYSIS OF THE ROTATIONAL SPECTRUM OF METHYL CYANATE UP TO 350GHZ

Detail laboratory measurements and analysis of the rotational spectra of potential interstellar molecules are indispensable for their subsequent search in the interstellar line surveys available from the astronomical telescopes. The aim of this work is to provide direct transition frequencies and molecular constants of methyl cyanide in its ground torsional state to the astronomical community. The experimental spectra of methyl cyanate were recorder in the millimeterwave domain from 130 to 350 GHz and internal rotation A- and E-symmetry components were analyzed simultaneously using the ERHAM program. The data set for the ground torsional state of methyl cyanate exceeds 700 transitions and allowed to derive a precise set of spectroscopic constants. These new spectroscopic data can be used to confidentially search the spectral features of methyl cyanate over a wide frequency range towards various interstellar sources.

XII.1. INTRODUCTION

Organic molecules containing the abundant interstellar elements H, C, N, and O have attracted both astrophysicists and spectroscopists to intensively search for in the interstellar medium (ISM) during many years. One of the simplest, isocyanic acid (HNCO) was detected with high abundances in a variety of Galactic sources as well as in the external galaxies [1-2]. Two energetically less stable isomers of isocyanic acid, namely cyanic acid (HOCN) and fulminic acid (HCNO), with predicted relative energies of 24.7 and 70.7 kcal mol^{-1}[3], were also successfully observed in space[2-5]. Owing to the detection of isocyanic acid and its isomers, their methyl substituted derivatives could be considered as the candidates for the astrophysical observations as well. Among the members of the open-chain methyl derivatives, methyl isocyanate (CH_3NCO) is the lowest-energy isomer followed by methyl cyanate (CH_3OCN), acetonitrile N-oxide (CH_3CNO), and methyl fulminate (CH_3ONC). The second most stable isomer, methyl cyanate, being higher in energy with respect to methyl isocyanate by 25.1 kcal mol^{-1} [6], is the subject of this work.

To observe methyl cyanate unambiguously in the interstellar medium requires a previous good knowledge of its rotational spectrum in the laboratory. Until the present work, only Stark-modulated spectra of methyl cyanate and its isotopic species were recorded up to 50 GHz[7] [8-9].

In the first study[7], the information about the spectroscopic constants and dipole moments was provided. Five years later, seven A- and seven E-components resulting from the methyl top internal rotation were reported for the ground torsional state with restriction to $J \leq 3$ and $K_a \leq 1$ quantum numbers[9] It becomes clear that the rotational and torsional constants obtained from the fit of these transitions cannot be used to predict reliably the higher frequency transitions due to large uncertainties involved at higher J and K_a values. Lack of the accurate laboratory millimeter wave data thus initiated new spectroscopic measurements over the frequency range from 130 to 350 GHz.
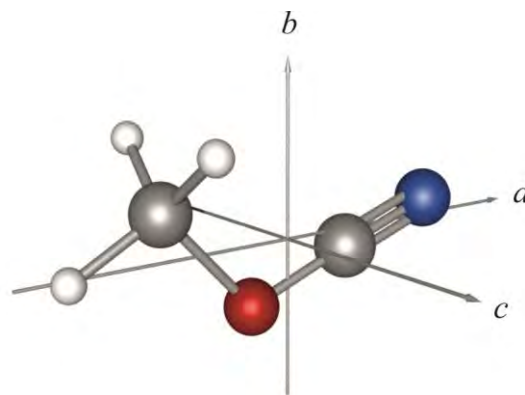
FIGURE XI.I: *Methyl cyanide depicted in the principal axis system*

New set of the spectroscopic constants together with the experimental frequencies and calculated intensities can be now used to guide confidently the astrophysical search for the millimeter wave features of methyl cyanate towards various interstellar sources.

XII.2. EXPERIMENTAL DETAILS

Methyl cyanate was generated[10]by gas-solid reaction of the evaporated O-methyl thiocarbamate ($CH_3OC(S)NH_2$) with yellow mercury oxide (HgO, Sigma Aldrich) packed into a tube in a vacuum line (0.3 mbar pressure). Sample of O-methyl thiocarbamate was prepared according to the method given by Davies *et al.*[11]. To remove the water, a by-product, the reaction products were passed through a short tube (15 cm) filled in half-section with phosphorus pentoxide (P_2O_5, Sigma Aldrich). Dried products were collected in the liquid nitrogen U-tube trap which was then connected directly to the Pyrex sample cell of the spectrometer. Vapor pressure of the trapped sample at -60°C was enough to fill the cell up to the total pressure of about 25 μbar. Undiluted methyl cyanate has been described as an extremely unstable compound at room temperature[12] and initial experiments were thus realized in the flow mode. Nonetheless, later it was found that the measurements could be performed in the closed cell during several hours. Isocyanic acid and methyl isocyanate were found as the major impurities.

The rotational spectra were recorded between 130 and 350 GHz using the millimeter wave spectrometer[13], which generates the millimeter wave radiation by multiplication of the fundamental Agilent E8257D synthesizer frequency by amplifier-multiplier chains from Virginia Diodes, Inc. The synthesizer output was frequency modulated at f = 10.2 kHz and the signal was detected by solid-state zero-bias detectors (Virginia Diodes, Inc.) and further processed by lock-in amplifier using $2f$ detection. The second derivative shape of the lines at the modulation depth of 30 kHz was fit to the Gaussian profile function with the uncertainty of the isolated well-developed lines to be better than 50 kHz.

XII.3. ANALYSIS OF THE SPECTRA

Methyl cyanate belongs to the group of near-prolate asymmetric top molecules with C_s symmetry and its molecular geometry is shown in Figure XII.1. The dipole moment component along the *a*-axis, $|\mu_a|$ = 4.07(6) D, is much larger than the component along the *b*-axis, $|\mu_b|$ = 1.24(40) D [7], therefore, the methyl cyanate rotational spectrum is dominated by strong *a*-type *R*-branch transitions. These transitions usually occur in groups with central part situated approximately at $(B+C)(J'' + 1)$. Each group corresponds to one $J'+ 1 \leftarrow J''$ and is formed by transitions with different K_a.

There are always two transitions for each $K_a > 0$ value and lower K_a pairs are more widely split than the higher K_a ones. Figure XII.2 illustrates an
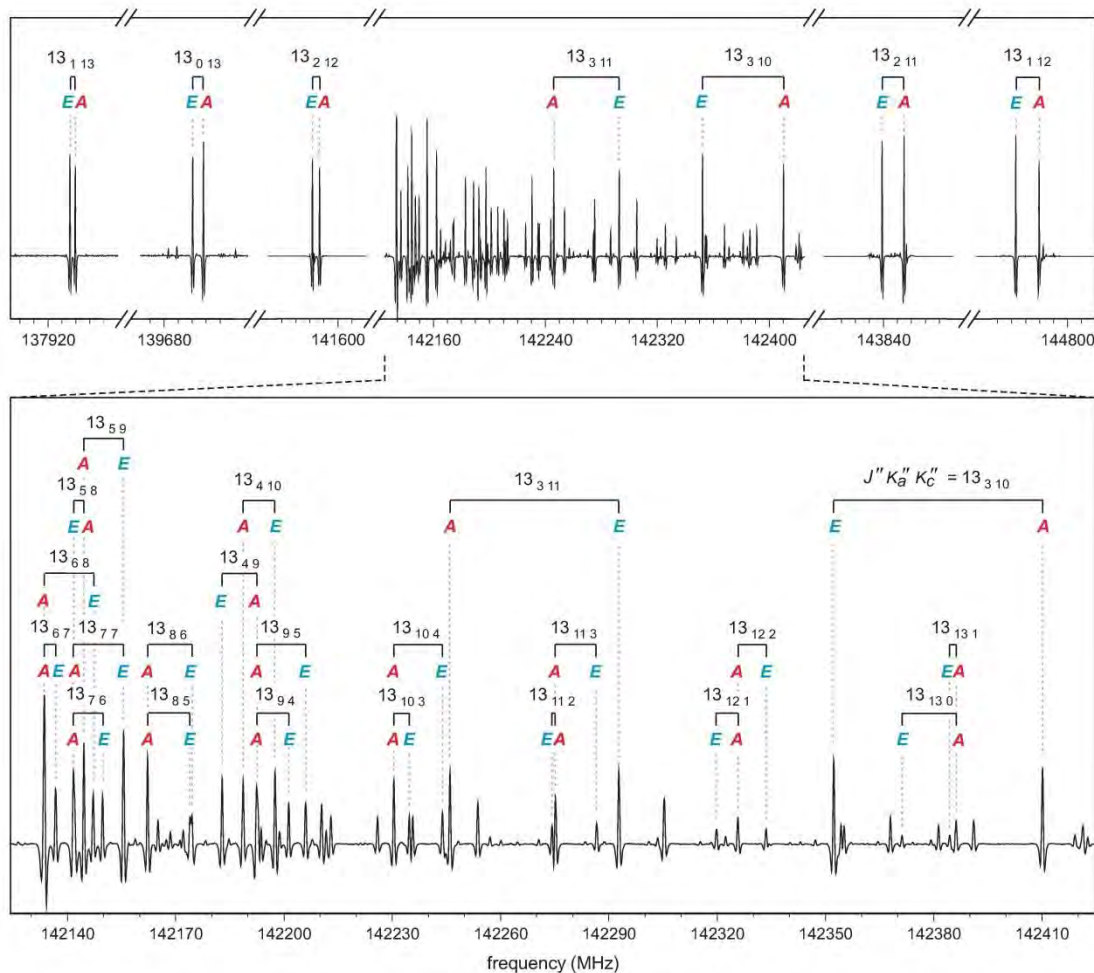
FIGURE XI.2. *Section of the methyl cyanate rotational spectrum with the assignment of the A-E doublets of the a-type R-branch transitions (ΔJ = +1, ΔK$_a$ = 0, ΔK$_c$ = +1) within the cluster for J″ = 13. The quantum numbers of the lower energy level, J″K$_a$″K$_c$″}$, are indicated. Transitions of the A-component for K$_a$ ≥5 are doubly degenerate.*

example of such a group for $J'' = 13$. The central region of the group contains all but the $K_a = 0$ and two $K_a = 1$ and two $K_a = 2$ lines which are situated apart. In addition, methyl cyanate contains one C_{3v} internal rotor (methyl group) which can undergo a torsion motion with respect to the rest of the molecule leading to the splitting of the rotational levels into A- and E-sublevels. The threefold barrier to the methyl top internal rotation was determined close to 400cm^{-1}[9] and is sufficient to complicate the rotational spectrum in the sense that all

transitions within the $J''+ 1 \leftarrow J''$ group appear as the A-E doublets. Separation of the A- and E-components reaches, in this case, from units to tens of MHz as shown in Figure XII.2. No quadrupole hyperfine structure has been observed in the rotational spectra.

Prior to the analysis of the millimeter wave spectra, predictions based on the previously published data[9] were made. After elimination of the lines corresponding to the isocyanic acid and methyl

Table XII.1. Ground torsional state molecular parameters of methylcyanate obtained from the fit using ERHAM program (A-reduction, I^r representation).

Constant[a]	Unit	Value[b]
A	MHz	38989.415 (62)
B	MHz	5322.2518 (13)
C	MHz	4821.3089 (11)
Δ_J	kHz	3.40871 (63)
Δ_{JK}	kHz	-81.4225 (99)
Δ_K	kHz	1745 (16)
δ_J	kHz	0.79100 (82)
δ_K	kHz	1.58 (11)
Φ_J	Hz	0.01011 (27)
Φ_{JK}	Hz	-0.2779 (36)
Φ_{KJ}	Hz	-8.363 (63)
φ_J	Hz	0.00440 (37)
ρ	---	0.186794 (63)
β	º	6.974 (15)
ε_1	MHz	-269.515 (82)
$[G_a]_1$	MHz	-3.768 (52)
$[G_{2a}]_1$	kHz	1.735 (82)
$[(B+C/2)]_1$	kHz	-1.56 (66)
$[(B-C/4)]_1$	kHz	5.68 (20)
$-[\Delta_J]_1$	Hz	-1.29 (20)
$-[\Delta_{JK}]_1$	Hz	-41.8 (14)
$-[\delta_K]_1$	Hz	-207.0 (89)
σ_{rms}[c]	kHz	93

[a] A, B, C are the rotational constants, Δ_J, Δ_{JK}, Δ_K, δ_J, δ_K, are quartic centrifugal distortion constants and Φ_K, Φ_{JK}, Φ_{KJ}, φ_J are the sextic centrifugal distortion constants. ρ and β represent the magnitude of the ρ-vector and the angle between the ρ-vector and principal a-axis, respectively. Tunneling parameters associated with the rotational and centrifugal distortion constants are given in the notation $[X]_1$, where X is a linear combination of the rotational constants or centrifugal distortion constants and the subscript designates the tunneling component, ε_1 is first energy tunneling parameter and $[G_a]_1$ and $[G_{2a}]_1$ are related to the Coriolis operators J_a and $(J_+^2 + J_-^2)J_a$, respectively[15-16]
[b] Numbers in parenthesis represent the 1σ uncertainty (67% confidence level) in units of the last decimal digit.
[c] Root mean square deviation of the fit.

isocyanate, the assignment was started searching the strongest low-K_a transitions subjected to the A-E splitting. Since these transitions were found within 10–20 MHz from the initial positions predicted, Loomis-Wood type plots (AABS package[14]), which allow to visualize a series of selected transitions with respect to their predicted locations, were very useful to reach the confident assignment of both A- and E-symmetry components. After having assigned and fitted the A-transitions with standard asymmetric top semirigid Hamiltonian to obtain a first set of the rotational and quartic

centrifugal distortion constants, the E-transitions were searched and added step by step starting at low J and K_a and going up progressively. Towards the end of the assignment, only a few very weak b-type R-branch transitions were found. In case of the lines composed from degenerate asymmetric rotor transitions, equal weights were assigned to the components of such blends. Any other transitions blended accidentally, as well as those corresponding to not related A- and E-components, were not included in the fit.

Both components of the internal rotation splitting were simultaneously fitted using the ERHAM program[17] which has been applied successfully to the analysis of complex rotational spectra of several interstellar molecules with one or two methyl tops[16, 18-20]. In this code, matrix elements of the effective Hamiltonian are expressed in terms of Fourier series whose coefficients are related to the rotational and centrifugal distortion constants as well as the so-called tunneling parameters for both Watson's[21] A- and S-reduction schemes.[15] The expressions for a molecule with the ab plane of symmetry and one internal rotor can be found in the literature[16, 20]. The same notation is used in this work. A total number of 22 spectroscopic parameters were determined from the nonlinear least-square fit of 385 A-transitions (295 distinct frequency lines due to the blended transitions) and 341 E-transitions (341 distinct frequency lines) within J''=10-35 and K_a''=0-13. The root mean square deviations of 77 kHz and 79 kHz were achieved for the sets of A- and E-symmetry

transitions, respectively. The list of the determined parameters is presented in Table XII.1. In addition to the parameters obtained from the fit, several other internal rotation parameters were derived from the ρ-vector, rotational, and energy tunneling parameters from Table XII.1 and their values can be found in Table XII.2. The observed and fitted experimental frequencies are collected in the online Table XI.S1 along with the assignments to the asymmetric top rotational quantum numbers J, K_a, K_c, ν_{obs}-ν_{calc} values where ν_{obs} and ν_{calc} are the observed and calculated frequencies, respectively,

and the symmetry number σ_1 labeling the *A*- and *E*-symmetry component.

Table XII.2. Derived internal rotation parameters.

Constant[a]	Unit	Value[b]
I_α	MHz	38989.415 (62)
F	MHz	5322.2518 (13)
ΔE_{E-A}	MHz	4821.3089 (11)
∡ (i,a)	°	3.40871 (63)
∡ (i,b)	°	-81.4225 (99)
∡ (i,c)	°	1745 (16)

[a]I_α is the moment of inertia of the methyl top, F is the reduced rotational constant, ΔE_{E-A} is the torsional energy difference, ∡ (i,a), ∡ (i,b), and ∡ (i,c) are the angles between the internal rotation axis i and the principal axis a, b, and c, respectively.
[b]Numbers in parenthesis represent the 1σ uncertainty (67% confidence level) in units of the last decimal digit.

XI.4. REFERENCES

[1]   D. Quan, E. Herbst, Y. Osamura, E. Roueff, *The Astrophysical Journal* **2010**, *725*, 2101.

[2]   S. Brünken, A. Belloche, S. Martín, L. Verheyen, K. M. Menten, *A&A* **2010**, *516*, A109.

[3]   S. Brünken, C. A. Gottlieb, M. C. McCarthy, P. Thaddeus, *The Astrophysical Journal* **2009**, *697*, 880.

[4]   N. Marcelino, J. Cernicharo, B. Tercero, E. Roueff, *The Astrophysical Journal Letters* **2009**, *690*, L27.

[5]   N. Marcelino, S. Brünken, J. Cernicharo, D. Quan, E. Roueff, E. Herbst, P. Thaddeus, *A&A* **2010**, *516*, A105.

[6]   T. Pasinszki, N. P. C. Westwood, *The Journal of Physical Chemistry A* **2001**, *105*, 1244-1253.

[7]   T. Sakaizumi, H. Mure, O. Ohashi, I. Yamaguchi, *Journal of Molecular Spectroscopy* **1990**, *140*, 62-70.

[8]   T. Sakaizumi, K. Sekishita, K. Furuya, Y. Tetsuda, K. Kaneko, O. Ohashi, I. Yamaguchi, *Journal of Molecular Spectroscopy* **1993**, *161*, 114-122.

[9]   T. Sakaizumi, M. Namikawa, O. Ohashi, *Journal of Molecular Structure* **1995**, *345*, 189-195.

[10]   T. Pasinszki, N. P. C. Westwood, *The Journal of Physical Chemistry* **1995**, *99*, 1649-1654.

[11]   W. Davies, J. Maclaren, *Journal of the Chemical Society (Resumed)* **1951**, 1434-1437.

[12]   M. Jensen, M. Due, A. Holm, C. Wentrup, *Acta Chem. Scand* **1966**, *19*, 438

[13]   A. Daly, L. Kolesniková, S. Mata, J. Alonso, *Journal of Molecular Spectroscopy* **2014**, *306*, 11-18.

[14]   Z. Kisiel, L. Pszczółkowski, I. R. Medvedev, M. Winnewisser, F. C. De Lucia, E. Herbst, *Journal of Molecular Spectroscopy* **2005**, *233*, 231-243.

[15]   P. Groner, *Journal of Molecular Spectroscopy* **2012**, *278*, 52-67.

[16]   A. Maeda, I. R. Medvedev, F. C. De Lucia, E. Herbst, P. Groner, *The Astrophysical Journal Supplement Series* **2008**, *175*, 138.

[17]   P. Groner, *The Journal of chemical physics* **1997**, *107*, 4483-4498.

[18]   P. Groner, S. Albert, E. Herbst, F. C. De Lucia, *The Astrophysical Journal* **1998**, *500*, 1059.

[19]   P. Groner, S. Albert, E. Herbst, F. C. De Lucia, F. J. Lovas, B. J. Drouin, J. C. Pearson, *The Astrophysical Journal Supplement Series* **2002**, *142*, 145.

[20]   P. Groner, M. Winnewisser, I. R. Medvedev, F. C. De Lucia, E. Herbst, K. Sastry, *The Astrophysical Journal Supplement Series* **2007**, *169*, 28.

[21]   J. K. G. Watson, *Vibrational Spectra and Structure, Vol. 6*, Elsevier: Amsterdam, **1977**.

CHAPTER XIII. DETECTION OF ILLICIT DRUGS BY DIRECT ABLATION OF SOLID SAMPLES

Analysis of illicit drugs rises as an interesting field of work given the high social impact presented by drugs in the modern society. Direct laser ablation of solid compounds enables their analysis without sampling or preparation procedures. For that purpose, we have constructed an experimental setup that combines laser ablation with time-of-flight mass spectrometry and ulteriorly perform studies on the mass spectra of such drugs as MDMA, commonly known as ecstasy. Analysis of the observed fragmentation pattern in mass spectra may elucidate upon the ablation-induced photofragmentation phenomena produced by ablation, which differs from those previously observed with conventional ionization methods.

XIII.1. INTRODUCTION

Direct chemical analysis of solid sample without chemical pretreatment can offer advantage over conventional dissolution techniques used in analysis of real samples such as high pressure liquid chromatography (HPLC) and gas chromatography (GS) coupled with mass spectrometry (MS).[1-2] Elimination of chemical solvents and wastes, reduced sample handling, and short analysis times are some offered by the benefits of direct solid sampling techniques. Laser ablation has raised considerable interest due to its proven applications in solid sample analysis and consequently different analytical techniques in combination with laser ablation have been developed during the past few decades. Laser-Induced breakdown spectroscopy (LIBS)[3-4] and laser ablation optical/mass spectrometry with inductively coupled plasma (LA-ICP-AES/MS)[5-10] appear to be amongst the most powerful analytical techniques for nearly non-destructive determination of elements. However, with the growing importance of biomedical and forensic investigations in organic analysis, the emphasis has been shifting towards detection of ever larger molecules. Hence, devoted laser-based mass spectrometry techniques such as laser microprobe mass analysis (LAMMA)[11-14] and laser desorption/ionization mass spectrometry (LDI-MS)[15-17] have been developed. Among all LDI systems, the matrix assisted laser desorption/ionization (MALDI)[18-20] is the most

extended due to its capacity to analyze samples up to 1.5 million of Daltons.[21] However, matrix selection presents itself as a crucial step since matrices are normally too specific and, furthermore, matrix to analyte molar ratio is difficult to adjust correctly.[22-23] Alternative assistants for LDI, such as metals,[17] surfaces,[24] nanoparticles[25] and polymers,[26] have been developed in order to circumvent the problems with the sample preparation in MALDI.

During the last decade, laser ablation has been successfully combined with Fourier transform microwave techniques to bring thermally unstable biomolecules into gas phase and reveal their most stable structures. Narrowband LA-MB-FTMW[27] and broadband CP-FTMW[28] techniques have overcome the drawback of vaporizing solid samples opening a new window to the high resolution rotational studies. In so doing, the conformational behavior of relevant building blocks such as amino acids,[29] sugars[30] and nucleic acid bases[31] could be unveiled. These techniques have also been tested in aspirin[32] and paracetamol.[33]

On the basis of previous experimental setups developed for identifying metallic contaminants[34] and taking advantage of our long experience on laser ablation techniques, we have configured an experimental setup, combining laser ablation with time-of-flight mass (LA-TOF-MS) spectrometry, dedicated to analyzing organic compounds. The

instrument configuration is described in the next section and preliminary results on several drugs (such as aspirin and paracetamol) and seized samples as the illicit drug MDMA (3,4-methylenedioxy-N-methylamphetamine) are reported.

XIII.2. EXPERIMENTAL SYSTEM

The LA-TOF-MS experimental setup has been developed in-house by using a combination of commercial components. Figure XIII.1 shows a diagram of the overall system. The ionization chamber is a multiport stainless steel vacuum cavity where samples are introduced through port 1. The samples present the shape of a pill, with 8 mm diameter and 5 mm long, and are linked to the holder via heat shrink tube. A gate valve is used to avoid vacuum loses each time a new sample is inserted. The horizontal position of the sample can be adjusted to obtain the best signal. Samples are vertically fixed at halfway point between the TOF extractor and repeller plates. Port 1 is coupled to the time-of-flight (TOF) tube in such a way that its extractor and repeller plates are located in the middle of the chamber. The TOF tube employed is a Jordan type tube of 1 meter long which can operate in reflectron mode (RM Jordan, model D-850). Along the tube, there are several voltage

FIGURE 1. *LA-TOF-MS instrument.*

adjustable plates that are adjust to optimize the signal of the samples. All of them are working in continuous mode with the exception of the repeller and extractor plates, which have been modified by two high voltage rapid switches in order to pulse them. The laser beam is introduced inside the ionization chamber though a glass window placed in port 3. This beam is aligned by two external mirrors in such a way that it is equally spaced from both extractor and repeller plates; as such, the laser ablation/ionization is produced perpendicularly to the sample. The laser employed is a Nd:YAG (Quantel Brilliant, model C07.BR) in the third harmonic (λ= 355 nm) with pulse width ~ 5 ns. Its power is adjusted modifying the time delay between the flash lamp and the Q-S pulse. A single lens (Melles Griot), with a focal distance of 750 mm, which is placed between the above mentioned two mirrors, is employed to focus the laser beam onto the sample. The distance from the lens to the target is tuned by employing a translation stage, which allows to modify the beam spot area in order to obtain a stable signal. The laser spot size is around 0.6 cm^2. Two turbo molecular pumps (Leybold, model TDL RS 458 and TURBOVAC, model 361) connected though port 4 and in the TOF tube are used to maintain the ultra high vacuum required for the experiment. The ionization chamber is generally at 10^{-7} Torr while the reflectron TOF is at 10^{-8} Torr.

The experimental sequence (Figure XIII.2) is controlled by a commercial delay generator
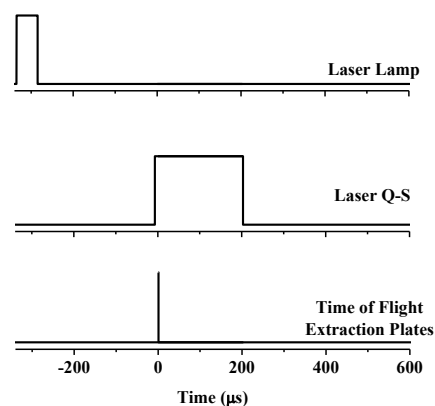
FIGURE XIII.2. *Operating sequence of LA-TOF-MS controlled by pulse delay generator.*

(Stanford Research Systems, model DG-645) working at a repetition rate of 10 Hz. Both flash lamp and Q-switch of the laser are externally triggered by the delay generator, being the Q-switch delayed from the flash lamp around 300μs; this time changes in function of the energy that requires the sample to be ionized. A few micro seconds after the Q-switch, the extractor and repeller plates are pulsed during a period that may range from less than a microsecond to 20μs. Delays and pulsed widths are tuned to accomplish the maximum signal of the interested ions. The most common experimental timings are summarized in Table XIII.1. The output signal of the extraction plates is used to trigger the oscilloscope (Agilent model 5464D, 2Gs/s), which digitalized the signal coming from the multichannel plate of the TOF tube. Afterwards, the data is sent to a computer where the analysis and graphing is performed.

Samples used for the analysis, such as aspirin (m.p.138ºC) or paracetamol (m.p. 169ºC), were purchased to Sigma Aldrich with the exception of MDMA (m.p.113ºC), which is a real sample (not pure), obtained from a seizure by Valladolid division of the Spanish Police Department. They were used without further purification. These samples were grounded and then introduced into an in-house designed cast and pressed into a hydraulic press at 50 bar in order to form pills with 8 mm diameter and 5 mm long. This procedure has been extensively described in our group reports.[27-33] The flight time data were converted to mass/charge based on the calibrations made with metals samples, (Ag and Cu see Figure XIII.2) which were

TABLE XII.1. Summary of the operating parameters of the LA-TOF-MS system

Laser	
Wavelengh	355nm
Pulse width	10 ns
Energy/pulse	0.5 – 15mJ
Rep rate	10Hz
Spot size	0.6 cm^2
Time of Flight	
Preassure	$\sim 10^{-7}$ Torr
Extraction plate	$\sim$ 2800 V
Repelling plate	$\sim$ 3250 V
Reflection plate 1	$\sim$ 1800 V
Reflection plate 2	$\sim$ 4000V
Deflection plates	$\sim$ 0 V
Detection plate	$\sim$ -4000V
Pulse delay generator	
Delay Flash lamps / Q-switch	300 – 350 μs
Delay Q-switch / Extraction plates	1-15 μs
Pulse width of extraction plates	0.5 - 5 μs

modeled with the same dimensions as the pills in our laboratory. .

XIII.3. RESULTS AND DISCUSSION

Prior to the analysis of the illicit drug MDMA, several organic compounds of similar physical characteristics (solids with similar melting points) have been proved by LA-TOF-MS. The pharmacological species paracetamol and aspirin were employed to optimize the experimental conditions and their mass spectra were successfully obtained using this technique (see Figure XIII.4). Both substances exhibit similar fragmentation pattern as those obtained by employing electron impact (EI), a more common ionization source.[35] However, the intensity ratio of the fragments is slightly different. In case of paracetamol, the cleavage between the carbonyl and amino groups

(pointed out in Figure XIII.4.a) has diminished drastically, leading to observe a major proportion of the parent ion (151u). Likewise, for aspirin, the ratio between the different possible cleavages has changed (see Figure XIII.4.b). For EI ionization, the most abundant fragment is by far that corresponding to 120u, with a mininal proportion of the 163u and 138u is minimal, being the latter slightly higher. In contrast, employing LA-TOF-MS, the 120u peak has decreased its intensity and, moreover, the proportion between 163u and 138u is inverted; in fact, the peak corresponding to 138u does not appear in our mass spectrum.
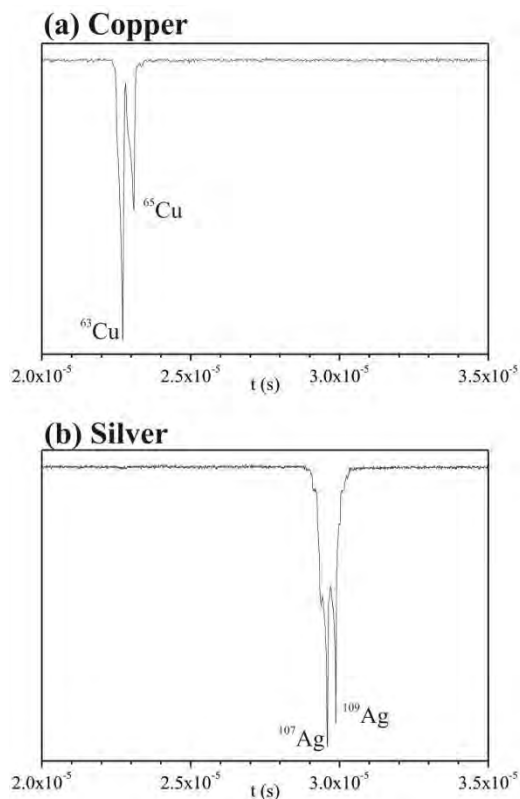
FIGURE XIII.3. *Mass spectra of some metals obtained from LA-TOF-MS instrument*

FIGURE XIII.4. *Mass spectra of paracetamol (151u) and aspirin (180u) obtained from LA-TOF-MS instrument*

In the MDMA spectrum at 5.7 mJ/pulse (Figure XII.4), besides the 194u fragment corresponding to the parent ion plus a proton ([MDMA+H]$^+$), several ions at m/z equal to 30, 42, 58, 122, 105, 135 and 163 can also be attributed to fragments from MDMA (Figure XIII.5). Between the three main possible cleavage sites for ecstasy molecule (Figure XIII.6) β- and γ-cleavages are given in higher proportion according to the almost equal intensity of the fragments m/z=135 and 163, representative of these two cleavages respectively. Both signals are about three times stronger than the parent ions, which can give us an idea of the fragmentation degree of MDMA under these experimental conditions.

Comparing this LA spectrum with those obtained from more conventional ionization methods, there are clear discrepancies in the relative intensities of the fragments which might indicate differences in the fragmentation procedure. In case of electron impact (EI) ionization (Figure XIII.7), β-cleavage dominates the mass spectrum, with negligible intensities of either other fragments or parent ion. This β-cleavage has also higher relevance related to α and γ in MALDI experiments,[36] although, in this case, the photofragmentation degree is minimum; the intensities of the fragment signals are almost
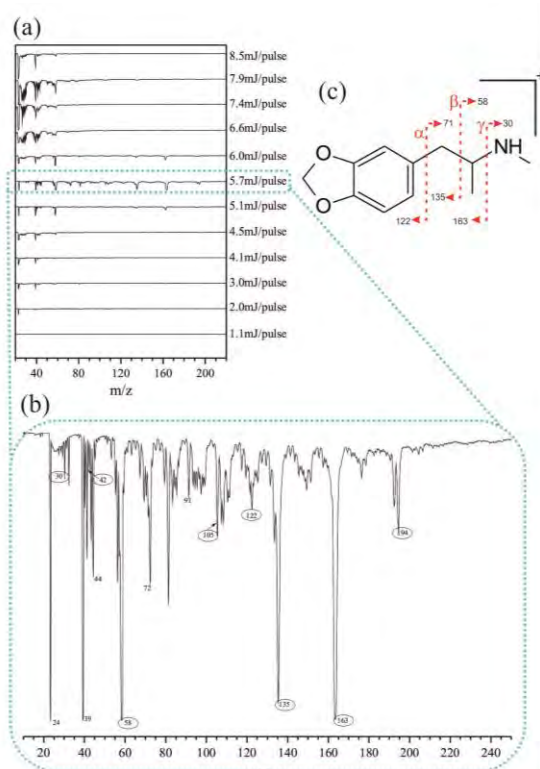
FIGURE XIII.5. *(a) Mass spectra of MDMA at different fluencies. (b) Mass spectrum of MDMA at 5.7mJ per pulse amplified. (c) α-, β-, and γ-cleavages of MDMA.*

exiguous in the spectrum. In contrast to these two ionization methods (EI and MALDI), electrospray ionization (ESI) produces a rupture via γ-cleavage[36] instead of the β-cleavage. On the other hand, as it was mentioned before, both γ- and β-cleavages are produced in almost equal amounts when LA is used to ionize the samples. Thus, LA fragmentation is not produced in exactly the same way as any of them, being more of a combination.

Deeper insight into the MDMA spectrum several reveals that signals with a relative high intensity non assignable to this illicit drug can be distinguished. One should take that the sample analyzed is not a pure sample (estimated purity 70%) into account,

otherwise, it was obtained from a seizure made by the Spanish police. Therefore, the presence of other analytes should be expected. By screening in to mass spectrum libraries,[35] it can be observed that several peaks are consistent with the existence of ethylamphetamine, sometimes present together with MDMA as a stimulant. This possible assignment is based on the signals at 72 and 91u and 44 and 119 that might correspond to the pair of ions produced by the break of ethylamphetamine through β- and δ-cleavages, respectively (Figure XIII.8). In this case, both types of cleavage have almost the same relevance, similar those in MDMA. However, in the latter, β-type is slightly more intense. The signal at 163u, assigned initially to a γ fragment of MDMA, could also have increased its contribution due to the parent peak of ethylamphetamine shedding some light on the intensity discrepancies between the two peaks produced by γ-cleavage (30u and 163u). Besides these two analytes, no more signals assignable to any other species could be identified in the spectrum..

XIII.4. Conclusions

To the best of our knowledge, this has been the first report of the utilization of conventional laser ablation/ionization TOF-MS spectrometry with the aim of detection the presence of illicit drugs in real samples. Our results have shown the capacity of this technique as a fast diagnostic method with a reduction of the sample processing, which constitute a major advantage, and serves as a foundation for future investigations about the implementation of laser ablation/ionization TOF-MS spectrometry applied to illicit drugs detection. Moreover, it was found that laser ablation produces different fragmentation patterns when compared to most conventional ionization methods (ESI, EI and MALDI). Hence, more work will be necessary to optimize the laser ablation conditions, for instance, using picosecond laser pulses.

XIII.5. REFERENCES

[1]   N. Pizarro, J. Ortuño, M. Farré, C. Hernández-López, M. Pujadas, A. Llebaria, J. Joglar, P. N. Roset, M. Mas, J. Segura, J. Camí, R. de la Torre, *Journal of Analytical Toxicology* **2002**, *26*, 157-165.

[2]   A. Namera, A. Nakamoto, T. Saito, M. Nagao, *Forensic Toxicol* **2011**, *29*, 1-24.

[3]   A. W. Miziolek, V. Palleschi, I. Schechter, *Laser Induced Breakdown Spectroscopy (LIBS): Fundamentals and Applications*, Cambridge University Press, New York, **2006**.

[4]   J. P. Singh, S. N. Thakur, *Laser Induced Breakdown Spectroscopy*, Elsevier, **2007**.

[5]   D. Günther, S. E. Jackson, H. P. Longerich, *Spectrochimica Acta Part B: Atomic Spectroscopy* **1999**, *54*, 381-409.

[6]   S. F. Durrant, *Journal of Analytical Atomic Spectrometry* **1999**, *14*, 1385-1403.

[7]   J. D. Winefordner, I. B. Gornushkin, D. Pappas, O. I. Matveev, B. W. Smith, *Journal of Analytical Atomic Spectrometry* **2000**, *15*, 1161-1189.

[8]   D. Günther, I. Horn, B. Hattendorf, *Fresenius J Anal Chem* **2000**, *368*, 4-14.

[9]   R. E. Russo, X. Mao, O. V. Borisov, *TrAC Trends in Analytical Chemistry* **1998**, *17*, 461-469.

[10]   R. E. Russo, X. L. Mao, O. V. Borisov, H. C. Liu, in *Encyclopedia of Analytical Chemistry* (Ed.: R. A. M. (Ed.)), Wiley, Chichester, **2000**, pp. 9485-9506.

[11]   F. Hillenkamp, E. UnsoLd, R. Kaufmann, R. Nitsche, *Nature* **1975**, *256*, 119-120.

[12]   L. Van Vaeck, J. Bennett, P. Van Epsen, E. Schweikert, R. Gijbels, F. Adams, W. Lauwers, *Organic Mass Spectrometry* **1989**, *24*, 782-796.

[13]   L. Van Vaeck, H. Struyf, W. Van Roy, F. Adams, *Mass Spectrometry Reviews* **1994**, *13*, 189-208.

[14]   L. Van Vaeck, H. Struyf, W. Van Roy, F. Adams, *Mass Spectrometry Reviews* **1994**, *13*, 209-232.

[15]   M. A. Posthumus, P. G. Kistemaker, H. L. C. Meuzelaar, M. C. Ten Noever de Brauw, *Analytical Chemistry* **1978**, *50*, 985-991.

[16]   R. J. Levis, *Annual Review of Physical Chemistry* **1994**, *45*, 483-518.

[17]   E. P. C. Lai, S. Owega, R. Kulczycki, *Journal of Mass Spectrometry* **1998**, *33*, 554-564.

[18]   K. Tanaka, H. Waki, Y. Ido, S. Akita, Y. Yoshida, T. Yoshida, T. Matsuo, *Rapid Communications in Mass Spectrometry* **1988**, *2*, 151-153.

[19]   M. Karas, F. Hillenkamp, *Analytical Chemistry* **1988**, *60*, 2299-2301.

[20]   K. Dreisewerd, *Chemical Reviews* **2003**, *103*, 395-426.

[21]   D. C. Schriemer, L. Li, *Analytical Chemistry* **1996**, *68*, 2721-2725.

[22]   E. T. P. Sze, T. W. D. Chan, G. Wang, *Journal of the American Society for Mass Spectrometry* **1998**, *9*, 166-174.

[23]   M. Vestling Martha, in *Time-of-Flight Mass Spectrometry, Vol. 549*, American Chemical Society, **1993**, pp. 211-224.

[24]   K. P. Law, J. Larkin, *Analytical and Bioanalytical Chemistry* **2011**, *399*, 2597-2622.

[25]   J. Nizioł, W. Rode, Z. Zieliński, T. Ruman, *International Journal of Mass Spectrometry* **2013**, *335*, 22-32.

[26]   A. Woldegiorgis, F. v. Kieseritzky, E. Dahlstedt, J. Hellberg, T. Brinck, J. Roeraade, *Rapid Communications in Mass Spectrometry* **2004**, *18*, 841-852.

[27]   J. L. Alonso, C. Perez, M. E. Sanz, J. C. Lopez, S. Blanco, *Physical Chemistry Chemical Physics* **2009**, *11*, 617-627.

[28]   S. Mata, I. Peña, C. Cabezas, J. C. López, J. L. Alonso, *Journal of Molecular Spectroscopy* **2012**, *280*, 91-96.

[29]   C. Bermúdez, S. Mata, C. Cabezas, J. L. Alonso, *Angewandte Chemie International Edition* **2014**, *53*, 11015-11018.

[30]   J. L. Alonso, M. A. Lozoya, I. Peña, J. C. Lopez, C. Cabezas, S. Mata, S. Blanco, *Chemical Science* **2014**, *5*, 515-522.

[31]   J. L. Alonso, V. Vaquero, I. Peña, J. C. López, S. Mata, W. Caminati, *Angewandte Chemie* **2013**, *48*, 5934-5936.

[32]   C. Cabezas, J. L. Alonso, J. C. López, S. Mata, *Angewandte Chemie International Edition* **2012**, *51*, 1375-1378.

[33]   M. Varela, C. Cabezas, J. C. López, J. L. Alonso, *The Journal of Physical Chemistry A* **2013**, *117*, 13275-13278.

[34]   R. E. Russo, G. L. Klunder, P. Grant, B. D. Andresen, *Appl Phys A* **1999**, *69*, S895-S897.

[35]   NIST Mass Spec Data Center, S. E. Stein, *Eds. P.J. Linstrom and W.G. Mallard, National Institute of Standards and Technology* **Nist Chemistry WebBook, NIST Standard Reference Database**, *Gaithersburg MD, 20899*, (retrieved 2014).

[36]   B.-H. Chen, J.-T. Liu, W.-X. Chen, H.-M. Chen, C.-H. Lin, *Talanta* **2008**, *74*, 512-517.

CHAPTER XIV. CONCLUSIONS AND FUTURE DIRECTIONS

The present Dissertation collects several research works concerning molecules of biological and astrophysical interest (see introduction in Chapter II). The vast majority of them were performed employing different approaches of rotational spectrometers presented in section III.I. Following, some conclusions and future directions are enunciated regarding not only to the molecular studies but also to the instrumental techniques.

Time domain spectrometers are employed to analyze the conformational behavior of biomolecules: fructose (Chapter IV), ketohexoses (Chapter V), deoxyribose (Chapter VI), glucosamine (Chapter VII), histidine (Chapter VIII), cytosine-water complex (Chapter IX) and synephrine (Chapter X).

The broadband technique LA-CP-FTMW has been revealed its capacity as a convenient and rapid acquisition method to obtain the rotational spectrum of sugars (Chapters IV-VII), allowing to unveiling for the first time its conformational behavior. Two, four, three and two species were identified with this approach for ketohexoses: D-fructose, D-tagatose, D-psicose and L-sorbose, respectively (Figure XIV.1). All of their most stable conformations show common conformational signatures that may be related to their sweetness, thus, to the way these substances are linked to the sweet receptors placed in the oral cavity. Further research is recommended to evaluate the influence on water in their conformational
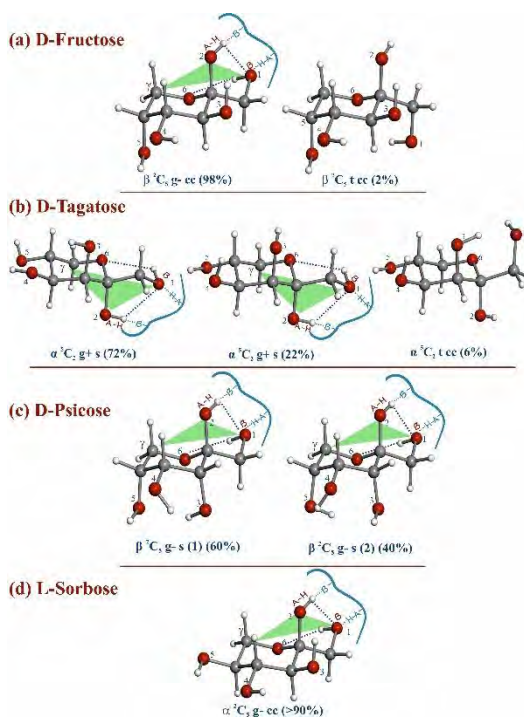
FIGURE XIV.I: *Observed conformations of ketohexoses. Dashed lines pointed out their H-bond. The proposed linkage to the receptor is signaled for the most abundant species (in parenthesis, their abundances). (a) D-Fructose. (b) D-Tagatose. (c) D-Psicose (d) L-Sorbose*

behavior as well as to try to identify if this conformational signature is present also in sweeteners of different characteristics, such as polyalcohols.

During the conformational investigation of glucosamine, it became evident the resolution limitations of the LA-CP-FTMW spectrometer, when regarding to analyze the hyperfine structure of this molecule. Figure XIV.2 compares the resolution of the hyperfine structure observed in the broadband experiment (b) and in the narrowband (a). While the first one allows a rapid acquisition of the whole spectrum, the latter provides higher resolution in order
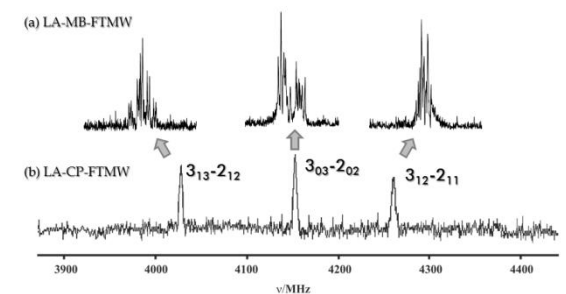
FIGURE XIV.2: *Hyperfine structure of D-glucosamine observed by (a) LA-MB-FTMW and (b) LA-CP-FTMW spectromenters.*

to sufficiently observe the quadrupole hyperfine components. The use of both approaches, LA-CP-FTMW to make the initial assignments and the LA-MB-FTMW to analyze the hyperfine structure, seems the perfect synergic combination to treat this biomolecules.

The analysis of the tautomeric/conformational behavior of the amino acid histidine challenged us due to the complexity quadrupole hyperfine structure as consequence of its three inequivalent ^{14}N. A new design of the LA-MB-FTMW spectrometer was built in order to measure the $1_{1\ 1} \leftarrow 0_{0\ 0}$ transition at 2.5GHz, where there are less hyperfine components and they are more spread in frequency. Although this transition was measured, the hyperfine analysis was complicated. The rotational parameters obtained indicated that the histidine species observed corresponded

FIGURE XIV.3: *Conformer of histidine observed in gas phase together with the hyperfine structure of the 11 1←0 0 0 transition.*

to the $N_\varepsilon H$ tautomer. Once completed this work, only two of the twenty natural amino acids remains to be analyzed by rotational spectroscopy. Promising results have been being obtained for dipeptide chains as well as for their microsolvation that may lead to a new research lines.

The formation of the cytosine water complex is not very effective during the ablation process; hence, transitions are not sufficiently intense to be detected under the standard conditions of the LA-MB-FTMW spectrometer. A step forward in the instrumentation was given by the implementation of the Multi-FID (Free Induction Decay) option, which allows to recording more than one spectrum per molecular pulse. In so doing, some new transitions, which were not observed before, could be assigned to the cytosine water complex. The hyperfine structure

of this substance has yet to be analyzed. The success involving the analysis of cytosine water complex may open a way to explore other complexes of nitrogen bases, as well as the base parings such as the adenine-thymine.

The frequency domain spectrometers (Stark and FM modulation) have been employed to perform the rotational analysis of propenal (Chapter XI), methyl isocyanate (Chapter X), ethyl cyanate (Appendix I) and vinyl cyanate (Appendix II). Prior to its analysis, it was necessary to upgrade the instrumentation that was hardly used after moving to the new building, which means: purchasing new devises (synthesizer, multipliers, power supply…), re-organization of the space and materials, checking the state of the old components, creating a working protocol, etc.

 Stark modulation spectroscopy was revealed itself as a powerful method of identification of new vibrational excited states in the pure rotational spectrum. Figure XIV.4 shows the vibrational excited states transitions of propenal that appear as satellites and all of them have the same transition pattern that makes them easily identified. This method was employed to obtain the initial assignments of the vibrational excited states of ethyl and vinyl cyanates and propenal. FM modulation spectrometers were then used to record the spectrum up to higher frequencies. On the basis of the Stark assignments it was relatively straightforward to follow the transition sequences; what was more complex was their analysis, especially in case of interactions between states. Further astronomical interesting molecules such as propynal, acrylic acid or methyl isocyanate can be analyzed to facilitate their detection in the ISM.
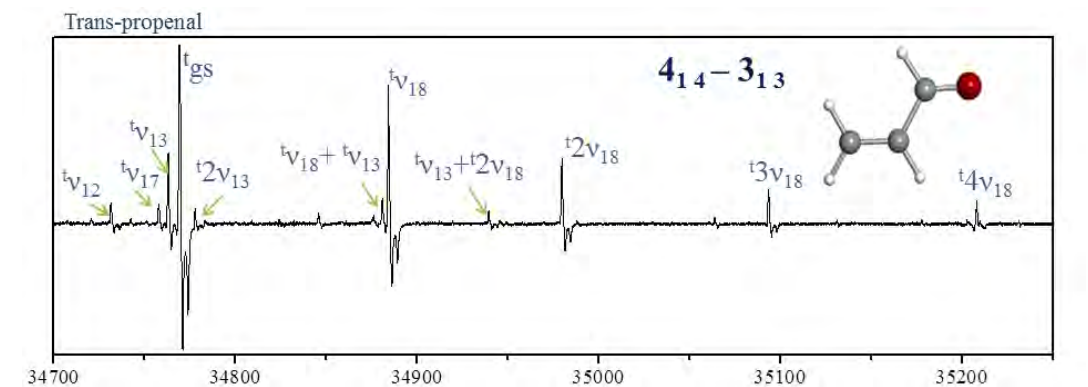
FIGURE XIV.4: *Vibrational excited state transition 414←313 in the Stark spectrum of transitions of trans-propenal.*

APENDIX I. LABORATORY CHARACTERIZATION AND ASTROPHYSICAL DETECTION OF VIBRATIONAL EXCITED STATES OF ETHYL CYANIDE

LABORATORY CHARACTERIZATION AND ASTROPHYSICAL DETECTION OF VIBRATIONALLY EXCITED STATES OF ETHYL CYANIDE

A. M. DALY[1], C. BERMÚDEZ[1], A. LÓPEZ[2], B. TERCERO[2], J. C. PEARSON[3], N. MARCELINO[4], J. L. ALONSO[1], AND J. CERNICHARO[2]

[1] Grupo de Espectroscopia Molecular (GEM), Edificio Quifima, Área de Química-Física, Laboratorios de Espectroscopia y Bioespectroscopia, Unidad Asociada del CSIC, Universidad de Valladolid, E-47005 Valladolid, Spain; adammichael.daly@uva.es, cbermu@qf.uva.es, jlalonso@qf.uva.es
[2] Department of Astrophysics, CAB, INTA-CSIC, Crta Torrejón, E-28850 Torrejón de Ardoz, Madrid, Spain; lopezja@cab.inta-csic.es, terceromb@cab.inta-csic.es, jcernicharo@cab.inta-csic.es
[3] Jet Propulsion Laboratory, California Institute of Technology, 4800 Oak Grove Dr., Padadena, CA 91109, USA; John.C.Pearson@jpl.nasa.gov
[4] National Radio Astronomy Observatory, 520 Edgemont Road, Charlottesville, VA 22903, USA; nmarceli@nrao.edu

ABSTRACT

Ethyl cyanide, CH_3CH_2CN, is an important interstellar molecule with a very dense rotational–vibrational spectrum. On the basis of new laboratory data in the range of 17–605 GHz and ab initio calculations, two new vibrational states, ν_{12} and ν_{20}, have been detected in molecular clouds of Orion. Laboratory data consist of Stark spectroscopy (17–110 GHz) and frequency-modulated spectrometers (GEM laboratory in Valladolid: 17–170, 270–360 GHz; Toyama: 26–200 GHz; Emory: 200–240 GHz; Ohio State: 258–368 GHz; and JPL: 270–318, 395–605 GHz). More than 700 distinct lines of each species were measured in J up to 71 and in K_a up to 25. The states were fitted with Watson's S-reduction Hamiltonian. The two new states have been identified in the interstellar medium toward the Orion Nebula (Orion KL). The ground state, the isotopologues of CH_3CH_2CN, and the vibrationally excited states have been fitted to obtain column densities and to derive vibrational temperatures. All together, ethyl cyanide is responsible for more than 2000 lines in the observed frequency range of 80–280 GHz.

Key words: ISM: abundances – ISM: individual objects (Orion KL) – ISM: molecules – line: identification – surveys

Online-only material: color figures, machine-readable tables

1. INTRODUCTION

Ethyl cyanide, CH_3CH_2CN, was first identified by Johnson et al. (1977) in the Orion Nebula and has subsequently been identified in several other high-mass star-forming regions (Miao & Snyder 1997; Cazaux et al. 2003). The isotopologues ^{13}C and ^{15}N in their ground state have been detected in Orion (Demyk et al. 2007; Margulès et al. 2009) using the line survey between 80 and 280 GHz carried out with the 30 m radio telescope of the Institute de Radio Astronomie Millétrique (IRAM; Tercero et al. 2010, 2011, 2012). The density of lines in this source, as observed with the 30 m telescope, makes this frequency survey a line confusion-limited one, despite very short integration times, and produces a forest of lines arising from isotopologues and vibrationally excited states of abundant species such as ethyl cyanide, methyl formate (Carvajal et al. 2009; Margulès et al. 2010; Kobayashi et al. 2007; Demyk et al. 2008; Tercero et al. 2012), methanol, SiS, SiO, OCS, CS, HCO^+, etc. (see, e.g., Tercero et al. 2010, 2011). If all the weak lines produced by these species are not identified and assigned, the quest for chemical complexity stops for line intensities larger than 1 K in sources such as Orion, and the detection of new molecular species becomes a very hard task. In Orion, Tercero and collaborators used values for the intensity of lines that are above the confusion limit of 0.03, 0.05, and 0.1 K (in antenna temperature) at 3, 2, and 1.3 mm wavelengths, respectively; values that are reached in a few minutes of observing time. The number of features in the line survey above these limits exceeds 15,000, and after assignment of the obvious features to the most abundant species (45 molecules), 4000 lines remain to be identified.

The detection of the isotopic species of ethyl cyanide (Demyk et al. 2007; Margulès et al. 2009) and the very intense spectrum measured of the parent species suggests that highly excited vibrational states of ethyl cyanide could be present in this source. This has been the case for objects with similar physical conditions such as Sgr B2, where Mehringer et al. (2004) have reported the detection of the in-plane bending vibration, $\nu_{13} = 1$, and the $\nu_{21} = 1$ torsional state toward Sgr B2(N-LMH). The increase in sensitivity of instruments such as ALMA and the opening of new spectral windows from space observatories (*Herschel*) will rely on the assignment of the low-lying vibrational states of abundant molecules to penetrate the line forest they produce. Without this spectral information, the full power of line surveys will be strongly limited and the data produced by new instruments will not be fully exploited. High-resolution spectroscopic work has been done for the ground state isotopologues of abundant species, but reliable rotational constants for a large number of low energy vibrational modes of polyatomic molecules, such as ethyl cyanide, have yet to be published. While the emission from isotopologues will depend on the isotopic abundances (e.g., $\simeq 40$–50 for $^{12}C/^{13}C$), the emission from low energy vibrationally excited states will depend on the vibrational temperature. In hot cores with $T_K \simeq 200$ K, the levels around 150–200 cm^{-1} above the ground state will have line intensities 1/3–1/5 of those of the ground state. A systematic study of the effect of temperature on the spectrums from 210 to 270 GHz and 570 to 645 GHz of this molecule has been performed by Fortman et al. (2010a, 2010b), who measured 9962 strong lines of ethyl cyanide in the range of 575–645 GHz and 3000 strong lines from 210 to 260 GHz in the laboratory. Not all of these states could be assigned to known vibrational states of ethyl cyanide, highlighting the importance of systematic studies that can identify vibrational states.

The ground state rotational a-type and b-type transitions of the parent ethyl cyanide have been assigned up to $J = 120$, with measurements in the laboratory reaching 1.6 THz
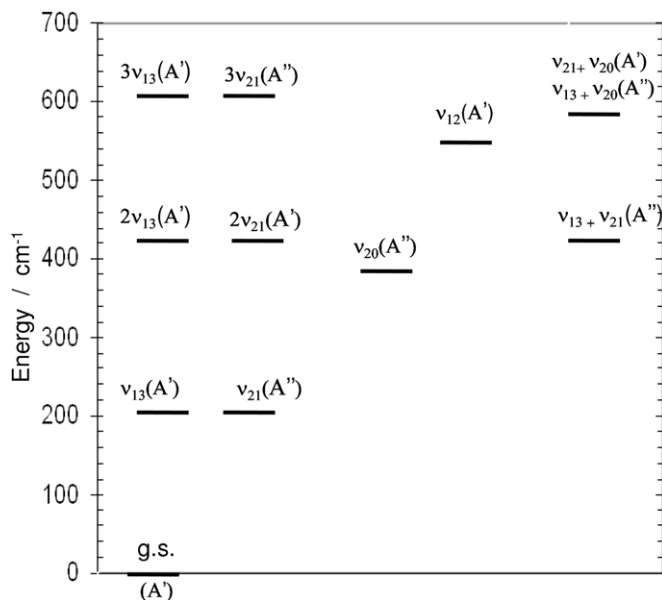
Figure 1. Vibrational states of ethyl cyanide below 700 cm^{-1}, excluding states made by difference.

(Pearson et al. 1994; Brauer et al. 2009). The dipole moments have been measured recently by Krasnicki & Kisiel (2011). Early observations of microwave transitions from excited vibrational states were assigned by Duncan & Janz (1955) and the gas-phase structure supporting the C_s symmetry was reported by Lerner & Dailey (1957). These states were identified by Laurie (1959) to arise from the two lowest energy states, the torsion (ν_{13} at 206 cm^{-1}) and in-plane bend (ν_{21} at 212 cm^{-1}) states, and were assigned to the A$'$ and A$''$, respectively, in Heise et al. (1981). The states below 700 cm^{-1} are shown in Figure 1 with their respective symmetries. The two overtone and combination bends also contribute to further complicating the spectrum. The first relatively unperturbed state was assigned and studied for the first time by Fukuyama et al. (1999); this was ν_{20} at 373 cm^{-1}. This study included the ground, ν_{13}, ν_{21}, and ν_{20} in a four-state fit, and μ_a and μ_b transitions were assigned up to $J = 16$ and $K_a = 4$. As part of our investigation of unassigned states of ethyl cyanide in the interstellar medium, we have continued the assignment of this state to obtain accurate spectroscopic constants for positive identification. The state ν_{12} at 534 cm^{-1} lies well above the three states of $2\nu_{13}$, $2\nu_{21}$, and $\nu_{13} + \nu_{21}$ at 410 cm^{-1} and just below the states at 570 cm^{-1} : $\nu_{13} + \nu_{20}$ and $\nu_{21} + \nu_{20}$ (see Figure 1). To disentangle these states, low frequency measurements using the Stark modulation spectrometer in Valladolid were performed. This technique is ideally suited for the identification of vibrational states due to the high sensitivity and distinct shape of the Stark pattern for each transition type. The vibrational satellite pattern around the ground state transition was modeled using ab initio calculations to help identify new states assigned in the Stark spectra. Fits of a previously unassigned state, ν_{12}, and additional measurements of ν_{20} up to 360 GHz have provided accurate rotational and distortion constants that have greatly aided the identification of two new states in the clouds of Orion. Subsequently, we combined data from the published studies of Toyoma (26–200 GHz; Fukuyama et al. 1999), OSU (210–270 GHz; Fortman et al. 2010a), and JPL (440–530 GHz; Pearson et al. 1994; Brauer et al. 2009) and previously unpublished measurements at OSU (258–368 GHz), Emory (200–240), and JPL (270–318, 395–605 GHz) to create a fit that includes transitions up to $J = 71$ and $K_a = 25$.

The new assignments of ν_{20} and ν_{12} were used successfully to identify both states for the first time in Orion using the data provided by the IRAM telescope. We have included data from this study, previously published data of the coupled state of ν_{21} and ν_{13}, and isotopic data in the ground vibrational state to present an analysis of the relative densities of vibrationally excited states to isotopologues in the ground vibrational state. We provide a wide analysis of the molecule and column densities have been calculated for all species detected from ethyl cyanide in a consistent way.

2. EXPERIMENTAL

Ethyl cyanide was purchased from Sigma Aldrich and was used without further purification. The sample was placed into a glass cell and degassed using the common freeze-pump-thaw method to remove air from the sample. Sample pressure was maintained between 2–3 × 10^{-2} mbar or about 20 mTorr. Experiments were performed first in the frequency range of 26–40 GHz using a newly configured computer-controlled Stark-modulated spectrometer whose principle components have been described in Lessari et al. (1991) and extended to 50–110 GHz by incorporation of multipliers and detectors from Virginia Diodes, Inc., which will be described in detail in a later publication. For most measurements, an accuracy of 50 kHz for peak frequencies is given, as unresolved ^{14}N-nuclear quadrupole splitting is present in our measurements. Voltages ranging from 100 to 700 V were used to sufficiently separate the modulated signals to obtain reliable determination of the center frequency. Scans were performed in both directions and the sum of both scans was used for frequency determination.

The experiments performed in Valladolid with frequency modulation (FM) from 110 to 170 GHz and 240 to 360 GHz were carried out in a static free space glass cell with Teflon windows fitted with ports to evacuate and maintain pressures of 20 mTorr with a 2 m length and 12 cm diameter (Alonso et al. 1993). Active multipliers and detectors from Virginia Diodes were used to obtain 240–360 GHz using FM modulation, and those detected at 2f will be described in detail soon. Software written in LabVIEW was used to control the synthesizer (13–20 GHz) and record the signal capable of scanning 30 GHz in 10 hr in 1 GHz sections with a step size of 50 kHz. Scans were performed in both directions, and the average of both directions was used for frequency measurements with an accuracy of 50 kHz. The spectra were imported into AABS (Kisiel et al. 2005), and frequencies were determined using a fit from a Gaussian line shape.

Additional measurements covering 270–318 GHz and 395–605 GHz were performed at the Jet Propulsion Laboratory (JPL) using the spectrometer described in Drouin et al. (2005) and Pearson et al. (2011) and at the Ohio State University with the FASSST spectrometer covering 268–368 GHz (Petkie et al. 1997). Some additional spectra covering 200–240 GHz were collected at Emory University and (the study peak list of Fukuyama et al. 1996) covering 26–200 GHz was utilized. Lines measured at JPL and Emory were peak picked and are assumed to be accurate to 50 kHz, with strong isolated lines being significantly more accurate. The spectrum in the JPL measurements above 270 GHz is line confused, assuring that lines are almost never isolated. The FASSST lines were collected with an early version of the system and are only accurate to 200 kHz. Agreement between common measurements suggests that the asserted accuracies are, on average, reasonable.

Table 1
Scaled Values of ab initio Predictions for the Ground State and the
Vibrational States ν_{20} and ν_{12}

	G.S.	ν_{20}	ν_{12}
ΔE (cm^{-1})	0	369	530
A (MHz)	27663.7	28374.9	27423.1
B (MHz)	4714.2	4716.6	4708.3
C (MHz)	4225.1	4240.8	4229.0

Note. Method MP2/6−311++G(d,p).

3. ASSIGNMENT OF THE EXCITED STATES

3.1. Identification of ν_{12}

Ethyl cyanide, $\mu_a = 3.816(3)$ D and $\mu_b = 1.235(1)$ D (Krasnicki & Kisiel 2011), has a strong a-type spectra and is dominated by strong a-type R-branch transitions in the region below 700 GHz. For this reason, long scans with the Stark spectrometer experiments were performed at room temperature at pressures of 20 mTorr concentrated on the $K_a = 1$ transitions of $J = 2$–8. As expected, several signals with the same Stark shape as the ground state transition were observed. Using the Fukuyama data, transitions assigned to ν_{13}, ν_{21}, and ν_{20} were readily identified. Unknown signals were recorded and preliminary fits were made. To help understand which vibrational states may be present, optimization and frequency calculations were performed with MP2/6−311++G** in the Gaussian09 (Frisch et al. 2009) suite using an anharmonic potential. This calculation will give the first-order correction to the ground state rotational constants and can be used to simulate the data with columns, $\alpha_i^A \alpha_i^B \alpha_i^C$. Vibrationally averaged rotational constants are given as the sum, $A_e - \sum_{i=0}^{n}(\alpha_i^A)(v+1/2)$. Since the ground state rotational constants are well known, the difference between the predicted and calculated rotational constants can be added to each state to effectively shift all the states equally. This is summarized in Table 1 for the states $\nu_{20} = 1$ and $\nu_{12} = 1$.

An example spectrum is shown in Figure 2 with the simulated spectrum produced from ab initio calculations using MP2/6−311++G** (Frisch et al. 2009) for the 7_{17}–6_{16}. The intensities of the lines were estimated using the vibrational partition function and are scaled by the ground state to 1.

A comparison of the ab initio predicted values shows both excellent predictions for the assigned ν_{20} and ν_{13} states in the frequency up to $J = 8$, and a poor prediction of the placement of the ν_{21} state. The poor prediction for the ν_{21} state is due to a $\Delta K = 2$ resonance with $\nu_{13} = 1$, which the ab initio calculation does not take into account. Also, it is clear from the spectra that there are no equally spaced progressions for any of the assigned states. The rotational transitions from the three states assigned by Fukuyama et al. (1999) are consistently higher in frequency than the ground state as measured up to $J = 8$. A transition consistently lower in frequency was observed. A fit was made of A, B, C as adjustable parameters with the distortion constants fixed to the ground state values given in Brauer et al. (2009) using SPFIT (Pickett 1991). The rotational constants obtained were consistent with the predicted values of ν_{12}. At a given transition, the ν_{12} CCC bending state lies at lower frequency than the ground state and all the other known low-lying vibrational states. Additionally, it exhibits no measurable torsional splittings in any of the transitions observed. As a result, the transitions are all single lines, giving them comparable intensity to torsionally split transitions lying 200 cm^{-1} lower in energy. The a-type

Table 2
Summary of s-representation

	Experimental	
	ν_{12}	ν_{20}
A (MHz)	28081.9841(95)	27445.4006(86)
B (MHz)	4707.35767(23)	4715.64665(32)
C (MHz)	4228.63011(19)	4240.78292(31)
$D_J \times 10^3$ (kHz)	2.980519(84)	3.01522(19)
D_{JK} (kHz)	−48.3584(50)	−46.5397(26)
D_K (kHz)	582.3(15)	518.14(94)
d_1 (kHz)	−0.680293(43)	−0.68374(11)
d_2 (kHz)	−0.033681(40)	−0.027800(27)
H_J (kHz)	0.009274(13)	0.009299(59)
H_{KJ} (Hz)	−0.956(27)	−1.330(11)
H_{JK} (Hz)	. . .	−0.1430(30)
H_K (Hz)	−976. (23)	−296.(26)
h_1 (Hz)	0.0037837(71)	0.003950(40)
h_2 (Hz)	0.0003052(68)	. . .
h_3 (Hz)	0.0000431(38)	. . .
L_J (mHz)	. . .	−0.0000456(61)
L_{JJK} (mHz)	−0.00781(15)	. . .
L_{JK} (mHz)	−2.1412(39)	. . .
L_K (mHz)	8232. (71)	. . .
l_1 (mHz)	. . .	−0.0000276(44)
l_2 (mHz)	. . .	0.0000538(10)
l_3 (mHz)	. . .	0.00001561(63)
P_{JK} (μHz)	0.0562 (14)	. . .
σ_{fit} (MHz)	0.087	0.095
σ_{rms} (MHz)	1.60	1.65
$N_{\text{total}}/N_{\text{excluded}}$	1109/128	971/180

Note. Lines excluded based on a measured frequency greater than five times the assigned uncertainty.

R-branch is well separated from the ground state, which makes the assignments relatively straightforward.

We were able to include lines from ν_{20} in the Stark spectrum after re-fitting the Fukuyama et al. (1999) data with several blended lines removed. This state was included in a global fit in that study, but the reference uses a structural model that does not allow for easy calculation of unmeasured transitions. Transitions of a-type R-branch and b-type Q-branch were measured for both states in the region of 17–110 GHz using Stark spectrometer data and 110–170 GHz using FM modulation. Predictions were made for the region of 240–360 GHz and a record of this range was made. These data were fit with the Watson S-reduction (Watson 1977) using SPFIT, with 265 transitions eventually included in the fit using the combined Stark and FM modulation data up to 360 GHz.

3.2. Assignment of ν_{12} and ν_{20} to 605 GHz

We have compiled the data from several sources in the literature of OSU (Fortman et al. 2010b) combined with Fukuyama et al. (1996), Pearson et al. (1994), and Brauer et al. (2009), which allowed us to extend the fit to JPL 605 GHz including transitions up to $J = 71$, $K_a = 25$ using the S-reduction. Both reductions were shown to give similar results in the study of the ground state.

These assignments were fit using the Hamiltonian in the S-reduction, including the octic (P^8) and a single decic term, P_{JK}, which are centrifugal constants for a semi-rigid molecule, and are given in Table 2. Tables of all the assigned transitions are given in the online journal for both states (tables sorted
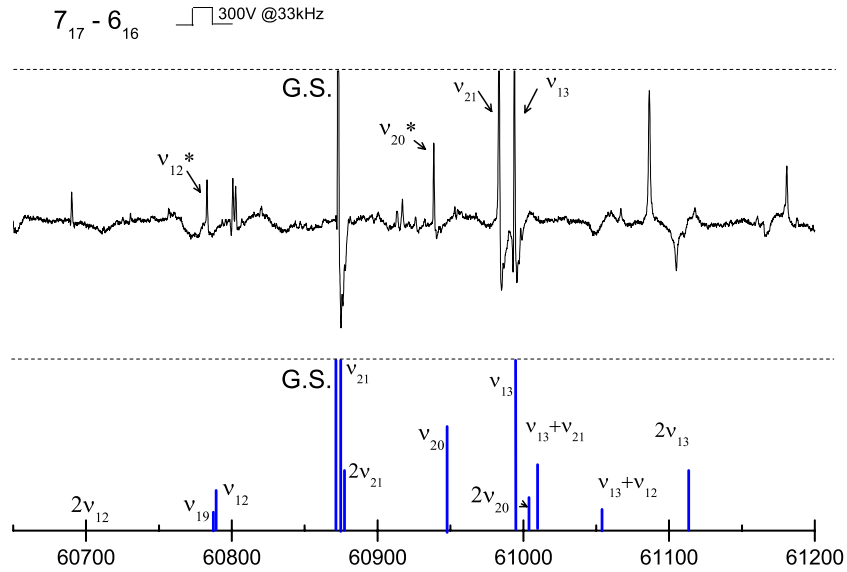
Figure 2. Plot of the 7_{17}–6_{16} scan using the Stark spectrometer and ab initio simulation of the data, above and below, respectively. Rotational constants used to predict the transitions are shifted by the ground state difference between prediction and experimental. Intensities are estimated using the vibrational partition function and have been scaled to the ground state. The graph is expanded to show the excited states.

(A color version of this figure is available in the online journal.)

by frequency and quantum number for ν_{20} and ν_{12} given in Tables 4–7). Excluding internal rotation and other types of coupling, are given as

$$
\begin{aligned}
H = {} & A J_a^2 + B J_b^2 + C J_c^2 - D_J J^4 - D_{JK} J^2 J_c^2 \\
& - D_K J_c^4 + d_1 J^2 (J_+^2 + J_-^2) + d_2 (J_+^4 - J_-^4) \\
& + H_J J^6 + H_{JK} J^4 J_c^2 + H_{KJ} J^2 J_c^4 + H_K J_c^6 \\
& + h_1 J^4 (J_+^2 + J_-^2) + h_2 J^2 (J_+^4 - J_-^4) + h_3 (J_+^6 - J_-^6) \\
& + L_J J^8 + L_{JJK} J^6 J_c^2 + L_{JK} J^4 J_c^4 + L_{KKJ} J^2 J_c^6 \\
& + L_K J^8 + l_1 J^6 (J_+^2 + J_-^2) + l_2 J^4 (J_+^4 - J_-^4) \\
& + l_3 J^2 (J_+^6 - J_-^6) + l_4 (J_+^8 - J_-^8) + P_{JK} J^6 J_c^4.
\end{aligned}
$$

In the ν_{20} and ν_{12} states, there are several K_a states that were found to be perturbed and have significant deviation from the fit or are split due to internal rotation. Lines were not included in the fit if the difference between predicted and assigned was found to be more than five times the assigned uncertainty. Torsional splittings were observed in all ν_{20} b-type transitions reported by Fukuyama et al. (1999), and they are observed in a-type transitions with $K_a = 2$, $K_a = 3$, and $K_a = 12$–14. Significant deviations for small ranges of J are observed for ν_{20} in $K_a = 4,6,7,11,12,14,15,16$ and for the states $K_a = 12,13$ in ν_{12}. The torsional effects observed in ν_{20} are an order of magnitude larger than those observed in the ground state. It is known that the couplings between ν_{20} and $2\nu_{21}$ and ν_{20} and $2\nu_{13}$ are weak. However, it is possible that there is a much stronger interaction with the same symmetry combination band $\nu_{21} + \nu_{13}$ that leads to the deviations in the K_a states. If the interaction originates from a quanta in the torsional state, the splitting, which has been ignored in this study, might be inverted relative to the normal ground state. The spectrum of ν_{20} and ν_{12} up to 605 GHz has been fit to be independent of any coupling from another torsion state ($2\nu_{21}$ 412 cm^{-1}, $2\nu_{13}$ 414 cm^{-1} and $\nu_{13} + \nu_{21}$ 419 cm^{-1}, and $\nu_{20}+ \nu_{13}$ 570 cm^{-1} and $\nu_{20}+ \nu_{21}$ 574 cm^{-1}, respectively). The lowest three states are most likely coupled with ν_{20} and the upper two are suspected to be coupled with ν_{12}. Future studies

with clear assignments of $2\nu_{21}$, $2\nu_{13}$, and $\nu_{13} + \nu_{21}$ may reveal the extent of coupling for the excited vibrational state of ν_{20}. A similar exercise would be required for $\nu_{20} + \nu_{13}$ and $\nu_{20} + \nu_{21}$ to determine the extent of interactions with ν_{12}, but for the purposes of astronomical assignments of the a-type spectrum to 300 GHz, these difficult steps can be neglected—though at higher frequencies than reported here ν_{12} clearly becomes perturbed.

There are several important points in utilizing the present analysis for astronomical searches. First, we have neglected the torsional splittings of the b-type transitions in the ν_{20} state. The b-type transitions in the ν_{20} state are all split by a few MHz, and the constants will give what we believe is the A-state line. Confirming that it is in fact the A-line will require understanding the origin of the torsional splittings, which is beyond the scope of the present effort. Second, interactions with higher states were neglected and very few b-type transitions changing K were included. As such, the H_K and L_K constants are not going to accurately predict the higher K b-type transitions. It is known that assignment of the high frequency b-type R-branch spectrum based on the present work is impossible. Finally, the spectrum becomes progressively more perturbed with increasing J, with the interactions spreading rapidly to lower K values. However, the majority of a-type R branches are predicted sufficiently well for astronomical assignments.

4. CH₃CH₂CN IN ORION KL

4.1. Observations and Overall Results of the Line Survey

Astronomical observations were carried out with the IRAM 30 m telescope from 2004 September to 2007 January in four different sessions, pointing toward the IRc2 source at $\alpha_{2000.0} = 5^h 35^m 14\overset{s}{.}5$, $\delta_{2000.0} = -5°22'30\overset{''}{.}0$ (J2000.0). Four SiS receivers were operating simultaneously at 3, 2, and 1.3 mm. Image side band rejections and system temperatures were in the ranges of 13–27 dB and 100–800 K, respectively, for all the frequency range covered. The calibration of the intensity scale was performed using two absorbers at different temperatures and

Table 3
Physical-chemical Conditions of Orion-KL from CH_3CH_2CN

	Hot Core 1	Hot Core 2	Hot Core 3
d_{sou} ($''$)	4	10	25
Offset ($''$)	5	5	5
v_{exp} (km s^{-1})	5	13	22
v_{LSR} (km s^{-1})	5	3	3
T_{ETL} (K)	275	110	65
$N(CH_3CH_2CN)$ (cm^{-2})	$(3.0 \pm 0.9) \times 10^{16}$	$(8 \pm 2) \times 10^{15}$	$(3.0 \pm 0.9) \times 10^{15}$
$N(CH_3CH_2CN\ \nu_{13} = 1/\nu_{21} = 1)$ (cm^{-2})	$(4 \pm 1) \times 10^{15}$	$(1.1 \pm 0.3) \times 10^{15}$	$(4 \pm 1) \times 10^{14}$
$N(CH_3CH_2CN\ \nu_{20})$ (cm^{-2})	$(1.7 \pm 0.5) \times 10^{15}$	$(4 \pm 1) \times 10^{14}$	$(1.7 \pm 0.5) \times 10^{14}$
$N(CH_3CH_2CN\ \nu_{12})$ (cm^{-2})	$(6 \pm 3) \times 10^{14}$	$(1.6 \pm 0.5) \times 10^{14}$	$(6 \pm 3) \times 10^{13}$
$N(^{13}CH_3CH_2CN)$ (cm^{-2})	$(7 \pm 2) \times 10^{14}$	$(1.9 \pm 0.6) \times 10^{14}$	$(7 \pm 2) \times 10^{13}$
$N(CH_3^{13}CH_2CN)$ (cm^{-2})	$(7 \pm 2) \times 10^{14}$	$(1.9 \pm 0.6) \times 10^{14}$	$(7 \pm 2) \times 10^{13}$
$N(CH_3CH_2^{13}CN)$ (cm^{-2})	$(7 \pm 2) \times 10^{14}$	$(1.9 \pm 0.6) \times 10^{14}$	$(7 \pm 2) \times 10^{13}$
$N(CH_3CH_2C^{15}N)$ (cm^{-2})	$(2 \pm 1) \times 10^{14}$	$(5 \pm 3) \times 10^{13}$	$(1.7 \pm 0.8) \times 10^{13}$
$N(A\text{-}CH_2DCH_2CN)$ (cm^{-2})	$\leqslant 6 \times 10^{14}$	$\leqslant 2 \times 10^{14}$	$\leqslant 6 \times 10^{13}$
$N(S\text{-}CH_2DCH_2CN)$ (cm^{-2})	$\leqslant 7 \times 10^{14}$	$\leqslant 1 \times 10^{14}$	$\leqslant 6 \times 10^{13}$
$N(CH_3CHDCN)$ (cm^{-2})	$\leqslant 6 \times 10^{14}$	$\leqslant 2 \times 10^{14}$	$\leqslant 6 \times 10^{13}$

Note. Physical-chemical conditions of Orion-KL from the analysis of ethyl cyanide emission lines in the range of 80–280 GHz.

the atmospheric transmission model (Cernicharo 1985; Pardo et al. 2001b). Observations were made in the balanced wobbler-switching mode, with a wobbling frequency of 0.5 Hz and a beam throw in the azimuth of $\pm 240''$. Quasars 0420−014 and 0528+134 were used to check pointing and focus. All spectra have 1 or 1.25 MHz of spectral resolution. As backends, two filter banks with 512×1 MHz channels and a correlator providing two 512 MHz bandwidths and 1.25 MHz resolution were used.

For further description of the observations and data reduction see Tercero et al. (2010).

Within the frequency domains 80–115.5, 130–178, and 196–281 GHz (168 GHz bandwidth covered), more than 15,000 spectral features have been detected. We found a total of 45 molecules, including 191 different isotopologues and vibrationally excited states. To date, more than 4000 spectral features are still unidentified (Tercero et al. 2010, 2011).

In the analysis of the emission lines of this line survey by Gaussian fits, we mainly found, in agreement with previous works, four different components characterized by different physical and chemical conditions (see Blake et al. 1987, 1996; Tercero et al. 2010, 2011, and references therein): (1) the *extended ridge* or ambient cloud ($T_k \simeq 60$ K, $n(H_2) \simeq 10^5$ cm^{-3}) at $v_{LSR} \simeq 9$ km s^{-1} and $\Delta v \simeq 4$ km s^{-1} traced by emission of simple molecules such us CO, CS, NS, or CCH; (2) the *compact ridge* ($v_{LSR} \simeq 8$ km s^{-1}, $\Delta v \simeq 3$ km s^{-1}, $T_k \simeq 110$ K, $n(H_2) \simeq 10^6$ cm^{-3}), a compact region rich in oxygen bearing and complex molecules such as HCOOCH$_3$, CH$_3$OH, and CH$_3$OCH$_3$ that was identified for the first time by Johansson et al. (1984); (3) the *plateau*, a mixture of outflows, shocks, and interactions with the ambient cloud ($v_{LSR} \simeq 6$–10 km s^{-1}, $\Delta v \gtrsim 25$ km s^{-1}, $T_k \simeq 150$ K, $n(H_2) \simeq 10^6$ cm^{-3}). This component is traced by molecules produced in shock chemistry (SO, SO$_2$, or SiO); and (4) a *hot core* component ($v_{LSR} \simeq 5$ km s^{-1}, $\Delta v \sim 10$ km s^{-1}, $T_k \simeq 225$ K, $n(H_2) \simeq 5 \times 10^7$ cm^{-3}) characterized by a N-rich chemistry. Molecules such as ethyl cyanide come mainly from this component.

4.1.1. 2D Survey Observations

In addition to the single pixel line survey of Orion KL, we also performed a 2D line survey between 210 and 275 GHz in

2008 and 2010. The maps covered an area of 140×140 arcsec^2 with a sampling of 4 arcsec. The observations were performed using the On-The-Fly mapping mode with reference position 10 arcmin west of Orion KL. This 2D line survey has been used to select different transitions of CH$_3$CH$_2$CN and to study the spatial extent of its emission. The EMIR single pixel heterodyne receivers were used for all observations except for the 220 GHz frequency setting, for which the HERA receiver array was used. The WILMA backend spectrometer was used for all observations, with a total bandwidth of 4 GHz and a spectral resolution of 2 MHz, corresponding to velocity resolutions of 5.4–2.5 km s^{-1} at 110 and 239 GHz, respectively. The telescope pointing was checked every 2 hr and found to have errors of typically less than 3 arcsec. The data were processed using the IRAM GILDAS software package.[5] Data reduction consisted of removing bad pixels, checking for image sideband contamination and emission from the reference position, and fitting and removing first-order baselines.

4.2. Detection of Excited Vibrational States and Isotopologues

4.2.1. Detection

The new laboratory and theoretical work presented above allows us to detect two new species (ν_{20} and ν_{12} vibrationally excited states of ethyl cyanide) in our line survey and for the first time in space. In the following sections, we will focus on the analysis of the detected spectral features from all species of ethyl cyanide (ground state, isotopologues, and vibrationally excited states). This analysis follows the proceedings of our previous works (Tercero et al. 2010, 2011, 2012; Demyk et al. 2007; Margulès et al. 2009, 2010; Carvajal et al. 2009; Motiyenko et al. 2012).

Ethyl cyanide (CH$_3$CH$_2$CN) shows emission from a large number of lines in this frequency band. Line detections in our survey include the ground vibrational state of five isotopologues (CH$_3$CH$_2$CN, ^{13}CH$_3$CH$_2$CN, CH$_3^{13}$CH$_2$CN, CH$_3$CH$_2^{13}$CN, CH$_3$CH$_2$C^{15}N; Demyk et al. 2007; Margulès et al. 2009), plus four vibrationally excited states of the main isotopologue ($\nu_{13} = 1/\nu_{21} = 1$; ν_{12}: torsion in the plane; and ν_{20}:

---

[5] http://www.iram.fr/IRAMFR/GILDAS
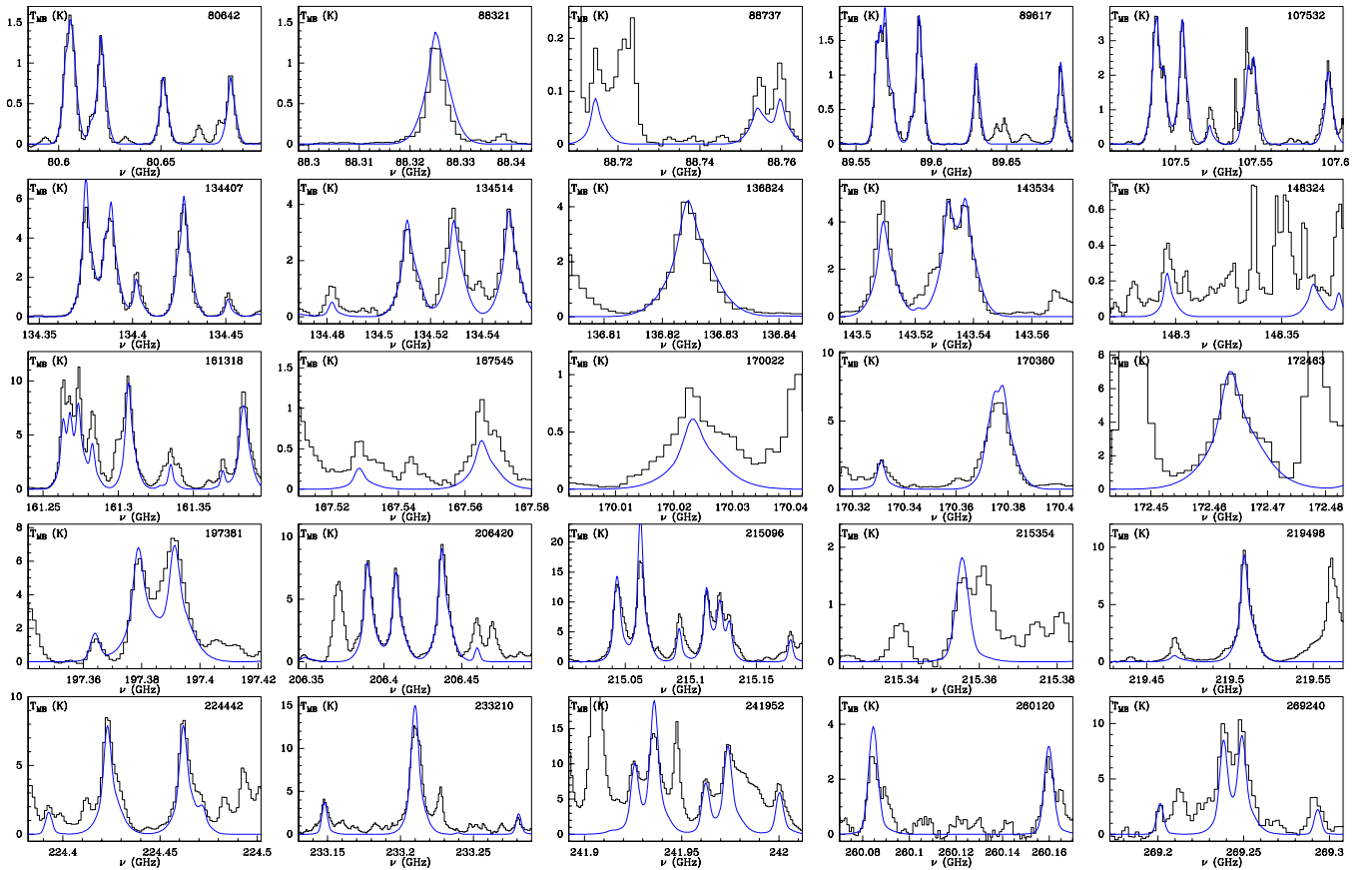
Figure 3. Observed lines from Orion KL (histogram spectra) and the model (thin curves) of ethyl cyanide in the ground state.
(A color version of this figure is available in the online journal.)

torsion out of the plane). The last two were detected here for the first time in space. Only a tentative detection is presented for the deuterated species, A/S-CH$_2$DCH$_2$CN and CH$_3$CHDCN (Margulès et al. 2009), because of the weakness of the features and/or their overlap with other spectral lines.

Isotopologue species have been characterized in Demyk et al. (2007) and Margulès et al. (2009). Here, we present observed line parameters and intensities, as well as the predicted frequencies, for all lines that are not strongly blended with other species from the vibrationally excited states (Tables 8–10 in the online version). In this paper, we provide a wide analysis of the molecule, and the column densities have been calculated in a consistent way for all species detected from ethyl cyanide.

The rotational constants were implemented in the MADEX code (Cernicharo 2012), which was used to calculate the emerging spectrum from the four cloud components. Table 10 gives the line intensity derived from the model predictions. In Tables 8–10, the observed brightness temperature has been obtained from the peak emission channel in the spectra. For that, the observed main beam temperature of weak blended lines is affected by the emission of the molecules that overlap in the same feature and this value, in those cases, has to be considered an upper limit. Hence, we have not showed highly blended lines in those tables. Nevertheless, the predicted intensities agree with the observations of the detected lines (see below, Figure 4).

For strong non-blended lines, we also provide the parameters of the lines derived by fitting Gaussian profiles with CLASS

software.[6] We note that the line parameters for these stronger lines match those of the hot core component. For the two new detected vibrationally excited states, ν_{20} and ν_{12}, we assigned 66 and 56 unblended lines, respectively.

Figures 3 and 4 show selected detected lines of ethyl cyanide in the ground state and in the three detected vibrational states, respectively, together with our best-fit-model line profiles.

Figure 4 shows many detected lines of CH$_3$CH$_2$CN ν_{20} and ν_{12} without blending with other species. The good fit between model and observations appears to be the first detection in space of both ethyl cyanide vibrationally excited states.

5. ASTRONOMICAL MODELING OF CH$_3$CH$_2$CN IN ORION KL

5.1. CH$_3$CH$_2$CN Maps

From the 2D survey data of Orion KL, maps of the integrated intensity of four ground state transitions of CH$_3$CH$_2$CN at different velocity ranges are shown in Figure 5 (line 1 to 4: $30_{2,28}-29_{2,27}$, $31_{2,30}-30_{2,29}$, $32_{0,32}-31_{0,31}$, and $32_{1,32}-31_{0,31}$, respectively). The velocity structure of the CH$_3$CH$_2$CN emission shows the contribution from two cloud components: a compact component at the position of the hot core and a more extended component. Note that there is not a spatial displacement of the emission peak with velocity. Particularly interesting is the spatial distribution of the red and blue wings at the largest

---

Figure 4. Observed lines from Orion KL (histogram spectra) and the model (thin curves) of vibrationally excited ethyl cyanide.
(A color version of this figure is available in the online journal.)
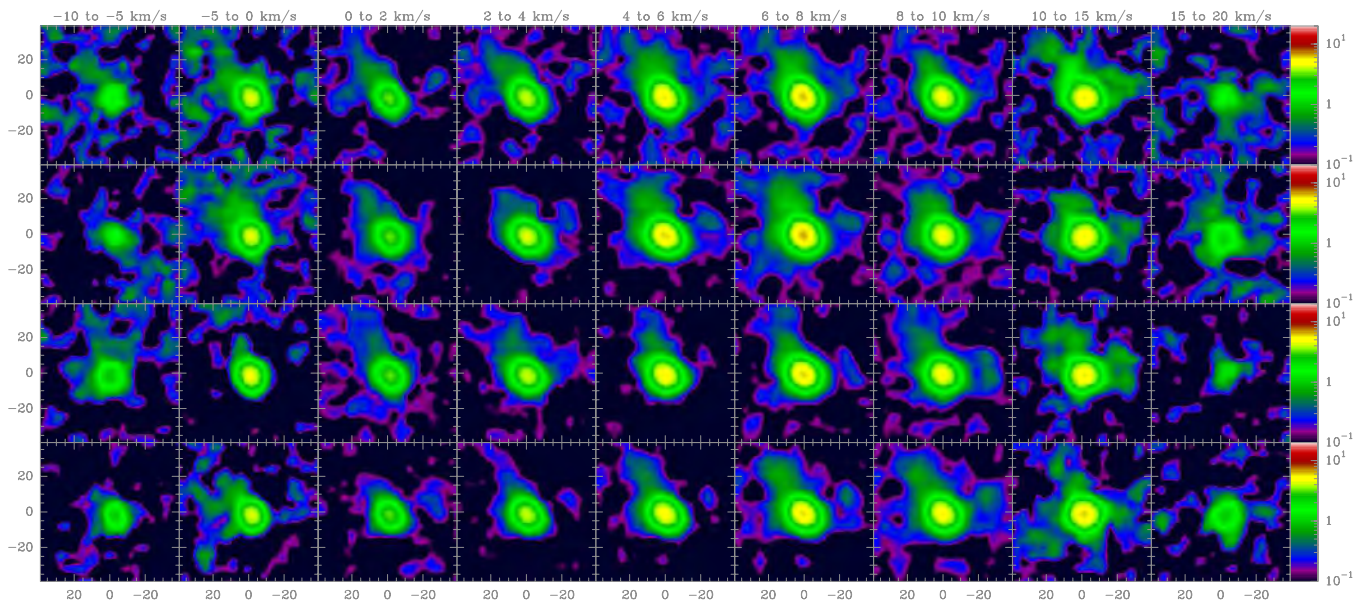
Figure 5. Integrated intensity of four transitions of ethyl cyanide (line 1 to 4: $30_{2,28}-29_{2,27}$, $31_{2,30}-30_{2,29}$, $32_{0,32}-31_{0,31}$, and $32_{1,32}-31_{0,31}$, respectively) at different velocity ranges (indicated in the top of each column). For each box, axes are in units of arcseconds ($\Delta\alpha$, $\Delta\delta$). Color logarithm scale is the integrated intensity ($\int T_A^* dv$) in units of K km s^{-1}.

(A color version of this figure is available in the online journal.)

velocities where we note the contribution of the plateau centering at the hot core position. The extended component appears at the northeast, at velocities from -5 to 15 km s^{-1}, following the delineation of the extended ridge (see, e.g., Wright et al. 1996). The observed structure in all transitions is in agreement with previous maps made with interferometric arrays by Wright et al. (1996) and Blake et al. (1996) in the 3 and 1.3 mm domains, respectively.

5.2. The Model

Radial velocities and line widths of the ethyl cyanide lines present in this line survey, together with the velocity maps shown above, suggest that the emission of these species comes mainly from the hot core. In addition, modeling the emission from the ^{13}C and ^{15}N isotopologues of ethyl cyanide (Demyk et al. 2007; Margulès et al. 2009), we found that the sum of two components, the hot core component and the plateau, is sufficient to reproduce all line intensities and profiles reasonably well.

For all detected ethyl cyanide species, column densities were calculated using an excitation and radiative transfer code developed by J. Cernicharo (Cernicharo 2012).

Owing to the lack of collisional rates for ethyl cyanide, we used LTE approximation. Nevertheless, as most of the emission comes from the hot core (a component with high density and temperature, see Section 4.1), the LTE approximation must work reasonably well. We assumed uniform physical conditions for the kinetic temperature, density, radial velocity, and line width (Table 3). These values are derived from the data analysis: the large number of transitions in a wide range of frequency allows us both to constrain these physical values by means of Gaussian fits and to attempt to simulate the line profiles with an LTE code. In addition, we performed a rotational diagram (Goldsmith & Langer 1999) of CH$_3$CH$_2$CN in its ground state (Figure 6), including 127 lines (transitions) free of blending with energies of the upper level from 23.5 to 449.2 K for two different Gaussian components of the emission lines. To quantify the beam telescope dilution, we considered a source diameter of 5″

and 10″ for the emitting region responsible for the narrow and broad profiles of the emission lines, respectively.

We have introduced a stratification of the hot core component to fit all the lines arising from ethyl cyanide species with the same physical source model (following the T_{rot} results of the rotational diagram). We considered three layers with different temperatures. Sizes and offsets from the pointing position (IRc2) of each component are taken into account in our model (maps of ethyl cyanide obtained with the 2D survey of Orion, N. Marcelino et al., in preparation, allow us to provide these parameters), and beam dilution is corrected for each line depending on their frequency. We did not observe any contributions from the error beam as most of cloud components are compact and lie inside the telescope beam. This setup gives the column density as the only free parameter. Sources of uncertainty are described in Tercero et al. (2010).

5.3. CH$_3$CH$_2$CN Column Densities

Column density results are shown in Table 3. Owing to the low intensity of the lines belonging to deuterated ethyl cyanide, implying larger overlap problems, we can only obtain upper limits for their column density. We estimate the uncertainty to be about 30% for the results of CH$_3$CH$_2$CN, CH$_3$CH$_2$CN $v_{13} = 1/v_{21} = 1$, CH$_3$CH$_2$CN v_{20}, and the ^{13}C isotopologues, whereas for CH$_3$CH$_2$CN v_{12} and CH$_3$CH$_2$C^{15}N we estimate the uncertainty to be 50% (due to the weakness of the observed lines for these species).

Figures 3 and 4 and Table 10 (in the online journal) show the comparisons between model and observations. Observed line intensities from all lines free of blending agree with the model predictions. For weaker observed lines, the lack of a good agreement is caused by overlap with other species.

Differences between column densities obtained with the rotational diagram and those derived from the model are mostly due to the source diameter considered in each component. We consider that this model fits these results better when taking into account all data introduced in it (rotational diagram results,
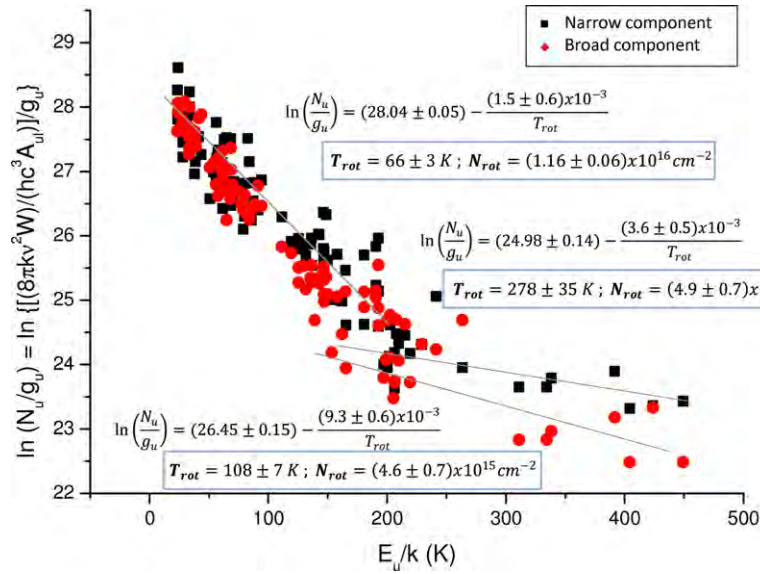
Figure 6. Rotational diagram of CH_3CH_2CN in its ground state.
(A color version of this figure is available in the online journal.)

Table 4
Measured Transitions of ν_{20} of Ethyl Cyanide Sorted by Frequency

J'	K_a'	K_c'	J''	K_a''	K_c''	ν_{obs}[a] (Hz)	ν_{obs}-ν_{cal}[b] (Hz)	Given Error[c] (Hz)	Flag[d]	Blended?[e]	Weighted Average Peak (Hz)
3	0	3	2	0	2	26839.519	−0.007	0.05			
3	1	2	2	1	1	27576.759	−0.067	0.05			
6	1	5	6	0	6	28352.470	−0.161	0.05			
7	1	6	7	0	7	30319.440	−0.087	0.05			
8	1	7	8	0	8	32665.470	−0.076	0.05			
6	0	6	5	1	5	33867.010	0.272	0.05	*		
4	1	4	3	1	3	34861.170	−0.083	0.05			
9	1	8	9	0	9	35422.430	0.011	0.05			
4	0	4	3	0	3	35751.461	0.021	0.05			
4	2	3	3	2	2	35820.625	−0.089	0.05			

Notes.
[a] Observed Frequency.
[b] Difference between observed and calculated frequencies.
[c] Error in ν.
[d] Non-fitted lines.
[e] Blended lines.

(This table is available in its entirety in a machine-readable form in the online journal. A portion is shown here for guidance regarding its form and content.)

diameters of the components following the 2D survey of Orion, velocity components from Gaussian fits, etc.).

We obtained a total column density of ethyl cyanide in the ground state of 4.1×10^{16} cm^{-2}. This result coincides with previous calculations: the source-averaged (hot core) CH_3CH_2CN column density was obtained by Comito et al. (2005) and Schilke et al. (2001) in their Orion surveys at high frequency (795–903 GHz and 607–725 GHz, respectively). However, Sutton et al. (1995) obtained a corrected-source-averaged column density of 2.4×10^{15} and 4.0×10^{15} for the hot core and compact ridge, respectively. In our line survey, we do not distinguish the spectral characteristic of the compact ridge in the ethyl cyanide lines.

For CH_3CH_2CN $\nu_{13} = 1/\nu_{21} = 1$, the derived column density (the same for each state) is one order of magnitude less than the derived column density of ethyl cyanide in the ground state. We obtained a total column density of $\simeq 2 \times 10^{15}$ and $\simeq 8 \times 10^{14}$ cm^{-2} for the ν_{20} and ν_{12} states, respectively.

5.4. Isotopic Abundances

From the derived column densities quoted above, we can now estimate the isotopic abundance ratios.

$^{12}C/^{13}C$. We obtained the same column density ratio for each ^{13}C isotopologue and cloud component: $\simeq 42 \pm 13$. Hence, no isotopic fractionation is found for these isotopologues of ethyl cyanide.

We obtain a factor of two lower than the solar isotopic abundance ($^{12}C/^{13}C = 90$; Anders & Grevesse 1989). This ratio is understood to be a direct measurement of the primary to secondary nuclear processing in stars (see Martín et al. 2010, and references therein) and is considered a sensitive indicator of the degree of galactic chemical evolution. Solar isotope value reflects conditions in the interstellar medium at an earlier epoch (Savage et al. 2002; Wyckoff et al. 2000).

In agreement with our study, Tercero et al. (2010) found an average value of $^{12}C/^{13}C = 45 \pm 20$. This result indicates a

Table 5
Measured Transitions of ν_{20} of Ethyl Cyanide[a]

J'	K_a'	K_c'	J''	K_a''	K_c''	ν_{obs}[b] (Hz)	$\nu_{obs}-\nu_{cal}$[c] (Hz)	Given Error[d] (Hz)	Flag[e]	Blended?[f]	Weighted Average Peak (Hz)
3	0	3	2	0	2	26839.519	−0.007	0.05			
4	0	4	3	0	3	35751.461	0.021	0.05			
5	0	5	4	0	4	44633.991	0.016	0.05			
6	0	6	5	0	5	53480.380	0.012	0.05			
7	0	7	6	0	6	62284.613	0.013	0.05			
8	0	8	7	0	7	71041.824	−0.011	0.05			
9	0	9	8	0	8	79748.976	0.065	0.05			
10	0	10	9	0	9	88404.817	0.023	0.05			
11	0	11	10	0	10	97010.865	0.007	0.05			
12	0	12	11	0	11	105570.915	0.039	0.05			

Notes.
[a] Lines sorted by type of transition: type of branch: R and Q; dipole moment: μ_a and μ_b; quantum number K_a; quantum number J.
[b] Observed Frequency.
[c] Difference between observed and calculated frequencies.
[d] Error in ν.
[e] Non-fitted lines.
[f] Blended lines.

(This table is available in its entirety in a machine-readable form in the online journal. A portion is shown here for guidance regarding its form and content.)

Table 6
Measured Transitions of ν_{12} of Ethyl Cyanide Sorted by Frequency

J'	K_a'	K_c'	J''	K_a''	K_c''	ν_{obs}[a] (Hz)	$\nu_{obs}-\nu_{cal}$[b] (Hz)	Given Error[c] (Hz)	Flag[d]	Blended?[e]	Weighted Average Peak (Hz)
2	1	2	1	1	1	17393.370	0.002	0.05			
2	0	2	1	0	1	17864.600	−0.002	0.05			
2	1	1	1	1	0	18350.740	−0.039	0.05			
3	1	3	2	1	2	26085.360	−0.038	0.05			
4	1	3	4	0	4	26097.404	−0.031	0.05			
5	1	4	5	0	5	27406.956	0.125	0.05			
3	1	2	2	1	1	27521.430	0.065	0.05			
6	1	5	6	0	6	29035.680	0.085	0.05			
7	1	6	7	0	7	31012.870	0.027	0.05			
6	0	6	5	1	5	33131.490	−0.042	0.05			

Notes.
[a] Observed Frequency.
[b] Difference between observed and calculated frequencies.
[c] Error in ν.
[d] Non-fitted lines.
[e] Blended lines.

(This table is available in its entirety in a machine-readable form in the online journal. A portion is shown here for guidance regarding its form and content.)

low opacity in the CH_3CH_2CN lines. Previous studies found a similar $^{12}C/^{13}C$ ratio in Orion (Johansson et al. 1984; Blake et al. 1987; Savage et al. 2002; Persson et al. 2007).

$^{14}N/^{15}N$. Our values of this ratio are very similar in all components. The $^{14}N/^{15}N$ average abundance ratio of our study is found to be 148 ± 74. In agreement with previous authors (Blake et al. 1987; Margulès et al. 2009) and within the observational errors, ^{15}N abundance obtained in this work appears to be similar to its terrestrial value ($^{14}N/^{15}N \simeq 274$; Anders & Grevesse 1989). Adande & Ziurys (2012) found that the $^{14}N/^{15}N$ ratio exhibits a distinct positive gradient with increasing distance from the Galactic center (toward 11 molecular clouds). This gradient is consistent with predictions of Galactic chemical evolution models in which ^{15}N has a secondary origin in novae.

D/H. We found a column density ratio for all deuterated species of 0.020 ± 0.010 in all considered components. In close agreement with our values, Tercero et al. (2010) found an $N(HDCS)/N(H_2CS)$ column density ratio of 0.05 ± 0.02 for the hot core component. Depending on the considered molecule and component, we found different values from the work of other authors: using $N(HDO)/N(H_2O)$, Pardo et al. (2001a) found an abundance ratio in the range 0.004–0.01 in the plateau component, and Persson et al. (2007) derived 0.005, 0.001, and 0.03 for the large velocity plateau, the hot core, and the compact ridge, respectively. Schilke et al. (1992) derived the DCN/HCN column density ratio in the hot core region, obtaining 0.001. A recent study of time dependence D/H fractionation from prestellar to protostellar cores (Aikawa et al. 2012) found that, even in warm regions, neutral species with high D/H ratios

Table 7
Measured Transitions of ν_{12} of Ethyl Cyanide[a]

J'	K_a'	K_c'	J''	K_a''	K_c''	ν_{obs}[b] (Hz)	$\nu_{obs}-\nu_{cal}$[c] (Hz)	Given Error[d] (Hz)	Flag[e]	Blended?[f]	Weighted Average Peak (Hz)
2	0	2	1	0	1	17864.600	−0.002	0.05			
4	0	4	3	0	3	35670.530	0.008	0.05			
5	0	5	4	0	4	44533.415	−0.032	0.05			
6	0	6	5	0	5	53360.500	−0.108	0.05			
7	0	7	6	0	6	62145.961	−0.045	0.05			
8	0	8	7	0	7	70884.747	−0.022	0.05			
9	0	9	8	0	8	79573.643	0.009	0.05			
10	0	10	9	0	9	88211.405	0.014	0.05			
11	0	11	10	0	10	96799.224	0.052	0.05			
12	0	12	11	0	11	105340.472	−0.003	0.05			

Notes.

[a] Lines sorted by type of transition: type of branch: R and Q; dipole moment: μ_a and μ_b; quantum number K_a; quantum number J.

[b] Observed Frequency.

[c] Difference between observed and calculated frequencies.

[d] Error in ν.

[e] Non-fitted lines.

[f] Blended lines.

(This table is available in its entirety in a machine-readable form in the online journal. A portion is shown here for guidance regarding its form and content.)

Table 8
Detected Lines of CH_3CH_2CN $\nu_{13} = 1/\nu_{21} = 1$

Transition[a] $J_{K_a,K_c,\nu} - J'_{K_a',K_c',\nu'}$	Predicted Frequency (MHz)	S_{ij}	E_u[b] (K)	ν_{LSR}[b,c] (km s^{-1})	$\delta\nu^2$ (km s^{-1})	T_{MB}[2] (K)	Area[b] (km s^{-1})
$9_{1,9,1}-8_{1,8,1}$	80481.139	15.20	330.5	4.3[1]		0.13	
$9_{2,8,0}-8_{2,7,0}$	80481.228*	15.20	330.5	4.6[1]		0.13	
				4.4 ± 0.5	10.6 ± 1.5	0.12	1.4 ± 0.2
$9_{2,8,1}-8_{2,7,1}$	80481.228*	15.20	330.5	0.7[1,3]		0.09	
$9_{3,7,0}-8_{3,6,0}$	80590.893	14.10	325.7	6.6[1,3]		0.09	
$9_{3,7,1}-8_{3,6,1}$	80592.859*	14.10	325.7	6.0[1,4]		0.13	
$9_{3,6,0}-8_{3,5,0}$	80715.621	14.10	325.6	6.6[1,4]		0.13	
$9_{4,6,0}-8_{4,5,0}$	80715.791*	14.10	325.6	4.0[1,4]		0.22	
$9_{4,5,2}-8_{4,4,2}$	80747.552	12.60	333.0	4.8[1,4]		0.22	
$9_{4,6,1}-8_{4,5,1}$	80747.778*	12.40	333.0	5.4[1,4]		0.22	

Notes.

[a] The line transition in the format $J_{K_a,K_c,\nu} - J'_{K_a',K_c',\nu'}$. The ν quantum number defines A and E states: $\nu = 0$ is A for the bend and $\nu = 3$ is A for the torsion; $\nu = 1$ and 2 are E for the bend and $\nu = 4$ and 5 are E for the torsion.

[b] The observed parameters are shown when the line is not blended with other molecule and no uncertainty is provided. Calculated parameters have uncertainties and mean the line can not be fitted like a Gaussian or there is some contribution from other molecule. (Narrow component (N), Wide component(W).)

[c] (1) peak line observed velocity. (2) peak line intensity. (3) blended with U-line. (4) blended with CH_3CH_2CN $\nu_{20} = 1$. (5) blended with $(CH_3)_2CO$. (6) blended with $HC^{13}CCN$. (7) blended with $HC^{13}CCN$ $\nu_7 = 1$. (8) blended with E-CH_3OD. (9) blended with $Si^{18}O$. (10) blended with E-$HCOOCH_3$. (11) blended with t-CH_3CH_2OH. (12) blended with $^{33}SO_2$. (13) blended with CH_3CHO $\nu_t = 2$. (14) blended with $SO^{18}O$. (15) blended with SO_2 $\nu_2 = 1$. (16) blended with HCOOH. (17) blended with $CH_3CH_2C^{15}N$. (18) blended with CH_2CHCN $\nu_{11} = 1$. (19) blended with CH_2CHCN $\nu_{15} = 1$. (20) blended with $^{34}SO_2$. (21) blended with HCCCN. (22) influence of CH_3CH_2CN $\nu_{12} = 1$. (23) blended with CH_3CH_2CN. (24) blended with A-$HCOOCH_3$. (25) blended with CH_3OH, $\nu_t = 0, 1$. (26) blended with g-CH_3CH_2OH. (27) blended with $^{13}CH_3OH$ $\nu_t = 0, 1$. (28) blended with $CH_2^{13}CHCN$. (29) blended with CH_3OCH_3. (30) blended with $SO^{17}O$. (31) blended with A-$HCOO^{13}CH_3$. (32) blended with E-$HCOO^{13}CH_3$.

(This table is available in its entirety in a machine-readable form in the online journal. A portion is shown here for guidance regarding its form and content.)

reflect the D/H ratio of those species that were injected from dust mantles (where icy material is highly deuterated by surface reactions with D atoms) to the hot gaseous medium. This is in agreement with other studies of hot core deuterium chemistry (Rodgers & Millar 1996). On the other hand, various complex organics (such us methyl formate) are formed via both gas-phase and grain surface reactions. Their high deuteration is mainly due to their formation from molecules with high deuteration (Aikawa et al. 2012). For ethyl cyanide, as a complex organic molecule, the process of deuteration most likely is the later case.

5.5. Vibrational Temperatures

We can estimate vibrational temperatures from

$$\frac{\exp\left(-\frac{E_{\nu_x}}{T_{vib}}\right)}{f_\nu} = \frac{N(CH_3CH_2CN\ \nu_x)}{N(CH_3CH_2CN)}, \quad (1)$$

where E_{ν_x} is the energy of the vibrational state (315.4, 531.2, and 763.4 K for ν_{21}, ν_{20}, and ν_{12}, respectively), T_{vib} is the vibrational temperature, f_ν is the vibrational partition function,

Table 9
Detected Lines of CH_3CH_2CN ν_{20}

Transition[a] $J_{K_a,K_c} - J'_{K'_a,K'_c}$	Predicted Frequency (MHz)	S_{ij}	E_u[b] (K)	ν_{LSR}[b,c] (km s^{-1})	$\delta\nu^2$ (km s^{-1})	$T_{MB}^{(2)}$ (K)	$T_{MB}^{(2)b}$ (K)
$9_{2,8}-8_{2,7}$	80470.356	8.55	567.6	$4.7^{(1)}$		0.03	
				5.8 ± 0.7	11.3 ± 1.5	0.03	0.40 ± 0.05
$9_{6,4}-8_{6,3}$	80470.356	8.55	567.6	$2.0^{(1,3)}$		0.25	
$9_{6,3}-8_{6,2}$	80665.506	5.00	602.9	$2.0^{(1,3)}$		0.25	
$9_{5,5}-8_{5,4}$	80665.506*	5.00	602.9	$7.6^{(1,3)}$		0.25	
$9_{5,4}-8_{5,3}$	80668.091*	6.22	590.8	$7.6^{(1,3)}$		0.25	
$9_{7,3}-8_{7,2}$	80668.091*	6.22	590.8	$5.7^{(1,3)}$		0.25	
$9_{7,2}-8_{7,1}$	80669.367*	3.56	617.2	$5.7^{(1,3)}$		0.25	
$9_{2,7}-8_{2,6}$	80669.367*	3.56	617.2	$6.1^{(1,4)}$		0.07	
$9_{1,8}-8_{1,7}$	81319.905	8.55	567.7	$6.1^{(1)}$		0.05	

Notes.

[a] The line transition in the format $J_{K_a,K_c} - J_{K'_a,K'_c}$.

[b] The observed parameters are shown when the line is not blended with other molecule and no uncertainty is provided. Calculated parameters have uncertainties and mean the line can not be fitted like a Gaussian or there is some contribution from other molecule. (Narrow component (N), Wide component (W).)

[c] (1) peak line observed velocity. (2) peak line intensity. (3) blended with CH_3OH $\nu_t = 0, 1$. (4) blended with $H_2C^{17}O$. (5) blended with U-line. (6) blended with ^{18}OCS. (7) blended with E-$HCOOCH_3$. (8) blended with CH_3CH_2CN ν_{13}/ν_{21}. (9) blended with A-$H^{13}COOCH_3$. (10) blended with E-$H^{13}COOCH_3$. (11) blended with $HCC^{13}CN$ $\nu_7 = 1$. (12) blended with SHD. (13) blended with $CH_3CH_2^{13}CN$. (14) influence of CH_3CH_2CN $\nu_{12} = 1$. (15) blended with A-$HCOOCH_3$. (16) blended with CH_3OCH_3. (17) blended with $(CH_3)_2CO$. (18) blended with CH_3CHDCN. (19) blended with $HCOO^{13}CH_3$. (20) blended with $^{33}SO_2$. (21) blended with $HC^{13}CCN$ $\nu_6 = 1$. (22) blended with CH_3-$^{13}CH_2CN$. (23) blended with $H^{15}NCO$.

(This table is available in its entirety in a machine-readable form in the online journal. A portion is shown here for guidance regarding its form and content.)

Table 10
Detected Lines of CH_3CH_2CN ν_{12}

Transition[a] $J_{K_a,K_c}-J'_{K'_a,K'_c}$	Predicted Frequency (MHz)	S_{ij}	E_u (K)	Observed Frequency[b] (MHz)	$\nu_{LSR}^{(1)}$ (km s^{-1})	Observed T_{MB} (K)	Model T_{MB} (K)
$9_{2,8}-8_{2,7}$	80288.056	8.55	799.3	80290.1	1.5	0.01	0.02
$9_{8,1}-8_{8,0}$	80495.806	1.89	867.3	80496.5	6.4	0.02	0.01
$9_{8,2}-8_{8,1}$	80495.806*	1.89	867.3	80496.5	6.4	0.02	0.01
$9_{4,6}-8_{4,5}$	80498.676	7.22	813.0	80499.8	4.8	0.02	0.02
$9_{4,5}-8_{4,4}$	80499.106*	7.22	813.0	80499.8	6.4	0.02	0.02
$9_{3,7}-8_{3,6}$	80528.735	8.00	805.0	80530.5	2.4	0.02	0.02
$9_{3,6}-8_{3,5}$	80560.434	8.00	805.0	80562.0	3.2	0.02	0.02
$9_{2,7}-8_{2,6}$	81129.013	8.55	799.5	81130.5	3.5	0.03	0.02
$10_{1,10}-9_{1,9}$	86693.722	9.90	799.6	$86694.4^{(2)}$	6.8	0.05	0.02
$10_{0,10}-9_{0,9}$	88211.372	9.98	799.0	88212.5	5.1	0.01	0.03

Notes.

[a] The line transition in the format $J_{K_a,K_c} - J_{K'_a,K'_c}$.

[b] (1) peak line observed velocity. (2) blended with U-line. (3) blended with ^{33}SO. (4) blended with A-$HCOOCH_3$. (5) blended with c-C_2H_4O. (6) blended with CH_2CHCN $\nu_{11} = 2$. (7) blended with CH_3CH_2CN ν_{13}/ν_{21}. (8) blended with NH_2D. (9) blended with H_2CCO. (10) blended with CH_3-$^{13}CH_2CN$. (11) blended with SO_2 $\nu_2 = 1$. (12) blended with E-$HCOOCH_3$. (13) blended with $^{13}CH_3CH_2CN$.

(This table is available in its entirety in a machine-readable form in the online journal. A portion is shown here for guidance regarding its form and content.)

$N(CH_3CH_2CN$ $\nu_x)$ is the column density of the vibrational state, and $N(CH_3CH_2CN)$ is the total column density of ethyl cyanide. Taking into account that $N(CH_3CH_2CN) = N(\text{ground}) \times f_\nu$, we only need the energy of each vibrational state and the calculated column densities to derive the vibrational temperatures.

We obtained the same T_{vib} in all cloud components for each vibrationally excited level, being $\simeq 160 \pm 50$ K, $\simeq 185 \pm 55$ K, and $\simeq 195 \pm 95$ K, for ν_{13}/ν_{21}, ν_{20}, and ν_{12}, respectively.

The values for ethyl cyanide $\nu_{13} = 1/\nu_{21} = 1$, ν_{20}, and ν_{12} in all components are similar to the averaged kinetic temperature we adopted in this model ($\simeq 150$ K). We assumed that both gases (ground state and vibrationally excited) are spatially coincident, so the calculated vibrational temperatures have to be considered as lower limits.

We note that the obtained T_{vib} for all levels is larger than the T_{rot} in the coldest component, pointing to an inner and hotter emitting region (shown in our model) for vibrationally excited ethyl cyanide. Comparing both temperatures is not an easy task, as temperature and density gradients in the region are required for the vibrational excitation. Collisional rates are necessary to ascertain whether either molecular collisions or IR dust photons dominate the vibrational excitation of ethyl cyanide.

6. CONCLUSION

Very sensitive low frequency Stark modulation experiments have been used to conclusively identify the excited vibrational state ν_{12} of ethyl cyanide. On the basis of fits made from

this work and the previously assigned ν_{20}, reliable rotational and distortion constants were obtained by measurements up to 605 GHz for both states.

The line survey of Orion KL with the IRAM 30 m telescope permitted the assignment of 66 and 56 free of blending spectral features that correspond to the first detection of the ethyl cyanide ν_{20} and ν_{12} species, respectively. The new detection of vibrationally excited ethyl cyanide, together with that of the three ^{13}C and the ^{15}N isotopologues and the tentative detection of deuterated ethyl cyanide (Demyk et al. 2007; Margulès et al. 2009) contributes more than 1000 lines in the 80–280 GHz domain covered by the Orion line survey of Tercero et al. (2010).

The present work clearly shows that the spectroscopic catalogs for heavy species could include the predicted spectra for all their vibrationally excited states with energies below three to four times the kinetic temperature of the gas. For vibrationally excited states with energies similar to the kinetic temperature of the gas, the intensities of their rotational lines will be much larger than those of the isotopologues of the ground state. For example, in Orion $^{12}C/^{13}C \simeq 50$, a vibrational level with $E_{vib} = T_K$ will have a population $\simeq 1/3$ of the ground state. The analysis of the spectral complexity of hot sources such as Orion requires a detailed laboratory study of the vibrational levels below 800 cm^{-1} of the most abundant species (CH$_3$CN, CH$_2$CHCN, CH$_3$CH$_2$CN, CH$_3$OH, CH$_3$OCOH, CH$_3$OCH$_3$, HCOOH, HNCO, and so on). Without this information, the analysis of future data coming from more sensitive instruments such as ALMA will be extremely limited.

REFERENCES

Adande, G. R., & Ziurys, L. M. 2012, ApJ, 744, 194
Aikawa, Y., Wakelam, V., Hersant, F., Garrod, R. T., & Herbst, E. 2012, ApJ, 760, 40
Alonso, J. L., Lessari, A. G., Leal, L. A., & López, J. C. 1993, JMoSp, 162, 4
Anders, E., & Grevesse, N. 1989, GeCoA, 53, 197
Blake, G. A., Mundy, L. G., Carlstrom, J. E., et al. 1996, ApJL, 472, L49
Blake, G. A., Sutton, E. C., Masson, C. R., & Philips, T. H. 1987, ApJ, 315, 621
Brauer, C. S., Pearson, J. C., Drouin, B. J., & Yu, S. S. 2009, ApJS, 184, 133
Carvajal, M., Margulès, L., Tercero, B., et al. 2009, A&A, 500, 1109
Cazaux, S., Tielens, A., Ceccarelli, C., et al. 2003, ApJL, 593, L51

Cernicharo, J. 1985, Internal IRAM Report (Granada: IRAM)
Cernicharo, J. 2012, in ECLA-2011: Proc. European Conf. on Laboratory Astrophysics, ed. C. Stehlé, C. Joblin, & L. d'Hendecourt (European Astronomical Society Publications Ser., Vol. 58; Cambridge: Cambridge Univ. Press), 251
Comito, C., Schilke, P., Philips, T. G., et al. 2005, ApJS, 165, 127
Demyk, K., Mäder, H., Tercero, B., et al. 2007, A&A, 466, 255
Demyk, K., Wlodarczak, G., & Carvajal, M. 2008, A&A, 489, 589
Drouin, B. J., Maiwald, F. W., & Pearson, J. C. 2005, RScI, 76, 093133
Duncan, N. E., & Janz, G. J. 1955, JChPh, 23, 434
Fortman, S. M., Medvedev, I. R., Neese, C. F., & De Lucia, F. C. 2010a, ApJ, 714, 476
Fortman, S. M., Medvedev, I. R., Neese, C. F., & De Lucia, F. C. 2010b, ApJ, 725, 1682
Frisch, M. J., Trucks, G. W., Schlegel, H. B., et al. 2009, Gaussian 09, Revision A.02 (Wallingford, CT: Gaussian, Inc.)
Fukuyama, Y., Odashima, H., Takagi, K., & Tsunekawa, S. 1996, ApJS, 104, 329
Fukuyama, Y., Omori, K., Odashima, H., Takagi, K., & Tsunekawa, S. 1999, JMoSp, 193, 72
Goldsmith, P. F., & Langer, W. D. 1999, ApJ, 517, 209
Heise, H. M., Winther, F., & Lutz, H. 1981, JMoSp, 90, 573
Johansson, L. E. B., Andersson, C., Elldér, J., et al. 1984, A&A, 130, 227
Johnson, D. R., Lovas, F. J., Gottlieb, C. A., et al. 1977, ApJ, 218, 370
Kisiel, Z., Pszczolkowski, L., Medvedev, I. R., et al. 2005, JMoSp, 233, 231
Kobayashi, K., Ogata, K., Tsunekawa, S., & Takano, S. 2007, A&A, 657, L17
Krasnicki, A., & Kisiel, Z. 2011, JMoSp, 270, 83
Laurie, V. W. 1959, JChPh, 31, 1500
Lerner, R. G., & Dailey, B. P. 1957, JChPh, 26, 678
Lessari, A. G., Charro, M. E., Villamañán, R. M., et al. 1991, JMoSp, 149, 317
Margulès, L., Huet, T. R., Demaison, J., et al. 2010, ApJ, 714, 1120
Margulès, L., Motiyenko, R., Demyk, K., et al. 2009, A&A, 493, 565
Martín, S., Aladro, R., Martín-Pintado, J., & Mauersberger, R. 2010, A&A, 522, 62
Mehringer, D. M., Pearson, J. C., Keene, J., & Phillips, T. G. 2004, ApJ, 608, 306
Miao, Y. T., & Snyder, L. E. 1997, ApJL, 480, L67
Motiyenko, R., Tercero, B., Cernicharo, J., & Margulès, L. 2012, A&A, 548, 71
Pardo, J. R., Cernicharo, J., Herpin, F., et al. 2001a, ApJ, 562, 799
Pardo, J. R., Cernicharo, J., & Serabyn, E. 2001b, ITAP, 49, 12
Pearson, J. C., Drouin, B. J., Maestrini, A., et al. 2011, RScI, 82, 093105
Pearson, J. C., Sastry, K., Herbst, E., & Delucia, F. C. 1994, ApJS, 93, 589
Persson, C. M., Olofsson, A. O. H., Koning, N., et al. 2007, A&A, 476, 807
Petkie, D. T., Goyette, T. M., Bettens, R. P. A., et al. 1997, RScI, 68, 1675
Pickett, H. M. 1991, JMoSp, 148, 371
Rodgers, S. D., & Millar, T. J. 1996, MNRAS, 280, 1046
Savage, C., Apponi, A. J., Ziurys, L. M., & Wyckoff, S. 2002, ApJ, 578, 211
Schilke, P., Benford, C. J., Hunter, T. R., Lis, D. C., & Philips, T. G. 2001, ApJS, 132, 281
Schilke, P., Walmsley, C. M., Pineau Des Forets, G., et al. 1992, A&A, 256, 595
Sutton, E. C., Peng, R., Danchi, W. C., et al. 1995, ApJS, 97, 455
Tercero, B., Cernicharo, J., Pardo, J. R., & Goicoechea, J. R. 2010, A&A, 517, 96
Tercero, B., Margulès, L., Carvajal, M., et al. 2012, A&A, 538, 119
Tercero, B., Vincent, L., Cernicharo, J., Viti, S., & Marcelino, N. 2011, A&A, 528, 26
Watson, J. K. G. 1977, in Vibrational Spectra and Structure, Vol. 6, ed. J. Durig (Amsterdam: Elsevier), 1
Wright, M. C. H., Plambeck, R. L., & Wilner, D. J. 1996, ApJ, 469, 216
Wyckoff, S., Kleine, M., Peterson, B. A., Wehinger, P. A., & Ziurys, L. M. 2000, ApJ, 535, 991

APENDIX II. LABORATORY CHARACTERIZATION AND ASTROPHYSICAL DETECTION OF VIBRATIONAL EXCITED STATES OF VINYL CYANIDE IN ORION KL. DETECTION OF THE ISOCYANIDE SPECIES.

Laboratory characterization and astrophysical detection of vibrationally excited states of vinyl cyanide in Orion-KL[*],[**]

A. López[1], B. Tercero[1], Z. Kisiel[2], A. M. Daly[3,4], C. Bermúdez[4], H. Calcutt[5], N. Marcelino[6], S. Viti[5], B. J. Drouin[3], I. R. Medvedev[7], C. F. Neese[8], L. Pszczółkowski[2], J. L. Alonso[4], and J. Cernicharo[1]

[1] Centro de Astrobiología (CSIC-INTA), Departamento de Astrofísica Molecular, Ctra. de Ajalvir Km 4, 28850 Torrejón de Ardoz, Madrid, Spain
   e-mail: lopezja@cab.inta-csic.es
[2] Institute of Physics, Polish Academy of Sciences, Al. Lotników 32/46, 02-668 Warszawa, Poland
[3] Jet Propulsion Laboratory, California Institute of Technology, 4800 Oak Grove Dr., Pasadena, CA 91109, USA
[4] Grupo de Espectroscopia Molecular (GEM), Unidad Asociada CSIC, Edificio Quifima,
   Laboratorios de Espectroscopia y Bioespectroscopia, Parque Cientfico UVa, Universidad de Valladolid, 47011, Valladolid, Spain
[5] Department of Physics and Astronomy, University College London, Gower Street, London WC1E 6B, UK
[6] NRAO, 520 Edgemont Road, Charlottesville, VA 22902, USA
[7] Wright State University, 3640 Colonel Glenn Hwy, Dayton, OH 45435, USA
[8] Ohio State University, 191 W. Wooddruff Ave., Columbus, OH 43210, USA

ABSTRACT

Context. We perform a laboratory characterization in the 18–1893 GHz range and astronomical detection between 80–280 GHz in Orion-KL with IRAM-30 m of CH_2CHCN (vinyl cyanide) in its ground and vibrationally excited states.
Aims. Our aim is to improve the understanding of rotational spectra of vibrationally excited vinyl cyanide with new laboratory data and analysis. The laboratory results allow searching for these excited state transitions in the Orion-KL line survey. Furthermore, rotational lines of CH_2CHCN contribute to the understanding of the physical and chemical properties of the cloud.
Methods. Laboratory measurements of CH_2CHCN made on several different frequency-modulated spectrometers were combined into a single broadband 50–1900 GHz spectrum and its assignment was confirmed by Stark modulation spectra recorded in the 18–40 GHz region and by ab-initio anharmonic force field calculations. For analyzing the emission lines of vinyl cyanide detected in Orion-KL we used the excitation and radiative transfer code (MADEX) at LTE conditions.
Results. Detailed characterization of laboratory spectra of CH_2CHCN in nine different excited vibrational states: $v_{11} = 1$, $v_{15} = 1$, $v_{11} = 2$, $v_{10} = 1 \Leftrightarrow (v_{11} = 1, v_{15} = 1)$, $v_{11} = 3/v_{15} = 2/v_{14} = 1$, $(v_{11} = 1, v_{10} = 1) \Leftrightarrow (v_{11} = 2, v_{15} = 1)$, $v_9 = 1$, $(v_{11} = 1, v_{15} = 2) \Leftrightarrow (v_{10} = 1, v_{15} = 1) \Leftrightarrow (v_{11} = 1, v_{14} = 1)$, and $v_{11} = 4$ are determined, as well as the detection of transitions in the $v_{11} = 2$ and $v_{11} = 3$ states for the first time in Orion-KL and of those in the $v_{10} = 1 \Leftrightarrow (v_{11} = 1, v_{15} = 1)$ dyad of states for the first time in space. The rotational transitions of the ground state of this molecule emerge from four cloud components of hot core nature, which trace the physical and chemical conditions of high mass star forming regions in the Orion-KL Nebula. The lowest energy vibrationally excited states of vinyl cyanide, such as $v_{11} = 1$ (at 328.5 K), $v_{15} = 1$ (at 478.6 K), $v_{11} = 2$ (at 657.8 K), the $v_{10} = 1 \Leftrightarrow (v_{11} = 1, v_{15} = 1)$ dyad (at 806.4/809.9 K), and $v_{11} = 3$ (at 987.9 K), are populated under warm and dense conditions, so they probe the hottest parts of the Orion-KL source. The vibrational temperatures derived for the $v_{11} = 1$, $v_{11} = 2$, and $v_{15} = 1$ states are 252 ± 76 K, 242 ± 121 K, and 227 ± 68 K, respectively; all of them are close to the mean kinetic temperature of the hot core component (210 K). The total column density of CH_2CHCN in the ground state is $(3.0 \pm 0.9) \times 10^{15}$ cm^{-2}. We report the detection of methyl isocyanide (CH_3NC) for the first time in Orion-KL and a tentative detection of vinyl isocyanide (CH_2CHNC). We also give column density ratios between the cyanide and isocyanide isomers, obtaining a $N(CH_3NC)/N(CH_3CN)$ ratio of 0.002.
Conclusions. Laboratory characterization of many previously unassigned vibrationally excited states of vinyl cyanide ranging from microwave to THz frequencies allowed us to detect these molecular species in Orion-KL. Column density, rotational and vibrational temperatures for CH_2CHCN in their ground and excited states, and the isotopologues have been constrained by means of a sample of more than 1000 lines in this survey.

Key words. ISM: abundances – ISM: molecules – stars: formation – line: identification – methods: laboratory: molecular – radio lines: ISM

1. Introduction

The rotational spectrum of vinyl cyanide (CH_2CHCN) was first studied in 1954 by Wilcox and collaborators and then later by Costain & Stoicheff (1959), who also investigated the singly-substituted ^{13}C species, as well as the ^{15}N, and the CH_2CDCN species. This molecule was detected for the first time in the interstellar medium (ISM) in 1973 toward the Sagittarius B2 (Sgr B2) molecular cloud (Gardner & Winnewisser 1975). Since then, CH_2CHCN has been detected toward different sources, such as Orion (Schilke et al. 1997), the dark cloud TMC-1 (Matthews & Sears 1983), the circumstellar envelope of the late-type star IRC+10216 (Agúndez et al. 2008), and the Titan atmosphere (Capone et al. 1981). CH_2CHCN is one of the molecules, whose high abundance and significant dipole moment allow radioastronomical detection even of its rare isotopologue species. Thus, vinyl cyanide makes an important contribution to the millimeter and submillimeter spectral emissions covered by high sensitivity facilities, such as ALMA and the *Herschel* Space Telescope. However, there has not yet been a comprehensive study of its low-lying vibrational excited states.

Vinyl cyanide is a planar molecule (six internuclear distances and five independent bond angles) and is a slightly asymmetric prolate rotor with two non-zero electric dipole moment components, which lead to a rich rotational spectrum. The first detailed discussion of the vinyl cyanide microwave spectrum was in 1973 by Gerry & Winnewisser. Subsequent studies of the rotational spectrum of vinyl cyanide resulted in the determination of its electrical dipole moment components by Stolze & Sutter (1985); these values were later improved by Krasnicki & Kisiel (2011) who reported the values $\mu_a = 3.821(3)\,D$, $\mu_b = 0.687(8)\,D$, and $\mu_{TOT} = 3.882(3)\,D$. Additional studies upgraded the molecular structure as Demaison et al. (1994), Colmont et al. (1997), and Krasnicki et al. (2011) successively derived more refined structural parameters from the rotational constants. The ^{14}N nuclear quadrupole hyperfine structure has been studied by Colmont et al. (1997), Stolze & Sutter (1985), and Baskakov et al. (1996).

Kisiel et al. (2009a) updated the rotational constants by simultaneously fitting the rotational lines of CH_2CHCN in its ground and lowest excited state $v_{11} = 1$. They fit the ground states of the ^{13}C and the ^{15}N isotopologues. More detailed analysis of the isotopologue spectra was later reported by Krasnicki et al. (2011). The ground state rotational a-type and b-type transitions of the parent vinyl cyanide have been assigned up to $J = 129$ with measurements in the laboratory reaching 1.67 THz (Kisiel et al. 2009a). They showed the influence of temperature on the partition function and consequently on the spectrum of vinyl cyanide. Figure 1 of Kisiel et al. (2009a) identifies this effect and the dominance of the millimeter and submillimeter region by the ^aR-type transitions. However, the b-type R-branch rotational transitions are one order of magnitude more intense than those of a-type due to smaller values of the rotational quantum numbers J at high frequencies (THz region).

The rotational transitions of CH_2CHCN in several of the lowest vibrational excited states, $v_{11} = 1,2,3$ and $v_{15} = 1$, were assigned by Cazzoli & Kisiel (1988), and the measurements were extended by Demaison et al. (1994) ($v_{11} = 1$ and the ground state). The data for $v_{11} = 3$ was more limited by hindering the determination of all sextic or even quartic constants. Recently, the analysis of broadband rotational spectra of vinyl cyanide revealed that there are perturbations between all pairs of adjacent vibrational states extending upwards from the ground state (g.s.), see Fig. 2 of Kisiel et al. (2009a). Kisiel et al. (2012) covered a broader frequency region (90–1900 GHz) identifying and
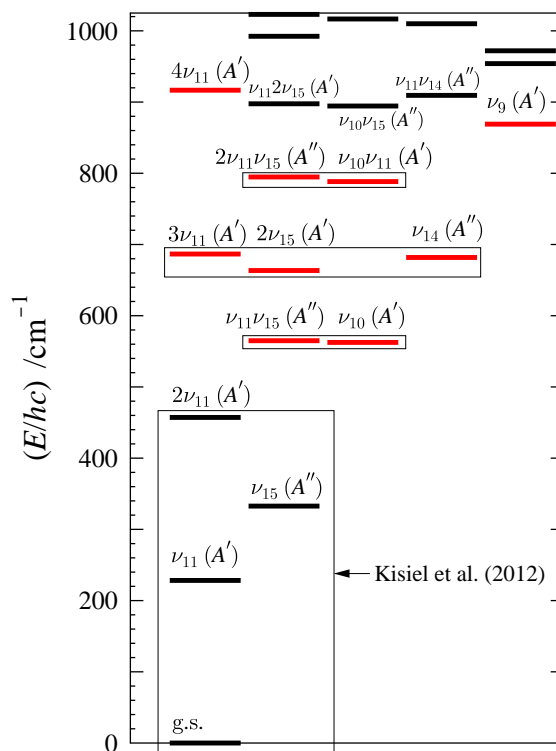
Fig. 1. All vibrational levels of vinyl cyanide up to 1000 cm^{-1}. The levels in red are those for which rotational transitions have been analyzed in this work. The boxes identify sets of levels treated by means of coupled fits accounting for interstate perturbations.

fitting the perturbations in frequencies of rotational transitions due to a-, b- or c-axis Coriolis-type or Fermi type interactions between the four lowest states of vinyl cyanide (g.s., $v_{11} = 1$, $v_{15} = 1$, and $v_{11} = 2$). The need for perturbation treatment of the $v_{10}/v_{11}v_{15}$ dyad at about 560 cm^{-1} and the $3v_{11}/2v_{15}/v_{14}$ triad of states at about 680 cm^{-1} was also identified, and initial results for the dyad were reported in Kisiel et al. (2011). Thus a meticulous analysis aiming toward an eventual global fit of transitions in all states of vinyl cyanide is necessary. The low resolution, gas-phase infrared spectrum of vinyl cyanide and its vibrational normal modes were studied by Halverson et al. (1948) and by Khlifi et al. (1999). Partial rotational resolution of the vibration-rotation spectrum of the two lowest wavenumber modes was also reported in the far-infrared study by Cole & Green (1973).

The first detection in the ISM of vinyl cyanide was in 1973 by means of the 2_{11}–2_{12} line in emission in Sgr B2 and was confirmed in 1975 by Gardner & Winnewisser (1975), suggesting the presence of the simplest olefin in the ISM, $CH_2=CH_2$ (ethylene) based on the evidence of the reactive vinyl radical. Betz (1981) observed the non-polar organic molecule $CH_2=CH_2$ toward the red giant C-rich star IRC+10216, for the first time; specifically, this is the v_7 band in the rotation-vibration spectral region (28 THz). Owing to the symmetry of ethylene the dipole rotational transitions are forbidden, and Occhiogroso et al. (2013) estimated a column density of 1.26×10^{14} cm^{-2} in standard hot cores for this molecule based on the abundance of its derivative molecule, hydrocarbon methylacetylene (CH_3CCH).

The dense and hot molecular clouds, such as Orion and Sgr B2, give rise to emission lines of vibrationally excited states of vinyl cyanide. Rotational transitions in the two lowest frequency modes v_{11} and v_{15} were detected in Orion by Schilke et al. (1997) (as tentative detection of three and two lines,
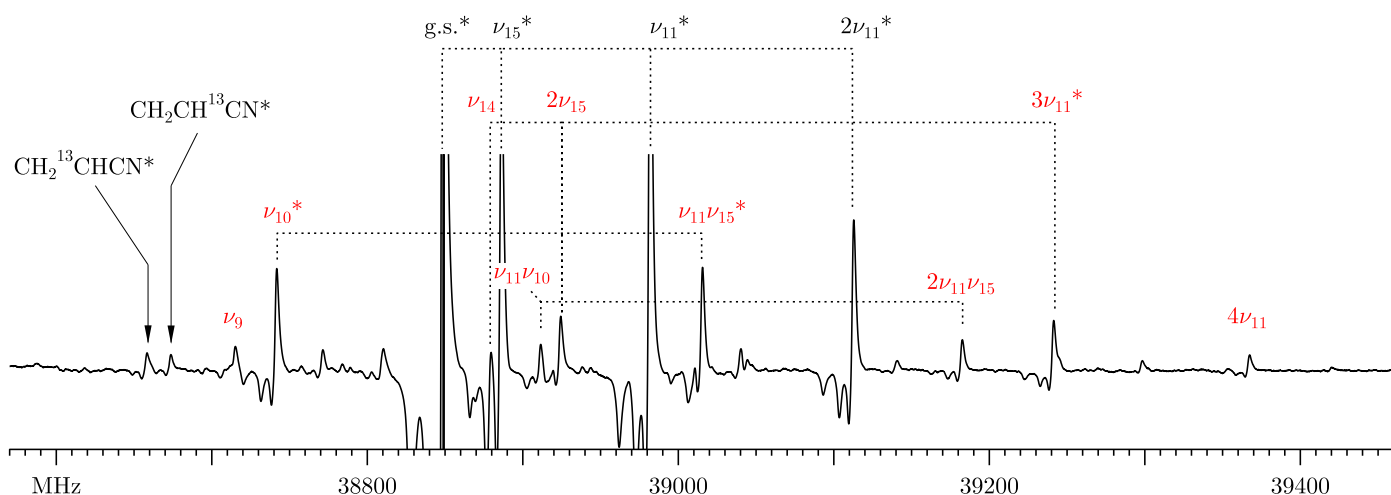
Fig. 2. Room-temperature laboratory spectrum of vinyl cyanide in the region of the $4_{13}-3_{12}$ rotational transition recorded with a Stark modulation spectrometer. All marked lines are for the $4_{13}-3_{12}$ transition in a given vibrational or isotopic species and display a characteristic pattern of negative lobes due to the non-zero field cycle of Stark modulation. Dotted lines connect vibrational states analyzed as perturbing polyads, red denotes vibrational states analyzed in the present work, and asterisks identify states detected presently in Orion-KL. It can be seen that laboratory analysis is now available for excited vibrational state transitions that are comparable in room-temperature intensity to those for ^{13}C isotopologues in terrestrial natural abundance.

respectively) and in Sgr B2 by Nummelin & Bergman (1999) (64 and 45 identified lines, respectively). The latter authors also made the tentative detection transitions in the $2v_{11}$ mode (five lines). Recently, Belloche et al. (2013) detected six vibrational states in a line survey of Sgr B2(N) ($v_{11} = 1, 2, 3, v_{15} = 1, 2$, $v_{11} = v_{15} = 1$) among which they detected the higher-lying vibrational states for the first time in space.

On the other hand, the ground states of rare isotopologues have been well characterized in the laboratory (Colmont et al. 1997; Müller et al. 2008; Kisiel et al. 2009a; Krasnicki et al. 2011). All monosubstituted species containing ^{13}C, ^{15}N, and D, and those of all ^{13}C-monosubstituted species of H$_2$C=CDCN of both cis- and trans- conformers of HDC=CHCN, HDC=CDCN, and D$_2$C=CDCN have been characterized. The double ^{13}C and ^{13}C^{15}N species have also been assigned by Krasnicki et al. (2011). The detection of ^{13}C species of vinyl cyanide in the ISM was carried out toward Sgr B2 by Müller et al. (2008) with 26 detected features.

The millimeter line survey of Orion-KL carried out with the IRAM-30 m telescope by Tercero and collaborators (Tercero et al. 2010, 2011; Tercero 2012) presented 8000 unidentified lines initially. Many of these features (near 4000) have been subsequently identified as lines arising from isotopologues, and vibrationally excited states of abundant species, such as ethyl cyanide and methyl formate, thanks to a close collaboration with different spectroscopic laboratories (Demyk et al. 2007; Margulès et al. 2009; Carvajal et al. 2009; Margulès et al. 2010; Tercero et al. 2012; Motiyenko et al. 2007; Daly et al. 2013; Coudert et al. 2013; Haykal et al. 2014). In this work, we followed the procedure of our previous papers, searching for all isotopologues and vibrationally excited states of vinyl cyanide in this line survey. These identifications are essential to probe new molecular species which reduce the number of U-lines and help to reduce the line confusion in the spectra. At this point we were ready to begin the search for new molecular species in this cloud by providing clues to the formation of complex organic molecules on the grain surfaces 1and/or in the gas phase (see the discovery of methyl acetate and *gauche* ethyl formate in Tercero et al. 2013, the detection of the ammonium ion in

Cernicharo et al. 2013, and the first detection of ethyl mercaptan in Kolesniková et al. 2014).

We report extensive characterization of 9 different excited vibrational states of vinyl cyanide (see Fig. 1) positioned in energy immediately above $v_{11} = 2$, which, up to this point, has been the highest vibrational state subjected to a detailed study (Kisiel et al. 2012). The assignment is confirmed by using the Stark modulation spectrometer of the spectroscopic laboratory (GEM) of the University of Valladolid and ab initio calculations. The new laboratory assignments of $v_{11} = 2$, $v_{11} = 3$, and $v_{10} = 1 \Leftrightarrow (v_{11} = 1, v_{15} = 1)$ vibrational modes of vinyl cyanide were used successfully to identify these three states in Orion-KL; the latter for the first time in the ISM. We also detected the $v_{11} = 1$ and $v_{15} = 1$ excited states in Orion-KL, as well as the ground state, and the ^{13}C isotopologues (see Sect. 4.2.1).

Because isomerism is a key issue for a more accurate understanding of the formation of interstellar molecules, we report observations of some related isocyanide isomers. Bolton et al. (1970) carried out the first laboratory study of the pure rotation (10–40 GHz) spectrum of vinyl isocyanide and also studied its 200–4400 cm^{-1} vibrational spectrum. Laboratory measurements were subsequently extended up to 175 GHz by Yamada & Winnewisser (1975) and the hyperfine structure of cm-wave lines was measured by Bestmann & Dreizler (1982). In Sect. 4.5, we searched for all isocyanides corresponding to the detected cyanides in Orion-KL: methyl cyanide (Bell et al. 2014), ethyl cyanide (Daly et al. 2013), cyanoacetylene (Esplugues et al. 2013b), cyanamide, and vinyl cyanide. In this study, we have tentatively detected vinyl isocyanide (CH$_2$CHNC) in Orion-KL (see Sect. 4.5). In addition, we observed methyl isocyanide (CH$_3$NC) for the first time in Orion-KL, which was observed firstly by Cernicharo et al. (1988) in the Sgr B2(OH) source, and we provide a tentative detection of ethyl isocyanide and isomers HCCNC and HNCCC of isocyanoacetylene. After the detection of cyanamide (NH$_2$CN) by Turner et al. (1975) in Sgr B2, we report the tentative detection of this molecule in Orion, as well as a tentative detection for isocyanamide.

Finally, we discuss and summarize all results in Sects. 5 and 6.

Table 1. Spectroscopic data sets for excited vibrational states of CH$_2$CHCN acquired in this work.

Excited state	E_{vib}[a] (cm^{-1})	ΔE[b] (cm^{-1})	N_{fitted}[c]	$N_{unfitted}$[d]	σ_{fit}[e] (MHz)	σ_{rms}[f]	J range	K_a range	Frequency range[g] (GHz)
v_{10}	560.5	0	2135[h]	55	0.324	1.446	2–99	0–22	37.0–1893.4
$v_{11}v_{15}$	562.9	2.391494(5)	1837[h]	136	0.382	1.872	3–100	0–20	39.0–1783.5
$2v_{15}$	663.5	0	1329[i]	52	0.265	1.980	1–70	0–17	18.6–1191.3
v_{14}	681.8	18.31812(2)	1287[i]	53	0.228	1.467	5–70	0–18	58.3–1891.1
$3v_{11}$	686.6	23.16415(3)	1250[i]	81	0.309	2.329	2–69	0–17	28.0–1196.5
$v_{10}v_{11}$	787.5	0	842[j]	3	0.137	1.289	3–68	0–12	37.1–639.3
$2v_{11}v_{15}$	793.9	6.44502(3)	860[j]	7	0.164	1.551	3–69	0–12	37.3–640.0
v_9	869.0		373	7	0.167	1.665	1–63	0–7	18.5–570.3
$4v_{11}$	916.7		225	17	0.250	2.496	3–43	0–5	37.4–410.9

Notes. [a] Estimated vibrational energy (see text in Sect. 3.2). [b] Energy difference relative to the lowest level in the relevant polyad obtained from the perturbation analysis. [c] The number of distinct frequency fitted lines. [d] The number of confidently assigned lines rejected from the fit at the 10σ cutoff criterion. [e] Deviation of fit for the vibrational subset. [f] Unitless deviation of fit for the vibrational subset. [g] Frequency coverage of transitions in the data set. [h,i,j] Transitions fitted jointly in a single fit accounting for interstate perturbations.

2. Experimental

The present spectroscopic analysis is based largely on the broadband rotational spectrum of vinyl cyanide compiled from segments recorded in several different laboratories. That spectrum provided a total of 1170 GHz of coverage and its makeup was detailed in Table 1 of Kisiel et al. (2012). In the present work, the previous spectrum has been complemented by two additional segments: 50–90 GHz and 140–170 GHz recorded at GEM by using cascaded multiplication of microwave synthesizer output. The addition of these segments provides practically uninterrupted laboratory coverage of the room-temperature rotational spectrum of vinyl cyanide over the 50–640 GHz region, which is key to the analysis of vibrational state transitions.

Another laboratory technique brought in by GEM is Stark spectroscopy at cm-wave frequencies. The Stark-modulation technique has the useful property of preferentially recording a given low-J rotational transition by a suitable choice of the modulation voltage. This is particularly the case for the lowest-J, $K_a = 1$ transitions. Due to asymmetry splitting, these transitions are significantly shifted in frequency relative to other transitions for the same J value. An example spectrum of this type is shown in Fig. 2 where all, but some of the weakest lines, correspond to the $4_{13}-3_{12}$ transition in either a vibrational state of the parent vinyl cyanide or the ground state of an isotopic species. Such spectra are particularly useful for an initial assignment since vibrationally induced frequency differences from the ground state are near additive. Relative intensities of transitions also give an immediate measure of relative population of assigned vibrational states and isotopic species.

The analysis of the spectra was carried out with the AABS graphical package for Assignment and Analysis of Broadband Spectra (Kisiel et al. 2005, 2012), which is freely available on the PROSPE database (Kisiel, 2001)[1]. The AABS package was complemented by the SPFIT/SPCAT program package (Pickett 1991)[2] used for setting up the Hamiltonian, fitting, and prediction.

Supporting ab initio calculations were carried out with GAUSSIAN 09[3] and CFOUR[4] packages. The key parameters for vibrational assignment are vibrational changes in rotational constants, which require relatively lengthy anharmonic force field calculations. Two strategies were used for this purpose: a relatively long basis set combined with a basic electron correlation correction (MP2/6-311++G(d,p)) and a more thorough correlation correction with a relatively simple basis set (CCSD(T)/6-31G(d,p)). The final results minimally favored the second approach but, in practice, both were found to be equally suitable.

3. Laboratory spectroscopy

3.1. Analysis of the excited vibrational states

An overview of the results of the spectroscopic analysis is provided in Table 1 and the determined spectroscopic constants necessary for generating linelists are given in Tables 2 and A.1–A.4.

The initial assignment was based on a combination of several techniques: (1) inspection of Stark spectra such as that in Fig. 2; (2) the use of the concept of harmonic behavior of rotational constant changes on vibrational excitation (linear additivity of changes); and (3) ab initio calculations of vibration-rotation constants. The final assignment of vibrational states is confirmed by the comparison of values of experimental vibration-rotation changes in rotational constants relative to the ground state with computed ab initio values, as listed in Table A.5.

Preliminary studies revealed a multitude of perturbations in rotational frequencies that necessitate the use of fits that account for interactions between vibrational states. The grouping of energy levels visible in Fig. 1 suggests that it was possible to break the treatment down into three isolated polyads above the last state studied in detail, namely $2v_{11}$. The symmetry classification of vibrational states (A' and A'', C_s point group) is marked in

---

[1] http://info.ifpan.edu.pl/~kisiel/prospe.htm
[2] http://spec.jpl.nasa.gov

[3] Frisch, M. J.; Trucks, G. W.; Schlegel, et al., Gaussian 09, Revision B.01; Gaussian: Wallingford, CT, 2010.
[4] Stanton, J. F., Gauss, J.; Harding, M. E. et al., CFOUR, a quantum chemical quantum package with integrated packages MOLECULE (Almlof, J.; Taylor, P. R.) and ECP routines (Mitin, A. V.; van Wüllen, C.), http://www.cfour.de

Table 2. Spectroscopic constants in the diagonal blocks of the Hamiltonian for the $v_{10} \Leftrightarrow v_{11}v_{15}$ and the $v_{11}v_{10} \Leftrightarrow 2v_{11}v_{15}$ dyads of vibrational states in vinyl cyanide compared with those for the ground state.

	Ground state	v_{10}	$v_{11}v_{15}$	$v_{11}v_{10}$	$2v_{11}v_{15}$
A/MHz	49850.69655(43)[a]	49550.03(63)	49890.72(61)	48861.72(62)	49124.87(56)
B/MHz	4971.212565(37)	4965.6692(98)	4992.6723(70)	4984.979(32)	5011.494(25)
C/MHz	4513.828516(39)	4509.6228(13)	4531.6029(13)	4517.9357(31)	4540.0924(32)
Δ_J/kHz	2.244058(13)	2.20646(19)	2.26839(18)	2.24034(23)	2.28278(27)
Δ_{JK}/kHz	−85.6209(35)	−89.854(83)	−80.615(83)	−88.79(17)	−63.97(17)
Δ_K/kHz	2715.4213(94)	2591.5(31)	2522.4(31)	2225.(16)	1842.(15)
δ_J/kHz	0.4566499(32)	0.44642(11)	0.465487(70)	0.46094(18)	0.47422(18)
δ_K/kHz	24.4935(22)	22.099(24)	25.225(14)	25.212(82)	24.683(96)
Φ_J/Hz	0.0064338(17)	0.006345(26)	0.006244(26)	0.006038(38)	0.005952(39)
Φ_{JK}/Hz	−0.00425(40)	0.0541(96)	0.0324(86)	−0.126(17)	−0.244(23)
Φ_{KJ}/Hz	−7.7804(39)	−5.74(11)	−5.18(11)	0.59(23)	1.52(22)
Φ_K/Hz	384.762(63)	399.73(71)	−86.8(11)	428.(396)	−1858.(389)
ϕ_J/Hz	0.00236953(79)	0.002405(22)	0.0021005(36)	0.002185(23)	0.002136(22)
ϕ_{JK}/Hz	0.14283(40)	0.1151(27)	0.1698(18)	0.145(13)	0.135(14)
ϕ_K/Hz	37.011(58)	51.4(12)	38.0(11)	17.1(27)	−5.6(38)
L_J/mHz	−0.000026315(71)	−0.0000263(15)	−0.0000202(14)	[0.]	[0.]
L_{JJK}/mHz	−0.001077(29)	−0.01178(86)	−0.00659(91)	[0.]	[0.]
L_{JK}/mHz	0.4279(30)	−0.0703(85)	[0.]	[0.]	[0.]
L_{KKJ}/mHz	0.012(12)	4.00(18)	−9.63(17)	[0.]	[0.]
L_K/mHz	−61.41(17)	−55.6(29)	462.9(45)	[0.]	[0.]
l_J/mHz	−0.000011602(36)	−0.0000165(13)	[0.]	[0.]	[0.]
l_{JK}/mHz	−0.000956(20)	[0.]	[0.]	[0.]	[0.]
l_{KJ}/mHz	−0.1436(46)	−1.79(11)	−0.86(12)	[0.]	[0.]
l_K/mHz	8.91(18)	[0.]	9.21(43)	[0..]	[0.]
P_{KJ}/mHz	−0.0000156(31)	−0.000147(14)	[0.]	[0.]	[0.]
P_{KKJ}/mHz	−0.0001977(57)	[0.]	[0.]	[0.]	[0.]
P_K/mHz	0.00867(15)	0.0286(23)	−0.3457(49)	[0.]	[0.]
ΔE^b/MHz		0.0	71695.20(16)	0.0	193216.69(90)
ΔE/cm^{-1}		0.0	2.391494(5)	0.0	6.44502(3)
N_{lines}^c	4490,0	2135,55	1837,136	842,3	860,7
σ_{fit}^d/MHz	0.144	0.324[e]	0.382[e]	0.137[f]	0.164[f]
σ_{rms}^d	0.713	1.446	1.872	1.289	1.551

Notes. [a] Round parentheses enclose standard errors in units of the last quoted digit of the value of the constant; square parentheses enclose assumed values. [b] The fitted vibrational energy difference relative to the lowest vibrational state in the respective dyad. [c] The number of distinct frequency fitted lines and the number of lines rejected at the 10σ fitting criterion of the SPFIT program. [d] Deviations of fit for the different vibrational subsets. [e] The coupled fit for the $v_{10} \Leftrightarrow v_{11}v_{15}$ dyad encompasses 3978 lines, at an overall σ_{fit} of 0.352 MHz and requires also the use of constants reported in Table A.2. [f] The coupled fit for the $v_{11}v_{10} \Leftrightarrow 2v_{11}v_{15}$ dyad encompasses 1702 lines, at an overall σ_{fit} of 0.151 MHz and requires also the use of constants reported in Table A.2.

Fig. 1 and states of different symmetry need to be connected by a- and b-type Coriolis interactions, while states of the same symmetry are coupled via c-type Coriolis and Fermi interactions. The Hamiltonian and the techniques of analysis used to deal with this type of problem have been described in detail in Kisiel et al. (2009a, 2012). This type of analysis is far from trivial, but its eventual success for the polyads near 560, 680, and 790 cm^{-1} is confirmed in Table 1 by the magnitudes of the deviations of fit in relation to the numbers of fitted lines and their broad frequency coverage. In the most extensive of the present analyses, for the $v_{10} = 1 \Leftrightarrow (v_{11} = 1, v_{15} = 1)$ dyad, the fit encompasses almost 4000 lines in addition to ^aR-type transitions that include ^bQ- and ^bR-types. We use the 10σ cutoff criterion of SPFIT to prevent lines perturbed by factors outside the model from unduly affecting the fit, and a moderate number of such lines (191) are rejected for this dyad. These are confidently assigned lines, generally in high-J tails of some transition sequences for higher

values of K_a, but their incompatibility suggests that there is hope for a final global fit with coupling between the polyads. At the present stage, the success of the perturbation fits is further reflected by additive vibrational changes in values of quartic centrifugal distortion constants and by the relative changes in perturbation constants between the two dyads listed in Table A.2, which are similar to those found for the well studied case of ClONO$_2$ (Kisiel et al. 2009b).

Unlike the situation in the ground state of vinyl cyanide (Kisiel et al. 2009a), the perturbations visible in the presently studied polyads are not a spectroscopic curiosity but affect the strongest, low-K_a, ^aR-type transitions. Such transitions occur in the mm- and submm-wave regions which are normally the choice for astrophysical studies. This effect is illustrated by the scaled plots in Fig. 3, which would have the form of near horizontal, very smoothly changing lines in the absence of perturbations. Perturbations lead to the marked spike shaped features in
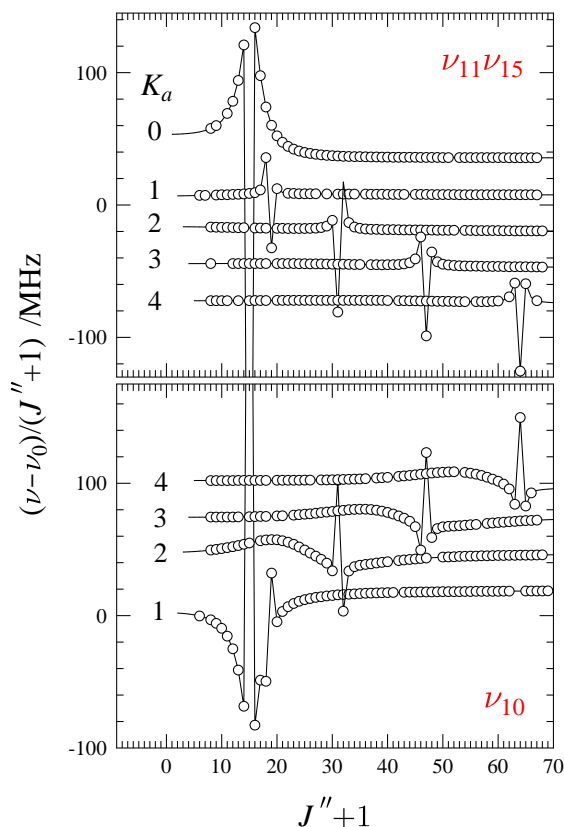
Fig. 3. Effect of vibration-rotation perturbations on frequencies of the strongest rotational transitions in the $v_{10} \Leftrightarrow v_{11}v_{15}$ dyad of vibrational states. The plotted quantities are scaled frequency differences relative to the same transitions in the ground state. Continuous lines are predictions from the final fit; circles mark assigned lines and traces in each panel have added vertical shifts to improve clarity.

these plots. Since evaluation of the Hamiltonian is made in separate blocks for each value of J, the perturbations affecting the two coupling states should have a mirror image form, as seen in Fig. 3. The scaled nature of these plots hides the reason that perturbations to the frequencies of many lines are considerable. For example, the peak of the rightmost spike in Fig. 3 corresponds to a perturbation shift of close to 50×64 MHz, namely 3.2 GHz. The frequencies of ^aR-transitions corresponding to the maximum perturbation peaks visible in Fig. 3 are 154.1, 183.4, 301.4, 456.5, and 620.8 GHz for v_{10}, and 131.9, 174.9, 290.3, 443.3, 604.9 GHz for $v_{11}v_{15}$. A significant number of transitions around such peaks are also clearly perturbed. The perturbations are not limited to frequency but also extend to intensities, which are often significantly decreased for pure rotation transitions near the perturbation maxima. The considerable energy level mixing in these cases leads instead to the appearance of transitions between the perturbing vibrational states. These transitions could only be predicted accurately in the final stages of the perturbation analysis but were easily found in the compiled broadband laboratory spectrum and are explicitly identified in the data files. Fortunately, the line lists generated from perturbation fits with the use of the SPCAT program reflect both frequency and intensity perturbations. Accounting for such effects at laboratory experimental accuracy is therefore the key to successful astrophysical studies.

Above the $v_{10}v_{11} \Leftrightarrow 2v_{11}v_{15}$ dyad, the density of vibrational states rapidly increases. The complexity of a thorough analysis appears to be too forbidding at this stage, but it is possible to

check how successfully some of these states can be encompassed by single state, effective fits. The v_9 vibrational state seems to be the most isolated, and its analysis could be taken up to $K_a = 7$ and transition frequencies of 570 GHz. In contrast, the easy to locate $4v_{11}$ state exhibited very incomplete sequences of transitions even at low values of K_a, so that its analysis could only be taken up to $K_a = 5$. The very fragmentary nature of line sequences for this state illustrates the limitations of single state approaches, but it nevertheless provides a useful starting point for any future work. The complete results of fit and the primary data files for the SPFIT program for all coupled and single-state effective fits are available online[5], while the predicted linelists will be incorporated in the JPL database.

3.2. Vibrational energies

In Table 1 we report a consistent set of vibrational energies for the studied excited states of vinyl cyanide, which are evaluated by taking advantage of results from the various perturbation analyses. The values for $3v_{11}$ and $4v_{11}$ are from v_{11} and the anharmonicity coefficient $x_{11,11}$ from Kisiel et al. (2012). The value for $v_{11}v_{15}$ comes from v_{11} and v_{15} augmented by $x_{11,15}$, which is calculated at the CCSD(T)/cc-PVDZ level that was benchmarked in Kisiel et al. (2012) as the optimum level for evaluating this type of constant for vinyl cyanide. The remaining vibrational energies in the lower dyad, and the triad are evaluated using the precise ΔE values from the perturbation analyses. Finally, $v_{10}v_{11}$ comes from v_{10} and v_{11} augmented by ab initio $x_{10,11}$. A double check of this procedure is provided by an alternative evaluation for $2v_{15}$ based on ab initio $x_{15,15}$, which gives a result within 0.5 cm^{-1} of the more reliable tabulated value. Only the vibrational energy for v_9 comes from the low resolution gas phase infrared spectrum (Halverson et al. 1948).

4. Astronomical detection of vinyl cyanide species

Thanks to these new laboratory data, we identified and detected the $v_{10} = 1 \Leftrightarrow (v_{11} = 1, v_{15} = 1)$ vibrational modes of CH$_2$CHCN for the first time in space. A consistent analysis of all detected species of vinyl cyanide have been made to outline the knowledge of our astrophysical environment. We also report the detection of methyl isocyanide for the first time in Orion KL and a tentative detection of vinyl isocyanide and calculate abundance ratios between the cyanide species and their corresponding isocyanide isomers.

4.1. Observations and overall results

4.1.1. 1D Orion-KL line survey

The line survey was performed over three millimeter windows (3, 2, and 1.3 mm) with the IRAM-30 m telescope (Granada, Spain). The observations were carried out between September 2004 and January 2007 pointing toward the IRc2 source at $\alpha_{2000.0} = 5^h35^m14.5^s$ and $\delta_{2000.0} = -5°22'30.0''$. All the observations were performed using the wobbler switching mode with a beam throw in azimuth of ±120″. System temperatures were in the range of 100–800 K from the lowest to the highest frequencies. The intensity scale was calibrated using the atmospheric transmission model (ATM, Cernicharo 1985; Pardo et al. 2001a). Focus and pointing were checked every 1–2 h. Backends provided a spectrum of 1–1.25 MHz of spectral resolution. All

---

spectra were single-side band reduced. For further information about observations and data reduction, see Tercero et al. (2010)[6].

All figures are shown in main beam temperature (T_{MB}) that is related to the antenna temperature (T_A^*) by the equation: $T_{MB} = T_A^*/\eta_{MB}$, where η_{MB} is the main beam efficiency which depends on the frequency.

According to previous works, we characterize at least four different cloud components overlapping in the beam in the analysis of low angular resolution line surveys of Orion-KL (see, e.g., Blake et al. 1987, 1996; Tercero et al. 2010, 2011): (i) a narrow (~4 km s^{-1} line-width) component at $v_{LSR} \simeq 9$ km s^{-1} delineating a north-to-south *extended ridge* or ambient cloud or an extended region with $T_k \simeq 60$ K, $n(H_2) \simeq 10^5$ cm^{-3}; (ii) a compact ($d_{sou} \simeq 15''$) and quiescent region, or the *compact ridge*, ($v_{LSR} \simeq 7$–8 km s^{-1}, $\Delta v \simeq 3$ km s^{-1}, $T_k \simeq 150$ K, $n(H_2) \simeq 10^6$ cm^{-3}); (iii) the *plateau*, or a mixture of outflows, shocks, and interactions with the ambient cloud ($v_{LSR} \simeq 6$–10 km s^{-1}, $\Delta v \gtrsim 25$ km s^{-1}, $T_k \simeq 150$ K, $n(H_2) \simeq 10^6$ cm^{-3}, and $d_{sou} \simeq 30''$); (iv) a *hot core* component ($v_{LSR} \simeq 5$ km s^{-1}, $\Delta v \simeq 5$–15 km s^{-1}, $T_k \simeq 250$ K, $n(H_2) \simeq 5 \times 10^7$ cm^{-3}, and $d_{sou} \simeq 10''$). Nevertheless, we found a more complex structure of that cloud (density and temperature gradients of these components and spectral features at a v_{LSR} of 15.5 and 21.5 km s^{-1} related with the outflows) in our analysis of different families of molecules (see, e.g., Tercero et al. 2011; Daly et al. 2013; Esplugues et al. 2013a).

4.1.2. 2D survey observations

We also carried out a two-dimensional line survey with the same telescope in the ranges 85−95.3, 105−117.4, and 200.4−298 GHz (N. Marcelino et al. priv. comm.) during 2008 and 2010. This 2D survey consists of maps of 140×140 arcsec^2 area with a sampling of 4 arcsec using a On-The-Fly mapping mode with a reference position 10 arcmin west of Orion-KL. The EMIR heterodyne receivers were used for all the observations except for 220 GHz frequency setting, for which the HERA receiver array was used. As backend, we used the WILMA backend spectrometer for all spectra (bandwidth of 4 GHz and 2 MHz of spectral resolution) and the FFTS (Fast Fourier Transform Spectrometer, 200 kHz of spectral resolution) for frequencies between 245−259, 264.4−278.6, and 289−298 GHz. Pointing and focus were checked every 2 h giving errors less than 3 arcsec. The data were reduced using the GILDAS package[7] by removing bad pixels, checking for image sideband contamination and emission from the reference position, and fitting and removing first order baselines. Six transitions of CH$_2$CHCN have been selected to study the spatial extent of their emission with this 2D line survey.

4.2. Results

4.2.1. Detection of CH$_2$CHCN: its vibrationally excited states and its isotopologues in Orion-KL

Vinyl cyanide shows emission from a large number of rotational lines through the frequency band 80–280 GHz. The dense and hot conditions of Orion-KL populate the low-lying energy excited states. Here, we present the first interstellar detection of the $v_{10} = 1 \Leftrightarrow (v_{11} = 1, v_{15} = 1)$ vibrational excited state.

Figures 4−8 and A.1 show selected detected lines of the g.s. of vinyl cyanide and five vibrationally excited states of the main isotopologue CH$_2$CHCN: in plane C-C≡N bending mode ($v_{11} = 1$, 228.1 cm^{-1} or 328.5 K), out of plane C-C≡N bending mode ($v_{15} = 1$, 332.7 cm^{-1} or 478.6 K), in plane C-C≡N bending mode ($v_{11} = 2$, 457.2 cm^{-1} or 657.8 K), in a combination state ($v_{10} = 1 \Leftrightarrow (v_{11} = 1, v_{15} = 1)$, 560.5/562.9 cm^{-1} or 806.4/809.9 K), and in plane C-C≡N bending mode ($v_{11} = 3$, 686.6 cm^{-1} or 987.9 K). The latter is in the detection limit, so we do not address the perturbations of this vibrational mode.

In addition, we detected the following isotopologues of vinyl cyanide in its ground state: ^{13}CH$_2$CHCN, CH$_2^{13}$CHCN, and CH$_2$CH^{13}CN (see Fig. 9). For CH$_2$CHC^{15}N and the deuterated species of vinyl cyanide, DCHCHCN, HCDCHCN, and CH$_2$CDCN (see Fig. A.2), we only provided a tentative detection in Orion-KL because of the small number of lines with an uncertainty in frequency less than 2 MHz (up to $K_a = 7$, 5, 15 for DCHCHCN, HCDCHCN, and CH$_2$CDCN, respectively), the weakness of the features, and/or their overlap with other molecular species.

Tables A.6−A.13 show observed and laboratory line parameters for the ground state, the vibrationally excited states, and the ^{13}C-vinyl cyanide isotopologues. Spectroscopic constants were derived from a fit with the MADEX code (Cernicharo 2012) to the lines reported by Kisiel et al. (2009a, 2012), Cazzoli & Kisiel (1988), and Colmont et al. (1997). For the $v_{10} = 1 \Leftrightarrow (v_{11} = 1, v_{15} = 1)$ state, spectroscopic constants are those derived in this work; dipole moments were from Krasnicki & Kisiel (2011). All these parameters have been implemented in MADEX to obtain the predicted frequencies and the spectroscopic line parameters. We have displayed rotational lines that are not strongly overlapped with lines from other species. Observational parameters have been derived by Gaussian fits (using the GILDAS software) to the observed line profiles that are not blended with other features. For moderately blended and weak lines, we show observed radial velocities and intensities given directly from the peak channel of the line in the spectra, so contribution from other species or errors in baselines could appear for these values. Therefore, the main beam temperature for the weaker lines ($T_{MB} < 0.1$ K) must be considered as an upper limit.

From the derived Gaussian fits, we observe that vinyl cyanide lines reflect the spectral line parameters corresponding to hot core/plateau components (v_{LSR} between 2–3 km s^{-1} for the component of 20 km s^{-1} of line width, and 5–6 km s^{-1} for the component of 6 km s^{-1} of line width). As shown by Daly et al. (2013) there is a broad component associated to the hot core that limits the accuracy of the derived velocities for the hot core and this broad component. Our velocity components for CH$_2$CHCN agree with those of CH$_3$CH$_2$CN obtained by Daly et al. (2013). Besides, for the vibrationally excited states, we found contribution of a narrow component with a v_{LSR} of 3–6 km s^{-1} and a line width of $\simeq 7$ km s^{-1}.

We rely on catalogs[8] to identify possible contributions from other species overlapping the detected lines (Tercero 2012), but it should be necessary to perform radiative transfer modeling with all the known molecules in order to precisely assess how much the contamination from other species influences the vinyl cyanide lines.

Fig. 4. Observed lines from Orion-KL (histogram spectra) and model (thin red curves) of vinyl cyanide in the ground state. The cyan line corresponds to the model of the molecules we have already studied in this survey (see text Sect. 4.4.2), including the CH$_2$CHCN species. A v_{LSR} of 5 km s^{-1} is assumed.

Table 3. Number of identified lines of CH$_2$CHCN species.

Species	Detectable	Unblended	Partially blended	Totally blended
CH$_2$CHCN g. s. (a-type)	350	204 (59%)	85 (24%)	61 (17%)
CH$_2$CHCN $v_{11} = 1$	307	111 (36%)	75 (25%)	121 (39%)
CH$_2$CHCN $v_{11} = 2$	253	59 (23%)	35 (14%)	159 (63%)
CH$_2$CHCN $v_{11} = 3$	245	30 (12%)	33 (14%)	182 (74%)
CH$_2$CHCN $v_{15} = 1$	287	68 (24%)	62 (22%)	157 (55%)
CH$_2$CHCN $v_{10} = 1 \Leftrightarrow (v_{11} = 1, v_{15} = 1)$	474	65 (14%)	64 (14%)	345 (73%)
(^{13}C)-CH$_2$CHCN	348	102 (29%)	115 (33%)	131 (38%)

Table 3 shows the number of lines of vinyl cyanide identified in this work. Our identifications are based on a whole inspection of the data and the modeled synthetic spectrum of the molecule we are studying (where we obtain the total number of detectable lines) and all species already identified in our previous papers. We consider blended lines when these are close enough to other stronger features. Unblended features are those, which present the expected radial velocity (matching our model with the peak channel of the line) (see, e.g., lines at 115.00 and 174.36 GHz in Fig. 5 or the line at 247.55 GHz in Fig. 8), and there are not another species at the same observed frequency (±3 MHz) with significant intensity. Partially blended lines are those which present either a mismatch in the peak channel of the line or significant contribution from another species at the peak channel of the feature (see, e.g., the line at 108.16 GHz in

Fig. 8). Generally, these lines also present a mismatch in intensity; see, e.g., line at 152.0 GHz in Fig. 6. If we do not found the line for the unblended frequencies we are looking for, then we do not claim detection, so we do not accept missing lines in the detected species. For species with quite strong lines (g.s., $v_{11} = 1$, and $v_{15} = 1$), most of the totally and partially blended lines are weaker due to the high energy of their transitions (see Tables A.6, A.8, and A.11). We observed a total number of ≃640 unblended lines of vinyl cyanide species. Considering also the moderately blended lines, this number rises to ≃1100. We detected lines of vinyl cyanide in the g.s. with a maximum upper level energy value of about 1400–1450 K by corresponding to a $J_{max} = 30$ and a $(K_a)_{max} = 24$. For the vibrational states we observed transitions with maximum quantum rotational numbers of $(K_a)_{max} = 20, 15, 17, 16, 15$ from the lowest energy vibrational

Fig. 5. Observed lines from Orion-KL (histogram spectra) and model (thin red curves) of CH$_2$CHCN of $v_{11} = 1$. The cyan line corresponds to the model of the molecules we have already studied in this survey (see text Sect. 4.4.2), including the CH$_2$CHCN species. A v_{LSR} of 5 km s^{-1} is assumed.

Fig. 6. Observed lines from Orion-KL (histogram spectra) and model (thin red curves) for the $v_{15} = 1$ vibrational state of CH$_2$CHCN. The cyan line corresponds to the model of the molecules we have already studied in this survey (see text Sect. 4.4.2), including the CH$_2$CHCN species. A v_{LSR} of 5 km s^{-1} is assumed.

Fig. 7. Observed lines from Orion-KL (histogram spectra) and model (thin red curves) for the $v_{11} = 2$ vibrational state of CH$_2$CHCN. The cyan line corresponds to the model of the molecules we have already studied in this survey (see text Sect. 4.4.2), including the CH$_2$CHCN species. A $v_{\rm LSR}$ of 5 km s^{-1} is assumed.

Fig. 8. Observed lines from Orion-KL (histogram spectra) and model (thin red curves) for combined vibrationally excited states of CH$_2$CHCN in the $v_{10} = 1 \Leftrightarrow (v_{11} = 1, v_{15} = 1)$ dyad. The cyan line corresponds to the model of the molecules we have already studied in this survey (see text Sect. 4.4.2), including the CH$_2$CHCN species. A $v_{\rm LSR}$ of 5 km s^{-1} is assumed.

state to the highest (i.e., from $v_{11} = 1$ to $v_{11} = 3$) and the same $J_{\max} = 30$ value up to the maximum $E_{\rm upp}$ between 1300–1690 K.

4.2.2. CH$_2$CHCN maps

Figure 10 shows maps of the integrated emission of six transitions in the g.s. of CH$_2$CHCN at different velocity ranges.

From line 1 to 6: $12_{1,12}-11_{1,11}$ (110 839.98 MHz, $E_{\rm upp}$ = 36.8 K), $24_{0,24}-23_{0,23}$ (221 766.03 MHz, $E_{\rm upp}$ = 134.5 K), $24_{2,23}-23_{2,22}$ (226 256.88 MHz, $E_{\rm upp}$ = 144.8 K), $26_{1,26}-25_{1,25}$ (238 726.81 MHz, $E_{\rm upp}$ = 157.4 K), $26_{2,25}-25_{2,24}$ (244 857.47 MHz, $E_{\rm upp}$ = 167.9 K), and $24_{10,15}-23_{10,14}$ and $24_{10,14}-23_{10,13}$ (228 017.34 MHz, $E_{\rm upp}$ = 352.0 K). These maps reveal the emission from two cloud components: a component

Fig. 9. Observed lines from Orion-KL (histogram spectra) and model (thin red curves) of ^{13}C isotopes for CH$_2$CHCN in the ground state. The subindex in ^{13}C$_i$ (i = 1, 2, 3) corresponds to the position of the isotope in the molecule (^{i_1}CH$_2^{i_2}$CH^{i_3}CN). The cyan line corresponds to the model of the molecules we have already studied in this survey (see text Sect. 4.4.2), including the CH$_2$CHCN species. A $v_{\rm LSR}$ of 5 km s^{-1} is assumed.

Fig. 10. Integrated intensity maps for 6 ground state transitions of vinyl cyanide. From line 1 (*top row*) to 6 (*bottom row*): $12_{1,12}-11_{1,11}$ (110 839.98 MHz, 36.8 K), $24_{0,24}-23_{0,23}$ (221 766.03 MHz, 134.5 K), $24_{2,23}-23_{2,22}$ (226 256.88 MHz, 144.8 K), $26_{1,26}-25_{1,25}$ (238 726.808 MHz, 157.4 K), $26_{2,25}-25_{2,24}$ (244 857.47 MHz, 167.9 K), and $24_{10,15}-23_{10,14}$ and $24_{10,14}-23_{10,13}$ (228017.34 MHz, 352.0 K) at different velocity ranges (indicated in the top of each column). Three boxes have been blanked because the emission at these velocities was blended with that from other well known species. For each box axis are in units of arcseconds ($\Delta\alpha$, $\Delta\delta$). Color logarithm scale is the integrated intensity ($\int T_A^* dv$) in units of K km s^{-1}.

Fig. 11. Rotational diagram of CH$_2$CHCN in its ground state. The *upper panel* displays the two components derived from the line profiles. The *middle panel* shows two linear fits to the narrow component points; these linear regressions yield temperatures and column densities of $T_{\rm rot} = 125 \pm 16$ K and $N = (1.3 \pm 0.1) \times 10^{15}$ cm^{-2} ($Q_{\rm rot} = 7.06 \times 10^3$), and $T_{\rm rot} = 322 \pm 57$ K and $N = (1.0 \pm 0.2) \times 10^{15}$ cm^{-2} ($Q_{\rm rot} = 2.92 \times 10^4$). Likewise, the *bottom panel* shows another two linear fits to the points corresponding to the wide component. The results of these fits are rotational temperatures of $T_{\rm rot} = 90 \pm 14$ K and $T_{\rm rot} = 227 \pm 130$ K, and column densities of $(2.9 \pm 0.5) \times 10^{15}$ cm^{-2} ($Q_{\rm rot} = 4.31 \times 10^3$) and $(1.2 \pm 0.9) \times 10^{15}$ cm^{-2} ($Q_{\rm rot} = 1.73 \times 10^4$), respectively.

at the position of the hot core at velocities from 2 to 8 km s^{-1} and a component with a slight displacement of the intensity peak at the extreme velocities. The intensity peak of the central velocities coincides with that of the -CN bearing molecules found by Guélin et al. 2008 (maps of one transition of ethyl and vinyl cyanide) and Daly et al. (2013) (maps of four transitions of ethyl cyanide). We note a more compact structure in the maps of the transitions at 352.0 K. Our maps do not show a more extended component found in the ethyl cyanide maps by Daly et al. (2013). We have obtained an angular source size between 7″– 10″ (in agreement with the hot core diameter provided by different authors; see, e.g., Crockett et al. 2014; Neil et al. 2013; Beuther & Nissen 2008) for central and extreme velocities by assuming emission within the half flux level and corrected for the size of the telescope beam at the observed frequency. These integrated intensity maps allow us to provide the offset position with respect to IRc2 and the source diameter parameters needed for modeling the vinyl cyanide species (see Sect. 4.4.1).

4.3. Rotational diagrams of CH$_2$CHCN (g.s., v_{11} = 1, 2, and v_{15} = 1)

To obtain an estimate of the rotational temperature ($T_{\rm rot}$) for different velocity components, we made rotational diagrams, which related the molecular parameters with the observational ones (Eq. (1); see e.g., Goldsmith & Langer 1999) for CH$_2$CHCN in its ground state (Fig. 11) and for the lowest vibrationally excited states v_{11} = 1, 2, and v_{15} = 1 (Fig. 12). Assumptions, such as LTE approximation and optically thin lines (see Sect. 4.4.4), are

required in this analysis. We have taken the effect of dilution of the telescope into account, which was corrected by calculation of the beam dilution factor (Demyk et al. 2008, Eq. (2)):

$$\ln\left(\frac{N_{\rm u}}{g_{\rm u}}\right) = \ln\left(\frac{8\pi k\nu^2 W_{\rm obs}}{hc^3 A_{\rm ul}g_{\rm u}}\right) = \ln\left(\frac{N}{Q_{\rm rot}}\right) - \frac{E_{\rm upp}}{kT_{\rm rot}} + \ln b, \qquad (1)$$

$$b = \frac{\Omega_{\rm S}}{\Omega_{\rm A}} = \frac{\theta_{\rm S}^2}{\theta_{\rm S}^2 + \theta_{\rm B}^2}, \qquad (2)$$

where $N_{\rm u}$ is the column density of the considered vinyl cyanide species in the upper state (cm^{-2}), $g_{\rm u}$ is the statistical weight in the upper level, $W_{\rm obs}$ (K cm s^{-1}) is the integrated line intensity ($W_{\rm obs} = \int T_{\rm MB_{\rm obs}}(v){\rm d}v$), $A_{\rm ul}$ is the Einstein A-coefficient for spontaneous emission, N (cm^{-2}) is the total column density of the considered vinyl cyanide species, $Q_{\rm rot}$ is the rotational partition function, which depends on the rotational temperature derived from the diagrams, $E_{\rm upp}$ (K) is the upper level energy, and $T_{\rm rot}$ (K) is the rotational temperature. In Eq. (2), b is the beam dilution factor, $\Omega_{\rm S}$ and $\Omega_{\rm A}$ are the solid angle subtended by the source and under the main beam of the telescope, respectively, and $\theta_{\rm S}$ and $\theta_{\rm B}$ are the angular diameter of the source and the beam of the telescope, respectively. We note that the factor b increases the fraction N_u/g_u in Eq. (1) and yields a higher column density than if it were not considered.

For the g.s., we used 117 transitions free of blending with upper level energies from 20.4 to 683.1 K with two different velocity components: one with $v_{\rm LSR}$ = 4–6 km s^{-1} and Δv = 4–7 km s^{-1} and the second one with $v_{\rm LSR}$ = 2–4 km s^{-1} and
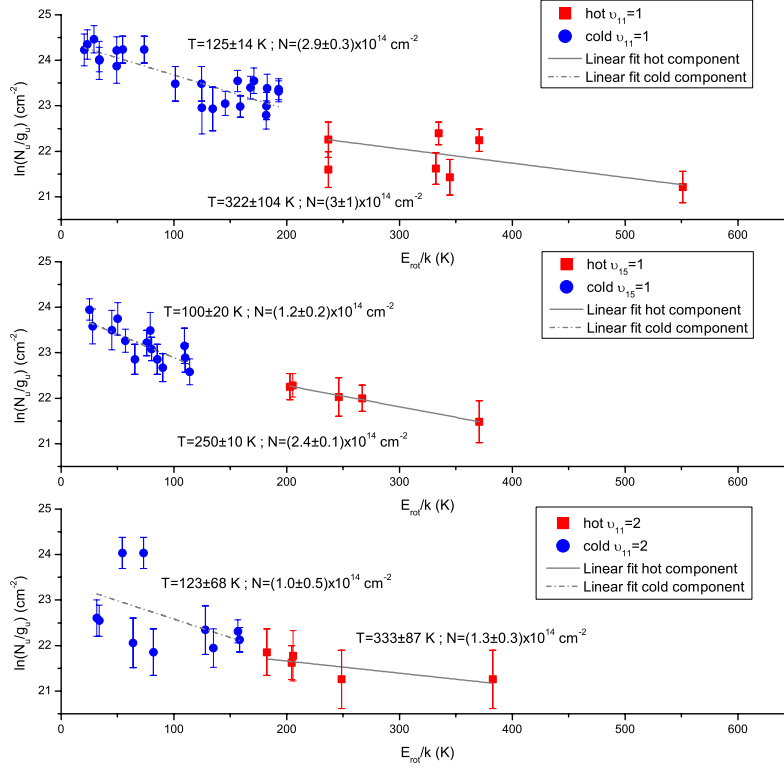
Fig. 12. Rotational diagrams for the vibrationally excited states of vinyl cyanide $v_{11} = 1$, $v_{15} = 1$, and $v_{11} = 2$ as a function of rotational energy (upper level energy corrected from the vibrational energy of each state), which sorted by increasing vibrational energy *from top to bottom*.

$\Delta v = 14$–$20 \, \text{km s}^{-1}$. For the vibrationally excited states, we considered 43 (40–550 K), 24 (30–380 K), and 33 (25–370 K) transitions with line profiles that can be fitted to a single velocity component ($v_{\text{LSR}} = 4$–$6 \, \text{km s}^{-1}$ and $\Delta v = 5$–$7 \, \text{km s}^{-1}$) for $v_{11} = 1, 2$, and $v_{15} = 1$, respectively.

The scatter in the rotational diagrams of CH_2CHCN g.s. is mainly due to the uncertainty of fitting two Gaussian profiles to the lines with the CLASS software. Rotational diagrams of the vibrationally excited states ($v_{11} = 1$ and $v_{15} = 1$) are less scattered because there is only one fitted Gaussian to the line profile. For the rotational diagram of the $v_{11} = 2$ state, the scatter is mostly due to the weakness of the observed lines for this species. We have done an effort to perform the diagrams with unblended lines; however, some degree of uncertainty could come from non-obvious blends. The individual errors of the data points are those derived by error propagation in the calculated uncertainty of $\ln(N_u/g_u)$, taking only the uncertainty of the integrated intensity of each line (W) provided by CLASS and an error of 20% for the source diameter into account. The uncertainty of the final values of T_{rot} and N has been calculated with the statistical errors given by the linear least squares fit for the slope and the intercept.

We assumed the same source diameter of $10''$ for the emitting region of the two components for the g.s. and the single component of the vibrationally excited states. In Fig. 11, the upper panel shows points in the diagram related with the wide and narrow components for the CH_2CHCN g.s. We observed two tendencies in the position of the data points up to/starting from an upper state energy of $\simeq 200 \, \text{K}$. From the narrow component, we derived two different rotational temperatures and column densities, $T_{\text{rot}} = 125 \pm 16 \, \text{K}$ and $N = (1.3 \pm 0.1) \times 10^{15} \, \text{cm}^{-2}$, and $T_{\text{rot}} = 322 \pm 57 \, \text{K}$ and $N = (1.0 \pm 0.2) \times 10^{15} \, \text{cm}^{-2}$. Likewise, from the wide component, we have determined cold and hot temperatures of about $T_{\text{rot}} = 90 \pm 14 \, \text{K}$ and $T_{\text{rot}} = 227 \pm 130 \, \text{K}$,

and column densities of $N = (2.9 \pm 0.5) \times 10^{15} \, \text{cm}^{-2}$ and $N = (1.2 \pm 0.9) \times 10^{15} \, \text{cm}^{-2}$, respectively.

To quantify the uncertainty derived from the assumed source size, we also have performed the rotational diagram of CH_2CHCN g.s. by adopting a source diameter of both $5''$ and $15''$. The main effect of changing the source size on the rotational diagram is a change in the slope and in the scatter. Table 4 shows the derived values of N and T_{rot} by assuming different source sizes. Therefore, as expected, derived rotational temperatures depend clearly on the assumed size with a tendency to increase T_{rot} when increasing the source diameter. The effect on the column density is less significant also due to the correction on the partition function introduced by the change in the rotational temperatures; in general, these values increased or decreased when we decreased or increased the source size, respectively (see Table 4).

In Fig. 12, the panels display the rotational diagrams of the three vinyl cyanide excited states $v_{11} = 1$, $v_{15} = 1$, and $v_{11} = 2$, which are sorted by the vibrational energy from top to bottom. In the x-axis we show the rotational energy which has been corrected from the vibrational energy to estimate the appropriate column density. We also observed the same tendency of the data points quoted above. The rotational temperature and the column density conditions for the $v_{11} = 1$ were $T_{\text{rot}} = 125 \pm 14 \, \text{K}$ and $(2.9 \pm 0.3) \times 10^{14} \, \text{cm}^{-2}$, and $T_{\text{rot}} = 322 \pm 104 \, \text{K}$ and $N = (3 \pm 1) \times 10^{14} \, \text{cm}^{-2}$. For the $v_{15} = 1$ state we determine $T_{\text{rot}} = 100 \pm 20 \, \text{K}$ and $N = (1.2 \pm 0.2) \times 10^{14} \, \text{cm}^{-2}$, and $T_{\text{rot}} = 250 \pm 10 \, \text{K}$ and $N = (2.4 \pm 0.1) \times 10^{14} \, \text{cm}^{-2}$. For the $v_{11} = 2$ state we find that $T_{\text{rot}} = 123 \pm 68 \, \text{K}$ and $N = (1.0 \pm 0.5) \times 10^{14} \, \text{cm}^{-2}$, and $T_{\text{rot}} = 333 \pm 87 \, \text{K}$ and $N = (1.3 \pm 0.3) \times 10^{14} \, \text{cm}^{-2}$. Owing to the weakness of the emission lines of the $v_{11} = 3$ and $v_{10} = 1 \Leftrightarrow (v_{11} = 1, v_{15} = 1)$ vibrational modes, we have not performed rotational diagrams for these species.

Table 4. N and $T_{\rm rot}$ from rotational diagrams of CH$_2$CHCN g.s. which assumes different source sizes.

	Hot narrow comp.	Cold narrow comp.	Hot wide comp.	Cold wide comp.
	$v_{\rm LSR}$ = 4–6 km s^{-1}	Δv = 4–7 km s^{-1}	$v_{\rm LSR}$ = 2–4 km s^{-1}	Δv = 14–20 km s^{-1}
$d_{\rm sou}$ = 5″	$N = (2.3 \pm 0.7) \times 10^{15}$ cm^{-2}	$N = (3.8 \pm 0.8) \times 10^{15}$ cm^{-2}	$N = (1.1 \pm 0.9) \times 10^{15}$ cm^{-2}	$N = (4.8 \pm 0.5) \times 10^{15}$ cm^{-2}
	$T_{\rm rot} = (334 \pm 89)$ K	$T_{\rm rot} = (100 \pm 20)$ K	$T_{\rm rot} = (210 \pm 132)$ K	$T_{\rm rot} = (71 \pm 5)$ K
$d_{\rm sou}$ = 10″	$N = (1.0 \pm 0.2) \times 10^{15}$ cm^{-2}	$N = (1.3 \pm 0.1) \times 10^{15}$ cm^{-2}	$N = (1.2 \pm 0.9) \times 10^{15}$ cm^{-2}	$N = (2.9 \pm 0.5) \times 10^{15}$ cm^{-2}
	$T_{\rm rot} = (322 \pm 57)$ K	$T_{\rm rot} = (125 \pm 16)$ K	$T_{\rm rot} = (227 \pm 130)$ K	$T_{\rm rot} = (90 \pm 14)$ K
$d_{\rm sou}$ = 15″	$N = (6.9 \pm 1.9) \times 10^{14}$ cm^{-2}	$N = (1.0 \pm 0.2) \times 10^{15}$ cm^{-2}	$N = (9 \pm 6) \times 10^{14}$ cm^{-2}	$N = (1.0 \pm 0.1) \times 10^{15}$ cm^{-2}
	$T_{\rm rot} = (326 \pm 85)$ K	$T_{\rm rot} = (166 \pm 55)$ K	$T_{\rm rot} = (250 \pm 125)$ K	$T_{\rm rot} = (100 \pm 10)$ K
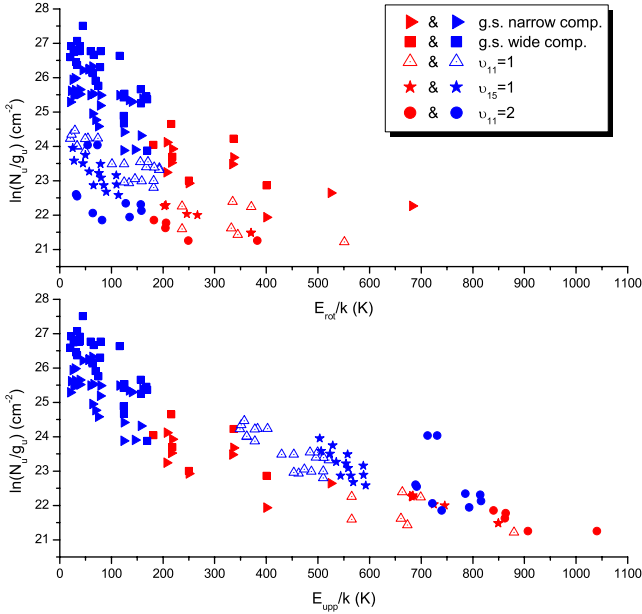
Fig. 13. Rotational diagram of CH$_2$CHCN in its ground and excited states as shown as a function of rotational energy corrected from the vibrational energy in the *upper panel*, while the *bottom panel* displays the ground state followed by CH$_2$CHCN $v_{11} = 1$, $v_{15} = 1$, and $v_{11} = 2$ excited states as a function of the upper level energy.

Figure 13 displays the combined rotational diagram for the ground state of CH$_2$CHCN and $v_{11} = 1$, $v_{15} = 1$, and $v_{11} = 2$ excited states. The upper panel is referred to the rotational level energies of the vinyl cyanide states, whereas the bottom panel shows the positions of the different rotational diagrams in the upper level energies when taking the vibrational energy for the excited states into account.

Owing to the large range of energies and the amount of transitions in these rotational diagrams we consider the obtained results ($T_{\rm rot}$) as a starting point in our models (see Sect. 4.4.1).

4.4. Astronomical modeling of CH$_2$CHCN in Orion-KL

4.4.1. Analysis: the Model

From the observational line parameters derived in Sect. 4.2.1 (radial velocities and line widths), the displayed maps, and the rotational diagram results (two components, cold and hot, for each derived Gaussian fit to the line profiles), we consider that the emission of CH$_2$CHCN species comes mainly from the four regions shown in Table 5, which are related with the hot core (those with Δv = 6–7 km s^{-1}) and plateau/hot core (those with Δv = 20 km s^{-1}) components. Daly et al. (2013) found that three components related with the hot core were enough to

properly fit their ethyl cyanide lines. The named "Hot Core 1" and "Hot Core 3" in Daly et al. (2013) are similar to our "Hot narrow comp." and "Cold wide comp." of Table 5, respectively. Interferometric maps performed by Guélin et al. (2008) of ethyl and vinyl cyanide and those of Widicus Weaver & Friedel (2012) of CH$_3$CH$_2$CN (the latter authors affirm that in their observations CH$_3$CH$_2$CN, CH$_2$CHCN, and CH$_3$CN are cospatial) show that the emission from these species comes from different cores at the position of the hot core and IRc7. The radial velocities found in the line profiles of vinyl cyanide (between 3–5 km s^{-1}) in this work with the cited interferometric maps could indicate that the four components of Table 5 are dominated by the emission of the hot core. For the vibrationally excited states and for the isotopologues, we found that two components (both narrow components) are sufficient to reproduce the line profiles (see Table 5). We note that we need a higher value in the line width for $v_{11} = 1$ and $v_{15} = 1$. This difference is probably due to a small contribution of the wide component in these lines.

Spectroscopic (Sect. 2) and observational parameters, such as radial velocity ($v_{\rm LSR}$), line width (Δv), temperature from rotational diagrams ($T_{\rm rot}$), source diameter ($d_{\rm sou}$) and offsets from the maps, were introduced in an excitation and radiative transfer code (MADEX) in order to obtain the synthetic spectrum. We have considered the telescope dilution and the position of the components with respect to the pointing position (IRc2). The LTE conditions have been assumed by owing to the lack of collisional rates for vinyl cyanide, which prevents a more detailed analysis of the emission of this molecule. Nevertheless, we expect a good approximation to the physical and chemical conditions due to the hot and dense nature of the considered components. Rotational temperatures (which coincide with the excited and kinetic temperatures in LTE conditions) have been slightly adapted from those of the rotational diagrams to obtain the best fit to the line profiles. These models allow us to obtain column density results for each species and components independently. The sources of uncertainty that were described in Tercero et al. (2010) have been considered. For the CH$_2$CHCN g.s., $v_{11} = 1$, and $v_{15} = 1$ states we have adopted an uncertainty of 30%, while we have adopted a 50% uncertainty for the ^{13}C isotopologues and the $v_{11} = 2$, $v_{11} = 3$, and $v_{10} = 1 \Leftrightarrow (v_{11} = 1, v_{15} = 1)$ states. Due to the weakness and/or high overlap with other molecular species, we only provided upper limits to the column densities of monodeuterated vinyl cyanide and the ^{15}N isotopologue.

4.4.2. Column densities

The column densities that best reproduce the observations are shown in Table 5 and used for the model in Figs. 4–9 and A.2. Although the differences between the intensity of the model and that of the observations are mostly caused by blending with other molecular species, isolated vinyl cyanide lines confirm a good

Table 5. Physico-chemical conditions of Orion-KL from ground and excited states of CH_2CHCN.

	Hot narrow comp.	Cold narrow comp.	Hot wide comp.	Cold wide comp.
d_{sou} (")	5	10	5	10
offset (")	2	2	0	0
Δv_{FWHM} (km s^{-1})	6(7*)	6(7*)	20	20
v_{LSR} (km s^{-1})	5	5	3	3
T_{rot} (K)	320	100	200	90
$N_{CH_2CHCN(g.s.)}$ (cm^{-2})	$(3.0 \pm 0.9) \times 10^{15}$	$(1.0 \pm 0.3) \times 10^{15}$	$(9 \pm 3) \times 10^{14}$	$(1.3 \pm 0.4) \times 10^{15}$
$N_{CH_2CHCN(v_{11}=1)}$(cm^{-2})	$(9 \pm 3) \times 10^{14}$	$(2.5 \pm 0.8) \times 10^{14}$	...	...
$N_{CH_2CHCN(v_{11}=2)}$(cm^{-2})	$(2 \pm 1) \times 10^{14}$	$(5 \pm 2) \times 10^{13}$	...	...
$N_{CH_2CHCN(v_{11}=3)}$(cm^{-2})	$\leq(2 \pm 1) \times 10^{14}$	$\leq(5 \pm 2) \times 10^{13}$	...	...
$N_{CH_2CHCN(v_{15}=1)}$(cm^{-2})	$(4 \pm 1) \times 10^{14}$	$(1.0 \pm 0.3) \times 10^{14}$	...	...
$N_{CH_2CHCN(v_{10}=1 \Leftrightarrow (v_{11}=1,v_{15}=1))}$(cm^{-2})	$(4 \pm 2) \times 10^{14}$	$(8 \pm 4) \times 10^{13}$	...	...
$N_{^{13}CH_2CHCN}$(cm^{-2})	$(4 \pm 2) \times 10^{14}$	$(5 \pm 2) \times 10^{13}$	...	...
$N_{CH_2^{13}CHCN}$(cm^{-2})	$(4 \pm 2) \times 10^{14}$	$(5 \pm 2) \times 10^{13}$	...	...
$N_{CH_2CH^{13}CN}$(cm^{-2})	$(4 \pm 2) \times 10^{14}$	$(5 \pm 2) \times 10^{13}$	...	...
$N_{CH_2CHC^{15}N}$(cm^{-2})	$\leq(1.0 \pm 0.5) \times 10^{14}$	$\leq(2 \pm 1) \times 10^{13}$	...	...
$N_{HCDCHCN}$(cm^{-2})	$\leq(4 \pm 2) \times 10^{14}$	$\leq(4 \pm 2) \times 10^{13}$	...	...
$N_{DCHCHCN}$(cm^{-2})	$\leq(4 \pm 2) \times 10^{14}$	$\leq(4 \pm 2) \times 10^{13}$	...	...
N_{CH_2CDCN}(cm^{-2})	$\leq(3 \pm 1) \times 10^{14}$	$\leq(3 \pm 1) \times 10^{13}$	...	...

Notes. Physico-chemical conditions of Orion-KL from vinyl cyanide (see text 4.4.1). * 7 km s^{-1} is only considered for $v_{11}=1$ and $v_{15}=1$ states.

agreement between model and observations. We found small differences between the column density values from the model and those from the rotational diagram, likely because of the source diameters that are considered in the determination of the beam dilution for the two components.

In Figs. 4–9, 15, 16, and A.1–A.5, a model with species all already studied that have been in this survey is included (cyan line). The considered molecules and published works containing the detailed analysis for each species are as follows: OCS, CS, H$_2$CS, HCS$^+$, CCS, CCCS species in Tercero et al. (2010); SiO and SiS species in Tercero et al. (2011); SO and SO$_2$ species in Esplugues et al. (2013a); HC$_3$N and HC$_5$N species in Esplugues et al. (2013b); CH$_3$CN in Bell et al. (2014); CH$_3$COOCH$_3$ and t/g-CH$_3$CH$_2$OCOH in Tercero et al. (2013); CH$_3$CH$_2$SH, CH$_3$SH, CH$_3$OH, CH$_3$CH$_2$OH in Kolesniková et al. (2014); ^{13}C-CH$_3$CH$_2$CN in Demyk et al. (2007); CH$_3$CH$_2$^{15}N, CH$_3$CHDCN, and CH$_2$DCH$_2$CN in Margulès et al. (2009); CH$_3$CH$_2$CN species in Daly et al. (2013); ^{13}C-HCOOCH$_3$ in Carvajal et al. (2009); DCOOCH$_3$ and HCOOCH$_3$ in Margulès et al. (2010); ^{18}O-HCOOCH$_3$ in Tercero et al. (2012); HCOOCH$_2$D in Coudert et al. (2013); ^{13}C-HCOOCH$_3$ v_t = 1, and HCOOCH$_3$ v_t = 1 in Haykal et al. (2014); NH$_2$CHO v_{12} = 1 and NH$_2$CHO in Motiyenko et al. (2007); CH$_2$CHCN species in this work; HCOOCH$_3$ v_t = 2 and CH$_3$COOH from López et al. (in prep.).

We obtained a total column density of vinyl cyanide in the ground state of $(6 \pm 2) \times 10^{15}$ cm^{-2}. This value is a factor 7 higher than the value in the Orion-KL hot core of Schilke et al. (1997), who detected the vinyl cyanide g.s. in the frequency range from 325 to 360 GHz with a column density (averaged over a beam of 10"–12") of 8.2×10^{14} cm^{-2} and a T_{rot} of 96 K. The difference between both results is mostly due to our more detailed model of vinyl cyanide which includes four components, two of them with a source size of 5" (half than the beam size in Schilke et al. 1997). Sutton et al. (1995) also derived a column density of 1×10^{15} cm^{-2} (beam size of 13.7") toward the hot core position. These authors found vinyl cyanide emission toward the compact ridge position but at typical hot core velocities. Previous authors derived beam averaged column densities

between 4×10^{13} and 2×10^{14} cm^{-2} (Johansson et al. 1984; Blake et al. 1987; Turner 1991; Ziurys & McGonagle 1993).

The column density of CH$_2$CHCN v_{11} = 1, $(1.0 \pm 0.3) \times 10^{15}$ cm^{-2} is four times smaller than that derived for the ground state in the same components. Moreover, we derived a column density of $(3 \pm 2) \times 10^{14}$, $\leq(3 \pm 2) \times 10^{14}$, $(5 \pm 2) \times 10^{14}$, and $(5 \pm 2) \times 10^{14}$ cm^{-2} for the v_{11} = 2, v_{11} = 3, v_{15} = 1, and v_{10} = 1 $\Leftrightarrow$ (v_{11} = 1,v_{15} = 1) states, respectively. Schilke et al. (1997) did not give column density results for the tentative detection of v_{11} = 1 and v_{15} = 1 bending modes. We also obtained a column density of $(4 \pm 2) \times 10^{14}$ cm^{-2} for each ^{13}C-isotopologue of vinyl cyanide.

4.4.3. Isotopic abundances

It is now possible to estimate the isotopic abundance ratio of the main isotopologue (^{12}C, ^{14}N, ^{1}H) with respect to ^{13}C, ^{15}N, and D isotopologues from the obtained column densities shown in Table 5. For estimating these ratios, we assume the same partition function for both the main and the rare isotopologues.

^{12}C/^{13}C: the column density ratio between the normal species and each ^{13}C isotopologue in Orion-KL, when the associated uncertainties are considered, vary between 4–20 for the hot narrow component and between 10–43 for the cold narrow component. The solar isotopic abundance (^{12}C/^{13}C = 90, Anders & Grevesse 1989) corresponds roughly to a factor 2–22 higher than the value obtained in Orion. The ^{12}C/^{13}C ratio indicates the degree of galactic chemical evolution, so the solar system value could point out earlier epoch conditions of this region (Wyckoff et al. 2000; Savage et al. 2002). The following previous estimates of the ^{12}C/^{13}C ratio in Orion-KL from observations of different molecules have been reported: 43±7 from CN (Savage et al. 2002), 30–40 from HCN, HNC, OCS, H$_2$CO, CH$_3$OH (Blake et al. 1987), 57 ± 14 from CH$_3$OH (Persson et al. 2007), 35 from methyl formate (Carvajal et al. 2009, Haykal et al. 2014), 45±20 from CS-bearing molecules (Tercero et al. 2010), 73 ± 22 from ethyl cyanide (Daly et al. 2013), and $\simeq$3–17 from cyanoacetylene in the hot core (Esplugues et al. 2013b). Considering the weakness of the ^{13}C lines, the derived ratios are compatible

Table 6. Line opacities.

Transition	Freq. (MHz)	E_{upp} (K)	Hot narrow comp. $d_{sou} = 10''$ $N = 1.6 \times 10^{15}$ cm^{-2}	Cold narrow comp. $d_{sou} = 15''$ $N = 3.6 \times 10^{14}$ cm^{-2}	Hot wide comp. $d_{sou} = 10''$ $N = 8.2 \times 10^{13}$ cm^{-2}	Cold wide comp. $d_{sou} = 15''$ $N = 9.2 \times 10^{14}$ cm^{-2}
$11_{0,11}-10_{0,10}$	103 575.4	29.9	$\tau = 2.76 \times 10^{-3}$	$\tau = 8.99 \times 10^{-3}$	$\tau = 1.22 \times 10^{-4}$	$\tau = 8.70 \times 10^{-3}$
$14_{3,11}-13_{3,10}$	133 030.7	67.3	$\tau = 3.83 \times 10^{-3}$	$\tau = 9.72 \times 10^{-3}$	$\tau = 1.58 \times 10^{-4}$	$\tau = 9.03 \times 10^{-3}$
$18_{0,18}-17_{0,17}$	167 728.4	77.1	$\tau = 6.33 \times 10^{-3}$	$\tau = 1.51 \times 10^{-2}$	$\tau = 2.57 \times 10^{-4}$	$\tau = 1.39 \times 10^{-2}$
$23_{0,23}-22_{0,22}$	212 788.7	123.8	$\tau = 8.89 \times 10^{-3}$	$\tau = 1.55 \times 10^{-2}$	$\tau = 3.31 \times 10^{-4}$	$\tau = 1.35 \times 10^{-2}$
$25_{4,21}-24_{4,20}$	237 712.0	182.8	$\tau = 8.78 \times 10^{-3}$	$\tau = 1.02 \times 10^{-2}$	$\tau = 2.93 \times 10^{-4}$	$\tau = 8.39 \times 10^{-3}$
$28_{0,28}-27_{0,27}$	257 646.2	181.4	$\tau = 1.10 \times 10^{-2}$	$\tau = 1.30 \times 10^{-2}$	$\tau = 3.68 \times 10^{-4}$	$\tau = 1.07 \times 10^{-2}$
$30_{0,30}-29_{0,29}$	275 588.1	207.4	$\tau = 1.25 \times 10^{-2}$	$\tau = 1.15 \times 10^{-2}$	$\tau = 3.71 \times 10^{-4}$	$\tau = 9.20 \times 10^{-3}$
Transition	Freq. (MHz)	E_{upp} (K)	$d_{sou} = 5''$ $N = 3.0 \times 10^{15}$ cm^{-2}	$d_{sou} = 10''$ $N = 1.0 \times 10^{15}$ cm^{-2}	$d_{sou} = 5''$ $N = 9.0 \times 10^{14}$ cm^{-2}	$d_{sou} = 10''$ $N = 1.3 \times 10^{15}$ cm^{-2}
$11_{0,11}-10_{0,10}$	103 575.4	29.9	$\tau = 5.07 \times 10^{-3}$	$\tau = 2.50 \times 10^{-2}$	$\tau = 1.37 \times 10^{-3}$	$\tau = 1.23 \times 10^{-2}$
$14_{3,11}-13_{3,10}$	133 030.7	67.3	$\tau = 7.06 \times 10^{-3}$	$\tau = 2.70 \times 10^{-2}$	$\tau = 1.78 \times 10^{-3}$	$\tau = 1.28 \times 10^{-2}$
$18_{0,18}-17_{0,17}$	167 728.4	77.1	$\tau = 1.16 \times 10^{-2}$	$\tau = 4.19 \times 10^{-2}$	$\tau = 2.89 \times 10^{-3}$	$\tau = 1.96 \times 10^{-2}$
$23_{0,23}-22_{0,22}$	212 788.7	123.8	$\tau = 1.64 \times 10^{-2}$	$\tau = 4.30 \times 10^{-2}$	$\tau = 3.72 \times 10^{-3}$	$\tau = 1.91 \times 10^{-2}$
$25_{4,21}-24_{4,20}$	237 712.0	182.8	$\tau = 1.62 \times 10^{-2}$	$\tau = 2.84 \times 10^{-2}$	$\tau = 3.30 \times 10^{-3}$	$\tau = 1.19 \times 10^{-2}$
$28_{0,28}-27_{0,27}$	257 646.2	181.4	$\tau = 2.02 \times 10^{-2}$	$\tau = 3.61 \times 10^{-2}$	$\tau = 4.14 \times 10^{-3}$	$\tau = 1.51 \times 10^{-2}$
$30_{0,30}-29_{0,29}$	275 588.1	207.4	$\tau = 2.14 \times 10^{-2}$	$\tau = 3.20 \times 10^{-2}$	$\tau = 4.18 \times 10^{-3}$	$\tau = 1.30 \times 10^{-2}$
Transition	Freq. (MHz)	E_{upp} (K)	$d_{sou} = 2''$ $N = 8.0 \times 10^{15}$ cm^{-2}	$d_{sou} = 5''$ $N = 4.8 \times 10^{15}$ cm^{-2}	$d_{sou} = 2''$ $N = 2.5 \times 10^{14}$ cm^{-2}	$d_{sou} = 5''$ $N = 4.4 \times 10^{15}$ cm^{-2}
$11_{0,11}-10_{0,10}$	103 575.4	29.9	$\tau = 1.35 \times 10^{-2}$	$\tau = 1.20 \times 10^{-1}$	$\tau = 3.80 \times 10^{-4}$	$\tau = 4.16 \times 10^{-2}$
$14_{3,11}-13_{3,10}$	133 030.7	67.3	$\tau = 1.88 \times 10^{-2}$	$\tau = 1.30 \times 10^{-1}$	$\tau = 4.94 \times 10^{-4}$	$\tau = 4.32 \times 10^{-2}$
$18_{0,18}-17_{0,17}$	167 728.4	77.1	$\tau = 3.11 \times 10^{-2}$	$\tau = 2.01 \times 10^{-1}$	$\tau = 8.02 \times 10^{-4}$	$\tau = 6.64 \times 10^{-2}$
$23_{0,23}-22_{0,22}$	212 788.7	123.8	$\tau = 4.36 \times 10^{-2}$	$\tau = 2.06 \times 10^{-1}$	$\tau = 1.03 \times 10^{-3}$	$\tau = 6.48 \times 10^{-2}$
$25_{4,21}-24_{4,20}$	237 712.0	182.8	$\tau = 4.31 \times 10^{-2}$	$\tau = 1.37 \times 10^{-1}$	$\tau = 9.16 \times 10^{-4}$	$\tau = 4.01 \times 10^{-2}$
$28_{0,28}-27_{0,27}$	257 646.2	181.4	$\tau = 5.39 \times 10^{-2}$	$\tau = 1.73 \times 10^{-1}$	$\tau = 1.15 \times 10^{-3}$	$\tau = 5.10 \times 10^{-2}$
$30_{0,30}-29_{0,29}$	275 588.1	207.4	$\tau = 5.71 \times 10^{-2}$	$\tau = 1.54 \times 10^{-1}$	$\tau = 1.16 \times 10^{-3}$	$\tau = 4.40 \times 10^{-2}$

Notes. Opacities for some lines of CH$_2$CHCN g.s. at different frequencies that consider different source diameters and column densities (see text, Sect. 4.4.4).

with a ^{12}C/^{13}C ratio between 30–45, which are found by other authors. Nevertheless, our results point out a possible chemical fractionation enhancement of the ^{13}C isotopologues of vinyl cyanide. The intensity ratios derived in Sect. 4.4.4 also indicate this possibility. This ratio might be underestimated if the lines from the g.s. were optically thick. However, our model for the assumed sizes of the source yields values of τ (optical depth) that are much lower than unity (see Sect. 4.4.4). In Sgr B2(N), Müller et al. (2008) derived from their observations of CH$_2$CHCN a ^{12}C/^{13}C ratio of 21 ± 6.

^{14}N/^{15}N: we obtained an average lower limit value for N(CH$_2$CHC^{14}N)/N(CH$_2$CHC^{15}N) of ≥33 for the two involved components. In Daly et al. (2013) (see Appendix B), we provided a ^{14}N/^{15}N ratio of 256 ± 128 by means of ethyl cyanide, which agree with the terrestrial value (Anders & Grevesse 1989) and with the value obtained by Adande & Ziurys (2012) in the local interstellar medium. The latter authors performed an evaluation of the ^{14}N/^{15}N ratio across the Galaxy (toward 11 molecular clouds) through CN and HNC. They concluded that this ratio exhibits a positive gradient with increasing distance from the Galactic center (which agree with chemical evolution models where ^{15}N has a secondary origin in novae).

D/H: for a tentative detection of mono-deuterated forms of vinyl cyanide we derived a lower limit D/H ratio of ≤0.12 (for HCDCHCN and DCHCHCN) and ≤0.09 (for CH$_2$CDCN) for the hot narrow component, whereas we obtain ≤0.04 (for HCDCHCN and DCHCHCN) and ≤0.03 (for CH$_2$CDCN) for the cold component. Studies of the chemistry of deuterated

species in hot cores carried out by Rodgers & Millar (1996) conclude that the column density ratio D-H remains practically unaltered during a large period of time when D and H-bearing molecules are released to the gas phase from the ice mantles of dust grains. These authors indicate that the observations of deuterated molecules give insight into the processes occurring on the grain mantles by inferring the fractionation of their parent molecules. Furthermore, the fractionation also helps us to trace the physical and chemical conditions of the region (Roueff et al. 2005). Values of this ratio were given by Margulès et al. (2010) from observations of deuterated methyl formate at obtained N(DCOOH$_3$/HCOOCH$_3$) = 0.04 for the hot core; Tercero et al. (2010) estimated an abundance ratio of N(HDCS)/N(H$_2$CS) being 0.05 ± 0.02, which is also for the hot core component. Neil et al. (2013) provided a N(HDCO)/N(H$_2$CO) ratio in the hot core of ≤0.005. Pardo et al. (2001b) derived a value between 0.004–0.01 in the plateau by means of N(HDO)/N(H$_2$O). Persson et al. (2007) also for N(HDO)/N(H$_2$O) derived 0.005, 0.001, and 0.03 for the large velocity plateau, the hot core, and the compact ridge, respectively, and Schilke et al. (1992) provided the DCN/HCN column density ratio of 0.001 for the hot core region.

4.4.4. Line opacity

The MADEX code gives us the line opacity for each transition for the physical components assumed in Table 5. Table 6 shows the opacities for the four cloud components shown in Table 5, which are obtained by varying the source diameter
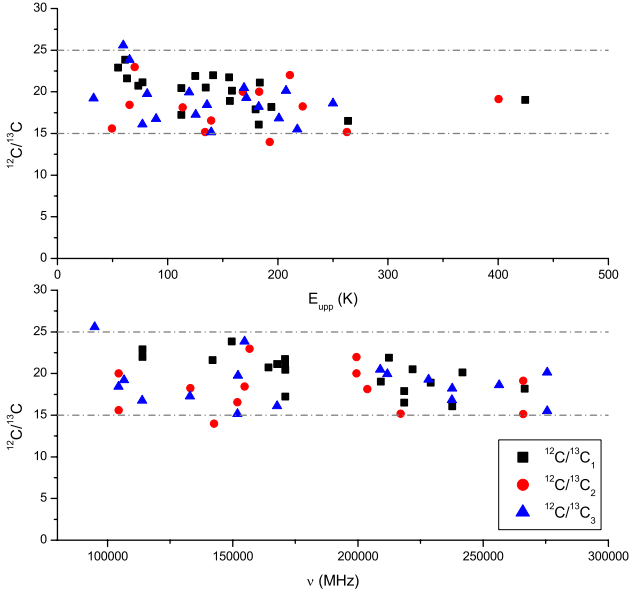
Fig. 14. $^{12}C/^{13}C$ ratios of the observed line intensities for a given transition as a function of the upper level energy (*top panel*) and the frequency (*bottom panel*).

and the column density (the last in order to obtain a good fit between the synthetic spectra and the observations). When we decreased the source diameter, we have to increase the column densities to properly fit the observations and, therefore, the opacities of the lines increment. The extreme case, where the hot and cold cloud components have diameters of 2″ and 5″, respectively, allow us to obtain the maximum total opacity of $\simeq 0.26$ (sum of the opacity of all cloud components) for the $30_{0,30}-29_{0,29}$ transition at 275 588 MHz. This value corresponds with a maximum correction of about 3–5% for our column density results. Column densities have to rise a factor 4 to obtain a total opacity of $\simeq 0.95$, which implies a large mismatch (a factor $\simeq 3$–4 in the line intensity) between model and observations.

Figure 14 shows the $^{12}C/^{13}C$ ratios of the observed line intensities for a given transition against its upper level energy and its frequency. As for the rotational diagrams, unblended lines have been used for deriving these ratios. We observe that most of these ratios are between 15 and 25, and we do not observe a clear decline of this ratio with either the increasing of upper state energy or the increasing of the frequency. In case of optically thick lines, we should expect these large opacities for lines at the end of the 1.3 mm window (240–280 GHz) where the upper state energies are above 150 K even for transitions of $K_a = 0,1$. Figure 14 suggests that the CH$_2$CHCN g.s. lines have $\tau < 1$. Nevertheless, if the bulk of the emission comes from a very small region (<1″), opacities will be larger than 1.

From Fig. 14 we can estimate the average intensity ratios for each ^{13}C isotopologue being 20 ± 6, 18 ± 5, and 19 ± 6 for $^{12}C/^{13}C_1$, $^{12}C/^{13}C_2$, and $^{12}C/^{13}C_3$, respectively. These results with the $^{12}C/^{13}C$ column density ratio derived in Sect. 4.4.3 suggests possible chemical fractionation enhancement of the ^{13}C isotopologues of vinyl cyanide.

4.4.5. Vibrational temperatures

We can estimate the vibrational temperature between the different vibrational modes of the vinyl cyanide according to

$$\frac{N(CH_2CHCN\ v_x)}{N(CH_2CHCN)} = \frac{\exp\left(-\frac{E_{v_x}}{T_{vib}}\right)}{f_\nu}, \qquad (3)$$

where v_x identifies the vibrational mode, E_{v_x} is the energy of the corresponding vibrational state (328.5, 478.6, 657.8, 806.4/ 809.9, and 987.9 K for $v_{11} = 1$, $v_{15} = 1$, $v_{11} = 2$, $v_{10} = 1 \Leftrightarrow$ ($v_{11} = 1, v_{15} = 1$), and $v_{11} = 3$, respectively), T_{vib} is the vibrational temperature, f_ν is the vibrational partition function, $N(CH_2CHCN\ v_x)$ is the column density of the vibrational state, and $N(CH_2CHCN)$ is the total column density of vinyl cyanide. Considering the relation $N(CH_2CHCN) = N_{g.s.} \times f_\nu$ and assuming the same partition function for these species in the ground and in the vibrationally excited states, we only need the energy of each vibrational state and the calculated column density to derive the vibrational temperatures. The vibrational temperature (T_{vib}) is given as a lower limit, since the vibrationally excited gas emitting region may not coincide with that of the ground state.

From the column density results, the T_{vib} in the hot narrow component for each vibrationally excited level were $\simeq 268 \pm 80$ K, $\simeq 246 \pm 74$ K, $\simeq 265 \pm 132$ K, $\simeq 402 \pm 201$ K, and $\simeq 385 \pm 192$ K for $v_{11} = 1$, $v_{15} = 1$, $v_{11} = 2$, $v_{10} = 1 \Leftrightarrow$ ($v_{11} = 1, v_{15} = 1$), and $v_{11} = 3$, respectively. In the same way, the T_{vib} in the cold narrow component for each vibrationally excited level were $\simeq 237 \pm 71$ K, $\simeq 208 \pm 62$ K, $\simeq 220 \pm 110$ K, $\simeq 324 \pm 162$ K, and $\simeq 330 \pm 165$ K for $v_{11} = 1$, $v_{15} = 1$, $v_{11} = 2$, $v_{10} = 1 \Leftrightarrow$ ($v_{11} = 1, v_{15} = 1$), and $v_{11} = 3$, respectively. The average vibrational temperature for $v_{11} = 1$, 2, and $v_{15} = 1$ from both narrow components was 252 ± 76 K, 242 ± 121 K, and 227 ± 68 K, respectively. In the case of $v_{10} = 1 \Leftrightarrow$ ($v_{11} = 1, v_{15} = 1$) and $v_{11} = 3$, the derived T_{vib} is larger than the T_{rot} in the hot narrow component (320 K), which could suggest an inner and hotter region for the emission of these vibrationally excited states of vinyl cyanide. Moreover, a tendency to increase the vibrational temperature with the vibrational energy of the considered state is observed. Vibrational transitions imply ro-vibrational states that may be excited by dust IR photons or collisions with the most abundant molecules in the cloud. Nevertheless, collisional rates are needed to evaluate the excitation mechanisms. The observed differences between T_{rot} and T_{vib} indicate either a far-IR pumping of the highly excited vibrational levels or the presence of a strong temperature gradient toward the inner regions. Some internal heating might be reflected in temperature and density gradients due to processes such as, for example, star formation.

4.5. Detection of isocyanide species

We searched for the isocyanide counterparts of vinyl, ethyl, and methyl cyanide, cyanoacetylene, and cyanamide in our line survey. In this section, we report the first detection toward Orion-KL of methyl isocyanide, and a tentative detection of vinyl isocyanide. The first to sixth columns of Table 7 show the cyanide and isocyanide molecules studied in Orion-KL, their column density values in the components where we assumed emission from the isocyanides, the column density ratio between the cyanide and its isocyanide counterpart, the same ratio obtained by previous authors in Sgr B2 and TMC-1 sources, and the difference of the bond energies between the -CN and -NC isomers.

Vinyl isocyanide (CH$_2$CHNC) is an isomer of the unsaturated hydrocarbon vinyl cyanide. The structure differences between the vinyl cyanide and isocyanide are due to the CNC and CCN linear bonds and their energies, where CCN displays shorter bond distances. The bonding energy difference between vinyl cyanide and isocyanide is 8658 cm^{-1} (24.8 kcal mol^{-1}) (Remijan et al. 2005) with the cyanide isomer being more stable than the isocyanide. We have tentatively detected vinyl isocyanide in our line survey (Fig. 15) with 28 unblended

Table 7. Column densities of the isocyanide species and N(-CN)/N(-NC) ratios.

Molecule	$N_{\rm TOTAL}$ (cm^{-2})	[N(-NC)/N(-CN)]			Isomerization energy
		Orion-KL	Sgr B2	TMC-1	(cm^{-1})
CH$_2$CHCN	$(4 \pm 1) \times 10^{15}$				
CH$_2$CHNC	$\leq(4 \pm 2) \times 10^{14}$	$\leq(1.0 \pm 0.5) \times 10^{-1}$	5×10^{-3a}		8658^a
CH$_3$CN	$(3.2 \pm 0.9) \times 10^{16}$				
CH$_3$NC	$(6.0 \pm 3.0) \times 10^{13}$	$(2 \pm 1) \times 10^{-3}$	2×10^{-2a}	$\geq 9 \times 10^{-2c}$	9486^a
			$(3\text{–}5) \times 10^{-2b}$		
CH$_3$CH$_2$CN	$(7 \pm 2) \times 10^{16}$				
CH$_3$CH$_2$NC	$\leq(2.0 \pm 0.6) \times 10^{14}$	$\leq(3 \pm 2) \times 10^{-3}$	$\leq 3 \times 10^{-1a}$		8697^a
HCCCN	$(4 \pm 1) \times 10^{15}$				
HCCNC	$\leq(3 \pm 1) \times 10^{13}$	$\leq(8 \pm 4) \times 10^{-3}$		$(2\text{–}5) \times 10^{-2d}$	6614^d
				8×10^{-3e}	
HNCCC	$\leq(3 \pm 1) \times 10^{13}$	$\leq(8 \pm 4) \times 10^{-3}$		$(2\text{–}6) \times 10^{-3f}$	$17\,745^d$
				1×10^{-3e}	
NH$_2$CN	$\leq(3 \pm 1) \times 10^{13}$				
NH$_2$NC	$\leq(5 \pm 2) \times 10^{13}$	...	...	...	$18\,537^g$

Notes. Derived column densities for the cyanide and isocyanide species (Col. 2). Columns 3–5 show the ratio between the cyanide and its isocyanide isomer in this work and that derived from other authors in Sgr B2 and TMC-1. Column 6 gives the energy difference for the isomerization between the isocyanide species and its corresponding cyanide.

References. [a] Remijan et al. (2005). [b] Cernicharo et al. (1988). [c] Irvine & Schloerb (1984). [d] Kawaguchi et al. (1992a). [e] Ohishi & Kaifu (1998). [f] Kawaguchi et al. (1992b). [g] Turner et al. (1975).
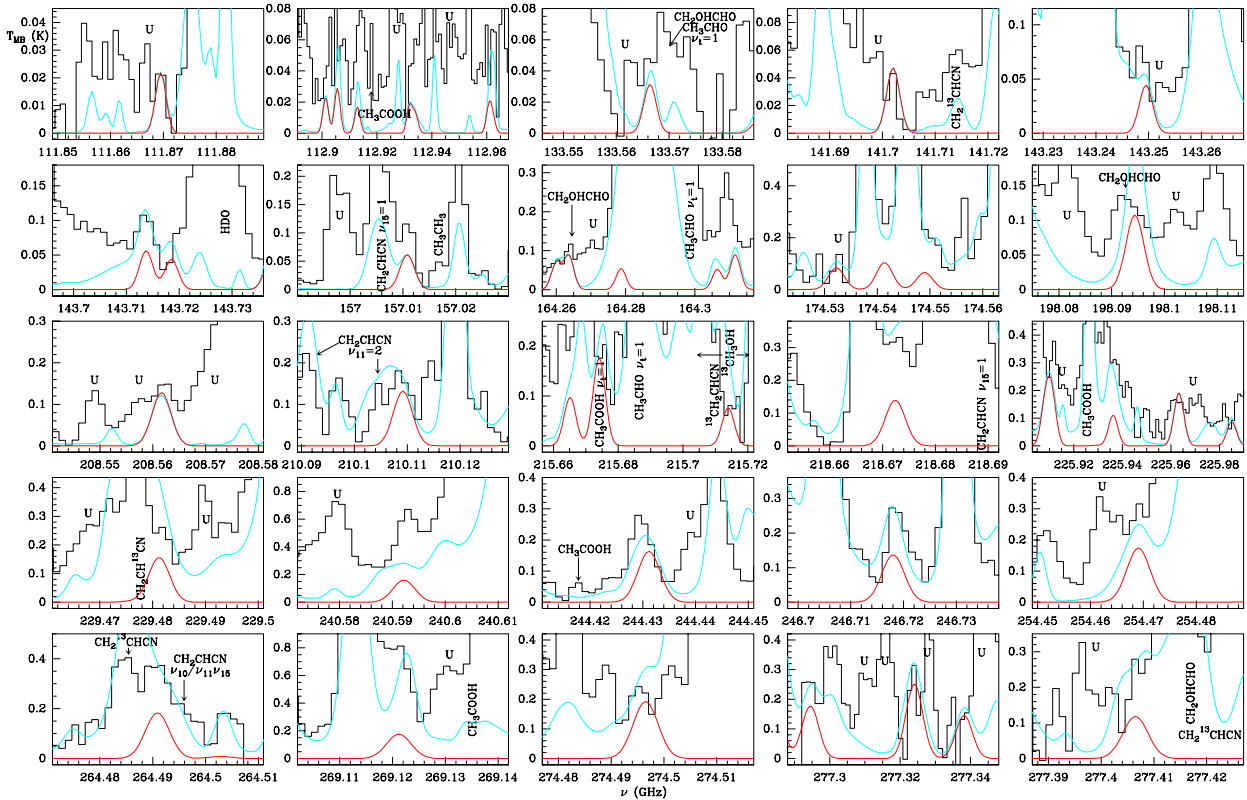
Fig. 15. Observed lines from Orion-KL (histogram spectra) and model (thin red curves) of vinyl isocyanide in its ground state. The cyan line corresponds to the model of the molecules we have already studied in this survey (see text Sect. 4.4.2) including the CH$_2$CHCN species. We consider the detection as tentative. A v$_{\rm LSR}$ of 5 km s^{-1} is assumed.

lines and 26 partially blended lines from a total of 96 detectable lines. This detection is just above the confusion limit. In Table A.14 we show spectroscopic and observational parameters of detected lines of vinyl isocyanide. Rotational constants were derived fitting all experimental data from Bolton et al. (1970), Yamada & Winnewisser (1975), and Bestmann & Dreizler (1982); the dipole moments were from Bolton et al. (1970). For modeling this molecule, we assume the same physical conditions as those found for the vinyl cyanide species

(where we consider both narrow components). We derived a column density of $\leq(3 \pm 2) \times 10^{14}$ cm^{-2} (hot narrow component) and $\leq(5 \pm 3) \times 10^{13}$ cm^{-2} (cold narrow component). We estimate a N(CH$_2$CHNC)/N(CH$_2$CHCN) ratio of $\leq 0.10 \pm 0.05$, while Remijan et al. (2005) derived a ratio of about ≤ 0.005 toward Sgr B2 with an upper limit for the vinyl isocyanide column density of $\leq 1.1 \times 10^{13}$ cm^{-2}.

Methyl cyanide (CH$_3$CN) is a symmetric rotor molecule whose internal rotor leads to two components of symmetry A
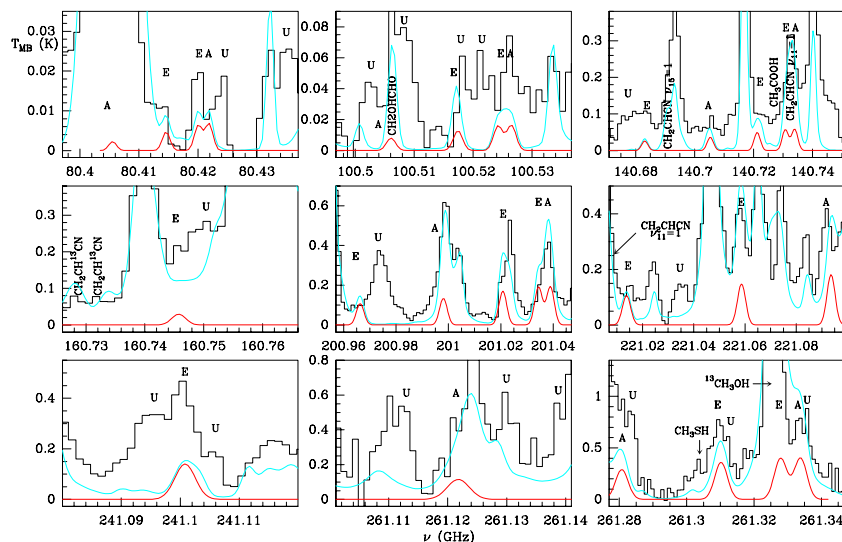
Fig. 16. Observed lines from Orion-KL (histogram spectra) and model (thin red curves) of methyl isocyanide in its ground state. The cyan line corresponds to the model of the molecules we have already studied in this survey (see text Sect. 4.4.2) including the CH$_2$CHCN species. A v_{LSR} of 5 km s^{-1} is assumed.

and E. The column densities of the ground state obtained for both A and E sub-states using an LVG model were derived by Bell et al. (2014) in Orion-KL. They separately fitted different series of K-ladders transitions ($J = 6-5$, $J = 12-11$, $J = 13-12$, $J = 14-13$). We averaged the model results for these four series at the IRc2 position deriving a column density of 3.1×10^{16} cm^{-2} and a kinetic temperature of $\simeq 265$ K. The CH$_3$CN molecule has a metastable isomer named methyl isocyanide (CH$_3$NC) that has been found in dense interstellar clouds (Sgr B2) by Cernicharo et al. (1988) and Remijan et al. (2005). The bonding energy difference between methyl cyanide and isocyanide is 9486 cm^{-1} (27.1 kcal mol^{-1}) (Remijan et al. 2005). We observed methyl isocyanide in Orion-KL for the first time (Fig. 16). For modeling the weak lines of methyl isocyanide we assume a hot core component ($T = 265$ K, $d_{sou} = 10''$, offset = 3$''$, $v_{LSR} = 5$ km s^{-1}, $\Delta v = 5$ km s^{-1}) that is consistent with those derived by Bell et al. (2014). Rotational constants were derived from a fit to the data reported by Bauer & Bogey (1970), Pracna et al. (2011). The constants H_J, L_J, and L_{JKKK} have been fixed to the values derived by Pracna et al. (2011). The constants A and D_K were from Pliva et al. (1995). Dipole moment was that of Gripp et al. (2000). We derived a column density of $(3.0 \pm 0.9) \times 10^{13}$ cm^{-2} for each A and E symmetry substates. We determined a N(CH$_3$NC)/N(CH$_3$CN) ratio of 0.002 which is a factor 15–25 lower than the value obtained by Cernicharo et al. (1988) toward Sgr B2. DeFrees et al. (1985) by means of chemical models predicted this ratio in dark clouds in the range of 0.1–0.4.

Ethyl cyanide (CH$_3$CH$_2$CN) is a heavy asymmetric rotor with a rich spectrum. In our previous paper (Daly et al. 2013), three cloud components were modeled in LTE conditions to determine the column density[9] of this molecule. We obtained a total column density of $(7 \pm 2) \times 10^{16}$ cm^{-2} for this species.

The bonding energy difference between ethyl cyanide and isocyanide is 8697 cm^{-1} (24.9 kcal mol^{-1}) (Remijan et al. 2005). The spectroscopic parameters used for ethyl isocyanide

(CH$_3$CH$_2$NC) were obtained from recent measurements in Lille up to 1 THz by Margulès et al. (in prep.). For CH$_3$CH$_2$NC we provide an upper limit to its column density of $(2 \pm 1) \times 10^{14}$ cm^{-2}. Then, we derived a N(CH$_3$CH$_2$NC)/N(CH$_3$CH$_2$CN) ratio of 0.003. This value is 100 times lower than the upper limit value obtained by Remijan et al. (2005) toward Sgr B2 of ≤0.3.

We observe that the upper limit for the CH$_2$CHNC column density is 5 times higher than the value of methyl isocyanide and holds a similar order of magnitude relationship with the upper limit column density of the tentatively detected ethyl isocyanide.

Cyanoacetylene (HCCCN) is a linear molecule with a simple spectrum. Its lines emerge from diverse parts of the cloud (Esplugues et al. 2013b), although mainly from the hot core. The model of the HCCCN lines was set up using LVG conditions. The authors determined a total column density of $(3.5 \pm 0.8) \times 10^{15}$ cm^{-2}.

Isocyanoacetylene (HCCNC) is a stable isomer of cyanoacetylene and has an energy barrier of 6614 cm^{-1} (18.9 kcal mol^{-1}). Owing to high overlap problems in our data, we only found one line of HCCNC free of blending at 99 354.2 MHz. To obtain an upper limit for its column density we assumed the same physical components as those of Esplugues et al. (2013b). Spectroscopic parameters were derived by fitting the lines reported by Guarnieri et al. (1992); the dipole moment was taken from Gripp et al. (2000). We obtained an upper limit to the HCCNC column density of ≤$(3 \pm 1) \times 10^{13}$ cm^{-2}. We estimated an upper limit for the N(HCCNC)/N(HCCCN) ratio of ≤0.008. The molecule HCCNC was observed for the first time toward TMC-1 (three rotational lines in the frequency range 40–90 GHz) by Kawaguchi et al. (1992a). They obtained a N(HCCNC)/N(HCCCN) ratio in the range 0.02–0.05 in that dark cloud, which is around 2–6 times higher than our upper limit. Ohishi & Kaifu (1998) provided an upper limit value of ≤0.001 also in TMC-1. This molecule has also been detected in the envelope of the carbon star IRC+10216 by Gensheimer (1997).

The other carbene-type isomer of HCCCN is 3-imino-1, 2-propadienylidene (HNCCC) that was predicted to have a relative energy of about 17744.6 cm^{-1} with respect to HCCCN (Kawaguchi et al. 1992b). We provided a tentative detection of this isomer in our survey (Fig. A.3). Its column density,

---

[9] We found a typographical error that is twice the difference in the column density of the hot core component 1 for the ground and excited states in our previous paper (Daly et al. 2013) hence the isotopic abundance has to be modified. We have attached the tables of column densities and that of isotopic abundance for CH$_3$CH$_2$CN in Appendix B.

$(3 \pm 1) \times 10^{13} \, \mathrm{cm}^{-2}$, has been obtained by assuming the same cloud components as those of Esplugues et al. (2013b). Spectroscopic parameters were derived from a fit to lines reported by Kawaguchi et al. (1992b) and Hirahara et al. (1993), and three lines observed in IRC+10216 with an accuracy of 0.3 MHz. The dipole moment was determined from Botschwina et al. (1992). We derived a $N(\mathrm{HNCCC})/N(\mathrm{HCCCN})$ upper limit ratio of 0.008. Kawaguchi et al. (1992a) obtained a $N(\mathrm{HNCCC})/N(\mathrm{HCCCN})$ ratio in the range 0.002–0.006 in TMC-1.

After the detection of cyanamide ($\mathrm{NH_2CN}$) by Turner et al. (1975), Cummins et al. (1986), and Belloche et al. (2013) in Sgr B2, we report a tentative detection of cyanamide ($\mathrm{NH_2CN}$) in Orion-KL (see Fig. A.4). Frequencies, energies, and line intensities for $\mathrm{O^+\text{-}NH_2CN}$ and $\mathrm{O^-\text{-}NH_2CN}$ were those published in the JPL catalog (based on the works of Read et al. 1986 and Birk 1988). We estimated a column density $\leq (3 \pm 1) \times 10^{13} \, \mathrm{cm}^{-2}$ ($\mathrm{O^+ + O^-}$) by assuming that its lines are coming only from one component (hot core) at 200 K ($v_{\mathrm{LSR}} = 5 \, \mathrm{km \, s^{-1}}$, $\Delta v = 5 \, \mathrm{km \, s^{-1}}$, $d_{\mathrm{sou}} = 10''$, offset $= 2''$). $\mathrm{NH_2CN}$ has an isomer differing only in the CN group, so that, the isomerization energy between the cyanamide and isocyanamide ($\mathrm{NH_2NC}$) is $18\,537 \, \mathrm{cm}^{-1}$ (Vincent & Dykstra 1980). In this work, we also provided only an upper limit column density of isocyanamide ($\mathrm{O^+ + O^-}$) being $\leq (5 \pm 1) \times 10^{13} \, \mathrm{cm}^{-2}$. Spectroscopic parameters were derived fitting the rotational lines reported by Schäfer et al. (1981). the dipole moment was determined by Ichikawa et al. (1982) from ab-initio calculations.

In Table 7, we give values of interconversion energies between cyanide and isocyanide molecules. These interconversion barriers are high, and under astronomical environments, such as the hot cores, it is unlikely that the isocyanide isomers are produced by rearrangement of the corresponding cyanide species. Remijan et al. (2005), proposed that non-thermal processes (such as shocks or enhanced UV flux in the surrounding medium) may be the primary route to the formation of interstellar isocyanides by the conversion of the cyanide to its isocyanide counterpart. Nevertheless, other formation routes have to be explored to explain their presence in environments dominated by thermal processes. Dissociative recombination reactions on the gas phase probably lead to the formation of the cyanide or isocyanide molecules. Depending on the structure of the protonated hydrocarbon and the branching ratios of the dissociative recombination pathway, the molecule $\mathrm{H_2C_3N^+}$ might produce cyanoacetylene and isocyanoacetylene, and similarly, the molecule $\mathrm{C_2H_4N^+}$ could yield methyl cyanide and methyl isocyanide (Green & Herbst 1979). DeFrees et al. (1985) found that the calculated ratio of the formation of the protonated precursor ions ($\mathrm{CH_3CNH^+}$ and $\mathrm{CH_3NCH^+}$) agrees with the detection of $\mathrm{CH_3NC}$ in dark clouds (Irvine & Schloerb 1984). In the same way, the recombination reaction of the molecule $\mathrm{C_2H_6N^+}$ could give ethyl isocyanide (Bouchoux et al. 1992). Once the isocyanides are formed, they remain as metastable species due to the high barrier quoted above supporting the possible existence of isolated isocyanides (Vincent & Dykstra 1980). On the other hand, a recent experimental study of the interaction of the diatomic radical CN and the π-system $\mathrm{C_2H_4}$ confirms that the possible pathway to $\mathrm{CH_2CHNC}$ becomes negligible even at temperatures as high as 1500 K (Balucani et al. 2000; Leonori et al. 2012). Since the cyanide molecules are strongly related to the dust chemistry (Blake et al. 1987; Charnley et al. 1992; Caselli et al. 1993; Rodgers & Charnley 2001; Garrod et al. 2008; Belloche et al. 2013), we also can infer a probable origin for the isocyanides from reactions on grain mantles.

5. Discussion

5.1. Abundances and column density ratios between the cyanide species

Table 8 shows the ground state abundances in the hot core (or hot core + plateau) component of the studied species in this work and the column density ratios between vinyl cyanide and other cyanide molecules. Results provided by different authors in Orion-KL, the well-studied star forming region Sgr B2, the star forming complex G34.3+0.2 (hot core), and the dark molecular cloud TMC-1 are also given in this table.

For Orion-KL, our study covers a wide frequency range allowing detailed modeling of the molecular emission. Moreover, the molecular abundances obtained from other authors, which are shown in Table 8, are often obtained with different telescopes and different assumptions on the size and physical conditions of Orion-KL. For this reason, these abundances are given in Table 8 for comparison purposes, but we focus on the results obtained in this work that have been derived from a common set of assumptions, sizes, and physical conditions for Orion-KL.

To estimate molecular abundances for the cyanide and isocyanide species, we assume that the column density of $\mathrm{H_2}$ ($N_{\mathrm{H_2}}$) is $4.2 \times 10^{23} \, \mathrm{cm}^{-2}$ for the hot core, $2.1 \times 10^{23} \, \mathrm{cm}^{-2}$ for the plateau, and $7.5 \times 10^{22} \, \mathrm{cm}^{-2}$ for the compact ridge and for the extended ridge, as derived by Tercero et al. (2010).

The total abundance for the $\mathrm{CH_2CHCN}$ ground state, as derived from all the components (hot core + mix hot core-plateau) (see Table 5), was $X(N_{\mathrm{CH_2CHCN}}/N_{\mathrm{H_2}}) = (2.0 \pm 0.6) \times 10^{-8}$. By means of the derived vibrational temperatures, we can estimate the vibrational partition function that follows the Eq. (4) for a Boltzmann distribution in both narrow components (1.7 and 1.5 for hot and cold narrow components, respectively) and correct the ground state column density to the total one (see Sect. 4.4.5). Considering these results for the vibrational partition function, we obtained $X_{\mathrm{CH_2CHCN}} \simeq (3.1 \pm 0.9) \times 10^{-8}$.

$$f_\nu = 1 + \sum_{x=1}^{n} d_x \exp\left(-\frac{E_{v_x}}{T_{\mathrm{vib}}}\right), \qquad (4)$$

where d_x is the degeneracy of the vibrational mode x and the low T_{vib} leads to $f_\nu \simeq 1$.

Assuming the column density values of $\mathrm{CH_3CN}$ of Bell et al. (2014), the abundance for $\mathrm{CH_3CN}$ ground state in the hot core component was $\simeq (1.0 \pm 0.3) \times 10^{-7}$. To estimate the correction of the column density of $\mathrm{CH_3CN}$ from excited vibrational states, we have derived the column density of this molecule in its $v_8 = 1$ lower energy state (525.2 K) and found a $N(\mathrm{CH_3CN}, v_8 = 1) \simeq 1.4 \times 10^{15} \, \mathrm{cm}^{-2}$ and $T_{\mathrm{vib}} \simeq 159$ K (considering only the hot core and plateau components). Hence, the vibrational partition function is ~ 1.04 and $X_{\mathrm{Total}} \simeq X_{\mathrm{ground}}$ for methyl cyanide.

For ethyl cyanide we use the column density results of Daly et al. (2013) (see Appendix B). We determine the $X(N_{\mathrm{CH_3CH_2CN}}/N_{\mathrm{H_2}})$ ratio being $(1.8 \pm 0.5) \times 10^{-7}$ for the ground state. Assuming the vibrational temperatures obtained in Daly et al. (2013) $\simeq 160 \pm 50$ K, $\simeq 185 \pm 55$ K, and $\simeq 195 \pm 95$ K for v_{13}/v_{21} ($E_{\mathrm{u}} = 306.3/315.4$ K), v_{20} ($E_{\mathrm{u}} = 531.2$ K), and v_{12} ($E_{\mathrm{u}} = 763.4$ K), respectively, the estimated vibrational partition function is 1.4, so we derived an abundance ratio $X \simeq (2.5 \pm 0.8) \times 10^{-7}$ for ethyl cyanide.

Esplugues et al. (2013b) derived an abundance of 7.3×10^{-9} for $\mathrm{HC_3N}$ (hot core + plateau) in the ground state.

Assuming a mean vibrational temperature of 360 K in the hot core that is calculated by these authors, the vibrational partition function from v_5 ($E_{\mathrm{u}} = 954.48$), v_6 ($E_{\mathrm{u}} = 718.13$), $v_7 = 1$

Table 8. Column density ratios and molecular abundances.

Molecule	Orion-KL		Sgr B2		G34.3+0.2		TMC-1	
	X	R	X	R	X	R	X	R
CH$_2$CHCN	$(2.0 \pm 0.6) \times 10^{-8\,\dagger}$	...	$6.2 \times 10^{-8\,j}$	...	$3.0 \times 10^{-10\,n}$	...	$1.0 \times 10^{-9\,p}$	...
	$1.5 \times 10^{-9\,a}$		$6.0 \times 10^{-8\,k}$					
	$1.8 \times 10^{-9\,b}$							
CH$_3$CN	$(1.0 \pm 0.3) \times 10^{-7\,\dagger\,d}$	$0.20^{\dagger\,d}$	$3.0 \times 10^{-8\,k}$	0.40^e	...	...	$7.5 \times 10^{-10\,p}$	1.3^p
	$4.0 \times 10^{-9\,a}$	0.39^a		2.0^k				
	$7.8 \times 10^{-9\,b}$	0.23^b		3.4^l				
	$5.1 \times 10^{-9\,c}$	1.7^e		0.40^m				
		$0.18\text{–}1.8^f$		0.37^o				
		0.48^g						
CH$_3$CH$_2$CN	$(1.8 \pm 0.5) \times 10^{-7\,\dagger\,h}$	$0.11^{\dagger\,h}$	$6.0 \times 10^{-10\,k*}$	0.72^e	$1.0 \times 10^{-8\,n}$	0.20^n	...	$>2.00^q$
	$3.0 \times 10^{-9\,a}$	0.50^a		11^l				
	$9.8 \times 10^{-9\,b}$	0.18^b		0.67^m				
		0.15^e		1.7^n				
		0.14^f		0.40^o				
		0.06^g						
HCCCN	$(7 \pm 2) \times 10^{-9\,\dagger\,i}$	$2.9^{\dagger\,i}$	$5.0 \times 10^{-9\,k}$	0.13^e	...	...	$7.5 \times 10^{-8\,p}$	0.01^p
	$1.8 \times 10^{-9\,a}$	0.86^a		12^k				
	$1.6 \times 10^{-9\,b}$	1.1^b		61^o				
	$1.8 \times 10^{-9\,c}$	2.11^e						
		$0.6\text{-}1.5^f$						
		0.16^g						
NH$_2$CN	$\leq(7 \pm 2) \times 10^{-11\,\dagger}$	$\geq 286^{\dagger}$	$9.0 \times 10^{-11\,k*}$	1.4^e	...	...	...	...
		30^e		14^o				

Notes. Abundances (X) and column density ratios between vinyl cyanide and some studied cyanides (R) in Orion-KL and other sources. [†] Values from this work. [a] Sutton et al. (1995), hot core, telescope beam ~13.7″. [b] Blake et al. (1987), hot core, telescope beam ~30″. [c] Persson et al. (2007), hot core, source size 10″. [d] Bell et al. (2014), hot core (different components between 5–10″) + plateau (10″). [e] Turner (1991). [f] Johansson et al. (1984). [g] Schilke et al. (1997). [h] Daly et al. (2013), hot core (4–10″) and mix hot core-plateau (25″). [i] Esplugues et al. (2013b) hot core (7–10″) and plateau (20″). [j] Müller et al. (2008). [k] Nummelin et al. (2000) small source-size averaged. [k*] Nummelin et al. (2000) beam averaged. [l] Remijan et al. (2005). [m] Belloche et al. (2009). [n] Mehringer & Snyder (1996). [o] Belloche et al. (2013). [p] Ohishi & Kaifu (1998). [q] Minh & Irvine (1991).

(E_u = 320.45), and v_7 = 2 (E_u = 642.67) is ~2.6 for the hot core components. Applying this correction in the hot core, we obtained a total abundance of $X_{HC_3N} \simeq 1.3 \times 10^{-8}$ (hot core + plateau).

For NH$_2$CN, we determine a molecular abundance $X(N_{NH_2CN}/N_{H_2})$ of $\leq(7 \pm 2) \times 10^{-11}$.

The column density ratio between the unsaturated hydrocarbon CH$_2$CHCN and other -CN bearing molecules, such as CH$_3$CH$_2$CN, CH$_3$CN, HC$_3$N, and NH$_2$CN, $N(CH_2CHCN)/N(X\text{-}CN)$, could be used to track a possible different evolutionary state described by different chemical models and to provide inputs for the chemical modeling of the cloud.

We obtain an abundance ratio $N(CH_2CHCN)/N(X\text{-}CN)<1$ for the saturated cyanide molecules (CH$_3$CH$_2$CN and CH$_3$CN); these ratios related with methyl and ethyl cyanide obtained by different authors are lower (in general) in Orion-KL than in the galactic center (Sgr B2). We also note that the relative abundance of CH$_3$CH$_2$CN with respect to vinyl cyanide in Orion is twice as much as in the hot core G34.3+0.2. In contrast, in the dark cloud TMC-1 vinyl cyanide is more abundant than the saturated -CN hydrocarbons.

The relative abundance between CH$_2$CHCN and HC$_3$N follows an opposite tendency than that of methyl and ethyl cyanide: HC$_3$N is less abundant than CH$_2$CHCN in Orion-KL and Sgr B2, whereas HC$_3$N is at least two orders of magnitude more abundant than CH$_2$CHCN in TMC-1. Nevertheless, we want to remark that we only address the hot core (or hot core + plateau) abundances in our work in Table 8. For vinyl and ethyl cyanide and cyanamide, these abundances correspond with the total abundance in the ground state in Orion-KL. However, cyanoacetylene appears in all the Orion-KL components, so its total abundance is higher than that of vinyl cyanide when we consider the whole Orion-KL region covered by our observations.

Finally, we find an lower limit of 286 for $X(CH_2CHCN)/X(NH_2CN)$.

The formation routes of the cyanide molecules in several environments have been extensively discussed by different authors. As ethyl cyanide was mainly detected in hot core regions (Johansson et al. 1984; Sutton et al. 1985; Blake et al. 1987), the grain surface production (by hydrogenation of HC$_3$N) seemed to be the main formation mechanisms for this molecule (Blake et al. 1987; Charnley et al. 1992; Caselli et al. 1993). On the other hand, vinyl cyanide has been detected in the dark could TMC-1 (Matthews & Sears 1983) and in hot cores (where appeared correlated with ethyl cyanide emission), indicating that gas phase production was also important for forming these species. Chemical models of Charnley et al. (1992) and
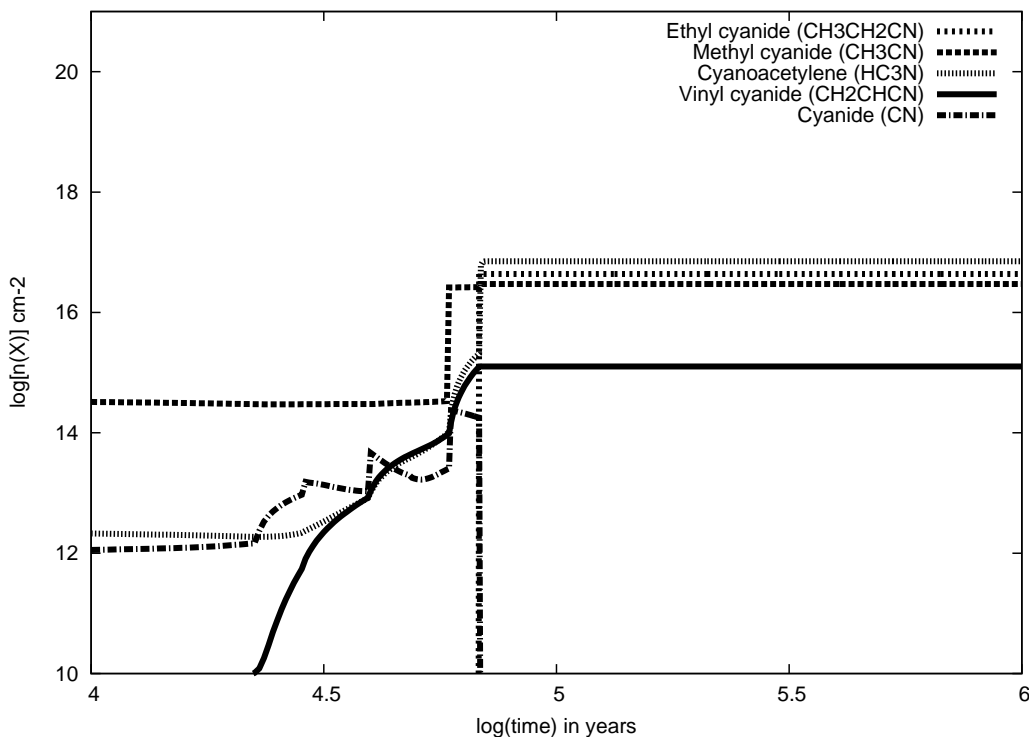
Fig. 17. Time evolution of the column densities of CH_2CHCN, CH_3CN, CH_3CH_2CN, HC_3N, and CN for a hot core chemical model.

Caselli et al. (1993) in hot cores predicted that CH_2CHCN forms in gas phase reactions involving CH_3CH_2CN. Caselli et al. (1993) derived a relation between the abundance ratio $X(CH_2CHCN)/X(CH_3CH_2CN)$ and the evolutionary stage of the core. This ratio has been used by several authors as a chemical clock to estimate the cloud age (Fontani et al. 2008; Müller et al. 2008). Belloche et al. (2009) performed a detailed analysis of the cyanide species detected in Sgr B2, including chemical models based on that of Garrod et al. (2008). Considering the observed relative abundances between these species, they conclude that the main formation mechanism for alkyl cyanides is probably the sequential addition of CH_2 or CH_3 radicals to CN, CH_2CN, and C_2H_4CN on the grain surfaces. Formation of methyl cyanide is dominated by reactions on the grains by addition of CH_3 and CN radicals, but it may also be formed by gas-phase processes after the evaporation of HCN. Vinyl cyanide is predominantly formed in the gas-phase through the reaction of CN with C_2H_4. Then CH_2CHCN accretes onto the grains by being a potential precursor, with HC_3N of ethyl cyanide and *n*-propyl cyanide. After the evaporation of the ice mantles, vinyl cyanide is efficiently formed again in the gas phase.

5.2. Chemical model

We have investigated the observed column densities of CH_2CHCN, CH_3CN, CH_3CH_2CN, HCCCN, and CN using a time and depth dependent gas-grain chemical model, UCL_CHEM. UCL_CHEM is a two-phase model, which follows the collapse of a prestellar core (Phase I), followed by the warming and evaporation of grain mantles (Phase II). In Phase II, we increase the dust and gas temperature up to 300 K to simulate the presence of a nearby infrared source in the core. For the hot core component, we model both a 10 $M_\odot$ and 15 $M_\odot$ star with a final density of 10^7 cm^{-3}. During the collapse, atoms and molecules collide with and freeze onto grain surfaces. The depletion efficiency is determined by the fraction of the gas-phase

material that is frozen on to the grains, which is dependent on the density, the sticking coefficient and other properties of the species and grains (see Rawlings et al. 1992). In our modeling, we have explored the uncertainty in grain properties and sticking coefficients by varying the depletion percentage. Initial atomic abundances are taken from Sofia & Meyer (2001), as in Viti et al. (2004). Gas-phase reaction rate coefficients are taken from the UMIST database of Woodall et al. (2007), however, some have been updated with those from the KIDA database (Wakelam 2009). We also include some simple grain-surface reactions (mainly hydrogenation) as in Viti et al. (2004). While COMs (complex organic molecules) may also form via surface reactions involving heavier (than hydrogen) species (e.g. Garrod et al. 2008), the mobility of most heavy species on grains has not been experimentally investigated; hence, for this qualitative analysis, we chose to adopt a simpler model where only the most efficient surface reactions occur. In this way we can give a lower limit to the formation of COMs which may be augmented by more complex reactions should they occur. In Phase I, non-thermal desorption is considered as in Roberts et al. (2007).

Within our grid of models, we find that models where we simulate a 10 $M_\odot$ star and 100% of CO frozen onto grain surfaces which most accurately reproduce the observed column densities of CH_2CHCN, CH_3CN, and CH_3CH_2CN. Figure 17 shows the column density as a function of time during phase II for this model. The column density produced by the model for HCCCN is an order of magnitude higher than the observed value. While our models simulate both gas phase and grain surface reactions for all of these species, the grain surface reactions are essential to reproduce the observed column densities. We therefore conclude that we are missing some grain surface destruction routes for HCCCN, and, consequently, overproduced this species in our models. Moreover, the deep decreased of the CN abundance when CH_3CH_2CN appears is observationally confirmed by the lack of the hot core component in the CN lines even at the HIFI frequencies (Crockett et al. 2014). For details of

the same surface chemistry approach, see Viti et al. (2004) and Bell et al. (2014).

5.3. Further issues for CH$_2$CHCN

Further observations of telescopes with higher sensitivity and spatial resolution, such as Atacama Large Millimeter/submillimeter Array (ALMA), could provide additional detections of other vibrationally excited states above $600\,cm^{-1}$, such as the outstanding states in the $3v_{11}/2v_{15}/v_{14}$ triad of states near $680\,cm^{-1}$ for which the spectroscopy is presently reported. In this study, we found that the $v_{11} = 3$ ($987.9\,K$ or $686.6\,cm^{-1}$) vibrational mode was near the detection limit, so we could not reliably address other vibrational components of the $3v_{11}/2v_{15}/v_{14}$ triad. We also note that Belloche et al. (2013) have recently detected the combination state $v_{15} = v_{11} = 1$ (809.9 K) but has not yet reported detection of the $v_{10} = 1$ (806.4 K) state toward Sgr B2(N). On the other hand, the $v_{15} = 2$ (960.2 K) excited state detected by these authors might be detected only at the limit in our study.

In the present work, we extended the laboratory coverage of the rotational spectrum of vinyl cyanide and the analysis of its vibrationally excited states to provide ample basis for detection of transitions from further excited vibrational states at even higher vibrational energies. The laboratory basis for detecting states up to as high as $v_9 = 1$ (1250 K) is now available. On the other hand, as implied by Fig. 1 and results for $4v_{11} = 4$, considerable spectroscopic analysis is required for satisfactory understanding of states above $v_9 = 1$.

6. Summary

Vinyl cyanide is one of the most abundant molecules in Orion-KL and a possible precursor of alanine. This study of the vinyl cyanide species improves the knowledge of the physical and chemical conditions of this high-mass star forming region. We have performed an identification of the ground state of CH$_2$CHCN and of its vibrationally excited states (up to 988 K) in the Orion-KL Nebula thanks to a new spectroscopic laboratory analysis by using Stark modulation and frequency-modulated spectrometers. Our results are based on rotational diagrams, integrated-frequency maps, and Gaussian fits to optimize the physical and chemical parameters that simulate the best synthetic spectrum of CH$_2$CHCN (using MADEX), which fit the observation conditions of the Orion-KL region in an accurate way. We have found N(CH$_2$CHCN) $\simeq (6 \pm 2) \times 10^{15}$ cm^{-2} from four cloud components of hot core/plateau nature (320-90 K). A total abundance of $(3.1\pm0.9)\times10^{-8}$ for vinyl cyanide is provided in this work. We have detected the CH$_2$CHCN $v_{11} = 2$, 3 vibrational modes for the first time in Orion-KL and the CH$_2$CHCN $v_{10} = 1 \Leftrightarrow (v_{11} = 1, v_{15} = 1)$ excited state for the first time in the space. We have seen that these species with those of the three monosubstituted ^{13}C and the ^{15}N isotopologues and the tentative detection of the three monodeuterated species of vinyl cyanide contribute with more than 1100 observed lines in the 80–280 GHz domain covered by the Orion line survey. We highlight the importance for spectroscopic catalogs to introduce vibrationally excited species in the astronomical detections.

The column density ratios between the vinyl cyanide g.s. and the vibrationally excited states have been used to obtain temperatures at which the vibrational modes are excited and to correct the ground column density from the vibrational partition function. The high vibrational temperature ($T_{vib} > T_{rot}$) for the states $v_{10} = 1 \Leftrightarrow (v_{11} = 1, v_{15} = 1)$ and $v_{11} = 3$ suggests a temperature

gradient toward the inner regions of the hot core. To infer the population mechanism of the vibrationally excited states (collisions and/or infrared radiation), collisional rates are needed.

Owing to the importance of isomerism for understanding a more precise way in forming interstellar molecules, we have included the study of ethyl isocyanide, methyl isocyanide, isocyanoacetylene, 3-imino-1, 2-propadienylidene, and isocyanamide in our work. We have provided the detection of methyl isocyanide for the first time in Orion-KL and tentative detections for the rest.

Finally, we have investigated the studied column densities of CH$_2$CHCN, CH$_3$CN, CH$_3$CH$_2$CN, and HCCCN using a time dependent gas-grain chemical model (UCL_CHEM) which reproduce the observed column densities for these molecules reasonably well, although it overestimates that for HCCCN. This is probably due to the efficiency for its formation on the grains being too high: a detailed investigation of the formation and destruction route for this species in chemical models is beyond the scope of this work. More quantitative models ought to be able to reproduce this molecule by investigating the efficiency of the formation of HCCCN on the grains.

References

Adande, G. R., & Ziurys, L. M. 2012, ApJ, 744, 194
Anderson, R. J., & Gwinn, W. D. 1968, J. Chem. Phys., 49, 39, 88
Agúndez, M., Cernicharo, J., Pardo, J. R., et al. 2008, Astron. Space Sci., 313, 229
Anders, E., & Grevesse, N. 1989, Geochim. Cosmochim. Acta, 53, 197
Balucani, N., Asvany, O., Huang, L. C. L., et al. 2000, ApJ, 545, 892
Baskakov, O. I., Dyubko, S. F., Ilyushin, V. V., et al. 1996, J. Mol. Spectr., 179, 94
Bauer, A., & Bogey, M. 1970, C. R. Acad. Sci. Paris, 271B, 892
Bell, T., Cernicharo, J., Viti, S., et al. 2014, A&A, 564, A114
Belloche, A., Garrod, T. D., Müller, H. S. P., et al. 2009, A&A, 499, 215
Belloche, A., Müller, H. S. P., Menten, K. M., Schilke, P., & Comito, C. 2013, A&A, 559, A47
Bera, P. P., Lee, T. J., & Schaefer, H. F. 2009, J. Chem. Phys., 131, 074303
Bestmann, G., & Dreizler, H. 1982, Z. Naturforsch, 37a, 58
Betz, A. L. 1981, ApJ, 244, L103
Beuther, H., & Nissen, H. D. 2008, ApJ, 679, L121
Birk, H. 1988, Ph.D. Thesis, Justus Liebig-Universit Giessen, Germany
Blake, G. A., Sutton, E. C., Masson, C. R., & Philips, T. G. 1987, ApJ, 315, 621
Blake, G. A., Mundy, L. G., Carlstrom, J., et al. 1996, ApJ, 472, L49
Bolton, K., Owen, N. L., & Sheridan, J. 1970, Spectrochim. Acta, 26, 909
Botschwina, P., Horn, M., Seeger, S., & Flgge, J. 1993, Chem. Phys. Lett., 195, 4, 427
Bouchoux, G., Nguyen, M. T., & Longevialle, P. 1992, J. Am. Chem. Soc., 114, 10000
Capone, L. A., Prasad, S. S., Huntress, W. T., et al. 1981, Nature, 293, 45
Carvajal, M., Margulés, L., Tercero, B., et al. 2009, A&A, 500, 1109
Caselli, P. 2005, Ap&SS Library, 324, 47
Caselli, P., Hasegawa, T. I., & Herbst, E. 1993, ApJ, 408, 548
Cazzoli, G., & Kisiel, Z. 1988, J. Mol. Spectr., 130, 303
Cernicharo, J. 1985, Internal IRAM report (Granada: IRAM)
Cernicharo, J. 2012, in ECLA-2011: Proc. of the European Conference on Laboratory Astrophysics, EAS Pub. Ser. 2012, eds. C. Stehl, C. Joblin, & L. d'Hendecourt (Cambridge: Cambridge Univ. Press), 58, 251
Cernicharo, J., Kahane, C., Guelin, M., & Gomez-Gonzalez, J. 1988, A&A, 189, L1
Cernicharo, J., Tercero, B. A., Fuente, A., et al. 2013, ApJ, 771, L10
Charnley, S. B., Tielens, A. G. G. M., & Millar, T. J. 1992, ApJ, 399, L71

Cole, A. R. H., & Green, A. A. 1973, J. Mol. Spectr., 48, 246
Colmont, J. M., Wlodarczak, G., Priem, D., et al. 1997, J. Mol. Spectr., 181, 330
Costain, C. C., & Stoicheff, B. P. 1959, J. Chem. Phys., 1959, 30, 777
Coudert, L. H., Drouin, B. J., Tercero, B., et al. 2013, ApJ, 779, 119
Crockett, N. R., Bergin, E. A., Neill, J. L., et al. 2014, ApJ, 787, 2
Cummins, S. E., Linke, R. A., & Thaddeus, P. 1986, ApJSS, 60, 819
Daly, A. M., Bermúdez, C., López, A., et al. 768, 81, ApJ, 2013
Demaison, J., Cosléou, J., Bocquet, R., & Lesarri, A. G. 1994, J. Mol. Spectr., 167, 400
Demyk, K., Mäder, H., Tercero, B., et al. 2007, A&A, 466, 255
Demyk, K., Wlodarczak, G., & Carvajal, M. 2008, A&A, 489, 589
DeFrees, D. J., McLean, A. D., & Herbst, E. 1985, ApJ, 293, 236
Ervasti, H. K., Jobst, K. J., Gerbaux, P., et al. 2009, Chem. Phys. Lett., 482, 211
Esplugues, G. B., Tercero, B., Cernicharo, J., et al. 2013a, A&A, 556, A143
Esplugues, G. B., Cernicharo, J., Viti, S., et al. 2013b, A&A, 559, A51
Fliege, E., & Dreizler, H. 1985, Z. Naturforsch., 40a, 43
Fontani, F., Caselli, P., Bourke, T. L., Cesaroni, R., & Brand, J. 2008, A&A, 477, L45
Gardner, F. F., & Winnewisser, G. 1975, ApJ, 195, L127
Garrod, R. T., Weaver, S. L. W., & Herbst, E. 2008, ApJ, 682, 283
Gensheimer, P. D. 1997, Ap&SS, 251, 199
Gerry, M. C. L., & Winnewisser, G. 1973, J. Mol. Spectr., 48, 1
Golsmith, P. F., & Langer, W. D. 1999, ApJ, 517, 209
Green, S., & Herbst, E. 1979, ApJ, 229, 121
Gripp, J., Guarnieri, A., Stahl, W., & Lentz, D. 2000, J. Mol. Struc. 526, 81
Guarnieri, A., Hinze, R., Krüger, M., et al. 1992, J. Mol. Spectr., 156, 1, 39
Guélin, M., Brouillet, N., Cernicharo, J., Combes, F., & Wooten, A. 2008, Ap&SS, 313, 45
Halverson, F., Stamm, R. F., & Whalen, J. J. 1948, J. Chem. Phys., 16, 808
Haykal, I., Carvajal, M., Tercero, B., et al. 2014, A&A, 568, A58
Heise, H. M., Lutz, H., & Dreizler, H. 1974, Z. Naturforsch., 29, 1345
Hirahara, Y., Ohshima, Y., & Endo, Y. 1993, ApJ, 403, L83
Hirota, T., Bushimata, T., Choi, Y. K., et al. 2007, PASJ, 59, 897
Ichikawa, K., Hamada, Y., Sugawara, Y., et al. 1982, Chem. Phys., 72, 301
Irvine, W. M., & Schloerb, F. P. 1984, ApJ, 282, 516
Irvine, W. M., Friberg, P., Hjalmarson, A., et al. 1988, ApJ, 334, L107
Johansson, L. B. E., Andersson, C., Elldèr, J., et al. 1984, A&A, 130, 227
Johnson, D. R., Lovas, F. J., Guélin, M., & Thaddeus, P. 1977, ApJ, 218, 370
Kawaguchi, K., Ohishi, M., & Ishikawa, S.-I. 1992a, ApJ, 386, L51
Kawaguchi, K., Takano, S., Ohishi, M., et al. 1992b, ApJ, 396, L49
Khlifi, M., Nollet, M., Paillous, P., et al. 1999, J. Mol. Spectr., 194, 206
Kim, M. K., Hirota, T., Honma, M., et al. 2008, PASJ, 60, 991
Kisiel, Z. 2001, in Spectroscopy from Space, eds. J., Demaison, et al. (Dordrecht: Kluwer Academic Publishers), 91
Kisiel, Z., Pszczolkowski, L., Medvedev, I. R., et al. 2005, J. Mol. Spectr., 233, 231
Kisiel, Z., Pszczolkowski, L., Drouin, B. J., et al. 2009a, J. Mol. Spectr., 258, 26
Kisiel, Z., Bialkowska-Jaworska, E., Butler, R. A. H, et al. 2009b, J. Mol. Spectr., 254, 78
Kisiel, Z., Pszczolkowski, L., Drouin, B. J., et al. 2011, talk MH09, 66th International Symp. on Molecular Spectroscopy, Columbus, Ohio, USA
Kisiel, Z., Pszczolkowski, L., Drouin, B. J., et al. 2012, J. Mol. Spectr., 280, 134
Kolesniková, L., Tercero, B., Cernicharo, J., et al. 2014, ApJ, 784, L7
Krasnicki, A., & Kisiel, Z. 2011, J. Mol. Spectr., 270, 83
Krasnicki, A., Kisiel, Z., Drouin B. J., & Pearson J. C. 2011, J. Mol. Struct., 1006, 20
Krüger, M., & Dreizler, H. 1992, Z. Naturforsch., 47a, 1067
Leonori, F., Petrucci, R., Wang, X., Casavecchia, P., & Balucani, N. 2012, Chem. Phys. Lett., 553, 1
Margulès, L., Motiyenko, R. A., Demyk, K., et al. 2009, A&A, 493, 565
Margulès, L., Huet, T. R., Demaison, J., et al. 2010, ApJ, 714, 1120
Mathews, H. E., & Sears, T. J. 1983, ApJ, 267, L53
Martinez Jr., O., Lattanzi, V., Thorwirth, S., & McCarthy, M. C. 2013, J. Chem. Phys., 138, 094316
Menten, K. M., Reid, M. J., Forbrich, J., & Brunthaler A. 2007, A&A, 474, 515
Mehringer, D. M., & Snyder, L. 1996, ApJ, 471, 897
Minh, Y. C., & Irvine, W. M. 1991, Ap&SS, 175, 165
Morris, M., Turner, B. E., Palmer, P., & Zuckerman, B. 1976, ApJ, 205, 82
Motiyenko, R. A., Tercero, B., Cernicharo, J., & Margulés, L. 2012, A&A, 548, A71
Müller, H. S. P., Thorwirth, S., Roth, D. A., & Winnewisser, G. 2001, A&A, 370, L49
Müller, H. S. P., Schlöder, F., Stutzki, J., & Winnewisser, G. 2005, J. Mol. Struct., 742, 215
Müller, H. S. P., Belloche, A., Menten, Comito, C., & Shilke, P. 2008, J. Mol. Spectr., 251, 319
Neil, J. L., Crockett, N. R., Bergin, E. A., Pearson, J. C., & Li-Hong, Xu 2013, ApJ, 777, 85
Nummelin, A., & Bergman, P. 1999, A&A, 341, L59
Nummelin, A., Bergman, P., Hjalmarson, Å., et al. 2000, ApJSS, 128, 213
Occhiogrosso, A., Viti, S., & Balucani, N. 2013, MNRAS, 432, 3423
Ohisi, M., & Kaifu, N. 1998, J. Chem. Soc. Faraday Discuss., 109, 205
Pardo, J. R., Cernicharo, J., & Serabyn, E. 2001a, IEEE Tras. Antennas and Propagation, 49, 1683
Pardo, J. R., Cernicharo, J., Herpin, F., Kawamura, J., et al. 2001b, ApJ, 562, 799
Persson, C. M., Olofsson, A. O. H., Koning, N., et al. 2007, A&A, 476, 2, 807
Petrie, S. A. H. 1991, Ph.D. Thesis, University of Canterbury, New Zealand (ir.canterbury.ac.nz)
Pickett, H. M. 1991, J. Mol. Spectr., 148, 371
Pickett, H. M., Poynter, R. L., Cohen, E. A., et al. 1998, J. Quant. Spectr. Rad. Transf., 60, 883
Pliva, J., Le, L. D., Johns, J. W. C., Lu, Z., & Bernheim, R. A. 1995, J. Mol. Spectr., 173, 2, 423
Pracna, P., Urban, J., Votava, O., et al. 2011, J. Phys. Chem. A., 115, 1063
Rawlings, J. M. C., Hartquist, T. W., Menten, K. M., & Williams, D. A. 1992, MNRAS, 255, 471
Read, W. G., Cohen, E. A., & Pickett, H. M. 1986, J. Mol. Spectr., 115, 316
Remijan, A. J., Hollis, J. M., Lovas, F. J., Plusquellic, D. F., & Jewell, P. R. 2005, ApJ, 632, 333
Roberts, J. F., Rawlings, J. M. C., Viti, S., & Williams, D. A. 2007, MNRAS, 382, 733
Rodgers, S. D., & Charnley, S. B. 2001, ApJ, 546, 324
Rodgers, S. D., & Millar, T. J. 1996, MNRAS, 280, 1046
Roueff, E., Lis, D. C., vanderTak, F. F. S., Gerin, M., & Goldsmith, P. F. 2005, A&A, 438, 585
Sandstrom, K. M., Peek, J. E. G., Bower, G. C., et al. 2007, ApJ, 667, 1161
Savage, C., Apponi, A. J., Ziurys, L. M., & Wyckoff, S. 2002, ApJ, 578, 211
Schäfer, E., & Winnewisser, M. 1982, Ber. Bunsenges. Phys. Chem., 86, 780
Schäfer, E., Winnewisser, M., & Christiansen, J. J. 1981, Chem. Phys. Lett., 81, 380
Schilke, P., Walmsley, C. M., Pineau Des Forets, G., et al. 1992, A&A, 256, 595
Schilke, P., Groesbeck, T. D., Blake, G. A., & Philips, T. G. 1997, ApJSS, 108, 301
Sofia, U. J., & Meyer, D. M. 2001, ApJ, 554, L221
Stolze, M., & Sutter, D. H. 1985, Z. Naturforsch. Teil A, 40a, 998
Sutton, E. C., Blake, G. A., Masson, C. R., & Phillips, T. G. 1985, A&A, 58, 341
Sutton, E. C., Peng, R., Danchi, W. C., et al. 1995, ApJSS, 97, 455
Tercero, B. 2012, Thesis UCM, Spain
Tercero, B., Cernicharo, J., Pardo, J. R., & Goicoechea, J. R. 2010, A&A, 517, A96
Tercero, B., Vincent L., Cernicharo, J., Viti S., & Marcelino, N. 2011, A&A, 528, A26
Tercero, B., Margulès, L., Carvajal, M., et al. 2012, A&A, 538, 119
Tercero, B., Kleiner, I., Cernicharo, J., et al. 2013, ApJ, 770, L13
Tielens, A. G. G. M. 2005, The Physics and Chemistry of the Interstellar Medium (Cambridge University Press)
Turner, B. E. 1991, ApJSS, 76, 617
Turner, B. E., Kyslyakov, A. G., Liszt, H. S., & Kaifu, N. 1975, ApJ, 201, L149
Vigren, E., Hamberg, M., Zhaunerchyk, V., et al. 2009, ApJ, 695, 317
Vincet, M. A., & Dykstra, C. E. 1980, J. Chem. Phys., 73, 3838
Viti, S., Collings, M. P., Dever, J. W., McCoustra, M. R. S., & Williams, D. A. 2004, MNRAS, 354, 1141
Wakelam, V. 2009, BAAS, 41, 665
Widicus Weaver, S. L., & Friedel, D. N. 2012, ApJS, 201, 16
Wilcox, W. S., Goldstein, J. H., & Simmons, J. W. 1954, J. Chem. Phys., 22, 516
Woodall, J., Agúndez, M., MarkwickKemper, A. J., & Millar, T. J. 2007, A&A, 466, 1197
Wyckoff, S., Kleine, M., Peterson, B. A., Wehinger, P. A., & Ziurys, L. M. 2000, ApJ, 535, 991
Yamada, K., & Winnewisser, M. 1975, Z. Naturforsch, A, 30, 672
Ziurys, L. M., & McGonagle, D. 1993, ApJSS, 89, 155

APENDIX III. Supplementary Information

SUPPLEMENTARY INFORMATION FOR CHAPTER IV

Table IV.S1: Table of molecular properties predicted *ab initio* for most stable conformers of α-D-fructopyranose.

α-pyranoses	cc α $^5C_2$ g-	cc α $^5C_2$ t	c α $^5C_2$ g+
A^a /MHz	1592.73	1555.89	1653.52
B /MHz	703.50	721.83	689.82
C /MHz	666.47	711.17	686.88
μ_a/D	1.2	2.9	-2.1
μ_b/D	1.0	3.0	-1.7
μ_c/D	0.1	1.6	-1.3
$\Delta E_{MP2}{}^b$ /cm^{-1}	0	231.11	970.45
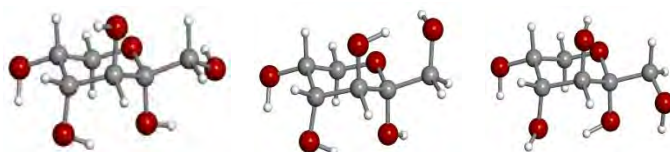
^{a}Ab initio calculations performed at the MP2/6-311++G(d,p) level of theory. A, B and C are the rotational constants; μ_a, μ_b and μ_c are the electric dipole moment components. ^{b}MP2/6-311++G(d,p) relative electronic energies.

Table IV.S2: Table of molecular properties predicted *ab initio* for most stable conformers of β-D-fructopyranose.

β-pyranoses	cc β $^2C_5$ g- (1)^c	cc β $^2C_5$ t	cc β $^2C_5$ g+	cc β $^2C_5$ g- (2)
A^a /MHz	1469.07	1244.58	1459.72	1434.43
B /MHz	777.03	843.84	791.09	802.08
C /MHz	614.09	717.72	629.35	637.40
μ_a/D	-0.2	-0.3	0.1	-0.8
μ_b/D	-0.0	-0.1	0.6	1.2
μ_c/D	1.4	3.6	1.7	1.3
$\Delta E_{MP2}{}^b$ /cm^{-1}	0	735.06	1087.91	1090.50
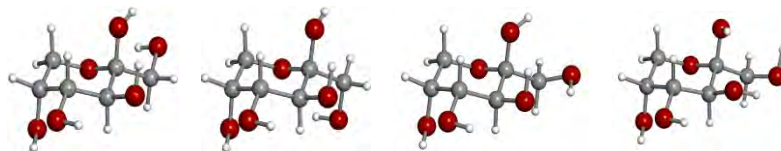
^{a}Ab initio calculations performed at the MP2/6-311++G(d,p) level of theory. A, B and C are the rotational constants; μ_a, μ_b and μ_c are the electric dipole moment components. ^{b}MP2/6-311++G(d,p) relative electronic energies. ^{c}A number has been added to provide MP2 energy ordering within the same family.

Table IV.S3. Observed frequencies and residuals (in MHz) for the rotational transitions of conformer cc β $^2C_5$ g- of fructose.

J'	K'_{-1}	K'_{+1}	J''	K''_{-1}	K''_{+1}	ν_{obs}	$\nu_{obs} - \nu_{cal}$
6	1	5	5	2	3	6530.00428	0.0085
3	2	2	2	1	2	6707.54220	0.0062
7	2	5	6	3	3	7010.00735	-0.0030
4	1	3	3	0	3	7146.06083	0.0037
7	1	6	6	2	4	7583.31269	-0.0040
3	3	0	2	2	0	8008.75703	0.0039
3	3	1	2	2	1	8031.09938	0.0045
4	2	3	3	1	3	8324.05101	0.0059
8	1	7	7	2	5	8394.04364	-0.0007
5	1	4	4	0	4	9012.29197	0.0004
4	3	1	3	2	1	9351.29076	0.0001
4	3	2	3	2	2	9454.72478	0.0017
5	2	4	4	1	4	10013.95919	-0.0012
5	3	2	4	2	2	10643.72540	-0.0023
5	3	3	4	2	3	10917.42665	-0.0026
4	4	0	3	3	0	10949.90271	-0.0050
4	4	1	3	3	1	10952.12859	-0.0041
6	1	5	5	0	5	10992.21327	-0.0036

Table IV.S4. Observed frequencies and residuals (in MHz) for the rotational transitions of conformer cc β $^2C_5$ t of fructose.

J'	K'_{-1}	K'_{+1}	J''	K''_{-1}	K''_{+1}	ν_{obs}	$\nu_{obs} - \nu_{cal}$
3	2	2	2	1	2	6236.5089	0.0146
3	3	0	2	2	0	6975.0480	0.0093
3	3	1	2	2	1	6996.7203	0.0017
4	1	3	3	0	3	7331.1284	0.0105
4	2	2	3	1	2	7544.0314	0.0168
4	2	3	3	1	3	7968.3694	0.0087
4	3	1	3	2	1	8490.9841	0.0111
4	3	2	3	2	2	8587.7400	0.0071
5	2	3	4	1	3	9185.2519	0.0078
5	1	4	4	0	4	9256.8697	-0.0126
4	4	0	3	3	0	9468.0368	0.0083
4	4	1	3	3	1	9470.8474	-0.0038
5	2	4	4	1	4	9754.6969	0.0076
5	3	2	4	2	2	9973.0034	-0.0012
5	3	3	4	2	3	10214.2357	-0.0128
6	2	4	5	1	4	10920.3944	-0.0007
5	4	1	4	3	1	11014.9909	-0.0046
5	4	2	4	3	2	11033.6094	-0.0156
6	1	5	5	0	5	11246.6565	-0.0057
6	3	3	5	2	3	11451.6508	-0.0165
5	5	0	4	4	0	11952.5895	0.0050
5	5	1	4	4	1	11952.8752	-0.0087

Table IV.S5: Cartesian coordinates for de *ab initio* predicted geometry (MP2/6-311++G(d,p) level of theory) of conformer cc β $^2C_5$ g- of D-fructopyranose.

```
                         Standard orientation:
---------------------------------------------------------------------
Center     Atomic      Atomic              Coordinates (Angstroms)
Number     Number      Type              X           Y           Z
---------------------------------------------------------------------
   1          6           0          1.469070    0.476407    0.449641
   2          6           0          1.706915   -1.018926    0.291881
   3          6           0          0.434624   -1.768941    0.644130
   4          8           0         -0.688651   -1.312048   -0.113395
   5          6           0         -0.964607    0.066635    0.036563
   6          6           0          0.248421    0.907059   -0.352835
   7          8           0          2.062135   -1.333394   -1.044346
   8          8           0         -1.262601    0.401895    1.377698
   9          6           0         -2.180779    0.313868   -0.845757
  10          8           0         -3.299524   -0.381885   -0.306175
  11          8           0          0.002469    2.298574   -0.179741
  12          8           0          2.634576    1.147752   -0.015743
  13          1           0          1.296075    0.700185    1.511926
  14          1           0          0.545533   -2.824746    0.391461
  15          1           0          2.755231   -0.704821   -1.282997
  16          1           0          0.232985   -1.664381    1.716899
  17          1           0          2.501051   -1.331593    0.986954
  18          1           0         -2.186780    0.143429    1.510968
  19          1           0          0.451933    0.754537   -1.415975
  20          1           0          2.384336    2.072544   -0.133360
  21          1           0         -3.079821   -1.318881   -0.371510
  22          1           0         -2.432470    1.374683   -0.838097
  23          1           0         -1.955767   -0.008802   -1.867772
  24          1           0         -0.381407    2.384078    0.703392
---------------------------------------------------------------------
Rotational constants (GHZ):      1.4690715    0.7770307    0.6140926
```

Table IV.S6: Cartesian coordinates for de *ab initio* predicted geometry (MP2/6-311++G(d,p) level of theory) of conformer cc β $^2C_5$ t of D-fructopyranose.

```
                        Standard orientation:
-----------------------------------------------------------------------
Center     Atomic      Atomic              Coordinates (Angstroms)
Number     Number      Type           X             Y             Z
-----------------------------------------------------------------------
    1         6           0        1.393111      0.605994      0.325807
    2         6           0        1.721904     -0.877738      0.256608
    3         6           0        0.607818     -1.663040      0.921582
    4         8           0       -0.675717     -1.373543      0.358140
    5         6           0       -1.044931     -0.012122      0.382626
    6         6           0        0.019628      0.868142     -0.273860
    7         8           0        1.834040     -1.309295     -1.088794
    8         8           0       -1.180949      0.477012      1.706143
    9         6           0       -2.377819      0.037239     -0.357281
   10         8           0       -2.273986     -0.498963     -1.658012
   11         8           0       -0.309034      2.250110     -0.178260
   12         8           0        2.396313      1.301804     -0.405334
   13         1           0        1.397442      0.923736      1.378699
   14         1           0        0.757538     -2.732182      0.762815
   15         1           0        2.404417     -0.662444     -1.523500
   16         1           0        0.601148     -1.448588      1.997220
   17         1           0        2.657734     -1.066596      0.804467
   18         1           0       -1.943410      0.037522      2.102315
   19         1           0        0.040040      0.627461     -1.338547
   20         1           0        2.044066      2.185237     -0.571013
   21         1           0       -1.847749     -1.358753     -1.556017
   22         1           0       -3.116177     -0.512633      0.248591
   23         1           0       -2.695239      1.076556     -0.455431
   24         1           0       -0.543419      2.402826      0.746440
-----------------------------------------------------------------------
Rotational constants (GHZ):     1.2445809     0.8438373     0.7177238
```

Reference 22:

M. J. Frisch, G. W. Trucks, H. B. Schlegel, G. E. Scuseria, M. A. Robb, J. R. Cheeseman, G. Scalmani, V. Barone, B. Mennucci, G. A. Petersson, H. Nakatsuji, M. Caricato, X. Li, H. P. Hratchian, A. F. Izmaylov, J. Bloino, G. Zheng, J. L. Sonnenberg, M. Hada, M. Ehara, K. Toyota, R. Fukuda, J. Hasegawa, M. Ishida, T. Nakajima, Y. Honda, O. Kitao, H. Nakai, T. Vreven, J. A. Montgomery, J. E. Peralta, F. Ogliaro, M. Bearpark, J. J. Heyd, E. Brothers, K. N. Kudin, V. N. Staroverov, T. Keith, R. Kobayashi, J. Normand, K. Raghavachari, A. Rendell, J. C. Burant, S. S. Iyengar, J. Tomasi, M. Cossi, N. Rega, J. M. Millam, M. Klene, J. E. Knox, J. B. Cross, V. Bakken, C. Adamo, J. Jaramillo, R. Gomperts, R. E. Stratmann, O. Yazyev, A. J. Austin, R. Cammi, C. Pomelli, J. W. Ochterski, R. L. Martin, K. Morokuma, V. G. Zakrzewski, G. A. Voth, P. Salvador, J. J. Dannenberg, S. Dapprich, A. D. Daniels, O. Farkas, J. B. Foresman, J. V. Ortiz, J. Cioslowski and D. J. Fox, Wallingford CT, 2010.

SUPPLEMENTARY INFORMATION FOR CHAPTER V

Table V.S1. Frequencies and residuals (in MHz) for the rotational transitions of conformer α $^5C_2$ g+ s of tagatose.

J'	K'_{-1}	K'_{+1}	J''	K''_{-1}	K''_{+1}	ν_{obs}	$\nu_{obs} - \nu_{cal}$
5	1	5	4	1	4	6123.3130	0.0049
5	0	5	4	0	4	6266.5299	0.0061
5	2	4	4	2	3	6413.0993	0.0013
5	2	3	4	2	2	6579.8950	0.0053
3	2	2	2	1	1	6648.9030	0.0042
5	1	4	4	1	3	6662.8266	0.0014
5	1	5	4	0	4	6669.5152	0.0049
3	2	1	2	1	1	6694.3786	0.0052
4	1	3	3	0	3	6700.4264	0.0063
3	2	2	2	1	2	6978.5885	0.0027
3	2	1	2	1	2	7024.0758	0.0155
6	0	6	5	1	5	7048.7925	-0.0003
6	1	6	5	1	5	7329.3883	0.0058
6	0	6	5	0	5	7451.7800	0.0007
6	2	5	5	2	4	7679.0760	-0.0010
6	1	6	5	0	5	7732.3609	-0.0079
4	2	3	3	1	2	7769.5981	0.0011
4	2	2	3	1	2	7903.2233	0.0031
6	2	4	5	2	3	7946.7318	0.0017
6	1	5	5	1	4	7962.6703	0.0078
5	1	4	4	0	4	8304.6172	-0.0118
7	0	7	6	1	6	8342.5302	0.0075
4	2	3	3	1	3	8428.5018	0.0120
7	1	7	6	1	6	8528.5812	0.0044
4	2	2	3	1	3	8562.1190	0.0059
7	0	7	6	0	6	8623.1184	0.0061
3	3	1	2	2	0	8779.1790	-0.0018
3	3	0	2	2	0	8779.6571	-0.0049
3	3	1	2	2	1	8788.3560	-0.0034
3	3	0	2	2	1	8788.8373	-0.0032
7	1	7	6	0	6	8809.1685	0.0021
5	2	4	4	1	3	8835.9955	0.0045

7	2	6	6	2	5	8936.3316	-0.0031
5	2	3	4	1	3	9136.3992	-0.0067
7	1	6	6	1	5	9240.8817	-0.0080
7	2	5	6	2	4	9317.6281	-0.0028
8	0	8	7	1	7	9603.0655	-0.0008
8	1	8	7	1	7	9721.7381	0.0013
8	0	8	7	0	7	9789.1194	-0.0010
6	2	5	5	1	4	9852.2445	0.0016
8	1	8	7	0	7	9907.7911	0.0002
5	2	4	4	1	4	9931.5927	0.0000
6	1	5	5	0	5	10000.7702	0.0026
4	3	2	3	2	1	10046.5716	-0.0092
4	3	1	3	2	1	10049.9345	-0.0011
4	3	2	3	2	2	10092.0559	0.0005
4	3	1	3	2	2	10095.4157	0.0055
8	2	7	7	2	6	10183.9091	0.0095
5	2	3	4	1	4	10232.0168	0.0091
6	2	4	5	1	4	10420.3137	0.0028
8	1	7	7	1	6	10492.3855	0.0094
8	2	6	7	2	5	10681.6381	-0.0201
7	2	6	6	1	5	10825.9191	0.0038
9	0	9	8	1	8	10836.5110	-0.0102
9	1	9	8	1	8	10909.9667	-0.0059
9	0	9	8	0	8	10955.1880	-0.0034
9	1	9	8	0	8	11028.6408	-0.0022
5	3	3	4	2	2	11279.0739	-0.0093
5	3	2	4	2	2	11292.3890	-0.0095
5	3	3	4	2	3	11412.7155	0.0089
9	2	8	8	2	7	11421.1688	-0.0065
5	3	2	4	2	3	11426.0163	-0.0054
6	2	5	5	1	5	11487.3534	-0.0081

Table V.S2. Frequencies and residuals (in MHz) for the rotational transitions of conformer α $^5C_2$ g+ cc of tagatose.

J'	K'_{-1}	K'_{+1}	J''	K''_{-1}	K''_{+1}	ν_{obs}	$\nu_{obs} - \nu_{cal}$
5	1	5	4	1	4	6146.7122	0.0088
5	2	3	4	2	2	6594.9417	-0.0031
3	2	1	2	1	1	6660.9177	-0.0022
5	1	4	4	1	3	6676.7429	-0.0079
4	1	3	3	0	3	6689.2552	0.0005
3	2	2	2	1	2	6940.2203	0.0088
6	1	6	5	1	5	7357.7974	-0.0121
6	0	6	5	0	5	7478.3347	0.0115
4	2	2	3	1	2	7874.5517	-0.0019
5	1	4	4	0	4	8291.3773	-0.0034
4	2	3	3	1	3	8390.8167	0.0003
3	3	0	2	2	0	8713.4589	-0.0029
3	3	1	2	2	1	8721.9929	0.0032
5	2	3	4	1	3	9111.9866	0.0051
8	0	8	7	0	7	9827.0427	-0.0010
5	2	4	4	1	4	9893.6779	-0.0099
6	1	5	5	0	5	9983.8099	0.0076
4	3	1	3	2	1	9987.6349	0.0088
4	3	2	3	2	2	10028.9239	-0.0046
6	2	4	5	1	4	10399.1249	0.0038
5	3	2	4	2	2	11234.5026	-0.0027
5	3	3	4	2	3	11352.4916	-0.0048

Table V.S3. Frequencies and residuals (in MHz) for the rotational transitions of conformer α $^5C_2$ t cc of tagatose.

J'	K'_{-1}	K'_{+1}	J''	K''_{-1}	K''_{+1}	ν_{obs}	$\nu_{obs} - \nu_{cal}$
5	1	5	4	1	4	6715.3664	0.0082
5	0	5	4	0	4	6829.1346	0.0075
5	2	4	4	2	3	6970.6230	0.0024
5	2	3	4	2	2	7132.1024	0.0000
5	1	4	4	1	3	7186.0259	-0.0116
6	1	6	5	1	5	8040.7446	0.0014
6	2	5	5	2	4	8348.3237	0.0205
6	1	5	5	1	4	8589.9334	0.0172
6	2	4	5	2	3	8603.0775	-0.0054
7	1	7	6	1	6	9359.9463	-0.0041
7	0	7	6	0	6	9427.6452	0.0093
7	1	6	6	1	5	9971.7566	-0.0109
8	1	8	7	1	7	10673.9426	-0.0128
8	0	8	7	0	7	10719.6337	-0.0059
8	1	7	7	1	6	11327.0848	-0.0047
8	2	6	7	2	5	11534.5266	-0.0008

Table V.S4: Molecular properties predicted *ab initio* for most stable conformers of α-D-tagatopyranose.

	α $^5C_2$ g+ s	α $^5C_2$ g+ cc	α $^5C_2$ t cc	α $^5C_2$ g- cc	α $^5C_2$ g- cc (2)
A^a /MHz	1636.6	1618.6	1474.9	1552.3	1562.1
B /MHz	701.9	703.6	750.3	738.2	733.3
C /MHz	592.3	595.7	653.6	603.7	608.0
$|\mu_a|$/D	1.9	1.0	2.7	2.3	0.8
$|\mu_b|$/D	1.7	0.1	1.4	0.7	0.6
$|\mu_c|$/D	1.4	1.7	0.0	0.3	1.8
ΔE^b/cm^{-1}	0	91	288	618	1406
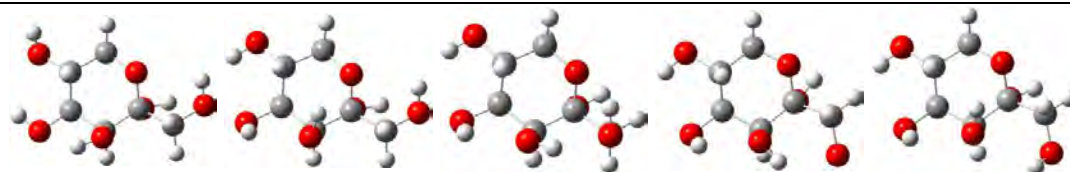
[a]Ab initio calculations performed at the MP2/6-311++G(d,p) level of theory. A, B and C are the rotational constants; $|\mu_a|$, $|\mu_b|$ and $|\mu_c|$ are absolute value of the electric dipole moment components. [b]MP2/6-311++G(d,p) relative electronic energies.

Table V.S5: *Ab initio* cartesian coordinates at MP2/6-311++G(d,p) level of theory for conformer $\alpha\ ^5C_2$ g+ s of D-tagatopyranose.

```
                        Standard orientation:
---------------------------------------------------------------------
Center     Atomic     Atomic           Coordinates (Angstroms)
Number     Number     Type         X            Y            Z
---------------------------------------------------------------------
   1          6          0       -1.370074     0.472842     0.543441
   2          6          0       -1.619500    -0.678317    -0.411362
   3          6          0       -0.464270    -1.668191    -0.314165
   4          8          0        0.757369    -1.016001    -0.658455
   5          6          0        1.074503     0.064000     0.213995
   6          6          0       -0.026614     1.122629     0.235367
   7          8          0       -2.862885    -1.263176    -0.014117
   8          6          0        2.402313     0.596838    -0.308910
   9          8          0        1.211636    -0.381228     1.540014
  10          8          0       -0.052560     1.753007    -1.035467
  11          1          0       -0.416504    -2.084638     0.698626
  12          1          0       -3.186948    -1.799167    -0.744319
  13          1          0       -0.583649    -2.482822    -1.033516
  14          1          0       -1.682712    -0.284074    -1.432240
  15          8          0        3.409861    -0.392103    -0.108918
  16          1          0        0.214536     1.846597     1.024383
  17          1          0       -0.874199     2.260473    -1.048628
  18          1          0        2.301426     0.874580    -1.360050
  19          1          0        2.698022     1.467393     0.279821
  20          1          0        3.171335    -1.126096    -0.686703
  21          1          0        2.091900    -0.782988     1.583839
  22          8          0       -2.356199     1.490581     0.399081
  23          1          0       -3.208397     1.039203     0.421506
  24          1          0       -1.360732     0.084086     1.569996
---------------------------------------------------------------------
```

Table V.S6: *Ab initio* cartesian coordinates at MP2/6-311++G(d,p) level of theory for conformer α $^5C_2$ g+ cc of D-tagatopyranose.

```
                          Standard orientation:
    ---------------------------------------------------------------------
    Center     Atomic      Atomic          Coordinates (Angstroms)
    Number     Number      Type         X            Y           Z
    ---------------------------------------------------------------------
       1          6          0       -1.376645     0.470841     0.550633
       2          6          0       -1.643206    -0.679896    -0.413449
       3          6          0       -0.459086    -1.636306    -0.427285
       4          8          0        0.742254    -0.919075    -0.754743
       5          6          0        1.064659     0.080807     0.218376
       6          6          0       -0.039057     1.134554     0.230462
       7          8          0       -2.791648    -1.415629    -0.029881
       8          6          0        2.429838     0.608384    -0.207429
       9          8          0        1.135258    -0.451819     1.510159
      10          8          0       -0.106583     1.812395    -1.024754
      11          1          0       -0.363426    -2.122128     0.548117
      12          1          0       -3.473109    -0.759615     0.161609
      13          1          0       -0.579757    -2.394855    -1.202339
      14          1          0       -1.782714    -0.269924    -1.426699
      15          8          0        3.401240    -0.415259    -0.017342
      16          1          0        0.186199     1.899172     0.978376
      17          1          0       -0.038517     1.132950    -1.707709
      18          1          0        2.402455     0.953103    -1.244071
      19          1          0        2.713533     1.435842     0.445850
      20          1          0        3.178492    -1.110642    -0.647243
      21          1          0        2.010971    -0.861683     1.575617
      22          8          0       -2.441780     1.413370     0.505594
      23          1          0       -2.269956     1.963195    -0.270665
      24          1          0       -1.353114     0.072421     1.569031
    ---------------------------------------------------------------------
```
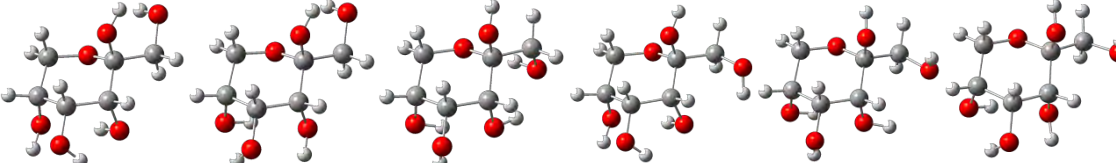
Table V.S7: *Ab initio* cartesian coordinates at MP2/6-311++G(d,p) level of theory for conformer α $^5C_2$ t cc of D-tagatopyranose.

```
                    Standard orientation:
---------------------------------------------------------------
Center     Atomic     Atomic        Coordinates (Angstroms)
Number     Number     Type        X          Y          Z
---------------------------------------------------------------
   1         6          0      -1.287815   0.519691   0.569891
   2         6          0      -1.602669  -0.428399  -0.579203
   3         6          0      -0.670959  -1.628035  -0.524975
   4         8          0       0.702736  -1.211031  -0.576201
   5         6          0       1.066734  -0.329450   0.465415
   6         6          0       0.179488   0.924839   0.511653
   7         8          0      -2.928455  -0.925822  -0.480383
   8         6          0       2.540886  -0.017431   0.209767
   9         8          0       0.917861  -0.920217   1.737278
  10         8          0       0.306828   1.742965  -0.644573
  11         1          0      -0.863207  -2.198612   0.390246
  12         1          0      -3.481324  -0.156469  -0.296868
  13         1          0      -0.818278  -2.275897  -1.390244
  14         1          0      -1.454848   0.103681  -1.527947
  15         8          0       2.761479   0.518590  -1.088243
  16         1          0       0.449126   1.489853   1.413820
  17         1          0       1.227106   1.706269  -0.943455
  18         1          0       2.881238   0.730214   0.929365
  19         1          0       3.117575  -0.941383   0.357107
  20         1          0       2.422986  -0.142739  -1.704986
  21         1          0       1.467426  -1.714033   1.748061
  22         8          0      -2.139323   1.659149   0.522110
  23         1          0      -1.771039   2.229279  -0.166124
  24         1          0      -1.499769   0.013490   1.515846
---------------------------------------------------------------
```

Table V.S8: Molecular properties predicted *ab initio* for most stable conformers of β-D-psicopyranose.

	β $^2C_5$ g- s (1)	β $^2C_5$ g- s (2)	β $^2C_5$ t cc	β $^2C_5$ g+ s (1)	β $^2C_5$ g+ cc	β $^2C_5$ g+ s (2)
A^a /MHz	1631.8	1635.8	1399.4	1447.9	1446.5	1504.8
B /MHz	728.3	728.3	792.6	805.7	794.8	778.7
C /MHz	665.3	664.9	759.3	691.3	690.7	679.8
$|\mu_a|$/D	-0.4	0.2	3.6	-1.0	2.9	0.5
$|\mu_b|$/D	1.4	0.7	2.6	1.5	2.0	2.2
$|\mu_c|$/D	0.0	0.0	0.1	-0.2	1.0	1.3
ΔE^b/cm^{-1}	0	73	828	1229	1295	1330

^{a}Ab initio calculations performed at the MP2/6-311++G(d,p) level of theory. A, B and C are the rotational constants; $|\mu_a|$, $|\mu_b|$ and $|\mu_c|$ are absolute value of the electric dipole moment components. ^{b}MP2/6-311++G(d,p) relative electronic energies.

Table V.S9. Frequencies and residuals (in MHz) for the rotational transitions of conformer β $^2C_5$ g- s (1) of psicose.

J'	K'_{-1}	K'_{+1}	J''	K''_{-1}	K''_{+1}	ν_{obs}	$\nu_{obs} - \nu_{cal}$
5	0	5	4	1	4	6197.3814	0.0063
3	2	2	2	1	1	6865.3783	0.0032
3	2	1	2	1	2	7066.9102	-0.0026
5	1	5	4	0	4	7415.6221	0.0066
6	0	6	5	1	5	7648.6072	0.0076
7	1	6	6	2	5	7676.5252	0.0043
4	2	3	3	1	2	8155.8918	0.0044
4	2	2	3	1	3	8573.8906	0.0012
6	1	6	5	0	5	8650.8672	-0.0002
3	3	1	2	2	0	8828.1887	-0.0039
3	3	0	2	2	1	8831.3667	-0.0066
7	0	7	6	1	6	9088.5986	0.0085
8	1	7	7	2	6	9258.7256	-0.0003
5	2	4	4	1	3	9415.4152	0.0075
7	1	7	6	0	6	9883.3235	-0.0029
5	2	3	4	1	4	10140.5512	0.0015
4	3	2	3	2	1	10205.8146	0.0023
4	3	1	3	2	2	10221.8552	-0.0015

8	0	8	7	1	7	10511.9921	-0.0068
6	2	5	5	1	4	10644.9556	-0.0054
9	1	8	8	2	7	10848.3285	-0.0100
8	1	8	7	0	7	11120.8076	-0.0075
5	3	3	4	2	2	11571.4618	-0.0020
5	3	2	4	2	3	11619.9159	0.0060

Table V.S10. Frequencies and residuals (in MHz) for the rotational transitions of conformer β $^2C_5$ g- s (2) of psicose.

J'	K'_{-1}	K'_{+1}	J''	K''_{-1}	K''_{+1}	ν_{obs}	$\nu_{obs} - \nu_{cal}$
4	1	4	3	0	3	6166.5409	-0.0020
3	2	2	2	1	1	6863.3901	0.0180
3	2	1	2	1	2	7070.5344	0.0081
5	1	5	4	0	4	7411.9792	0.0050
4	2	3	3	1	2	8153.1792	0.0052
4	2	2	3	1	3	8583.2011	0.0137
6	1	6	5	0	5	8646.1000	-0.0059
3	3	1	2	2	0	8825.3679	0.0004
3	3	0	2	2	1	8828.7279	0.0056
7	0	7	6	1	6	9103.2970	0.0107
8	1	7	7	2	6	9298.5276	-0.0078
5	2	4	4	1	3	9411.1912	-0.0036
4	3	2	3	2	1	10204.3316	-0.0128
4	3	1	3	2	2	10221.2653	-0.0043
5	3	3	4	2	2	11570.6964	-0.0159

Table V.S11: *Ab initio* cartesian coordinates at MP2/6-311++G(d,p) level of theory for conformer β $^2C_5$ g- s (1) of D-psicopyranose.

```
                      Standard orientation:
---------------------------------------------------------------------
Center     Atomic     Atomic           Coordinates (Angstroms)
Number     Number     Type          X           Y           Z
---------------------------------------------------------------------
   1          6          0      -0.210924   -1.056740    0.263409
   2          6          0      -1.426112   -0.308259    0.823400
   3          6          0      -1.614155    1.041040    0.124009
   4          6          0      -0.310219    1.821483    0.118787
   5          8          0       0.732044    1.052835   -0.488518
   6          6          0       1.013196   -0.147964    0.223618
   7          8          0      -2.587143   -1.116297    0.666663
   8          8          0      -2.126265    0.850342   -1.192963
   9          8          0       1.347590    0.115522    1.561983
  10          6          0       2.200459   -0.759866   -0.508997
  11          8          0       3.343523    0.067757   -0.308411
  12          1          0      -1.266908   -0.138349    1.893130
  13          1          0      -0.416583    2.715881   -0.497840
  14          1          0      -1.445995    0.355702   -1.673048
  15          1          0      -0.030223    2.103864    1.139942
  16          1          0      -2.378903    1.618620    0.654831
  17          1          0       2.275131    0.395051    1.542840
  18          1          0      -3.047062   -0.754853   -0.103766
  19          1          0       3.156542    0.889635   -0.776539
  20          1          0       2.435105   -1.730333   -0.066959
  21          1          0       1.962869   -0.881640   -1.567731
  22          8          0      -0.453675   -1.486350   -1.075763
  23          1          0      -1.224213   -2.065100   -1.018458
  24          1          0       0.018166   -1.917108    0.904312
---------------------------------------------------------------------
```
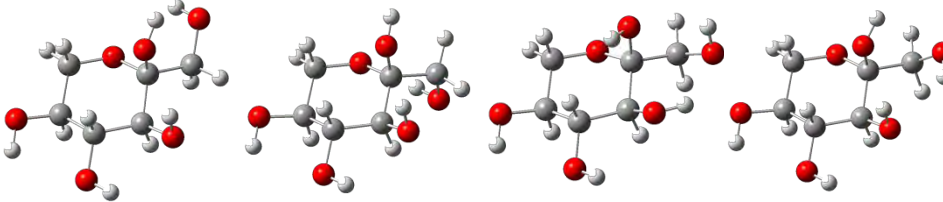
Table V.S12: Ab initio coordinates at MP2/6-311++G(d,p) level of theory for conformer β $^2C_5$ g- s (2) of D-psicopyranose.

```
                       Standard orientation:
-------------------------------------------------------------------
Center     Atomic     Atomic           Coordinates (Angstroms)
Number     Number      Type        X           Y           Z
-------------------------------------------------------------------
   1          6          0      -0.213975   -1.063167    0.198009
   2          6          0      -1.407563   -0.336971    0.822514
   3          6          0      -1.607504    1.037738    0.173909
   4          6          0      -0.302845    1.813069    0.134922
   5          8          0       0.740276    1.053467   -0.481191
   6          6          0       1.016905   -0.159885    0.211109
   7          8          0      -2.589105   -1.117460    0.677934
   8          8          0      -2.061750    0.893015   -1.174385
   9          8          0       1.331915    0.073303    1.559971
  10          6          0       2.216113   -0.754318   -0.515408
  11          8          0       3.353052    0.074393   -0.286993
  12          1          0      -1.218524   -0.198638    1.891528
  13          1          0      -0.421817    2.706350   -0.480841
  14          1          0      -2.908270    0.433206   -1.113836
  15          1          0      -0.012721    2.098948    1.151766
  16          1          0      -2.342773    1.609661    0.756869
  17          1          0       2.260458    0.350401    1.562240
  18          1          0      -2.418056   -1.713371   -0.063811
  19          1          0       3.164518    0.906164   -0.736797
  20          1          0       2.448930   -1.731311   -0.086998
  21          1          0       1.995817   -0.860835   -1.579711
  22          8          0      -0.522459   -1.496077   -1.122046
  23          1          0      -0.778198   -0.696735   -1.609046
  24          1          0       0.008409   -1.967761    0.771986
-------------------------------------------------------------------
```

Table V.S13: Molecular properties predicted *ab initio* for most stable conformers of α-L-sorbopyranose.

	α $^2C_5$ g- cc	α $^2C_5$ t cc	α $^2C_5$ g+ cc (1)	α $^2C_5$ g+ cc (2)
A^a /MHz	1527.89	1353.26	1570.64	1587.65
B /MHz	727.52	759.86	734.11	726.92
C /MHz	559.03	626.42	572.7	567.72
$|\mu_a|$/D	0.8	1.0	1.5	0.6
$|\mu_b|$/D	0.1	0.7	1.3	0.7
$|\mu_c|$/D	0.1	2.2	0.0	0.3
ΔE^b/cm^{-1}	0	813	1021	1099

[a]Ab initio calculations performed at the MP2/6-311++G(d,p) level of theory. A, B and C are the rotational constants; $|\mu_a|$, $|\mu_b|$ and $|\mu_c|$ are absolute value of the electric dipole moment components. [b]MP2/6-311++G(d,p) relative electronic energies.

Table V.S14. Frequencies and residuals (in MHz) for the rotational transitions of conformer α $^2C_5$ g- cc of sorbose.

J'	K'_{-1}	K'_{+1}	J''	K''_{-1}	K''_{+1}	ν_{obs}	$\nu_{obs} - \nu_{cal}$
5	0	5	4	0	4	6021.2268	0.0059
5	2	4	4	2	3	6339.2743	0.0027
5	4	1	4	4	0	6443.2885	0.0163
5	3	3	4	3	2	6451.2005	0.0097
5	3	2	4	3	1	6492.3986	0.0054
5	1	4	4	1	3	6682.1359	0.0106
5	2	3	4	2	2	6707.5563	0.0120
6	1	6	5	1	5	7033.7343	0.0068
6	0	6	5	0	5	7119.3808	0.0106
6	2	5	5	2	4	7565.9460	0.0075
6	3	4	5	3	3	7747.3909	0.0046
6	3	3	5	3	2	7851.4857	0.0160
6	2	4	5	2	3	8110.1274	-0.0009
7	1	7	6	1	6	8163.9426	-0.0007
7	0	7	6	0	6	8215.2508	0.0059
7	2	6	6	2	5	8772.4819	-0.0037
7	3	5	6	3	4	9036.4786	0.0099

7	4	4	6	4	3	9055.9529	0.0025
7	4	3	6	4	2	9073.0216	0.0028
7	1	6	6	1	5	9112.3107	0.0096
7	3	4	6	3	3	9249.7965	-0.0100
8	1	8	7	1	7	9286.7967	0.0012
8	0	8	7	0	7	9315.3224	-0.0018
7	2	5	6	2	4	9487.1106	-0.0051
8	2	7	7	2	6	9958.4199	-0.0095
8	1	7	7	1	6	10243.5991	-0.0065
8	3	6	7	3	5	10312.7610	-0.0099
8	4	5	7	4	4	10370.1118	-0.0154
9	1	9	8	1	8	10404.8701	-0.0115
9	0	9	8	0	8	10419.9641	-0.0039
8	3	5	7	3	4	10682.1180	-0.0048
8	2	6	7	2	5	10823.0925	-0.0109
9	1	8	8	1	7	11337.2271	0.0006
9	3	7	8	3	6	11571.3693	-0.0072

Table V.S15: Ab initio coordinates at MP2/6-311++G(d,p) level of theory, for conformer $\alpha\ ^2C_5$ g- cc of L-sorbopyranose.

```
                      Standard orientation:
---------------------------------------------------------------------
Center     Atomic     Atomic          Coordinates (Angstroms)
Number     Number     Type         X           Y           Z
---------------------------------------------------------------------
   1          6          0       0.569869   -1.756057    0.111748
   2          8          0      -0.675946   -1.295459   -0.424963
   3          6          0      -1.039560    0.004705    0.008886
   4          6          0       0.037377    1.024325   -0.362348
   5          6          0       1.396911    0.567030    0.148891
   6          6          0       1.696312   -0.837468   -0.334242
   7          8          0      -1.175316    0.070918    1.411602
   8          6          0      -2.381384    0.272093   -0.659105
   9          1          0       0.714636   -2.763647   -0.280322
  10          1          0       0.529503   -1.792331    1.205650
  11          1          0      -2.706109    1.288577   -0.434772
  12          1          0      -2.278561    0.144838   -1.742090
  13          8          0      -3.360440   -0.605581   -0.114660
  14          1          0      -3.086836   -1.494880   -0.368846
  15          1          0      -2.051130   -0.293770    1.608039
  16          8          0      -0.277897    2.320109    0.131234
  17          1          0      -0.540018    2.184861    1.052013
  18          8          0       2.434559    1.415748   -0.327781
  19          1          0       2.172752    2.318227   -0.109703
  20          8          0       2.903311   -1.334896    0.218892
  21          1          0       3.567050   -0.651134    0.069612
  22          1          0       0.082979    1.112821   -1.452955
  23          1          0       1.745996   -0.827832   -1.433167
  24          1          0       1.386420    0.559790    1.248959
---------------------------------------------------------------------
```

SUPPLEMENTARY INFORMATION FOR CHAPTER VI

Experimental Section

2-deoxy-D-ribose (m.p.: 89-90ºC) was purchased from Sigma-Aldrich, without further purification, and prepared by mixing the powder of the solid with a commercial binder (Methylcellulose). The mixture was pressed to form cylindrical rods, which were placed in a laser ablation nozzle[12] to be vaporized using a 20 ps Nd:YAG laser (10 mJ/pulse). The vaporized molecules were seeded in the Ne carrier gas at backing pressure of 15 bar, to expand adiabatically into the vacuum chamber, and probed by broadband CP-FTMW (Valladolid)[21] or Balle-Flygare FTMW (Bilbao)[12] spectroscopies.

The conformational survey used advanced Monte-Carlo and large-scale-low-mode MM methods to obtain a large set of plausible starting geometries, later classified in five structural families: α-/β-pyranoses, α-/β-furanoses and open–chain conformations (see Fig. S3 and Tables S12-S14 of Supporting Information). All geometries in each structural class within energy windows of 15 kJ mol^{-1} are later fully reoptimized with the three quantum mechanical methods (B3LYP, M06-2X and MP2). The Gaussian09 suite[35] was used in all the cases running in two supercomputers (SGI-IZO and i2Basque) with a maximum of 96 processors per calculation.

Reference 35:

Gaussian 09, Revision B.01, M. J. Frisch, G. W. Trucks, H. B. Schlegel, G. E. Scuseria, M. A. Robb, J. R. Cheeseman, G. Scalmani, V. Barone, B. Mennucci, G. A. Petersson, H. Nakatsuji, M. Caricato, X. Li, H. P. Hratchian, A. F. Izmaylov, J. Bloino, G. Zheng, J. L. Sonnenberg, M. Hada, M. Ehara, K. Toyota, R. Fukuda, J. Hasegawa, M. Ishida, T. Nakajima, Y. Honda, O. Kitao, H. Nakai, T. Vreven, J. A. Montgomery, Jr., J. E. Peralta, F. Ogliaro, M. Bearpark, J. J. Heyd, E. Brothers, K. N. Kudin, V. N. Staroverov, R. Kobayashi, J. Normand, K. Raghavachari, A. Rendell, J. C. Burant, S. S. Iyengar, J. Tomasi, M. Cossi, N. Rega, J. M. Millam, M. Klene, J. E. Knox, J. B. Cross, V. Bakken, C. Adamo, J. Jaramillo, R. Gomperts, R. E. Stratmann, O. Yazyev, A. J. Austin, R. Cammi, C. Pomelli, J. W. Ochterski, R. L. Martin, K. Morokuma, V. G. Zakrzewski, G. A. Voth, P. Salvador, J. J. Dannenberg, S. Dapprich, A. D. Daniels, Ö. Farkas, J. B. Foresman, J. V. Ortiz, J. Cioslowski, and D. J. Fox, Gaussian, Inc., Wallingford CT, 2010.

Table VI.S1. Experimental spectroscopic parameters for the six observed conformers of 2-deoxy-D-ribose.

Parameter	Rotamer I c-β-pyr $^1C_4$	Rotamer II cc-β-pyr $^1C_4$	Rotamer III c-β-pyr $^4C_1$	Rotamer IV cc-β-pyr $^4C_1$	Rotamer V cc-α-pyr $^4C_1$	Rotamer VI c-α-pyr $^4C_1$
$A^{[a]}$ /MHz	2437.82389(32)[e]	2449.4937 (10)	2934.16159	2921.37984	2484.4138 (40)	2505.0150 (12)
B /MHz	1510.72826 (24)	1508.31836	1271.16880	1266.99318	1517.76532	1521.47507
C /MHz	1144.98038 (27)	1137.47992	1022.34668	1020.28439	1238.99757	1246.45004
D_J /kHz	0.0954 (47)	...	...	0.090 (20)	0.1063 (47)	0.107 (24)
D_{JK} [kHz]	...	...	0.207 (17)	...	...	...
D_K [kHz]	0.238 (22)	...	0.339 (82)	...	...	...
d_I [kHz]	-0.0117 (19)	...	-0.0138 (32)	...	...	...
$\mu_a^{[b]}$/D	Obs^f	Obs	Obs	...	Obs	Obs
μ_b /D	Obs	Obs	Obs	Obs	...	...
μ_c /D	Obs	Obs	...	Obs	...	Obs
$\sigma^{[c]}$ / KHz	5.2	7.3	5.3	7.0	1.8	4.0
$N^{[d]}$	67	21	45	20	19	16

[a] A, B and C are the rotational constants; Watson's quartic centrifugal distortion constants in the *S* reduction (D_J, D_K, D_{JK}, d_1). [b] Electric dipole moment.1 D ≈ 3.3356×10^{-30} C m. [c] Rms deviation of the fit. [d] Number of fitted transitions.[e] Standard error in parenthesis in the units of the last digit. [f] Observation of a-, b-, and c-type transitions for each structure.

Table VI.S2. Measured rotational transitions (in MHz) assigned to conformer c-β-pyr $^1C_4$-1.

J'	K'_{-1}	K'_{+1}	J''	K''_{-1}	K''_{+1}	ν_{obs}	$\nu_{obs} - \nu_{cal}$
5	3	3	5	2	4	6197.119	-0.003
5	2	4	5	1	5	6273.829	0.008
5	2	4	5	0	5	6355.121	0.010
6	1	5	6	1	6	6760.802	-0.001
6	3	4	6	2	5	6782.753	-0.005
6	1	5	6	0	6	6794.030	0.011
6	4	2	6	3	3	6893.377	-0.000
2	1	1	1	0	1	6970.006	0.001
3	0	3	2	1	2	6992.325	-0.000
5	2	4	4	3	1	7175.708	0.020
5	4	1	5	3	2	7321.567	0.006
5	3	3	5	1	4	7333.391	0.009
3	1	3	2	1	2	7368.466	-0.000
6	2	5	6	1	6	7416.783	0.002
6	3	4	6	1	5	7438.733	-0.004
6	2	5	6	0	6	7450.001	0.004
4	3	2	4	1	3	7531.385	0.004
4	4	0	4	3	1	7554.370	0.007
7	3	5	7	2	6	7577.221	-0.004
3	0	3	2	0	2	7642.293	-0.000
4	4	1	4	3	2	7646.419	0.001
5	4	2	5	3	3	7654.174	0.002
6	4	3	6	3	4	7735.180	0.001
3	3	1	3	1	2	7896.466	0.009

7	3	5	7	1	6	7912.382	0.007
3	2	2	2	2	1	7967.117	0.001
3	1	3	2	0	2	8018.434	0.000
3	2	1	2	2	0	8291.938	-0.000
3	1	2	2	1	1	8451.804	0.000
2	2	1	1	1	0	8458.445	-0.000
2	2	0	1	1	0	8547.065	-0.000
7	2	6	7	1	7	8667.018	0.002
7	2	6	7	0	7	8679.946	-0.002
2	2	1	1	1	1	8824.195	0.002
4	1	3	3	2	2	8834.523	-0.001
2	2	0	1	1	1	8912.813	-0.000
5	2	3	4	3	2	9434.836	0.014
4	0	4	3	1	3	9563.080	-0.000
4	1	4	3	1	3	9748.085	0.000
2	2	0	1	0	1	9839.914	0.006
4	0	4	3	0	3	9939.220	-0.000
3	3	0	3	1	3	10090.931	-0.010
4	1	4	3	0	3	10124.225	-0.000
3	1	2	2	0	2	10199.015	0.001
4	2	3	3	2	2	10552.875	-0.000
3	2	2	2	1	1	10748.382	-0.018
4	3	2	3	3	1	10766.046	0.003
4	3	1	3	3	0	10845.995	0.001
4	1	3	3	1	2	11131.119	-0.000
3	2	1	2	1	1	11161.841	-0.001
4	2	2	3	2	1	11234.665	-0.001
5	1	4	4	2	3	11946.307	-0.004
5	0	5	4	1	4	12009.428	-0.000
5	1	5	4	1	4	12090.718	0.001
5	0	5	4	0	4	12194.434	0.001
3	2	1	2	1	2	12259.085	0.000
5	1	5	4	0	4	12275.723	0.001
4	2	3	3	1	2	12849.473	0.002
5	2	4	4	2	3	13082.573	0.001
5	3	3	4	3	2	13466.664	-0.000
5	4	2	4	4	1	13474.421	0.002
3	3	1	2	2	0	13478.354	-0.003
5	4	1	4	4	0	13488.434	-0.000
3	3	0	2	2	0	13492.260	-0.001
5	1	4	4	1	3	13664.662	-0.001
5	3	2	4	3	1	13721.233	-0.004
5	2	3	4	2	3	14152.614	-0.005

Table VI.S3. Measured rotational transitions (in MHz) assigned to conformer cc-β-pyr $^1C_4$-1.

J'	K'_{-1}	K'_{+1}	J''	K''_{-1}	K''_{+1}	ν_{obs}	$\nu_{obs} - \nu_{cal}$
3	0	3	2	1	2	6948.235	0.005
2	1	1	1	0	1	6974.454	0.006
3	1	3	2	1	2	7330.469	0.010
3	0	3	2	0	2	7608.318	-0.011
3	2	2	2	2	1	7937.391	-0.004
3	1	3	2	0	2	7990.567	0.008
3	2	1	2	2	0	8266.460	-0.000
3	1	2	2	1	1	8428.904	-0.002
2	2	1	1	1	0	8485.963	0.002
2	2	0	1	1	0	8575.710	-0.014
4	1	3	3	2	2	8766.842	-0.001
2	2	0	1	1	1	8946.561	-0.002
4	0	4	3	1	3	9508.279	-0.000
4	1	4	3	1	3	9696.414	0.007
4	0	4	3	0	3	9890.497	-0.011
4	1	4	3	0	3	10078.645	0.009
4	2	3	3	2	2	10512.356	-0.002
3	2	2	2	1	1	10760.917	-0.004
4	1	3	3	1	2	11098.859	0.002
3	2	1	2	1	1	11179.763	0.013
5	0	5	4	1	4	11942.134	-0.011

Table VI.S4. Measured rotational transitions (in MHz) assigned to conformer c-β-pyr $^4C_1$-1.

J'	K'_{-1}	K'_{+1}	J''	K''_{-1}	K''_{+1}	ν_{obs}	$\nu_{obs} - \nu_{cal}$
2	1	2	1	0	1	6001.204	0.004
3	2	2	3	1	3	6124.073	-0.005
7	2	6	6	3	3	6355.121	0.009
3	1	3	2	1	2	6491.901	0.003
4	2	3	4	1	4	6648.594	-0.003
3	0	3	2	0	2	6778.821	0.004
7	1	6	7	0	7	6864.596	-0.002
3	2	2	2	2	1	6880.546	0.005
3	2	1	2	2	0	6982.275	0.003
3	1	2	2	1	1	7236.671	0.004
5	2	4	5	1	5	7310.123	-0.000
4	0	4	3	1	3	7777.357	0.000
5	1	4	4	2	3	7785.713	0.002
5	2	4	5	0	5	7893.328	-0.005
3	1	3	2	0	2	7931.954	0.002
6	3	3	6	2	4	7982.490	0.014

6	2	5	6	1	6	8105.866	0.010
5	3	2	5	2	3	8375.656	-0.007
4	1	4	3	1	3	8629.349	-0.001
4	3	1	4	2	2	8660.335	-0.006
3	3	0	3	2	1	8826.483	0.003
4	0	4	3	0	3	8930.495	0.001
3	3	1	3	2	2	8952.398	-0.002
4	3	2	4	2	3	9019.645	-0.002
5	3	3	5	2	4	9149.676	0.003
4	2	3	3	2	2	9153.870	0.001
4	3	2	3	3	1	9221.117	0.001
4	3	1	3	3	0	9231.210	0.002
6	3	4	6	2	5	9365.125	-0.007
4	2	2	3	2	1	9397.346	0.000
6	3	3	6	2	5	9501.843	0.013
4	1	3	3	1	2	9614.543	0.002
2	2	1	1	1	0	9824.825	0.004
4	1	4	3	0	3	9782.486	-0.000
2	2	0	1	1	1	10099.532	0.003
5	0	5	4	1	4	10165.358	-0.006
6	1	5	5	2	4	10628.094	0.002
5	0	5	4	0	4	11017.350	-0.008
5	1	5	4	0	4	11600.564	-0.004
5	2	4	4	2	3	11410.098	-0.003
5	4	2	4	4	1	11525.011	-0.001
5	4	1	4	4	0	11525.741	-0.002
5	3	3	4	3	2	11540.123	-0.004
5	3	2	4	3	1	11574.897	-0.014
5	1	4	4	1	3	11957.887	0.004

Table VI.S5. Measured rotational transitions (in MHz) assigned to conformer cc-β-pyr $^4C_1$.

J'	K'_{-1}	K'_{+1}	J''	K''_{-1}	K''_{+1}	ν_{obs}	$\nu_{obs} - \nu_{cal}$
4	2	3	4	1	4	6608.584	-0.008
2	1	1	1	0	1	6722.354	-0.003
5	2	4	5	1	5	7264.448	0.010
4	0	4	3	1	3	7759.706	-0.012
5	1	4	4	2	3	7769.847	0.013
3	1	3	2	0	2	7909.778	-0.006
3	3	0	3	2	1	8779.458	-0.004
3	3	1	3	2	2	8903.937	-0.008
4	3	2	4	2	3	8970.444	0.008
3	1	2	2	0	2	9388.367	-0.000

4	1	4	3	0	3	9757.655	-0.004
2	2	1	1	1	0	9784.423	0.002
2	2	0	1	1	0	9810.020	0.013
2	2	1	1	1	1	10031.127	-0.003
2	2	0	1	1	1	10056.717	0.001
5	0	5	4	1	4	10141.575	-0.002
7	2	5	7	1	7	11424.185	-0.005
5	1	5	4	0	4	11573.100	-0.004
3	2	2	2	1	1	11824.984	0.002
3	2	1	2	1	1	11951.143	0.008

Table VI.S6. Measured rotational transitions (in MHz) assigned to conformer cc-α-pyr $^4C_1$.

J'	K'_{-1}	K'_{+1}	J''	K''_{-1}	K''_{+1}	ν_{obs}	$\nu_{obs} - \nu_{cal}$
3	1	3	2	1	2	7822.126	-0.001
3	0	3	2	0	2	8072.940	-0.001
3	2	2	2	2	1	8270.277	-0.001
3	2	1	2	2	0	8467.612	-0.002
3	1	2	2	1	1	8652.222	0.003
4	1	4	3	1	3	10381.349	0.002
4	0	4	3	0	3	10588.401	-0.003
4	2	3	3	2	2	10986.165	0.001
4	3	2	3	3	1	11115.169	0.003
4	3	1	3	3	0	11151.538	-0.003
4	2	2	3	2	1	11424.175	0.002
4	1	3	3	1	2	11460.043	0.000
5	1	5	4	1	4	12913.571	0.002
5	0	5	4	0	4	13049.443	0.000
5	2	4	4	2	3	13668.374	0.001
5	4	2	4	4	1	13899.148	-0.002
5	3	3	4	3	2	13907.452	0.001
5	3	2	4	3	1	14028.156	-0.002
5	1	4	4	1	3	14186.647	-0.001

Table VI.S7. Measured rotational transitions (in MHz) assigned to conformer c-α-pyr $^4C_1$-1.

J'	K'_{-1}	K'_{+1}	J''	K''_{-1}	K''_{+1}	ν_{obs}	$\nu_{obs} - \nu_{cal}$
2	1	1	1	0	1	7069.446	0.001
3	1	3	2	1	2	7862.368	0.000
3	0	3	2	0	2	8113.674	0.002
3	2	2	2	2	1	8303.775	-0.006
3	2	1	2	2	0	8493.892	0.001
3	1	2	2	1	1	8681.631	-0.003
2	2	0	1	1	0	8811.546	0.006

2	2	1	1	1	1	9036.517	-0.003
3	1	2	2	0	2	10265.272	0.006
4	1	4	3	1	3	10436.609	0.003
4	0	4	3	0	3	10647.125	0.004
4	2	3	3	2	2	11032.447	-0.006
4	3	2	3	3	1	11156.739	0.001
4	2	2	3	2	1	11456.475	0.003
3	2	1	2	1	1	11494.543	-0.006
4	1	3	3	1	2	11502.650	-0.004

Table VI.S8. Observed rotational transitions (MHz) and residuals (kHz) of minor isotopologues of 2-deoxyribose c-β-Pyr-$^1C_4$-1.

Transitions	$^{13}C_1$	v_{obs}-v_{cal}	$^{13}C_2$	v_{obs}-v_{cal}	$^{13}C_3$	v_{obs}-v_{cal}	$^{13}C_4$	v_{obs}-v_{cal}	$^{13}C_5$	v_{obs}-v_{cal}	$^{18}O_5$	v_{obs}-v_{cal}
$3_{03} \leftarrow 2_{12}$	6942.1003	0.4	6987.1524	0.2	6975.7366	0.3	6969.6833	0.0				
$3_{13} \leftarrow 2_{02}$									7965.1194	-0.5		
$3_{13} \leftarrow 2_{12}$	7327.0071	-0.4	7349.7413	-0.7	7348.4263	-0.3	7344.0087	-1.1	7338.7600	-1.7	7284.2816	0.0
$4_{04} \leftarrow 3_{03}$	9888.2201	0.6	9908.3737	0.8	9911.0952	-0.4	9906.0527	-0.7	9891.0875	1.0	9823.7085	-0.1
$4_{14} \leftarrow 3_{13}$	9694.8223	-1.1	9722.0102	0.1	9721.2635	-1.3	9715.8323	-0.3	9706.6109	-0.2	9635.8298	0.0
$4_{13} \leftarrow 3_{12}$	11060.3123	0.2	11105.2967	0.1	11102.0494	0.2	11092.3557	-0.4	11093.5978	0.7	11010.4457	0.0
$4_{22} \leftarrow 3_{21}$	11152.1414	-0.2	11219.7208	-0.1	11207.6567	0.0	11195.4496	0.5	11213.7831	-0.2		
$5_{05} \leftarrow 4_{04}$	12132.5900	0.3	12156.9209	-0.4	12159.8720	1.3	12154.0597	1.5	12135.2693	2.0	12051.9080	0.2
$5_{15} \leftarrow 4_{14}$											11950.5764	0.0

Table VI.S9. Rotational parameters of the monosubstituted isotopologues of 2-deoxyribose c-β-Pyr-$^1C_4$-1.

	$^{13}C_1$	$^{13}C_2$	$^{13}C_3$
A (MHz)[a]	2432.69120(95)	2417.58510(79)	2428.9117(12)
B (MHz)	1499.57198(11)	1508.364680(91)	1507.07202(14)
C (MHz)	1139.154470(67)	1141.810570(55)	1141.769070(88)
D_J (kHz)	[0.09954]	[0.09954]	[0.09954]
D_K (kHz)	[0.238]	[0.238]	[0.238]
d_1 (kHz)	[-0.0117]	[-0.0117]	[-0.0117]
N[b]	7	7	7
σ / kHz	0.6	0.5	0.8

	$^{13}C_4$	$^{13}C_5$	$^{18}O_5$
A (MHz)[a]	2427.9974(14)	2410.4330(20)	2408.85090(61)
B (MHz)	1505.32374(16)	1507.65325(22)	1495.280720(43)
C (MHz)	1141.295570(99)	1139.73973(16)	1131.441210(20)
D_J (kHz)	[0.09954]	[0.09954]	[0.09954]
D_K (kHz)	[0.238]	[0.238]	[0.238]
d_1 (kHz)	[-0.0117]	[-0.0117]	[-0.0117]
N	7	7	6
σ / kHz	0.8	1.1	0.1

[a] Rotational constants (A, B, C). [b] Number of transitions (N) and rms deviation (σ) of the fit. [c] Standard error in parenthesis in units of the last digit

Table VI.S10. Substitution coordinates of the c-β-Pyr-$^1C_4$-1 conformer of 2-deoxyribose (principal-inertial-axis coordinates in Å; *ab initio* data according to MP2(full)/6-311++G(d,p).

Atom	Substitution Coordinates			MP2 (full) Coordinates		
	/a/	/b/	/c/	a	b	c
C_1	1.4691(10)	0.3239(46)	0.5824(26)	-1.46187	-0.34001	0.58392
C_2	0.083(18)	1.1034(14)	0.7247(21)	-0.15252	-1.09720	0.73596
C_3	0.8033(19)	0.7745(19)	0.4092(37)	0.81216	-0.77729	-0.40406
C_4	0.9446(16)	0.7321(20)	0.5581(27)	0.93198	0.73590	-0.56189
C_5	0.4194(36)	1.3612(11)	0.7179(21)	-0.44313	1.35212	-0.72649
O_5	1.2458(12)	1.0569(14)	0.4180(36)	-1.25148	1.05558	0.41822

Table VI.S11. The c-β-pyr[1]C$_4$-1 structure of free 2-deoxyribose, and comparison with the β-pyr[1]C$_4$ crystal structure (bond lengths and valence angles in Ångström and degrees, respectively).

	Gas-phase[a]			Crystal[b]
	r_s	r_0	r_e	
r(C$_1$-C$_2$)	1.596(20)[c]	1.574(23)	1.520	1.500
r(C$_2$-C$_3$)	1.477(17)	1.485(11)	1.527	1.486
r(C$_3$-C$_4$)	1.5205(49)	1.5222(43)	1.526	1.532
r(C$_4$-C$_5$)	1.5106(65)	1.4982(76)	1.516	1.529
r(C$_5$-O$_6$)	1.4347(78)	1.452(10)	1.432	1.405
r(O$_6$-C$_1$)	1.4084(70)	1.419(11)	1.421	1.446
r(C$_1$-O$_1$)		1.4322(48)	1.409	1.413
r(C$_3$-O$_3$)			1.417	1.430
r(C$_4$-O$_4$)			1.429	1.399
∠(C$_1$-C$_2$-C$_3$)	110.13(74)	110.77(72)	111.4	107.2
∠(C$_2$-C$_3$-C$_4$)	110.59(55)	110.50(25)	109.5	111.5
∠(C$_3$-C$_4$-C$_5$)	109.82(34)	110.20(29)	110.1	108.2
∠(C$_4$-C$_5$-O$_6$)	110.33(47)	110.19(27)	109.9	109.0
∠(C$_5$-O$_6$-C$_1$)	113.02(46)	113.10(61)	112.3	112.6
∠(O$_1$-C$_1$-C$_2$)		109.66(52)	107.4	133.0
∠(O$_3$-C$_3$-C$_4$)		109.37(71)	111.6	106.6
∠(O$_4$-C$_4$-C$_5$)		110.28(51)	109.8	112.3
τ (C$_1$-C$_2$-C$_3$-C$_4$)	52.7(12)	52.27(86)	50.4	56.8
τ (C$_2$-C$_3$-C$_4$-C$_5$)	-56.4(12)	-56.07(85)	-53.9	-57.1
τ (C$_3$-C$_4$-C$_5$-O$_6$)	58.69(72)	58.49(35)	59.4	57.2
τ (C$_4$-C$_5$-O$_6$-C$_1$)	-61.39(69)	-60.75(85)	-62.1	-61.1
τ (O$_1$-C$_1$-C$_2$-C$_3$)		70.03(97)	69.9	55.1
τ (O$_3$-C$_3$-C$_2$-C$_1$)		174.69(24)	173.2	177.3
τ (O$_4$-C$_4$-C$_3$-O$_2$)		66.1(12)	68.4	65.1

[a]This work. [b]Ref. 9.

Table VI.S12. Conformational search (>20 kJmol[-1]) of 2-deoxyribose according to B3LYP/6-311++G** (Electronic energies, zero-point energy corrections, Gibbs free energy and electric dipole moment components denoted respectively Δ(E+ZPVE), ΔG, μa, μb, μc).

Conformer	Δ(E + ZPVE) (kJ/mol)	ΔG (kJ/mol)	μ$_a$ (Debye)	μ$_b$ (Debye)	μ$_c$ (Debye)
Deoxyribose_lineal_10	9.1	0.0	1.2	0.6	-0.2
AlphaDeoxyriboPyr_2	0.0	0.1	2.9	0.2	0.4
Deoxyribose_lineal_3	8.5	0.8	-0.3	-0.7	0.1
Deoxyribose_lineal_5	10.3	1.8	1.4	-1.6	1.1
AlphaDeoxyriboFur_2	7.0	3.5	-0.6	-2.5	-0.5
BetaDeoxyriboPyr_1	5.1	4.0	-2.5	1.3	0.5
AlphaDeoxyriboFur_1	8.3	4.4	-1.3	-1.9	1.6

Deoxyribose_lineal_7	14.5	5.2	-1.0	-0.6	-1.4
Deoxyribose_lineal_13	13.6	5.5	2.4	-1.6	-0.5
AlphaDeoxyriboPyr_4	5.9	5.7	-3.1	0.6	1.5
BetaDeoxyriboPyr_2	7.8	6.3	-0.9	-2.1	-0.7
AlphaDeoxyriboPyr_1	7.7	6.5	-1.7	1.6	-1.8
Deoxyribose_lineal_22	15.5	6.6	0.5	-0.9	-0.1
AlphaDeoxyriboPyr_7	7.5	7.2	-3.6	-0.8	2.8
Deoxyribose_lineal_1	18.6	7.3	-3.9	-0.9	1.6
BetaDeoxyriboPyr_3	9.0	7.5	-0.2	-1.0	-2.2
AlphaDeoxyriboFur_3	11.9	7.9	1.9	-1.9	-0.5
AlphaDeoxyriboFur_7	14.8	8.0	-1.1	-0.2	1.4
BetaDeoxyriboPyr_5	9.9	8.0	-1.7	-2.0	0.0
BetaDeoxyriboPyr_7	10.4	8.6	-0.2	2.2	-1.0
BetaDeoxyriboFur_2	14.1	8.7	2.0	-0.9	0.5
BetaDeoxyriboPyr_4	12.8	8.9	-0.4	0.0	0.0
BetaDeoxyriboPyr_8	10.8	8.9	-2.0	-0.6	-1.0
AlphaDeoxyriboFur_14	15.1	9.1	0.1	-0.9	0.7
AlphaDeoxyriboFur_37	15.1	9.1	0.5	0.9	-0.6
AlphaDeoxyriboFur_9	13.9	9.9	-0.9	-2.4	-0.4
Deoxyribose_lineal_18	21.1	10.0	-3.0	-1.3	-0.5
BetaDeoxyriboFur_6	15.4	10.1	-0.7	-2.5	-0.5
Deoxyribose_lineal_9	19.7	10.1	0.8	-0.4	-3.3
BetaDeoxyriboFur_1	16.1	10.2	-3.0	-0.5	0.8
Deoxyribose_lineal_11	20.9	10.3	1.6	0.3	-0.7
BetaDeoxyriboFur_5	13.8	10.3	0.6	0.1	1.2
AlphaDeoxyriboPyr_3	11.9	10.5	-0.2	0.8	-0.1
AlphaDeoxyriboFur_5	14.2	10.6	0.2	2.1	1.6
BetaDeoxyriboFur_3	14.2	10.6	0.7	-1.7	-0.3
AlphaDeoxyriboFur_11	15.2	10.7	0.4	-3.2	1.5
BetaDeoxyriboFur_7	17.1	10.8	-1.1	-0.5	0.7
Deoxyribose_lineal_2	20.0	10.9	-0.7	-1.4	2.2
AlphaDeoxyriboFur_6	15.0	11.1	1.3	2.3	-0.2
BetaDeoxyriboFur_4	13.8	11.2	-0.3	-2.0	1.8
AlphaDeoxyriboPyr_9	11.6	11.2	1.0	3.3	1.6
Deoxyribose_lineal_4	22.7	11.2	-4.0	-1.1	0.6
Deoxyribose_lineal_19	20.7	11.3	-0.7	-1.2	-1.6
Deoxyribose_lineal_27	22.3	11.5	0.2	-0.1	1.0
BetaDeoxyriboFur_16	17.4	11.7	-0.3	-1.6	1.3
BetaDeoxyriboFur_10	17.7	11.7	-2.1	-1.2	-1.5
BetaDeoxyriboPyr_10	13.7	11.8	2.3	-1.4	2.1
AlphaDeoxyriboFur_13	17.3	11.8	1.5	-2.6	1.8

Deoxyribose_lineal_26	21.7	11.8	-1.1	1.4	0.3
AlphaDeoxyriboFur_4	15.9	12.1	-0.2	3.1	1.5
AlphaDeoxyriboFur_10	19.1	12.1	-2.3	0.7	2.8
AlphaDeoxyriboPyr_8	13.9	12.1	0.1	-1.4	-2.8
AlphaDeoxyriboFur_29	16.7	12.4	-1.6	-1.3	1.7
AlphaDeoxyriboFur_8	16.7	12.7	-1.8	3.0	3.0
Deoxyribose_lineal_25	22.8	12.7	3.2	3.1	-0.2
AlphaDeoxyriboFur_15	17.7	12.7	3.5	0.7	1.8
Deoxyribose_lineal_12	19.2	12.8	-0.6	-0.7	-2.3
AlphaDeoxyriboPyr_6	15.1	13.1	1.5	-2.0	-1.3
Deoxyribose_lineal_23	19.6	13.2	2.2	-0.9	-2.7
AlphaDeoxyriboFur_26	18.5	13.2	0.2	-2.0	0.3
Deoxyribose_lineal_14	22.3	13.4	-1.0	0.0	0.7
Deoxyribose_lineal_8	23.7	13.6	1.2	-0.2	0.1
AlphaDeoxyriboFur_22	20.0	13.6	-0.4	0.2	2.4
Deoxyribose_lineal_24	25.2	13.8	-3.9	0.7	-0.8
BetaDeoxyriboFur_18	21.9	14.1	-0.9	-1.7	-0.5
BetaDeoxyriboFur_9	20.0	14.1	1.3	-0.3	0.2
AlphaDeoxyriboPyr_16	16.1	14.4	1.4	-0.1	-3.9
Deoxyribose_lineal_21	22.7	14.4	0.0	-0.8	-1.4
AlphaDeoxyriboFur_18	21.1	14.4	-0.3	2.2	0.3
BetaDeoxyriboFur_11	21.4	14.6	3.0	0.8	1.3
AlphaDeoxyriboFur_28	19.4	14.6	2.5	1.2	0.0
Deoxyribose_lineal_15	23.4	14.7	-0.9	-1.3	0.7
BetaDeoxyriboFur_20	18.7	14.8	-1.2	-2.3	-1.4
BetaDeoxyriboFur_21	19.3	14.8	-1.9	0.3	-0.8
BetaDeoxyriboFur_45	24.0	14.9	-2.2	-0.9	0.3
AlphaDeoxyriboPyr_11	16.8	14.9	2.8	-0.8	-2.3
AlphaDeoxyriboFur_16	20.0	15.0	0.8	-0.8	2.3
BetaDeoxyriboFur_12	20.2	15.2	1.2	2.0	-0.5
Deoxyribose_lineal_16	22.9	15.2	-0.7	2.7	1.4
AlphaDeoxyriboFur_25	21.7	15.4	0.7	1.3	-0.4
AlphaDeoxyriboFur_17	20.2	15.6	2.9	2.3	1.4
Deoxyribose_lineal_6	24.7	15.6	-2.2	0.1	-1.6
Deoxyribose_lineal_17	26.2	15.8	-1.0	-0.9	-0.7
Deoxyribose_lineal_20	23.3	16.0	1.5	-2.2	1.2
AlphaDeoxyriboFur_34	20.4	16.0	1.1	2.0	1.4
BetaDeoxyriboFur_26	22.4	16.1	0.3	1.3	1.7
BetaDeoxyriboFur_25	21.1	16.1	-1.5	-1.4	-0.3
BetaDeoxyriboFur_44	20.9	16.2	-0.6	-4.0	-0.7
AlphaDeoxyriboFur_27	24.9	16.2	1.3	-0.4	0.9

AlphaDeoxyriboFur_21	21.1	16.3	3.9	2.4	-0.4
BetaDeoxyriboFur_30	23.3	16.4	-1.4	0.0	-0.2
BetaDeoxyriboFur_31	23.9	16.5	-0.9	-0.3	1.3
AlphaDeoxyriboFur_31	21.3	16.6	2.3	1.2	3.1
BetaDeoxyriboFur_39	20.8	16.7	-0.7	-2.1	0.9
BetaDeoxyriboFur_17	20.3	17.0	0.6	-2.9	-0.7
BetaDeoxyriboFur_33	24.6	17.1	1.7	0.8	0.4
AlphaDeoxyriboFur_23	23.4	17.5	2.6	-0.9	0.6
BetaDeoxyriboPyr_9	19.4	17.5	-0.1	0.1	-0.3
BetaDeoxyriboFur_19	22.7	17.7	-2.6	1.8	0.6
BetaDeoxyriboFur_37	22.8	17.7	-2.2	0.7	-1.4
BetaDeoxyriboFur_36	22.0	17.7	-1.5	0.2	1.7
BetaDeoxyriboFur_41	23.7	17.8	2.5	-1.3	1.3
AlphaDeoxyriboFur_24	25.6	17.9	-1.8	3.0	1.4
BetaDeoxyriboFur_22	25.7	18.1	0.5	-0.8	-1.8
BetaDeoxyriboFur_34	25.3	18.3	0.6	0.7	-0.1
BetaDeoxyriboFur_28	24.3	18.6	1.1	-2.3	0.2
BetaDeoxyriboPyr_12	20.5	18.6	-3.1	-1.2	-0.4
AlphaDeoxyriboFur_36	23.8	18.6	-2.1	2.0	2.4
AlphaDeoxyriboPyr_5	20.0	18.8	-2.8	0.0	-0.4
BetaDeoxyriboFur_38	25.6	18.9	-1.9	2.1	3.1
AlphaDeoxyriboFur_32	26.2	18.9	-0.1	2.3	1.1
BetaDeoxyriboFur_47	24.3	18.9	1.2	-0.7	1.9
BetaDeoxyriboFur_27	25.8	19.0	-1.0	0.5	2.3
BetaDeoxyriboFur_32	23.5	19.3	0.4	4.9	-1.2
BetaDeoxyriboFur_56	26.7	19.4	-0.4	1.8	1.7
BetaDeoxyriboFur_53	27.7	19.5	2.9	-1.1	2.3
BetaDeoxyriboFur_29	25.9	19.6	0.0	2.0	2.1
BetaDeoxyriboFur_48	27.2	19.7	0.8	-0.1	2.3
AlphaDeoxyriboFur_33	27.0	19.9	-1.7	1.4	-0.7

Table VI.S13. Conformational search (>20 kJmol^{-1}) of 2-deoxyribose according to M06-2X/6-311++G** (Electronic energies, zero-point energy corrections, Gibbs free energy and electric dipole moment components denoted respectively Δ(*E+ZPVE*), Δ*G*, μ*a*, μ*b*, μ*c*).

Conformer	Δ(E + ZPVE) (kJ/mol)	ΔG (kJ/mol)	μ$_a$ (Debye)	μ$_b$ (Debye)	μ$_c$ (Debye)
AlphaDeoxyriboPyr_2	0.0	0.0	2.9	0.2	0.3
BetaDeoxyriboPyr_1	6.0	5.0	-2.6	1.2	0.5
AlphaDeoxyriboPyr_4	5.4	5.3	-3.1	0.5	1.4
AlphaDeoxyriboPyr_7	7.8	7.6	-3.6	-0.9	2.8
BetaDeoxyriboPyr_2	10.0	8.6	-0.9	-2.1	-0.7
AlphaDeoxyriboPyr_1	10.1	9.0	-1.8	1.6	-1.8
AlphaDeoxyriboFur_2	12.2	9.2	-0.6	-2.6	-0.6
BetaDeoxyriboPyr_3	11.8	10.5	-0.2	-1.0	-2.2
BetaDeoxyriboPyr_7	13.0	11.2	-0.3	2.2	-1.0
AlphaDeoxyriboPyr_9	11.6	11.3	0.9	3.4	1.5
BetaDeoxyriboPyr_5	13.0	11.4	-1.8	-2.0	0.1
AlphaDeoxyriboFur_1	15.3	11.6	-1.3	-1.9	1.5
BetaDeoxyriboPyr_8	14.0	12.1	-2.2	-0.5	-1.0
BetaDeoxyriboPyr_4	15.9	13.1	-0.5	-0.2	0.1
AlphaDeoxyriboPyr_3	14.6	13.4	-0.2	0.8	-0.1
AlphaDeoxyriboFur_3	17.9	14.2	2.0	-2.0	-0.5
BetaDeoxyriboPyr_10	17.0	15.5	2.4	-1.5	2.0
AlphaDeoxyriboPyr_8	17.6	15.7	0.2	-1.4	-2.8
BetaDeoxyriboFur_2	22.3	16.3	1.3	2.1	0.1
BetaDeoxyriboFur_4	19.2	16.5	-0.5	-1.9	1.8
AlphaDeoxyriboFur_5	19.9	16.9	0.2	2.1	1.6
AlphaDeoxyriboPyr_6	18.9	17.0	1.6	-2.0	-1.3
AlphaDeoxyriboPyr_13	18.9	17.0	0.7	-1.4	-2.3
BetaDeoxyriboPyr_9	19.2	17.2	-0.1	0.0	-0.3
BetaDeoxyriboFur_8	20.6	17.5	0.5	0.2	1.4
AlphaDeoxyriboFur_6	20.9	17.5	1.3	2.3	-0.2
BetaDeoxyriboFur_3	20.8	17.5	0.6	-1.5	-0.3
AlphaDeoxyriboFur_9	21.8	17.7	-1.0	-2.4	-0.4
BetaDeoxyriboFur_5	23.6	18.2	-0.2	-1.0	0.7
AlphaDeoxyriboFur_11	23.1	18.5	0.4	-3.2	1.5
AlphaDeoxyriboPyr_16	20.9	19.2	1.5	0.0	-3.8
AlphaDeoxyriboPyr_5	20.3	19.5	-2.9	0.0	-0.2
AlphaDeoxyriboFur_4	23.3	19.6	-0.2	3.1	1.4
BetaDeoxyriboFur_6	24.4	19.8	-0.7	-2.7	-0.5
AlphaDeoxyriboFur_29	24.3	19.9	-1.9	-1.3	1.6

Table VI.S14. Conformational search (>20 kJmol-1) of 2-deoxyribose according to MP2(Full)/6-311++G** (Electronic energies, zero-point energy corrections, Gibbs free energy and electric dipole moment components denoted respectively Δ(*E+ZPVE*), Δ*G*, μ*a*, μ*b*, μ*c*).

Conformer	Δ(E + ZPVE) (kJ/mol)	ΔG (kJ/mol)	μ_a (Debye)	μ_b (Debye)	μ_c (Debye)
AlphaDeoxyriboPyr_2	0.0	0.0	2.9	0.3	0.3
BetaDeoxyriboPyr_1	4.3	3.3	-2.6	1.2	0.5
AlphaDeoxyriboFur_2	6.7	3.5	-0.6	-2.6	-0.6
AlphaDeoxyriboPyr_4	4.7	4.7	-3.0	0.6	1.4
BetaDeoxyriboPyr_2	7.0	5.6	-1.0	-2.1	-0.6
AlphaDeoxyriboPyr_7	6.6	6.0	-3.6	-0.7	2.8
AlphaDeoxyriboFur_1	10.2	6.5	-1.3	-2.0	1.5
BetaDeoxyriboPyr_4	8.6	6.7	-1.2	2.6	-0.3
AlphaDeoxyriboPyr_1	8.0	6.7	-1.8	1.6	-1.9
BetaDeoxyriboPyr_3	8.4	6.8	-0.2	-1.1	-2.2
AlphaDeoxyriboFur_3	12.0	8.5	1.9	-2.0	-0.5
BetaDeoxyriboPyr_5	10.7	8.9	-1.7	-2.0	0.2
BetaDeoxyriboPyr_8	11.5	9.4	-2.2	-0.6	-1.1
BetaDeoxyriboPyr_7	11.4	9.6	-0.2	2.2	-1.0
AlphaDeoxyriboPyr_9	11.2	10.6	1.0	3.3	1.6
AlphaDeoxyriboFur_5	13.9	10.7	0.2	2.1	1.6
BetaDeoxyriboFur_2	17.0	11.6	1.9	0.7	0.4
AlphaDeoxyriboPyr_3	13.2	11.8	-0.3	0.7	-0.2
AlphaDeoxyriboFur_6	15.3	12.0	1.3	2.2	-0.3
AlphaDeoxyriboFur_9	16.2	12.3	-1.0	-2.4	-0.4
AlphaDeoxyriboFur_11	16.9	12.4	0.4	-3.3	1.4
AlphaDeoxyriboPyr_8	14.7	13.0	0.2	-1.3	-2.8
BetaDeoxyriboFur_6	17.9	13.0	-0.5	-2.7	-0.6
BetaDeoxyriboPyr_10	14.9	13.1	2.3	-1.4	1.9
Deoxyribose_lineal_3	21.3	13.7	0.0	-0.6	0.0
AlphaDeoxyriboFur_7	20.0	13.9	-1.1	-0.2	1.3
AlphaDeoxyriboPyr_15	19.0	13.9	0.4	0.2	-1.8
BetaDeoxyriboFur_4	16.2	14.0	-0.4	-1.9	1.7
Deoxyribose_lineal_10	23.5	14.2	1.0	0.5	-0.2
AlphaDeoxyriboFur_14	20.2	14.3	0.0	-1.0	0.6
AlphaDeoxyriboFur_4	18.1	14.3	-0.2	3.1	1.4
AlphaDeoxyriboPyr_6	16.4	14.5	1.5	-2.0	-1.3
BetaDeoxyriboFur_8	17.2	14.5	0.5	0.1	1.4

AlphaDeoxyriboFur_15	19.4	14.5	3.6	0.6	1.6
BetaDeoxyriboFur_3	17.5	14.7	0.6	-1.6	-0.3
AlphaDeoxyriboPyr_13	17.4	14.9	1.3	2.3	0.0
AlphaDeoxyriboFur_8	18.9	15.0	-1.8	3.0	3.0
BetaDeoxyriboFur_1	20.5	15.1	-3.1	-0.8	0.8
AlphaDeoxyriboFur_29	19.3	15.2	-1.9	-1.4	1.5
AlphaDeoxyriboPyr_16	17.3	15.3	1.5	0.0	-3.9
BetaDeoxyriboFur_16	21.1	15.3	-0.2	-1.6	1.2
Deoxyribose_lineal_5	23.7	15.5	1.7	-1.4	1.1
AlphaDeoxyriboPyr_14	19.3	15.7	0.4	0.3	-1.7
BetaDeoxyriboFur_7	21.8	16.3	-1.0	-0.8	0.7
AlphaDeoxyriboPyr_11	18.5	16.3	2.9	-0.8	-2.3
AlphaDeoxyriboFur_13	21.7	16.5	1.5	-2.7	1.7
BetaDeoxyriboFur_15	21.6	16.6	2.3	0.4	2.9
AlphaDeoxyriboFur_17	20.6	16.7	2.9	2.4	1.5
BetaDeoxyriboFur_10	22.5	17.2	-2.0	-1.4	-1.5
AlphaDeoxyriboFur_16	22.3	17.4	0.8	-0.7	2.2
AlphaDeoxyriboFur_28	22.0	17.6	2.5	1.3	-0.1
BetaDeoxyriboPyr_12	19.5	17.7	-3.2	-1.2	-0.3
BetaDeoxyriboFur_21	21.8	17.9	-1.9	0.4	-0.6
Deoxyribose_lineal_7	27.3	17.9	-1.1	-0.5	-1.5
BetaDeoxyriboFur_12	22.1	18.0	1.0	2.1	-0.4
AlphaDeoxyriboFur_21	21.9	18.0	4.0	2.5	-0.4
BetaDeoxyriboFur_9	23.2	18.3	1.2	-0.1	0.1
BetaDeoxyriboFur_20	21.9	18.4	-1.3	-2.1	-1.0
AlphaDeoxyriboFur_31	23.1	18.5	2.4	1.1	3.1
AlphaDeoxyriboFur_10	25.1	18.5	-2.4	0.7	2.7
BetaDeoxyriboPyr_9	19.0	18.6	-0.3	-0.4	-0.1
Deoxyribose_lineal_13	26.6	18.6	2.7	-1.5	-0.4
AlphaDeoxyriboFur_26	23.9	18.7	0.1	-2.0	0.2
AlphaDeoxyriboFur_34	22.9	18.8	1.0	2.0	1.5
BetaDeoxyriboFur_25	23.7	19.2	-1.5	-1.4	-0.1
BetaDeoxyriboFur_18	25.6	19.5	-1.0	-1.7	-0.1
BetaDeoxyriboFur_44	24.6	19.8	-0.5	-3.8	-0.5
Deoxyribose_lineal_22	28.8	19.8	0.6	-0.8	-0.1
BetaDeoxyriboFur_11	25.3	20.0	2.8	1.5	1.3
BetaDeoxyriboFur_17	22.6	20.0	0.8	-3.1	-0.8

Figure VI.S1. Interconversion barrier between conformers c-β-pyr $^4C_1$-2 ↔ c-β-pyr $^4C_1$-1 of 2-deoxyribose calculated at the MP2 level of theory.

c-β-pyr$^4C_1$-2

c-β-pyr$^4C_1$-1

~100

angle HOCC / degrees

ΔE/ cm^{-1}
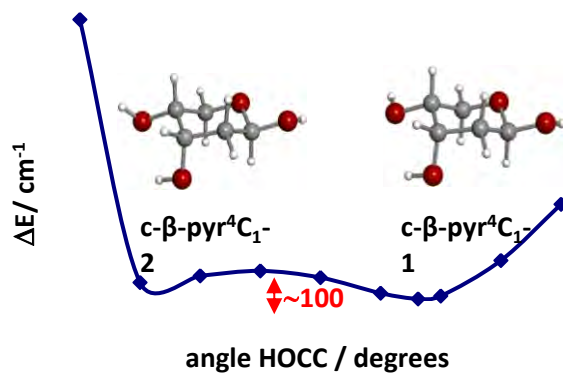
Figure VI.S2. Interconversion barrier between conformers c-α-pyr $^4C_1$-2 ↔ c-α-pyr $^4C_1$-1 of 2-deoxyribose calculated at the MP2 level of theory.

c-α-pyr$^4C_1$-2

c-α-pyr$^4C_1$-1

~220

angle HOCC / degrees

ΔE/ cm^{-1}
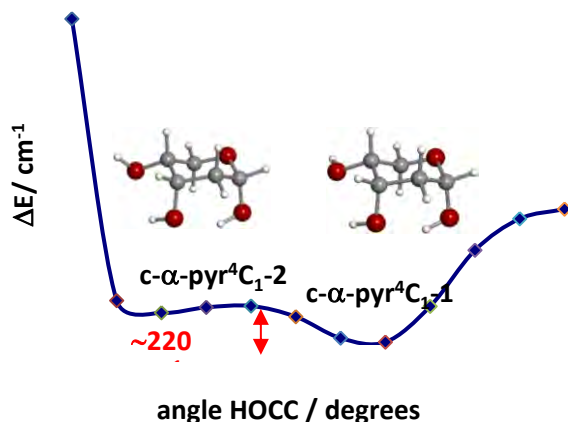
Figure *VI.S3*. Conformational distribution in 2-deoxyribose.
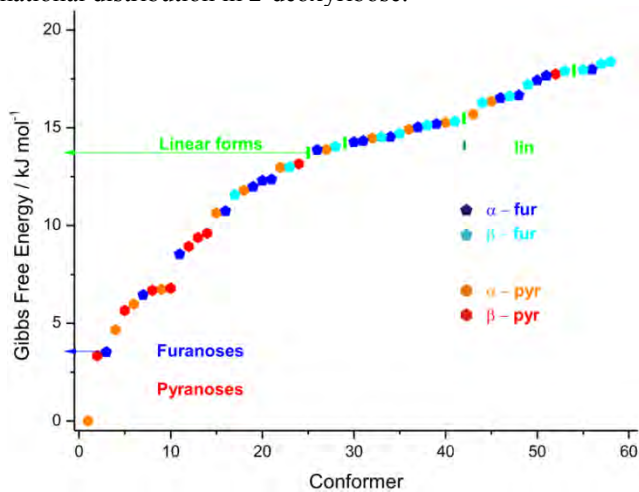
SUPPLEMENTARY INFORMATION FOR CHAPTER VII

Table VII.S1. Measured rotational transitions (in MHz) assigned to conformer α-G-g+/*cc*/t using CP-FTMW spectroscopy.

J'	K'_{-1}	K'_{+1}	J''	K''_{-1}	K''_{+1}	ν_{obs}	$\nu_{obs} - \nu_{cal}$
5	0	5	4	1	4	6088.345	0.004
5	1	5	4	1	4	6126.814	0.040
5	2	4	4	2	3	6679.013	0.011
6	0	6	5	1	5	7280.228	-0.004
6	1	6	5	1	5	7295.506	0.051
6	0	6	5	0	5	7318.660	-0.003
6	1	6	5	0	5	7333.884	-0.002
7	0	7	6	1	6	8450.718	0.010
7	1	7	6	1	6	8456.507	0.052
7	0	7	6	0	6	8465.941	0.011
7	1	7	6	0	6	8471.655	-0.022
4	3	1	3	2	2	8553.878	0.008
6	2	4	5	2	3	8724.034	0.017
7	1	6	6	2	5	8990.076	0.006
7	2	6	6	2	5	9146.439	0.014
4	4	0	3	3	1	9578.099	-0.002
7	3	5	6	3	4	9597.705	-0.031
8	0	8	7	1	7	9611.657	-0.013
8	0	8	7	0	7	9617.444	0.028
8	1	8	7	0	7	9619.535	0.021
7	2	5	6	2	4	10075.498	-0.053
8	1	7	7	2	6	10267.183	-0.006
8	2	7	7	2	6	10337.607	0.008
9	0	9	8	1	8	10768.752	-0.004
9	1	9	8	1	8	10769.484	-0.018
9	0	9	8	0	8	10770.829	-0.024
9	1	9	8	0	8	10771.591	-0.007
8	3	6	7	3	5	10893.323	0.009
9	1	8	8	2	7	11481.371	-0.004
9	2	8	8	2	7	11511.103	-0.008
9	2	8	8	1	7	11581.477	-0.045

Table VII.S2. Measured rotational transitions (in MHz) assigned to conformer α-*G*+*g*-/*cc*/*t* using CP-FTMW spectroscopy.

J'	K'_{-1}	K'_{+1}	J''	K''_{-1}	K''_{+1}	ν_{obs}	$\nu_{obs} - \nu_{cal}$
5	2	4	4	2	3	6328.266	0.017
5	3	3	4	3	2	6577.787	0.064
6	0	6	5	1	5	6769.014	0.003
6	1	6	5	1	5	6785.799	0.045
6	0	6	5	0	5	6811.457	0.032
6	1	6	5	0	5	6828.174	0.004
5	2	3	4	2	2	7009.604	-0.008
6	2	5	5	2	4	7497.333	0.051
7	0	7	6	1	6	7848.754	0.003
7	1	7	6	1	6	7855.079	0.028
7	1	7	6	0	6	7871.843	0.048
6	3	4	5	3	3	7874.877	-0.033
6	2	4	5	2	3	8390.817	0.007
7	1	6	6	2	5	8457.100	-0.005
7	2	6	6	2	5	8629.428	0.030
8	0	8	7	1	7	8917.972	0.014
8	1	8	7	1	7	8920.234	-0.016
8	0	8	7	0	7	8924.252	-0.007
8	1	8	7	0	7	8926.555	0.005
7	3	5	6	3	4	9137.467	0.013
7	4	4	6	4	3	9282.154	-0.003
8	1	7	7	2	6	9654.960	0.017
7	2	5	6	2	4	9672.504	-0.051
8	2	7	7	2	6	9732.253	0.002
4	4	1	3	3	0	9786.838	-0.002
4	4	0	3	3	1	9797.798	0.000
9	0	9	8	1	8	9982.884	-0.007
9	1	9	8	1	8	9983.682	-0.021
9	0	9	8	0	8	9985.183	0.001
9	1	9	8	0	8	9985.979	-0.015
8	3	6	7	3	5	10357.322	0.046
8	5	4	7	5	3	10613.756	-0.040
9	1	8	8	2	7	10782.884	0.032
9	2	8	8	2	7	10815.378	-0.007
8	2	6	7	2	5	10834.473	-0.033
1	0	10	9	1	9	11046.177	-0.023
1	1	10	9	1	9	11046.453	-0.030
1	0	10	9	0	9	11047.008	-0.005
1	1	10	9	0	9	11047.265	-0.030
5	4	1	4	3	2	11134.931	-0.006
8	3	5	7	3	4	11249.799	-0.022
9	3	7	8	3	6	11532.592	-0.016

Table VII.S3. Measured rotational transitions (in MHz) assigned to conformer α-*Tg*+/*cc*/*t* using CP-FTMW spectroscopy.

J'	K'_{-1}	K'_{+1}	J''	K''_{-1}	K''_{+1}	ν_{obs}	$\nu_{obs} - \nu_{cal}$
6	1	6	5	1	5	6822.801	0.023
6	0	6	5	0	5	6869.392	0.024
6	2	5	5	2	4	7467.283	0.005
7	1	7	6	1	6	7905.067	0.023
7	0	7	6	0	6	7927.498	-0.007
6	2	4	5	2	3	8224.086	0.001
7	2	6	6	2	5	8623.150	0.041
8	1	8	7	1	7	8981.471	0.018
8	0	8	7	0	7	8991.615	0.006
7	3	5	6	3	4	9024.174	-0.010
7	2	5	6	2	4	9555.592	0.014
8	2	7	7	2	6	9751.287	-0.005
9	1	9	8	1	8	10054.828	-0.012
9	0	9	8	0	8	10059.2275	-0.011
8	3	6	7	3	5	10265.375	-0.014
9	2	8	8	2	7	10857.373	-0.009
9	1	8	8	1	7	10956.891	-0.011
1	1	10	9	1	9	11126.796	-0.004
1	0	10	9	0	9	11128.595	-0.051
9	3	7	8	3	6	11473.195	-0.007
1	2	9	9	2	8	11947.931	0.016

Table VII.S4. Measured rotational transitions (in MHz) assigned to conformer α-G-g+/*cc*/t using LA-MB-FTMW spectroscopy.

J'	K'_{-1}	K'_{+1}	F'	J''	K''_{-1}	K''_{+1}	F''	ν_{obs}	$\nu_{obs} - \nu_{cal}$
4	0	4	3	3	1	3	2	4853.910	0.005
4	0	4	5	3	1	3	4	4853.989	0.003
4	0	4	4	3	1	3	3	4854.143	0.000
4	1	4	4	3	1	3	3	4944.265	0.002
4	1	4	5	3	1	3	4	4944.309	0.004
4	0	4	5	3	0	3	4	5043.431	0.002
4	0	4	3	3	0	3	2	5043.508	0.000
4	1	4	5	3	0	3	4	5133.751	0.003
4	1	4	3	3	0	3	2	5133.881	0.002
4	1	3	4	3	1	2	3	5710.490	0.001
4	1	3	5	3	1	2	4	5710.616	-0.000
4	1	3	3	3	1	2	2	5710.767	-0.002
5	0	5	4	4	1	4	3	6088.312	0.001
5	0	5	6	4	1	4	5	6088.337	0.000
5	0	5	5	4	1	4	4	6088.343	0.001
5	1	5	5	4	1	4	4	6126.717	0.001
5	1	5	4	4	1	4	3	6126.776	-0.000
5	1	5	6	4	1	4	5	6126.787	0.001
5	0	5	5	4	0	4	4	6178.463	0.000

5	0	5	6	4	0	4	5	6178.658	0.002
5	0	5	4	4	0	4	3	6178.680	-0.001
5	1	5	5	4	0	4	4	6216.839	0.002
5	1	5	6	4	0	4	5	6217.106	-0.000
5	1	5	4	4	0	4	3	6217.150	0.003
5	1	4	5	4	1	3	4	6991.716	-0.000
5	1	4	6	4	1	3	5	6991.982	-0.002
5	1	4	4	4	1	3	3	6992.101	0.000
6	1	6	6	5	1	5	5	7295.388	-0.003
6	1	6	5	5	1	5	4	7295.449	-0.006
6	1	6	7	5	1	5	6	7295.458	-0.004
6	0	6	6	5	0	5	5	7318.559	-0.004
6	0	6	7	5	0	5	6	7318.681	-0.002

Table VII.S5. Measured rotational transitions (in MHz) assigned to conformer α-G+g-/cc/t using LA-MB-FTMW spectroscopy.

J'	K'_{-1}	K'_{+1}	F'	J''	K''_{-1}	K''_{+1}	F''	ν_{obs}	$\nu_{obs} - \nu_{cal}$
4	0	4	3	3	1	3	2	4514.534	0.000
4	0	4	5	3	1	3	4	4514.602	0.001
4	0	4	4	3	1	3	3	4514.659	-0.000
4	1	4	4	3	1	3	3	4614.533	0.001
4	1	4	3	3	1	3	2	4614.562	0.000
4	1	4	5	3	1	3	4	4614.598	0.001
4	0	4	4	3	0	3	3	4724.829	0.000
4	0	4	5	3	0	3	4	4725.048	-0.000
4	1	4	4	3	0	3	3	4824.703	0.002
4	1	4	5	3	0	3	4	4825.046	0.001
4	1	4	3	3	0	3	2	4825.110	0.002
4	1	3	4	3	1	2	3	5474.860	0.000
4	1	3	5	3	1	2	4	5474.983	0.001
4	1	3	3	3	1	2	2	5475.082	0.001
5	0	5	5	4	1	4	4	5665.462	0.003
5	0	5	6	4	1	4	5	5665.482	0.000
5	1	5	5	4	1	4	4	5707.836	0.000
5	1	5	6	4	1	4	5	5707.908	0.002
5	1	5	5	4	0	4	4	5807.708	-0.000
5	1	5	6	4	0	4	5	5807.902	-0.001
5	1	4	5	4	1	3	4	6678.236	-0.001
5	1	4	6	4	1	3	5	6678.441	-0.001
5	1	4	4	4	1	3	3	6678.515	-0.002
6	0	6	6	5	1	5	5	6768.967	-0.003
6	0	6	7	5	1	5	6	6769.015	-0.002
6	0	6	6	5	0	5	5	6811.346	-0.000
6	0	6	5	5	0	5	4	6811.433	-0.002
6	0	6	7	5	0	5	6	6811.442	0.001
6	1	6	6	5	0	5	5	6828.076	-0.000
6	1	6	7	5	0	5	6	6828.188	-0.001

Table VII.S6. Measured rotational transitions (in MHz) assigned to conformer α-*Tg+*/*cc*/*t* using LA-MB-FTMW spectroscopy.

J'	K'_{-1}	K'_{+1}	F'	J''	K''_{-1}	K''_{+1}	F''	ν_{obs}	$\nu_{obs} - \nu_{cal}$
4	0	4	4	3	0	3	3	4761.448	0.002
4	0	4	5	3	0	3	4	4761.766	-0.000
4	0	4	3	3	0	3	2	4761.869	0.001
4	1	3	4	3	1	2	3	5404.677	0.000
4	1	3	5	3	1	2	4	5404.743	0.002
4	1	3	3	3	1	2	2	5404.894	0.001
5	1	5	5	4	1	4	4	5730.265	0.001
5	1	5	6	4	1	4	5	5730.327	-0.001
5	0	5	5	4	0	4	4	5817.484	-0.000
5	0	5	6	4	0	4	5	5817.721	-0.002
5	0	5	4	4	0	4	3	5817.766	0.001
5	0	5	4	4	1	4	3	5643.506	-0.001
5	0	5	6	4	1	4	5	5643.549	0.001
5	0	5	5	4	1	4	4	5643.632	-0.001
5	1	4	5	4	1	3	4	6646.291	-0.002
5	1	4	6	4	1	3	5	6646.492	-0.001
6	1	6	6	5	1	5	5	6822.699	0.001
6	1	6	5	5	1	5	4	6822.765	-0.001

SUPPLEMENTARY INFORMATION FOR CHAPTER VIII

Table VIII.S1. Measured frequencies and residuals (in MHz) for the nuclear quadrupole coupling hyperfine components of histidine.

J'	K'_{-1}	K'_{+1}	J''	K''_{-1}	K''_{+1}	F'_1	F'_2	F'	F''_1	F''_2	F''	ν_{obs}	$\nu_{obs}-\nu_{cal}$
1	1	1	0	0	0	2	2	1	1	1	1	2591.8881	0.0027
						0	1	2	1	2	3	2591.9708	0.0018
						2	1	0	1	0	1	2592.1041	0.0037
						2	2	3	1	1	2	2592.5997	-0.0012
						0	1	1	1	1	1	2593.1625	-0.0044
						2	3	4	1	2	3	2593.4948	0.0007
						1	2	3	1	2	2	2593.7008	-0.0030
						2	3	3	1	2	3	2594.0987	0.0004
						2	1	1	1	2	2	2595.3370	0.0006
						2	1	2	1	1	2	2595.3818	-0.0025
2	1	2	1	1	1	3	4	5	2	3	4	3069.4436	0.0020
						2	3	4	1	2	3	3069.4819	0.0015
						3	4	4	2	3	3	3069.5193	-0.0001
2	0	2	1	0	1	3	4	5	2	3	4	3150.0738	0.0006
						2	3	4	1	2	3	3150.0889	0.0009
						3	4	4	2	3	3	3150.1196	0.0025
2	1	1	1	1	0	3	4	4	2	3	3	3240.9537	-0.0015
						3	4	5	2	3	4	3240.9999	-0.0012
						1	2	3	2	1	2	3241.0357	0.0008
						3	4	3	2	3	2	3241.0976	-0.0028
2	1	2	1	0	1	3	3	2	2	2	1	4084.0661	0.0005
						3	3	4	2	2	3	4084.3272	-0.0005
						2	2	3	1	1	2	4084.4197	-0.0014
						1	2	3	0	1	2	4085.2867	-0.0012
						3	4	5	2	3	4	4085.3506	0.0004
						3	2	3	2	2	3	4085.5313	-0.0004
						2	3	4	1	2	3	4085.6356	-0.0021
						3	4	4	2	3	3	4086.0266	0.0015
						2	3	3	1	2	2	4086.2490	0.0009
						3	2	3	2	1	2	4086.7377	0.0010
						2	1	2	2	1	2	4087.0727	-0.0009
						2	1	1	2	1	0	4087.1150	-0.0001
3	1	3	2	1	2	4	5	6	3	4	5	4601.0869	0.0001
3	0	3	2	0	2	4	4	5	3	3	4	4712.1537	0.0006
						3	3	4	2	2	3	4712.1751	0.0007

						4	5	6	3	4	5	4712.2347	-0.0008
						3	4	5	2	3	4	4712.2706	-0.0048
						4	5	5	3	4	4	4712.3144	-0.0009
						3	4	4	2	3	3	4712.3412	0.0023
						4	3	4	3	2	3	4712.3660	0.0011
3	1	2	2	1	1	3	3	3	2	2	2	4858.0021	-0.0032
						3	4	4	2	3	3	4858.1296	-0.0002
						4	4	4	3	3	3	4858.1485	-0.0005
						3	4	5	2	3	4	4858.1753	-0.0009
						4	5	5	3	4	4	4858.2022	0.0002
						4	5	6	3	4	5	4858.2170	-0.0013
						3	2	3	3	2	3	4858.2989	-0.0001
						4	4	3	3	3	2	4858.3539	0.0016
						4	4	5	3	3	4	4858.3976	0.0012
3	1	3	2	0	2	4	4	3	3	3	2	5535.2364	0.0008
						4	4	5	3	3	4	5535.4262	0.0043
						3	3	4	2	2	3	5535.6358	0.0043
						4	5	6	3	4	5	5536.3659	-0.0031
						3	4	5	2	3	4	5536.6652	-0.0020
						4	5	5	3	4	4	5537.0443	0.0006
						3	4	4	2	3	3	5537.2958	0.0033
						4	3	3	3	2	2	5537.5194	-0.0024
4	1	4	3	1	3	5	6	7	4	5	6	6129.1638	0.0018
						5	6	6	4	5	5	6129.2063	0.0040
						5	6	5	4	5	4	6129.2423	0.0000
4	0	4	3	0	3	3	4	5	2	3	4	6259.6101	0.0015
						5	6	7	4	5	6	6259.6216	-0.0007
						4	5	4	3	4	3	6259.6401	-0.0001
						4	5	6	3	4	5	6259.6697	-0.0004
						5	4	5	4	3	4	6259.6873	0.0001
						4	3	4	3	2	3	6259.7386	0.0017
						5	6	6	4	5	5	6259.7844	-0.0039
						4	5	5	3	4	4	6259.8209	-0.0012
4	1	3	3	1	2	4	4	4	3	3	3	6470.9716	-0.0046
						4	5	6	3	4	5	6471.0527	0.0004
						5	6	7	4	5	6	6471.0636	0.0007
						4	4	5	3	3	4	6471.0857	0.0002
						5	5	6	4	4	5	6471.1291	0.0005
						4	3	4	3	2	3	6471.1608	-0.0002
						5	4	5	4	3	4	6471.2294	-0.0001

Figure VIII.S1. Variation of the quadrupole coupling constants calculated at the MP2/6-311++G(d,p)level with the dihedral angle <HNCC for histidine conformer εII_a.

Table VIII.S2. Cartesian coordinates for the εII_a conformer of histidine. The geometry has been optimized *ab initio* at the MP2/6-311++G(d,p) level of theory.

```
                         Standard orientation:
---------------------------------------------------------------------
Center     Atomic     Atomic            Coordinates (Angstroms)
Number     Number     Type         X           Y           Z
---------------------------------------------------------------------
   1          7          0       -2.558340   -0.862911   -0.398551
   2          6          0       -1.509677   -1.104038    0.457380
   3          6          0       -0.935527    0.134820    0.687170
   4          7          0       -1.610762    1.111324   -0.021923
   5          6          0       -2.583667    0.475140   -0.664757
   6          6          0        0.293374    0.454607    1.475112
   7          6          0        1.495879    0.661776    0.536189
   8          6          0        1.758479   -0.658794   -0.211910
   9          8          0        1.855161   -0.519046   -1.538076
  10          7          0        1.309919    1.747960   -0.436248
  11          8          0        1.860447   -1.720646    0.362304
  12          1          0        0.323859    2.003538   -0.500193
  13          1          0        2.392751    0.853691    1.136587
  14          1          0        0.522444   -0.367369    2.158331
  15          1          0        0.134160    1.367030    2.059515
  16          1          0       -1.249332   -2.093961    0.801134
  17          1          0       -3.320243    0.928062   -1.313273
  18          1          0       -3.194215   -1.554721   -0.769854
  19          1          0        1.729042    0.451892   -1.666165
  20          1          0        1.837795    2.573699   -0.177961
---------------------------------------------------------------------
Rotational constants (GHZ):     1.8174613   0.8621925    0.7715727
```

Table VIII.S3. Cartesian coordinates for the εII$_b$ conformer of histidine. The geometry has been optimized *ab initio* at the MP2/6-311++G(d,p) level of theory.

```
                        Standard orientation:
-----------------------------------------------------------------
Center     Atomic     Atomic          Coordinates (Angstroms)
Number     Number     Type         X           Y           Z
-----------------------------------------------------------------
   1          7          0       3.365123   -0.515438   -0.252728
   2          6          0       2.206573   -1.232600   -0.062389
   3          6          0       1.255705   -0.299660    0.314737
   4          7          0       1.820462    0.961125    0.353636
   5          6          0       3.090234    0.796243    0.005431
   6          6          0      -0.189522   -0.518457    0.623300
   7          6          0      -1.115895    0.090711   -0.443942
   8          6          0      -2.551512   -0.335763   -0.107999
   9          8          0      -3.286817    0.641067    0.443368
  10          7          0      -1.022029    1.555445   -0.426840
  11          8          0      -2.953879   -1.463819   -0.280561
  12          1          0      -0.088369    1.843357   -0.134595
  13          1          0      -0.865880   -0.352916   -1.415668
  14          1          0      -0.432693   -0.065751    1.593206
  15          1          0      -0.400125   -1.590208    0.687567
  16          1          0       2.156769   -2.302538   -0.199936
  17          1          0       3.837327    1.574194   -0.065152
  18          1          0       4.263327   -0.892958   -0.519862
  19          1          0      -2.685855    1.421326    0.414677
  20          1          0      -1.177325    1.936747   -1.355995
-----------------------------------------------------------------
Rotational constants (GHZ):    2.9931597    0.5676125    0.5011361
```

Table VIII.S4. Cartesian coordinates for the δII$_a$ conformer of histidine. The geometry has been optimized *ab initio* at the MP2/6-311++G(d,p) level of theory.

```
                          Standard orientation:
 ---------------------------------------------------------------------
 Center     Atomic     Atomic              Coordinates (Angstroms)
 Number     Number     Type            X           Y           Z
 ---------------------------------------------------------------------
    1          6          0         1.799147   -0.618432    0.013468
    2          6          0         1.428293    0.820243    0.413234
    3          8          0         1.650947   -1.565168    0.758176
    4          8          0         2.308747   -0.725463   -1.214657
    5          1          0         2.225692    0.184414   -1.580794
    6          7          0         1.316539    1.630796   -0.802832
    7          1          0         0.349179    1.636945   -1.127311
    8          1          0         1.592397    2.592447   -0.635196
    9          6          0         0.172700    0.811142    1.304483
   10          1          0         2.280329    1.192122    0.996114
   11          6          0        -1.025090    0.320663    0.561706
   12          6          0        -2.095713    0.983882   -0.023150
   13          7          0        -2.943355    0.103131   -0.654257
   14          6          0        -2.394807   -1.090136   -0.464153
   15          7          0        -1.239988   -1.008157    0.261678
   16          1          0        -2.303852    2.045846    0.008821
   17          1          0        -0.618684   -1.767520    0.517145
   18          1          0        -2.787603   -2.031581   -0.822170
   19          1          0         0.367742    0.193641    2.186564
   20          1          0        -0.022295    1.834174    1.643030
 ---------------------------------------------------------------------
 Rotational constants (GHZ):      1.9172176    0.8258574    0.7292662
```

Table VIII.S5. Cartesian coordinates for the δI$_a$ conformer of histidine. The geometry has been optimized *ab initio* at the MP2/6-311++G(d,p) level of theory.

```
                      Standard orientation:
---------------------------------------------------------------------
Center     Atomic     Atomic          Coordinates (Angstroms)
Number     Number     Type          X           Y           Z
---------------------------------------------------------------------
   1          6          0       1.537260    0.492987    0.642722
   2          6          0       1.654188   -0.576377   -0.427667
   3          8          0       1.767799   -0.365771   -1.614262
   4          8          0       1.640325   -1.810035    0.122095
   5          1          0       1.690784   -2.436373   -0.615584
   6          7          0       1.445695    1.802673   -0.010307
   7          1          0       2.066963    1.830325   -0.815527
   8          1          0       1.742924    2.528064    0.636076
   9          6          0       0.283029    0.249265    1.503183
  10          1          0       2.428117    0.388723    1.281544
  11          6          0      -0.940870    0.068805    0.666786
  12          6          0      -1.928640   -0.904832    0.647943
  13          7          0      -2.865173   -0.639599   -0.324266
  14          6          0      -2.450814    0.484390   -0.898686
  15          7          0      -1.305595    0.954831   -0.322597
  16          1          0      -2.002867   -1.775989    1.285332
  17          1          0      -2.938446    0.990928   -1.719909
  18          1          0      -0.703150    1.717364   -0.618006
  19          1          0       0.423954   -0.649086    2.110583
  20          1          0       0.177323    1.101732    2.187334
---------------------------------------------------------------------
Rotational constants (GHZ):     1.8052882    0.8468902    0.7848799
```
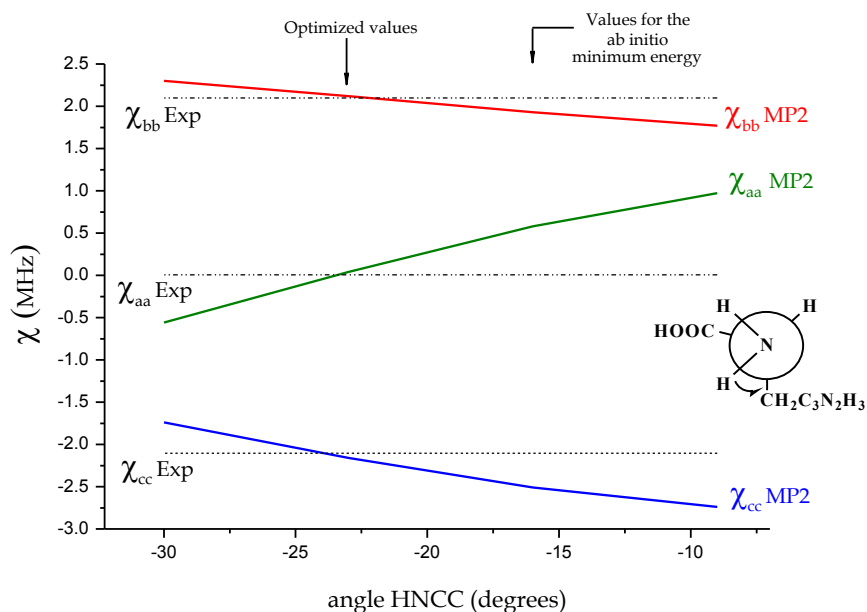
Table VIII.S6. Cartesian coordinates for the εII$_a$ conformer of histidine. The geometry has been optimized *ab initio* at the MP2/cc-pVTZ level of theory.

```
                        Standard orientation:
 ---------------------------------------------------------------------
 Center     Atomic      Atomic            Coordinates (Angstroms)
 Number     Number      Type         X           Y           Z
 ---------------------------------------------------------------------
    1          6           0      -2.577156    0.485901   -0.680604
    2          7           0      -2.562446   -0.849090   -0.429549
    3          6           0      -1.526907   -1.104712    0.429339
    4          6           0      -0.947071    0.121400    0.676972
    5          7           0      -1.608404    1.107169   -0.024799
    6          6           0       0.270079    0.423095    1.478836
    7          6           0       1.474901    0.648125    0.557326
    8          7           0       1.300553    1.742391   -0.403571
    9          6           0       1.765269   -0.653231   -0.202764
   10          8           0       1.802274   -1.735069    0.337582
   11          8           0       1.979063   -0.469125   -1.507406
   12          1           0       0.307058    1.931552   -0.523943
   13          1           0       2.360863    0.843298    1.163833
   14          1           0       0.494178   -0.409170    2.142985
   15          1           0       0.107595    1.318287    2.079242
   16          1           0      -1.276321   -2.094131    0.765687
   17          1           0      -3.299883    0.948209   -1.329785
   18          1           0      -3.198104   -1.529358   -0.809898
   19          1           0       1.855567    0.507367   -1.608884
   20          1           0       1.735757    2.590744   -0.069837
 ---------------------------------------------------------------------
 Rotational constants (GHZ):     1.8388175    0.8592330    0.7689911
```

SUPPLEMENTARY INFORMATION FOR CHAPTER IX

Table IX.S1. Measured frequencies and residuals (in MHz) for the rotational transitions of the observed rotamer of cytosine water complex.

J'	K'$_{-1}$	K'$_{+1}$	J"	K"$_{-1}$	K"$_{+1}$	ν_{obs}	$\nu_{obs} - \nu_{cal}$
2	1	2	1	1	1	3312.78	0.05
2	0	2	1	0	1	3505.17	-0.08
1	1	1	0	0	0	4502.95	0.23
3	1	3	2	1	2	4962.56	0.10
3	0	3	2	0	2	5230.92	0.06
3	1	2	2	1	1	5572.10	-0.24
2	1	2	1	0	1	6057.56	0.18
4	1	4	3	1	3	6605.10	0.37
4	0	4	3	0	3	6925.42	0.22
3	1	3	2	0	2	7514.18	-0.41

SUPPLEMENTARY INFORMATION FOR CHAPTER X

Table X.S1. Observed frequencies and residuals (in MHz) for the nuclear quadrupole coupling hyperfine components of the rotamer I of synephrine.

J′	K′$_{-1}$	K′$_{+1}$	J′′	K′′$_{-1}$	K′′$_{+1}$	F′	F′′	$n_{obs.}$	$n_{obs.}$-$n_{cal.}$
2	1	1	1	0	1	3	2	3872.6771	0.0017
						2	1	3872.9006	0.0010
5	1	5	4	1	4	6	5	3938.0789	0.0019
5	0	5	4	0	4	5	4	4012.2456	0.0006
						6	5	4012.2578	0.0031
						4	3	4012.2983	-0.0022
5	1	4	4	1	3	6	5	4097.0777	0.0035
						5	4	4097.1352	0.0023
3	1	3	2	0	2	3	2	4532.9559	-0.0010
						4	3	4533.7254	-0.0033
						4	3	4724.3066	0.0018
3	1	2	2	0	2	3	2	4724.7265	-0.0009
6	1	6	5	1	5	7	6	4724.7976	0.0036
						6	5	4724.8152	0.0008
6	0	6	5	0	5	6	5	4810.9581	0.0000
						7	6	4810.9776	0.0016
						5	4	4811.0057	-0.0007
6	1	5	5	1	4	7	6	4915.5281	-0.0006
						6	5	4915.5637	0.0014
						5	4	4915.5757	0.0041
4	1	4	3	0	3	4	3	5273.9107	-0.0004
						5	4	5274.6173	0.0001
						3	2	5274.8760	0.0010
7	1	7	6	1	6	8	7	5511.0331	-0.0019
						7	6	5511.0462	0.0014
7	0	7	6	0	6	7	6	5607.6705	-0.0007
						8	7	5607.6942	-0.0017
						6	5	5607.7175	-0.0023
7	1	6	6	1	5	8	7	5733.4217	-0.0032
						7	6	5733.4411	-0.0033
						6	5	5733.4540	-0.0033

Table X.S2. Observed frequencies and residuals (in MHz) for the nuclear quadrupole coupling hyperfine components of the rotamer II of synephrine.

J'	K'_{-1}	K'_{+1}	J''	K''_{-1}	K''_{+1}	F'	F''	$n_{obs.}$	$n_{obs.}-n_{cal.}$
5	1	5	4	1	4	6	5	3943.3160	0.0039
						5	4	3943.3565	0.0016
5	0	5	4	0	4	5	4	4012.8274	-0.0014
						6	5	4012.8358	0.0023
						4	3	4012.8795	0.0006
5	1	4	4	1	3	6	5	4091.6041	0.0011
						5	4	4091.6622	0.0007
3	1	3	2	0	2	3	2	4541.3981	-0.0016
						4	3	4542.0797	-0.0007
						2	1	4542.4835	-0.0011
3	1	2	2	0	2	4	3	4719.8427	0.0015
						3	2	4720.1695	0.0001
6	1	6	5	1	5	7	6	4731.1924	-0.0011
						5	4	4731.2014	0.0029
						6	5	4731.2181	0.0015
6	0	6	5	0	5	6	5	4812.1432	-0.0017
						7	6	4812.1599	0.0029
						5	4	4812.1848	-0.0025
6	1	5	5	1	4	7	6	4909.0942	0.0016
						6	5	4909.1252	-0.0017
						5	4	4909.1345	0.0022
4	1	4	3	0	3	4	3	5286.4873	0.0010
						5	4	5287.1000	-0.0008
						3	2	5287.3375	0.0017
7	1	7	6	1	6	8	7	5518.6570	-0.0017
						7	6	5518.6720	0.0011
7	0	7	6	0	6	7	6	5609.7145	-0.0026
						8	7	5609.7320	-0.0031
						6	5	5609.7555	-0.0027
7	1	6	6	1	5	8	7	5726.0982	-0.0012
						7	6	5726.1210	0.0011

Table X.S3. Observed frequencies and residuals (in MHz) for the nuclear quadrupole coupling hyperfine components of the rotamer III of synephrine.

J´	K´$_{-1}$	K´$_{+1}$	J´´	K´´$_{-1}$	K´´$_{+1}$	F´	F´´	$n_{obs.}$	$n_{obs.}$-$n_{cal.}$
5	1	5	4	1	4	4	3	3877.3231	0.0023
						6	5	3877.3550	0.0029
						5	4	3877.3854	0.0032
5	0	5	4	0	4	5	4	3921.1871	0.0037
						6	5	3921.1987	0.0006
						4	3	3921.2474	0.0029
3	1	3	2	0	2	3	2	4337.7117	0.0008
						4	3	4339.0497	-0.0014
						2	1	4339.6872	0.0004
6	1	6	5	1	5	6	5	4652.5098	0.0022
						5	4	4652.4796	0.0020
						7	6	4652.4937	-0.0014
6	0	6	5	0	5	6	5	4704.0660	-0.0019
						7	6	4704.0900	-0.0020
						5	4	4704.1229	-0.0014
6	1	5	5	1	4	7	6	4762.3099	0.0030
						6	5	4762.3462	0.0003
						5	4	4762.3712	0.0017
4	1	3	3	0	3	3	2	5269.6916	-0.0011
						5	4	5269.9016	0.0021
						4	3	5271.0003	0.0007
7	0	7	6	0	6	7	6	5486.2158	-0.0045
						8	7	5486.2468	-0.0056
7	1	6	6	1	5	8	7	5555.5518	-0.0021
						7	6	5555.5759	-0.0010
5	1	5	4	0	4	5	4	5825.8375	-0.0006
						6	5	5827.0897	-0.0006
						4	3	5827.3894	-0.0001

Table X.S4. Observed frequencies and residuals (in MHz) for the nuclear quadrupole coupling hyperfine components of the rotamer IV of synephrine.

J'	K'_{-1}	K'_{+1}	J''	K''_{-1}	K''_{+1}	F'	F''	$n_{obs.}$	$n_{obs.}-n_{cal.}$
5	1	5	4	1	4	4	3	3888.2896	0.0041
						6	5	3888.3195	0.0034
						5	4	3888.3526	0.0040
5	0	5	4	0	4	5	4	3924.0673	0.0012
						6	5	3924.0765	0.0015
						4	3	3924.1233	0.0016
5	1	4	4	1	3	6	5	3962.3287	0.0037
						5	4	3962.3967	0.0027
6	0	6	5	0	5	6	5	4707.9960	0.0032
						7	6	4708.0094	-0.0006
						5	4	4708.0386	-0.0037
6	1	5	5	1	4	7	6	4754.5836	-0.0010
						5	4	4754.6486	0.0013
						6	5	4754.6271	0.0011
7	0	7	6	0	6	7	6	5491.4336	-0.0046
						8	7	5491.4565	-0.0061
						6	5	5491.4802	-0.0057
3	1	3	2	0	2	3	2	4347.2253	-0.0003
						4	3	4348.5639	0.0009
						2	1	4349.2007	-0.0004

Table X.S5. Observed frequencies and residuals (in MHz) for the nuclear quadrupole coupling hyperfine components of the rotamer V of synephrine.

J'	K'_{-1}	K'_{+1}	J''	K''_{-1}	K''_{+1}	F'	F''	$n_{obs.}$	$n_{obs.}-n_{cal.}$
3	1	3	2	0	2	3	2	4058.2337	-0.00002
						4	3	4058.4760	-0.00199
6	0	6	5	1	5	5	4	4636.6293	0.00149
						7	6	4636.6433	-0.00157
						6	5	4636.8178	0.00001
4	1	4	3	0	3	4	3	4959.9368	-0.00009
						5	4	4960.1392	0.00194
						3	2	4960.2353	-0.00153
5	1	5	4	0	4	5	4	5849.5637	0.00025
						6	5	5849.7417	0.00249
						4	3	5849.8048	0.00182
6	1	6	5	0	5	6	5	6728.3590	-0.00024
						7	6	6728.5143	-0.00365
						5	4	6728.5640	0.00095

Table X.S6. Observed frequencies and residuals (in MHz) for the nuclear quadrupole coupling hyperfine components of the rotamer VI of synephrine.

J'	K'_{-1}	K'_{+1}	J''	K''_{-1}	K''_{+1}	F'	F''	$n_{obs.}$	$n_{obs.}-n_{cal.}$
3	1	3	2	0	2	3	2	4062.8027	-0.0025
						4	3	4062.9565	-0.0008
						2	1	4063.1170	0.0012
3	1	2	2	0	2	3	2	4217.3152	0.0014
						4	3	4217.3891	0.0006
						2	1	4217.5211	0.0013
6	0	6	5	1	5	7	6	4635.0423	0.0005
						6	5	4635.1351	-0.0005
4	1	4	3	0	3	4	3	4968.4379	-0.0005
						5	4	4968.5504	0.0043
						3	2	4968.6179	-0.0050
4	1	3	3	0	3	4	3	5225.8944	0.0001
						5	4	5225.9200	-0.0027
						3	2	5225.9799	0.0008
5	1	5	4	0	4	5	4	5862.6219	0.0012
						6	5	5862.7083	0.0032
						4	3	5862.7481	-0.0030
6	1	6	5	0	5	6	5	6746.4581	-0.0001
						7	6	6746.5289	0.0007
						5	4	6746.5587	-0.0004